

A Theory of Unified Gravitation

By Gil Raviv

Abstract:

The theory presented here, entitled the theory of unified gravitation, holds that the nuclear strong interaction and gravitation are one and the same force. Detailed and relatively simple mathematics are shown to lead to an explicit strong/gravitational force equation that relies on only three independent parameters, identical to the parameters used in Newton's gravitational theory. The theory is applied on various distance scales to explain a broad range of phenomena, and is shown to provide an unparalleled level of agreement with observations, without requiring an assumption of dark matter, dark energy or inflation. Most notable is its ability to reproduce the morphologies of various types of galaxies and nebulae, as well as the complex structure of Saturn's main body of rings. Additional large-scale phenomena explained by unified gravitation include

- The constant rotation curve observed in spiral galaxies
- The nature of density waves in spiral galaxies
- The mechanism underlying star formation and fragmentation
- The parameters that determine galactic (or nebular) morphology and classification
- The clustering of nearby galaxies, repulsion between distant galaxies, and the creation of galactic voids
- The accelerated expansion of the universe
- The cause of the observed redshift periodicity
- The mechanism responsible for the creation of galactic and stellar wind
- The sudden expansion of gas and matter observed in novae and supernovae
- The formation of planetary ring systems and the composition of planets
- The mechanism responsible for the creation of the planetary and galactic magnetic fields
- A possible mechanism for the creation of the solar corona
- The process of ionization that produces the vast amount of plasma in the universe.

On nuclear scale, the theory is demonstrated to account for the observed weak fall-off of the deep inelastic scattering cross section, and to provide a scaling behavior similar to the observed Bjorken scaling.

Copyright © 2010 by Gil Raviv

All rights reserved

The theory was initially developed, presented and copyrighted in 2007 (copyright registration number/date TXu001599680/2007-11-07 under the title: A Theory of Unified Gravitation (UG): The Unification of the Strong Interaction and the Gravitational Force) and later copy righted again in 2010.

For information about this article write to Gil Raviv at

UGRaviv@gmail.com

Executive Editor: Ayelette Raviv

Edited by Ayelette Raviv
Nataly Raviv

Contents

Introduction	1
Not all is well with gravitation; Or: Why look for an alternative theory?	15
Chapter I: The Theory of Unified Gravitation- The Unification of the Strong Interaction and the Gravitational Force	20
I-1 The Logic Leading to the Theory of Unified Gravitation	21
Chapter II: The UG Characteristics at Non-Relativistic Velocities	31
II-1 The UG Gravitational Zones at Non-Relativistic Velocities	38
II-2 Superheavy Particles Embedded in Ordinary Matter	41
Chapter III: The UG Equations of Astronomical Objects	50
III-1 The UG Morphology Model- The Non-Relativistic Approach	50
III-2 The UG Morphology Model- The Relativistic Approach	58
III-3 The Creation and Motion of SHP groups	64
III-4 The Issue of the Tail Wagging the Dog	67
Chapter IV: Applying the UG Theory to Model Galaxy Morphology	69
IV-1 Two Dimensional Potential Energy Mapping and Derivation of Morphology	69
IV-1-1 Low Velocity SHP Group Rotation	71
IV-1-2 Star formation via Binary SHP Groups	74
IV-1-3 Butterfly Formations in Planetary Nebulae	79
IV-1-4 Hourglass Structures	80
IV-1-5 Ring Morphologies in Galaxies and Nebulae	84
IV-2 The Influence of SHP Group Rotation on Morphology and the Creation of Spiral Galaxies	84
IV-2-1 The Creation of Spiral Structures via Two Non-Relativistic Rotating SHP Groups	84
IV-2-2 Relativistic SHP groups and the Creation of the Grand Design Spiral Morphology	91
IV-2-3 Flocculent Spiral Structures	99
IV-2-4 Lenticular Galaxies	100
IV-3 The Red Square and the Red Rectangle	100
IV-4 Companion Galaxies	102
IV-5 Multiple SHP Groups	103
Chapter V: Applying the Theory of Unified Gravitation to Saturn's Ring System	104
V-1 Summary of Current Theories	104
V-2 The D, C, B, A, and F Rings and the Cassini Division of Saturn	106
V-3 The Phenomenon of Spokes	123
V-4 The Non-Circular Shape of the B Ring	126
V-5 The Dynamics of Ring Variability Over Time and Azimuth	126
V-6 Estimating the Overall Mass and Abundance of Superheavy Particles of Mass M_1	127
V-7 Summary	131
Chapter VI: The Potential Energy Spiral and the Constant Velocity Curve	132
VI-1 The Formation of Galactic Density Waves	133
VI-2 The Outflow of Gas and Matter From Galaxies	135

VI-3	The Constant Galaxy Rotation Curve	137
VI-4	The Influence of SHP Group Rotation on Star Formation in Galaxies	148
Chapter VII: The Effect of UG Theory on Cosmology		156
VII-1	The General Theory of Relativity and Unified Gravitation	156
VII-2	Unified Gravitation and Black Holes	159
VII-3	The Effect of Unified Gravitation on Cosmology- The Big Bang and the Expansion of the Universe	159
VII-4	Galactic Lock Out	160
VII-5	The Construction of a Barrier, the Effect of a Barrier on the Fragmentation of a Collapsing Cloud and the Creation of a Series of Distinct Galactic Entities	163
VII-6	UG Repulsion and the Generation of Stellar Novae and Supernovae	165
VII-7	The Fragmentation of a Galactic Entity and the Creation of Galactic Substructures	166
VII-8	Gravitational Repulsion Between Galaxies	168
VII-9	The Expansion of the Universe	170
VII-10	Additional Comments About Unified Gravitation and the Big Bang Model	171
VII-11	The Galactic Halo and the Transition From a Spiral to an Elliptical Galaxy	173
VII-12	Elliptical Morphology and Properties of Elliptical Galaxies	174
VII-13	Boxiness vs. Diskiness of Elliptical Galaxies	175
Chapter VIII: Gravitational Ionization		176
Chapter IX: The General Structure and Composition of Planets and the Creation of their Magnetic Fields		181
IX-1	Planetary Ring and Satellite Systems of Terrestrial and Gas Planets	181
IX-2	Unified Gravitation and the Surface Structure of Gas and Terrestrial Planets	183
IX-3	The Composition of Earth's Core	184
IX-4	The Creation of Planetary, Stellar and Galactic Magnetic Fields via Unified Gravitation	184
IX-5	The Solar Corona	196
Chapter X: The Question of Galactic Redshift Periodicity		188
X-1	Galactic Redshift Periodicity	188
X-2	Unified Gravitation and the Redshifts of Quasars	196
Chapter XI: The UG Theory and Deep Inelastic Scattering (DIS)		198
XI-1-1	The Effect of the Velocity of Colliding Particles on Their UG Interaction	200
XI-1-2	The Effect of Quantum Mechanics on DIS	205
XI-2-1	The Effect of Special Relativity on the Range of the UG Interaction	208
XI-2-2	DIS and the Relativistic Effect of the Folding and Unfolding of the Particles' Zonal Structure	209
XI-3	The Weak Fall-off of the DIS Cross Section	215
XI-4	Unified Gravitation and the Phenomenon of Bjorken Scaling	225
Appendix A: The UG Scaling Theorems		239
A-1	The First UG Scaling Theorem	239
A-2	The Second UG Scaling Theorem	241
References		243
Index		247

Introduction

At any given time, our knowledge of the natural world can be summarized by means of physical laws. These laws are used to construct mathematical models to describe essential aspects of an existing physical system. As we broaden our domain of observation, we must constantly verify whether these models, and their embedded laws, continue to be valid. Ideally, an existing model should be repeatedly tested and critiqued via an iterative process, in which new experiments are conducted and their results compared with the predictions of the mathematical model. A model that remains consistent with all measurements and observations will gain in status. In cases where its predictions deviate from the results of new experiments, a model must be adjusted to fit both the prior and the new sets of results. As science progresses and the number of iterations grows, an existing model may become increasingly difficult to adjust. Eventually a paradigm shift might offer radical simplification, and a new model may emerge to replace the old one.

This process should be governed by the principle of Occam's Razor, which states that the explanation of any phenomenon should make as few assumptions as possible. This principle can be expressed as, 'If all other things being equal, the simplest solution is the best.' In accordance with Occam's Razor, most successful models are initially developed with a relatively simple structure of few variables governed by few equations. However, in most cases there is a clear trade-off between the simplicity of a model and its accuracy. As new measurements deviate from the model's predictions by an amount that cannot be discounted simply as measurement noise or measurement error, the model must be adjusted in order to fit reality. Inevitably, this iterative process increases the model's complexity. Therefore, it is important not only to verify (after each iteration) that the modified model is consistent with the entire database of new and old experiments, but also to substantiate that the model is still consistent with Occam's Razor, namely that the modified model is still the simplest model that explains the behavior of the given physical system. This second criterion, however, is often overlooked or lost in the process.

One of the most fundamental and powerful models used in physics combines Newton's classical mechanics, which describes the relationship between force and the motion of bodies, and Newton's law of universal gravitation. Newton based his theory on three simple postulates and two simple equations that have since been demonstrated to provide an efficient and astonishingly accurate model of most ordinary mechanical situations. Over 200 years of scientific advances transpired before measurements started to suggest the need for a departure from the Newtonian model.

Newton's law of universal gravitation and his laws of motion were based on prior work done by Galileo and Kepler. Johannes Kepler, a German mathematician, studied observations of planetary dynamics tabulated by the Danish astronomer Tycho Brahe and developed an ad hoc mathematical model to describe the empirical observations via three laws of planetary motion.¹

¹ Kepler's first law: the orbit of a planet around a star is an ellipse, with the star located at one of the foci.
Kepler's second law: identified that the line joining a planet and its star sweeps out equal areas during equal intervals of time.

Kepler's laws provided a clear blueprint with which an astronomer of the time could calculate and predict the location and the periodicity of planets in the Solar System. While his achievement was incredibly important, Kepler's mathematical laws were empirical in nature, and were not derived from any basic underlying principles. The rationale and explanation of the theoretical principles driving these rules emerged over half a century later with Newton's publication of his *Philosophiae Naturalis Principia Mathematica*.

As Newton's mathematical model was based on a more profound understanding of fundamental principles, the shortcomings of the Keplerian model became apparent. Kepler's laws were found to be inaccurate when the mass of an orbiting object is not negligible in comparison to the mass of the object being orbited. Furthermore, Kepler's laws did not deal with situations in which the smaller body is moving faster than the escape velocity, as in the case of comets. Under such circumstances, the small body trajectory becomes an open parabolic or hyperbolic orbit, rather than a closed elliptical orbit. In addition, Kepler's laws assumed a two-body system and could not be applied accurately to systems containing three or more bodies.² Newton's insight therefore provided a simpler and more accurate way of calculating planetary trajectories, which not only resolved the limitations of Keplerian dynamics, but also substantially increased the scope of applications covered by the model.

The basic framework for Newton's theory was also inspired by the work of Italian astronomer Galileo Galilei, introduced in 1638. Before Galileo, ideas about the motion of bodies were based on Aristotle's assertion that the natural state of a body was to be at rest and that a resting body will move only if driven by a force or impulse. Aristotle further intuited that a heavy body should fall faster than a lighter one, as the heavy body should by nature experience greater pull toward the earth. Galileo put these notions to a test. By rolling balls of different weights down a smooth slope, Galileo created an effect similar to bodies falling vertically, and found that contrary to Aristotle's predictions, the speed of all bodies increased at the same rate regardless of their mass (as long as air resistance and friction can be neglected). In other words, the gravitational acceleration of an object is independent of its mass. This idea led Einstein, almost three centuries later, to his equivalence principle and to the development of the general theory of relativity. Galileo's experiment further demonstrated that the effect of a force is to change the speed of a body, rather than simply to set it in motion. It followed that a body moving on a level surface will continue to travel in the same direction at constant speed unless disturbed, a principle that became Newton's first law. Galileo also formed the principle of Galilean relativity, stating that dynamical laws are precisely the same when referred to in any non-accelerating frame of reference, where reference frames travel at constant velocity relative to each other. Hence, there is no experiment that can differentiate between a system at rest and a system in uniform motion, and there is no absolute motion or absolute rest state. This principle

Kepler's third law: the square of the sidereal period of an orbiting planet is directly proportional to the cube of the orbit's semi-major axis, or $T^2 \propto R^3$.

² Kepler's laws are inadequate, for example, for calculating the orbit of the Moon, as the calculation requires taking into account three heavenly bodies, the Sun, the Earth and the Moon.

initially provided the basic framework for Newton's theory and later on inspired Einstein's special theory of relativity.

Newton's original formulation of his laws of motion stated the principle of Galilean relativity as one of five or six fundamental laws. Later on, however, Newton adopted the notion of absolute space and simplified his model to rely on only three independent laws:

Newton's First Law: A particle will stay at rest or continue to move at a constant velocity following a straight line unless acted upon by an external unbalanced force.

Newton's Second Law: Observed from an inertial frame (a frame at rest or moving at constant velocity) the net force on a particle is equal to the particle mass times its acceleration, or $\vec{F} = m\vec{a}$.

Newton's Third Law: Whenever a particle A exerts force on a second particle B, B simultaneously exerts a force of same magnitude in the opposite direction on particle A.

Newton then formulated a law to describe the gravitational force, stating that two point objects of mass m and M attract each other along the line that connects them via a force that is proportional to the product of their masses divided by the square of the distance r that separates them. Expressed mathematically,

Equation 1-1

$$\vec{F} = \frac{GmM}{r^2} \hat{r}$$

where \vec{F} is the gravitational vector force applied on either point particle, G is a gravitational constant, and \hat{r} is the unit vector in the direction toward the other point object. Newton's gravitational force thus describes a central force, which can also be stated as a conserving force that is derived from a potential energy function V via

Equation 1-2

$$\vec{F} = -\vec{\nabla}V = \frac{\partial V}{\partial r} \hat{r}, \text{ where } V = -\frac{GmM}{r}$$

Remarkably, just a few simple rules result in an extraordinarily powerful and versatile theory that predicts the behaviors of macroscopic objects with great accuracy, as long as their speeds are non-relativistic. For his theory to work Newton had to assume, against his own judgment and instincts, that gravity is instantaneous, or in other words that the speed of gravity is infinite. Newton was also quite uncomfortable with the notion implied by his equations that gravity is an "action at a distance," without direct contact between the bodies involved.

While no mathematical model can exactly reproduce an actual physical system, the Newtonian theory remained virtually unchallenged for over 200 years. That is, until Albert Einstein introduced his revolutionary special theory of relativity, which provided a more accurate model in the case of object velocities that approach the speed of light, and his new gravitational

theory, the general theory of relativity, which resolved a number of shortcomings within Newton's theory of gravitation. Special relativity, and to a larger extent general relativity, significantly increased the mathematical complexity of both mechanical dynamics and gravitation, resulting in a set of non-linear equations that often require resolution via computer-based simulations. However, both theories are complete and self-consistent theories based on strikingly simple postulates. Special relativity relies on the principle of relativity and also postulates that the speed of light is the same in all inertial frames. General relativity relies on the principles of special relativity and on the equivalence principle.³ Both theories converge to the Newtonian gravitational model in the limiting case of slow velocities (in the case of special relativity) or weak gravitational fields (in the case of general relativity), where their equations approach Newton's equations. Due to the minimalistic nature of their assumptions, special relativity and general relativity can be considered to comply with the spirit of Occam's Razor, regardless of their substantial computational complexities. However, the simplicity of Newton's model, and the fact that the majority of known systems are non-relativistic, make it the preferred choice for most applications. Therefore, in spite of the somewhat reduced accuracy of the Newtonian model relative to general relativity or special relativity, it is still the most frequently used model in earthbound engineering applications, as well as in most areas of space exploration.

As our domain of observation has broadened considerably in the recent century, studies have begun to show significant inconsistencies between observations and the predictions of both, Newton's theory and general relativity. Some of the new discoveries were attributed to non-gravitational phenomena, as in the case of the strong interaction between nucleons, which was classified as an entirely new force unrelated to gravitation and became part of the standard model. Other inconsistencies clearly related to gravitation were reconciled by modification of the gravitational model of the Universe in an iterative process, resulting in a significant increase in the complexity of the overall gravitational model. Ideally, every iteration step should have been tested to uphold the following criteria:

1. Can the modified model explain, quantify and be consistent with all prior known phenomena, as well as the new discoveries?
2. Is the modified model still the simplest one available? Or alternatively, can it be replaced by an equally successful, yet substantially simpler model?

The risk in the failure to uphold the second criterion is that even a flawed model that agrees with all prior known phenomena can be modified to agree with new contradicting data by simply increasing the number of independent variables used, thus creating a more complex and still flawed model. The best way to eliminate flawed models, but by no account the easiest route to take, is by searching and testing for simpler alternative models.

The current astronomical model of the universe, which describes the motion of a system of gravitating bodies, is based on the general theory of relativity (and therefore indirectly on the

³ The equivalence principle will be discussed later in this chapter.

less complete Newtonian theory). The amount of visible matter observed in galaxies and galactic clusters is insufficient to explain the motion of stars in galaxies, or the motion of galaxies within clusters. We can therefore conclude that either the current understanding of gravitation is incorrect, or additional non-visible matter must exist. At present, most astrophysicists prefer the latter explanation, and consequently a new variable of dark matter has been added to the current paradigm. The addition of the dark matter concept made possible the formation of a plausible model that is consistent with observations without shaking the theoretical foundation of the established gravitational model. Since undetected, dark matter is believed to consist of non-baryonic matter and to interact through the gravitational force. To fit observations, dark matter must account for about 90% of the average galaxy mass, and furthermore must dominate the mass of the galaxy up to several hundred kiloparsecs from its center. However, no trace of dark matter has ever been observed directly and no effects of such matter can be measured within our own Solar System. The complexity of the dark matter model, and the lack of direct observational evidence, should raise the question of whether modification of the cosmological model with the inclusion of dark matter still provides the simplest possible model to explain the observed properties of galaxies as well as stellar and galactic motions, or whether a simpler model exists.

Additional variables have been incorporated into the current accepted cosmological model in a series of iterations geared to resolve paradoxes related mainly to the Big Bang theory. The added variables include the assumption of the existence of dark energy, which together with dark matter brings the total amount of non-visible and undetected matter in the universe to as large as 96%, as well as a theory of inflation, which indicates that at some initial period of time, space expanded at a rate much higher than the speed of light.

Newton never published the reasoning that guided him to his equation of universal gravitation, and we can only speculate the process by which he arrived at this final form, however, history provides us with a clear sense of the information available to Newton at the time. On no account could he have known about the phenomenon of constant rotation curves in spiral galaxies, where stars travel around the galactic center with roughly constant rotational speed, rather than at a speed decreasing inversely to the square root of the star's radius of orbit. While Galileo had observed a system of rings around Saturn prior to Newton's work, its characteristics were not yet understood. The difficulties of fully explaining planetary rings within the Newtonian theory have since proved to be formidable, as attested by the fact that almost 400 years later we are still very far from understanding the root of their existence. Newton did not have access to deep inelastic scattering experiments that have since brought to light the behavior of particles on a subatomic scale and could not have known about the existence of the short-range strong forces between nucleons within the nucleus. Such forces were later observed to be strong enough to overcome the Coulomb rejection force between protons, and therefore must be greater than 10^{36} times the strength of the gravitational force predicted by Newton's formula, at nuclear distances of the order of $0.65 * 10^{-15} m$. Although the strong force is considered as a separate force, entirely distinct from gravitation, it appears to share some of gravitation's

essential defining qualities. Similar to the gravitational force, for instance, the subatomic force appears to be (at least approximately) a central force between a pair of point-like particles with strong dependency on the respective masses of the interacting particles.⁴ An interesting yet speculative question is whether Newton would have attempted to integrate the additional observed phenomena into his theory of gravitation had the above information been available to him? We can only suppose Newton's course of action, but the question that should be addressed and may be contemplated is whether such phenomena, from long-range force interactions to force interactions on a nuclear level, can be explained by a single equation that provides a simpler and more accurate model than the current paradigm.

In fact, there is a whole family of equations that, given the limited observation technology available to Newton and for about 230 years thereafter, would have provided virtually indistinguishable results and predictions from those developed by Newton at the measured distance ranges available at the time. However, on extremely small scales, and in some cases on galactic or cosmic scale distances, the predictions formulated by these equations may differ from each other, and from the predictions of the Newtonian equation. These distinctions could not have been addressed during Newton's time and would have been irrelevant to his reasoning, since the alternative equations are slightly more complex and would have been discounted in accordance with Occam's Razor.

If a simpler model does exist, it is likely to be based on a modified gravitational equation. To explore this notion, let us first analyze some simple alternative equations for the gravitational potential energy, starting with the exponential energy equation,

Equation 1-3

$$V = -\frac{GmM}{a}(e^{a/r} - 1) \rightarrow -\frac{GmM}{r} \text{ as } r \rightarrow \infty$$

Note that a is a constant with a dimension of distance. For reasons that will become apparent in the next chapter, a good choice for a could be in the vicinity of $a = 5.7 * 10^{-14} \text{ m}$. This will result in the following force equation:

Equation 1-4

$$\vec{F} = -\vec{\nabla}V = \frac{\partial V}{\partial r} \hat{r} = \frac{GmM}{r^2} e^{a/r} \hat{r} \rightarrow \frac{GmM}{r^2} \hat{r} \text{ as } r \rightarrow \infty$$

The choice made in equation 1-3 may seem odd and non-intuitive. However, equation 1-3 is practically indistinguishable from Newton's equation of potential energy (1-2) at the distance range of $r \gg a$. Similarly, at these distances, the results of equation 1-4 cannot be distinguished from those of Newton's equation of force (1-1). Although the force in equation 1-4 is exponential, rather than proportional to $\frac{1}{r^2}$, the difference between the force calculated via equation 1-4 and the Newtonian force calculated via equation 1-1 merely amounts to about 0.1% at a distance of $r = 5.3 * 10^{-11} \text{ m}$, which is the Bohr radius, or roughly the radius of the

⁴ To be further discussed in Chapter II.

hydrogen atom. At a distance of $10^{-9} m$ the difference reduces to about 0.0057%, and at distances above one micrometer ($10^{-6} m$), there is virtually no difference between the two calculated forces. In other words, if Newton had used the slightly more complex equation 1-4 (or 1-3) rather than equation 1-1 (or 1-2), he would have obtained the exact same results. Nevertheless, had the thought of using an exponential function occurred to Newton, the inability at the time to experimentally differentiate between the two sets of equations would have most likely steered him toward the simpler equation 1-1, in accordance with Occam's Razor. While equations 1-3 and 1-4 are also quite simple, they contain an additional universal constant a and require the calculation of an exponential function, which was not an easy task in the pre-calculator era of the 17th century.

Today data is available on interactions at distances at which the predictions of Newton's equations of force and potential energy differ from those of equations 1-4 and 1-3, and the results of the two sets of equations are no longer identical within all measurement ranges. Had Newton selected equation 1-3 (or 1-4) as his law of gravitation, then three centuries later the discovery of a strong nuclear force may have possibly been perceived as an additional triumph for the theory of gravitation. After all, the newly discovered strong force was found to be approximately a central force⁵ between a pair of particles that is mainly dependent on the particle masses, and to demonstrate explosive growth at the distances $r < 10^{-15} m$, just as predicted by equations 1-3 and 1-4 due to the explosive growth of the exponential term $e^{a/r}$ at distances $r \lesssim a$.

The finding that a single mathematical equation may display behaviors that resemble at least some key characteristics of the strong force at extremely short distance ranges, while converging with Newton's gravitational equation at larger distances, does not necessarily imply that the two forces are one and the same. However, such a theory does not appear to have ever been considered. Instead, the strong force became a part of an extensive new theory called the standard model.⁶ Based on Newton's law of gravitation, the standard model was developed with the underlying assumption that the gravitational force is negligible at atomic and sub-atomic distances.

Exponential equations such as 1-3 or 1-4 are not the only possible alternatives to Newton's gravitational equations 1-1 and 1-2. Of interest are also equations of the type

Equation 1-5

$$V_2 = -\frac{GmM}{B(m,M)} \sin\left(\frac{B(m,M)}{r}\right) \rightarrow -\frac{GmM}{r} \text{ as } \frac{r}{B(m,M)} \rightarrow \infty$$

and

⁵ As matter of fact, the strong force was shown to deviate slightly from being a central force. This will be explained to be a relativistic effect, similar to the one that makes central Coulomb force appear as a non-central magnetic force when viewed from an inertial frame moving at high velocity relative to the charges.

⁶ Interestingly, one of the declared goals of the standard model is to eventually unify the four fundamental forces of nature; the electromagnetic force, the strong interaction, the weak interaction and the gravitational force.

Equation 1-6

$$\vec{F}_2 = \vec{\nabla}V_2 = \frac{GmM}{r^2} \cos\left(\frac{B(m,M)}{r}\right) \hat{r} \rightarrow \frac{GmM}{r^2} \hat{r} \text{ as } \frac{r}{B(m,M)} \rightarrow \infty$$

where $B(m, M)$ is either a constant or a function of the particle masses. Equations 1-5 and 1-6 provide a perfect Newtonian attractive force at distances $r \gg B(m, M)$, where they become virtually indistinguishable from the Newtonian equations. At shorter distances of $r \lesssim B(m, M)$, the potential energy V_2 begins to oscillate between a series of constant maxima and minima ($\frac{GmM}{B(m,M)}$ and $-\frac{GmM}{B(m,M)}$ respectively), at which point the force can also become repulsive. The cyclical nature of these equations may be functional in addressing the cause of the ring and spiral structures demonstrated in galaxies and planets, as well as for the shell structure and resonances of the atom's nucleus. However, in this form, these equations are unlikely to be consistent with the strong force, since it is not possible to find a function $B(m, M)$ that can simultaneously provide the high amplitude required at short distance ranges and the abrupt and explosive growth of the force at the distance range of $r \lesssim 10^{-15} m$.

As it turns out, neither equation 1-3 nor equation 1-5 can reproduce and explain the entire range of observational data. However, merging these two concepts will be shown to provide a simpler and more accurate theory than the current paradigm, with the ability to explain a large number of yet unexplained phenomena.

The hypothesis presented here, entitled the theory of unified gravitation (UG), holds that the nuclear strong interaction and gravitation are actually one and the same force, viewed at different distance scales. This force is predominantly a central force between a pair of fundamental particles,⁷ and can be derived from a central potential given by

Equation 1-7

$$V_g = -\frac{GmM}{a} \left(e^{a/r} \cos\left(\frac{bmM}{r}\right) - 1 \right)$$

The equation uses the gravitational constant G , as well as two additional universal constants, a and b . Variables M and m represent the respective masses of two particles, and r is the distance between the pair of particles.

When applied to objects consisting exclusively of ordinary particles at distances significantly larger than 10 micrometers, the UG force equations developed in the first two chapters will be shown to yield results indistinguishable from those derived by Newtonian calculations within the experimental level of reliability.⁸ However, when applied to much heavier particles, the results obtained by the UG and Newtonian equations may diverge at much larger distance ranges, and the UG potential and its derived force are able to elucidate many thus far unexplained observations in the cosmic, galactic, planetary and nuclear realms. The ability of

⁷ Fundamental particles include any baryon, meson or lepton, while ordinary matter refers to any matter constructed exclusively from protons, neutrons and/or electrons.

⁸ The experimental margin of error is derived from the published variability of the gravitational constant G .

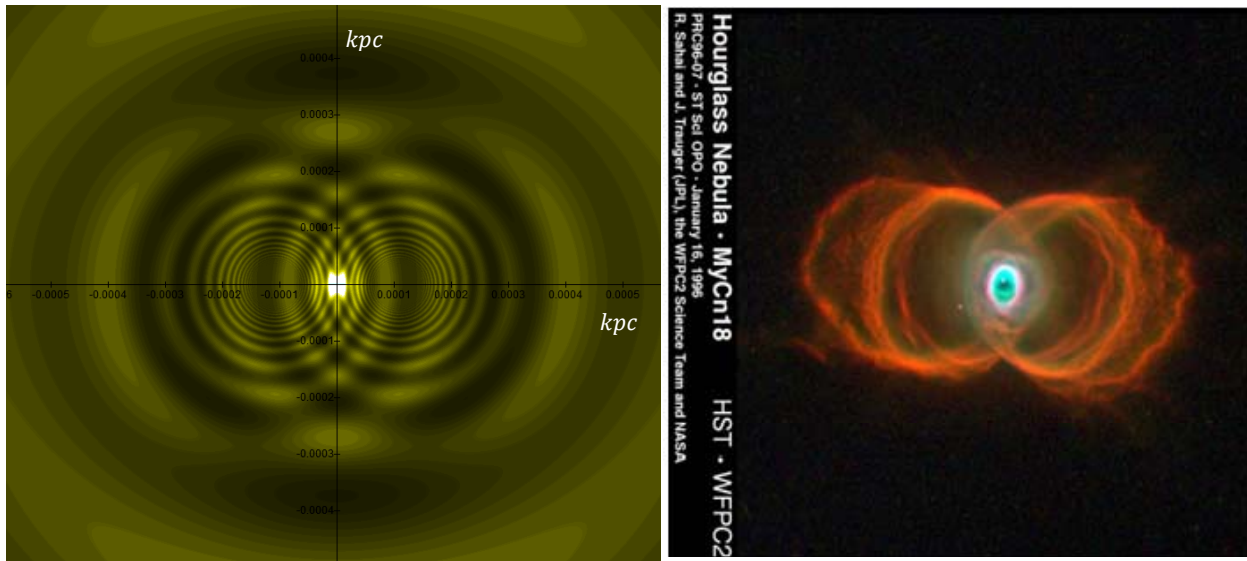
larger particles to form is demonstrated by high-energy collisions between electrons and positrons, which have been shown to produce particles that are more than 350,000 times their mass. Therefore, a secondary, but essential assumption of the UG theory holds that the high pressure and temperature conditions at the cores of large satellites, planets, stars, and galaxies provide the energy and means necessary to produce superheavy particles (SHPs) and to prevent their decay.

The present book is intended to introduce the theory of Unified Gravitation (UG). It would be unreasonable to expect that the capability of any new theory to provide better agreement in one particular area is sufficient to challenge a well-established fundamental theory that for centuries provided a clear picture of the known universe. Therefore, the UG theory must be applied successfully to the analysis of a wide range of phenomena in multiple areas of physics. The purpose of this book, therefore, is to demonstrate sufficient evidence of the viability and the advantages of unified gravitation, in order to challenge and motivate the physics community toward further testing.

The first three chapters are dedicated to developing the UG postulates and gravitational equations. The theory will subsequently be applied on solar, galactic and cosmological scales to explain a broad selection of observed phenomena. In the fourth and fifth chapters, a simple UG-based model will be demonstrated to provide for a number of the observed morphologies of astronomical systems. In Chapter IV, a simple model will be employed to reproduce a variety of complex morphologies observed in planetary nebulae and galaxies, from bipolar structures in figure 4-4 to ring structures in figure 4-5, to simple spiral structures in figure 4-8 to flocculent spirals in figure 4-9.⁹

Figure 4-4d

Figure 4-4e



Figures 4-4d and 4-4e: A comparison between a bipolar structure calculated by the UG equations (figure 4-4d) and MyCn 18, the hourglass nebula (figure 4-4e). Image credit for figure 4-4e: R. Sahai and J. Trauger, Photo AURA/STScI/NASA/JPL (NASA photo # STScI-PRC96-07) <http://apod.nasa.gov/apod/ap020615.html>.

⁹ Note that the figures are numbered according to their numbering in the chapters in which they are presented.

Figure 4-5a

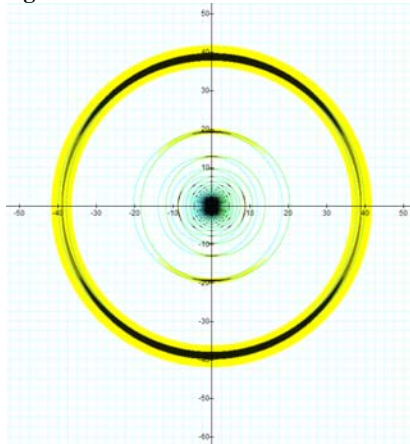


Figure 4-5b

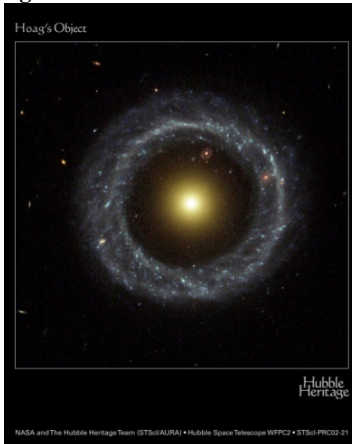


Figure 4-5c



Figure 4-5a: A UG calculated image of a ring morphology (on the left), compared with Hoag's object and the planetary nebula Abell 39.

Figure 4-5b: Hoag's Object, image credit: NASA and the Hubble Heritage Team (STScI/AURA) Acknowledgment: R. Lucas(STScI/AURA) <http://www.nasaimages.org/luna/servlet/detail/NVA2~4~4~4753~105279:Hoag-s-Object--A-Strange-Ring-Galaxy>.

Figure 4-5c: The Planetary Nebula Abell 39, WIYN Observatory's 3.5-m (138-inch) telescope at Kitt Peak National Observatory, Tucson, AZ. Image credit: "NOAO/AURA/NSF."

Figure 4-8e

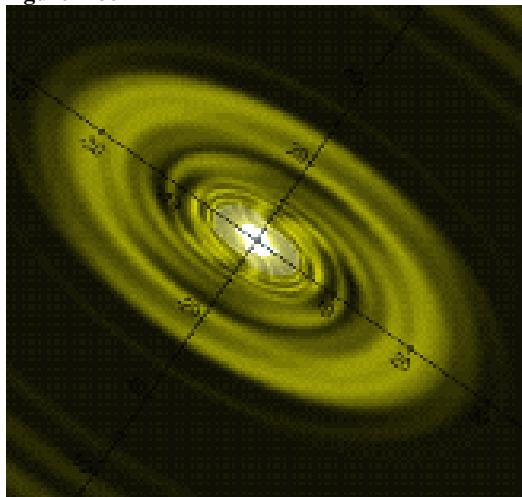


Figure 4-8f



Figure 4-8e: A modeled galaxy compared with the observed spiral galaxy M81 (figure 4-8f).

Figure 4-8f: M81 image credit: NASA's Spitzer and Hubble space telescopes and NASA's Galaxy Evolution (NASA/JPL-Caltech/ESA /Harvard-Smithsonian CfA), http://www.nasa.gov/mission_pages/spitzer/multimedia/spitzer-20070604.html.

Figure 4-8i: NGC 4622 observed



Figure 4-8j: Calculated

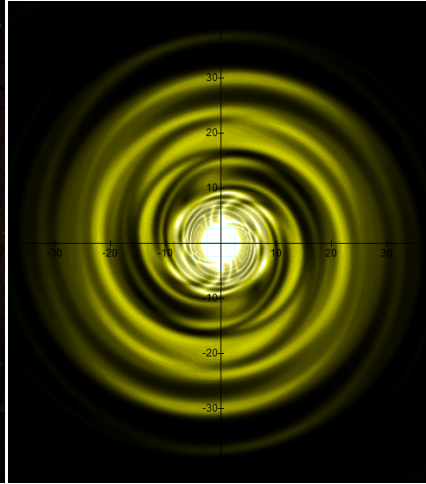


Figure 4-8i: NGC 4622, image credit: G. Byrd, R. Buta, (Univ. Alabama, Tuscaloosa), T. Freeman (Bevill State College), NASA <http://apod.nasa.gov/apod/ap040221.html>.

Figure 4-8j: A modeled spiral galaxy compared with the observed galaxy NGC 4622 (figure 4-8i), which displays both trailing and leading spiral arms.

Figure 4-9a: Calculated

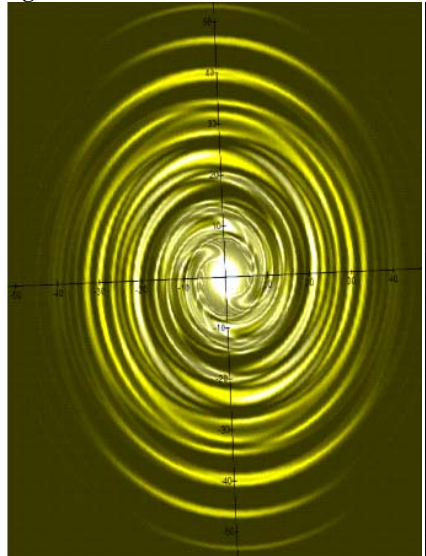


Figure 4-9b



Figure 4-9a: A modeled spiral galaxy compared with the observed galaxy NGC 488 (figure 4-9b), demonstrating a flocculent structure.

Figure 4-9b: NGC 488, image credit: Johan Knapen and Nik Szymanek, Isaac Newton group of telescopes; http://images.google.co.uk/imgres?imgurl=http://www.ing.iac.es/PR/newsletter/news6/johan4.jpg&imgrefurl=http://www.ing.iac.es/PR/science/ngc488.html&usg=__wsWG6nhi5biMN2pbNEcaq-cdASU=&h=1143&w=1000&sz=110&hl=en&start=6&um=1&tbnid=tOUIfhc2uTM-nM:&tbnh=150&tbnw=131&prev=/images%3Fq%3DNGC%2B488%2Bpicture%26hl%3Den%26sa%3DX%26um%3D1.

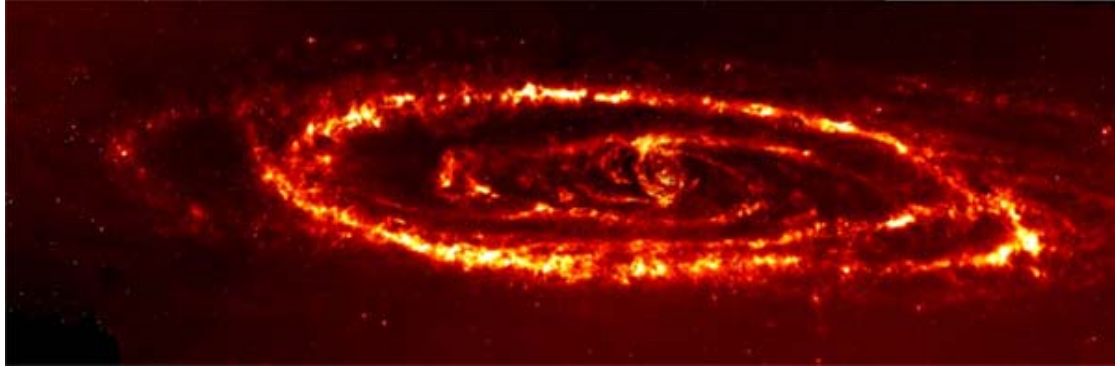


Figure 4-7c: An infrared view of the Andromeda Galaxy taken by NASA’s Spitzer Space Telescope. Image credit: NASA/JPL-Caltech/K. Gordon (University of Arizona), <http://www.spitzer.caltech.edu/Media/releases/ssc2005-20/ssc2005-20a.shtml>.

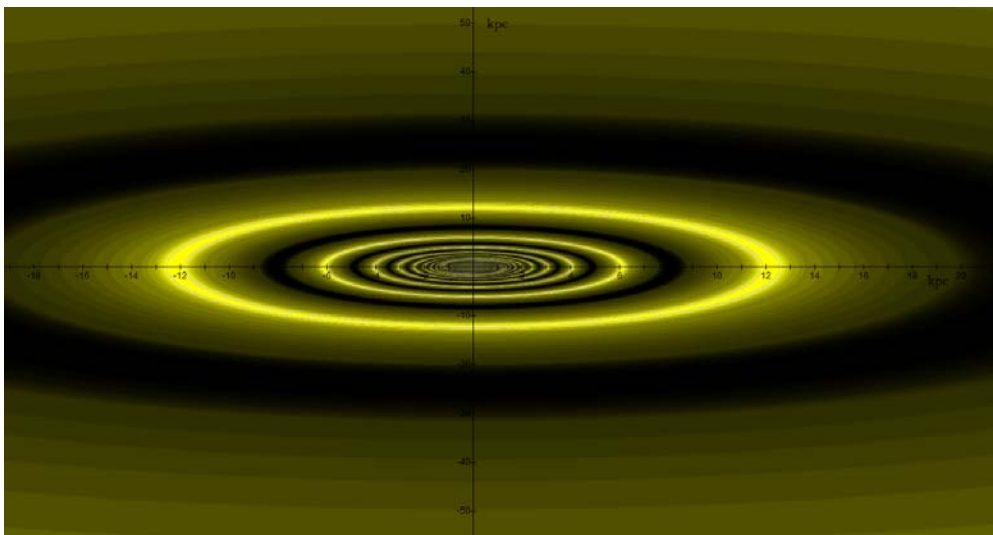


Figure 4-7d: A UG calculated image of the Andromeda Galaxy.

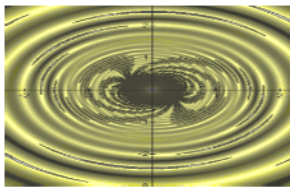


Figure 4-7e: Calculated

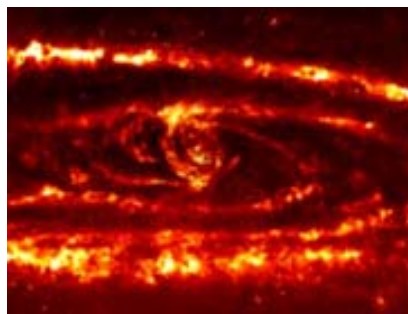


Figure 4-7f: Observed

In figures 4-7d and e, a UG modeled galaxy is demonstrated to bear a resemblance to the general morphology and properties of the Andromeda galaxy. Note that the rotating distorted hourglass structure at the center of the calculated galaxy (figure 4-7e) bears a resemblance to the general structure of Andromeda’s nucleus (figure 4-7f), additionally accounting for the two short spirals observed to extend from the nucleus and for the ansae reported by Beaton et al. in 2005 ^(Beaton et al., 2005).

Figure 4-12a: Calculated

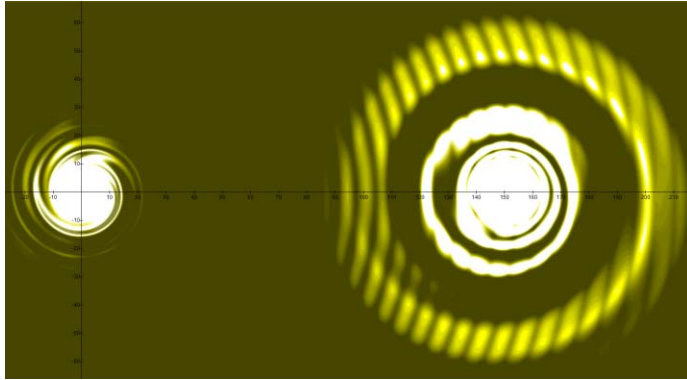


Figure 4-12b: Observed Galaxy ESO 350-40



Figure 4-12a: Depicts an image of the effect of a companion galaxy on a modeled galaxy, compared with the observed cartwheel galaxy ESO 350-40 (figure 4-12b). Note that both galaxies demonstrate clumps of star formation.

Figure 4-12b: The Cartwheel Galaxy, ESO 350-40. Image credit: NASA, ESA, and K. Borne (STScI), <http://hubblesite.org/gallery/album/pr2007017d>.

In Chapter V, the UG theory is applied to model the general structure of Saturn's main body of rings. Saturn's ring system was first observed by Galileo nearly 400 years ago, 77 years prior to Newton's discovery of the gravitational force. Despite the extensive study of planetary rings, the origin and many of the properties of Saturn's complex ring system remain a mystery. Figure 5-1 provides a comparison between a UG calculated model and a computer-generated image of Saturn's ring system using RSS 3-wavelength occultation data.

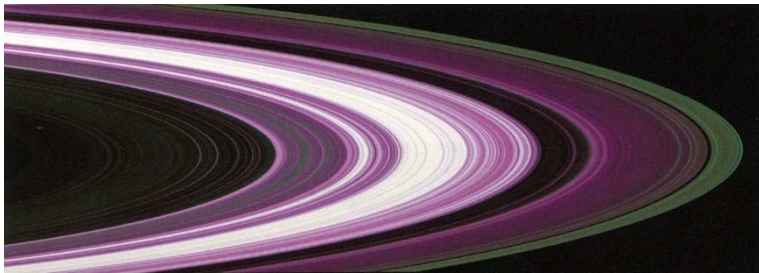


Figure 5-1a: Credit: NASA/JPL

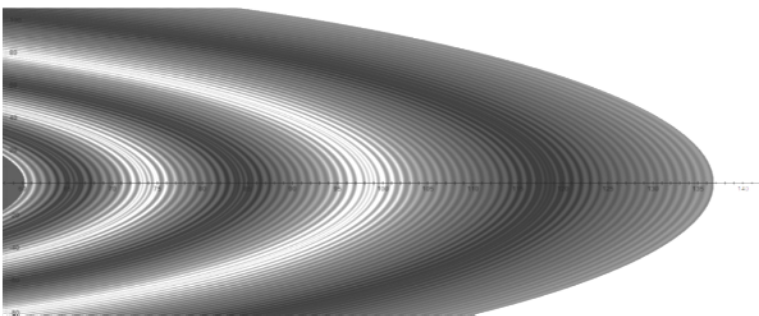


Figure 5-1b: UG Calculated

A detailed, high resolution image of Saturn's D ring is displayed in Figure 5-2. Figure 5-7a displays a detail of Saturn's A ring interior to the Encke Gap taken by the Cassini ISS instrument. On the right the image reveals spiral bending waves, where the wavelength decreases inwards, and on the left a succession of spiral density waves, where the wavelength decreases outwards. The same structure is revealed in the calculated image 5-7c.

Figure 5-2a: Saturn's D ring

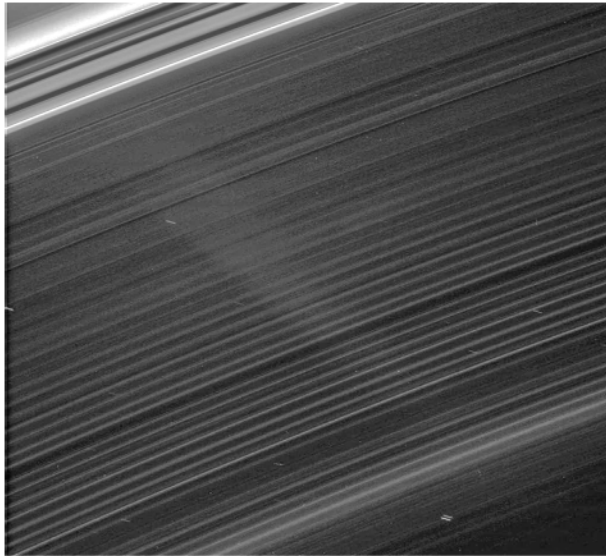


Figure 5-2c: UG Calculated D ring

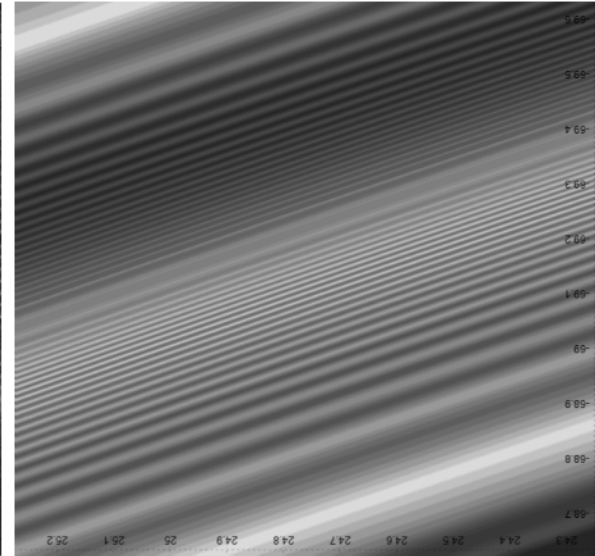


Figure 5-2a: Saturn's D ring, NASA/JPL/Space Science Institute, <http://photojournal.jpl.nasa.gov/catalog/?IDNumber=PIA08990>.

Figure 5-2c: A comparison between a calculated image of Saturn's D ring (figure 5-2c) and the observed D ring (figure 5-2a).

Figure 5-7a: Saturn's A ring interior to the Encke Gap

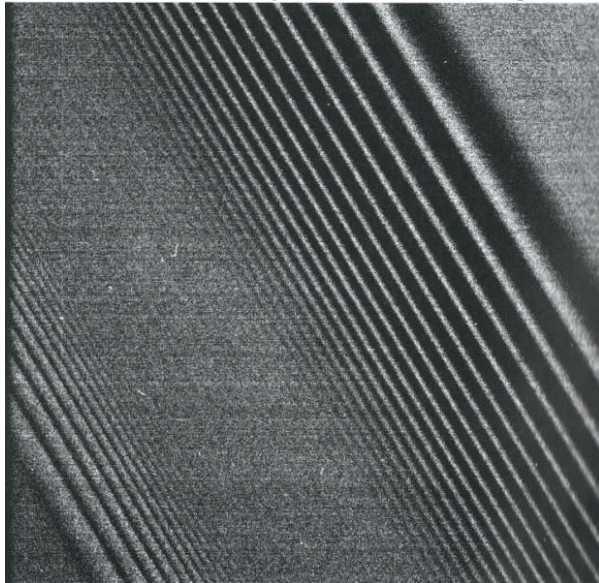


Figure 5-7c: UG Calculated A ring section

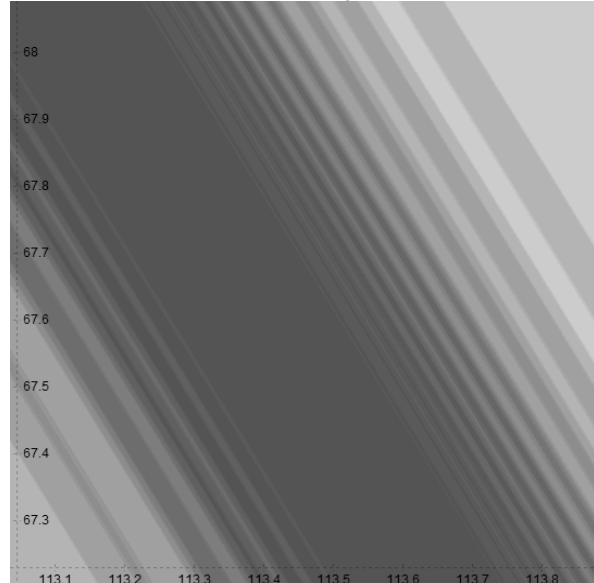


Figure 5-7a: Saturn's A ring interior to the Encke Gap. Image credit: NASA/JPL/Space Science Institute; <http://photojournal.jpl.nasa.gov/catalogue/PIA06093>.

Building on the same equations, the UG theory will be applied in Chapter VI to explain galactic dynamics. The unified gravitational equations will be shown to provide for the constant velocity curve observed in spiral galaxies, as well as for high stellar velocities, without relying

on the auxiliary hypothesis of dark matter. The chapter will additionally discuss the origin of galactic wind and the mechanism underlying star formation and fragmentation.

Chapter VII will discuss the implications of unified gravitation on general relativity and on the current cosmological model. In addition, the formation of galactic voids, the triggering mechanism and the driving forces behind the massive outflow of gas and matter observed during novae or supernovae, the clustering of nearby galaxies, and the effective repulsion between distant galaxies will be addressed. Finally, the theory of unified gravitation will be demonstrated to provide an explanation for the observed expansion of the universe while avoiding the dilemmas that led to the adaptation of inflation theory and to the assumptions of dark matter and dark energy, thus providing a significantly simpler model.

Additional applications of the UG equation will be discussed in the following chapters. Chapter VIII is concerned with the processes of ionization and their sources of energy. Chapter IX will discuss the structure and composition of planets and the mechanisms that determine whether a given planet will develop into a terrestrial or gas planet, and whether or not a given planet will demonstrate a ring system. The chapter will additionally propose a possible explanation for the generation of planetary magnetic fields. In Chapter X the question of galactic redshift periodicity will be contemplated.

As the fundamental premise of the UG theory is the unification of gravitation and the strong interaction, the final chapter will demonstrate the applicability of the unified gravitational equations on nuclear scales, where the UG theory will be demonstrated to account for the observed weak fall-off of the deep inelastic scattering cross section, and to provide a scaling behavior similar to Bjorken scaling.

Not all is well with gravitation; Or: Why look for an alternative theory?

Since their development, Newton's gravitational theory and the general theory of relativity have served as the foundation for our understanding of the construction and dynamics of the universe. In the recent century, however, a growing body of experimental observations has demonstrated inconsistencies within both theories. The following is a brief review of the problems pertaining to the scope of the UG theory.

1. The problem of "missing mass" in galaxies and galactic clusters

As early as 1933, Fritz Zwicky ^(Zwicky, 1933) concluded that the calculated gravitational force of the visible galaxies in the Coma Cluster is far too small to account for the observed high speed stellar orbits. Later studies of the rotation curves of spiral galaxies ^(Rubin et al., 1970; 1980) reported that contrary to the prediction of Keplerian dynamics, most stars rotate around the galaxy center at a roughly constant or slightly increasing speed, rather than at a speed decreasing inversely to the square root of the star's radius of orbit. These disparities led to the conclusion that the amount of visible matter in galaxies is insufficient to explain the observed motion of

their stars, or the motion of galaxies within clusters. Further investigation confirmed these findings, leading to two possibilities; either the current understanding of gravitation is incorrect, or additional non-visible matter must exist and account for about 90% of the galactic mass. At present, astrophysicists tend to prefer the second explanation, that additional matter explains the observed motion of galaxies within the existing theory. Consequently, a new variable of dark matter has been introduced to the current paradigm.

2. Problems with Big Bang cosmology

Hubble's discovery that the universe is not static, but expanding, and the earlier introduction of the general theory of relativity, led to the development of the Big Bang cosmological model, which attributes the beginning of our universe to an explosion from a very dense point singularity at about 14.5 billion years ago. The consensus in the physics community accepts the Big Bang as the most reasonable theory for the origin and evolution of the universe. Nevertheless, throughout its development the Big Bang model encountered significant problems; notably, the flatness problem, the horizon problem, as well as problems of age, structure and isotropy.

According to the Friedman-Lemaitre-Robertson-Walker metric, the curvature of the universe depends on its energy density. The flatness problem arises from the fact that even an extremely small departure of one part in 10^{60} of the energy density from the critical density would have caused the universe to either collapse in a big crunch at an earlier stage, or to expand too fast for any substantial structure to form. In either case, the current universe would have developed in an entirely different form than observed. Furthermore, the age of the universe estimated from its current size and rate of expansion has posed a dilemma, as certain globular clusters studied in the mid-1990s appeared to be older than the time passed since the Big Bang according to these calculations.¹⁰ The finite age of the universe and the finite speed of light place a limit on the maximum distance that light could have traveled since the Big Bang. Given that matter in the universe must travel at a velocity lower than the speed of light, it is impossible for regions separated by greater than this maximum distance to have ever interacted. The horizon problem results from the observation that all regions of the universe, including regions separated by greater than this maximum distance, have the same temperature and share the same physical properties, pointing to past interactions at an equilibrium or steady state.

The horizon and the flatness problems were resolved by the introduction of Guth's inflation theory, postulating an initial phase of rapid exponential expansion, at which space itself (rather than matter) expanded at a rate much higher than the speed of light ^(Guth, 1981). Nevertheless, the visible density of matter in the universe amounts to only about 3% to 4% of the critical density of its mass and energy. The inclusion of dark matter provides for only about 26% of this critical density. Furthermore, counter to Newton's theory, the expansion of the universe

¹⁰ Note that the age problem is largely believed to have been resolved in the late 1990s when computer simulations reduced the estimated age of the globular clusters ^(Navabi & Riazi, 2003).

has been found to accelerate, rather than to decelerate. Resolving these issues without modification of the current paradigm requires the addition of a repulsive element to Einstein's field equations, as well as accounting for the missing 74% of mass or energy. This has led to the reintroduction of the cosmological constant, and to the concept of dark energy, which together with dark matter brings the total amount of non-visible and undetected matter in the universe to about 96% of the overall mass and energy of the universe. To date, neither dark matter nor dark energy has ever been directly observed.

In addition, a structure problem arises from the question of how a universe that began in equilibrium, in a perfectly homogenous state, could have exploded into an inhomogeneous universe. At the same time, the observed inhomogeneous structure of the universe conflicts with the Big Bang theory's reliance on the cosmological principle,¹¹ which requires that the universe be homogeneous and isotropic on a large scale. Redshift surveys of the night sky, however, provide convincing evidence that the universe is not perfectly homogeneous, as the observed patterns of galaxies reveal that they are clearly not distributed randomly across the sky. Observations additionally reveal the existence of immense voids, or vacant regions of loosely spherical structure measuring up to 140 megaparsecs across (Rudnick et al., 2007). Deviations from homogeneity are currently explained by the Big Bang model (and by inflation theory) to result from a quantum effect in the early universe, where Heisenberg's uncertainty principle guaranteed density fluctuations. These density fluctuations were then "frozen" as inflation expanded the universe at an exponential rate far too rapid for the particles to interact. Voids of this magnitude, as well as the discovery of large walls of galaxies, challenge the Big Bang cosmological model, as they are observed to exceed the scales predicted by the quantum effect and inflation.

3. Problems of infinities and singularities

The equations of quantum mechanics and general relativity often encounter predictions of physical values becoming infinite. In quantum theory, infinities appear whenever one attempts to use quantum mechanics to describe fields, such as electromagnetic fields. Some of these difficulties were averted by the introduction of renormalization techniques. Once regarded as controversial, renormalization is carried out by using rationalized procedures to scale out equation terms that diverge to infinity, while finite terms are kept as valid. However, renormalization breaks down when applied to gravitation; and consequently, to date, all efforts to consolidate general relativity with quantum mechanics have proven unsuccessful. Furthermore,

¹¹ The cosmological principle states that on large distance scales the distribution of matter in the universe is homogenous. According to the cosmological principle, the density of matter, when averaged over a sufficiently large volume of space, has the same value anywhere at the present time. This principle is known not to hold on small scales, where matter tends to cluster. The transition to homogeneity is currently believed to occur on scales between 100 and 1000 *Mpc* (which is large in comparison to the size of galactic clusters and small relative to the size of the visible universe). The cosmological principle can be derived from the Copernican principle, which holds that our own planet does not inhabit a special location in the universe, meaning that the laws of physics on Earth are the same and can be applied everywhere in the universe. Observations reveal that the distribution of galaxies, as viewed from Earth, is isotropic on large angular scales. As the Copernican principle requires that the distribution of galaxies appear to be isotropic when viewed from all locations of the universe, it follows that the special distribution of matter on large scales must be homogeneous.

the equations of general relativity lead to singularities, such as black holes. Singularities have resulted in inconsistencies which stem from the inability of current physics to deal with infinite density and infinite temperature. In addition, as the Big Bang theory postulates that the universe began at a point singularity, the structure of the observed universe requires matter and radiation to have escaped from the singularity, a process that is prohibited by general relativity. These inconsistencies were simply sidestepped by the assumption that our current physics is invalid at sub-Planck distances, and that further explanation would require a new and yet undiscovered quantum theory of gravitation.

4. The problem of accurately calculating the value of Newton's gravitational constant G

Physics has encountered a long-standing dilemma in determining the value of the gravitational constant G . Whereas all other fundamental constants in physics are known to parts per billion, or parts per million at worst, the gravitational constant G stands alone with a measurement reliability of only about one part in 7000 (Gillies, 1997). Numerous attempts to improve the precision of the value of G over the last 200 years have resulted in marginal improvements at best, in spite of vast improvement in technology. Inconsistencies in the measured value of G have been proven to occur within distance ranges starting as small as several micrometers up to cosmic scale. The reason underlying these inconsistencies has not yet been determined. When an equation in science accurately describes an observed phenomenon, the values of its constant(s) can be determined with a high level of accuracy. However, the constants of an equation that only approximates a given phenomenon must vary somewhat with the range of its variables. Therefore, the inability to establish the value of G may suggest a deviation between Newton's gravitational equation and the actual law of gravitation.

5. The increasing number of unexplained phenomena and the increased complexity of the cosmological model

The effort of consolidating major discrepancies within Newton's theory, general relativity and the standard model has resulted in a substantial increase in the number of independent parameters and constants.¹² Although much theoretical progress has been made, many open questions remain to this date. The fifth problem is a growing list of observed phenomena that cannot be explained by a cohesive gravitational theory. Rather, the following phenomena either require auxiliary hypotheses to comply with current theory, or remain unaccounted for. In the realm of galaxies, the ability of current theory to explain galactic structure and dynamics is limited. Images emerging from the Hubble space telescope reveal

¹² This list of parameters/auxiliary hypotheses includes dark matter, dark energy and inflation, while the list of constants includes the cosmological constant as well as about twenty adjustable constants within the framework of the standard model. For the most part, this list contains many freely adjustable constants that can have almost any value from theoretical point of view, as their values can only be determined experimentally. Lee Smolin has stated, "If you think of the standard model as a calculator, then the constants will be dials that can be set to whatever positions you like each time the program is run" (Smolin, 2006).

large-scale astronomical objects such as galaxies and nebulae with complex and varied morphologies, from various types of spiral and lenticular structures to elliptical, ring and irregular structures. While different mechanisms have been proposed to influence certain galactic properties, the mechanisms underlying their diverse morphologies are not yet well-understood. For example, the nature of density waves, which are theorized to drive spiral morphology in galaxies, is not yet well-understood. Furthermore, it is not clear what determines whether a spiral galaxy is normal or barred, or why star formation in barred spirals is concentrated mainly at the ends of the bar. There are also questions as to what drives the fragmentation of stars within galaxies, what activates the sudden expansion of gas observed in novae and supernovae, as well as the physical mechanisms underlying the creation of galactic and stellar wind and the magnetic fields of galaxies.

Inconsistencies between theory and observation are not limited to galactic or cosmic scales. In the Solar System, Newton's laws of motion, together with his law of gravitation, have been experimentally verified to provide excellent agreement with the observed trajectories and orbital periods of planets, and most of the trajectories and orbital periods of satellites.¹³ Nevertheless, Newtonian-based theories have had only limited success in explaining the origin and structure of planetary ring systems. Whereas some of the observed characteristics of individual rings and gaps can be accounted for by orbital resonances, or by other mechanisms such as shepherd satellites, embedded moons or Lorentz resonances, the vastness of these ring systems and a significant portion of their properties remain unexplained. Furthermore, although gravitation is the dominant force on solar scale, a number of phenomena within our Solar System remain unaccounted for. Current gravitational theories do not explain planetary composition; in particular, we do not know why the outer planets Jupiter, Saturn, Uranus and Neptune are composed of gas, or why, in contrast to the inner terrestrial planets, gas planets display extensive ring systems and a large number of satellites. There are additional unanswered questions as to what are the mechanisms underlying the formation of the Asteroid belt, the Kuiper belt and the Kuiper cliff within our Solar System? What mechanism is responsible for the generation of planetary magnetic fields?¹⁴ What causes the solar corona? What causes the flyby anomaly, where an unexpected and unexplained energy increase is observed during Earth flybys of a spacecraft? Recently, the current locations of Pioneer 10 and Pioneer 11 were reported to deviate by about 5,000 *km* from their expected trajectories. If no observational errors are found, the Pioneer anomaly might require modification of current theory.

This partial list of problems and inconsistencies between observations and the predictions of the current paradigm, as well as the vastly increased complexity of the cosmological model, raise serious questions as to whether the actual law of gravitation differs from the gravitational force described by Newton's theory or by general relativity.

¹³ The largest exception is the precession of the perihelion of Mercury's orbit, where Newton's solution deviated from the observed orbit and required a correction provided by Einstein's general relativity.

¹⁴ It is currently believed that the magnetic field of Earth is generated by electrical currents within its liquid core. However, if so, it is unclear what causes these currents.

Chapter I: The Theory of Unified Gravitation

The Unification of the Strong Interaction and the Gravitational Force

The theory of unified gravitation is based on the assumption that the nuclear strong interaction and gravitation are one and the same force, viewed at different distance scales, and that a single equation can describe both interactions on nuclear as well as on cosmological scales. In particular, it is assumed that similar to Newton's theory of gravitation, the unified gravitational force is predominantly a central and conserving force between a pair of particles. At large distances, the UG force equation should asymptotically approach Newton's classical force equation, when applied to ordinary matter composed of protons, neutrons and electrons, and should fully comply with all experimental measurements of gravitation that are currently available. In addition, the UG force must comply with the behavior of the nuclear forces between nucleons, which have been observed to be substantially stronger than the Coulomb interaction at below sub-Fermi distances. Accordingly, the UG force must produce an explosive growth at distances below $1 fm$,¹⁵ and is thus assumed to demonstrate exponential behavior. At a microscopic distance range of approximately $r > 1.5 fm$, the UG force between two protons must be negligible in comparison to the Coulomb force. It is further assumed that the force is independent of velocity and spin, as their effects are either relatively small, or are part of the electromagnetic forces. However, it should be noted that as energy and force equations are not invariant under the Lorenz transformations, the force may not be central and may become dependent on particle velocity when the particles move at relativistic velocities. The UG theory must also be capable of explaining the observed nuclear resonance patterns, as well as planetary (and galactic) ring patterns, which consist of thousands of ringlets (oscillation patterns). The large area occupied by planetary and galactic rings rules out quantum mechanics as the cause of the oscillations, thus indicating that the UG potential must be driven by a periodic function. As most gravitational systems do not demonstrate cyclical behavior, the oscillating term must be suppressed under ordinary conditions.

Newton never published the reasoning that guided him to his gravitational force equation and never attempted to prove the equation on a theoretical basis. This is quite understandable, given that fundamental principles cannot be proven to be correct and may be regarded as valid only as long as they are not rendered false by experimental results. The basic UG equation 1-7 has the same limitation and cannot be proven correct. The equation will simply be required to survive a continuous inflow of experimental data that may either confirm or refute its accuracy. In the case that it is proven to be incorrect, the equation should either be adjusted or its theoretical foundation discarded. The logic underlying equation 1-7 is laid out in the following section of this chapter, where it will be shown that mathematically a family of very similar equations may be compatible with the aforementioned requirements. Equation 1-7 has been selected as virtually the simplest equation fulfilling the criteria.

¹⁵ $1 fm = 10^{-15} m$.

Section I-1: The Logic leading to the Theory of Unified Gravitation

The UG theory for the strong interaction and gravitation is based on four postulates leading to a family of possible gravitational equations. While the different possible equations may provide different potential energy values, they share major properties that can be shown to provide a simpler and more accurate theory than the one currently used, with the ability to explain a large number of unexplained observed phenomena. The first UG postulate states,

UG Postulate I: The nuclear strong interaction and gravitation are actually one and the same interaction, viewed on different distance scales. Therefore, a single equation can describe both interactions from the sub-nuclear scale to the cosmological scale.

Newton's gravitational equations 1-1 and 1-2 describe a central and conserving force between a pair of particles. The force depends on the distance between the two particles and on the product of their masses. Therefore, a natural starting point for the UG theory is to assume that the UG force is also a central and conserving force between a pair of particles, and that the force depends exclusively on the distance between the particles and on their respective masses. The short-range strong force was also shown to depend on inter particle distances and on particle masses, and to be dominated by central forces. However, the strong force has also been shown to contain a non-central component, and furthermore to depend relatively weakly on the charge and spin of the particles. Thus, the assumption of a central force that is entirely dependent on particle mass and distance can be challenged for distances of the order of $r \lesssim 10^{-15} m$. The weak dependency of the overall nuclear force on particle charge and spin can be attributed to electromagnetic interactions between the charged particles, or between their charges and the magnetic fields generated by their motion and spin. The existence of a non-central component can be attributed to a relativistic effect caused by high particle velocities. Whereas two charges at rest exert a central Coulomb force on each other, two relativistic charges are known to exert a non-central magnetic force on each other, in addition to the central Coulomb force. This phenomenon was explained by Einstein to be a simple relativistic effect. The underlying cause for this effect is that a force, under special relativity, is not an invariant entity. In other words, due to the relativistic phenomena of distance contraction and time dilation, force equations are not the same when viewed in different inertial frames that move at relativistic velocities relative to each other. Consequently, a central force between two particles at rest would not be viewed as a central force when both particles are moving at relativistic speeds relative to the observer. These relativistic effects provide a mechanism by which the central Coulomb force, as well as any other central force between two particles at rest, can create a substantial non-central force component (for further discussion see Chapter III). Therefore, the existence of a strong central UG force and an electromagnetic force between two massive charged particles can be consistent with observations of non-central components, with some weaker dependencies on the charge and spin of the interacting particles. This enables the UG assumption that when viewed from an inertial

rest frame of one of the interacting particles, the unified gravitational force is predominantly a central and conserving force between a pair of particles, depending exclusively on the absolute value of the distance between the particles and on their respective masses, where the distance and masses are measured relative to the given inertial rest frame. In cases where the test particle has a relativistic velocity relative to the source particle, its perceived mass and distance are altered by the relativistic effect. For the time being, the discussion is limited to the non-relativistic case, where the particle velocities, relative to each other and relative to the observer, are significantly lower than the speed of light. The discussion will be broadened in the third chapter of this book to deal with relativistic particles as well.

As the UG force is assumed to be a central and conserving force, it can be written as a gradient of a potential energy scalar function

$$\vec{F}_g(m, M, r) = \vec{\nabla}V_g = \frac{\partial V_g(m, M, r)}{\partial r} \hat{r}$$

where the distance vector between the two particles is given by $\vec{r} = \vec{r}_1 - \vec{r}_2$, where \vec{r}_1 and \vec{r}_2 are the locations of the interacting particles and where $r = |\vec{r}|$, and \hat{r} is defined as the unit vector in the direction of \vec{r} . The respective rest masses of the particles are denoted M and m , the potential energy function is given by $V_g(m, M, r)$, and for reasons of symmetry, the potential energy of each particle should be the same when the particle masses are exchanged. Therefore, $V_g(m, M, r) = V_g(M, m, r)$.

Additionally, at sufficiently large distances, the UG potential energy equation converges toward Newton's equation 1-2, which depends implicitly on the product of the masses of interacting particles, rather than on their individual masses. There is also no evidence of strong forces acting between particles where either one or both particles have zero mass. Therefore, for any particle mass M , $V_g(0, M) = V_g(M, 0) = V_g(0,0) = 0$. This strongly suggests that the potential energy function V_g actually depends on only two variables: the distance r , and the product of the two masses mM . Therefore, the second UG postulate can be stated as,

UG Postulate II: The unified gravitational force is a force between a pair of particles. When viewed at an inertial rest frame of one of the interacting particles (the source particle), the unified gravitational force applied on the second particle (the test particle) is predominantly a central and conserving force that depends exclusively on the absolute distance between the particles and on the product of their masses.¹⁶

This leads to

¹⁶ The distinction between the source particle and the test particle is only required for cases where their velocity v relative to each other is relativistic. Note that the distance between the particles and the mass of the test particle are viewed from the inertial rest frame of the source particle. Therefore, the test particle mass used by the UG equations is given by $m\gamma(v)$, where m is defined as the test particle's rest mass and $\gamma(v) = \frac{1}{\sqrt{1-\frac{v^2}{c^2}}}$. The significance of this distinction will become clear in Chapter III.

Equation 1-2-1

$$V_g = V_g(mM, r)$$

$$\vec{F}_g = \vec{F}_g(mM, r) = \nabla V_g = \frac{\partial V_g(mM, r)}{\partial r} \hat{r}$$

An important question that needs to be addressed is how the UG force and the UG potential energy depend on the distance r ($r = |\vec{r}|$). In accordance with the first UG postulate, at large distances¹⁷ the UG force equation should asymptotically approach the classical Newtonian force equation and should fully comply with all experimental measurements of gravitation that are currently available, leading to

Equation 1-2-2

$$V_g(Mm, r) \approx -\frac{GmM}{r} \text{ and } \vec{F}_g(mM, r) \approx \frac{GmM}{r^2} \hat{r} \text{ at } r > 10^{-6} \text{ m}$$

where m and M are the masses of ordinary particles such as protons, neutrons and electrons.

In addition, according to the first postulate, the UG force must comply with the behavior of the nuclear forces between nucleons, which have been observed to be substantially stronger than the Coulomb interaction at below approximately 0.65 fm . Observations further dictate that at distances $r > 1.5 \text{ fm}$, the nuclear force between two protons must be negligible in comparison to the Coulomb force acting between them. Accordingly, the UG potential energy must produce an explosive growth at about 1 fm , thus leading to the third postulate.

UG Postulate III: The UG potential energy has an exponential dependency on the distance r .

The simplest mathematical function that complies with the aforementioned requirements is the function $V_1 = -B(e^{A/r} - 1)$, where A is of the order of 0.5 fm to 10 fm . This function demonstrates exponential growth, as well as substantial amplitude at $r < 1 \text{ fm}$, and relatively negligible amplitude at $r > 1.5 \text{ fm}$. In addition, this function and its derivative are practically indistinguishable from the Newtonian function $V_N = -\frac{GmM}{r}$ and its derivative at $r > 10^{-6} \text{ m}$, as long as the value of A is sufficiently small. Expressed mathematically,

Equation 1-2-3

$$V_1 = -B(e^{A/r} - 1) = -B\left(1 + \frac{A}{r} + O\left(\left(\frac{A}{r}\right)^2\right) - 1\right) \rightarrow \frac{-AB}{r} = \frac{-GmM}{r} \text{ for } r \gg A$$

Therefore, if $AB = GmM$ and $r \gg A$ then $V_1 \rightarrow V_N$. Similarly, for the derivative of V_1 (or the force),

¹⁷ “Large distances” refers to distances where the UG and the Newtonian equations are indistinguishable. In the case of matter composed of protons, neutrons and electrons, large distances refers to $r \gg 5 * 10^{-6} \text{ m}$, which provides the range of distances at which experiments were conducted, confirming within 1 part in 7000 the accuracy of Newton’s formula.

Equation 1-2-4

$$\vec{F}_1 = \frac{dV_1}{dr} \hat{r} = \frac{AB}{r^2} e^{A/r} \hat{r} = \frac{AB}{r^2} \left(1 + \frac{A}{r} + O\left(\left(\frac{A}{r}\right)^2\right) \right) \hat{r} \rightarrow \frac{AB}{r^2} \hat{r} = \frac{GmM}{r^2} \hat{r}$$

where $r \gg A$. Note that while Newton's force and potential energy equations depend linearly on the particle mass m through the product of mM , the second UG postulate does not require that the UG force or potential energy be linear with m . Such linearity is possible if the variable B of equation 1-2-3 is proportional to mM , or if A is independent of mM , and therefore a constant. However, in order to comply with the first UG postulate, the UG theory should be capable of explaining the patterns of nuclear resonances, as well as planetary and galactic rings patterns, which may consist of many thousands of ringlets, as observed in Saturn's complex ring system. Both phenomena demonstrate strong oscillation patterns. The existence of nuclear resonances, which demonstrate a series of discrete nuclear energy levels that depend mainly on the masses of nucleons, strongly suggests the presence of a shell structure in the nucleus. The existence of such a shell structure, however, does not necessarily infer a cyclical UG potential energy. After all, the Coulomb potential energy of the proton-electron system given by the equation $V_c = \frac{Kq^2}{r}$ is non-cyclical, but still produces the atomic electron shell structure due to quantum effects. However, quantum effects occur on microscopic distance scales and thus cannot be responsible for planetary or galactic rings, as the large size of the area occupied by the planetary and galactic rings simply rules them out as a reasonable cause. Attempts to explain ring structures via electromagnetic forces have proven to be unsuccessful, and attempts to explain planetary rings and gaps as a result of orbital resonances between rings (or the gaps) and certain satellites have been only partially successful, as they do not explain the vastness of the ring systems (see Chapter V), nor the entirety of the observed rings and gaps. In order to provide a mechanism capable of producing the vast planetary ring systems, as well as the ring and spiral structures observed in galaxies (see Chapter IV), the UG potential energy equation must also contain a periodic function. As most of the gravitational systems familiar to us do not demonstrate cyclical behavior, the oscillating term must somehow be suppressed at distances larger than $10 \mu m$ when applied to protons, neutrons and electrons. Whereas nuclear resonances occur at distances of approximately $10^{-15} m$, planetary rings occur at distances below $150,000 km$, and rings are observed in galaxies at distance ranges of the order of $3 kpc$ to $120 kpc$.¹⁸ Therefore, the distance range of the oscillations must vary for different systems, yet must still depend exclusively on the mass of the interacting particles. Theoretically, ring and galaxy formations could also be explained by some odd distribution of dark matter, or by collisions between systems; however, to date these explanations have provided only limited success for a limited number of systems, while resulting in models with escalating complexity. Instead, a different approach is attempted by the UG theory.

¹⁸ $1 pc = 3.0857 * 10^{16} m$.

The simplest cyclical function that can concurrently provide diminished oscillations as $r \rightarrow \infty$ and produce a derivative that, similar to the Newtonian force, is proportional to $1/r^2$, is the function $\cos\left(\frac{D}{r} + \varphi\right)$, which oscillates at $r \lesssim D$ and approaches the constant value $\cos(\varphi)$ as $r \rightarrow \infty$. If D were independent of particle mass, rings should always occur at the exact same interparticle distances, regardless of the masses of the two interacting particles, in disagreement with observations that different planetary and galactic systems often demonstrate concentric sets of rings at varying radii. This leads to the conclusion that D must be dependent on the masses of the particles, or specifically on their product mM , as required by the second postulate.

Therefore, the simplest functions that comply with the above requirements are of the form

Equation 1-2-5

$$V_g = -B \left(e^{A/r} \cos\left(\frac{D}{r} + \varphi\right) - \cos(\varphi) \right)$$

where D must be dependent on mM , and B, A and φ may either be constants or functions of mM . The term $-\cos(\varphi)$ was added to assure that $\lim_{r \rightarrow \infty} V_g = 0$.¹⁹ The requirement that at large distances V_g should approach its Newtonian counterpart leads to

Equation 1-2-6

$$\begin{aligned} \lim_{r \rightarrow \infty} V_g &= \lim_{r \rightarrow \infty} \left[-B \left(e^{A/r} \cos\left(\frac{D}{r} + \varphi\right) - \cos(\varphi) \right) \right] \rightarrow \\ &\rightarrow \left[-B \left(\left(1 + \frac{A}{r}\right) \left(\cos\left(\frac{D}{r}\right) \cos(\varphi) - \sin\left(\frac{D}{r}\right) \sin(\varphi) \right) - \cos(\varphi) \right) \right] \rightarrow \\ &\rightarrow \left[-B \left(\left(1 + \frac{A}{r}\right) \left(\left(1 - \left(\frac{D}{r}\right)^2\right) \cos(\varphi) - \frac{D}{r} \sin(\varphi) \right) - \cos(\varphi) \right) \right] \rightarrow \\ &\rightarrow \left[-\frac{B}{r} (A \cos(\varphi) - D \sin(\varphi)) \right] \xrightarrow{r \rightarrow \infty} -\frac{GmM}{r} \end{aligned}$$

or

Equation 1-2-7

$$B(A \cos(\varphi) - D \sin(\varphi)) = GmM$$

Using the same process for its derivative (or force),

¹⁹ Note that equations of the type $V_g = -\frac{B}{r} \left(e^{A/r} \cos\left(\frac{D}{r} + \varphi\right) \right)$ are not considered, as they would fail to provide the constant rotation curve observed in spiral galaxies (see Chapter VI). A more complex equation such as $V_g = -B \left(e^{A/r} \cos\left(\frac{D}{r} + \varphi\right) - \frac{kmM}{r} \right)$ cannot simply be ruled out. However, to fit the observations listed above, at distances of $r \lesssim A$ or $r \lesssim D$ the term $\frac{kmM}{r}$ must become relatively insignificant, while at $r \gg A$ and $r \gg D$, the UG potential energy V_g becomes indistinguishable from Newton's V_N . Therefore, the term $\frac{kmM}{r}$ would provide a significant contribution only within a relatively narrow range of distances.

Equation 1-2-8

$$\begin{aligned}
 \lim_{r \rightarrow \infty} F_g &= \lim_{r \rightarrow \infty} \nabla V_g = \lim_{r \rightarrow \infty} \left[-\frac{B e^{A/r}}{r^2} \left(-A \cos\left(\frac{D}{r} + \varphi\right) + D \sin\left(\frac{D}{r} + \varphi\right) \right) \right] \rightarrow \\
 &\rightarrow \left[\frac{B(1 + A/r)}{r^2} \left(A \left(\cos\left(\frac{D}{r}\right) \cos(\varphi) - \sin\left(\frac{D}{r}\right) \sin(\varphi) \right) - D \left(\sin\left(\frac{D}{r}\right) \cos(\varphi) + \cos\left(\frac{D}{r}\right) \sin(\varphi) \right) \right) \right] \rightarrow \\
 &\rightarrow \left[\frac{B(1 + A/r)}{r^2} \left(A \left(\left(1 - \left(\frac{D}{r}\right)^2 \right) \cos(\varphi) - \frac{D}{r} \sin(\varphi) \right) - D \left(\frac{D}{r} \cos(\varphi) + \left(1 - \left(\frac{D}{r}\right)^2 \right) \sin(\varphi) \right) \right) \right] \rightarrow \\
 &\rightarrow \frac{B}{r^2} (A \cos(\varphi) - D \sin(\varphi)) \rightarrow \frac{GmM}{r^2}
 \end{aligned}$$

Again, in agreement with equation 1-2-7,

Equation 1-2-9

$$B(A \cos(\varphi) - D \sin(\varphi)) = GmM$$

This leaves us with three degrees of freedom, where setting three out of the four functions A , B , D or φ will uniquely determine the fourth function.²⁰ However, there are a few constraints. As discussed above, D must be dependent on mM , otherwise all planets and galaxies would demonstrate rings at exactly the same sets of radii. According to equation 1-2-7 (or the identical equation 1-2-9), either B , or alternatively $A \cos(\varphi) - D \sin(\varphi)$, must be equal to or approach zero if either m or M are equal to or approach zero. Therefore, either one or both B or $A \cos(\varphi) - D \sin(\varphi)$ must depend implicitly on mM .

If function A is negative, the UG potential energy would be monotonically attenuated, becoming zero as r approaches zero. The function A must therefore be positive in order to explain both gravitation and the strong nuclear interaction. The existence of rings suggests that the UG cosine term of equation 1-2-5 oscillates within the radius of the farthest observed ring, requiring that $r \leq D$. The fact that gravitational fields do not demonstrate explosive exponential growth in the vicinity of the observed galactic or planetary rings further requires that within the distance range of the rings, $r \gg A$. In the range of distances $A \ll r < D$, equation 1-2-5 can be reduced to $V_g = -B \left(\cos\left(\frac{D}{r} + \varphi\right) - \cos(\varphi) \right)$, and therefore oscillates with virtually constant amplitude B . It is reasonable to assume that particles of greater mass should produce a larger UG potential energy amplitude within this oscillation range. This suggests that B should also be dependent on mM . While these constraints eliminate many possible combinations of functions A , B , D and φ , a substantial number of possibilities remain, and a significant amount of experimental data is required before the number of possible equations can be reduced to a bare

²⁰ Unless the fourth function is φ , which can only be determined within an integer multiple of 2π .

minimum. However, once the values of m and M are set, A , D and φ can be treated as a set of constants (denoted A , D and Φ) and equation 1-2-5 becomes

Equation 1-2-10

$$V_g = -\frac{GmM}{A\cos(\Phi) - D\sin(\Phi)} \left(e^{A/r} \cos\left(\frac{D}{r} + \Phi\right) - \cos(\Phi) \right)$$

Among the mathematically possible sets of functions A , B , D and Φ , the simplest and most logical are those where the exponent operand A is a positive constant ($A \equiv a > 0$) and the phase Φ is set as zero. This leads to $B = \frac{GmM}{a}$. As D must depend on the particle masses, $D = bmM$ is selected for simplicity, where b is a constant.

Using this simplified set, the UG potential energy can be written as

Equation 1-2-11

$$V_g = -\frac{GmM}{a} \left(e^{a/r} \cos\left(\frac{bmM}{r}\right) - 1 \right)$$

Equation 1-2-11 was derived by searching for the simplest function that is compatible with the UG postulates. While in agreement with the spirit of Occam's Razor, the selection of the simplest equation is somewhat subjective, and cannot necessarily be regarded as proven. After all, nature is not required to guarantee simplicity. However, the simplest model is usually a good starting point. If experimental data is found to conflict with the predictions of equation 1-2-11, new sets of functions should be evaluated.

The inclusion of a cosine term (or in general, a cyclical term) in the UG equation, and the dependency of its operand on the particle masses, is probably the most fundamental deviation of the UG theory from Newton's theory and general relativity. According to Newton's equation, the external gravitational force applied on an object is always an attractive force that is linearly proportional to its total mass m . Newton's gravitational theory holds that the external force is the same whether a point-like object consists of few heavy fundamental particles or of many light fundamental particles, as long as the total sum of all of their masses are the same. For example, according to the Newtonian equation, the gravitational force applied by an external point-like and electromagnetically neutral object of mass M on a point-like object containing a single particle of mass m is virtually equal to the gravitational force applied by the same external object from the same distance on a point-like object containing 100 particles of mass $m/100$. The UG theory makes the distinction that the UG force is linear with the number of fundamental particles if they are all of the same mass. However, the UG force and potential energy are not linear functions of the fundamental particle masses, and therefore are not necessarily linear with the total mass of the object. As an example, the Newtonian gravitational potential energy V_N between two atoms, one containing N_p protons, N_n neutrons and N_e electrons of respective mass m_{prot} , m_n and m_e and the other containing K_p protons, K_n neutrons and K_e electrons, is given

by $V_N = -\frac{G_n(N_p m_{prot} + N_n m_n + N_e m_e)(K_p m_{prot} + K_n m_n + K_e m_e)}{r} = -\frac{G_n m_1 m_2}{r}$, where the distance r between the two atoms is assumed to be significantly larger than the diameter of either atom.²¹ The total mass of each atom is given by m_1 and m_2 , and G_n is the Newtonian gravitational constant.

The UG potential energy V_g of the same interaction is provided by

$$V_g = -\frac{G_u}{a} \left[N_p m_{prot} K_p m_{prot} \left(e^{a/r} \cos\left(\frac{b m_{prot}^2}{r}\right) - 1 \right) + N_p m_{prot} K_n m_n \left(e^{a/r} \cos\left(\frac{b m_{prot} m_n}{r}\right) - 1 \right) + N_p m_{prot} K_e m_e \left(e^{a/r} \cos\left(\frac{b m_{prot} m_e}{r}\right) - 1 \right) + N_n m_n K_p m_{prot} \left(e^{a/r} \cos\left(\frac{b m_{prot} m_n}{r}\right) - 1 \right) + N_n m_n K_n m_n \left(e^{a/r} \cos\left(\frac{b m_n^2}{r}\right) - 1 \right) + N_n m_n K_e m_e \left(e^{a/r} \cos\left(\frac{b m_n m_e}{r}\right) - 1 \right) + N_e m_e K_p m_{prot} \left(e^{a/r} \cos\left(\frac{b m_{prot} m_e}{r}\right) - 1 \right) + N_e m_e K_n m_n \left(e^{a/r} \cos\left(\frac{b m_n m_e}{r}\right) - 1 \right) + N_e m_e K_e m_e \left(e^{a/r} \cos\left(\frac{b m_e m_e}{r}\right) - 1 \right) \right]$$

V_N and V_g are not identical at sufficiently short distances where $e^{a/r}$ is distinguishable from $\left(1 + \frac{a}{r}\right)$, or if $\cos\left(\frac{b m_n m_n}{r}\right)$ is still oscillating or has not yet converged to 1.²² At these distance ranges, the cosine terms within V_g are not all equal, and the total sum within the brackets does not add up to the product of the overall mass of the atoms. At large distances, where $r \gg a$ and $r \gg b m_n m_n$, V_g does converge toward $-\frac{G_u(N_p m_{prot} + N_n m_n + N_e m_e)(K_p m_{prot} + K_n m_n + K_e m_e)}{r} = -\frac{G_u m_1 m_2}{r}$, and with $G_u = G_n$, the two potential energies converge.

Therefore, with a constant a that is significantly less than the diameter of a hydrogen atom, and with a constant b that complies with $b m_n m_n \ll 10^{-6} m$, the two potential energy functions are indistinguishable at distances greater than $10^{-6} m$. However, for interactions involving fundamental particles of a mass significantly larger than the mass of a proton or neutron, the deviation from the Newtonian equation would become significant at greater distance ranges. Theoretically, these distances can extend to tens of thousands of kilometers if sufficiently large fundamental particles exist at the center of planets, or may further extend to the order of tens of kpc if substantially heavier particles exist at the galactic centers, leading to the fourth UG postulate.

UG Postulate IV: The extreme temperature and pressure conditions that exist at the cores of entities such as planets, stars and galaxies produce relatively stable superheavy particles (SHPs). Substantially higher temperature and pressure produce substantially more massive fundamental particles.

²¹ For simplicity, the small reduction of the proton, neutron or electron masses due to atomic bonding is neglected in this discussion. Furthermore, only the gravitational potential energy of the interaction between the two atoms is taken into consideration. Therefore, electromagnetic interactions, or any UG interactions within each atom, and the rest energy of the particles, are not taken into account.

²² Since $m_n > m_{prot}$ and $m_n \gg m_e$, the cosine term $\cos\left(\frac{b m_n m_n}{r}\right)$ requires the farthest distance before converging toward 1.

The production of very massive fundamental particles, coupled with the UG equations (equations 1-2-5, 1-2-10 or 1-2-11), can provide a mechanism for generating planetary or galactic rings within the distance range where the cosine term demonstrates oscillations. High-energy collisions between electrons and positrons have been shown to create particles that are heavier than 350,000 times their mass. Consistent with postulate IV, experimental data shows that higher energy particle collisions are capable of producing more massive particles. However, the masses of the heaviest particles produced via collision experiments are far smaller than the extreme masses required for the production of planetary or galactic rings via equation 1-2-11. Furthermore, the heaviest particles produced by high-energy collision experiments exist for only an instant before decaying into a barrage of lighter particles. Note, however, that the energy levels at the cores of planets, stars and galaxies are many orders of magnitude greater than those created by particle accelerators, and therefore the postulation that they can produce particles of substantially greater mass is logical. The relative stability of planetary ring systems suggests that if rings are in fact produced by superheavy particles in the vicinity of the central core of a planet, then the number of superheavy particles involved must be about constant. This can be explained via two different processes. First, the steady-state conditions within the core of a planet dictate that on average, the rate of production of a particular type of SHP should be equal to its rate of decay. Second, although free neutrons are known to be unstable and to decay, a neutron becomes stable when bonded with a proton in an atom nucleus. A similar mechanism may be at work for the large superheavy particles within galactic, stellar or planetary cores, where the superheavy particles may become bonded to each other or to the central core of ordinary matter, and thus become stable.²³ A more restrictive assertion, known as quark confinement, is made by the standard model, in which quarks are assumed to be stable only when they are bonded together.

We must also question whether it is reasonable to assume the possibility of the existence of fundamental particles of masses of many orders of magnitude greater than the most massive particle ever observed (10^{30} times heavier). To answer this question we should bear in mind that according to the UG postulate IV, such large particles can be produced and maintained only within violent environments of extremely high energy, temperature and pressure, as exist at the cores of planets, stars and galaxies. These violent environments are simply not accessible for direct and close observation. However, according to the UG theory, their effects can be observed from far distances in the form of planetary rings, ring and spiral galaxies, and as rejection forces that drive galaxies away from each other. The idea that a gravitational collapse could generate massive superheavy particles of many orders of magnitude larger than the heaviest particles observed can understandably be viewed as almost inconceivable. It should be noted, however, that this postulate is very mild relative to the accepted notion of the existence of black holes.

²³ Such an occurrence is extremely unlikely in the case of scattering experiments, where the production of a superheavy particle via a brief violent collision is an isolated event, and where the newly produced particle is subsequently immersed in a very mild (low energy) environment and does not have the opportunity to bond with any other SHP or to a massive object such as the core of planets or stars.

According to the no-hair theorem,²⁴ a black hole is viewed by an external observer to behave like a particle with enormous mass. However, the masses of black holes, which are believed to be produced by gravitational collapse, may exceed the SHP masses contemplated here by factors of 10^{26} to 10^{52} . Therefore, to make it easier to comprehend the fourth postulate in terms of current belief, the postulate can be described as an assumption that the extreme conditions generated by the collapse of gas clouds produces small black holes (SHPs) near the center of the planet, star or galaxy. With this approach, the main and fundamental difference between the UG theory and the current paradigm (Newton's gravitational theory and general relativity) is the use of equation 1-2-11, rather than equation 1-2, to describe the potential energy of the interaction.

²⁴ According to the no-hair theorem, all stationary black hole solutions of the Einstein equations of general relativity and the Maxwell equations of electromagnetism can be completely characterized by four numbers (in addition to their location and velocity): The total mass (energy), the angular momentum (spin), the total charge, and possibly, the total magnetic monopole charge (which is believed to be 0, reducing the number to only three). Consequently, a black hole is viewed by an external observer as a particle.

Chapter II: The UG Characteristics at Non-Relativistic Velocities.

Before proceeding further, it is important to address the oscillating behavior of the UG potential energy demonstrated in figures 2-3 to 2-6.

Equation 2-1-1

$$V_g = -\frac{GmM}{a} \left(e^{a/r} \cos\left(\frac{bmM}{r}\right) - 1 \right)$$

Whereas the gravitational force described by Newton's equation increases monotonically with a reduction in the distance between a pair of particles and is purely attractive, the UG potential equation incorporates a cosine term. The cosine enables a cyclical function to alternate between -1 and 1, and its inclusion in equation 2-1-1 implies that at short distances ($r < bmM/\pi$) the UG equation alternates between zones of attraction and zones of repulsion. The cosine term further implies that there are an infinite number of distances at which the UG force or potential energy cross zero, as well as an infinite number of distances at which they assume local maxima or minima.

Figure 2-1 illustrates that the cyclical behavior of the UG equation can be restricted to very short distances, well below the range of distances where gravitation has been tested experimentally. The graph uses an example of the general function $Y = \cos\left(\frac{bmM}{r}\right)$ compared to unity. When $r \rightarrow \infty$, $Y = 1$. As the value of r decreases, Y reduces monotonically, yet remains almost indistinguishable from 1 until a distance of about $r = 1.2 * 10^6 \text{ fm}$, which is slightly larger than the size of a typical atom or molecule. As r is further reduced, Y continues to drop monotonically until it becomes equal to zero at $r = \frac{2bmM}{\pi}$. At $r = \frac{bmM}{\pi}$, Y reaches its first minimum at $Y = -1$. As r continues to decrease, Y begins oscillating between -1 and 1 with growing frequency. Similarly, figure 2.2 compares the behavior of $Z = -GmM \left(\frac{e^{a/r}-1}{a}\right)$ with the behavior of $Y = \frac{-GmM}{r}$. The two functions are indistinguishable from each other at distances of $r \gg 5 * 10^{-13} \text{ m}$. Therefore, using the set of numbers given in the previous example, both terms, $\left(\frac{e^{a/r}-1}{a}\right)$ and $\cos\left(\frac{bmM}{r}\right)$ are, for all practical purposes, indistinguishable from $1/r$ and 1 respectively at distances of $r > 10^{-9} \text{ m}$.²⁵ In figures 2-3 to 2-6, the exponent and the cosine terms are combined into the UG potential energy equation 2-1-1. Again, using the same selected values and the given display scales, the UG potential energy V_g can hardly be distinguished from the Newtonian potential V_N at distances of $r > 1.2 * 10^{10} \text{ fm} = 1.2 * 10^{-5} \text{ m}$. Under the assumption that the UG force is a conserving force, the UG gravitational force \vec{F}_g between two particles of respective mass M and m can be calculated by computing the gradient of V_g , given by equation 2-1-1. As the force is further assumed to be a central force, equation 2-1-1 is

²⁵ The reasoning behind the specific selected values for the constants a and b will be explained later on in this chapter.

dependent only on the distance r , and independent of any orientation angle.²⁶ Therefore, only the radial derivative must be taken into account, leading to

Equation 2-1-2

$$\vec{F}_g = \vec{\nabla}V_g = \frac{\partial V_g}{\partial r} \hat{r} = \frac{GmM}{r^2} e^{a/r} \left(\cos\left(\frac{bmM}{r}\right) - \frac{bmM}{a} \sin\left(\frac{bmM}{r}\right) \right) \hat{r}$$

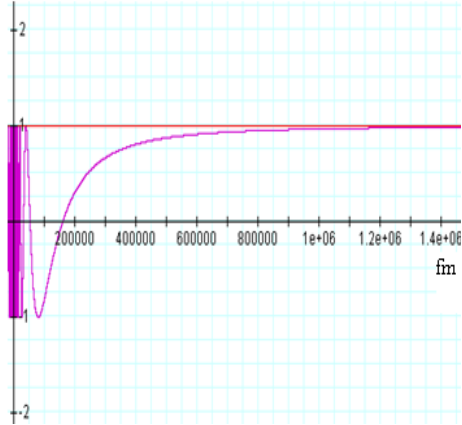


Figure 2-1: Comparison between $y = \cos\left(\frac{bmM}{r}\right)$ and $y = 1$ using $b = 9 * 10^{43} \text{ m/kg}^2$, $M = m = 1.674 * 10^{-27} \text{ kg}$. The x axis provides the distance r in fm . The two functions converge at about $r > 1.2 * 10^6 \text{ fm} = 1.2 * 10^{-9} \text{ m}$.

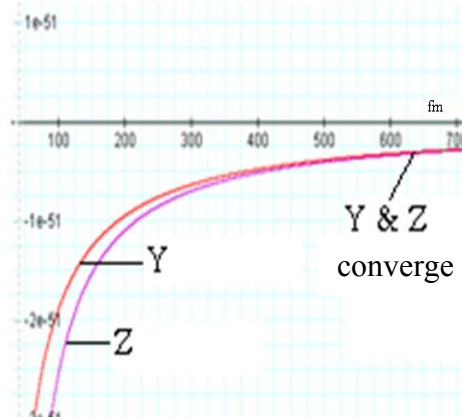


Figure 2-2: Compares $y = -GmM\left(\frac{e^{a/r}-1}{a}\right)$, denoted as Z, to $y = -\frac{GmM}{r}$, denoted as Y, where $a = 5.7 * 10^{-14} \text{ m}$.

In the general case of two objects consisting of a variety of particles, where the first object is composed of an ensemble of particles of particle mass M_i and the second object is composed of an ensemble of particles of particle mass M_j , the UG potential energy between the two objects is given by

Equation 2-1-3

$$V_g = -\frac{G}{a} \sum_i \sum_j M_i M_j \left[e^{a/r_{ij}} \cos\left(\frac{bM_i M_j}{r_{ij}}\right) - 1 \right]$$

²⁶ The assumption that the UG force is a central force is valid only as long as the particle velocities are non-relativistic. Relativistic velocities will be discussed in Chapter III.

Figure 2-3

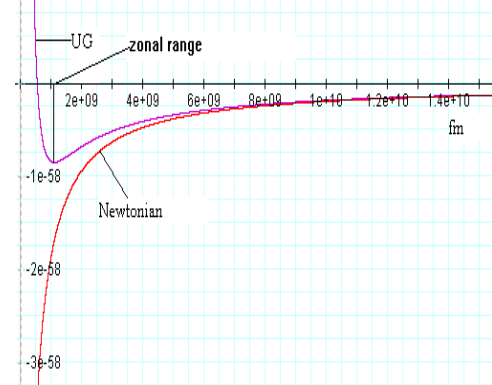


Figure 2-3: The UG and Newtonian potential equations are compared in a display range of $10^9 fm < r < 15 * 10^9 fm$, using values of $a = 5.7 * 10^{-14} m$, $b = 9 * 10^{43} m/kg^2$, $G = 6.674 * 10^{-11} Nm^2/kg^2$, and $M = m = 1.674 * 10^{-27} kg$. The two functions converge at about $r > 10^{10} fm$.

Figure 2-4

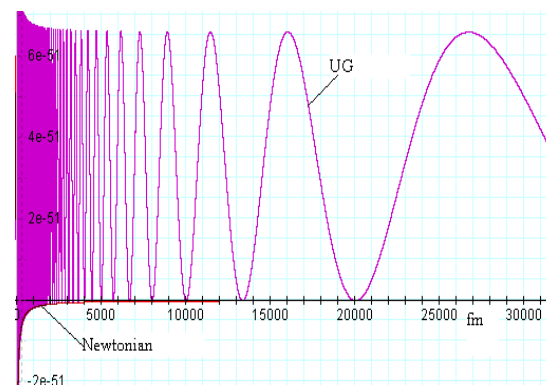


Figure 2-4: Displays the same comparison as figure 2.3, viewed in a display range of $0 < r < 30,000 fm$. In this range, as long as $a \ll r$, the UG potential energy V_g oscillates with a large, almost constant amplitude (relative to the Newtonian potential), and with increasing frequency as r approaches zero. Note that V_g is essentially positive, and only briefly negative near its minima that reside on the Newtonian curve.

Figure 2-5

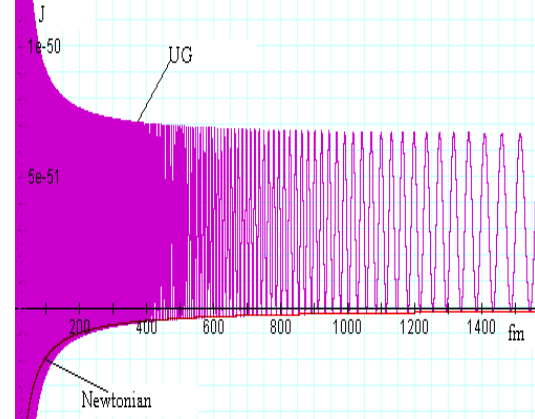
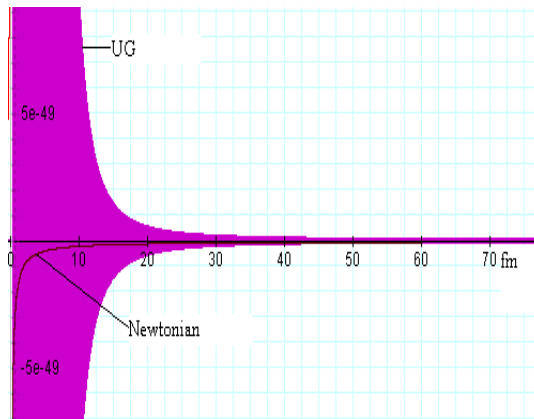


Figure 2-6



Figures 2-5 and 2-6: Comparison between the UG and Newtonian potential equations, viewed in display ranges of $0 < r < 1,500 fm$ and $0 < r < 80 fm$ respectively. Note that at low r values (below about $150 fm$) there is an explosive increase in amplitude, saturating the display scale almost instantly.

The summations over i and j include all of the particles in objects 1 and 2 respectively, and r_{ij} is the distance between the particle of mass M_i in the first object and the particle of mass M_j in the second object.

For simplicity, let it be assumed that the first object is composed of N_M identical particles of particle mass M and the second object is composed of N_m identical particles of particle mass m . Furthermore, the distance r between the two objects is assumed to be substantially larger than the size (or diameter) of either object. Consequently, the potential energy equation is given by

Equation 2-1-4

$$V_g = -\frac{GmN_mMN_M}{a} \left(e^{a/r} \cos\left(\frac{bmM}{r}\right) - 1 \right)$$

Similarly, the unified gravitational force \vec{F}_g is provided by

Equation 2-1-5

$$\vec{F}_g = \nabla V_g = \frac{\partial V_g}{\partial r} \hat{r} = \frac{GmN_mMN_M}{r^2} e^{a/r} \left[\cos\left(\frac{bmM}{r}\right) - \frac{bmM}{a} \sin\left(\frac{bmM}{r}\right) \right] \hat{r}$$

Therefore, at distances $r \gg a$, $r \gg bmM$ and $r \gg \frac{(bmM)^2}{a}$, where $e^{a/r}$ and $\cos\left(\frac{bmM}{r}\right)$ approach 1 and $\frac{bmM}{a} \sin\left(\frac{bmM}{r}\right) \approx \frac{(bmM)^2}{ra}$ approaches zero, the UG force equation converges to

Equation 2-1-6

$$\vec{F}_g \cong \frac{GmN_mMN_M}{r^2} \hat{r} = \vec{F}_n$$

where \vec{F}_n denotes the Newtonian force, thereby demonstrating that the UG and Newtonian forces converge at far distances.²⁷ In general, at the limit $\lim_{b \rightarrow 0 \text{ and } a \rightarrow 0} \vec{F}_g = \vec{F}_n$. Thus, both theories provide the same results for any gravitational system that is composed of ordinary particles, as long as the constants a and b are sufficiently small, and the distance r is not sub-microscopic.

The underlying postulate that the unified gravitational force equation can also be applied to the strong interaction suggests that in the nucleus of an atom, where the distance between the nucleons is about $r \cong 0.65 * 10^{-15} \text{ m}$, the UG potential energy between two protons will be virtually equal in amplitude to the Coulomb potential. Therefore,²⁸ using equation 2-1-1 and Coulomb's law,

Equation 2-1-7

$$\frac{Gm_{prot}^2}{a} e^{a/r} \cong \frac{Kq_e^2}{r}$$

Multiplying by the constant a and taking the log of both sides provides

Equation 2-1-8

$$\frac{a}{r} \cong \ln\left(\frac{Kq_e^2}{Gm_{prot}^2}\right) + \ln\left(\frac{a}{r}\right)$$

²⁷ See figure 2-8.

²⁸ The Coulomb interaction is clearly dominant at $r > 1.5 \text{ fm}$ and negligible compared with the strong interaction at approximately $r < 0.5 \text{ fm}$. Therefore, the UG potential energy must be approximately equal to the electromagnetic (Coulomb's) potential energy somewhere in between those two distances. This provides a margin of error of about 30% for the constant a .

Substituting $q_e = 1.602 * 10^{-19} C$ for the proton charge, $m_{prot} = 1.673 * 10^{-27} kg$ for the proton mass, $K = 9 * 10^9 Nm^2/c^2$, $G = 6.674 * 10^{-11} Nm^2/kg^2$, and $r = 0.65 * 10^{-15} m$, and solving equation 2-1-8 via iterations provides the approximate value of the constant $a \cong 5.7 * 10^{-14} m$.

Evaluating the exponential values at distances of $0.4 fm$, $0.65 fm$, and $1 fm$, with the assumption that $a = 5.7 * 10^{-14} m$ will increase the UG force by a factor of about $2.13 * 10^{13}$ between $1 fm$ and $0.65 fm$, and by a factor of about $6.3 * 10^{23}$ between $0.65 fm$ and $0.4 fm$. Therefore, equations 2-1-1 and 2-1-2 provide the necessary explosive growth at approximately $1 fm$ and below, while asymptotically converging to the Newtonian force for ordinary particles at distances significantly larger than about $10 \mu m$.

Finding the value of the constant b is more complicated, as the oscillations could have started at distance ranges where the amplitude of the UG potential energy is negligible compared with the electromagnetic potential energy, and are thus difficult to detect.

A lower bound for the constant b can be attained by taking into account the stability of the nucleus, where the distances between the nucleons average about $0.65 * 10^{-15} m$, requiring that a minimum occur at about this distance. For a minimum to occur, the interaction between the nucleons at $0.65 * 10^{-15} m$ must be within the oscillation range of the cosine term, or

$$\frac{bm_p^2}{\pi} > 0.65 * 10^{-15} m, \text{ leading to } b > 7.28 * 10^{38} m/kg^2.^{29}$$

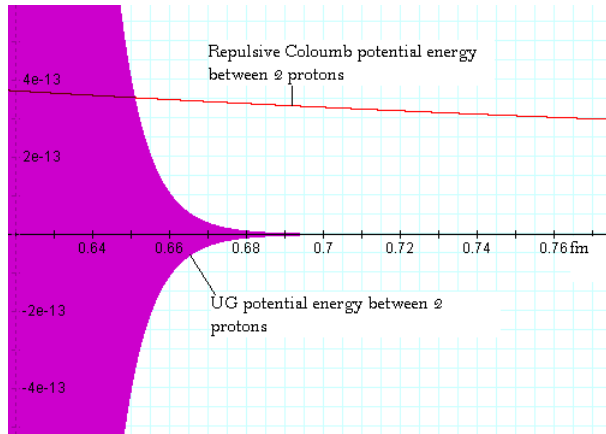


Figure 2-7: The graph demonstrates the explosive growth of the UG potential energy at the nuclear boundaries. As calculated in the case of two proton interactions, the amplitude of the UG potential energy is equal in magnitude to the Coulomb potential energy at about $0.65 fm$. At distances below $0.65 fm$, the UG potential energy completely dominates over the electromagnetic potential energy (with the exception of the UG zero crossings). At just above $0.65 fm$, however, the UG potential energy becomes negligible.

The requirement that the UG force equation be consistent with the Newtonian force equation within the level of measurement reliability can be used for estimating an upper bound

²⁹ The term m_p is used here for either the mass of a proton m_{prot} , the mass of a neutron m_n , or the mass of Hydrogen 1_1H . Therefore, an approximate average of $m_p = 1.674 * 10^{-27} kg$ was used for the calculation.

for the value of the constant b . To date, all measurements of G have been conducted at distances $r > 5\mu m$, where $r \gg a$. Therefore, the exponential term can be replaced by a value of 1, leading to $\lim_{b \rightarrow 0} \vec{F}_g = \vec{F}_n$, assuring that the two forces are indistinguishable at the distance range of interest when the value of b is sufficiently small. The variation in the measurement of the gravitational constant G (one part in 7000 for $r > 20\text{ cm}$ ^(Gillies, 1997)) can provide the upper bound of the constant b by calculating the range of the acceptable deviation between the forces calculated by the UG and the Newtonian equations. This level of variation in G may be caused by the following:

1. Measurement error- Since the gravitational force is significantly weaker than the electromagnetic force, the signal-to-noise ratio is low. In addition, as there is no negative mass, the external gravitational fields cannot be masked out.
2. The presence of additional (relatively light) superheavy particles that interact according to equations 2-1-1 and 2-1-2, but do not dominate the interaction.
3. Variation between the gravitational force and Newton's equations when applied to ordinary matter.

The failure to find an exact value of G despite substantial improvements in measurement technology suggests that measurement error alone cannot entirely account for the deviation. As no stable SHP has ever been detected on the surface of Earth, the second option seems unlikely. Therefore, the variability of G is presumably a consequence of the deviation of gravity from the Newtonian equation. Finding the accurate value of b requires a detailed analysis that takes into account the geometry of the specific experiment, as well as the fact that ordinary matter molecules contain electrons, protons and neutrons of different masses.

As an example, assume that the experiment for measuring the gravitational constant G is conducted by measuring the force between two identical homogeneous spheres of density ρ (in units of number of molecules per cubic meter) with radius R . When measurements take place, the two centers of the spheres are Δ meters apart along the x axis. Each molecule of the matter enclosed in the two spheres contains n_1 protons of mass m_1 , an average of n_2 neutrons of mass m_2 (the number of neutrons must be averaged from all stable isotopes), and n_3 electrons of mass m_3 (due to molecular neutrality $n_1 = n_3$).

According to Newton's law,

Equation 2-1-9a

$$\vec{F}_n = \frac{GM^2}{\Delta^2} = \frac{G\rho^2 \left(\frac{4}{3}\pi R^3 (\sum_{i=1}^3 n_i m_i) \right)^2}{\Delta^2} \vec{x}$$

while according to the UG theory,

Equation 2-1-9b

$$\vec{F}_g = G\rho^2 \left\{ \sum_{i=1}^3 \sum_{j=1}^3 n_i n_j m_i m_j \left[\int_{r_1=0}^R \int_{r_2=0}^R \int_{\theta=0}^{2\pi} \int_{\vartheta=0}^{2\pi} \int_{\phi=-\pi/2}^{\pi/2} \int_{\varphi=-\pi/2}^{\pi/2} \left[\frac{e^{-a/r}}{r^2} \left(\cos\left(\frac{bm_i m_j}{r}\right) - \frac{bm_i m_j}{a} \sin\left(\frac{bm_i m_j}{r}\right) \right) r_1^2 r_2^2 \cos\varphi \cos\phi \, d\varphi d\phi d\vartheta d\theta dr_2 dr_1 \hat{r} \right] \right\}$$

where $r = ((\vec{r}_1 - \vec{r}_2) \cdot (\vec{r}_1 - \vec{r}_2))^{1/2}$, $\hat{r} = \frac{(\vec{r}_1 - \vec{r}_2)}{r}$, and

$$(\vec{r}_1 - \vec{r}_2) = (\Delta + r_2 \cos\vartheta \cos\varphi - r_1 \cos\theta \cos\phi, r_2 \sin\vartheta \cos\varphi - r_1 \sin\theta \cos\phi, r_2 \sin\vartheta - r_1 \sin\theta).$$

The terms r_1 , θ and ϕ respectively provide the distance from the center, the azimuth and the elevation angles of the volume point within the first sphere, and r_2 , ϑ and φ are their counterparts in the second sphere. As the two spheres are not in contact, Δ must be larger than $2R$ and all possible pairs of particles split between the two spheres must be separated by a distance of at least $\Delta - 2R \gg a$. Therefore, the term $e^{-a/r}$ can be replaced by 1.

Equation 2-1-9c

$$\frac{|\Delta G|}{G} = \frac{|\vec{F}_g - \vec{F}_n|}{|\vec{F}_n|}$$

\vec{F}_n and \vec{F}_g are given by equations 2-1-9a and 2-1-9b, and the calculated $\frac{\Delta G}{G}$ is consequently dependent on the value of the constant b . Therefore, the optimal value of b can then be estimated by finding the range of values that provide the best fit between the calculated and measured $\frac{\Delta G}{G}$ at different values of R and Δ . It is clear from the discussion above that ΔG should approach zero as $\frac{R}{\Delta}$ approaches zero, as long as $\Delta \gg b(m_2)^2/\pi$ and $\Delta \gg a$.

In the absence of such an experiment, the value of b could be estimated from the reported range of variation of the value of G . The gravitational contribution of an electron and the effect of the small difference between the proton and neutron masses are relatively small in comparison to the contribution of either a proton or a neutron. Therefore, the contribution of the electrons to the gravitational force is assumed to be negligible, while protons and neutrons are assumed for simplicity to have an equal mass of $m_p = 1.674 * 10^{-27} \text{ kg}$. In addition, the distance r must be between $\Delta - 2R < r < \Delta + 2R$. Using equations 2-1-9a, 2-1-9b and 2-1-9c for the case where bm_p^2 and R are significantly smaller, but not negligible compared with the distance Δ , provides

Equation 2-1-9d

$$\frac{|\Delta G|}{G} \approx \left| \cos\left(\frac{bm_p^2}{\Delta}\right) - \frac{bm_p^2}{a} \sin\left(\frac{bm_p^2}{\Delta}\right) - 1 \right| \approx \left| 1 - \left(\frac{bm_p^2}{\Delta}\right)^2 - \frac{(bm_p^2)^2}{a\Delta} - 1 \right| \leq \frac{1}{7000}$$

Given that $\Delta \gg a$ or $1/a \gg 1/\Delta$,

$$\frac{|\Delta G|}{G} \approx \left| \frac{(bm_p^2)^2}{a\Delta} \right| \leq \frac{1}{7000}.$$

Since the deviation in $\frac{|\Delta G|}{G}$ can reach the value of 1/7000 from time to time, b should be of the order of $b \approx \frac{\sqrt{\Delta}}{m_p^2} \left(\frac{a}{7000} \right)^{1/2} \approx \frac{\sqrt{\Delta}}{(1.674 \times 10^{-27})^2} \left(\frac{5.7 \times 10^{-14}}{7000} \right)^{1/2} = 1.02 \times 10^{45} \sqrt{\Delta}$. As typical high precision laboratory-based experiments were conducted at distances of the order of $\Delta \approx 20 \text{ cm}$, the value of the constant b is likely to be in the general range of $b \approx 4.4 \times 10^{44} \text{ m/kg}^2$. This estimated value is only an approximation, however, and may be off by as much as one to two orders of magnitude. For the purpose of discussion, as the exact values of the constants a and b are not known, values of $a = 5.7 \times 10^{-14}$ and $b = 0.9 \times 10^{44} \text{ m/kg}^2$ will be assumed for the remainder of this book. Furthermore, the gravitational contribution of the electrons and the effect of the small difference between proton and neutron masses will also be assumed to be insignificant.³⁰ Instead, a mass of $m_p = 1.674 \times 10^{-27} \text{ kg}$ will be used for either a nucleon or the hydrogen atom ${}^1_1\text{H}$. The term “ordinary particle” (or “ordinary matter”) will be used throughout this book to refer to either a proton, a neutron or an electron (or to matter composed of these particles), while an ordinary particle of mass m_p will refer specifically to either the hydrogen atom ${}^1_1\text{H}$, a proton or a neutron. An object composed of ordinary matter that contains one or more atoms or molecules with one or more nucleons will be regarded as having N particles of mass m_p , where N is the overall number of nucleons in the object. Finally, for the remainder of this chapter, particle velocities will be assumed to be non-relativistic.

Section II-1: The UG Gravitational Zones at Non-Relativistic Velocities

According to equations 2-1-1 and 2-1-2, the UG interaction between a particle of mass M at a given location and a second particle of mass m divides the space surrounding the first particle into zones that define the force and potential energy acting on the second particle by the first at any location within this space. The equations below have been developed for the non-relativistic case to quantify the widths and boundaries of the zones, and to find where they reach a local maximum or minimum.

The local potential energy maxima and minima (where the force is equal to zero) are given by

Equation 2-1-10

$$\vec{\nabla} V_g = \frac{\partial V_g}{\partial r} \hat{r} = \frac{GmM}{r^2} e^{a/r} \left(\cos\left(\frac{bmM}{r}\right) - \frac{bmM}{a} \sin\left(\frac{bmM}{r}\right) \right) \hat{r} = 0$$

³⁰ This is justified as the number of electrons must equal the number of protons (for reasons of electrical neutrality), and the mass of a proton is about 1,837 times heavier than the mass of an electron. Similarly, the difference between the masses of protons and neutrons is only about 0.166% of the proton mass.

or

Equation 2-1-11

$$\tan\left(\frac{bmM}{r}\right) = \frac{a}{bmM}$$

or

Equation 2-1-12

$$R_{n,ext} = \frac{bmM}{n\pi + \arctan\left(\frac{a}{bmM}\right)} \text{ for } n = 0, 1, 2 \dots$$

with minima at even n values and maxima at odd n values. Similarly, applying equation 2-1-1 and the relation $V_g(R_{n,0}) = 0$ may provide the zero intersections $R_{n,0}$ of the potential energy function V_g ,

Equation 2-1-13

$$V_g = -\frac{GmM}{a} \left(e^{a/r} \cos\left(\frac{bmM}{r}\right) - 1 \right) = 0$$

or $\cos\left(\frac{bmM}{R_{n,0}}\right) = e^{-a/R_{n,0}}$, thus

Equation 2-1-14

$$R_{n,0} = \frac{bmM}{2n\pi \pm \arccos\left(e^{\frac{-a}{R_{n,0}}}\right)}$$

For distances $R_{n,0} \gg a$, $e^{\frac{-a}{R_{n,0}}} \cong 1$, and therefore³¹

Equation 2-1-15

$$R_{n,0} \cong \frac{bmM}{2n\pi}, \text{ for } n = 1, 2 \dots$$

A zone is defined as the area of space enclosed between a minimum curve and an immediate neighboring maximum curve. Any zone n_+ , refers to the zone situated between the minimum indexed n and the maximum indexed $n + 1$, while any zone n_- refers to the zone situated between the same minimum n and the maximum curve indexed $n - 1$. The distance between two successive maxima or two successive minima can be found by using equation 2-1-12 for the usual case of $a \ll bmM$, or for the case of $n\pi \gg \pi/2$. Since $\left| \arctan\left(\frac{a}{bmM}\right) \right| \leq \pi/2$,

³¹ Note, however, that at $a \ll R_{n,0} \ll \frac{bmM}{\pi}$ each zero is split into two very close consecutive zeroes, since the relatively large positive potential energy very briefly becomes negative, with a minimum coinciding with the relatively negligible Newtonian potential energy (see figures 2-4 and 2-5).

Equation 2-1-16

$$\Delta R_{n,ext} = R_{n,ext} - R_{n+2,ext} \approx bmM \left(\frac{1}{n\pi} - \frac{1}{(n+2)\pi} \right) = \frac{2bmM}{n(n+2)\pi} \approx \frac{2R_{n,ext}}{(n+2)} \rightarrow \frac{2R_{n,ext}}{n} \text{ as } n \rightarrow \infty$$

Similarly, it can be shown that $\Delta R_{n,0} \approx \frac{bmM}{2n\pi} - \frac{bmM}{2(n+1)\pi} = \frac{2bmM}{4n(n+1)\pi} = \frac{R_{n,0}}{(n+1)} \rightarrow \frac{R_{n,0}}{n}$ as $n \rightarrow \infty$.

Figures 2-3 to 2-6 illustrate the behavior of the function V_g (using equation 2-1-1) compared with the Newtonian gravitational potential at different distance ranges. As demonstrated in figure 2-3, the two functions are virtually identical at distances sufficiently greater than the first minimum ($n = 0$), which according to equation 2-1-12 occurs at

Equation 2-1-17a

$$R_0 = \frac{bmM}{\arctan\left(\frac{a}{bmM}\right)}$$

Below this point the behaviors of the UG and the Newtonian functions diverge substantially, as the UG potential V_g changes direction and begins to exhibit an oscillation pattern with $\frac{1}{r}$.

Initially, when $r \gg a$, the oscillation amplitude of the potential energy remains almost constant at a value close to $\frac{GmM}{a}$. As r approaches or becomes smaller than the constant a , both the amplitude and frequency of the oscillations increase sharply with the reduction of distance r .

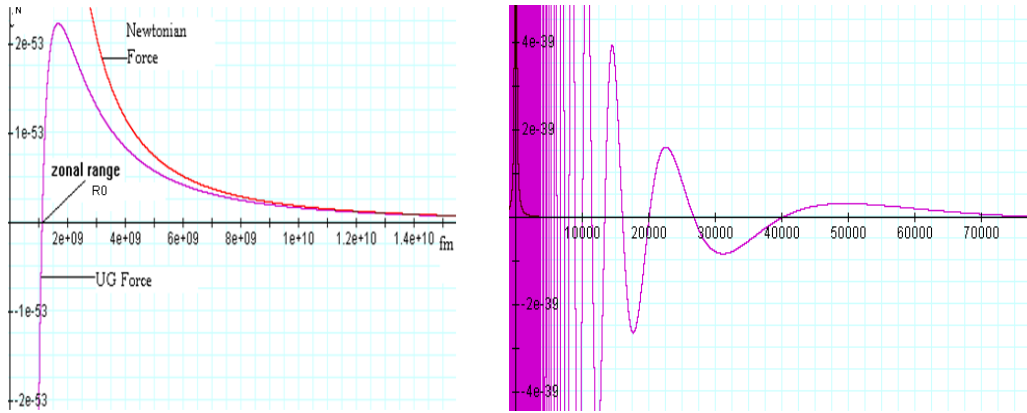
Since the oscillation frequency approaches infinity as $r \rightarrow 0$, the potential energy continues to alternate between rapidly growing positive and negative potentials, which converge exponentially into positive and negative infinities. An infinite amount of energy is thus required to reduce the distance between the two particles to zero. **Therefore, the particles can never “meet,” and singularity is avoided.** If proven correct, this will have a profound effect on the concept of black holes (black holes will be discussed in section VII-2). R_0 , defined above as the distance of the first minimum, serves as an indicator for how close the two particles must be from each another before their gravitational interaction begins to deviate strongly from the classical Newtonian behavior and proceeds into a pattern of sinusoidal zones. For its significance, the distance R_0 will be referred to as the **zonal range** of the particles. In the case of two objects consisting of many types of particles, the zonal range between the heaviest particle in each object will be defined as the **maximal zonal range** of the objects. For example, in the comparison between F_g and F_N in figure 2-8, we can observe that sufficiently far beyond the zonal range distance R_0 , the UG and the Newtonian forces are indistinguishable. In other words, starting at somewhat beyond their zonal range R_0 , the force between a pair of superheavy particles of mass M and m is equivalent to the force between two objects that are positioned at the same distance r from each other, where the first object is composed of $\frac{M}{m_p}$ ordinary particles and the second object consists of $\frac{m}{m_p}$ ordinary particles. This, however, is not the case for distances within the particles' zonal range. For larger superheavy particles of mass M , which will be shown to be capable of generating planetary rings, $bm_pM \gg a$. The SHP zonal range with ordinary particles

R_0 is given by equation 2-1-17a and is inversely proportional to $\arctan\left(\frac{a}{bm_pM}\right)$. In cases where $bm_pM \gg a$, $\arctan\left(\frac{a}{bm_pM}\right)$ is very small, and the SHP zonal range R_0 is located at an extremely large distance from the central core of the planet (see equation 2-1-17a), significantly beyond the distance where the UG potential energy oscillations cease. The amplitude at this zonal minimum is also negligible. For this reason, a second important distance, termed the **zonal oscillation range** is defined as the radius of the first maximum ($n = 1$) given by

Equation 2-1-17b

$$R_1 = \frac{bmM}{\pi + \arctan\left(\frac{a}{bmM}\right)}$$

where the potential energy becomes virtually $\frac{2GMm}{a}$.



Figures 2-8 and 2-9: A comparison between the UG force and the Newtonian gravitational force, given the same parameters used in figures 2-3 to 2-6. The two functions converge at about $r > 10^{10} \text{ fm}$ (10^{-5} m).

Section II-2: Superheavy Particles Embedded in Ordinary Matter

According to the UG equation, a single massive superheavy particle embedded in a large amount of ordinary matter can completely dominate a significant amount of the surrounding region, yet remain completely undetected at very long or short-range distances. In order to demonstrate this concept, consider the following example of a hypothetical object composed of 10^{30} ordinary particles of particle mass $m_p = 1.674 * 10^{-27} \text{ kg}$ arranged in spherically symmetric distribution within a distance R of a single superheavy particle of mass $M = 10^{-13} \text{ kg}$. Figures 2-10 and 2-11 provide the comparison between the absolute value of the contribution of the 10^{30} ordinary particles and the contribution of the single SHP of mass 10^{-13} kg to the potential energy of a given ordinary particle at a distance $r > R$. At distances significantly greater than the SHP zonal range with ordinary matter, where the UG equation and the Newtonian equations converge, the overall larger mass of the ordinary matter dominates the interaction, and the SHP effect is completely negligible (smaller by a factor of $1.674 * 10^{17}$). As r reduces to below about 243 km , the superheavy particle contribution begins to dominate.

The SHP dominance peaks at the $n = 1$ maximum, where its contribution becomes about 18.7 times larger than the contribution of ordinary particles. As r reduces below 280.4 m , the ratio r/a falls to a level at which the SHP effect is diminished by the excessive mass of ordinary particles, and the ordinary matter contribution once again becomes dominant. As r continues to drop, the contribution of the superheavy particle becomes completely negligible, as long as r remains greater than R .

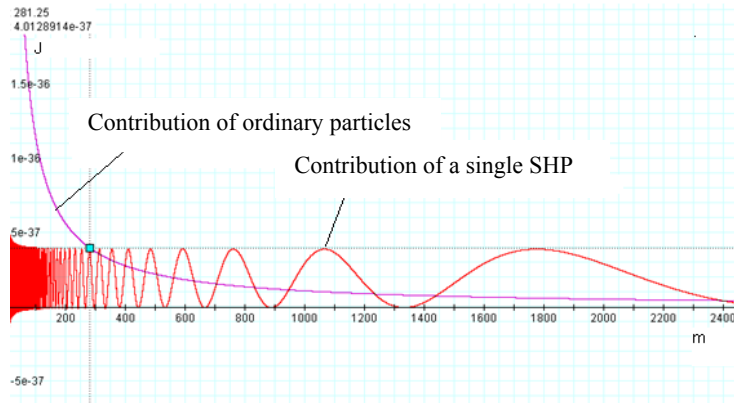


Figure 2-10: A comparison between the inverted contribution of 10^{30} ordinary particles and the contribution of a single SHP of mass 10^{-13} kg to the potential energy of an ordinary particle at distance r (x axis). The ordinary particles clearly dominate at distances $r < 280$ m , while the SHPs begin to dominate at $r > 280$ m .

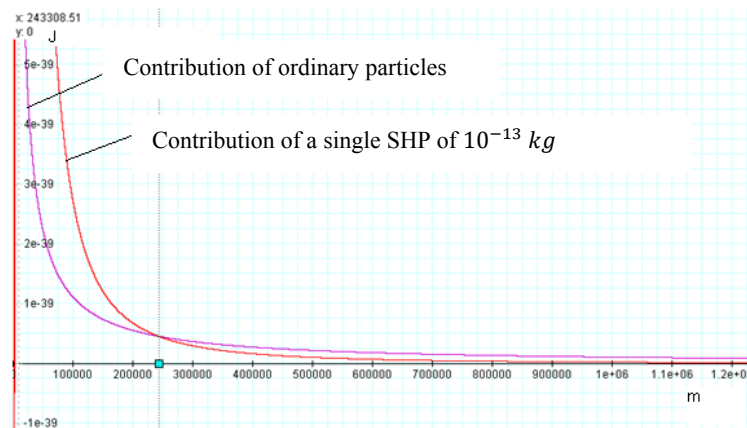


Figure 2-11: Using the same parameters as figure 2-10, the SHP dominance is terminated at 243.3 km , as ordinary matter begins to dominate the interaction at larger distances.

Between those extreme circumstances, however, there is a third condition of a “nearly Newtonian environment.” This environmental classification is comprised of ordinary matter and superheavy particles, where the distances between objects are adequately large that the SHP effect is detectable, but can be treated as a small perturbation to the Newtonian equations (an example of this is the formation of planetary rings, discussed in Chapter V). A relatively simple way to estimate whether a cosmological system is a “nearly Newtonian environment” is to verify that the orbital motions of its bodies are in accordance with Kepler’s laws of motion. The interactions between the Sun, planets, and other objects in our Solar System, for instance, are

included in the “nearly Newtonian” class. However, in the case of galaxies, or deep inside stars, planets or large satellites, the environment can depart significantly from being “nearly Newtonian.”

The UG interaction between two objects can be broken down to the sum of two distinct groups according to the following equation:

Equation 2-1-18

$$V_g = -\frac{G}{a} \sum_i \sum_j \left[M_i M_j \left(e^{a/r} \cos\left(\frac{bM_i M_j}{r}\right) - 1 \right) \right]$$

$$= \left[\frac{-G \sum_i M_i (M_L - \sum_{j_i} M_{j_i})}{r} \right] - \frac{G}{a} \sum_i \sum_{j_i} \left[M_i M_{j_i} \left(e^{a/r} \cos\left(\frac{bM_i M_{j_i}}{r}\right) - 1 \right) \right]$$

where the first summation of index i includes all of the particles in the first object, where the summation of index j includes all of the particles in the second object, and where the summation on j_i includes only the object 2 particles of mass M_{j_i} that are within ten times of their oscillation zonal range with the particle M_i (and therefore, does not include particles of the second object which comply with $r > \frac{10bM_i M_j}{\pi}$ or $M_j < \frac{\pi r}{10bM_i}$).³² Combined with the requirement that $r \gg a$, the contributions to the UG potential energy of all pairs of particles i of object 1 and particles j of object 2 that are not in the j_i sub-group are reduced to approximately their Newtonian interactions. As the overall mass of this group is equal to $M_L - \sum_{j_i} M_{j_i}$, where M_L represents the total mass of the larger object 2, their overall contribution can be replaced by the first term of equation 2-1-18. While the first term describes a classical Newtonian gravitational potential, the second term includes the interactions of all pairs for which their calculated UG contribution to the potential energy of the first object departs significantly from their calculated Newtonian contribution. A similar approach can be taken to calculate the UG force, where

Equation 2-1-19

$$\vec{F}_g = \vec{\nabla} V_g = \frac{\partial V_g}{\partial r} \hat{r} = \frac{G \sum_i M_i (M_L - \sum_{j_i} M_{j_i})}{r^2} \hat{r} +$$

$$+ G \sum_i \sum_{j_i} \left[\frac{M_i M_{j_i}}{r^2} e^{a/r} \left(\cos\left(\frac{bM_i M_{j_i}}{r}\right) - \frac{bM_i M_{j_i}}{a} \sin\left(\frac{bM_i M_{j_i}}{r}\right) \right) \hat{r} \right]$$

In the present case, both conditions of $\frac{bM_i M_j}{r} < \pi/10$ and $\frac{(bM_i M_j)^2}{ar} < 0.1$ (or $M_j < \frac{\pi r}{10bM_i}$ and $M_j < \frac{(ar)^{1/2}}{10bM_i}$) are required in order for the particle j of object 2 to be in the first term of equation 2-1-19. The main benefit of distinguishing between the two terms is that the linear Newtonian

³² The number 10 was arbitrarily selected. The value needs to be sufficiently large to allow the convergence of the UG and Newtonian potentials within the required level of accuracy.

term is in compliance with important Newtonian properties, specifically Newton’s shell theorem, which states the following:

1. A spherically symmetric body affects external objects gravitationally as though all of its mass were concentrated at its center point.
2. An object inside a spherically symmetric shell feels no gravitational force exerted by the shell, regardless of the object’s location within the shell.
3. Within a solid sphere of constant density, the gravitational force varies linearly with distance from the center, becoming zero at the center of the mass.

While the shell theorem holds true when applied to the first term ($\frac{G \sum_i M_i (M_L - \sum_{j_i} M_{j_i})}{r^2} \hat{r}$), the shell theorem does not hold true for the general UG force, and therefore does not hold true for the second terms of equations 2-1-18 and 2-1-19. In summary, when the second terms of equations 2-1-18 and 2-1-19 are small relative to the first Newtonian terms, but still detectable, the gravitational interaction between the two objects can be classified as “nearly Newtonian”³³

Although equation 2- 1-12 provides the minima $R_{n,min} = R_{n,ext}$ (for even n) of the V_g potential energy, the smaller object can become trapped exactly at a minimum only if its velocity v is equal to zero. In the more general case, where the small object velocity is not zero, the orbit will deviate slightly outward from the calculated circular radii of the potential V_g minima. For example, consider the gravitational interaction between a large, spherically symmetric object of mass M_L , and a significantly smaller spherically symmetric object of mass M_s traveling in circular orbit around the large object at non-relativistic velocity. The larger object is assumed to consist of N_M identical superheavy particles of mass M residing in a relatively small core at the center of the object, and of ordinary particles of particle mass m_p and an overall total ordinary particle mass of $M_{Lp} = (M_L - N_M M)$ distributed throughout the object in a spherically symmetric form. Similarly, the small orbiting object is assumed to consist of N_m identical particles of particle mass m and a total mass of $M_s = N_m m$. The circular orbital radius r is assumed to be much greater than the sum of the radius of the small object, the radius of the large object, and the zonal range between the particles of masses m and m_p . Since the orbit is assumed to be circular,³⁴

Equation 2-1-20

$$F_g = \frac{M_s v^2}{r}$$

³³ The process applied here, of separating the contribution of the interaction into a Newtonian term and a non-Newtonian term under the assumption that ordinary matter is positioned in spherically symmetric distribution within either or both objects, significantly reduced the complexity of the equations. Therefore, this approach will often be used in the following chapters.

³⁴ The assumption of a circular orbit is very reasonable, given that at non-relativistic velocities the minima contours of the UG potential energy are spherically symmetric with steep slopes.

Therefore, the kinetic energy T of the small object is given by

Equation 2-1-21

$$T = \frac{1}{2} M_S v^2 = \frac{1}{2} r F_g$$

and the overall sum of the small object potential and kinetic energies is provided by

Equation 2-1-22

$$E = V_g + T = V_g + \frac{1}{2} r F_g$$

Substituting the number of particles in each object and their respective masses into equations 2-1-18 and 2-1-19 yields

Equation 2-1-23

$$\begin{aligned} V_g &= -\frac{G}{a} \sum_i \sum_j \left[M_i M_j (e^{a/r} \cos\left(\frac{bM_i M_j}{r}\right) - 1) \right] \\ &= -\frac{G}{a} m N_m M N_M (e^{a/r} \cos\left(\frac{b m M}{r}\right) - 1) - \frac{G}{a} m N_m m_p N_{m_p} (e^{a/r} \cos\left(\frac{b m_p m}{r}\right) - 1) \end{aligned}$$

Since r is assumed to be much larger than both a and the zonal range between particles of mass m and m_p (therefore $e^{a/r} \approx 1 + \frac{a}{r}$ and $\cos\left(\frac{b m_p m}{r}\right) \approx 1$), and since both objects are assumed to contain a spherically symmetric distribution of matter,

Equation 2-1-24

$$V_g = -\frac{G}{a} m N_m M N_M (e^{a/r} \cos\left(\frac{b m M}{r}\right) - 1) - \frac{G m N_m m_p N_{m_p}}{r}$$

or using $m_p N_{m_p} = (M_L - M N_M)$,

Equation 2-1-25

$$V_g = -\frac{G}{a} m N_m M N_M (e^{a/r} \cos\left(\frac{b m M}{r}\right) - 1) - \frac{G m N_m (M_L - M N_M)}{r}$$

Similarly, the force can be derived from equation 2-1-19, leading to

Equation 2-1-26

$$\vec{F}_g = \frac{G m N_m (M_L - M N_M)}{r^2} \hat{r} + \frac{G m N_m M N_M}{r^2} e^{a/r} \left(\cos\left(\frac{b m M}{r}\right) - \frac{b m M}{a} \sin\left(\frac{b m M}{r}\right) \right) \hat{r}$$

Substituting equations 2-1-25 and 2-2-26 into equation 2-1-22,

Equation 2-1-27

$$E = \frac{G m M N_M N_m}{2r} e^{a/r} \left[\cos\left(\frac{b m M}{r}\right) - \frac{b m M}{a} \sin\left(\frac{b m M}{r}\right) \right] - \frac{G m N_m M N_M}{a} \left[(e^{a/r} \cos\left(\frac{b m M}{r}\right) - 1) \right] + G m N_m (M_L - M N_M) \left(\frac{1}{2r} - \frac{1}{r} \right)$$

leading to

Equation 2-1-28

$$E = GmMN_M N_m \left\{ e^{a/r} \left[\left(\frac{1}{2r} - \frac{1}{a} \right) \cos \left(\frac{bmM}{r} \right) - \frac{bmM}{2ar} \sin \left(\frac{bmM}{r} \right) \right] + \frac{1}{a} \right\} - GmN_m \left(\frac{M_L - MN_M}{2r} \right)$$

Thus,

Equation 2-1-29

$$\begin{aligned} \frac{\partial E}{\partial r} &= \frac{GmMN_M N_m}{r^2} e^{a/r} \left[\left(1 - \frac{a}{2r} \right) \cos \left(\frac{bmM}{r} \right) + \frac{bmM}{2r} \sin \left(\frac{bmM}{r} \right) \right] + \\ &GmMN_M N_m e^{a/r} \left[-\frac{1}{2r^2} \cos \left(\frac{bmM}{r} \right) + \left(\frac{1}{2r} - \frac{1}{a} \right) \left(\frac{-bmM}{r^2} \right) \left(-\sin \left(\frac{bmM}{r} \right) \right) \right] + \\ &+ GmMN_M N_m e^{a/r} \left[\frac{bmM}{2ar^2} \sin \left(\frac{bmM}{r} \right) - \left(\frac{bmM}{2ar} \right) \left(\frac{-bmM}{r^2} \right) \cos \left(\frac{bmM}{r} \right) \right] + GmN_m \left(\frac{M_L - MN_M}{2r^2} \right) \\ &= \frac{GmMN_M N_m}{r^2} e^{a/r} \left[\left(1 - \frac{a}{2r} \right) - \frac{1}{2} + \frac{(bmM)^2}{2ar} \right] \cos \left(\frac{bmM}{r} \right) + \\ &+ \frac{GmMN_M N_m}{r^2} e^{a/r} \left[\frac{bmM}{2r} + \left(\frac{1}{2r} - \frac{1}{a} \right) bmM + \frac{bmM}{2a} \right] \sin \left(\frac{bmM}{r} \right) + GmN_m \left(\frac{M_L - MN_M}{2r^2} \right) \\ \frac{\partial E}{\partial r} &= \frac{GmMN_M N_m}{r^2} e^{a/r} \left\{ \left(\frac{1}{2} \left(1 - \frac{a}{r} + \frac{(bmM)^2}{ar} \right) \right) \cos \left(\frac{bmM}{r} \right) + bmM \left(\frac{1}{r} - \frac{1}{2a} \right) \sin \left(\frac{bmM}{r} \right) \right\} + GmN_m \left(\frac{M_L - MN_M}{2r^2} \right) \end{aligned}$$

If the large object does not consist of any ordinary particles ($M_{Lp} = (M_L - N_M M) = 0$), the orbit will comply with the following equation:

$$\frac{\partial E}{\partial r} = 0 \rightarrow \tan \left(\frac{bmM}{r} \right) = \frac{ar - a^2 + (bmM)^2}{(r - 2a)bmM}$$

or

Equation 2-1-30

$$r = \frac{bmM}{n\pi + \arctan \left(\frac{ar - a^2 + (bmM)^2}{(r - 2a)bmM} \right)}$$

To calculate the closest maximum or minimum in the vicinity of $2a$,

Equation 2-1-31

$$r \cong 2a \cong \frac{bmM}{(n_{2a} \pm \frac{1}{2})\pi}$$

In cases where $r \ll a$,

Equation 2-1-32

$$r \cong \frac{bmM}{n\pi + \arctan\left(\frac{a}{2bmM} - \frac{bmM}{2a}\right)}$$

When $r \ll a$ and $bmM \gg a$,

Equation 2-1-33

$$r \cong \frac{bmM}{n\pi - \arctan\left(\frac{bmM}{2a}\right)} \cong \frac{bmM}{(n - 1/2)\pi}$$

When $r \ll a$ and $bmM \ll a$,

Equation 2-1-34

$$r \cong \frac{bmM}{n\pi + \arctan\left(\frac{a}{2bmM}\right)} \cong \frac{bmM}{(n + 1/2)\pi}$$

In cases where $r \gg a$,

Equation 2-1-35

$$r \cong \frac{bmM}{n\pi + \arctan\left(\frac{a}{bmM} + \frac{bmM}{r}\right)}$$

When $r \gg a$ and $bmM \gg a$,

Equation 2-1-36

$$r \cong \frac{bmM}{n\pi + \arctan\left(\frac{bmM}{r}\right)}$$

When $bmM \gg r \gg a$,

Equation 2-1-37

$$r \cong \frac{bmM}{\left(n + \frac{1}{2}\right)\pi}$$

However, in most cases the overall mass of ordinary matter is expected to exceed the total SHP mass, or $M_L \gg MN_M$. At distances far greater than the size of an atom nucleus, $r \gg a \rightarrow a/r \ll 1$, and $e^{a/r}$ can be replaced by 1. Therefore, equation 2-1-29 will become

Equation 2-1-38

$$\frac{\partial E}{\partial r} = 0 \rightarrow \left(1 + \frac{(bmM)^2}{ar}\right) \cos\left(\frac{bmM}{r}\right) - \left(\frac{bmM}{a}\right) \sin\left(\frac{bmM}{r}\right) + \frac{M_L}{MN_M} = 0$$

For the usual case of $\frac{bmM}{a} \gg 1$ and $\frac{bmM}{r} > 1$ (where the orbiting object is within the zonal oscillation range), this equation reduces to

Equation 2-1-39

$$\frac{\partial E}{\partial r} = 0 \rightarrow \frac{bmM}{r} \cos\left(\frac{bmM}{r}\right) - \sin\left(\frac{bmM}{r}\right) = -\frac{aM_L}{bmM^2N_M}$$

The case of $\frac{aM_L}{bmM^2N_M} \ll 1$:

In the case of $\frac{aM_L}{bmM^2N_M} \ll 1$ equation 2-1-39 leads to $\frac{bmM}{r} \cos\left(\frac{bmM}{r}\right) - \sin\left(\frac{bmM}{r}\right) \approx 0$ or to the same conclusion as in equation 2-1-36

Equation 2-1-40

$$R_{n,ext} \approx \frac{bmM}{n\pi + \arctan\left(\frac{bmM}{R_{n,ext}}\right)} \text{ where } n = 0, 1, 2, \dots$$

with minima at even n values and maxima at odd n values. Thus minima occur at

$$R_{2n,ext} \approx \frac{bmM}{2n\pi + \arctan\left(\frac{bmM}{R_{n,ext}}\right)}, \text{ where } n = 0, 1, 2, \dots$$

The case of $\frac{aM_L}{bmM^2N_M} \gg 1$:

In the case of $\frac{aM_L}{bmM^2N_M} \gg 1$, the $\sin\left(\frac{bmM}{r}\right)$ term in equation 2-1-39 is negligible (as $\left|\sin\left(\frac{bmM}{r}\right)\right| < 1 \ll \frac{aM_L}{bmM^2N_M}$), thus

Equation 2-1-41

$$\cos\left(\frac{bmM}{r}\right) \approx -\frac{aM_L r}{(bm)^2 M^3 N_M}$$

Consequently, minima and maxima occur at

Equation 2-1-42

$$r_n = \frac{bmM}{(2n+1)\pi \pm \arccos(\psi)}$$

where $\psi = \frac{aM_L}{(bm)^2 M^3 N_M} r_n > 0$ and $r_n \ll bmM$ or $n \gg 1$, and where minima occur at the

$$r_n = \frac{bmM}{(2n+1)\pi - \arccos(\psi)}$$

Equation 2-1-41 can be solved only if $0 \leq \psi \leq 1$. Therefore, for minima (and maxima) to occur, the distance r must comply with

Equation 2-1-43

$$r \leq \frac{(bm)^2 M^3 N_M}{aM_L}$$

Note that since $\psi \geq 0$, the arccosine term is limited to the range $0 \leq \arccos(\psi) \leq \pi/2$ and $\lim_{r \rightarrow 0} \arccos(\psi) = \lim_{n \rightarrow \infty} \arccos(\psi) = \arccos(0) = \pi/2$. Additionally, equation 2-1-41 becomes accurate only where $n \gg 1$. As $n \rightarrow \infty$, $r_n \rightarrow 0$. Therefore, for all practical purposes, if the condition of equation 2-1-42 is fulfilled, the minima are expected to occur at

Equation 2-1-44

$$r_n \xrightarrow{n \rightarrow \infty} \frac{bmM}{(2n+1/2)\pi}$$

As a reminder, the given scenario assumes that $n \gg 1$, $a \ll r_n$, $M_L \gg MN_M$,

$$r_n \leq \frac{(bm)^2 M^3 N_M}{aM_L}, \text{ and that } \frac{aM_L}{bmM^2 N_M} \gg 1.$$

The case of $\frac{aM_L}{bmM^2 N_M} \approx 1$

In cases of $\frac{aM_L}{bmM^2 N_M} \approx 1$, equation 2-1-39 leads to $\left| \cos\left(\frac{bmM}{r}\right) \right| = \left| \frac{r}{bmM} \left(\sin\left(\frac{bmM}{r}\right) - \frac{aM_L}{bmM^2 N_M} \right) \right| \leq \frac{2r}{bmM} \ll 1$. Therefore, $\left| \cos\left(\frac{bmM}{r}\right) \right| \approx 0$, and consequently, for an integer $n \gg 1$, $r_n \approx \frac{bmM}{(n+1/2)\pi}$, where minima occur at approximately $r_n \approx \frac{bmM}{(2n+1/2)\pi}$.

Chapter III: The UG equations of Astronomical Objects

Section III-1: The UG Morphology Model- The Non-Relativistic Approach

The goal of this chapter is to develop the equations and tools required for the application of the UG theory to the quantitative analysis of large astronomical objects, such as galaxies and nebulae. For convenience, the reader should keep in mind that throughout this chapter, the term “galaxy” will be broadened to refer to galaxies as well as all types of nebulae, and that the tools and equations developed here are general, and are not limited to galaxies and nebulae. The same tools and equations will be applied in later chapters for the analysis of cosmic voids, planetary rings, as well as to additional astronomical phenomena.

The UG theory is rooted in the assumption that the dominant superheavy particles in a galaxy are produced in areas of extremely high pressure and temperature, and are therefore most likely to be situated at the center, or in orbits at close proximity to the center of the galactic bulge. Each of these superheavy particles can be viewed as part of a point-like group, where a “group” is defined as either a single SHP, or a tight group of SHPs of the same mass that share the same orbit, location and velocity.³⁵ Note that the superheavy particles within a single group, or within different SHP groups, are prevented from collapsing into each other by the UG rejection zones generated between them.³⁶

Although there is no reason to assume that a galaxy center should contain only a single type of SHP, it will be demonstrated via the UG theory that even simple configurations can explain a large portion of the observed galactic morphologies. Figure 3-1 provides a schematic of the two simplest interactions possible between an object composed of ordinary particles located within the galaxy plane at time t_0 and superheavy particles arranged in either a single or binary grouping. Figure 3-1a demonstrates the interaction between the object and a single SHP group orbiting in circular motion of radius A and constant angular velocity w around the center of the galaxy. Figure 3-1b presents the interaction between the object and a binary grouping of identical superheavy particles in circular orbit of radius A around the center of the galaxy.³⁷ It will be demonstrated that the morphology of a galaxy is determined mainly by the velocities and orbital radii of the dominant SHP groups, while the size of the galaxy is determined mainly by the mass of the dominant SHP type, and to a lesser degree by their velocity.³⁸

³⁵ Note that more than one SHP group can share the same space, orbit and velocity. This may occur when superheavy particles of different masses are bonded together to form a single object.

³⁶ While the zonal maxima are the main elements preventing the different individual superheavy particles from collapsing into each other, the conservation of angular momentum also plays a role.

³⁷ Note that there is a distinction between binary SHP groups and any two groups arbitrarily selected. Binary SHP groups share the same orbit, and are always co-linear with the center of the galaxy. Therefore, in the case of binary SHPs, if the spherical coordinates of the first group at any given time t are $(A, \theta, 0)$, the coordinates of the second group at time t must be $(A, \theta + \pi, 0)$. In contrast, in the case of two arbitrary groups, the second group can be located almost anywhere.

³⁸ The dominant SHP types are those which exert the greatest effect on the local morphology or on the properties of the galaxy. Whether a specific type of SHP is dominant in a given area of the galaxy depends on the SHP mass and prevalence relative to other SHPs, on the location of the given area, and on the velocity and distribution of the superheavy particles.

Figure 3-1a

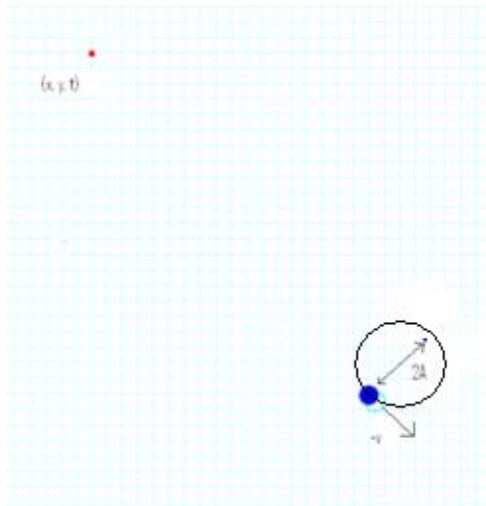


Figure 3-1b

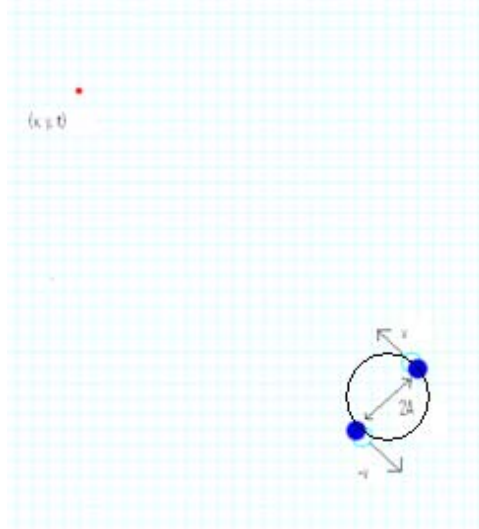


Figure 3-1: Provides a schematic of the two simplest interactions possible between an object composed of ordinary particles located within the galaxy plane at time t_0 (represented by the red point) and SHPs arranged in either a single or binary grouping. Figure 3-1a demonstrates the interaction between the object and a single group orbiting in circular motion of radius A and constant speed around the center of the galaxy. Figure 3-1b presents the interaction between the object and binary SHP groups in circular motion of radius A around the galactic center. The small open circles (cyan) denote the locations of the SHP groups at time t_0 , while the full circles (blue) provide the given SHP locations at time $t_0 - r_i/c$, where r_i/c provides the time required for the gravitational signal to travel from the i^{th} SHP group to the remote particle at distance r_i . This delay will be demonstrated to play an important role in creating the spiral structure.

For simplicity, the provided analysis of galactic morphology will be guided by the following assumptions:

1. The unified gravitational formula of the UG potential energy between two interacting fundamental particles moving at non-relativistic speeds relative to the center of the galaxy is given by equation 2-1-1,

$$V_g = -\frac{GmM}{a} \left(e^{a/r} \cos\left(\frac{bmM}{r}\right) - 1 \right)$$

2. A free-falling frame of reference that covers the entire spacetime of a galaxy during the local time of the entire period of observation³⁹ can be regarded as an inertial frame of reference. This assumption is in line with the conclusion of the currently accepted cosmological model, which states that the effects of general relativity are negligible on the scale of galaxies and galactic clusters.^{40 41} A convenient choice for an inertial frame

³⁹ The observation time is the period of time observed from the point of view of the galaxy, rather than the time measured by the observer. As the observed galaxy is located far from Earth, the detected radiation must have been emitted long ago (for example, several billions years ago). In addition, the radiation detected on Earth is redshifted, since at the time of emission the galaxy was moving away from Earth at high speed relative to our galaxy. Therefore, from the point of view of the observer on Earth, the local clock on Earth runs faster than the same clock in the observed galaxy. The time period studied from the inertial frame of the galaxy should thus be shorter than the length of time perceived by earthbound observation.

⁴⁰ See sections VII-1 to VII-3.

is to set the origin of the frame at the center of the galaxy. For the case of a flat galactic disk, the z axis of the frame can be chosen to be perpendicular to the galactic plane. This specific inertial frame of reference will be referred to as frame S .

3. On their journey from the galaxy to the observer on Earth, photons pass through the gravitational fields of other galaxies. Therefore, the trajectories of the photons may be bent by gravitation, causing a distortion in the perceived morphology of the galaxy via gravitational lensing. The present discussion will be limited to cases where gravitational lensing is too small to significantly affect the perceived morphology of the galaxy.

Radiation redshift, due either to the speed of the observed galaxy relative to the observer, or due to gravitation, affects the wavelength and frequency of galactic radiation, but not the perceived morphology of the galaxy. In addition, the second and third assumptions allow the analysis of galactic morphology to ignore possible distortions due to external gravitational effects on the galaxy, on the observer, or on the spacetime anywhere along the path of the radiation emitted by the galaxy and intercepted by the observer, and to instead rely exclusively on the UG theory and on special relativity within the limits of the given galaxy.⁴²

To further simplify the analysis, the discussion will be restricted to galaxies with the following properties:

4. The galaxy center contains either a single SHP group or a binary grouping in circular orbit of radius A around the galaxy center, where the group(s) consist of a single type of superheavy particles of identical mass.
5. The observer views the galaxy face-on.
6. Due to its rotation, the galaxy is confined to a flat disk with negligible depth, designated as the $z = 0$ plane of the inertial frame S .
7. Tidal forces and other external influences of nearby galaxies are relatively small and can be ignored.
8. The diameter of the galaxy is very small relative to its distance from the observer.
9. The orbiting objects are composed of ordinary matter, and their size is negligible relative to their radius of orbit around the galaxy center.
10. The orbital radii of the objects are significantly greater than the distance between the SHP group(s) and the center of the galaxy.

The above limitations serve to reduce mathematical complexity, and to focus the discussion on the most important factors that influence galaxy morphology. There is nothing preventing the use of the same tools developed here for the case of more complex galaxies that may involve multiple SHP types contained in a number of groups, or for galaxies that are viewed

⁴¹ This assumption does not hold true in the immediate vicinity of a collapsed star, such as a neutron star or a black hole.

⁴² Strong external gravitational fields applied on the galaxy create tidal forces. Therefore, in the presence of strong external gravitational fields, no single inertial frame can cover the entire galaxy. The influence of substantial external gravitational fields on the spacetime along the path of the radiation will result in a gravitational lensing effect, which may distort the observed morphology of the galaxy. In addition, strong external gravitation applied on the observer will result in strong accelerations, and may cause additional morphology distortions.

at different orientations (other than face-on observation), or for cases where the galaxies are influenced by external galaxies, or where the orbiting matter is composed of SHPs as well as ordinary particles. The same types of tools can also be used for the analysis of stellar and planetary systems, and will be applied in Chapter V for the more complex analysis of Saturn's rings.

In principle, the effective distance photons travel on their way from the emitting atom within the galaxy toward the observer depends on the location of the galaxy and on its relative velocity compared to the observer as well as on the velocity and the location of the emitting atom within the galaxy.⁴³ Given assumptions 5, 6 and 8 we are assured that the velocity of the particle that emitted an observed photon is perpendicular to the photon's path. Therefore, regardless of the position or the velocity of the emitting atoms within the galaxy disk at the time of the photon emission, the effective distance between the emitting atoms and the observer and the time it takes the photons to reach the observer are virtually identical and depend only on the distance and velocity of the galaxy relative to the observer.⁴⁴ Furthermore, assumptions 5 and 8 and the observation that the object within the galactic disk moves at non-relativistic velocities relative to the galactic center, assure us that for all practical purposes, any two photons that are detected simultaneously by the observer have traveled the same distance and the same amount of time regardless of the location from which they were emitted within the given galaxy.⁴⁵

Galaxy morphology is typically determined by the spatial distribution of the radiation emitted by ordinary matter within the galaxy that is detected by the observer. The observer's perception of galactic shape is strongly affected by the contrast between areas of high radiation (and therefore, high brightness) and areas of low radiation. The amount of radiation emitted by any given region of a galaxy is related to the density of ordinary matter within this region. The density of ordinary matter, and thus the radiation level, is expected to be higher at locations where the overall energy of orbiting ordinary matter has a local minimum. Thus, identifying the local minima, predominantly those that produce sharp brightness contrast to their background, will provide the theoretical morphology of the galaxy.

The task at hand is to use the UG equation to analyze the energy patterns formed by the combined effect of superheavy particles (either stationary or rotating) at the central core of a galaxy and the surrounding ordinary matter; In particular, to identify the minimum points, contours and arcs, and how they change over time. Establishing this task will facilitate in confirming the initial hypothesis, that in all or most cases, the observed shape and properties of a galaxy can be explained by the configuration of its dominant superheavy particles.

The following equations, developed to identify the local minima, will initially use the symbols c for the speed of light and c_g for the speed of gravitation. The assumption that the propagation speed of gravity is equal to the speed of light will only be made at a later stage. As gravity propagates at a finite speed c_g , the gravitational signal requires time to reach the orbiting

⁴³ The dependency on the relative velocity of the galaxy and the emitting atom is due to relativistic distance contraction.

⁴⁴ This does not include the case of radiation emitted from an atom in the vicinity of a collapsed star.

⁴⁵ The discussion is limited to galactic morphologies driven by self-generated radiation, rather than by absorption or reflection of externally generated radiation.

object. Consider an object with an orbital radius of $r_0 = (x_0^2 + y_0^2 + z_0^2)^{1/2} \gg A$. The gravitational signal (or graviton) detected by the orbiting object at $\vec{X} = (x_0, y_0, z_0)$ at time t_0 in frame S was actually emitted by a superheavy particle at the S position \vec{S}_i at an earlier time t_i , where the emittance time t_i and location \vec{S}_i are related by $t_i = t_0 - \frac{|\vec{X} - \vec{S}_i|}{c_g}$. The period $t_0 - t_i$ presents a delay that increases with the distance $|\vec{X} - \vec{S}_i|$.

The velocity of matter located in the galaxy halo is typically non-relativistic at about a few hundred km/s . For non-relativistic SHP groups with velocities $v = Aw \ll c$, the entire calculation can take place in the rest frame of the center of the galaxy. In this frame, the potential energy of an object composed of N_{m_p} ordinary particles located in the galaxy halo is given approximately by

Equation 3-1-1

$$E(\vec{r}_0, \vec{r}_1, \vec{r}_2) = \frac{-Gm_p M N_{m_p} N_M}{a} \left(e^{\frac{a}{|\vec{r}_0 - \vec{r}_1|}} \cos\left(\frac{bm_p M}{|\vec{r}_0 - \vec{r}_1|}\right) - 1 \right) - \frac{Gm_p M N_{m_p} N_M \Gamma}{a} \left(e^{\frac{a}{|\vec{r}_0 - \vec{r}_2|}} \cos\left(\frac{bm_p M}{|\vec{r}_0 - \vec{r}_2|}\right) - 1 \right) - \frac{Gm_p N_{m_p} M_G}{r_0} Z$$

where \vec{r}_0 denotes the location of the object at time t_0 , and \vec{r}_1 and \vec{r}_2 represent the locations of the two groups of superheavy particles at the time they emitted the gravitational signals intercepted by the object at time t_0 . For simplicity, the total mass of ordinary matter in the galaxy, given by M_G , is assumed to be homogeneously distributed around the galaxy center within a radius R . The value Γ is a positive number defined as the ratio between the number of SHPs in group 2 and group 1. Setting $\Gamma = 0$ for the case of a single SHP group rotating around the center of the galaxy, and $\Gamma = 1$ for the case of identical binary groups, will allow the same set of equations to cover both scenarios. In the case of binary groups where $\Gamma > 0$, both groups are assumed to follow a circular orbit of radius A around the galaxy center with the same constant speed v . It is further assumed that the two SHP groups and the galaxy center are co-linear,⁴⁶ The last term of 3-1-1, which represents the interaction between the ordinary matter of the galaxy and the ordinary matter of the orbiting object includes the variable Z , defined as $Z = 1$ when $r_0 > R$, and as $Z = \frac{1}{2} \left(3 - \frac{r_0^2}{R^2} \right)$ when $r < R$.

The orbiting stars and interstellar gas in a galaxy are expected to gravitate strongly toward regions of lower potential energy, creating areas of increased density in their vicinity. As $M \gg m_p$, the interaction between the galaxy's ordinary matter and the object provides a relatively smooth and slow-changing potential energy curve compared with the rapid oscillations of the potential energy of the object due to its interaction with the galaxy's SHPs. Therefore, as demonstrated in figure 3-2, it is likely that even if the contribution of a galaxy's ordinary matter

⁴⁶ In cases involving two or more SHP groups that are not co-linear with the center of the galaxy, or in cases of groups that rotate at different speeds or at different orbital radii, the potential energy of the orbiting object can be calculated by obtaining the sum of the contributions of all SHP groups, where equation 3-1-1 is applied for all individual (non-binary) groups with a value of $\Gamma = 0$.

to the potential energy of an object is significantly larger than the overall contribution of the galaxy's superheavy particles, the locations of the potential energy minima of the interaction are determined almost entirely by the SHP masses, velocities and locations, while the influence of the galaxy's ordinary matter on the minima locations is almost negligible.⁴⁷

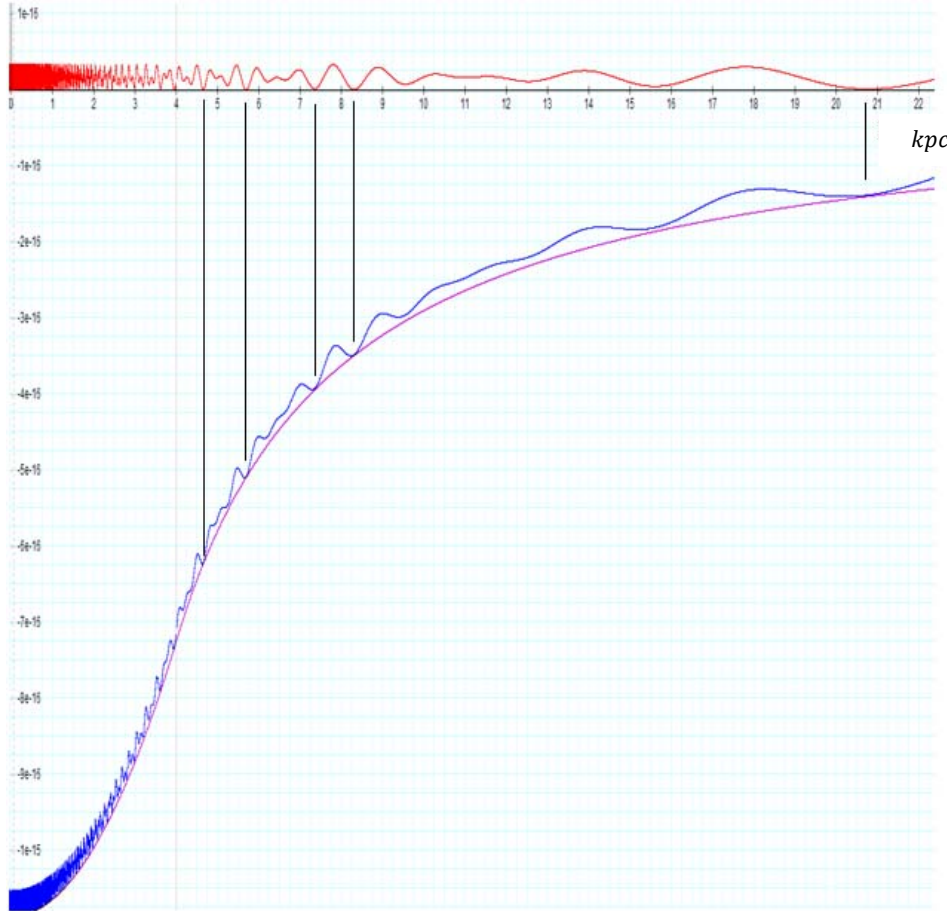


Figure 3-2: Presents the potential energy of a single ordinary particle of mass m_p as a function of its distance from the galaxy center. The red curve provides the potential energy due to the influence of two stationary SHP groups, each containing 54 SHPs of mass $8 \times 10^4 \text{ kg}$, located at a distance of 0.5 kpc from the galaxy center. The two groups are assumed to be positioned in a linear alignment with the galactic center, on either side of the center. The purple curve provides the potential energy of the particle due to $8 \times 10^{41} \text{ kg}$ of ordinary matter distributed homogeneously within a sphere of 4 kpc centered around the galaxy center. The combined effect of both SHP groups and of the galaxy's ordinary matter is demonstrated by the blue curve. The black vertical lines indicate the deepest minima contours between $4.5 \text{ kpc} < r < 22 \text{ kpc}$, demonstrating that the minima occur almost precisely at the same distances, whether or not the effect of the ordinary matter is included. Ordinary matter is expected to be concentrated in the vicinity of the local minima, with higher densities at the deeper minima. Although the potential energy in this example is dominated by the object's interaction with ordinary matter (at least at $r < 22 \text{ kpc}$), the galactic ordinary matter is demonstrated to have little influence on the positions of substantial minima. Note, however, that shallow minima contributed by the two SHP groups may become washed out by the contribution of the galactic ordinary matter. For example, the two shallow minima between 6 kpc and 7 kpc , and the two minima between 10 kpc and 14 kpc in the red curve do not remain minima after the inclusion of the ordinary matter contribution, as shown by the blue curve.

⁴⁷ It will be demonstrated that in the case of relativistic SHP groups, the locations of the object's potential energy minima may depend on the velocity of the SHP as well.

Therefore, locations of high density matter would not be notably affected by the Newtonian term in equation 3-1-1, and can consequently be found in the minima of the following equation:

Equation 3 - 1 - 2

$$\xi(\vec{r}_0, \vec{r}_1, \vec{r}_2) = \frac{-Gm_p M N_{m_p} N_M}{a} \left(e^{\frac{a}{|\vec{r}_0 - \vec{r}_1|}} \cos\left(\frac{bm_p M}{|\vec{r}_0 - \vec{r}_1|}\right) - 1 \right) - \frac{Gm_p M N_{m_p} N_M \Gamma}{a} \left(e^{\frac{a}{|\vec{r}_0 - \vec{r}_2|}} \cos\left(\frac{bm_p M}{|\vec{r}_0 - \vec{r}_2|}\right) - 1 \right)$$

First, the locations at which the gravitational signal was emitted \vec{r}_1 and \vec{r}_2 must be calculated. Due to the finite speed of gravitation, the object located at $\vec{r}_0 = (x_0, y_0, z_0)$ at time t_0 in the inertial frame S simultaneously receives the UG gravitational signals that were emitted by the two respective groups at earlier S times $t_1(x_0, y_0, z_0, t_0)$ and $t_2(x_0, y_0, z_0, t_0)$ by the two respective groups, which were located at $\vec{r}_1 = (x_1(x_0, y_0, z_0, t_0), y_1(x_0, y_0, z_0, t_0), 0)$ and $\vec{r}_2 = (x_2(x_0, y_0, z_0, t_0), y_2(x_0, y_0, z_0, t_0), 0)$ at the time of the signal emissions. Therefore,

$$\begin{aligned} \begin{pmatrix} \vec{r}_1 \\ t_1 \end{pmatrix} &= \begin{pmatrix} x_1 \\ y_1 \\ 0 \\ t_1 \end{pmatrix} = \begin{pmatrix} A * \cos(\omega t_1) \\ A * \sin(\omega t_1) \\ 0 \\ t_1 \end{pmatrix} = \\ &\begin{pmatrix} A * \cos\left(w\left(t_0 - \left((x_0 - A * \cos(\omega t_1))^2 + (y_0 - A * \sin(\omega t_1))^2 + z_0^2\right)^{1/2} / c_g\right)\right) \\ A * \sin\left(w\left(t_0 - \left((x_0 - A * \cos(\omega t_1))^2 + (y_0 - A * \sin(\omega t_1))^2 + z_0^2\right)^{1/2} / c_g\right)\right) \\ 0 \\ t_0 - \left((x_0 - A * \cos(\omega t_1))^2 + (y_0 - A * \sin(\omega t_1))^2 + z_0^2\right)^{1/2} / c_g \end{pmatrix} \end{aligned}$$

and

Equation 3-1-3b

$$\begin{aligned} \begin{pmatrix} \vec{r}_2 \\ t_2 \end{pmatrix} &= \begin{pmatrix} x_2 \\ y_2 \\ 0 \\ t_2 \end{pmatrix} = \begin{pmatrix} -A * \cos(\omega t_2) \\ -A * \sin(\omega t_2) \\ 0 \\ t_2 \end{pmatrix} = \\ &= \begin{pmatrix} -A * \cos\left(w\left(t_0 - \left((x_0 + A * \cos(\omega t_2))^2 + (y_0 + A * \sin(\omega t_2))^2 + z_0^2\right)^{1/2} / c_g\right)\right) \\ -A * \sin\left(w\left(t_0 - \left((x_0 + A * \cos(\omega t_2))^2 + (y_0 + A * \sin(\omega t_2))^2 + z_0^2\right)^{1/2} / c_g\right)\right) \\ 0 \\ t_0 - \left((x_0 + A * \cos(\omega t_2))^2 + (y_0 + A * \sin(\omega t_2))^2 + z_0^2\right)^{1/2} / c_g \end{pmatrix} \end{aligned}$$

Therefore x_1 and y_1 are explicit functions of t_1 , and their dependency on x_0, y_0, z_0 and t_0 is only through t_1 . Similarly, x_2 and y_2 are explicit functions of t_2 , and thus are indirectly dependent on x_0, y_0, z_0 and t_0 .

The minus signs preceding the terms $A * \cos(wt_2)$ and $A * \sin(wt_2)$ in the equation for the second group are due to the requirement that at any given S time, the two groups and their common center of mass are drawn along a straight line, and are thus half a cycle apart. Since the distances between the orbiting object and the two groups in the inertial frame S are usually different, the amount of time required for the gravitational signal to propagate from each group to the object will vary, and frequently $t_1 \neq t_2$. However, as the maximum difference between the two groups is $2A$, $|t_1 - t_2| \leq \frac{2A}{c_g}$.

The values t_1 and t_2 are essential for conducting successful calculations of galactic shapes and properties. Unfortunately, finding a direct analytical solution for equations 3-1-3a and 3-1-3b is not that simple. Instead, it is more practical to use an iterative approach, where the first order of titration is given by

Equation 3-1-4

$$t_1^{(0)} = t_2^{(0)} = t_0 - (x_0^2 + y_0^2 + z_0^2)^{1/2}/c_g$$

Followed by n additional titrations,

$$t_1^{(n+1)} = t_0 - \left((x_0 - A * \cos(wt_1^{(n)}))^2 + (y_0 - A * \sin(wt_1^{(n)}))^2 + z_0^2 \right)^{1/2} / c_g$$

and for the second group,

$$t_2^{(n+1)} = t_0 - \left((x_0 + A * \cos(wt_2^{(n)}))^2 + (y_0 + A * \sin(wt_2^{(n)}))^2 + z_0^2 \right)^{1/2} / c_g$$

At the final stage, the emission times in frame S are assigned the values $t_1 = t_1^{(n+1)}$ and $t_2 = t_2^{(n+1)}$. For the following examples, it is assumed that in the case of $(x_0^2 + y_0^2 + z_0^2)^{1/2} \gg A$, a single iteration can provide sufficiently accurate results. Therefore,

Equation 3-1-5

$$t_1 = t_0 - \frac{\left((x_0 - A * \cos(w(t_0 - (x_0^2 + y_0^2 + z_0^2)^{1/2}/c_g)))^2 + (y_0 - A * \sin(w(t_0 - (x_0^2 + y_0^2 + z_0^2)^{1/2}/c_g)))^2 + z_0^2 \right)^{1/2}}{c_g}$$

and

Equation 3-1-6

$$t_2 = t_0 - \frac{\left((x_0 + A * \cos(w(t_0 - (x_0^2 + y_0^2 + z_0^2)^{1/2}/c_g)))^2 + (y_0 + A * \sin(w(t_0 - (x_0^2 + y_0^2 + z_0^2)^{1/2}/c_g)))^2 + z_0^2 \right)^{1/2}}{c_g}$$

Given the small value of the constant a ($a \approx 5.7 * 10^{-14}$), at galactic distance ranges the exponent terms $e^{\frac{a}{|\vec{r}_0 - \vec{r}_1|}}$ and $e^{\frac{a}{|\vec{r}_0 - \vec{r}_2|}}$ can be replaced by 1. As we are looking for the minima of

equation 3-1-1, the highest density of matter is expected to be concentrated in the vicinity of the deepest minima, which occur at the lowest points of the following equation:

Equation 3-1-7

$$\xi(\vec{r}_0, \vec{r}_1, \vec{r}_2) \cong \frac{Gm_p N_{m_p} N_M M}{a} \left(1 - \cos\left(\frac{bm_p M}{|\vec{r}_0 - \vec{r}_1|}\right)\right) + \frac{Gm_p N_{m_p} N_M M \Gamma}{a} \left(1 - \cos\left(\frac{bm_p M}{|\vec{r}_0 - \vec{r}_2|}\right)\right)$$

Note that at the limit $a/r \rightarrow 0$, $\xi(\vec{r}_0, \vec{r}_1, \vec{r}_2)$ is always greater than or equal to zero. With $0 < a \ll |\hat{r}_0 - \hat{r}_1| \ll bm_p M$ and $0 < a \ll |\hat{r}_0 - \hat{r}_2| \ll bm_p M$, the lowest minima, and therefore the highest density distribution, will occur in the vicinity of the locations \vec{r}_0 that comply with $\xi(\vec{r}_0, \vec{r}_1, \vec{r}_2) < \epsilon$, where $0 < \epsilon \approx 0$. This will happen at locations where both cosine terms are simultaneously equal to 1. Note that at higher levels of potential energy, the discussion can be extended to areas of lower density by simply allowing a range of higher values for ϵ . This method of dividing the range of possible potential energies into slices of ϵ values will be used in the next few chapters to provide the two dimensional contour maps (or isophotes) of the potential energy profile of a galaxy, and to demonstrate the resulting features, such as rings or spiral arms.

III-2: The UG Morphology Model- The Relativistic Approach

The dynamic calculations required for the case of a group of superheavy particles moving at relativistic velocity relative to the inertial frame of reference are somewhat more complex. Force and potential energy are not invariant under Lorentz transformations, and may change form when viewed in different inertial frames moving at relativistic velocities relative to each other. Therefore, a force law must be defined in a specific inertial frame. Prior to Einstein's special theory of relativity, Coulomb's law was known to accurately provide the electromagnetic force applied on a test charge moving at any constant velocity only when the source charge is at rest. When the source charge is not stationary relative to the observer, it generates a magnetic field that applies an additional force on the test particle, resulting in an overall force which may or may not be a central force. Einstein showed that on the basis of Coulomb's force and special relativity alone, one can generate a quantitative description of electric and magnetic interactions between charges moving with arbitrary constant velocities, and that what appears as a purely magnetic field, or as a combination of an electric and a magnetic field, when viewed in one coordinate system may be simply an electric (Coulomb) field when viewed in another coordinate system. The key to developing all of the electromagnetic kinematic and dynamic quantities is to use Coulomb's law only when the calculations are performed in the inertial rest frame of the source charge. Thus, when the source charge moves in respect to a given S frame, the procedure entails the following three steps:

- Step 1: The kinematic and dynamic parameters of the test particle must first be transformed to frame $S1$, in which the source charge is at rest.

- Step 2: Apply the Coulomb force (or potential energy) equation to the test particle.
- Step 3: Transform the particles' parameters back from frame $S1$ to frame S .

All transformations are done via the Lorentz transformations ^(French, 1968). The realization that a force is not invariant under Lorentz transformations, and that the same force that appears as a central force from the point of view of one inertial frame may appear as a non-central force and may be described by a different equation form when viewed in a different inertial frame, led to the language used in the second UG postulate given in Chapter II and repeated below:

UG Postulate II:

The Unified Gravitational force is a force between a pair of particles. When viewed at an inertial rest frame of one of the interacting particles (the source particle), the unified gravitational force applied on the second particle (the test particle) is predominantly a central and conserving force that depends exclusively on the absolute distance between the particles and on the product of their masses.

This basic postulation further led, in conjunction with three additional postulates (as well as the application of the principle of Occam's Razor), to a family of possible gravitational equations, where equation 2-1-1 was selected as the simplest potential energy equation that complies with the given postulates. An additional assumption was made at the beginning of this chapter, stating that a free-falling frame of reference that covers the entire spacetime of a given galaxy during the local time of the observation can be regarded as an inertial frame throughout the galaxy, with the exception of the immediate vicinity of collapsing stars. Under the provided postulates and assumptions, the galaxy can be correctly analyzed via equation 2-1-5 and special relativity. As this equation is only valid in the rest frame of a source particle, calculating the UG force applied to a moving test particle requires a procedure similar to the three-step procedure described above for the case of the Coulomb force. However, there is an important difference: the Coulomb force depends on the particle charges, which are the same in any frame of reference. The UG force equation, however, depends on the particle masses, which are not invariant under the Lorentz transformations.

Therefore, the mass of the test particle m in equation 2-1-5 provides the mass as viewed by the source particle, which is equal to $m_{rest}\gamma(v)$, where m_{rest} is the rest mass of the test particle and $\gamma(v) = \frac{1}{\sqrt{1-\frac{v^2}{c^2}}}$. The same procedure can be used to calculate the potential energy of the test particle via equation 2-1-1.

Therefore, in order to assess the UG effect applied by either SHP group on the object, the calculation must take place in the inertial frame where the group is momentarily at rest, denoted by $S1$ for the first group and $S2$ for the second group. The relativistic velocity of the object relative to the SHP groups can theoretically result from either the relativistic velocities of either

one of the SHP groups $v(t_1)$ and $-v(t_2)$, or from the relativistic velocity of the object ($\vec{u}(t_0)$) relative to the center of the galaxy, or from both. However, matter in the galaxy disk and halo has typically been observed to travel at non-relativistic velocities between 70 km/s and 400 km/s relative to the galactic center. Therefore, to the extent that relativistic effects occur in galaxies, they must be attributed to the relativistic velocities of their SHP groups. The speed of the object thus becomes negligible compared with the relativistic speed of the groups. In such cases, the relativistic velocity between a given SHP group and a given object can be regarded as equal to the velocity of the group.⁴⁸

As mentioned above, the UG force or potential energy equations 2-1-5 and 2-1-1 applied on an orbiting object are not invariant under Lorentz transformation, and are assumed to be valid exclusively in the inertial frame of the source at rest. For the relativistic case of a galaxy consisting of two SHP groups, the UG equation of each group must therefore be calculated in different inertial frames; specifically, in inertial frame $S1$, where the first group is momentarily at rest at the S time t_1 , and in inertial frame $S2$, where the second group is momentarily at rest at S time t_2 . As a reminder, t_1 and t_2 are the S time at which the respective groups emitted the gravitational signals, which were simultaneously intercepted by the orbiting object at S time t_0 . Time t_1 and t_2 are given by equation 3-1-5 and 3-1-6 respectively.

Calculating the potential energy at any arbitrary point (x_0, y_0, z_0, t_0) in the S inertial frame requires the Lorentz transformation of coordinates from frame S to frames $S1$ and $S2$, where the UG equations 2-1-1 or 2-1-5 can be applied. The results are then transformed back to the S frame and combined to provide the overall potential energy or force.

Starting with group 1, the first task is to calculate the magnitude and direction of its velocity at S time t_1 . As assumed above, the coordinates of the first group within the S frame at the S emission time t_1 are given by

Equation 3-1-8

$$x_1(t_1) = A * \cos(\omega t_1) \text{ and } y_1(t_1) = A * \sin(\omega t_1) \text{ and } z_1(t_1) = 0$$

Consequently, the velocity of the SHP group within the S frame is given by the derivative of equation 3-1-8,

Equation 3-1-9

$$\left(v_{x_1}(t_1), v_{y_1}(t_1), v_{z_1}(t_1) \right) = \left(\frac{dx_1(t_1)}{dt_1}, \frac{dy_1(t_1)}{dt_1}, \frac{dz_1(t_1)}{dt_1} \right) = A\omega(-\sin(\omega t_1), \cos(\omega t_1), 0)$$

And

Equation 3-1-10

$$v = \left(v_{x_1}^2 + v_{y_1}^2 + v_{z_1}^2 \right)^{1/2} = A\omega$$

⁴⁸ The mechanism by which the superheavy particles are accelerated to relativistic velocities will be discussed at the end of this chapter.

Note that the angular velocity w may be positive for counterclockwise rotation and negative for clockwise rotation.

As discussed, applying the UG equation 2-1-1 requires the use of the inertial frame where the source mass, in this case group 1, is momentarily at rest. Note that as group 1 travels in circular motion around the center of the galaxy, it is accelerating. Therefore, the group will remain at rest in frame $S1$ for only an infinitesimal period of time.

The distance D_s in frame S between the frame S location of the orbiting object (x_0, y_0, z_0) at the interception time t_0 , and the frame S location of group 1 $(x_1(t_1), y_1(t_1), 0)$ at the time of emission t_1 is given by

Equation 3-1-11

$$D_s = \left((x_0 - x_1(t_1))^2 + (y_0 - y_1(t_1))^2 + z_0^2 \right)^{1/2}$$

where t_1 , $x_1(t_1)$ and $y_1(t_1)$ are given by equation 3-1-3a. Since group 1 is at rest in frame $S1$ at S time t_1 , $S1$ travels at a velocity given by equation 3-1-9 and 3-1-10 relative to the inertial frame S . Therefore, the distance \dot{D}_{s1} between the orbiting object and group 1 in the inertial frame $S1$ is almost always contracted. In calculating the distance \dot{D}_{s1} , it is more convenient to separately calculate the parallel and vertical components of the velocity of group 1 within the rotation plane $Z = 0$.

The component of the distance D_s in the S frame that is parallel to the velocity of group 1 at time t_1 is given by

$$D_{s\parallel} = \left| \frac{((x_0, y_0, z_0) - (x_1(t_1), y_1(t_1), 0)) \circ (v_{x_1}(t_1), v_{y_1}(t_1), 0)}{|(v_{x_1}(t_1), v_{y_1}(t_1), 0)|} \right|$$

where the value of $|(v_{x_1}(t_1), v_{y_1}(t_1), 0)| = v = wA$, as given by equation 3-1-10. Additionally, in circular motion the velocity of the SHP group is perpendicular to the vector connecting the rotating group to the center of the circle. Therefore,

$((x_1(t_1), y_1(t_1), 0)) \circ (v_{x_1}(t_1), v_{y_1}(t_1), 0) = 0$. Consequently,

Equation 3-1-12

$$D_{s\parallel} = \left| \frac{Aw(-x_0 \sin(wt_1) + y_0 \cos(wt_1))}{Aw} \right| = |x_0 \sin(wt_1) - y_0 \cos(wt_1)|$$

Since $D_{s\perp}$ is defined to be perpendicular to $D_{s\parallel}$, and both are contained in the galaxy plane $Z = 0$,

Equation 3-1-13

$$D_{s\perp}^2 = D_s^2 - D_{s\parallel}^2 - z_0^2$$

Since the distance $D_{s\perp}$ is perpendicular to the velocity of group 1, it is not altered by the Lorentz transformation from the S frame to the $S1$ frame of reference. However, the parallel component $D_{s\parallel}$ is contracted via division by $\gamma(v_1)$, where $\gamma(v_1) = \left(1 - \frac{v_1^2}{c^2}\right)^{-1/2}$. In addition, the velocity $\vec{v}_1(\vec{v}, \vec{u})$ is the relative velocity between group 1 and the object, and $v_1 = |\vec{v}_1|$. Therefore,

Equation 3-1-14

$$\dot{D}_{s1\perp} = D_{s\perp} \text{ and } \dot{D}_{s1\parallel} = D_{s\parallel}/\gamma(v_1)$$

Using equations 3-1-13 and 3-1-14

Equation 3-1-15

$$\dot{D}_{s1}^2 = \dot{D}_{s1\perp}^2 + \dot{D}_{s1\parallel}^2 + z_0^2 = D_{s\perp}^2 + \left(D_{s\parallel}/\gamma(v_1)\right)^2 + z_0^2 = D_s^2 + D_{s\parallel}^2 \left[\left(\gamma(v_1)\right)^{-2} - 1\right] = D_s^2 - \frac{v_1^2}{c^2} D_{s\parallel}^2$$

Substituting equations 3-1-11 and 3-1-12 into equation 3-1-15,

Equation 3-1-16

$$\dot{D}_{s1}^2 = (x_0 - x_1(t_1))^2 + (y_0 - y_1(t_1))^2 + z_0^2 - \frac{v_1^2}{c^2} (x_0 \sin(wt_1) - y_0 \cos(wt_1))^2$$

where the $(x_0 - x_1(t_1))^2 + (y_0 - y_1(t_1))^2 + z_0^2$ term is the same as in the non-relativistic case, and the term $-\frac{v_1^2}{c^2} (x_0 \sin(wt_1) - y_0 \cos(wt_1))^2$ provides the relativistic distance contraction. Applying equation 3-1-8, and the fact that $x_1^2(t_1) + y_1^2(t_1) = A^2$,

Equation 3-1-17a

$$\dot{D}_{s1} = \left(x_0^2 + y_0^2 + z_0^2 + A^2 - 2A(x_0 \cos(wt_1) + y_0 \sin(wt_1)) - \frac{v_1^2}{c^2} (x_0 \sin(wt_1) - y_0 \cos(wt_1))^2 \right)^{1/2}$$

In the case of a binary grouping, a phase shift of π must be added to the operand of each cosine and sine term of the second group and the time t_1 should be replaced by t_2 to provide

Equation 3-1-17b

$$\dot{D}_{s2} = \left(x_0^2 + y_0^2 + z_0^2 + A^2 + 2A(x_0 \cos(wt_2) + y_0 \sin(wt_2)) - \frac{v_2^2}{c^2} (x_0 \sin(wt_2) - y_0 \cos(wt_2))^2 \right)^{1/2}$$

When only the contribution of group 1 is taken into account, the object's energy as viewed at the $S1$ inertial frame (at a point denoted by the S coordinates (x_0, y_0, z_0, t_0)) is given by

Equation 3-1-18a

$$\dot{E}_1 = -\frac{GN_M MN_{m_p} m_p \gamma(v_1)}{a} \left(e^{a/\dot{D}_{s1}} \cos\left(\frac{bMm_p \gamma(v_1)}{\dot{D}_{s1}}\right) - 1 \right) + N_{m_p} \gamma(v_1) m_p c^2$$

where the mass of the object's ordinary matter (in the $S1$ inertial frame) can be substituted by the product of its rest mass m_p and $\gamma(v_1)$.

At S time t_2 the second group travels at a velocity of $-\vec{v}(t_2)$ relative to the inertial frame S . Therefore, the object's velocity relative to group 2 is $\vec{v}_2(-\vec{v}, \vec{u})$ (and $v_2 = |\vec{v}_2|$). When only the contribution of group 2 is taken into consideration, a similar analysis of the energy of an object in the $S2$ inertial frame of group 2 is provided by

Equation 3-1-18b

$$\dot{E}_2 = -\frac{GN_M MN_{m_p} m_p \gamma(v_2) \Gamma}{a} \left(e^{a/\dot{D}_{s_2}} \cos\left(\frac{bM m_p \gamma(v_2)}{\dot{D}_{s_2}}\right) - 1 \right) + N_{m_p} \gamma(v_2) m_p c^2$$

To find the overall energy of the object in the S frame, the energy due to group 1 in frame $S1$ and the energy due to group 2 in frame $S2$ (including the object's rest energy) must first be identified and transformed via Lorentz transformations, i.e. $E_i = \gamma(v_i)(\dot{E}_i - v_i \gamma(v_i) m_p v_i)$, where $i = 1$ or $i = 2$. The total energy E can then be derived by adding E_1 and E_2 , and since the energy derived from the object's rest mass was counted twice (once in either inertial frame), it must also be subtracted once. In addition, as stated above, the velocity $\vec{u}(t_0)$ of the object in frame S (typically less than 400 km/s) is non-relativistic, and therefore in the case of relativistic superheavy particles, $u \ll v$. Consequently, $v_1 \approx v_2 \approx v$ and $\gamma(v_1) \approx \gamma(v_2) \approx \gamma(v)$.⁴⁹ This approximation serves to simplify the math, as it removes the need to know the exact direction of the velocity \vec{u} at the S time t_0 ; however, it also eliminates the non-relativistic kinetic energy of the object, which must therefore be added back into the equation. Taking the above, as well as the contribution of the influence of non-relativistic ordinary matter into consideration, the overall energy of the object in the S inertial frame is given by

Equation 3-1-19

$$E = \gamma(v) (\dot{E}_1 - v \gamma(v) N_{m_p} m_p v) + \gamma(v) (\dot{E}_2 - v \gamma(v) N_{m_p} m_p v) - N_{m_p} m_p c^2 + \frac{1}{2} N_{m_p} m_p u^2 - \frac{G m_p N_{m_p} M_G}{r_0} Z$$

Using the identity $\gamma^2(v)(c^2 - v^2) = c^2$ leads to

Equation 3-1-20

$$E = -\frac{GN_M MN_{m_p} m_p \gamma^2(v)}{a} \left(e^{a/\dot{D}_{s_1}} \cos\left(\frac{bM m_p \gamma(v)}{\dot{D}_{s_1}}\right) - 1 \right) - \frac{GN_M MN_{m_p} m_p \gamma^2(v) \Gamma}{a} \left(e^{a/\dot{D}_{s_2}} \cos\left(\frac{bM m_p \gamma(v)}{\dot{D}_{s_2}}\right) - 1 \right) + N_{m_p} m_p c^2 + \frac{1}{2} N_{m_p} m_p u^2 - \frac{G m_p N_{m_p} M_G}{r_0} Z$$

Recall that the morphology of a galaxy is determined by the distribution of the radiation detected by an observer. The observer's perception of morphology is strongly affected by the areas of high radiation (or brightness), and by their contrast with the background level of brightness. The

⁴⁹ According to Lorentz transformations, $v_{1\parallel} = \frac{(u_{1\parallel} + v)}{1 + u_{1\parallel} v/c^2}$ and $v_{1\perp} = \frac{u_{1\perp} / \gamma(v)}{1 + u_{1\parallel} v/c^2}$. Typically, $|u| \ll 1000 \text{ km/s}$, while v is assumed to be relativistic. Therefore, $|u| \ll |v|$, $v_1^2 = v_{1\parallel}^2 + v_{1\perp}^2 \approx v^2$, and consequently $\gamma(v_1) \approx \gamma(v)$. The same holds true for v_2 and $\gamma(v_2)$.

amount of radiation emitted by any given area of the galaxy is largely related to its size and the density of its ordinary matter. The density, however, is expected to be higher at locations where the total energy of the object E has a local minimum, particularly at the relatively deep minima, which are significantly lower than their neighboring minima (as shown in figure 3-2). Since the term $N_{m_p} m_p c^2$ in equation 3-1-20 is independent of location (and time), it does not have any effect on the location of the minima and can be removed. The term $\frac{1}{2} N_{m_p} m_p u^2$ will cause the total energy minima to depart slightly from the potential energy minima, and will shift the orbits of objects in the outward direction, away from the potential energy minimum contours (thus creating a force to balance the centrifugal force). Adhering to the same logic used in equation 3-1-7, the Newtonian term $\frac{G m_p N_{m_p} M_G}{r_0} Z$ bears little influence on the location of the minima. Thus, the high density concentrations should occur where

Equation 3-1-21a

$$\xi = -\frac{G N_M M N_{m_p} m_p \gamma^2(v)}{a} \left(e^{a/\dot{D}_{s_1}} \cos\left(\frac{b M m_p \gamma(v)}{\dot{D}_{s_1}}\right) - 1 \right) - \frac{G N_M M N_{m_p} m_p \gamma^2(v) \Gamma}{a} \left(e^{a/\dot{D}_{s_2}} \cos\left(\frac{b M m_p \gamma(v)}{\dot{D}_{s_2}}\right) - 1 \right) < \epsilon$$

where $0 < \epsilon \approx 0$, and where $e^{a/\dot{D}_{s_1}}$ and $e^{a/\dot{D}_{s_2}}$ can be replaced by 1, resulting in a non-negative energy value for ξ .⁵⁰

Equation 3-1-21b

$$0 < \xi = \frac{G N_M M N_{m_p} m_p \gamma^2(v)}{a} \left(1 - \cos\left(\frac{b M m_p \gamma(v)}{\dot{D}_{s_1}}\right) \right) + \frac{G N_M M N_{m_p} m_p \gamma^2(v) \Gamma}{a} \left(1 - \cos\left(\frac{b M m_p \gamma(v)}{\dot{D}_{s_2}}\right) \right) < \epsilon$$

Equation 3-1-21b holds true in the immediate vicinity of the coordinates at which both $\cos\left(\frac{b M m_p \gamma(v)}{\dot{D}_{s_1}}\right) = 1$ and $\cos\left(\frac{b M m_p \gamma(v)}{\dot{D}_{s_2}}\right) = 1$ at the inertial frame S , where \dot{D}_{s_1} and \dot{D}_{s_2} are given by equations 3-1-17a and 3-1-17b using t_1 and t_2 respectively. As expected, when applied to non-relativistic SHP velocity v , the relativistic equation 3-1-21 provides identical results to the non-relativistic equation 3-1-7, since at non-relativistic velocities $\lim_{v/c \rightarrow 0} \dot{D}_{s_1} = D_{s_1} = |\vec{r}_0 - \vec{r}_1|$, $\lim_{v/c \rightarrow 0} \dot{D}_{s_2} = D_{s_2} = |\vec{r}_0 - \vec{r}_2|$ and $\lim_{(v/c) \rightarrow 0} \gamma(v) = 1$.

Section III-3: The Creation and Motion of SHP groups

Current theories commonly attribute the creation of planets, stars and galaxies to the gravitational collapse of clouds of gas. According to UG Postulate IV, the extreme temperature and pressure conditions that exist at the cores of large astronomical bodies produce superheavy particles. As theorized here, the vast amount of energy that is required for the creation of massive superheavy particles is likely to originate from the energy released by the collapse of ordinary matter towards the center of the astronomical bodies, and by the high level of pressure

⁵⁰ Theoretically, the lowest minima of equation 3-1-21a are negative, however their amplitudes are completely negligible since $a \ll r$ by many orders of magnitude (typically by a factor of 10^{35}).

and temperature at their central core.⁵¹ By the time that an astronomical body reaches a steady state condition, its center comprises of a dense core that contains a significant portion of its ordinary matter, which rotates as a rigid body with constant angular velocity w around its axis of rotation. The assumed circular orbits of the SHP groups around the center of the astronomical body may or may not be located within the central core. In either case, the interaction between orbiting SHP groups and the core ordinary matter produces rotating zones, with maxima and minima contours that intersect with the volume of the core. When the angular velocity of any of the SHP groups is equal to w , these maxima and minima rotate in unison with the ordinary matter of the central core, allowing both the core and the SHP groups to maintain their angular velocity. Conversely, when the angular velocity of any of the SHP groups orbiting the center of the astronomical body varies from w , the angular velocity of the resultant zonal pattern differs from the angular velocity of the core ordinary matter. In such a scenario, ordinary matter within the core will periodically either pass or be overtaken by the maxima and minima of the rotating zone structure. The forces that result from such encounters apply strong torques which accelerate (or decelerate) the rotational velocity of the SHP group, forcing it to converge to the angular velocity of the central core. Therefore, a group composed of superheavy particles of mass $M_1 > \frac{\pi A_1}{bm_p \gamma}$ in a circular orbit of radius $A_1 < c/w$ must rotate at the same angular velocity as the central core.⁵² Consequently, the speed of any SHP group j of SHP mass $M_j > \frac{\pi A_j}{bm_p \gamma}$ with an orbital radius of A_j is given by⁵³

⁵¹ In the case of galaxies, stars, and possibly large planets, some of the energy can be attributed to nuclear reactions deep within their cores.

⁵² Note that the large forces that equalize the angular velocity of the SHP group with that of the central rotating core can only attain sufficient strength if the center of the planet is within the zonal oscillation range of the group's superheavy particles. This will occur only if $A_1 < \frac{bM_1 m_p \gamma}{\pi}$ or $M_1 > \frac{\pi A_1}{bm_p \gamma}$. To avoid violating special relativity, the velocity of the SHP group $v_1 = wA_1$ must be lower than the speed of light, leading to $A_1 = v_1/w < c/w$. Consequently, a group of superheavy particles of mass $M_1 > \pi A_1 / bm_p \gamma$ cannot maintain a circular orbit of radius $A_1 \geq c/w$, and will either be pulled toward the core or ejected outward to an orbit beyond the zonal oscillation range of the given SHP-ordinary matter interaction. Beyond this range the UG gravitational force reduces to the Newtonian force, and the SHP group may orbit at an angular velocity significantly lower than w .

⁵³ This raises the question of whether the UG force is sufficiently strong to keep a relativistic SHP group in a circular orbit. Assume, for example, that the central core rotates at 100 rotations per second and that the orbital radius of the SHP group is 100 km. The resultant speed of the group is thus equal to 62,832 km/sec = 0.21c. The force required to balance the centrifugal force at non-relativistic velocities is equal to $\frac{M_1 v_1^2}{A_1} = 4 * 10^{10} M_1 \text{ m/s}^2$ (note that the relativistic correction may change this number. However, for the purpose of estimating the order of magnitude of the acceleration, the non-relativistic force is sufficiently accurate). Assuming a very small central core (of radius $r \ll A_1$), the acceleration of the superheavy particles is given by $\vec{a} \approx \frac{\vec{F}}{M_1} \approx \frac{G \gamma^2 M_c e^{a/D_{s_1}}}{D_{s_1}^2} \left(\cos\left(\frac{bM_1 \gamma m_p}{D_{s_1}}\right) - \frac{bM_1 \gamma m_p}{a} \sin\left(\frac{bM_1 \gamma m_p}{D_{s_1}}\right) \right) \approx \frac{GM_1 \gamma^3 M_c m_p b}{A_1^2 a} \sin\left(\frac{bM_1 \gamma m_p}{A_1}\right)$, where M_c provides the overall mass of the ordinary matter in the central core, where the value of D_{s_1} is of the order of A_1 , where $a \ll D_{s_1}$ or $e^{a/D_{s_1}} = 1$, and where $\frac{bM_1 \gamma m_p}{a} \gg 1$. Therefore, the terms $\frac{bM_1 \gamma m_p}{a} \approx 2.643 * 10^{30}$ and M_c (which may be of the order of 10^{26} kg) provide the SHP group with the enormous acceleration levels needed to maintain a circular orbit at relativistic velocities. However, this logic cannot be applied to objects composed entirely of ordinary matter, or for SHPs with an oscillation range that is substantially shorter than their radii of orbit around the center of the galaxy. In the latter case, the forces enacted by the rotating center on the SHP group at distance A_1 are outside of the zonal range of the interacting SHP-ordinary particle pairs. Hence, $\sin\left(\frac{bM_1 \gamma m_p}{A_1}\right) \ll 1$, $\frac{bM_1 \gamma m_p}{a} \sin\left(\frac{bM_1 \gamma m_p}{D_{s_1}}\right) \ll 1$ and $\cos\left(\frac{bM_1 \gamma m_p}{D_{s_1}}\right) \approx 1$. The UG force equation therefore converges to the Newtonian force

Equation 3-3-1

$$v_j = wA_j$$

This provides two very important rules that apply to superheavy particles in circular orbit around the center of an astronomical body with a massive rotating central core, where the zonal oscillation ranges of these SHPs are longer than the radius of their orbit around the center of the astronomical body:

Rule 1: In a steady state condition, all orbiting superheavy particles fulfilling the above conditions share the same angular momentum w , where w is the angular velocity of the central core of the astronomical body.

Rule 2: As a consequence of equation 3-3-1, and the requirement that the velocity of a superheavy particle cannot surpass the speed of light, the orbital radii of all superheavy particles that fulfill the above conditions must be shorter than c/w .

There are a few important questions regarding the nature and characteristics of superheavy particles that must be addressed. What is the mechanism that allows for and enables the generation of superheavy particles? What mechanism forces superheavy particles into nearly circular orbits around the center of the galaxy and accelerates them to relativistic velocities? What prevents their immediate annihilation or decay?

The process by which SHPs are created may be similar to the process that generates a particle and an anti-particle of the same mass, such as an electron and positron pair from photons. If that is the case, the momentum and energy of the newly created SHP and anti-SHP are determined by the energy and momentum of the high-energy photons from which they originated. Newly created SHPs that do not have sufficient kinetic energy to escape the (UG) gravitation of the central core will enter an orbit around it. However, as the superheavy particles settle into orbits, they are accelerated over a relatively short period of time by the mechanisms described above, and forced to move at an angular velocity equal to the angular velocity w of the rotating central core. Therefore, according to equation 3-3-1, when the orbital radii of the SHPs are sufficiently large, their velocities become relativistic. Note that complete stability of a superheavy particle orbit can be achieved only if the orbit becomes almost exactly circular (note that the orbit may become slightly deformed by relativistic effects). A non-circular orbit will create a wobbling effect of the zonal pattern relative to the rotating ordinary particles within the planet's central core. This wobbling effect will generate strong torques that force the SHP into a

equation, and is not sufficiently strong to keep relativistic SHP groups in a circular orbit. In the specific case of an object composed exclusively of ordinary matter, the force exerted on the object by the ordinary matter of the central core is also Newtonian, and the UG force generated by the SHPs is proportional to $\frac{GM_1\gamma^3 M_1 m_p b}{A_1^2 a} \sin\left(\frac{bM_1\gamma m_p}{A_1}\right)$, and therefore smaller by a factor of M_1/M_c (of the order of less than 10^{-35}). Hence, the object does not experience sufficiently large forces or torques to force the SHP group to move at the angular velocity of the central core w . Consequently, ordinary matter within this range of distances will not be able to keep pace with the rotation rate of the central core, and will orbit at a much lower angular velocity.

circular orbit where its velocity is perpendicular to the distance vector between the SHP location and the center of the core, and where the angular velocity of the zonal maxima and minima that cross the volume of the core is exactly the same as the angular velocity of the core particles. Upon entering into orbit, the SHP's velocity is still only a small fraction of its final speed when its angular momentum becomes equal to w . Consequently, when a superheavy particle enters an orbit with relatively low velocity, other superheavy particles along the same orbit with an angular velocity of w are moving at much higher speeds, and are therefore able to catch up and bond⁵⁴ with the new particle within a very short period of time, generating a group of superheavy particles. This process may be repeated many times as the SHP groups grow to include multiple superheavy particles.

In regard to the question of how superheavy particles remain stable, avoiding either annihilation or decaying into smaller particles, all known particles aside from protons and electrons (as well as their anti-particles) are unstable when they are free or un-bonded. However, the neutron, which is also unstable when free, is known to become stable when it is bonded to a proton(s). The fact that SHPs are bonded to the central core of the planet or to other SHPs (within a group) may explain how they remain stable and avoid decay. Moreover, the strong rejection zones between SHPs and anti-SHPs may keep them apart and prevent their annihilation while in orbit around the same center of rotation.

Section III-4: The Issue of the Tail Wagging the Dog

At first sight the UG theory seems to pose the inherent problem of the “tail wagging the dog.” As will be shown in the following chapters, UG calculations suggest that SHP groups of a total mass of the order of few hundreds of kilograms dictate the overall structure of Saturn's ring and satellite system, which amounts to an overall mass of approximately 10^{24} kg. Similarly, SHP groups of a total mass of the order of 10^4 kg to 10^7 kg will be shown to determine the overall morphology of a galaxy of a mass of about 10^{38} kg to 10^{43} kg. The force that a superheavy particle of a mass of $1.15 * 10^{-8}$ kg is capable of exerting on ordinary matter within its zonal oscillation range at distances of $a \ll r < \frac{bM_1m_p}{\pi} \approx 552,000$ km is about $\frac{bM_1m_p}{a} \approx 3.04 * 10^{22}$ times larger than the Newtonian force applied by a point-like sphere of ordinary matter of a total mass of M_1 from the same distance.⁵⁵

However, as the mass of the SHP groups is negligible in comparison to the mass of ordinary matter within a galactic disk, or within a system of planetary rings and satellites, the SHP orbits should be profoundly affected by the gravitational influence of ordinary matter. Furthermore, the overall SHP effect exerted on the heavier ordinary matter should be minimal, as the overall mass of the ordinary matter of a galactic or planetary system is larger by many orders of magnitude. Yet, as will be seen, the model here assumes, for example, that in the case of

⁵⁴ via the UG force acting between two superheavy particles.

⁵⁵ These calculated numbers are even larger when the relativistic corrections are taken into account.

planetary systems, the orbits of SHP groups are completely unaffected by the matter in the rings and satellites, while the rings and the satellite orbits are curved by the effect of the SHP groups.

The logic behind this assumption is quite simple. The SHP groups are not free, and are held in circular orbit by the central rotating core of the planet. As the superheavy particles transfer energy and angular momentum to orbiting matter outside of the massive central core, they may lose angular momentum and energy to the orbiting objects, yet are prevented from slowing down or leaving their orbit around the central core, which is few orders of magnitude heavier than the overall mass of the planet's ring and satellite system. Moreover, the same mechanism which led to equation 3-3-1 ($v_j = wA_j$) forces the SHPs to rotate around the center of the planet at the exact same angular velocity w as the central core. In addition, the SHP group is prevented from significantly reducing or increasing its radius of orbit by the nearby maxima that confined its orbit. Therefore, the energy and angular momentum lost (or gained) by the SHP to the ring and satellite system must be replenished immediately by the far more massive rotating central core. Consequently, the SHP group will maintain the same angular velocity as that of the rotating center and the same orbit and speed. An analogy to this concept is the image of a free rigid rod of almost no mass pushing a small ship. As the mass of the rod is negligible compared with the mass of the ship, the force acting between the two objects will essentially influence the momentum and velocity of the rod, bearing virtually no effect on the momentum and velocity of the ship. However, if the rod is attached to a much larger ship that is using the rod to push the small ship, the opposite effect will occur, and there will be minimal change in the momentum and speed of the rigid rod, which is now part of the much larger ship, while the momentum and velocity of the small ship will change significantly.

Chapter IV: Applying the UG Theory to Model Galaxy Morphology

Images emerging from the Hubble space telescope have revealed a number of planetary nebulae and galaxies with complex and varied morphologies. While different mechanisms have been proposed to influence certain galactic forms, the mechanisms that drive the diverse morphologies are not yet well-understood.

The goal of this Chapter is to apply the UG theory to large astronomical objects, such as nebulae and galaxies, and to demonstrate the viability of the theory by explaining how relatively simple SHP configurations can provide the mechanism which drives the creation and maintenance of a number of poorly understood galactic morphologies and properties, including the mechanism responsible for the creation and maintenance of the various types of spiral galaxies.

Section IV-I: Two Dimensional Potential Energy Mapping and Derivation of Morphology

The structure and dynamics of galaxies and nebulae can be analyzed using the equations developed in Chapter III. Specifically, equation 3-1-20 will be applied to a number of observed morphologies with the anticipation that the level of radiation emitted from a given section of a galaxy should be greater in areas of higher density. The maxima and minima of the radiation are thus expected to follow the respective patterns of the minima and maxima of the ordinary matter potential energy.

Equation 3-1-20

$$E = -\frac{GN_M MN_{m_p} m_p \gamma^2(v)}{a} \left(e^{a/\dot{D}_{s_1}} \cos\left(\frac{bMm_p \gamma(v)}{\dot{D}_{s_1}}\right) - 1 \right) - \frac{GN_M MN_{m_p} m_p \gamma^2(v) \Gamma}{a} \left(e^{a/\dot{D}_{s_2}} \cos\left(\frac{bMm_p \gamma(v)}{\dot{D}_{s_2}}\right) - 1 \right) + N_{m_p} m_p c^2 + \frac{1}{2} N_{m_p} m_p u^2 - \frac{Gm_p N_{m_p} M_G}{r_0}$$

N_M and ΓN_M denote the number of superheavy particles of SHP mass M in the first and second SHP groups of a binary, where both groups travel in a circular orbit of radius A around the center of the galaxy at a constant speed v and are collinear with the center. A vast majority of the ordinary matter M_G is assumed to be distributed in a spherically symmetric⁵⁶ organization within a sphere of radius $R < r_0$ around the center of the given galaxy. The orbiting object is assumed to contain N_{m_p} particles of mass m_p , and to move at a non-relativistic velocity \vec{u} relative to the center of the galaxy. The terms \dot{D}_{s_1} and \dot{D}_{s_2} provide the distances traveled by the gravitational signals between the time of their emission by the two groups (S times t_1 and t_2) and the S time t_0 of their interception by the object as measured in the respective SHP group inertial frames of reference at the time of emission, and are given by (see equations 3-1-17a and b of Chapter III)

⁵⁶ At $r_0 > R$, this simplifying assumption can replace the more restrictive assumption of a homogeneous distribution of ordinary matter within the galaxy or nebula.

Equation 3-1-17a

$$\dot{D}_{s1} = \left(x_0^2 + y_0^2 + A^2 - 2A(x_0 \cos(wt_1) + y_0 \sin(wt_1)) - \frac{v_1^2}{c^2} (x_0 \sin(wt_1) - y_0 \cos(wt_1))^2 + z_0^2 \right)^{1/2}$$

and

Equation 3-1-17b

$$\dot{D}_{s2} = \left(x_0^2 + y_0^2 + A^2 + 2A(x_0 \cos(wt_2) + y_0 \sin(wt_2)) - \frac{v_2^2}{c^2} (x_0 \sin(wt_2) - y_0 \cos(wt_2))^2 + z_0^2 \right)^{1/2}$$

The times t_1 and t_2 are approximated by

Equation 3-1-5

$$t_1 = t_0 - \frac{\left(\left(x_0 - A * \cos \left(w(t_0 - (x_0^2 + y_0^2 + z_0^2)^{1/2}/c) \right) \right)^2 + \left(y_0 - A * \sin \left(w(t_0 - (x_0^2 + y_0^2 + z_0^2)^{1/2}/c) \right) \right)^2 + z_0^2 \right)^{1/2}}{c}$$

and

Equation 3-1-6

$$t_2 = t_0 - \frac{\left(\left(x_0 + A * \cos \left(w(t_0 - (x_0^2 + y_0^2 + z_0^2)^{1/2}/c) \right) \right)^2 + \left(y_0 + A * \sin \left(w(t_0 - (x_0^2 + y_0^2 + z_0^2)^{1/2}/c) \right) \right)^2 + z_0^2 \right)^{1/2}}{c}$$

where the speed of gravitation c_g is assumed to be equal the speed of light c and $\gamma(v) =$

$\left(1 - \frac{v^2}{c^2} \right)^{-1/2}$. Equation 3-1-20 includes two potential energy terms contributed by the two SHP groups,

$$-\frac{GN_M MN_{m_p} m_p \gamma^2(v)}{a} \left(e^{a/\dot{D}_{s1}} \cos \left(\frac{bM m_p \gamma(v)}{\dot{D}_{s1}} \right) - 1 \right) \text{ and } -\frac{GN_M MN_{m_p} m_p \gamma^2(v) \Gamma}{a} \left(e^{a/\dot{D}_{s2}} \cos \left(\frac{bM m_p \gamma(v)}{\dot{D}_{s2}} \right) - 1 \right),$$

a potential energy term contributed by the galaxy's ordinary matter $-\frac{Gm_p N_{m_p} M_G}{r_0}$, as well as the

non-relativistic object's kinetic energy term $\frac{1}{2} N_{m_p} m_p u^2$ and its rest mass energy term $N_{m_p} m_p c^2$.

The kinetic energy term shifts the actual orbit of the object in the outward direction from the potential energy minima (to balance the centrifugal force). However, the existence of kinetic energy simply pushes the n^{th} energy minimum contour to somewhere between the n^{th} potential energy minimum and the $n - 1$ maximum contour. The visual effect of this shift on the morphology of the galaxy is relatively small and should not bear a significant influence on the galaxy's overall morphology. Moreover, the rest mass energy term is independent of the location of the particle within the galaxy and therefore does not affect the location of the minima or, consequently, the galaxy's morphology. Therefore, the following two dimensional maps will omit the kinetic energy and the rest mass energy terms, and will display only the relevant potential energy terms. Overall, these changes lead to the highest levels of ordinary matter (and

therefore the highest level of radiation) at close proximity to the minima of the following equation:

Equation 4-1-1a

$$E = -\frac{GN_M MN_{m_p} m_p \gamma^2(v)}{a} \left(e^{a/\dot{D}_{s_1}} \cos\left(\frac{bMm_p \gamma(v)}{\dot{D}_{s_1}}\right) - 1 \right) - \frac{GN_M MN_{m_p} m_p \gamma^2(v) \Gamma}{a} \left(e^{a/\dot{D}_{s_2}} \cos\left(\frac{bMm_p \gamma(v)}{\dot{D}_{s_2}}\right) - 1 \right) - \frac{Gm_p N_{m_p} M_G}{r_0}$$

or

Equation 4-1-1b

$$E = -GN_M N_{m_p} \left[\frac{Mm_p \gamma^2(v)}{a} \left(e^{a/\dot{D}_{s_1}} \cos\left(\frac{bMm_p \gamma(v)}{\dot{D}_{s_1}}\right) - 1 \right) + \frac{Mm_p \gamma^2(v) \Gamma}{a} \left(e^{a/\dot{D}_{s_2}} \cos\left(\frac{bMm_p \gamma(v)}{\dot{D}_{s_2}}\right) - 1 \right) + \frac{m_p (M_G/N_M)}{r_0} \right]$$

Note that the observational resolution within galaxies and nebulae is of the order of 1 pc (1 pc is about $3.08 * 10^{16}$ m), which is far greater than $a = 5.7 * 10^{-14}$ m. The term $e^{a/r}$ is therefore indistinguishable from 1, and may be replaced by it.

The following succession of examples will illustrate how the different parameters A , M , N_M , w (or equivalently $v = wA$), M_G and Γ of equation 4-1-1a (or 4-1-1b) affect the morphology, dynamics and classification of a galaxy (or nebula) and its interaction with companion galaxies. Note that multiplying equation 4-1-1b by any constant greater than zero would not affect the location of its minima, and therefore would not alter the morphology of the nebula or galaxy. Therefore, the morphology is independent of the number of ordinary particles of mass m_p of the object, denoted N_{m_p} , and setting the value $N_{m_p} = 1$ will provide the same morphology. Similarly, when the equation is written in the form given by 4-1-1b (where M_G is replaced by M_G/N_M within the parentheses) the morphology of the galaxy is unaltered by the replacement of N_M by 1 (as long as M_G is replaced by the original value of M_G/N_M).⁵⁷

The general approach taken here is to modify the remaining parameters one or two at a time, and to review how morphology (and therefore morphological classification, such as the Hubble classification) changes continuously with variation of the individual parameters. We begin with the parameters Γ and A , followed by v , M and M_G/N_M .

Section IV-1-1: Low Velocity SHP Group Rotation

In the following discussion it is assumed that while the rotational velocity of the given galaxy as a whole is fast enough to flatten the galactic plane into a rotating disk, the velocities of

⁵⁷ For clarification, while the energy of the object is modified by these transformations, the galaxy morphology, which is driven by the location of the minima, is unaffected by the reduction of N_M and N_{m_p} to 1. However, the amount of galactic radiation will decrease (see theorem A-2 in Appendix A).

its SHP groups are still relatively low. For the provided examples, ‘slow’ SHP group rotation implies that the velocity of the SHP group(s) is non-relativistic ($v = wA \ll c$) and that the distance traveled by the SHP group during the time it takes the gravitational signal to propagate from the SHP group to the orbiting object is negligible.

The density of matter begins to decline rapidly beyond the farthest major minimum contour (beyond the radius of the $n = 2$ minimum r_2 of the dominant SHP) at $r > r_2 \approx \frac{bm_p M}{2\pi}$. Therefore, the galaxy is mainly visible at $r \lesssim r_2$, which defines the outer borders of the galactic disk. For the case of an object located at a distance r from the galaxy center where $A \ll r \lesssim r_2$, it takes the gravitational signal approximately $r/c \lesssim r_2/c$ seconds to pass the distance between the SHP group and the orbiting object. During this period of time the SHP group(s) rotates by an angle of $\varphi \lesssim w r_2/c = \frac{v r_2}{Ac} \approx \frac{v}{Ac} \frac{bm_p M}{2\pi}$. For this amount of rotation to be insignificant v must comply with⁵⁸

Equation 4-1-2

$$v \ll \frac{2\pi Ac}{bm_p M}$$

Figure 4-1 presents a two dimensional map of the calculated potential energy of an ordinary particle of mass m_p as a function of its location $(x_0, y_0, 0, t_0)$ in the rotational disk plane of a simple hypothetical object containing a single stationary SHP of mass $0.156 * 10^4 \text{ kg}$ at its center. The figure was derived via equation 4-1-1a using the parameters $\Gamma = 0$, $A = 0 \text{ km}$, $N_M = 1$, $N_{m_p} = 1$, $M = 0.156 * 10^4 \text{ kg}$, $v \approx 0 \text{ km/s}$, and $M_G = 0 \text{ kg}$). The potential energy is demonstrated via a color-coded map, where brighter color values indicate lower potential energy and darker colors represent higher potential energy levels. The upper curve provides the potential energy along the x axis, and its minima and maxima thus correspond to the light and dark color values respectively along the x axis. In order to create the two dimensional map, a set of K energy threshold levels $\{\varepsilon_k\}$ were selected, where k is an integer ($0 \leq k \leq K$ and $\varepsilon_k > \varepsilon_l$ when $k > l$). Each location (x_0, y_0) on the rotating disk at $z_0 = 0$ at time t_0 was layered in yellow once for each k value, where $E(x_0, y_0, 0, t_0)$ of equation 4-1-1a is greater than ε_k . Therefore, an area where the potential energy is higher than the highest energy threshold ε_K is layered $K + 1$ times and appears very dark. An area where the potential energy E complies with $\varepsilon_0 < E(x_0, y_0, z_0, t_0) < \varepsilon_1$ is layered by a single layer of color and appears as light yellow. An

⁵⁸ Note that the energy required for the creation of superheavy particles is assumed to be generated by the vast amount of energy released during the collapse of a cloud of gas composed of ordinary matter toward its center. In the process of collapse, the moment of inertia of the collapsing gas cloud is reduced by a large factor, or $I_{final} \ll I_{initial}$. As the total angular momentum of the cloud needs to be preserved, or $w_{final} I_{final} = w_{initial} I_{initial}$, even a very small initial angular velocity $w_{initial}$ will be accelerated to high angular velocity $w_{final} = w_{initial} \frac{I_{initial}}{I_{final}} \gg w_{initial}$. Therefore, the angular velocity of the galaxy’s central core and its SHPs should become elevated immediately after the collapse. However, over time the galaxy’s angular momentum may be reduced substantially by a number of mechanisms, such as galactic wind or collisions between galaxies, resulting in a gradual slowing of the rotation of the galactic core and its superheavy particles.

area with a potential energy $E(x_0, y_0, z_0, t_0) < \varepsilon_0$ remains unlayered and consequently appears white.

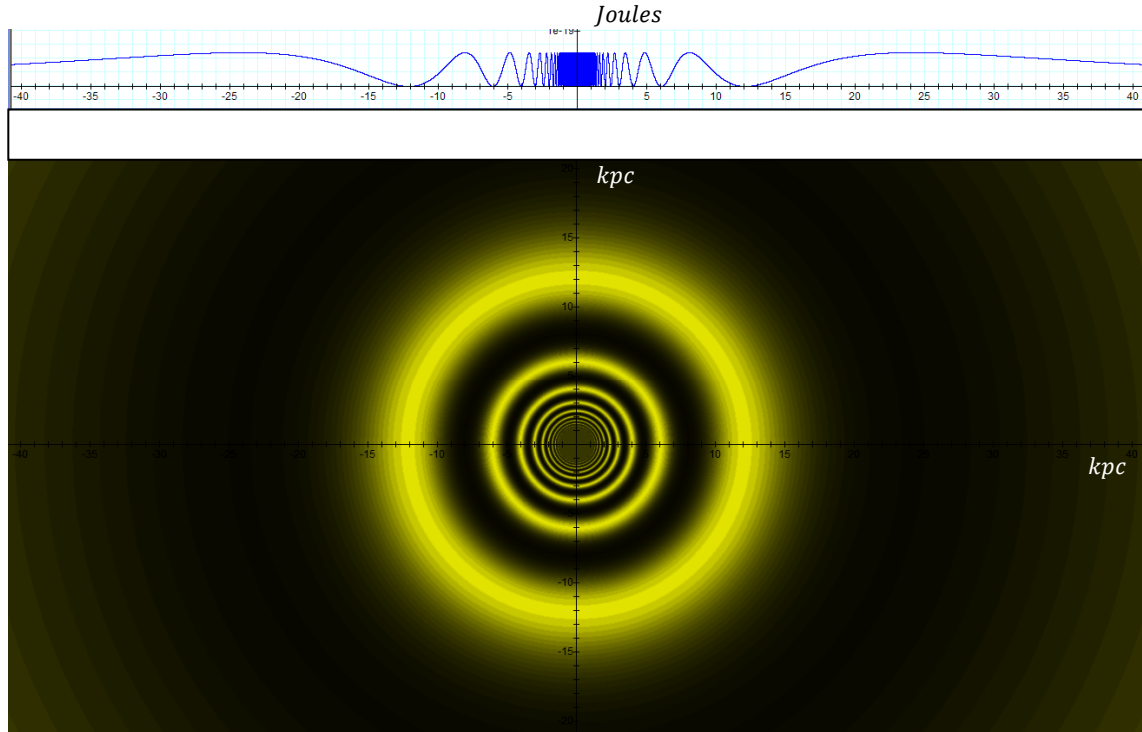


Figure 4-1: The lower image displays the two dimensional color map of the calculated potential energy of an ordinary particle of mass m_p as a function of its location $(x_0, y_0, 0, t_0)$ for the case of a single stationary SHP group located at $(0,0,0)$ and composed of a single SHP of mass M . The upper image provides the potential energy along the x axis, and is displayed in order to identify the exact minima locations. A contour that is brighter than its immediate neighboring contours is at a local minimum of the potential energy, while a contour that is darker than its immediate neighboring contours is at a local maximum. Calculations were performed via equation 4-1-1a using the following values: $\Gamma = 0$, $M = 0.156 * 10^5 \text{ kg}$, $v = 0 \text{ m/s}$, $A = 10^{-9} \text{ kpc}$, $c = 300,000 \text{ km/s}$, $M_G = 0$, $N_M = 1$, $N_{m_p} = 1$, $m_p = 1.674 * 10^{-27} \text{ kg}$.

The resultant two dimensional map displays concentric contours of maxima and minima, with an increasing density of zones as the distance to the galaxy center is reduced. Since on galactic scales $r \gg a$, the potential energy of the maxima is equal to $\frac{2GMm_p}{a}$, while the minima contours are virtually at zero energy.⁵⁹

The pattern of the matter density of a galaxy centered around a single SHP group provides for the existence of rings, however does not account for the existence of stellar systems. Stellar systems can be explained with the introduction of the concept of multiple SHP groups. In

⁵⁹ Recall that at distances $r \gg a$, the exponent $e^{a/\hat{D}_{s1}} = e^{a/\hat{D}_{s2}} = 1$, and that the maxima and the minima of equation 4-1-1a occur when both $\cos\left(\frac{bMm_p\gamma(v)}{\hat{D}_{s1}}\right)$ and $\cos\left(\frac{bMm_p\gamma(v)}{\hat{D}_{s2}}\right)$ are equal to -1 or 1 respectively. Using the assumed values of $M_G = 0$, $N_M = 1$, $N_{m_p} = 1$, $\Gamma = 0$, and $v \ll c$ (and therefore $\gamma = 1$), the resultant potential energy is given as $E = \frac{2GMm_p}{a}$ at the maxima, and as virtually zero energy at the minima. Further note that the overall color value at the center of this hypothetical galaxy is relatively dark. This is due to the arbitrary and unrealistic assumption that the galaxy contains only SHPs and no ordinary matter ($M_G = 0$). In a more realistic model, where M_G is substantially large, the center appears brighter than the surrounding galaxy (see figures 4-4d, 4-8e, 4-9a and 4-10a).

the following section, star formation will be addressed in the special case of stationary or very slow rotating binary SHP groups.

Section IV-1-2: Star Formation via Binary SHP groups

A two dimensional map of a hypothetical galaxy containing two identical stationary superheavy particle groups separated by some arbitrary distance $2A$ is demonstrated in figures 4-2a to 4-2e (using $\Gamma = 1$, $A > 0$, $N_M = N_{m_p} = 1$, $v = 0$ and $M_G = 0$). The two sets of concentric minima contours contributed by the two SHP groups to the overall potential energy of the test particle are shown in 4-2a to 4-2d, where the minima of SHP group 1 are indicated in blue and the minima of SHP group 2 are indicated in violet.⁶⁰ As the discussion is limited to the case where both SHP groups are composed of the same single SHP of mass M , the two sets of circular contours are identical and are shifted from each other by a distance of $2A$. Any pair of minima circles respectively generated by SHP group 1 and SHP group 2 may either intersect at one or two points, or may not intersect at all. As the overall potential energy of a test particle at any given location is equal to the sum of the potential energy contributed by each of the SHP groups, the lowest minima will occur at any point where a minimum circular contour produced by group 1 intersects with a circular minimum contour produced by group 2. At these points, both cosine terms in equation 4-1-1a are equal to 1.⁶¹ The density of ordinary matter is thus expected to peak at these local minima, where dense clouds of gas are subsequently formed. The collapse of these dense and massive clouds may lead to star formation and to the creation of the panoramic night sky view on a global scale.⁶²

A minimum circle created by the first SHP group will not intersect with a minimum circle created by the second SHP group if the sum of their radii is shorter than $2A$, or when the difference between their two radii is larger than $2A$. Pairs of minima circles, where the sum of their radii is greater than $2A$ and the difference between their radii is less than $2A$, intersect at exactly two distinct points. Theoretically, when the sum or the difference of the two radii are exactly $2A$, the pair of circles can intersect only at a single point. However, in reality, when the sum or the difference of the radii approach the exact value of $2A$, the two intersecting points approach each other, and the two circular arcs located between the two intersecting points nearly overlap to create a minimum arc at which the density of matter is high.⁶³

⁶⁰ Note that according to equation 4-1-1a, the radii of the minima circles are dependent on the SHP mass and are independent of the number of superheavy particles in each SHP group.

⁶¹ This is correct since typically \dot{D}_{s_1} and \dot{D}_{s_2} are greater than or of the order of $10^{16} m$, while $a = 5.7 * 10^{-14} m$. Therefore, $e^{a/\dot{D}_{s_1}} = 1$. In addition, the influence of ordinary matter is assumed to be negligible at this point of the discussion.

⁶² A more detailed explanation of how stars are formed and the influence of rotation on the process will be discussed later on in chapter VI. A similar mechanism on larger scale can create entire galaxies (within clusters), which in turn generates a large population of stars. Thus, the panoramic view of the night sky consists of galaxies and stars.

⁶³ When the two intersecting points are sufficiently close, two nearby star systems are likely to form. If the two stars are sufficiently massive, the gravitational interaction between them may become stronger than their interaction with the galaxy center, and they may consequently begin to orbit around each other as well as around the galaxy center. This can explain the occurrence of binary star systems, as well as their low abundance relative to the number of single star systems. This may further be applied within the Solar System to provide a possible explanation for how the Earth and Moon system was created.

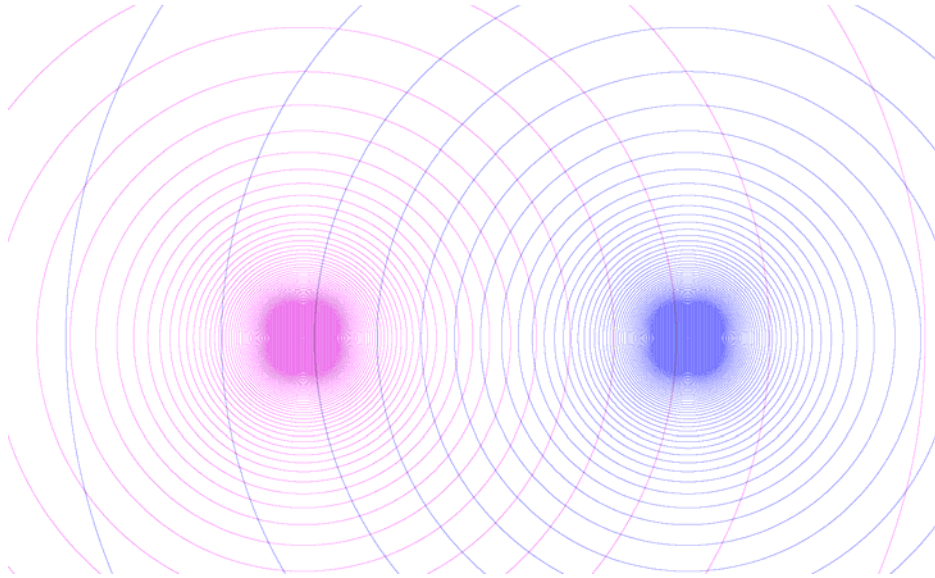


Figure 4-2a: The intersections of the minima contours of two SHP groups create local minima where clouds of gas are formed. The collapse of these clouds generates star formation.

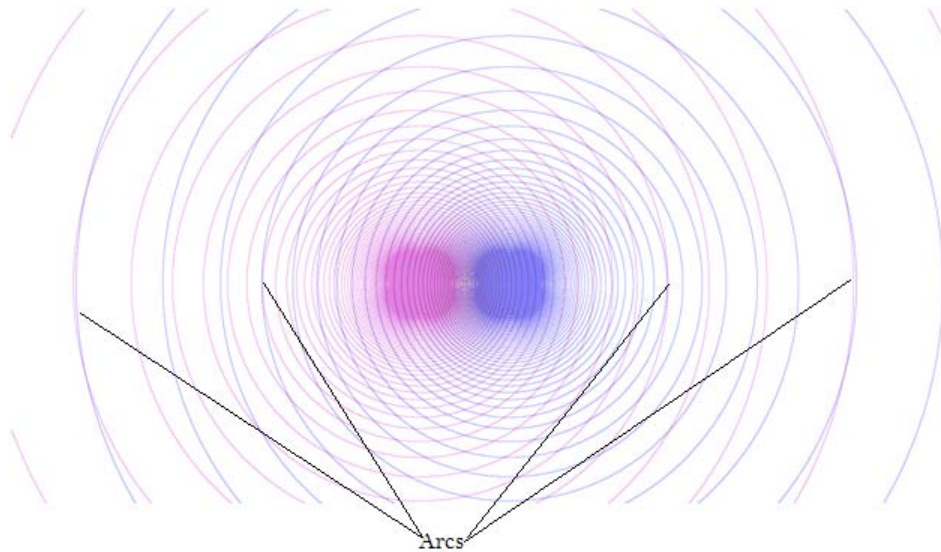


Figure 4-2b: Decreasing the distance between the SHP groups substantially increases the number of intersections (and thus the number of stars formed). Note the occasional occurrence of arcs, which resemble the appearance of filaments.

As demonstrated in figures 4-2b and c, such arcs (or filaments) are formed by the intersection of minima circles with radii that comply with $|R_1 \pm R_2| \approx 2A$. Note that the arcs are perpendicular to the line connecting the two SHP groups. As the respective radii R_1 and R_2 of the intersecting circles increase, the length of the arc increases as well. At sufficiently low zonal indices, where the difference between two successive minima is larger than $2A$, the two circular contours can intersect only if their radii are equal ($R_1 = R_2 \gg A$), creating two arcs around the two intersection points.⁶⁴

⁶⁴ This is true as long as the assumption that the two groups consist of superheavy particles of equal mass holds true.

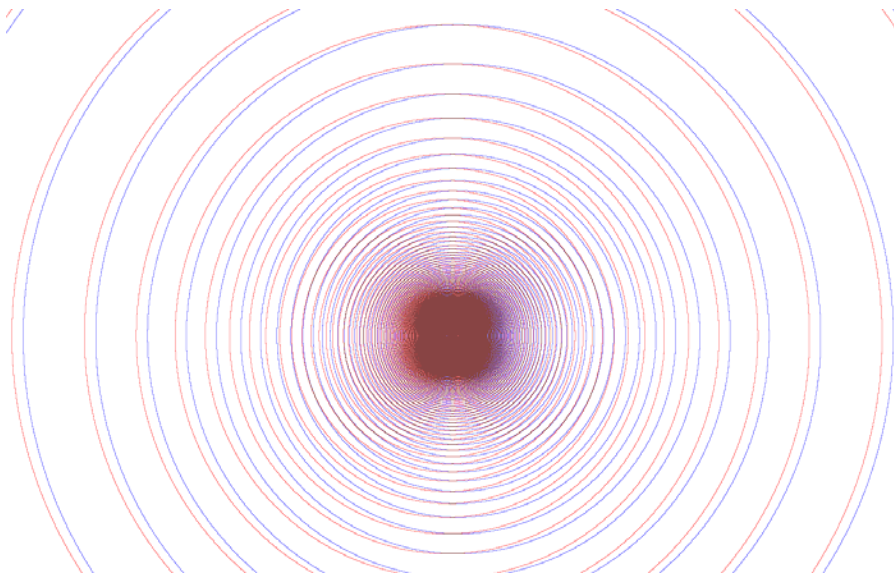


Figure 4-2c: As the distance between the SHP groups reduces, further pattern changes can be noted in the geometrical pattern near the center of the galaxy. In addition, at large distances only contours of the same radius (or zonal index) can intersect.

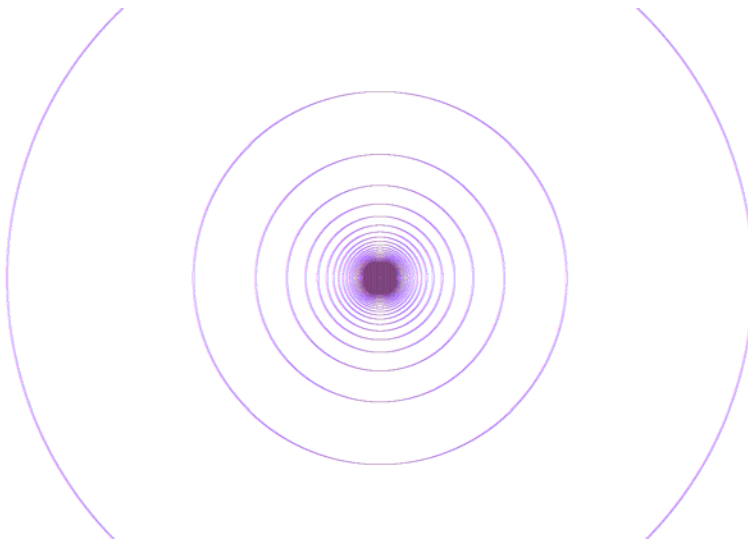


Figure 4-2d: At a very short distance A , concentric contours are produced and the galaxy becomes almost indistinguishable from a galaxy containing a single stationary SHP group located at its center.

In figure 4-2d, as the distance R_1 (and therefore R_2) increases, the two arcs approach each other to create a full circle, or a ring. In general, when the ratio between the orbital radius of the SHP group(s) and the distance of the object from the galaxy center $A/r \rightarrow 0$, equation 4-1-1a results in a galaxy or nebula that demonstrates essentially the same form as provided by a single SHP group (see figure 4-1a), where the total number of superheavy particles in the group is given by the sum $N_M + \Gamma N_M$. As can be deduced from equation 4-1-1a and demonstrated by figures 4-2a to 4-2d, the number of intersections between the two sets of concentric minima

circles increases as the distance $2A$ between the two SHP groups is reduced, creating more star systems.

Figure 4-2e provides the two dimensional contour map of the overall potential energy pattern generated by two identical SHP groups positioned at $x = \pm 1.8 \text{ kpc}$, $y = 0$ and $z = 0$. The number of minima (represented by the brightest areas) increases and their individual sizes reduce with decreasing distance from either SHP group. Consequently, stars created in the immediate areas surrounding the SHP groups are expected to be smaller and more abundant than those produced at more distant locations. As shown in the figure, some very large stars should be generated from the gas trapped at the minima, located for example at $(x, y, z) = (0, 6, 0)$, $(0, -6, 0)$, $(8, 0, 0)$ and $(-8, 0, 0)$. The size of the minima, and therefore the size of the stars produced within them, should decrease, and the number of stars should increase as their distance from the SHP groups is reduced. Note that the darkest areas within close proximity to the SHP groups (within a radius of about 1 kpc) are not continuous and appear so due to the limited resolution of the figure. These areas actually consist of many distinct minima separated by maxima, where many thousands of small stars can be created. Note that some of the minima may be too small to cause a collapse.

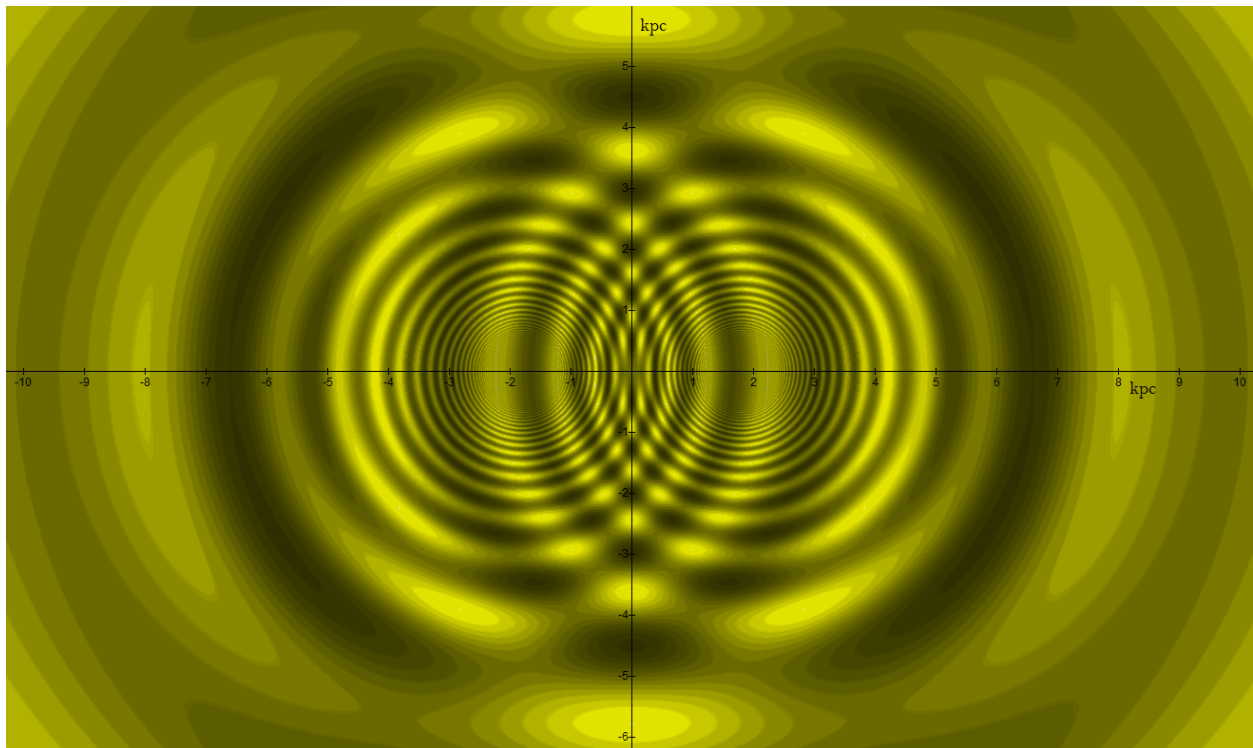


Figure 4-2e: A two dimensional contour map of the overall potential energy pattern generated by two identical SHP groups (positioned at $x = \pm 1.8 \text{ kpc}$, $y = 0$ and $z = 0$, where the z axis is perpendicular to the page). Star formation may occur at the isolated minima (displayed as bright circles or bright segments (or filaments)). The size and the abundance of stars are determined by their distances from the two SHP groups. Note that the stars in the center or mid-region of the galaxy are significantly larger in size and smaller in number than those near the SHP groups. Further note the broad arcs produced at a great distance from the galaxy center.

The sizes of the stars are therefore dependent on the distance parameter A , which determines the closest point of intersection to either one of the SHP groups, and therefore the minimum size of stars produced within the galaxy.⁶⁵ As the galaxy center is relatively far from both SHP groups (by as much as 1.8 *kpc* in this example), the stars produced at the intersection points close to the center are expected to be fewer in number and larger in size than those produced closer to either one of the SHP groups. This phenomenon was observed near the core of the Milky Way Galaxy (Courtland, 2008).

An important factor left out of the above discussion is that most of the galactic SHP groups in the observed galaxies should be rotating. In the static scenario, where either no rotation or a very slow rotation takes place, each intersection is potentially capable of producing a single star, which then remains trapped within the local minima. However, in the case of rapid SHP group rotation, it will be shown that following the collapse of a gas cloud, the pattern generated by the rotating SHP groups will move too fast for the newly generated stars to keep pace. As the pattern rotates away from the newly formed stars, new clouds of gas emerge and are forced to collapse into the shifted minima intersections. This process may repeat continuously, resulting in the steady creation of a large number of stars, as long as there is no shortage of interstellar gas. A more detailed description of the process of star formation, fragmentation, and the influence of the rotation of SHP groups will be provided in Chapter VI.⁶⁶

Extending the discussion, equation 4-1-1a will be applied to map and evaluate a series of known morphologies that may have been generated by binary SHP groups. The resultant models will then be compared with morphologies observed in various galaxies and nebulae. Features such as multiple rings, arcs, spirals and ansae will also be considered and explained. Current theories suggest that some of these features may in part be determined by binary central stars, external interactions, stellar winds and magnetic fields in the case of planetary nebulae, or by the gravitational influence of companions or collisions in the case of galaxies; however the exact mechanisms which drive the diverse morphologies are not yet well-understood, and certainly not proven.

We begin using the above scenario of binary SHP groups, each containing a single type of superheavy particle. The SHP groups may either remain stationary or may rotate around each other at relatively low velocity.⁶⁷ In such a system, the morphology will be shown to be determined mainly by the value of the parameter A , which is equal to the orbital radius of a single or binary SHP groups around the center of the core of the galaxy or nebula.

⁶⁵ In the example provided in the figure, the closest intersection to the SHP groups is at a distance of about 0.2 *kpc* to 0.3 *kpc* from one group, and about 4 *kpc* from the other. It is possible to estimate the minimum star size by either zooming the display around the minimum point to a sufficient display resolution, or by applying equation 2-1-12 to calculate the indices n of the contours generated by each SHP group and equation 2-1-16 to calculate their estimated widths.

⁶⁶ See section VI-4.

⁶⁷ In the Newtonian scenario, the SHP groups must rotate around each other, or otherwise collapse into each other. Thus, the scenario of no rotational velocity is unstable. According to the UG theory, this is not necessarily the case for two massive superheavy particles, since two SHPs can be kept apart by the rejection zones (or maxima) created by their interaction.

Section IV-1-3: Butterfly Formations in Planetary Nebulae

Figure 4-3a provides the two dimensional map of a nebula generated by two stationary (or slow rotating) SHP groups separated by a distance of $2A$, where $A = 0.6 pc$, $M = 2.625 g$, $v \approx 0 m/s$ and the overall mass of ordinary matter in the cloud is about $M_G = 10^{23} kg$ (using a single cut-off value of $E < -5 * 10^{-32} J$). The resultant image appears as a butterfly structure composed of narrow arcs, bearing a close resemblance to the morphology of a number of axially symmetric, or “butterfly” nebulae (see NGC 6302 in figure 4-3b, NGC-2346 in figure 4-3c and the Boomerang Nebula in figure 4-3d).⁶⁸ The width of the two outer lobes, or the “wings” of the butterfly formation, is determined by the value of A . The span of the two wings increases as A is reduced, becoming a full circle as $A/r \rightarrow 0$. Reduction of the ordinary matter effect M_G will strengthen the butterfly morphology. However, increasing M_G by a factor larger than ten (in this example) may eliminate the butterfly pattern, instead creating a pattern of concentric spheres or circles. Note that for the case of a static or slow-rotating nebula, the nebular structure is not reduced to a thin rotating disk and retains substantial depth. Therefore, the minima arcs become spherical sub-sections that appear to overlap when viewed from our Solar System, obscuring the view of the arcs but not the general view of the butterfly wings.

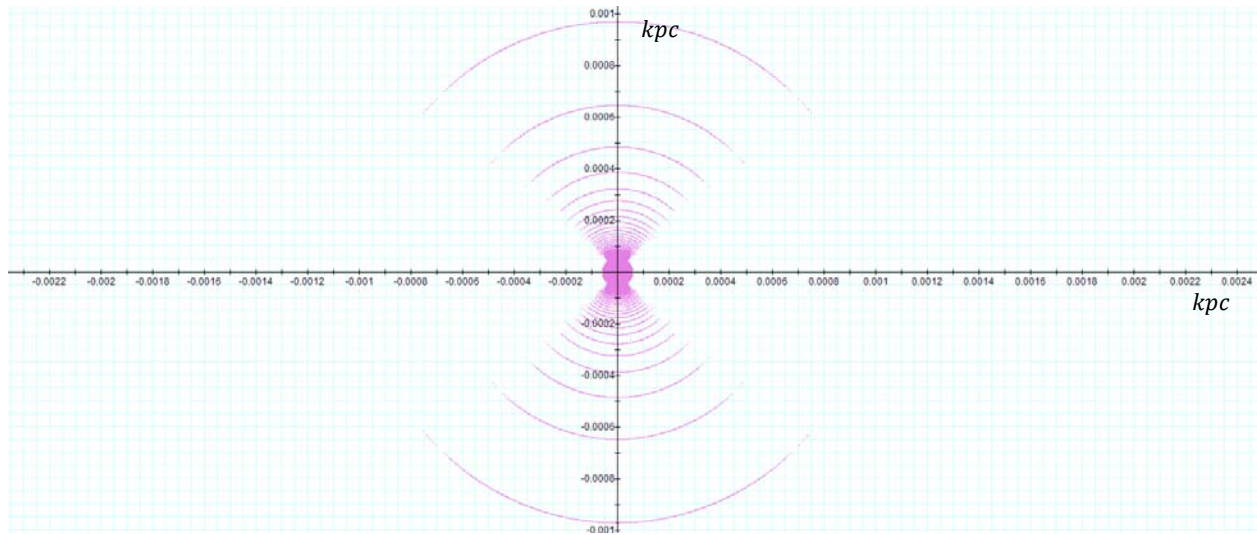


Figure 4-3a: Displays the two dimensional map of the potential energy minima contours of an ordinary particle of mass m_p as a function of its location in the galaxy plane $z = 0$, calculated by applying equation 4-1-1a to a nebula with stationary or low velocity SHP groups separated by the distance $2A$ from each other. The resulting morphology resembles the general structure of the Bug Nebula NGC-6302, the Butterfly Nebula NGC-2346 and the Boomerang nebula shown in figures 4-3b, 4-3c and 4-3d respectively.

⁶⁸ Nebulae of this type are currently believed to have been formed by the outflow of gas from a massive central star and to be relatively short-lived phenomena, lasting only a few tens of thousands of years. According to unified gravitation, the structure of a nebula is determined by the mass of its core of ordinary matter and by the size, quantity and orbit of its SHP groups. Therefore, as long as the above parameters are not subject to significant change, nebular morphology is a long-lasting phenomenon.

4-3b



4-3c



4-3d



Figure 4-3b: An image of NGC 6302, or the Bug Nebula, taken by the refurbished Hubble Space Telescope, shows a celestial object that looks like a delicate butterfly. The image, provided by NASA, was released Wednesday, Sept. 9, 2009 (AP Photo/NASA); <http://nasa-satellites.blogspot.com/2009/09/excellent-images-from-refurbished.html>.

Figure 4-3c: NGC 2346, the Butterfly Nebula, courtesy of Massimo Stiavelli (STScI) and NASA; <http://www.nasaimages.org/luna/servlet/detail/NVA2~4~4~7989~108515:NGC-2346--A-Butterfly-Shaped-Planet>.

Figure 4-3d: A Hubble space telescope image of the Boomerang Nebula provided by NASA; <http://www.spacetelescope.org/images/html/heic0301a.html>.

Section IV-1-4: Hourglass Structures

The same methodology can be applied toward producing the hourglass structure observed in MyCn 18 (figure 4-4e), or at the center of the Southern Crab Nebula (figure 4-4b). Such structure requires at least two superheavy particle groups. The highly symmetrical structure of the hourglass morphology suggests the existence of two dominant groups of equal SHP mass. The value of Γ is more difficult to estimate, however the selection of $\Gamma = 1$ is a reasonable starting point. Equation 4-1-1b can be divided by $N_M N_{m_p}$ without bearing any effect on the overall morphology, as the potential energy minima will remain at the exact same locations as long as M_G is also divided by N_M . Therefore, $N_M = N_{m_p} = 1$ can be selected. Since $A \rightarrow 0$ was shown to produce concentric spheres or circles, a larger distance A should be tested. Initially, we can arbitrarily select values of $M = 2.5 * 10^5 \text{ kg}$ and $M_G = 0$ and then apply the first scaling theorem of the UG theory for correction.⁶⁹ Comparing the two dimensional maps generated by different values of A with the desired morphology provides a relatively good fit at $A = 0.18 \text{ kpc}$. The resultant map in figure 4-4a demonstrates a close resemblance to the central section of the Southern Crab Nebula in the constellation of Centaurus. Plotting the concentric equi-potential minima contours of the two SHP groups provides vivid insight into how such a pattern is formed at the intersections of the various minima contours. Note that finding the right value of A is not difficult since the general hourglass structure appears within a wide range of A values, and can easily be fined-tuned via trial and error to generate the desired x - y proportions.

⁶⁹ The first scaling theorem is discussed in Appendix A.

Using the above parameters results in a galactic-scale radius of 16.4 kpc , which is about 111,000 times larger than the desired dimensions of a nebula of roughly 0.15 pc . With the aid of the first scaling theorem of the UG theory, the transformation of $M \rightarrow M/111,000 \approx 2.25 \text{ kg}$, $A \rightarrow A/111,000 \approx 0.0016 \text{ pc}$ and $\omega \rightarrow 111,000\omega \approx 0$ will provide the exact same morphology in the typical scale of planetary nebulae.⁷⁰ MyCn 18 (figure 4-4e), known as the Engraved Hourglass nebula, provides a similar bipolar morphology, but differs in two important aspects: First, the dramatic, bright central core observed at the center of the Hourglass nebula does not appear in the calculated model of figure 4-4a. In addition, the two sets of concentric circles are observed to overlap significantly, rather than simply intersecting at a single point at the center (as is the case in figures 4-4a and 4-4b). The results obtained by applying the scaled-down parameters $M = 2.25 \text{ kg}$ and $A = 0.0045 \text{ pc}$ using a potential energy cut-off of $-1.17 * 10^{-24} \text{ J}$ and adding into the equation the contribution of ordinary matter of $M_G = 3 * 10^{28} \text{ kg}$ at the center of the nebula are presented in figure 4-4c. The resultant object is of the size of a typical nebula, and retains its general morphology beyond the central area of the structure. The addition of a large mass of ordinary matter at the center of the galaxy produces a strong gravitational pull inward towards the center. The gravitational pull is especially robust at low radii, resulting in the formation of a circular bulge at the galactic core, where the size of the central bulge increases with the amount of ordinary matter near the center of the galaxy.

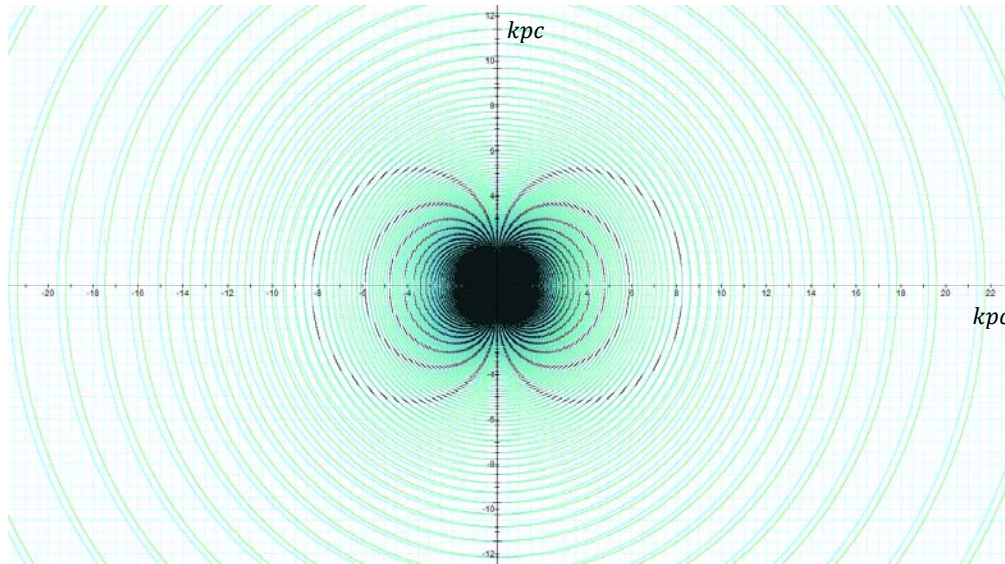


Figure 4-4a: Demonstrates an hourglass morphology generated by two stationary single-particle SHP groups of SHP mass $M = 2.5 * 10^5 \text{ kg}$, where the SHP velocity $v = 0$, and the distance between the SHP groups and center of rotation is approximately $A = 0.18 \text{ kpc}$. The calculated pattern bears a close resemblance to the center of the Southern Crab Nebula, displayed in figure 4-4b. Also shown are the two identical sets of concentric minima contours produced by group 1 (green) and group 2 (cyan), which are displaced by a distance of $2A = 0.36 \text{ kpc}$. The overall potential energy minima are given by the intersections between the two sets of minima contours respectively generated by each of the two SHP groups, and are indicated in blue. Note that the calculated morphology depicts an additional set of arcs along the galaxy's axis of symmetry (the y axis) that were not detected in the observed images (these two additional calculated arcs provide spiral arms in cases of rapidly rotating SHP groups).

⁷⁰ In this example, $w = 0$ and $M_G = 0$, and do not need to be taken into account.

To resolve the lack of overlap between the two sets of contours generated by the two SHP groups in the modeled galaxy (relative to the observed image of MyCn 18), a greater distance value can be used. Figure 4-4d demonstrates that the relatively large overlapping area between the two sets of circular contours in MyCn 18 may be generated by introducing a much larger distance $A = 0.108 \text{ pc}$. Application of this value, using $M_G = 2 * 10^{28} \text{ kg}$, $M = 0.75 \text{ kg}$, $\Gamma = 1$, and $v = 0 \text{ m/s}$ provides two sets of concentric overlapping contours, as well as a central accumulation of matter, resulting in an almost identical morphology to the Hourglass nebula.

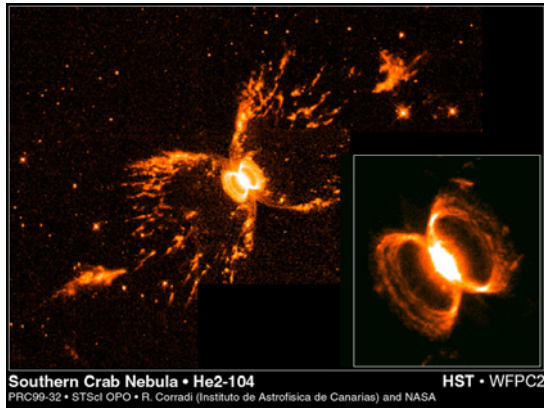


Figure 4-4b: The Southern Crab Nebula, image credit: Romano Corradi Instituto de Astrofísica de Canarias, Tenerife, Spain, Mario Livio, Space Telescope Science Institute, Baltimore, MD, Ulisse Munari, Osservatorio Astronomico Di Padova-Asiago, Italy, Hugo Schwarz Nordic Optical Telescope Canarias Spain, and NASA.

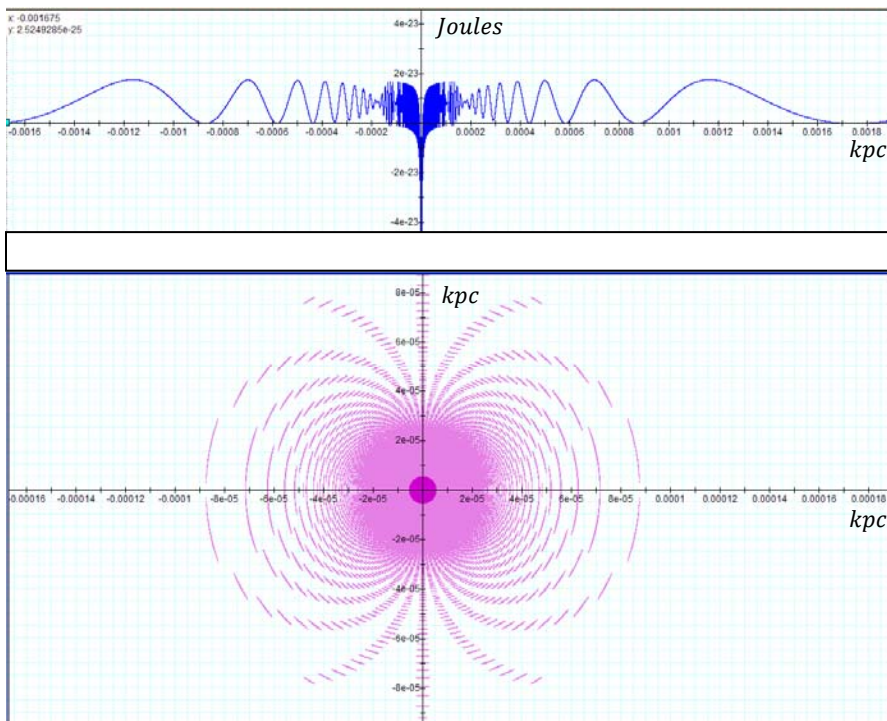


Figure 4-4c: Scaling down by a factor of about 1/111,000 and adding the contribution of $3 * 10^{28} \text{ kg}$ of ordinary matter at the center of the structure provides the dimensions of a typical nebula, and an internal central bulge similar to the center of the hourglass nebula shown in figure 4-4e.

Figure 4-4d

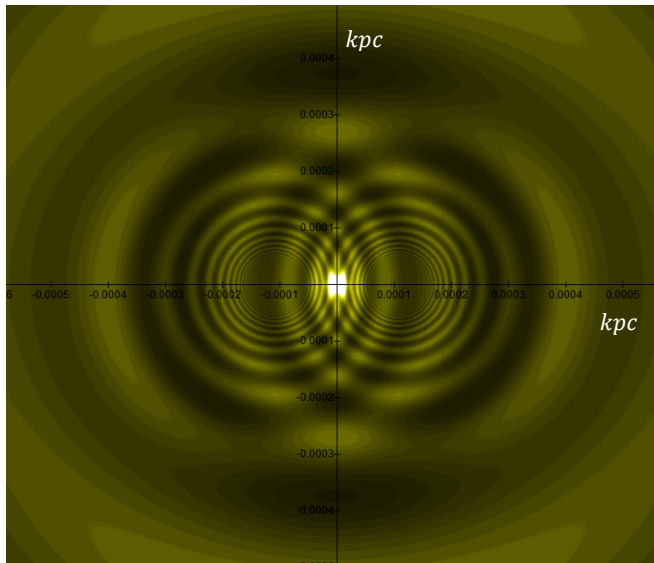


Figure 4-4e

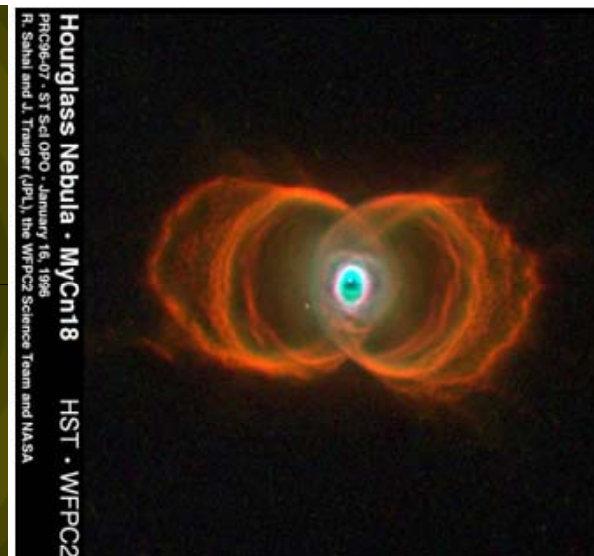


Figure 4-4d: Demonstrates a calculated hourglass morphology generated by two stationary single-particle SHP groups of SHP mass $M = 0.75 \text{ kg}$, where the SHP velocity $v = 0$, the distance between the SHP groups and their common center of mass $A = 0.108 \text{ pc}$, and the overall mass of ordinary matter $M_G = 2 * 10^{28} \text{ kg}$. The calculated pattern bears a significant resemblance to the center of the Hourglass nebula MyCn 18 displayed in figure 4-4e.

Figure 4-4e: The Hourglass Nebula, MyCn 18. Image credit: R. Sahai and J. Trauger, Photo AURA/STScI/NASA/JPL (NASA photo # STScI-PRC96-07); <http://apod.nasa.gov/apod/ap020615.html>.

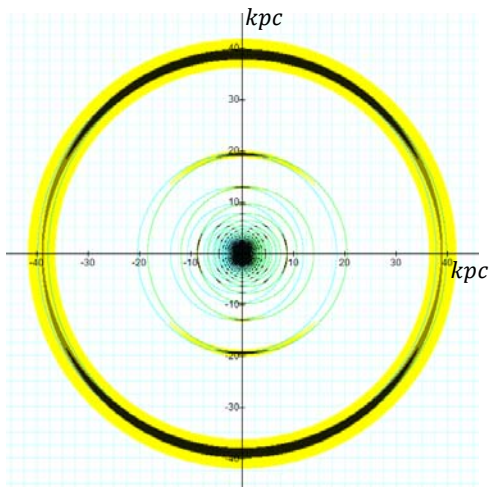


Figure 4-5a

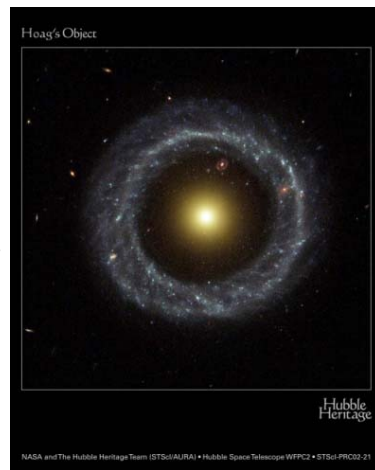


Figure 4-5b



Figure 4-5c

Figure 4-5a: Displays a two dimensional map of the potential energy contours of an ordinary particle of mass m_p as function of its location in the galactic disk for a galaxy similar to the one used in figure 4-4a, using a superheavy particle of mass $M = 50,000 \text{ kg}$. The black contours include the lowest minima regions, where $0 < \xi < 2.5 * 10^{-21} \text{ J}$, while the yellow contours provide the range where $2.5 * 10^{-21} \text{ J} < \xi < 20 * 10^{-21} \text{ J}$. Ordinary matter is expected to concentrate at the minima contours (mainly at the black contours, and to a lesser degree at the yellow contours), resulting in a ring morphology. Also displayed are the circular minima contours of the potential energy contribution of each of the two SHP groups (in green and cyan). Note the resemblance to the planetary nebula Abell 39 in figure 4-5c and to Hoag's object in figure 4-5b. The following parameters were used: $M = 50,000 \text{ kg}$, $v = 0 \text{ m/s}$, $M_G = 0$, and $A = 1 \text{ kpc}$.

Figure 4-5b: Image credit: NASA and the Hubble Heritage Team (STScI/AURA) Acknowledgment: R. Lucas(STScI/AURA) <http://www.nasaimages.org/luna/servlet/detail/NVA2~4~4~4753~105279:Hoag-s-Object--A-Strange-Ring-Galaxy>.

Figure 4-5c: The Planetary Nebula Abell 39, WIYN Observatory's 3.5-m (138-inch) telescope at Kitt Peak National Observatory, Tucson, AZ, image credit: "NOAO/AURA/NSF."

Section IV-1-5: Ring Morphologies in Galaxies and Nebulae

Figure 4-5a depicts a similar galaxy of SHP mass $M = 0.5 * 10^5 \text{ kg}$ and orbital radius $A = 1 \text{ kpc}$, viewed in a substantially increased display threshold using two cut-off energy levels $0 < \epsilon < 2.5 * 10^{-21} \text{ J}$ and $2.5 * 10^{-21} \text{ J} < \epsilon < 20 * 10^{-20} \text{ J}$ to show only the vicinity of the minima (where darker color values indicate lower potential energy). The resultant morphology transforms into a ring structure, bearing a resemblance to a number of galactic systems with external rings, such as Hoag's Object in figure 4-5b (Hoag, 1950), as well as NGC 6028 (Vorontsov-Velyaminov, 1959), NGC 2859 (Sandage, 1961), UGC 9562 and NGC 3081. The model may be scaled down to the dimensions of a typical nebula (via the first scaling theorem of the UG theory given in Appendix A) to explain the structure of ring nebulae such as Abell 39 in figure 4-5c.

Section IV-2: The Influence of SHP Group Rotation on Morphology and the Creation of Spiral Galaxies

Section IV-2-1: The Creation of Spiral Structures via Two Non-Relativistic Rotating SHP groups

The morphology of galaxies can be sorted into four main categories according to the Hubble Classification System, dividing regular galaxies into three broad classes- elliptical, spiral and lenticular galaxies, as well as a fourth class of galaxies with an irregular appearance.⁷¹ The Hubble sequence shows significant variation even within its broad morphological classes, and the transitions between them are relatively smooth. Thus, classification provides only an approximate procedure, where two skilled astronomers may arrive at two different classifications for the same galaxy.

Among the morphological classes, spiral galaxies have proven to be particularly intriguing and challenging, as understanding their evolution and the variation among their local properties has shown to be one of the more complex undertakings in astrophysics. Drawing on earlier work by Bertil Lindblad, C.C. Lin and Frank Shu suggested that the spiral pattern can be viewed as a manifestation of low-amplitude “density waves” that rotate throughout the galaxy with fixed angular speed called pattern speed, causing a periodic compression and rarefaction of the disk surface (Lin & Shu, 1964). As the compression wave rotates, it triggers star formation on the leading edge of the spiral arms. Lin and Shu also assumed that in the large-scale spiral structure, the appearance of spiral arms remains stable over many orbital periods.⁷² At present, near-infrared images of nearby galaxies have provided convincing evidence that the large-scale spiral structure is a density wave. However, emerging theories suggest that the spiral pattern is far from stationary, and that spiral structure may result from a wide variety of causes. The study of the dynamics of differentially rotating disks has since developed into an extensive density wave

⁷¹ Additional classes and sub-classes have been added over time, for example Arp's peculiar class, which includes a class of ring galaxies.

⁷² Alternatively, Lin and Shu assumed that the spiral pattern is a long lasting stationary density wave.

theory. The theory has achieved relative success in explaining how spiral patterns can persist for a greater length of time than the particular arms we see at a given moment, leading to a semi-empirical approach for modeling different spiral morphologies. Other theories suggest that the formation and evolution of spirals, as well as a broad range of galactic morphologies, can be explained via gravitational encounters or collisions between galaxies. Nevertheless, in their book *Galactic Dynamics*, James Binney and Scott Tremaine stated “The number of reviews of spiral-structure theory is disappointingly small” (Binney & Tremaine, 2008). While observations provide persuasive evidence of the existence of density waves, the exact nature of the density wave is not yet well-understood and the number of galaxies successfully modeled (quantitatively) is small.

By means of the UG theory, spiral morphology can be generated by the interaction between a test object and two (or more) SHP groups rotating at non-relativistic speeds of $\frac{2\pi Ac}{bm_p M} \lesssim v \ll c$, or by a single (or more than one) SHP group rotating at a relativistic speed.

According to equation 4-1-1a, the size and morphology of a galaxy depends on the mass of its dominant superheavy particles, the rotational velocity of the SHP groups, and their radii of orbit around the center of the galaxy. The mass of superheavy particles in equation 4-1-1a affects the potential energy amplitude through the term $\frac{GN_{m_p}m_p N_M M \gamma^2(v)}{a}$, and the size of the galactic disk through the term $\cos\left(\frac{bm_p M \gamma(v)}{\dot{D}_{s_i}}\right)$. Note that the SHP contribution to the object’s potential energy increases its potential energy amplitude by a factor of $\gamma^2(v)$. Therefore, the rotational velocity of the SHP groups increases the effective size of the galaxy by a factor between $\gamma(v)$ (in the direction perpendicular to the direction of the velocity of the SHP group) and $\gamma^2(v)$ (in the direction parallel to the direction of the SHP velocity).⁷³ The farthest substantial zonal minimum from the center is located at $\dot{D}_{s_i} \approx bm_p M \gamma(v) / 2\pi$ in the relativistic case (which is reduced to $\dot{D}_{s_i} \approx r_2 \approx bm_p M / 2\pi$ in the non-relativistic case). The farthest substantial minimum provides the distance of the last significant outer contour (or isophote) containing a high density of matter,⁷⁴ and therefore defines the visible edge of the galaxy, or the galactic disk radius. In figures 4-1 to 4-5, the morphology appears to be far more sensitive to the radius A of the SHP group(s) than to changes in the number of SHPs within the SHP group(s), or to changes in the SHP mass (at least for the case of a single dominant SHP).

⁷³ The dependency of the size of the galaxy in the direction parallel to the direction of the velocity of a superheavy particle group can be proportional to $\gamma^2(v)$, due to the contribution of $\gamma(v)$ in the denominator of the cosine operand, and the fact that \dot{D}_{s_i} can be reduced by a factor of $\gamma(v)$ in the parallel direction.

⁷⁴ The radius of the most external minimum actually resides at a farther distance, at approximately $r_0 = bm_p M / \arctan(a/bm_p M) \gg r_2$. However, at this distance the UG equation becomes almost indistinguishable from the Newtonian equation, and since the total mass of the superheavy particles is significantly smaller than the total mass of ordinary matter in the galaxy, the minimum contour at r_0 would not be noticeable. Instead, a minimum contour occurs somewhere between the maximum contour r_1 and the minimum contour r_0 at the point where the rate of change of the ordinary matter contribution to the potential energy of the object is equal in magnitude, but opposite in sign to the rate of change of the galaxy’s SHP contribution. As this minimum occurs at greater distance from the galaxy’s main body, where the UG equation becomes almost indistinguishable from the Newtonian equation, and as the contribution of the galaxy’s ordinary matter to the potential energy of the object is also substantially reduced at the given distance, the visual effect of this additional minimum contour is relatively small.

Recall that as a cloud of gas collapses inward under its own gravitational force to form a galaxy, the law of conservation of angular momentum dictates that its rotation must accelerate as it becomes more and more compressed. According to the UG postulates, the extreme conditions generated by the collapse lead to the creation of massive superheavy particles. As of equation 3-3-1, the velocity of SHP groups is proportional to their radius of orbit, and may therefore be relativistic.

In the case of two stationary or very slow rotating binary SHP groups, an hourglass pattern similar to the observed nebula MyCn 18, or to the center of the Southern Crab nebula, can be generated at distances r not much larger than the order of A . As the distance between the SHP group and the object increases well beyond A , the morphology begins to change into a butterfly pattern, and eventually forms a concentric ring structure at $r \gg A$, where the distance separating two successive rings increases with their distance from the SHP groups.

The rotation of SHP groups will be shown to result in the formation of spiral structures. The mechanism responsible for the creation of spirals at low velocities differs from the mechanism responsible for the creation of spirals at relativistic velocities. At low rotational speeds, a minimum of two SHP groups are necessary in order to create a spiral structure. In the relativistic case, however, due to the effect of relativistic distance contraction in the direction parallel to the direction of the SHP velocity, and to the lack of relativistic contraction in the perpendicular directions, even a single SHP group may be sufficient to produce spiral morphology.

We begin with the non-relativistic case. Figure 4-6 displays a two dimensional map of the potential energy minima contours of an object composed of a single ordinary test particle of mass m_p as a function of its location within the galactic disk plane. The provided galaxy contains two SHP groups of SHP mass $M = 0.8 * 10^5 \text{ kg}$ traveling at a velocity of $v = 0.03c$ at a radius of $A = 0.048 \text{ kpc}$, where $\Gamma = 1$ and $M_G = 2 * 10^{35} \text{ kg}$. The minima contours of the overall potential energy were again calculated via equation 4-1-1a, and the display provides the regions where the test particle's potential energy complies with $-10^{-21} \text{ J} < E < 0 \text{ J}$. The particle's potential energy minima, indicated in black, are shown to be located at the intersections of the minima contours of the two SHP groups, indicated in cyan and green respectively. The figure demonstrates a clear spiral structure at the central part of the galaxy. The spiral arms are constructed from arcs, which appear relatively short near the galaxy center and grow longer as the test particle's distance from the center increases.

The mechanism at work to produce the spiral structure at non-relativistic velocities requires at least two SHP groups, where each group generates a set of concentric minima around itself. Equation 4-1-1a provides minima at the coordinates at which the two cosine terms are either equal to or very close to 1. At these locations a circular minimum contour produced by a single SHP group (in cyan) coincides with a circular minimum contour produced by the other SHP group, forming a set of arcs at and near their intersection points. As the distance between the minimum intersections and the central SHP groups increases, a greater amount of time is required for the gravitational signal traveling at a relativistic velocity c to arrive. This lengthens

the distance traveled by the two SHP groups between the time(s) that the gravitational signals (or gravitons) were emitted, as well as the time of their simultaneous interception by the orbiting object. Consequently, the arcs that are farther away from the galaxy center will lag behind those closer to the center, in effect creating a spiral pattern.

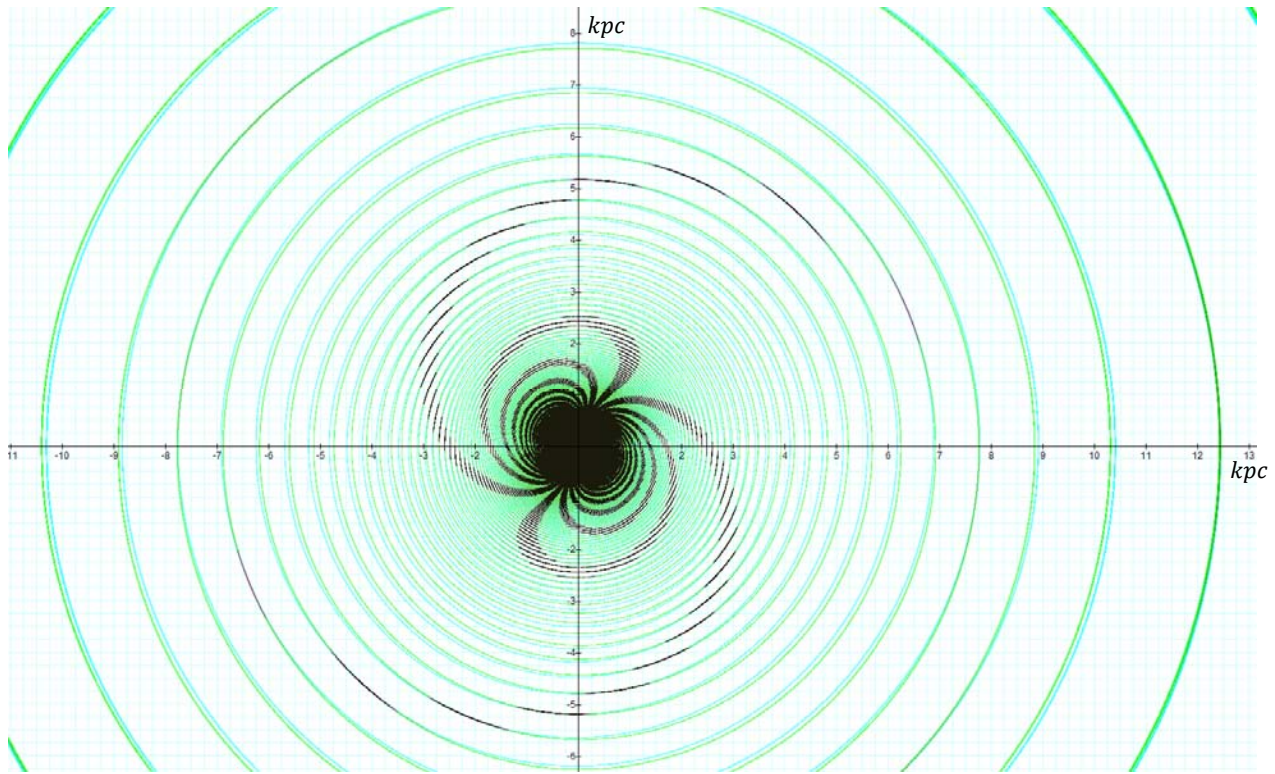


Figure 4-6: Depicts the contours that fulfill equation 4-1-1a, where both SHP groups rotate at a non-relativistic speed of $v = 0.03c$. A clear spiral structure appears at the central part of the galaxy, created at the intersection points of the two sets of concentric circular contours generated by the two rotating SHP groups.

The complete mathematical formulation leading to the spiral is given by equations 4-1-1a, 3-1-17a, 3-1-17b and 3-1-20. The following explanation, while making some approximations, can make these mathematical results somewhat more intuitive.

Following equation 2-1-12, the radii of a set of potential energy minima generated by a stationary SHP group can be approximated by $r_n \approx \frac{bm_p M}{n\pi}$ (for $n = 2, 4, 6, \dots$). A second factor affecting the minima locations is the displacement of the SHPs during the finite time it takes the gravitational signal to reach the orbiting ordinary particle. This results in different sections of spacetime being affected by the gravitational pull created by the SHP groups at different times and different locations. For the case where the speed of SHP groups is small relative to the speed of light, or $v \ll c$, the difference in the amount of time it takes the gravitational signal to propagate between the two successive minima contours indexed $n - 2$ and n is $\Delta t \approx$

$$\frac{\left(\frac{bm_p M}{(n-2)\pi} - \frac{bm_p M}{n\pi}\right)}{c} = \frac{2bm_p M}{n(n-2)\pi c},$$

in which time the two SHP groups were displaced by the angle of

$\Delta\varphi = w\Delta t = \frac{v}{A}\Delta t = \frac{2bm_p Mv}{n(n-2)\pi Ac}$. Therefore, as long as $\frac{2bm_p Mv}{n(n-2)\pi Ac} \ll 1$ and $A \ll r$, the effect of the SHP group rotation is negligible, and a standard hourglass morphology will result. When $\frac{2bm_p Mv}{n(n-2)\pi Ac}$ becomes more substantial, but still significantly smaller than 2π (for example, $\frac{2bm_p Mv}{n(n-2)\pi Ac} \approx \pi/20$), the small angular displacement between the successive minima contours creates a clear spiral structure. At larger distances of $\frac{2bm_p Mv}{n(n-2)\pi Ac} \gtrsim \pi$, where A is very small compared with $r_n \approx \frac{bm_p M}{n\pi}$, the pattern displays both ring and spiral morphology. At distances where $r_n \approx \frac{bm_p M}{n\pi} \gg A$, the pattern becomes a ring galaxy (as long as the relative influence of the galaxy's ordinary matter is sufficiently small). Therefore, a galaxy (of non-relativistic SHP velocities) may contain at least one outer ring, as well as an inner spiral structure located between the central core and the outer ring. Such morphology may occur when $A \ll \frac{bm_p M}{2\pi}$ and $0 \ll \frac{2bm_p Mv}{n(n-2)\pi Ac} \ll 2\pi$, and is observed in M31 the Andromeda galaxy. However, the relative effect of the galaxy's ordinary matter may be sufficiently large to eliminate the outer rings.

The results of substituting the values $\Gamma = 1$, $M = 0.156 * 10^4 \text{ kg}$, $A = 0.05 \text{ kpc}$, $v = 0.1c$ and $M_G = 1.5 * 10^{36} \text{ kg}$ into equation 4-1-1a are depicted in figure 4-7a, providing a structure that bears a resemblance to a smoothed version of the Andromeda galaxy. The modeled galaxy, viewed in face-on orientation, displays a central hourglass structure (which appears slightly distorted by the rotation of the central SHP groups) and a series of rings, where the most prominent outer rings (bright minima of $n = 2, 4$ and 6) are located at about 12 kpc , 6 kpc and 4 kpc , as well as a more diffused inner structure. A tilted version of the computed galaxy is displayed in figure 4-7b. The model also depicts two trailing spiral arms in between the central bulge and the ring at 4 kpc (see the enlarged view in figure 4-7g). These features of the modeled galaxy fit well with the properties demonstrated by the Andromeda galaxy in figures 4-7c and 4-7f, which depict two tightly wound trailing spiral arms that extend outward and transition into a ring galaxy between 3 kpc and 4 kpc . The rotating hourglass structure at the center of the modeled galaxy (figure 4-7g) also bears a resemblance to the general structure of Andromeda's nucleus (figure 4-7f), additionally accounting for the ansae reported by Beaton et al. in 2007 ^(Beaton et al., 2007). Note that the model predicts the existence of virtually an infinite number of ansae, which may be perceived as a single ansa on each side when viewed in insufficient resolution.

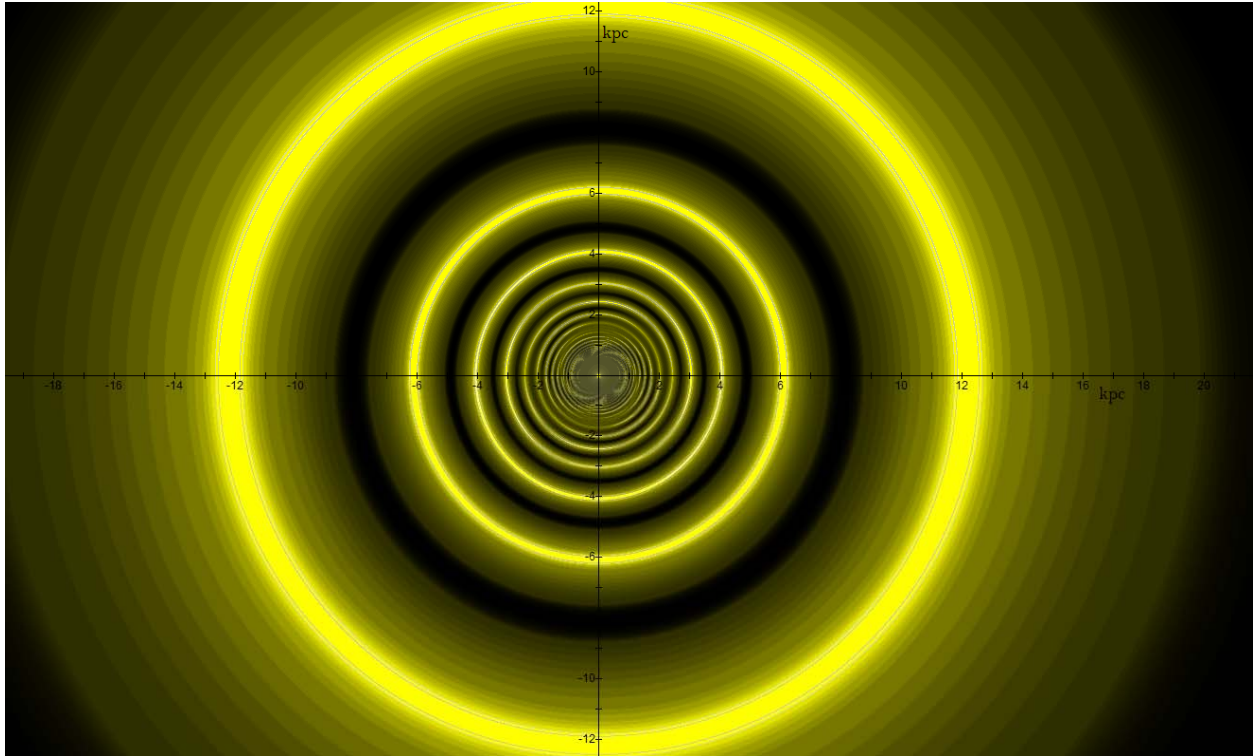


Figure 4-7a: Substituting $\Gamma = 1$, $M = 0.156 * 10^4 \text{ kg}$, $A = 0.05 \text{ kpc}$, $v = 0.1c$ and $M_G = 1.5 * 10^{36} \text{ kg}$ into equation 4-1-1a provides a face-on view of a series of rings, where the most prominent outer rings (bright minima of $n = 2, 4$ and 6) are located at about 12 kpc , 6 kpc and 4 kpc , as well as a central hourglass structure that is slightly distorted by the rotation of the central SHP groups. The resultant structure bears a significant resemblance to a smoothed version of the Andromeda galaxy (see figure 4-7c). Note that the lowest few energy contours were displayed in black to increase the contrast between the central disk and the surrounding environment.

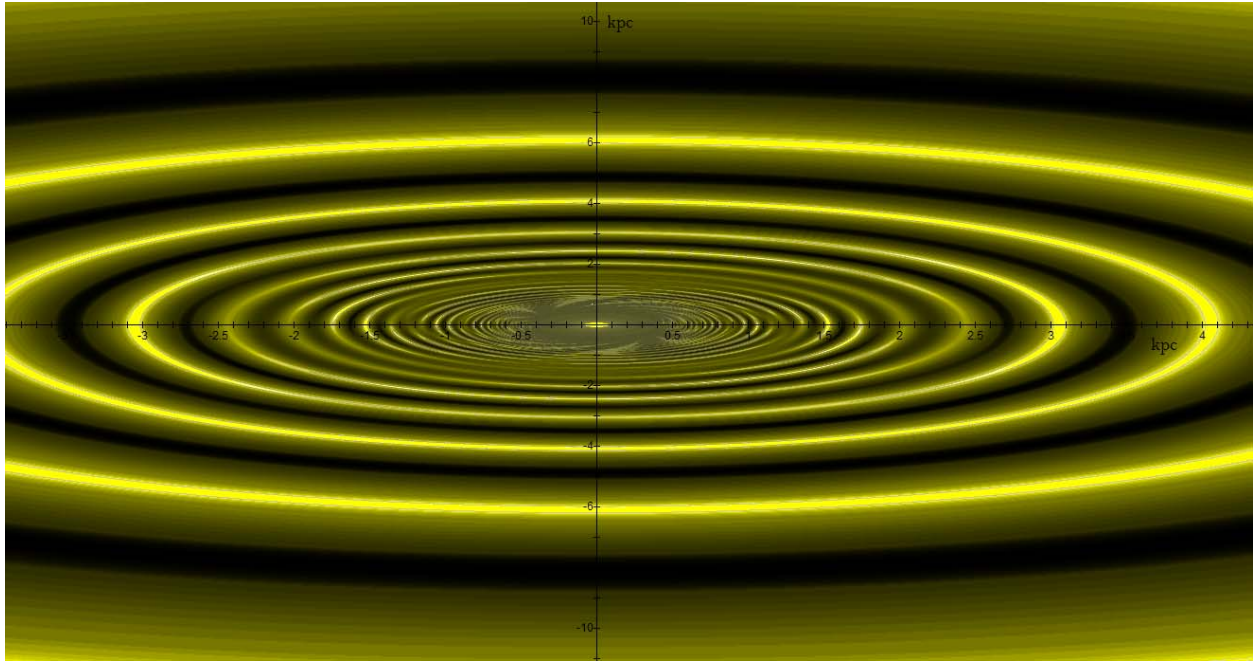


Figure 4-7b: Display of the same modeled galaxy tilted at nearly 75.5° around the x axis.

Note that this simple model does not take into account the influence of Andromeda's companion galaxy M32 on its morphology. A companion galaxy will be shown to explain distortions in the ring or spiral structures of galaxies such as Andromeda, as well as the appearance of "beads on a string." The influence of a companion galaxy on galactic systems will be demonstrated in section IV-4.

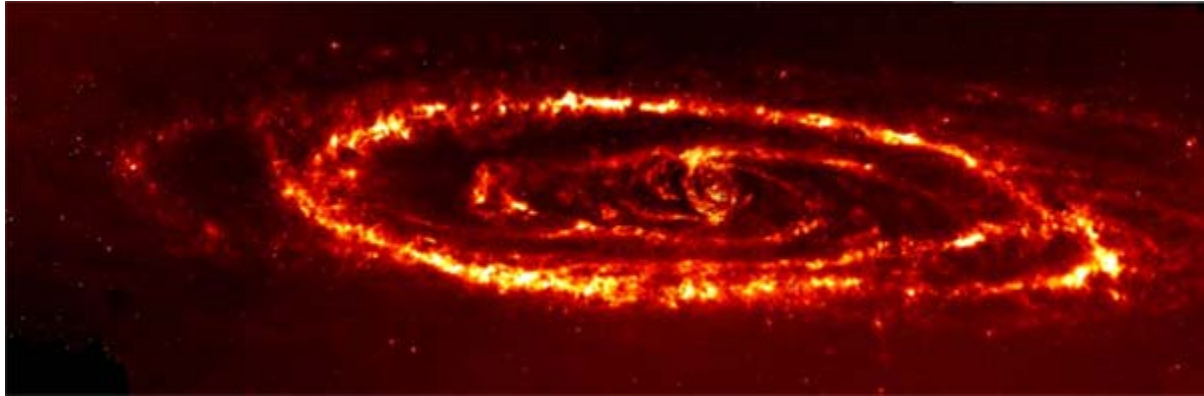


Figure 4-7c: An infrared view taken by NASA's Spitzer Space Telescope revealed a dust ring deep within the Andromeda galaxy. Combined with previous data of an outer ring, the image was interpreted as evidence that the neighboring dwarf galaxy M32 collided with the Andromeda Galaxy about 210 million years ago, plunging through its central disk. According to the UG theory, Andromeda's rings are a direct consequence of equation 4-1-1a, while the appearance of "beads on a string" and the split of the outer rings are due to the gravitational effect of a companion galaxy (see section IV-5).
Image credit: NASA/JPL-Caltech/K. Gordon (University of Arizona, <http://www.spitzer.caltech.edu/Media/releases/ssc2005-20/ssc2005-20a.shtml>).

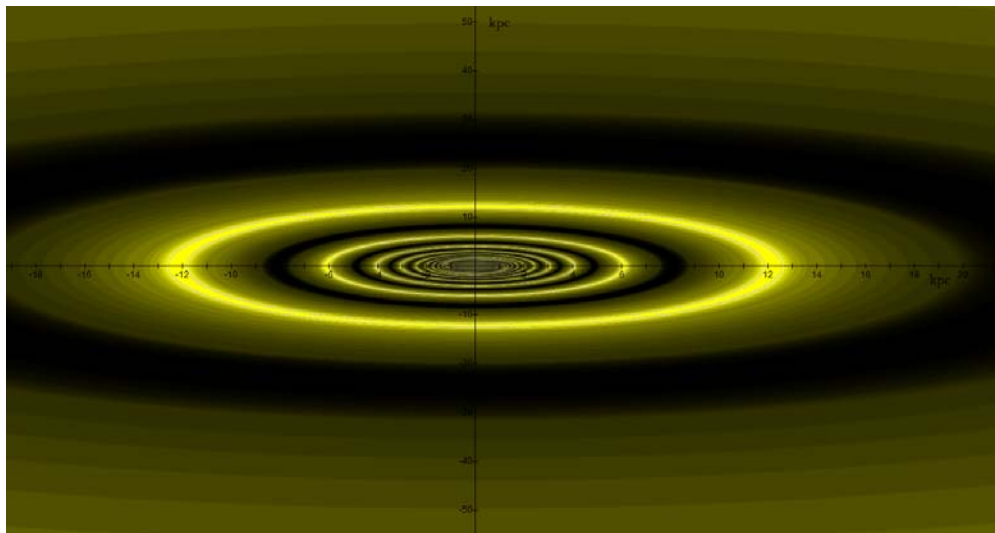


Figure 4-7d: Provides a direct comparison between the calculated galaxy of figures 4-7b and the observed image in figure 4-7c.

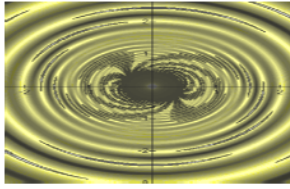


Figure 4-7e

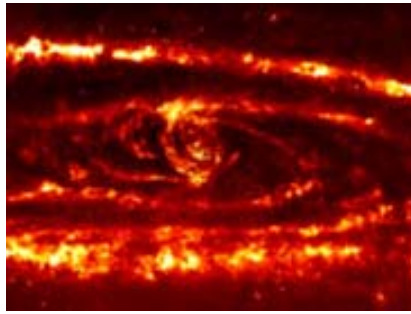


Figure 4-7f

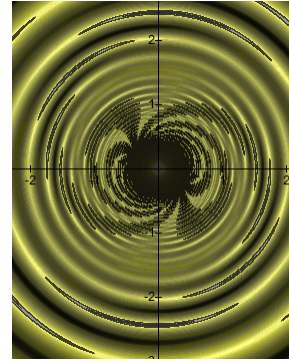


Figure 4-7g

Figure 4-7e: Provides the tilted version of the calculated image of the center of the Andromeda galaxy. Note the ansae and two spiral arms displayed at the central bulge and the similarities between the calculated image in figure 4-7e and the observed center of Andromeda in figure 4-7f.

Figure 4-7f: A view of the center of figure 4-7c.

Figure 4-7g: Provides a clear view of the calculated central disk of the modeled galaxy. Note the appearance of ansae, as well as two short tightly wound trailing spiral arms extend outward and transition into a ring galaxy between 1.5 kpc and 4 kpc . The lowest few energy contours are depicted in black to increase the display contrast between the central disk and the surrounding environment.

Section IV-2-2: Relativistic Rotational Speeds of SHP Groups and the Creation of the Grand Design Spiral Morphology

Accounting for the morphologies of certain grand design and flocculent spiral structures may require relativistic SHP velocities. Some examples are shown in figures 4-8a to 4-8k. Figure 4-8a depicts a two dimensional map of the potential energy contours of an ordinary particle of mass m_p within the rotation plane of a galaxy generated by identical binary SHP groups ($\Gamma = 1$), each containing a single SHP of mass $0.156 * 10^5 \text{ kg}$, traveling at a constant velocity $v = 0.3c$ (which translates to an angular velocity of $w = \frac{v}{A} \approx 5.122 * 10^{-5} \text{ rd/year}$) in a circular orbit of radius 1.8 kpc around the galaxy center. The influence of the galaxy's remaining ordinary matter ($M_G = 0$) is initially neglected. The resultant minima resemble slightly distorted elliptical (almost circular) isophotes of various sizes and orientations. These contours change smoothly in accordance with the distance of the ordinary particle from the galactic center, creating rings and arcs at the minima and relative voids at the maxima, as well as a slightly distorted or twisted hourglass pattern at the center of the galaxy. Figure 4-8b displays the minima contours of the potential energy of an ordinary particle within the galaxy's rotation plane using a similar scenario, where the speed of the SHP groups is increased to $v = 0.4c$. This increase in rotational velocity can be observed to result in a significant distortion of the morphology of the potential energy contours. Applying the same parameters, figure 4-8c demonstrates the asymmetry produced by the influence of a single SHP group, or $\Gamma = 0$, rather than binary superheavy particles. Note that in the case of a single SHP group, the lack of intersection between different minima contours prevents the generation of a massive amount of stars. If such structures exist, they should appear as asymmetric galaxies containing little or no stars.⁷⁵

⁷⁵ Some stars may form due to interactions of the single dominant SHP group and lesser SHP groups (smaller in size or quantity), or due to gravitational interactions with companion galaxies or nebulae.

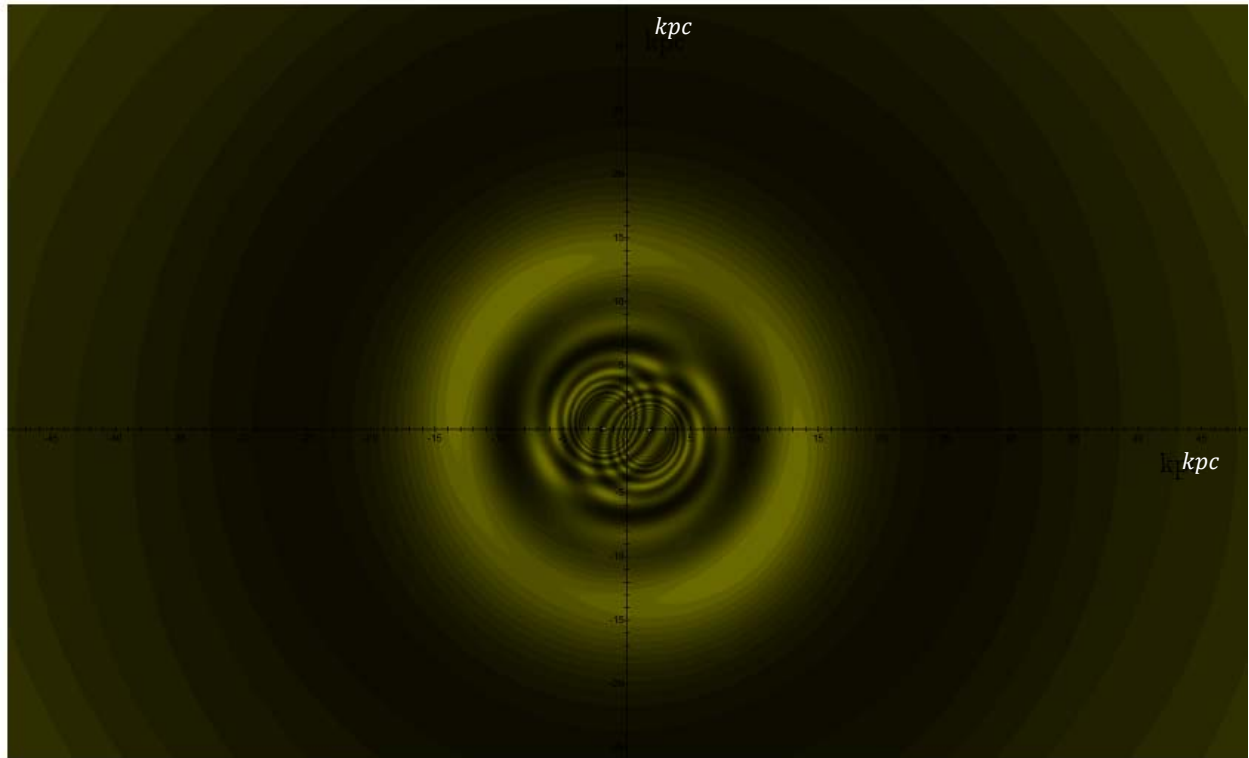
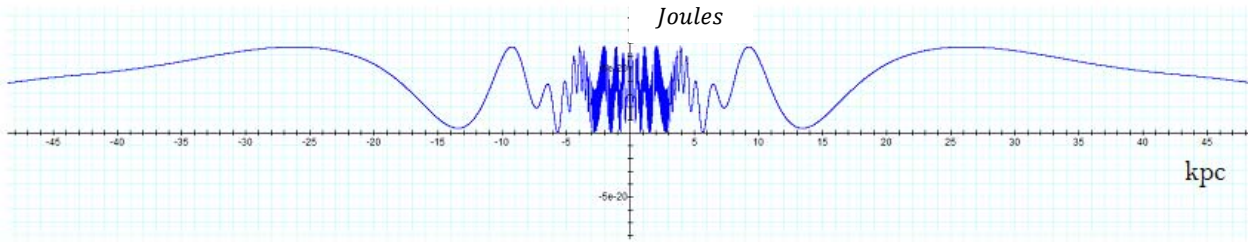


Figure 4-8a: The lower image provides the two dimensional color map of the calculated potential energy of an ordinary particle of mass m_p as a function of its location $(x_0, y_0, 0, t_0)$, substituting $\Gamma = 1, M = 0.156 * 10^5 \text{ kg}, v = 0.3c, A = 1.8 \text{ kpc}, M_G = 0, N_M = 1, N_{m_p} = 1, m_p = 1.674 * 10^{-27}$. The upper curve provides the potential energy along the x axis. The resultant minima contours resemble slightly distorted elliptical (almost circular) isophotes of various sizes and orientations. These contours change smoothly in accordance with the distance of the ordinary particle from the galaxy center, creating rings and arcs at the minima (the brightest contours) and relative voids at the maxima (at the darkest contours) as well as a slightly distorted hourglass pattern at the center of the galaxy.

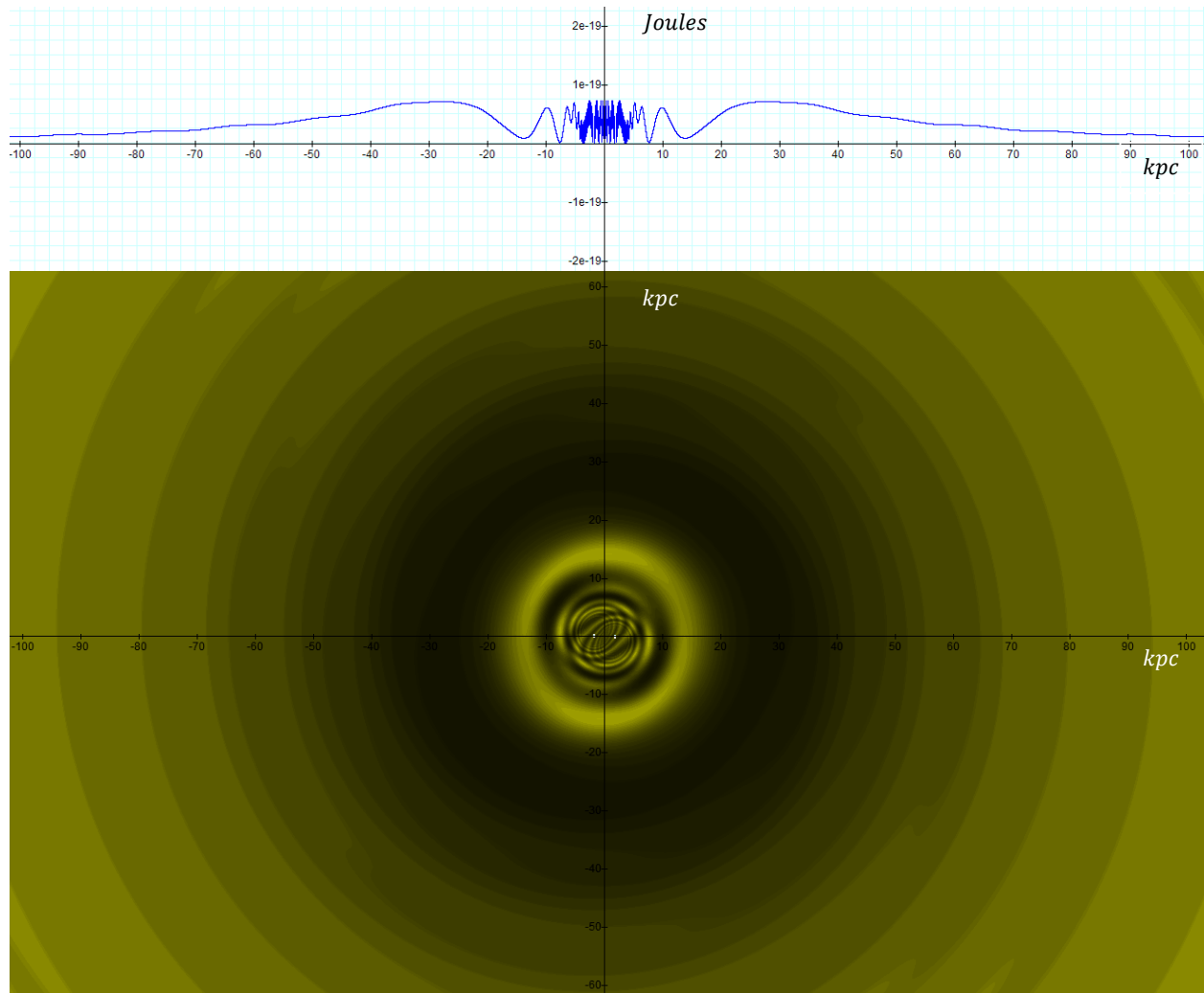


Figure 4-8b: Displays a galaxy generated using the same parameters as figure 4-8a, where v is increased to $0.4c$. Note that a decreased display resolution is used.

Note that the isophote patterns in figures 4-8a and 4-8b are still approximately circular and do not yet provide a spiral structure. However, when the SHP velocity is increased to $v = 0.6c$, as shown in Figure 4-8d, the potential energy of the galactic disk begins to form into a spiral structure with two trailing arms, and the hourglass morphology at the center of the galaxy begins to shift into a bar-like structure. It is generally quite difficult to determine simply by observation whether a spiral arm is leading or trailing. However, in almost all cases where the result is unambiguous, the spiral arms are found to be trailing. This can be expected according to the UG explanation. The underlying reason for the formation of the spiral morphology is that it takes longer for the gravitational signal to reach the farthest sections of the spiral arms than to the sections located closer to the galaxy center. The farthest sections of the spiral are thus influenced by earlier locations of the SHP groups, and therefore lag behind their counterparts at the inner portion of the same spiral. Consequently, the outer edge of a spiral arm should be

trailing, while the inner edge should be leading.⁷⁶ Increasing the velocity of the SHP group to $v = 0.68c$ and $v = 0.75c$ strengthens the spiral structure. As displayed in figures 4-8e and 4-8g, the spiral becomes tighter, further defining the central bar.

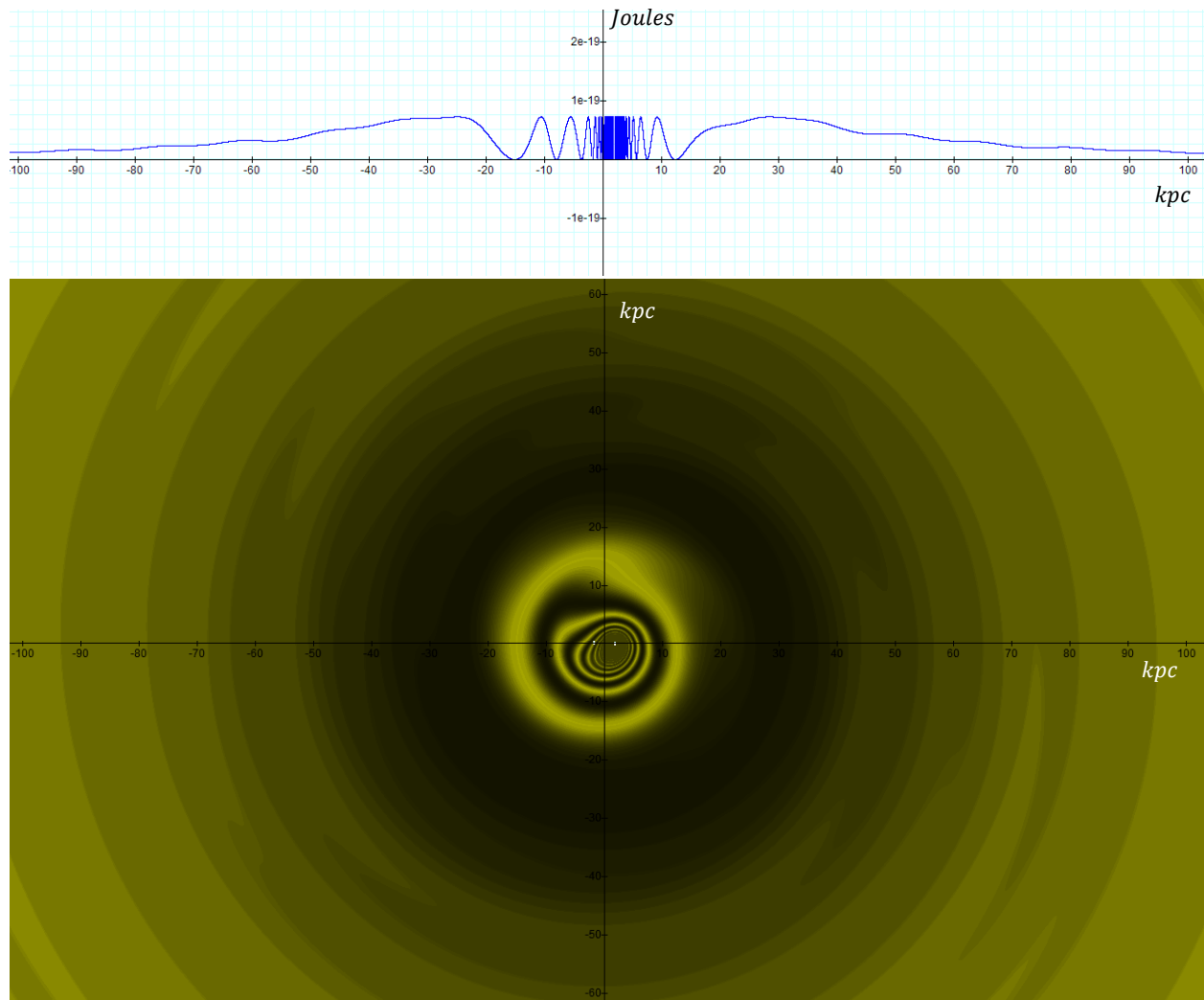


Figure 4-8c: Depicts a galaxy generated via the same parameters as figure 4-8b with only a single superheavy particle ($\Gamma = 0$), producing clear asymmetry.

⁷⁶ Further explanation is provided in Chapter VI.

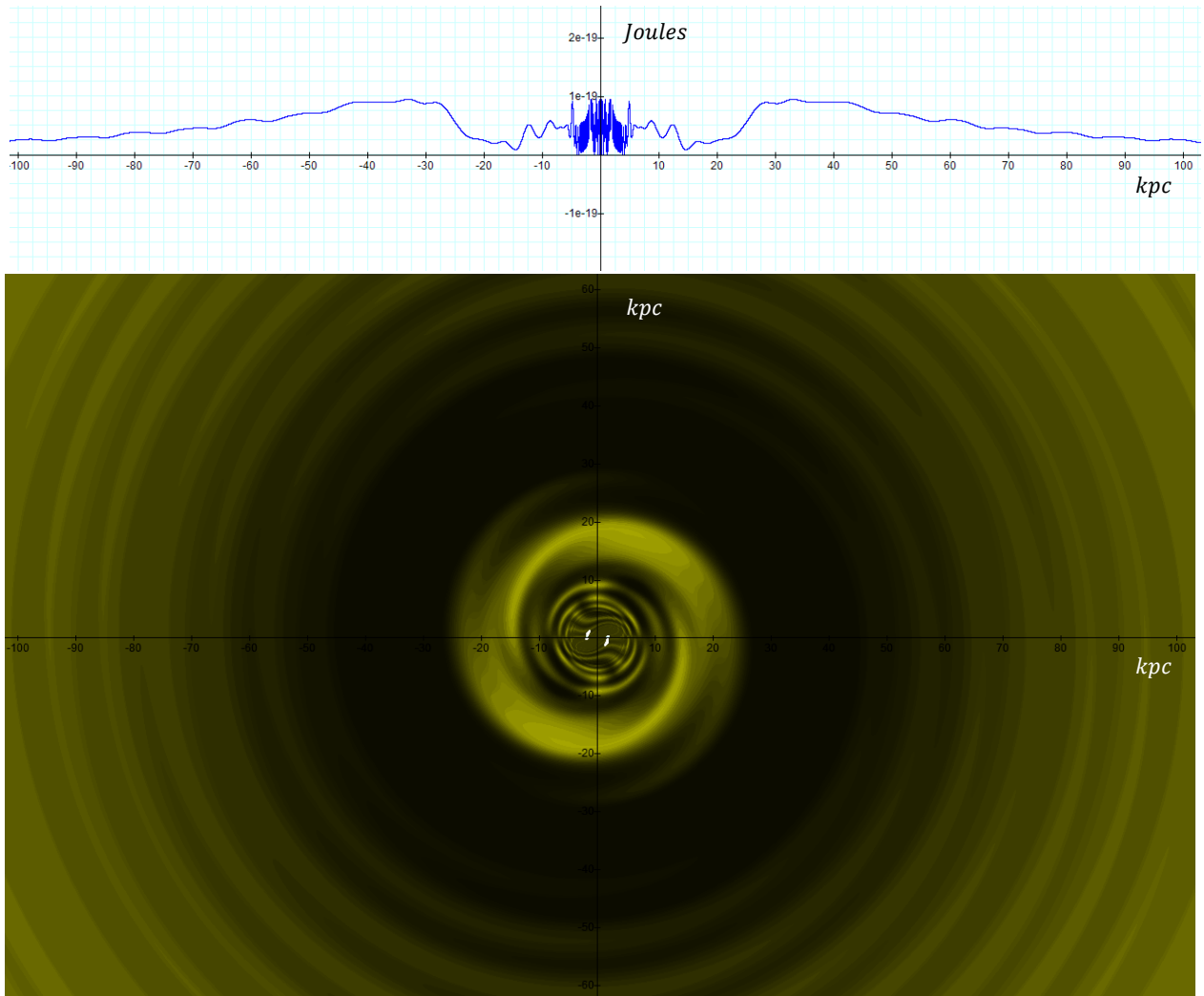


Figure 4-8d: When the velocity of the SHP group is increased to $v = 0.6c$ (using the same parameters of $\Gamma = 1$, $M = 0.156 * 10^5 \text{ kg}$, $A = 1.8 \text{ kpc}$, $M_G = 0$, $N_M = 1$, $N_{m_p} = 1$ and $m_p = 1.674 * 10^{-27}$), the potential energy at the galactic disk begins to form into a spiral structure with two trailing arms, and the central hourglass morphology begins to shift into a bar structure.

Figure 4-8e

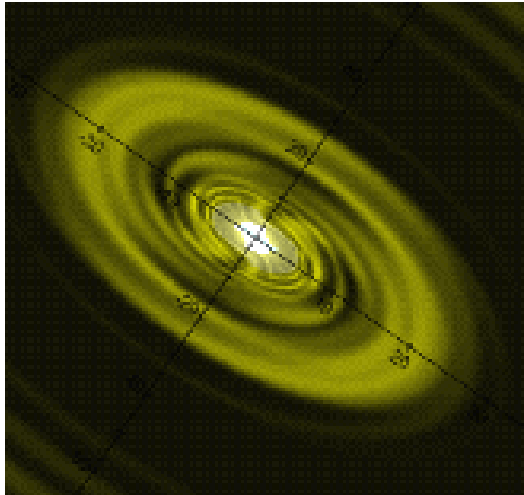


Figure 4-8f

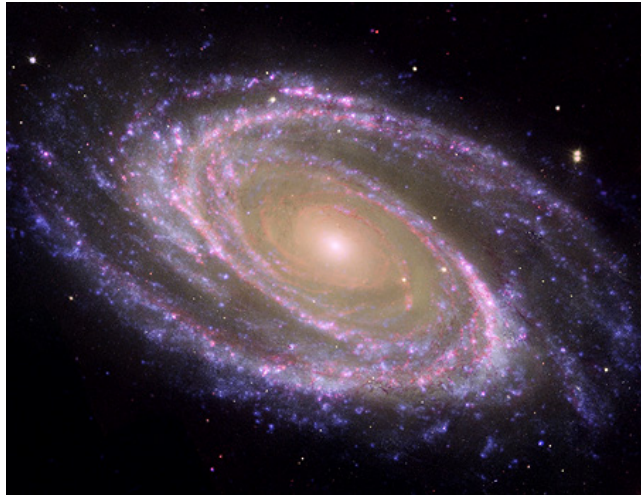


Figure 4-8e: Setting the parameters $M_G = 4 * 10^{38} kg$ and $v = 0.68c$, the calculated model bears a close resemblance to the morphology of the galaxy M81.

Figure 4-8f: provides a composite of M81 from NASA's Spitzer and Hubble space telescopes and NASA's Galaxy Evolution. Image credits: NASA's Spitzer and Hubble space telescopes and NASA's Galaxy Evolution (NASA/JPL-Caltech/ESA /Harvard-Smithsonian CfA); http://www.nasa.gov/mission_pages/spitzer/multimedia/spitzer-20070604.html.

Note the similarity between the calculated pattern displayed tilted in figure 4-8e and the image of the galaxy M81 shown in figure 4-8f after modifying $M_G = 4 * 10^{38} kg$ and $v = 0.68c$.

The dark section between approximately $40 kpc < r < 50 kpc$ in figure 4-8g provides the external maximum at $n = 1$. The galaxy's visible border is located at its $n = 2$ minimum contour at approximately $35 kpc$, and the area enclosed within this radius thus constitutes the galactic disk. A focused view of the central part of $r \lesssim 35 kpc$ is provided in figure 4-8h, demonstrating a spiral morphology with two external trailing arms as well as an internal spiral that consists of both trailing and leading arms. While the trailing spirals are located at the outer end of the visible spiral arms, the leading spirals are located at the inner end of the spiral arms.⁷⁷ Note that this model bears a close resemblance to the galaxy NGC-4622 depicted in figure 4-8i.

⁷⁷ It will be demonstrated that in the case of rapid SHP rotational velocities, the visible galactic arms are actually part of a larger trailing spiral structure that begins at the central nucleus and continues far beyond the galactic disk. However, only some sections of the spiral have sufficiently low potential energy and a high enough density of matter to emit substantial radiation. The perceived morphology therefore displays shorter segments of spirals with leading inner and trailing outer edges.

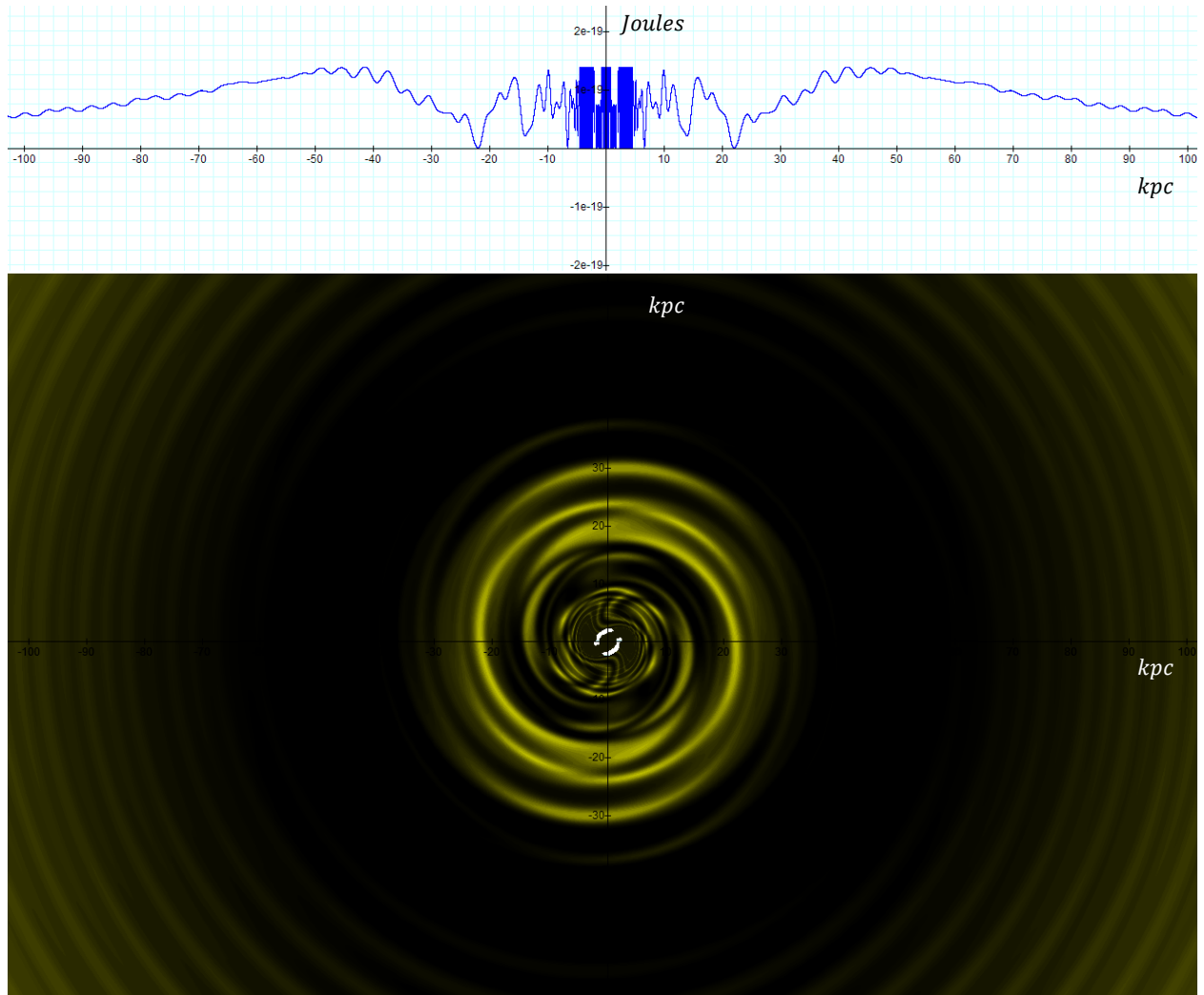


Figure 4-8g: Increasing the speed of the SHP groups to $0.75c$ further strengthens the spiral structure and demonstrates both leading and trailing spiral arms, providing a morphology that resembles the galaxy NGC 4622.

However, there is a clear difference between the modeled galaxy and the observed NGC 4622 galaxy. While the modeled galaxy provides a strong bar at its center, NGC 4622 demonstrates an unbarred or oval structure. Accounting for the additional influence of ordinary matter of mass of $2 * 10^{38} kg$ at the core of the modeled galaxy results in a non-barred spiral morphology, shown in figure 4-8j. Therefore, the principal factor that determines whether or not a spiral galaxy is barred or oval is likely to be the relative amount of ordinary matter at its central core, or the ratio M_G/MN_M .

Figure 4-8h

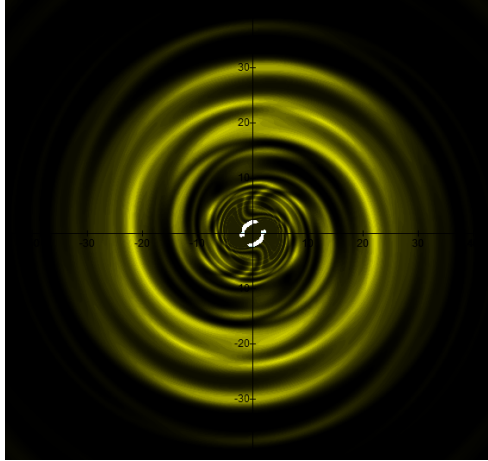


Figure 4-8i



Figure 4-8j

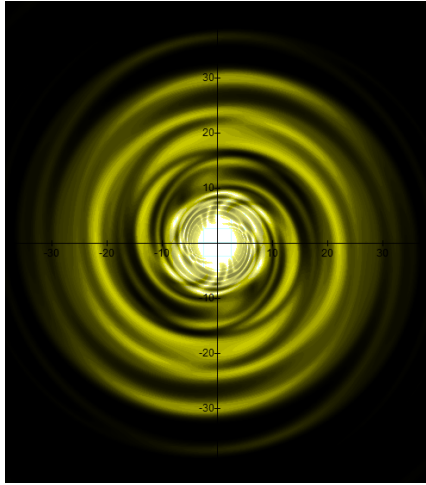


Figure 4-8i



Figure 4-8k

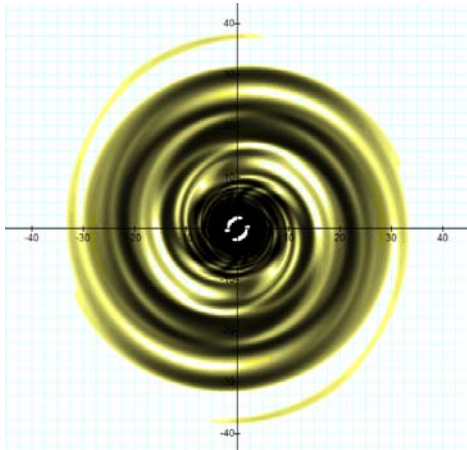


Figure 4-8i



Figures 4-8h and 4-8i: Comparison of the calculated galaxy to NGC-4622 using $\Gamma = 1$, $M = 0.156 * 10^5 \text{ kg}$, $v = 0.75c$, $A = 1.8 \text{ kpc}$, $M_G = 0$, $N_M = 1$, $N_{m_p} = 1$, and $m_p = 1.674 * 10^{-27}$. Credit for Figure 4-8i: G. Byrd, R. Buta, (Univ. Alabama, Tuscaloosa), T. Freeman (Bevill State College), NASA; <http://apod.nasa.gov/apod/ap040221.html>.

Figures 4-8j and 4-8i: Same comparison as displayed in figure 4-8h and 4-8i, however the amount of ordinary matter in the central disk at $r \ll r_0$ is set to $2 * 10^{38} kg$. The central bar structure of figure 4-8f is replaced by an oval bulge.

Figures 4-8k and 4-8i: As the dark background of figure 4-8j provides limited contrast with the color of the calculated spiral arms, a similar comparison is displayed in figures 4-8i and 4-8k, where an inverted color scale is used (the maxima are indicated in light color values and the minima are indicated in dark values).⁷⁸

Section IV-2-3: Flocculent Spiral Structures

As the velocity of the SHP groups increases to $v = 0.85c$ in figure 4-9a, the arms of the modeled galaxy become more tightly wound and segmented in appearance, bearing a resemblance to flocculent structures, as observed in the galaxy NGC 488. To attain a better fit, the rotation of the two SHP groups was reversed relative to the previous modeled galaxies to a clockwise rotation (by using $-w$ rather than w), and the total mass of ordinary matter at the central core of the galaxy was increased to $2.5 * 10^{38} kg$.

Figure 4-9a

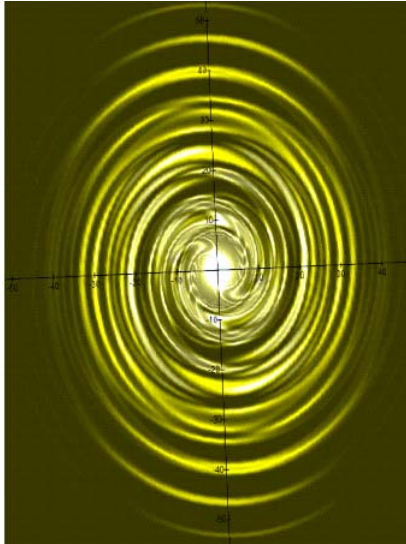


Figure 4-9b NGC 488



Figures 4-9a and 4-9b: Comparison between a tilted view of the calculated galaxy and NGC 488, using the same parameters $\Gamma = 1$, $M = 0.156 * 10^5 kg$, $A = 1.8 kpc$, $M_G = 2.5 * 10^{38} kg$, $N_M = 1$, $N_{m_p} = 1$, $m_p = 1.674 * 10^{-27}$ and an increased speed of $v = 0.85c$. The rotational direction of the SHP groups was reversed to clockwise.⁷⁹

Figure 4-9b: NGC 488, image credit: Johan Knapen and Nik Szymanek, Isaac Newton group of telescopes.

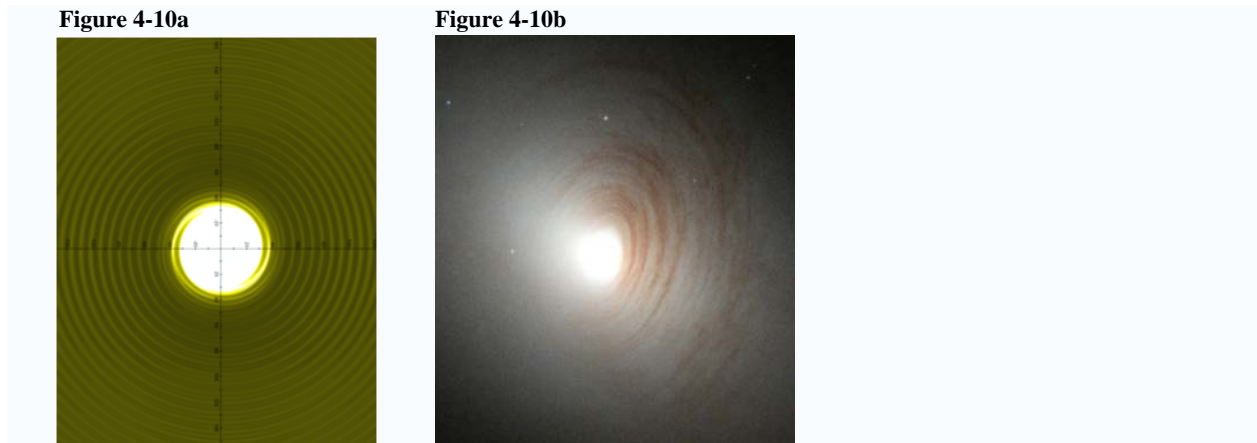
http://images.google.co.uk/imgres?imgurl=http://www.ing.iac.es/PR/newsletter/news6/johan4.jpg&imgrefurl=http://www.ing.iac.es/PR/science/ngc488.html&usg=__wsWG6nhi5biMN2pbNEcaq-dASU=&h=1143&w=1000&sz=110&hl=en&start=6&um=1&tbnid=tOUIfhc2uTM-nM:&tbnh=150&tbnw=131&prev=/images%3Fq%3DNGC%2B488%2Bpicture%26hl%3Den%26sa%3DX%26um%3D1

⁷⁸ Note that the two white arcs at the central bulge are simply a calculation artifact, which occurs at extremely high potential energies where calculated numbers exceed the numeric range of the computer/graphical program. In such cases the pixel remains white. However, even those artifacts can provide useful information as they indicate the general areas where the SHP groups are located.

⁷⁹ Note that the image was calculated in a face-on orientation, and then tilted 35° around the y axis and 2.5° around the z axis, both counter-clockwise.

Section IV-2-4: Lenticular Galaxies

Lenticular galaxies are regarded as transitional objects between elliptical and spiral galaxies. Similar to spiral galaxies they contain a rapidly rotating disk and a central bulge, and similar to elliptical galaxies they are often smooth and featureless, contain little or no cool gas, and have minimal or no star formation. As the transition between the various morphological classifications is generally smooth, it is likely that more than one type of morphology can fall under the broad definition of lenticular galaxies. Figure 4-10a provides an example of a calculated lenticular morphology. Similar parameters to those used to model NGC 4622 in figure 4-8h were applied,⁸⁰ however the mass of ordinary matter at the center of the galaxy was increased to $M_G = 2 * 10^{39} \text{ kg}$. Subsequently, the central bulge expanded to cover all of the minima contours up to the zonal minimum indexed $n = 2$ (therefore, the central bulge almost extends throughout the entire rotating galactic disk). The resultant morphology resembles the lenticular galaxy NGC 2787, displayed in figure 4-10b.



Figures 4-10a and 4-10b: Comparison between a UG calculated galaxy (with face-on orientation) and the lenticular galaxy NGC 2787, using the following parameters for the calculation: $\Gamma = 1$, $M = 0.156 * 10^5$, $N_M = 1$, $A = 1.8 \text{ kpc}$, $M_G = 2 * 10^{39} \text{ kg}$ and $v = 0.75c$. Image credit for figure 4-10b: Marcella Carollo (ETHZ), Hubble Heritage, NASA; <http://apod.nasa.gov/apod/ap020408.html>.

Section IV-3: The Red Square and the Red Rectangle

An interesting finding is made when zooming the display around one of the SHP groups to about 100pc, as shown in figure 4-11a. The figure depicts several concentric crisscrossing isophotes, which emerge in patterns that bear a striking resemblance to MCW 922, the Red Square Nebula, and to the Red Rectangle provided by figures 4-11b and 4-11c respectively. In 2007 Peter Tuthill and James Lloyd reported the Red Square nebula to consist of a box-shaped X structure which necks down into identical opposing hyperbolic bicones, a series of orthogonal linear rungs, and a series of radial linear features resembling a comb that lie along the bicone surfaces (between the rung and the outer edge of the nebula). They additionally noted that the

⁸⁰ The following parameters were used: $\Gamma = 1$, $M = 0.125 * 10^5$, $N_M = 1$, $A = 1.8 \text{ kpc}$, $M_G = 2 * 10^{39} \text{ kg}$ and $v = 0.45c$.

structures are, to a remarkable extent, reflection symmetric about the principle axis (Tuthill & Lloyd, 2007). All of these features appear in the marked sections of figure 4-11a. According to Tuthill and Lloyd, “The finding of a cousin to the Red Rectangle, but with differing spectrum and a hotter central star, implies that the conditions of formation for these elegant bipolar ladders may not be so singular and unique as formerly thought.” Indeed, the fact that several (at least four) such structures were found in this single model figure, and that they are very similar in general appearance yet somewhat differ in particular features, suggests that there may be many such structures even within a single galaxy.

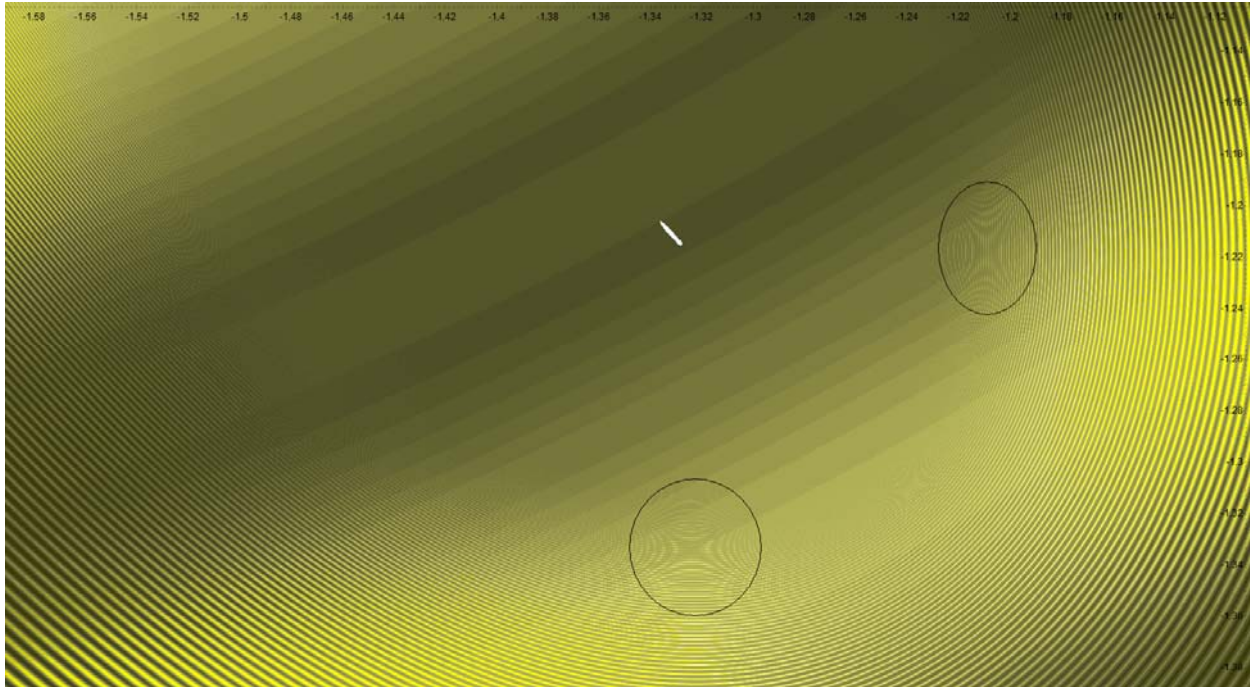


Figure 4-11a

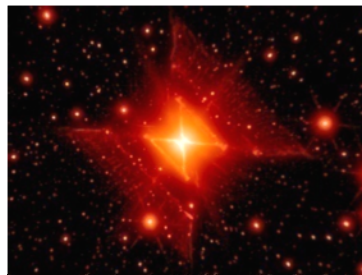


Figure 4-11b



Figure 4-11c

Figure 4-11a: Provides a high resolution image of the same galaxy modeled in figure 4-8h, using $\Gamma = 1$, $M = 0.156 * 10^5$, $N_M = 1$, $A = 1.8 \text{ kpc}$, $M_g = 10^{36} \text{ kg}$, and $v = 0.75c$. The display is zoomed to about 100 pc around one of the SHP groups. The circled areas bear a striking resemblance to MCW 922, the Red Square Nebula, and to the Red Rectangle shown in figures 4-11b and 4-11c respectively (note that aside from the two circled patterns, there are few more similar unmarked patterns). Note that for the purpose of clarity, the color scheme is reversed, where the darker color values indicate lower potential energy.

Figure 4-11b: MWC 922: The Red Square Nebula credit (Tuthill & Lloyd, 2007); <http://apod.nasa.gov/apod/ap070416.html>.

Figure 4-11c: The Red Rectangle, Image credit: H. Van Winckel (KULeuven), M. Cohen (UC Berkely), H. Bond (STScI), T. Gull (GSFC), ESA, NASA; <http://www.nasaimages.org/luna/servlet/detail/NVA2~4~4~5326~105852>: Rungs-of-the-Red-Rectangle.

Section IV-4: Companion Galaxies

Figure 4-12a provides the calculated potential energy of an ordinary particle of mass m_p within the plane of a galaxy with one companion. The parameters of the main galaxy are given by $\Gamma_1 = 0$, $M_1 = 0.156 * 10^5$, $N_{M_1} = 1$, $A_1 = 1.8 \text{ kpc}$, $M_{G_1} = 7 * 10^{38} \text{ kg}$ and $v_1 = 0.8c$, and the parameters of the companion galaxy are given by $x = 150 \text{ kpc}$, $\Gamma_2 = 0$, $M_2 = 0.6 * 10^5$, $N_{M_2} = 1$, $A_2 = 1.8 \text{ kpc}$, $M_{G_2} = 7 * 10^{38} \text{ kg}$ and $v_2 = 0.4c$ (figure 4-12a). The general structure of the calculated morphology bears a resemblance to the cartwheel galaxy shown by the Hubble Space Telescope (HST) image (figure 4-12b). The two galaxies on the left side of the image are companion galaxies. A similar pattern of “beads on a string” was spotted in Andromeda and number of other galaxies with nearby companion. A comparable pattern is also apparent in figure 4-13, displaying the effect of a companion on supernova 1987A.

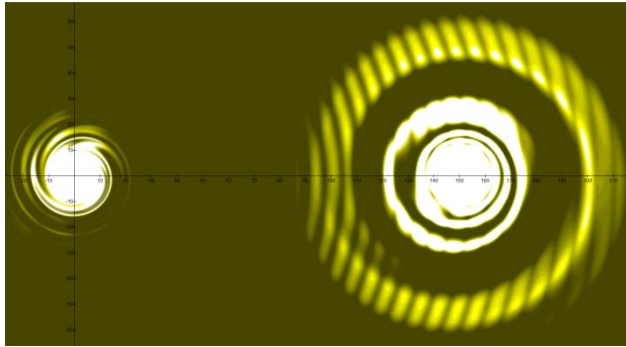


Figure 4-12a: UG calculated image



Figure 4-12b

Figure 4-12b: Observed Cartwheel Galaxy ESO 350-40, image credit: NASA, ESA, and K. Borne (STScI) <http://hubblesite.org/gallery/album/pr2007017d>.



Figure 4-13: Supernova 1987A, image credit: NASA, ESA, P. Challis and R. Krushner (Harvard-Smithsonian Center of Astrophysics); [http://www.nasa.gov/multimedia/imagegallery/image feature 773.html](http://www.nasa.gov/multimedia/imagegallery/image%20feature%20773.html).

Section IV-5: Multiple SHP Groups

In the above examples, a simple model based on as little as four or five independent parameters (M , A , w (or v), M_G/N_M and Γ (for the case of binary SHP groups)) of a single galaxy composed of a single or binary SHP groups and ordinary matter was demonstrated to account for a variety of galactic and nebular morphologies. However, as real physical systems are likely to contain multiple types of superheavy particles and multiple SHP groups, the UG model may be extended to cover more complex cases. To start, a galaxy may contain multiple SHP groups rotating around the central core at different velocities and at various orbital radii. However, following the logic provided in section III-3, the orbits of the SHP groups are nearly circular and their rotational velocities are determined uniquely by their radii via equation 3-3-1, where $v_j = wA_j$. Therefore, any additional SHP group requires the addition of three or four independent variables (M_j , N_{M_j}/N_M , A_j and Γ_j). Following the third section of chapter III, all of the SHP groups with orbital radii shorter than their zonal oscillation range with ordinary matter must comply with $A_j < c/w$, and must rotate together as a rigid body, in unison with the central core of the galaxy. A model of multiple SHP groups will be applied in the following chapter for a UG analysis of Saturn's ring system.

The UG model can be further extended by allowing some SHP orbits to deviate from the rotational plane of the galaxy. Substantial deviation, for instance a deviation of 90° , may explain the structure of polar ring galaxies while a lesser amount of deviation may explain the structure of ESO 510-G13, displayed in Figure 4-14.



Figure 4-14: An edge-on view of the galaxy ESO 510-G13, image credit: NASA, the Hubble Heritage Team, and C. Conselice; <http://heritage.stsci.edu/2001/23/caption.html>.

Chapter V: Applying the Theory of Unified Gravitation to Saturn's Ring System

Section V-1: Summary of Current Theories

It has been nearly four hundred years since Galileo first observed Saturn's extensive ring system, and about 20 to 30 years since smaller ring systems were discovered around Jupiter, Uranus and Neptune. Despite the extensive study of planetary rings and major improvements in theory, as more detailed measurements become available, observations reveal increasingly complex systems, and many features within the rings have not yet been adequately explained.⁸¹

Current theories explaining the observed planetary ring structures for the most part describe gravitational interactions between ring material, nearby satellites and the parent planet. As the mass of each of the four solar gas planets exceeds the mass of their respective satellites by several orders of magnitude, the planetary influence on the behavior of ring particles is likely to be far greater than that of the satellites. When applied to an isolated planet-ring system (without the influence of nearby satellites), Newton's theory of gravitation allows a rotating object to occupy one of an infinite number of possible Keplerian orbits, however does not maintain any intrinsic preference for one orbit over another. Hence, an elaborate ring structure, as observed in the Saturnian system, is unlikely to be explained simply by Newton's predicted gravitational interaction between ring particles and their parent planet. Such structure, even if formed, would be expected to decay over time. Current theories thus mainly center on orbital resonances between ring particles and satellites as the possible underlying cause for the planetary ring structure.

Large bodies cannot form spontaneously at orbital radii below the Roche limit of a planet, where the tidal forces acting on different portions of the bodies become stronger than the gravitational force that acts between them to keep them intact. Therefore, satellites may form spontaneously only at radii exceeding their planet's Roche limit. In all four gas planets, the number of satellites decreases outside of the Roche limit, while their size and the space between them increase with distance from the planet. As the orbits of the planetary satellites and ring matter are Keplerian, their orbital periods change continuously with distance from the planet, and their speeds reduce proportionally to $1/r^{1/2}$. Therefore, there are a large yet countable number of radii where the orbital period of the ring particles is a simple integer fraction of a given satellite's orbital period, referred to as an orbital resonance. At ring distances at which orbital resonances do not occur, the location of the closest encounter between the satellite and the ring particle varies and the average satellite's influence on the ring particle tends to cancel out over time. However, as a result of orbital resonances, periodic close encounters occur at fixed locations and the small gravitational forces from the satellite repeatedly act on the same ring material. After some number of orbits this may cause a notable disturbance.⁸² The migration of

⁸¹ A summary of what is known about the planetary ring systems, the current leading theories, and which features within the rings have not yet been adequately explained is provided in *Planetary Ring Systems* by Miner et. al (Miner, Wessen and Cuzzi, 2007).

⁸² Another mechanism, known as a Lorentz resonance, is theorized to be capable of creating planetary rings with dust-size particles, by which small particles located slightly inward to or outward from the Lorentz resonance radius experience small

material away from the radii of the resonances is believed to explain some of the gaps within the rings. In certain cases, a gap may be produced by an embedded satellite that is large enough to clear a space in the ring, as in the case of the moons, Pan and Daphnis, respectively located within the Encke and Keeler gaps in Saturn's ring system. A mechanism by which the gravity of a local moonlet, or shepherd moon, pushes ring material away was also thought to explain how narrow ringlets are confined and prevented from spreading out.⁸³

Although the current Newtonian-based theories have been successful in accounting for a small number of planetary rings and gaps, a broad and conclusive theory has not yet been developed to explain the structure and vastness of the known ring systems, or their specific patterns. The relatively simpler ring systems of Jupiter, Uranus and Neptune are far from being understood, however they present far less of a challenge than the A and B rings of Saturn, where the origin of the rings and their unique properties are still unknown. Explanation of certain A and B ring characteristics via orbital resonances requires an enormous amount of embedded satellites, all less than a kilometer in diameter.⁸⁴ Even then, the cause of the irregular structure of the inner half of the B ring remains unaccounted for. In the case of Uranus's less extensive ring system, none of the known satellites provide the gravitational forces needed to confine its ring particles. A thorough search to locate satellites closer to the planet than Cordelia restricts the possible size of satellites to be too small to effectively shape and confine the Uranian rings via gravitational shepherding.⁸⁵ Further questions address the mechanisms that determine the sharpness and ellipticity of planetary rings. It is unclear why some rings are sharp and narrow while others are wide and diffused, or why some of the rings are more elliptical than others, or what causes the formation of arcs. There are also questions as to how the planetary ring and satellite systems were created, their ages, and how they persist and change over time. According to current theories, rings can essentially form in two ways: (1) Planetary rings may be a remnant of material from the distant past of a planet that was prevented from coalescing into individual satellites, or (2) ring material may be comprised of the remaining debris of former satellites that wandered too close to the planet and were torn apart by its gravitational tides, or of satellites shattered by collision with an interplanetary object. Certain rings may also be replenished by meteoroid bombardment, or by eruptions from a nearby satellite.⁸⁶ When applied to the estimated timescale of the rings, data from NASA's Voyager Spacecraft in the 1970s, and later from NASA's Hubble Space Telescope, led scientists to infer that Saturn's present rings could not have existed for more than tens of millions of years, a small fraction of the age of the Solar System. Planetary rings were thus believed to be a temporary feature created by some

forces that push them away from the resonance radius. Over time, the region around the ring may become depleted of dust-size particles. This process, however, cannot explain the existence of rings consisting of larger objects.

⁸³ Saturn's F ring and the dense, narrow rings of Uranus rings were initially thought to have formed via gravitational shepherding. However, new discoveries have challenged this theory.

⁸⁴ With the current available observation resolution, any satellites with a diameter larger than one kilometer should have already been detected.

⁸⁵ An alternative theory suggests that the Uranian rings were formed by the trapping of outward drifting particles between resonances of the planet's inner satellites (Fridman & Gorkavyi, 1994). After their formation, the rings left the resonances that produced them and drifted hundreds of kilometers toward their current positions.

⁸⁶ It is current belief that eruptions from the moon Enceladus are the main source of material replenishment for Saturn's E ring.

cataclysmic event(s) and expected to dissipate over time. However, it is very difficult to understand how such a massive ring system as Saturn's could be so finely divided by those same processes over time periods lasting only tens, or at most hundreds of millions of years, especially when an interplanetary meteoroid flux is thought to have been almost depleted for a much longer period of time. Features observed by NASA's Cassini mission indicate that Saturn's finely divided rings could not have resulted from a single cataclysmic event, and instead may persist through a recycling of material. Observations show that even when ring objects fragment into groups of smaller particles, they tend to re-clump together to sustain the overall ring structure. Support is subsequently escalating for the theory that the Saturnian ring system formed with the creation of the planet and Solar System, in contradiction to many existing theories.⁸⁷

Finally, current theories that explain the structure of ring systems via interactions between their ring particles and satellites do not address questions as to why gas planets have a large number of satellites, or why those satellites rotate at their specific orbital locations. Careful analysis of the orbital periods of satellites reveals that the resonances that occur between rings are of the same kinds that occur between satellites and rings, or between different satellites. This strongly suggests that satellites and rings were formed from the same material via the same mechanism. It is proposed by the UG theory that planetary satellites follow the same orbits previously occupied by former rings. This view is further strengthened by the observation that both Saturn and Uranus have rings and satellites that share the same orbits. Therefore, we are left with the classic chicken and egg question: which came first, the rings which formed the satellites or the satellites which formed the rings?

Although Newton's theory of gravitation (as well as general relativity) has been repeatedly tested and proven to work well in our Solar System, a four hundred year old question, which is older than the Newtonian theory itself, regarding the origin and the mechanisms underlying Saturn's ring structure remains unsolved. This query will be evaluated via a UG analysis of the Saturnian ring system. The present goal, however, is to demonstrate the power of the UG theory and its ability to provide the general morphology and characteristics of complex systems on all distance scales. Therefore, the current UG analysis of planetary rings will be limited to Saturn's main body of rings, specifically rings D, C, B, A and the Cassini Division. Nevertheless, the same methods and techniques used here may be applied to the remaining planetary ring systems.

Section V-2: The D, C, B, A, and F Rings and the Cassini Division of Saturn

Following equation 3-3-1 developed in chapter III-3, the velocity of the SHP groups in orbit around the center of an astronomical body is given by

⁸⁷ NASA (December 12, 2007). "Saturn's Rings May be Old Timers." Press release. Retrieved 2007-12-27. Archive copy at the Internet Archive http://www.nasa.gov/mission_pages/cassini/media/cassini20071212.html.

Equation 5-1

$$v_j = wA_j$$

where the following rules must be fulfilled:

Rule 1: In a steady state condition, all orbiting SHP groups with a zonal oscillation range exceeding their orbital radius A_j around the center of an astronomical body share the same angular velocity w , where w is the angular velocity of the central core of the astronomical body.

Rule 2: As a consequence of equation 5-1, and the requirement that the velocity of a superheavy particle cannot surpass the speed of light, all superheavy particles with a zonal oscillation range greater than A_j must reside within the distance $A_j < c/w$ from the center.

A direct consequence of equation 5-1 is that the velocity of a superheavy particle of mass $M_j > \frac{\pi A_j}{b m_p \gamma}$ is relativistic when $A_j \rightarrow c/w$.⁸⁸ According to the theory developed in Chapter III (and demonstrated for galaxies in chapter IV), the existence of wide rings and extensive spiral structure requires some SHP groups to orbit at relativistic speeds.⁸⁹ Hence, achieving the vast and almost continuous spread of Saturn's main body of rings requires that some of its SHP groups rotate at relativistic velocities. However, the surface matter of the planet rotates at far below relativistic speeds. This leads to the conclusion that Saturn's central core must rotate at a far greater angular velocity than the planetary surface. In the contrary case, if Saturn's central core, and therefore its relativistic SHP groups, travel at an angular velocity lower than or equal to the angular velocity of the planet's surface, the orbital radii of the relativistic SHP groups would need to exceed the radius of the planet by several orders of magnitude, resulting in an entirely different structure than observed. As discussed in Chapter IV, ordinary matter accumulates to form rings or spirals in the vicinity of the deep minima contours created by the interaction between the dominant, centrally located SHP groups and ordinary matter.⁹⁰ In the case of stationary superheavy particles (or low SHP velocities), the density of the ordinary matter is expected to increase in the vicinity of the resultant stationary (or low velocity) zonal minima. For the case where the angular velocity of the SHP groups exceeds the angular velocity of the orbiting object, the SHP-generated minima move faster than the ability of the object to follow. Thus, a higher density of ordinary matter can be expected at the minima of the average potential energy, where the average potential energy is calculated over a period of time equal to $2\pi/w$ seconds. In areas where the density of ordinary matter is sufficiently high and the gravitational tidal forces are not too strong, ring matter will begin to coalesce into satellites or other relatively

⁸⁸ The zonal oscillation range of a superheavy particle of mass M_j and an ordinary particle of mass m_p is given by $bM_j m_p \gamma / \pi$. The planetary center is within the oscillation range of the SHP, which orbits at a radius A_j when $M_j > \frac{\pi A_j}{b m_p \gamma}$.

⁸⁹ In contrast, a superheavy particle group in orbit around the central core moving at a speed of $v_j = wA_j \ll c$ creates a narrow circular ring of the type demonstrated by Uranus.

⁹⁰ Planetary ring particles or objects are assumed to be too small to support superheavy particles of their own, thus they contain only ordinary matter.

large objects. As the UG equations of motion have a linear dependency on the number of particles involved, and the process of coalescence is assumed to simply “glue” particles together while conserving their types and their numbers, the orbit of a newly constructed object should be approximately equal to the average of the prior orbits of its individual particles. Furthermore, as the velocities of Saturn’s satellites and ring matter are observed to obey Keplerian dynamics, the angular velocity of the newly created object is expected to be slightly higher than the angular velocities of adjacent particles at larger orbital radii, and lower than the angular velocities of adjacent particles at smaller orbital radii. In either case, the rotating object will periodically encounter nearby orbiting matter. Over time the gravitational pull of the object, which is magnified by the accumulating effect of many synchronized periodic encounters, causes a disturbance and a shift in the orbits of surrounding matter. Adjacent orbiting matter may consequently be absorbed into the forming object, or expelled away from their initial orbital locations, creating a small gap around the object’s orbit. As the mass of the object increases, its gravitational reach expands, allowing for the consumption or ejection of material from a larger range of distances, consequently widening the gap. The mass of the object and the size of the gap continue to grow as long as there is an available supply of matter in the vicinity of the object, and as long as the entire object is located beyond the planet’s Roche limit.⁹¹

The strength of a theory is determined by its ability to explain all observed phenomena using a minimal number of variables and assumptions, as well as its ability to correctly predict the outcome of new experiments. The goal of the current exercise is to demonstrate the ability of the UG theory to explain the observed structure of Saturn’s main body of rings, specifically rings D, C, B, A, F and the Cassini Division, using a simple model of very few variables. As discussed, a UG-based model that is capable of explaining a vast and complicated structure such as Saturn’s ring system requires superheavy particles orbiting at relativistic velocities. The simplest possible UG model that fulfills this requirement consists of a single SHP group with

⁹¹ Based on Newtonian gravitation, a planet’s Roche limit resides at about $r = \left(\frac{f_r \bar{\rho}_s}{\bar{\rho}_m}\right)^{1/3} R_s$, where R_s is the radius of the planet, $\bar{\rho}_s$ and $\bar{\rho}_m$ provide the average densities of the planet and the object respectively, and f_r is a constant, where $f_r = 2$ for the case of a rigid satellite and $f_r = 2.423$ for the case of a fluid satellite. Relying only on Newtonian gravitation, it is difficult to explain the range of radii where both rings and satellites are observed to coexist (for example, in the range starting with the Encke gap, which contains the satellite Pan, up to Pandora’s radius of orbit between the A ring and the F ring). The intermingling of rings and satellites can be explained relatively easily via the UG theory, as the potential energy of the object due to the contribution of SHP groups contains cosine terms that oscillate as a function of the inverse of their distance from the object. In the range of radii in the vicinity of the classical Roche limit, or $r \approx \left(\frac{f_r \bar{\rho}_s}{\bar{\rho}_m}\right)^{1/3} R_s$, the additional oscillating terms create sub-zones in which the tidal forces of Saturn prevent additional coalescence, where planetary rings can consequently be retained. These sub-zones are separated by a second set of sub-zones in which the tidal forces enhance coalescence, or are simply too weak to prevent it, possibly resulting in the formation of a satellite and in the consumption and/or ejection of the enclosed ring material. Therefore, in this range of radii, a series of narrow rings and small satellites can coexist. However, the amplitudes of the SHP-generated oscillations are relatively small compared with the amplitude of the potential energy contributed by the planet’s ordinary matter. Consequently, the oscillations affect the process by which matter coalesces to form a satellite mainly in the vicinity of the classical Roche limit. Outside this range of radii, the UG-based model becomes consistent with the results of the classical Roche model. Hence, in agreement with the Newtonian theory, no satellites can form below the vicinity of $r \approx \left(\frac{f_r \bar{\rho}_s}{\bar{\rho}_m}\right)^{1/3} R_s$, while beyond this range, planetary rings coalesce into satellites over time. However, contrary to the prediction of Newton’s theory, in the vicinity of $r \approx \left(\frac{f_r \bar{\rho}_s}{\bar{\rho}_m}\right)^{1/3} R_s$, rings and small satellites may coexist.

N_{M_1} superheavy particles of particle mass M_1 rotating at a speed of $v_1 = wA_1$ in a circular orbit of radius A_1 around the planetary center (using a total of five independent parameters w , N_{M_1} , M_1 , A_1 , and M_S , where M_S denotes the overall mass of Saturn's ordinary matter). This simple model will be demonstrated to successfully explain the general structure of the Saturnian ring system, as well as a number of principal ring characteristics. In particular, the model will address the origin and stability of the current ring structure, spiral wave patterns within the rings,⁹² the observed dynamic changes in structure occurring over time, and the phenomenon of spokes.

While successful in explaining the general ring structure down to a scale of a few hundred kilometers, the simplified model does not produce the observed fine structure of Saturn's rings. Resolving this issue thus requires the addition of at least one more SHP group. To keep the complexity of the model to a minimum, a second group of N_{M_2} SHPs of the same mass M_1 rotating at a velocity of $v_2 = wA_2$ around the center of the planet in a circular orbit of radius A_2 can be added, increasing the total number of independent variables to seven. In this example the variables M_1 , v_1 , v_2 , A_1 , N_{M_1} , $\frac{N_{M_2}}{N_{M_1}}$ and M_S/N_{M_1} were selected. For simplicity, w was replaced by v_1 , where $w = v_1/A_1$, and A_2 was replaced by v_2 , where $A_2 = v_2/w = A_1 v_2/v_1$.⁹³ The above analysis will be shown to produce a fairly accurate model of the general structure as well as the underlying fine-scale structure of Saturn's main body of rings.

An initial rough estimation of the mass of the superheavy particle that dominates the structure of Saturn's ring system can be deduced from the characteristics of the outermost E ring, extending from about 183,000 *km* to beyond 483,000 *km* from the planetary center. As the E ring provides the observed external boundary of Saturn's rings, it can be assumed to reside in the vicinity of the outermost maximum contour of the SHP group that dominates within the range of 62,000 *km* < r < 600,000 *km*. Consequently, it is reasonable to assume that the outer maximum associated with the dominant SHP occurs somewhere between about 483,000 *km* and 600,000 *km* from the planetary center. Using the non-relativistic equation 2-1-42, the external maximum is given by

Equation 5-2

$$r_1 \approx \frac{bM_1m_p}{\pi + \arccos(\Psi_1)}$$

where Saturn's entire collection of ordinary matter and remaining superheavy particles (other than those of group 1) influences the location of this maximum exclusively through the term $\arccos(\Psi_1)$, where $0 \leq \arccos(\Psi_1) \leq \pi$ and 483,000 *km* $\leq r_1 \leq$ 600,000 *km*. Substituting these inequalities into equation 5-2, where the denominator of the equation is between π and 2π , yields 10^{-8} *kg* $\leq M_1 \leq 2.5 * 10^{-8}$ *kg*. To further narrow down the values of the dominant SHP group responsible for the general structure of Saturn's ring system, equation 3-1-20 for the case of a single SHP group (or $\Gamma = 0$) reduces to

⁹² As matter of fact, the UG theory leads to the conclusion that the rings are composed almost entirely of tight spirals.

⁹³ As will be shown, the effect of N_{M_1} and M_S/N_{M_1} on the morphology is relatively small, therefore reducing the minimum number of independent variables required to explain and emulate the rings of Saturn to five.

Equation 5-3a

$$E_1(x_0, y_0, z_0, t_0) = -\frac{GN_{M_1}M_1N_{m_p}m_p\gamma^2(v_1)}{a}\left(e^{a/\dot{D}_{s_1}}\cos\left(\frac{bM_1m_p\gamma(v_1)}{\dot{D}_{s_1}}\right) - 1\right) - \frac{GN_{m_p}m_pM_S}{r_0}Z + N_{m_p}m_p c^2 + \frac{1}{2}N_{m_p}m_p u^2$$

The term $N_{m_p}m_p c^2$ is independent of the locations of the minima, and thus bears no influence on the morphology of the rings. Consequently, this term may be dropped. As the ring particles reside above the surface of Saturn, $Z = 1$. Furthermore, since the orbits of Saturn's rings and satellites are in compliance with Kepler's laws of motion, the following approximation can be made:⁹⁴

Equation 5-3b

$$-\frac{GN_{m_p}m_pM_S}{r_0} + \frac{1}{2}N_{m_p}m_p u^2 = -\frac{GN_{m_p}m_pM_S}{2r_0}$$

Therefore, the maxima and minima of equation 5-3a are, for all practical purposes, identical to the maxima and minima of

Equation 5-3c

$$E_1(x_0, y_0, z_0, t_0) = -\frac{GN_{M_1}M_1N_{m_p}m_p\gamma^2(v_1)}{a}\left(e^{a/\dot{D}_{s_1}}\cos\left(\frac{bM_1m_p\gamma(v_1)}{\dot{D}_{s_1}}\right) - 1\right) - \frac{GN_{m_p}m_pM_S}{2r_0}$$

The morphology of planetary rings is determined mainly by the locations of the potential energy minima, rather than by the local magnitude of the potential energy level. Although substantial (or even dominant), the contribution of Saturn's ordinary matter term $-\frac{GN_{m_p}m_pM_S}{2r_0}$ to the overall energy level of the object changes very gradually with distance relative to the rate of change of the rapidly oscillating contribution of the superheavy particles. Therefore, the influence of Saturn's ordinary matter on the local frequency and general shape of the potential energy oscillations, as well as on the locations of the local minima, is small. Consequently, the locations of the minima of $E_1(x_0, y_0, z_0, t_0)$ can be approximated by finding the locations of the minima of

Equation 5-3d

$$\xi_1(x_0, y_0, z_0, t_0) = -\frac{GN_{M_1}M_1N_{m_p}m_p\gamma^2(v_1)}{a}\left(e^{a/\dot{D}_{s_1}}\cos\left(\frac{bM_1m_p\gamma(v_1)}{\dot{D}_{s_1}}\right) - 1\right)$$

⁹⁴ Equation 5-3b can be proven with the aid of the centrifugal force equation $\frac{N_{m_p}m_p u^2}{r_0} = \frac{GM_S N_{m_p}m_p}{r_0^2}$, leading to $u^2 = \frac{GM_S}{r_0}$.

Subsequently, substituting $u^2 = \frac{GM_S}{r_0}$ in the kinetic energy term on the left side of equation 5-3b proves this equation. Note that the orbiting object velocity \vec{u} is non relativistic, and that observations have established that the deviations of the motion of Saturn's rings objects and satellites from Kepler's laws are minimal, thus the contribution of the SHPs to the overall force must be very small. Therefore, the non-relativistic centrifugal force, which neglects the contribution of the SHPs to the overall amplitude of the force, should provide a good approximation.

where the contribution of Saturn's ordinary matter is absent.⁹⁵ Equation 5-3d was employed to construct two dimensional color-coded maps of the resultant calculated energies as functions of the SHP mass M_1 , the velocity of the SHP group v_1 and its radius of orbit A_1 .⁹⁶ The constructed maps were then compared with published images of Saturn's main body of rings, which comprise of rings D, C, B, A and the Cassini Division.

Figure 5-1 provides a UG calculated map in comparison to an observed image of Saturn's ring system generated using RSS 3-wavelength occultation data recorded by NASA's Cassini satellite, which samples a single trace radially through the rings. A reasonably good fit was found using a single group of SHP mass $M_1 = 1.15 * 10^{-8} \text{ kg}$ rotating at a speed of $v_1 = 0.3c$ in a circular orbit of radius $A_1 = 100 \text{ km}$ around the center of Saturn. The calculated map of Saturn's ring plane, drawn between the planet and the edge of the A ring at $136,775 \text{ km}$, reveals large spiral structures encircling the planet. A low level of potential energy, and therefore a high density of matter, can be observed in the lighter areas of the UG map (demonstrated in the vicinity of $74,000 \text{ km}$ and $98,000 \text{ km}$), and a high level of potential energy, and therefore a low density of matter, or even gaps are observed in darker regions (viewed in the vicinity of $66,000 \text{ km}$, $85,000 \text{ km}$ and $118,000 \text{ km}$ from the planetary center). At a display resolution of lower than approximately 100 km , the calculated map bears a significant resemblance to the observed large-scale structure of Saturn's ring system. However, figure 5-1a, as well as other observed images recorded by Cassini and Voyager, reveals additional fine structure that is not present in the simple calculated model of a single SHP group. As discussed, in order to provide for the general large-scale as well as the fine-scale structure of Saturn's rings (while keeping the complexity of the model to a minimum), a second orbiting SHP group of the same SHP type was added.

Following equation 5-1, the velocity v_2 and the orbital radius A_2 of the second group are related via $w = \frac{v_2}{A_2} = \frac{v_1}{A_1}$. The velocity v_2 and the radius of orbit A_2 were calculated using the fine structure observed in the D ring.

Closest to Saturn, the D ring consists of a number of faint, narrow ringlets. The inner edge of the D ring is indistinct, and the forces that sustain this part of the ring are poorly understood. Furthermore, as shown in figure 5-2a, a new type of regular pattern, yet unexplained, was detected in the gap between the D73 ringlet and the C ring. This pattern was found to consist of a fine structure of a wavelength of approximately 30 km (Hedman, Burns & Showalter, 2007).

⁹⁵ In mathematical terms, ordinary matter affects the location of the minima through the \arccos term in the denominator of equation 2-1-42. As $0 \leq \arccos(\Psi_1) \leq \pi$, the ordinary matter effect is significantly smaller than $(2n + 1)\pi$ for any case where $n \gg 0$, and diminishes as n increases. At low n indices, the influence of ordinary matter is limited to shifting the minima locations, causing a relatively mild distortion to the overall ring structure. Inclusion of the ordinary matter contribution in the UG calculations requires the use of a wide range of energy scales in the two dimensional maps, which would overwhelm the SHP contribution, flattening the oscillations contributed by the SHP groups to the point where the local maxima and minima become almost indistinguishable. Therefore, the term $\frac{GN_{m_p}m_pM_S}{2r_0}$ was left out.

⁹⁶ Grayscale was applied to indicate the energy level at any given display point, where darker shades represent higher potential energy levels.

In order to calculate the parameters of the second SHP group, equation 5-3d must be modified to include its contribution to the potential energy of the object, leading to

Equation 5-4

$$\begin{aligned} \xi(x_0, y_0, z_0, t_0) &= -\frac{GN_{M_1}M_1N_{m_p}m_p\gamma^2(v_1)}{a}\left(e^{a/\tilde{D}_{s_1}}\cos\left(\frac{bM_1m_p\gamma(v_1)}{\tilde{D}_{s_1}}\right)-1\right) \\ &\quad -\frac{GN_{M_2}M_1N_{m_p}m_p\gamma^2(v_2)}{a}\left(e^{a/\tilde{D}_{s_2}}\cos\left(\frac{bM_1m_p\gamma(v_2)}{\tilde{D}_{s_2}}\right)-1\right) \\ &= N_{M_1}\left[-\frac{GM_1N_{m_p}m_p\gamma^2(v_1)}{a}\left(e^{a/\tilde{D}_{s_1}}\cos\left(\frac{bM_1m_p\gamma(v_1)}{\tilde{D}_{s_1}}\right)-1\right)\right. \\ &\quad \left.-\frac{G(N_{M_2}/N_{M_1})M_1N_{m_p}m_p\gamma^2(v_2)}{a}\left(e^{a/\tilde{D}_{s_2}}\cos\left(\frac{bM_1m_p\gamma(v_2)}{\tilde{D}_{s_2}}\right)-1\right)\right] \end{aligned}$$

where again, the exponent values can be replaced by 1. The same values of M_1 , A_1 and v_1 used in figure 5-1b were applied in conjunction with a new set of independent parameters, v_2 and N_{M_2}/N_{M_1} ,⁹⁷ to calculate two dimensional maps based on equation 5-4. A relatively good fit, which retained the large-scale pattern while successfully producing the 30 km wavelength of the fine structure along the outer edge of the D ring and into the C ring, was achieved with the addition of a group of superheavy particles of the same particle mass $M_1 = 1.15 * 10^{-8} kg$, rotating in a circular orbit around the center of Saturn at a relativistic speed of about $v_2 = 0.9c$ (the value of $v_2 = 0.895c$ was used). The corresponding radius of the second group is therefore equal to $A_2 = \frac{A_1v_2}{v_1} = 298.333 km$. According to observations, Saturn's main body of rings contains areas of abundant ultra-fine structure separated by areas with little or no fine structure. This restricts the value of the ratio N_{M_2}/N_{M_1} to the order of 0.007. In the following discussion the value of $N_{M_2}/N_{M_1} = 0.00665$ will be used.⁹⁸

Although application of $v_2 = 0.895c$ provided reasonable agreement with observations, the range of possible velocities is not narrow, and in some of the following images a higher value, somewhere in the range between $v_2 = 0.895c$ and $0.94c$,⁹⁹ may provide better results. Figure 5-2 displays a calculated section of Saturn's D ring, compared with a view of the fine structure between the D73 ringlet and the C ring taken with the Cassini Spacecraft narrow-angle camera. In figure 5-2b, the UG pattern calculated with $v_2 = 0.895c$ provides for the faint features of the D ring, as well as the inner region of the C ring, visible at the upper left corner of the images. The pattern further produces a regular pattern with a wavelength of 30 km. However, the calculated figure notably demonstrates fewer waves than observed by Cassini in figure 5-2a. Increasing the velocity to $v_2 = 0.94c$ in figure 5-2c resulted in improved agreement, but reduced the wavelength of the fine structure to a range of about 12 km to 25 km,

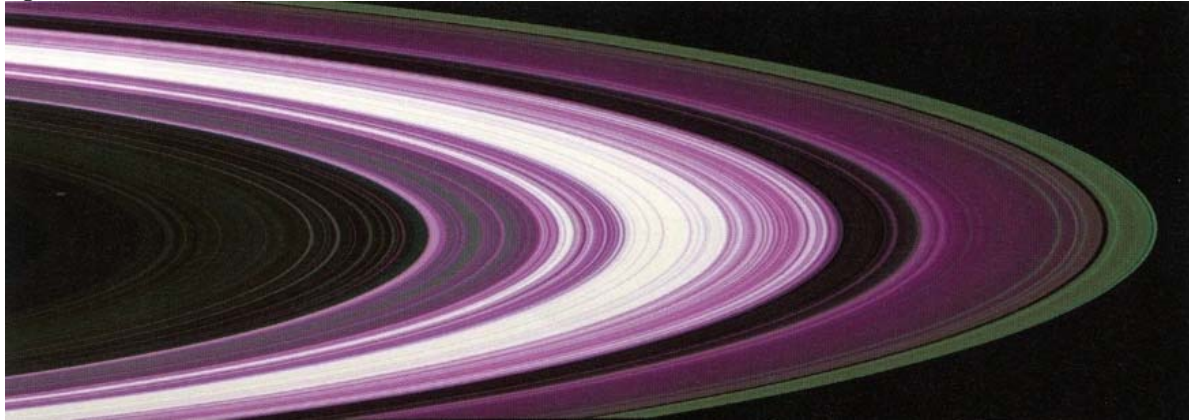
⁹⁷ Note that the multiplication by N_{M_1} in equation 5-4 does not affect the morphology of the ring system, reducing the number of independent parameters needed to five.

⁹⁸ This approximate value was obtained via trial and error, by simply calculating the map of the various rings to determine the range of values that correctly provided areas of abundant fine structure and areas of little or no fine structure.

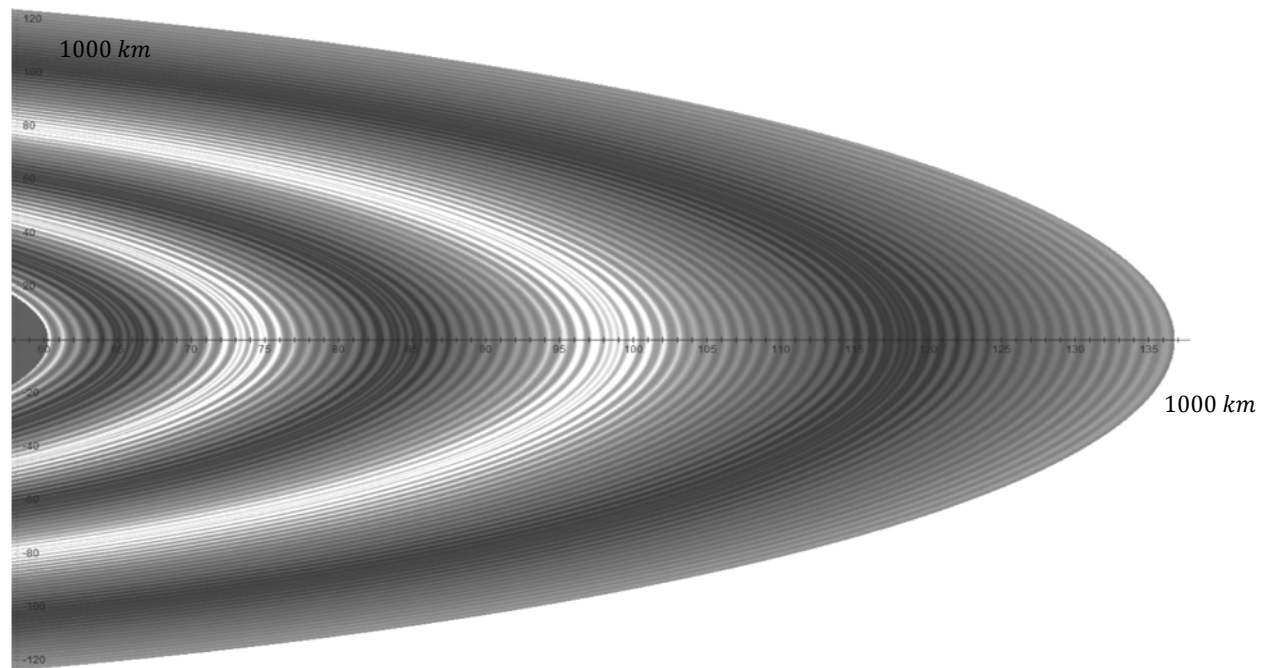
⁹⁹ Note that Cassini reported the existence of ultra-fine structure with kilometer scale in the inner A ring, which may require an additional third SHP group with a velocity $v > 0.94c$. An extremely rapid SHP group may also explain the structure of Saturn's dusty rings, such as the G and E rings.

which is less than the reported 30 *km* wavelength (Hedman, Burns & Showalter, 2007). Therefore, the precise velocity is expected to fall somewhere between $v_2 = 0.895c$ and $v_2 = 0.94c$.¹⁰⁰

Figure 5-1a



5-1b: UG calculated image of Saturn's main rings.



Figures 5-1a and 5-1b: Displays a comparison between the UG calculated zones providing rings D,C,B, A and the Cassini Division (figure 5-1b) and Saturn's observed ring profile (figure 5-1a). In figure 5-1a areas depicted in green and blue are dominated by small particles, and areas indicated in violet consist mainly of large particles. White areas indicate regions that were so opaque that the size of particle could not be determined.

Image credit for figure 5-1a: NASA/JPL; <http://photojournal.jpl.nasa.gov/catalogue/PIA07872>.

¹⁰⁰ Note that it is possible that the mass of the superheavy particles in the second group may differ slightly from M_1 .

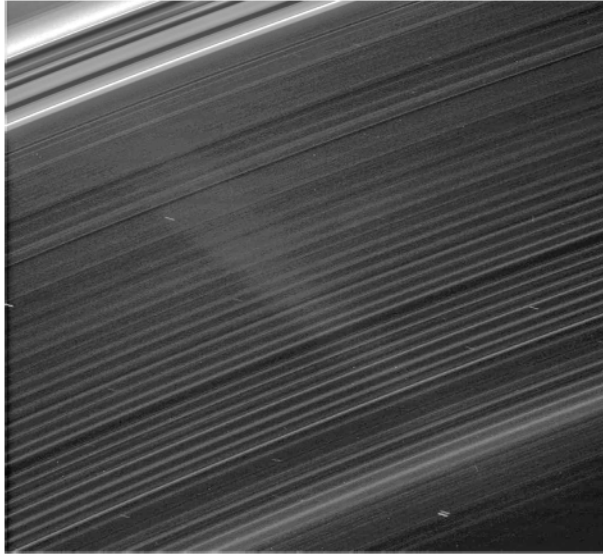


Figure 5-2a: Image obtained from NASA/JPL/Space Science Institute. <http://photojournal.jpl.nasa.gov/catalog/?IDNumber=PIA08990>.

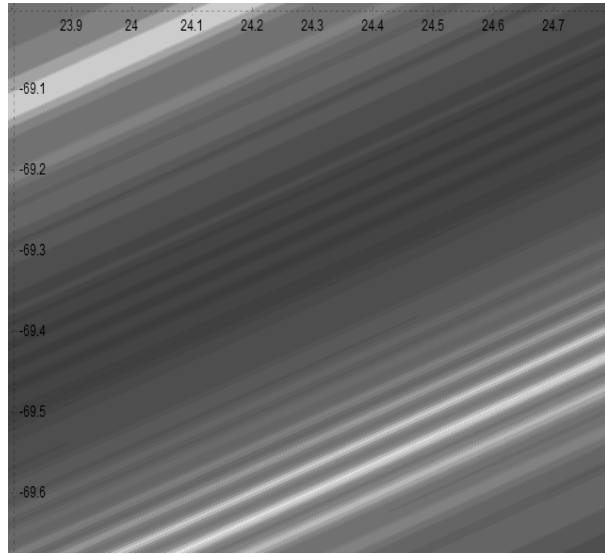


Figure 5-2b: Calculated using $v_2 = 0.895c$

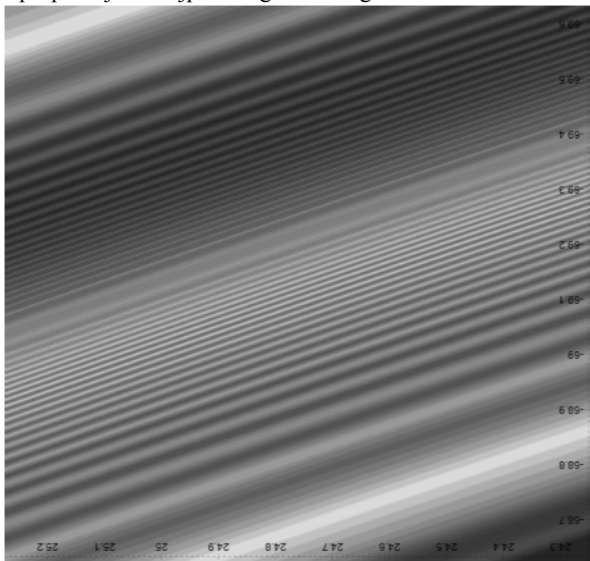


Figure 5-2c: Calculated using $v_2 = 0.94c$

Figure 5-3 displays the calculated narrow radial section of the D ring in the range of $66,000 \text{ km} < r < 74,200 \text{ km}$, providing a number of faint, narrow ringlets, in agreement with observations.

The C ring displays several empty gaps containing sharp, eccentric ringlets. While according to current theory, a few of the gaps may be identified with satellite resonances, a number of observed gaps remain unexplained. The ring pattern consists of spiral waves, as well as bright regions of high particle density informally referred to as “plateaus.” The density of particles is relatively uniform within the boundaries of the plateaus, and their sharp structure is maintained despite the expected spreading or diffusion of material. A view of the outer C ring and the surrounding Maxwell gap is displayed in figure 5-4, providing the comparison between a calculated section (figure 5-4a) and an observed view of the ring obtained by Cassini (figure 5-4b). Both images reveal a series of regularly spaced plateau structures of about 300 km wide,

nearly symmetrically placed around the Maxwell Gap. Note that there is no known satellite or resonant structure to explain this symmetrical placement.

The B ring is dense, bright, massive and radially extensive, demonstrating successive regions of abundant fine-scale structure as well as irregular regions with little or no fine structure occurring on a scale of 100 km or more. There are no clear gaps in the ring, however the Huygens gap, which contains an eccentric ringlet, resides at its outer edge. Whereas the confining mechanism of the B ring's inner boundary is unknown, its outer boundary is currently thought to be caused by a 2:1 resonance with the satellite Mimas.

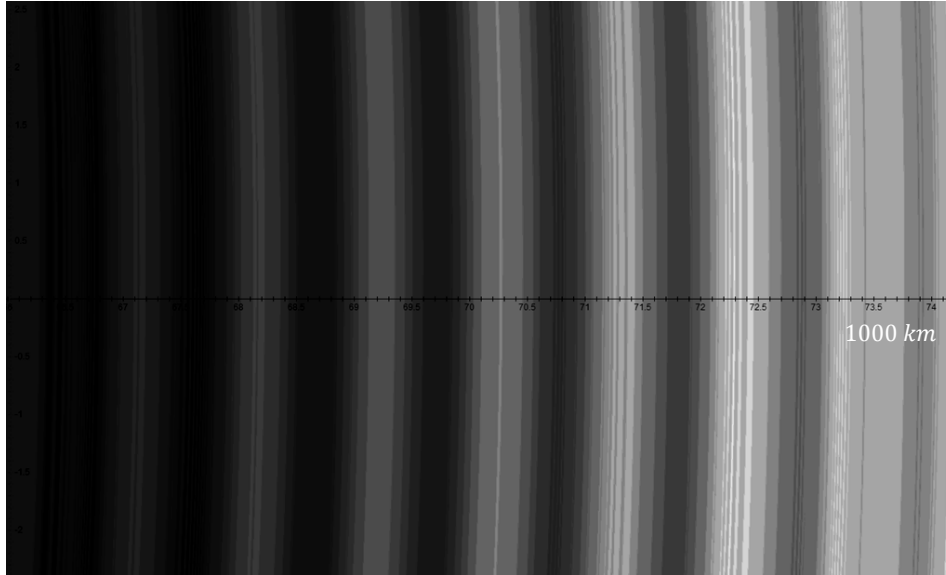


Figure 5-3: Display of the calculated structure of narrow ringlets within the D ring using the parameters $M_1 = 1.15 \times 10^{-8} \text{ kg}$, $v_1 = 0.3c$, $v_2 = 0.895c$, $A_1 = 100 \text{ km}$, and $N_{M_1}/N_{M_2} = 0.00665$.

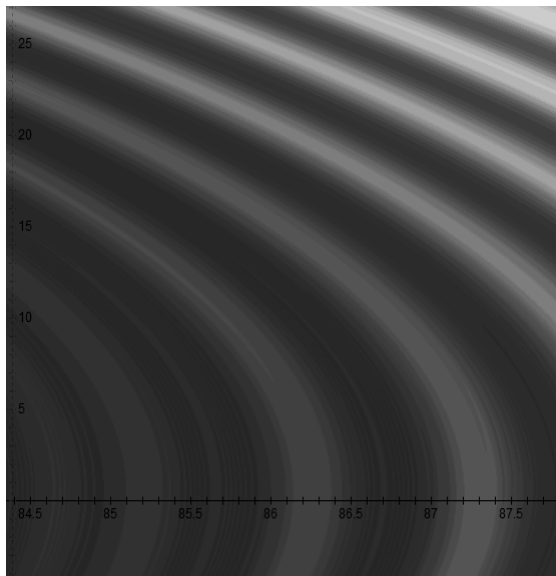


Figure 5-4a:¹⁰¹ UG calculated

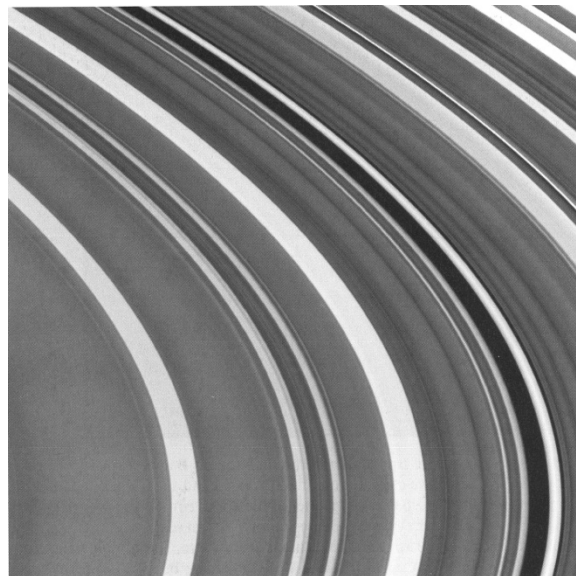


Figure 5-4b: Image credit: NASA/JPL/Space Science Institute; <http://photojournal.jpl.nasa.gov/catalog/PIA06540>.

¹⁰¹ A tilting effect was achieved by reducing the scale of the y axis.

Figure 5-5 displays a calculated section of the B ring (figure 5-5a)¹⁰² compared with an image shuttered by NASA’s Cassini satellite of the lit face of its middle region (figure 5-5b). Both figures demonstrate abundant structure with a scale of a few hundred kilometers and very little ultrafine-scale structure. Very-fine-scale structure is observed in the outer B ring, shown in figure 5-6c.

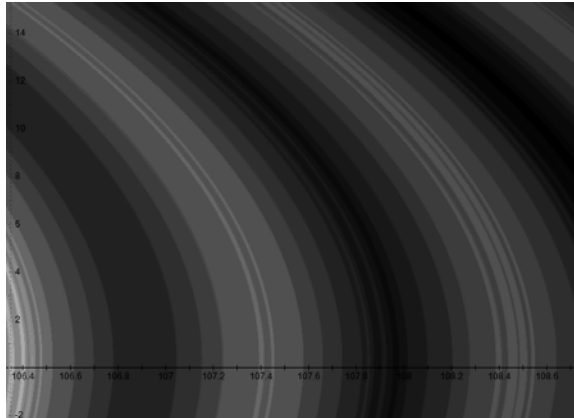


Figure 5-5a: UG calculated B ring section.

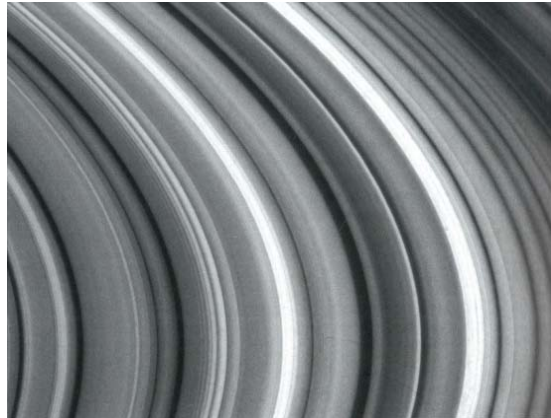


Figure 5-5b: Image credit: NASA/JPL/Space Science Institute; <http://photojournal.jpl.nasa.gov/catalog/PIA06535>.

Figure 5-6a provides the calculated two dimensional map of the outer B ring, the Cassini Division and the lower A ring. Areas of abundant ultra-fine structure can be noted within this region. Figures 5-6b and c provide a comparison between the calculated region of the Cassini division external to the bright outer B ring (figure 5-6b)¹⁰³ and an observed image obtained by Cassini (figure 5-6c). The calculated zonal structure provides the general regular pattern observed in the rings of the Cassini division.

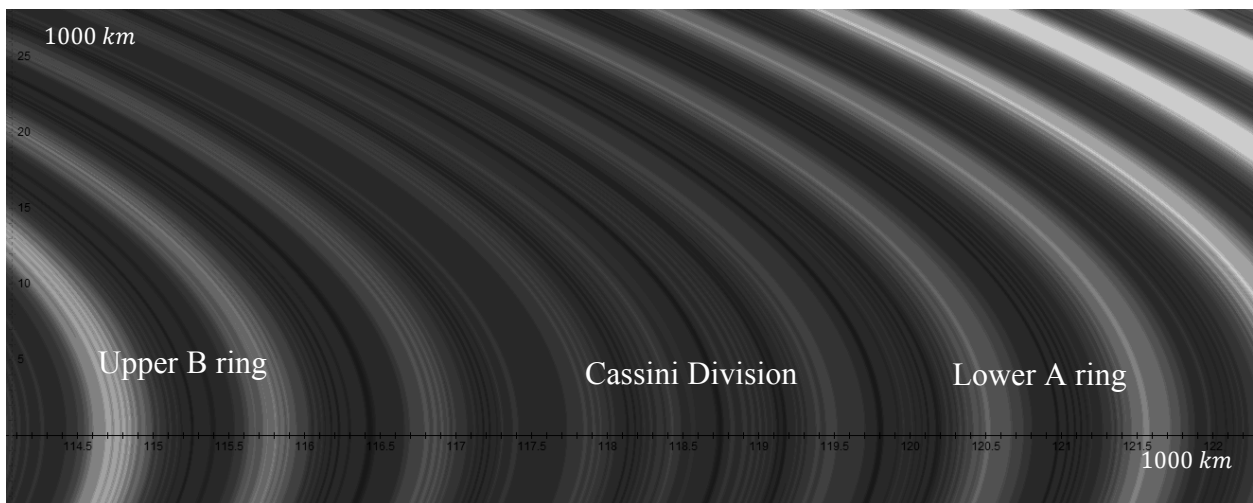


Figure 5-6a: A UG calculated two dimensional map of the outer B ring, the Cassini Division and the lower A ring.

¹⁰² The resolution of the y axis was reduced by a factor of ten relative to the x axis in order to mimic the tilting of the ring plane relative to the viewing angle of the telescope in figure 5-5b.

¹⁰³ Figure 5-6b is displayed in lower resolution relative to figure 5-6a, in order to fit with the resolution of the observed ring.

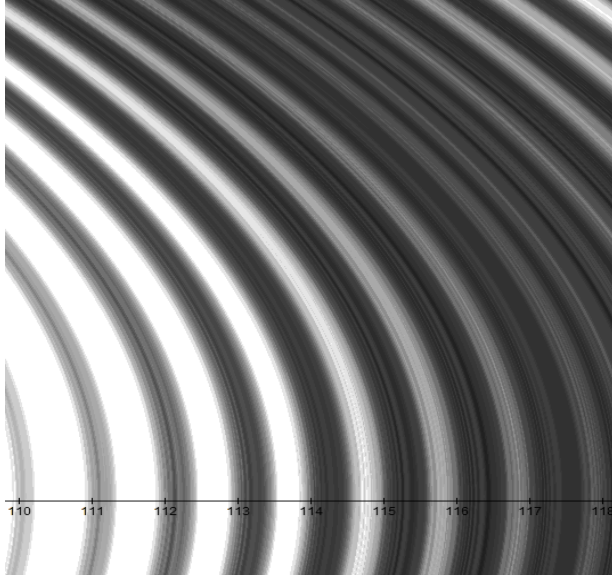


Figure 5-6b: UG Calculated B ring section.

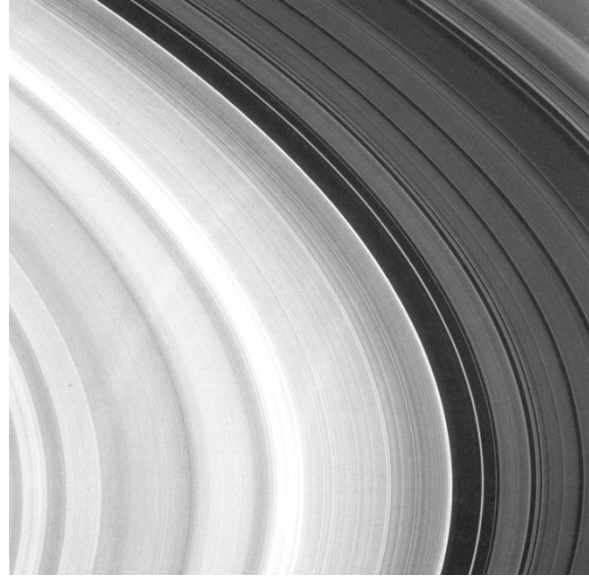


Figure 5-6c: Outer B ring, image credit: NASA/JPL/Space Science Institute;
<http://photojournal.jpl.nasa.gov/catalogue/PIAA06535>.

Figure 5-7a displays a detail of Saturn's A ring interior to the Encke gap taken by the Cassini ISS instrument. On the right the image reveals spiral bending waves, where the wavelength decreases inwards, and on the left a succession of spiral density waves, where the wavelength decreases outwards. As the image is viewed from the unlit side of the rings, opaque regions appear darker. In the calculated UG model similar patterns of spiral density and bending waves were found in several rings. A section of spiral waves in the A ring is demonstrated in figures 5-7b, 5-7c and 5-7d. Note that in figure 5-7b, drawn with $v_2 = 0.895c$, the calculation provides fewer waves than observed. Elevating the velocity of the second SHP group to $v_2 = 0.94c$ increases the number of waves, and in the case of the D ring, results in better agreement with observation, as displayed in low resolution in figure 5-7c and in higher resolution in figure 5-7d. In addition, both the calculated and observed images of figure 5-7 reveal regions of abundant fine-scale structure adjacent to smooth regions of little or no fine-scale structure. Note that figure 5-7c, where the velocity of the second of SHP group $v_2 = 0.94c$, bears a particularly close resemblance to the observed A ring.

The spiral that produces the F ring is likely to be a continuation of the spiral which forms the D, C, B, and A rings and the Cassini division. Following the discussion in footnote 91 of this chapter, the Roche midsection, where rings and satellites coexist, starts at about the radius of the satellite Pan. The gaps observed between the A ring and the F ring and beyond the F ring may be located at the UG sub-zones where the cosine terms either enhance coalescence, or are too small to prevent the ring particles from coalescing into satellites. These gaps may also be cleared by the gravitational effect of nearby satellites, such as Atlas, Prometheus, Pandora or Mimas, via resonances or the mechanism summarized in section V-1. Therefore, the F ring is likely to be a narrow ring that is contained within a zone in which matter cannot coalesce, surrounded from both sides by areas where matter is swept away. Recall that the value of v_2

between $0.895c$ and $0.94c$ was derived from the observed wavelength of the ringlets in the D ring, and seems to be confirmed by the agreement between the calculated and the observed ring sections provided in figures 5-1 to 5-7. This range of velocity provides for fine structure in the range of 12 km to 30 km in wavelength. However, Saturn's rings appear to contain some ultra-fine structure in the range of few kilometers or less. Consequently, for stronger agreement between theory and observation, three or more SHP groups may be required.

There is still the question of what provides for the stability of these wide rings. In the Newtonian scenario, during each orbital rotation a ring object must lose a minute amount of energy in the form of gravitational radiation. As the object's energy is reduced continuously, its orbit is expected to draw closer and closer to the planet, until eventually becoming consumed by it. This process may last for at most few tens of millions of years before the ring system dissipates completely. Within this timeline, Saturn's rings would be expected to have existed for 100 million years at most, a period which is too short to allow for the presence of the elaborate fine structure observed. For Saturn's ring system to remain stable over the length of time required for the formation of its fine structure, there must be a continuous source of new energy or new matter to replenish the ring system.

The answer to this question is much simpler in the case of non-relativistic SHP velocities, as is probably the case with Uranus, where a majority of the potential energy minima (and therefore a majority of the rings) are very narrow. In cases of non-relativistic SHP groups, the minima within the ring plane are arranged in sets of stationary concentric circular contours. To escape from any of these stationary minima, the energy of the ring particle must be elevated; thus, the most stable state of the matter within the ring is to remain at its given minimum. However, the situation is slightly more complicated in the case of relativistic SHP groups, as in the case of Saturn, where the density waves produced by the SHP groups rotate at a much faster rate than the ring matter. Hence, the minima locations are not stationary, and the orbiting object moves too slowly to keep pace with its minimum. Therefore, the object crosses paths with both the local minimum and the local maximum on a periodic basis.¹⁰⁴ In this case, the rotating zonal pattern driven by the rotating SHP groups can provide a mechanism to replenish any energy losses due to radiation, or attributed to other bodies interacting with the ring matter. As previously discussed, due to the finite propagation speed of gravitation, the relativistic rotation of SHP groups around the planetary center generates rapidly rotating potential energy spiral structures. Consequently, an orbiting ring particle in the path of the rapidly rotating spiral structure encounters an endless series of rapid oscillations that, along with their maxima and minima, propagate outward at relativistic speeds.¹⁰⁵

¹⁰⁴ For a more detailed analysis, see Chapter VI.

¹⁰⁵ A good analogy to this process is the Archimedes screw pump, which consists of a screw rotating inside a hollow pipe, historically used to transfer water from a low-lying body of water into irrigation ditches. As the screw rotates endlessly around its axis without any forward motion, it elevates a volume of water by pushing it forward along its axis of rotation. In the present case of the orbiting ring object, the SHP contribution to the force acting on the object is small relative to the Newtonian contribution of the planet's ordinary matter. Therefore, the rotating spiral is powerful enough to replenish the minute amount of energy lost by the ring particles in less than 0.007 seconds it takes the SHP groups to complete a full rotation around the center of Saturn, but not sufficiently powerful to advance the particles outwards. A more complete analogy will be provided in Chapter

Figure 5-7a: Spiral bending waves (right) and density waves in Saturn's A ring interior to the Encke Gap. **Figure 5-7b:** Calculated using $v_2 = 0.895c$.

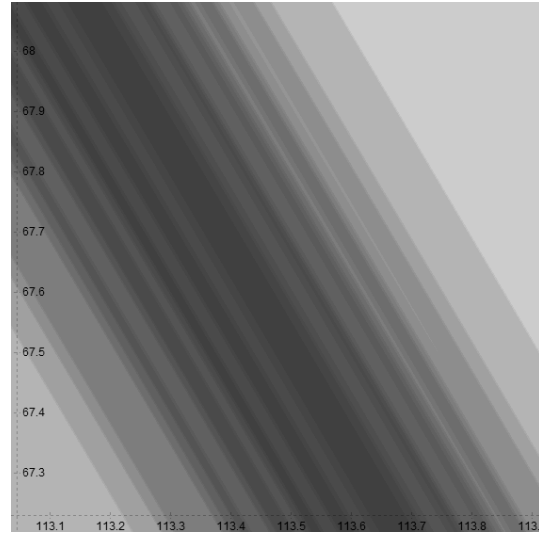
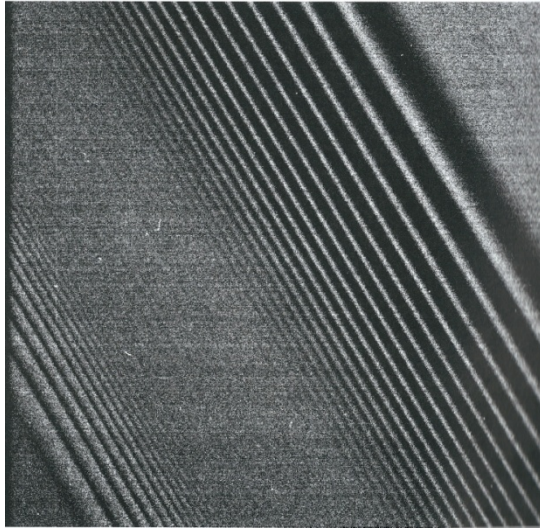


Figure 5-7c: Calculated using $v_2 = 0.94c$.

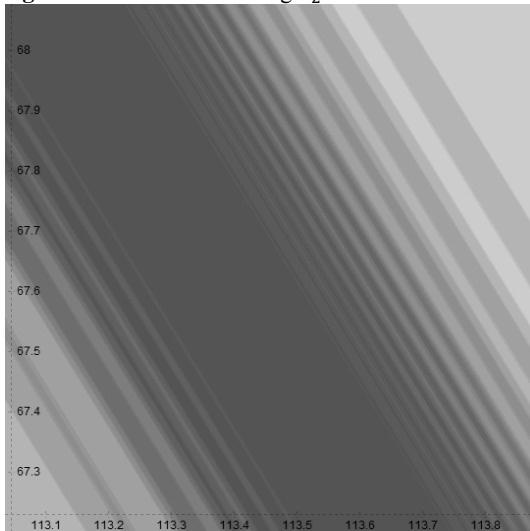


Figure 5-7d: Calculated at higher resolution using $v_2 = 0.94c$.

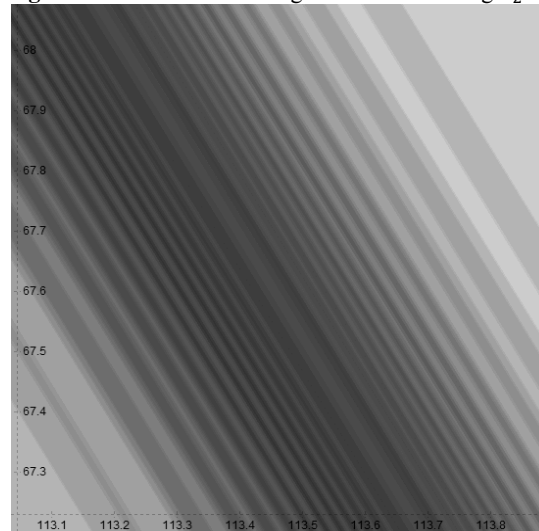


Figure 5-7a: Image credit: NASA/JPL/Space Science Institute; <http://photojournal.jpl.nasa.gov/catalogue/PIA06093>.

As the observed orbital period of the ring matter is Keplerian, the overall force exerted on the ring particles is very close to Newton's gravitational force (see section V-6), and consequently, the particles cannot be accelerated to the high velocities needed to keep up with the high propagation speed of the minima of the rotating pattern of the potential energy. Therefore, the rapid, outward moving maxima and minima contours will encounter the orbiting object on a periodic basis, where the time between two successive respective encounters is less than or approximately equal to 0.007 seconds, the approximate time it takes the SHP groups to complete

VI for the case of galaxies, where the rotating spirals demonstrate sufficient strength to pump out ordinary matter in the form of galactic wind.

one full rotation.¹⁰⁶ As the object must encounter an oscillation maximum every 0.007 seconds or less, the minute amount of energy lost during one orbital period will be replenished by the next encounter with the following maximum. These periodic encounters create a barrier that prevents the object from gradually losing energy and falling towards the planet. Hence, the orbiting object behaves as a driven harmonic oscillator, where the force applied on the object by the rotating spiral pattern of the SHP groups provides a periodic driving force. As the overall motion of the object is in accordance with Kepler's laws, this driving force is substantially smaller, yet not negligible relative to the force applied by Saturn's ordinary matter. Thus, the force exerted by the orbiting SHP groups provides a small perturbation to the overall force exerted by the planetary ordinary matter, causing the rotating object to oscillate slightly around its Keplerian orbit.

Consequently, the force generated by the rapidly rotating SHP groups is demonstrated to provide a mechanism by which the energy lost by orbiting material is replenished to maintain the ring structure over time, thus allowing for the long-term stability of planetary ring systems. The oscillating waves created by the rotating spiral are calculated to propagate outwards at relativistic speeds, and are certainly not stationary. Conversely, images of Saturn's rings reveal relatively little fluctuation in the orbital locations of certain rings or gaps over time. The rapid movement of the calculated oscillating patterns, however, does not contradict observations of stable ring orbits and gaps, since our perception of the ring characteristics at a given location is driven by the amplitude and frequency of the oscillating waves, rather than by their phase.¹⁰⁷

In figure 5-8 three waveforms are overlaid with two dimensional calculated images of the potential energy of the given object.¹⁰⁸ The oscillating waveform displayed entirely above the x axis provides the total contribution of both SHP groups, without the contribution of Saturn's ordinary matter. The second waveform, characterized by distinct trains of rapid oscillations, is displayed entirely below the x axis and provides the exclusive contribution of the second SHP group (with $v_2 = 0.895c$). The third smooth waveform crossing the x axis provides the overall contribution of Saturn's ordinary matter and the significantly smaller contribution of both SHP groups (given by the first waveforms).¹⁰⁹ As demonstrated in the figure, the potential energy of the SHP contribution is highest within the area covered by the Cassini Division (between approximately 117,000 km and 122,000 km) where the oscillations of the upper waveform appear to almost flatten, with significant reduction in amplitude and

¹⁰⁶ The time T it takes the SHP groups to complete a full rotation around Saturn center is approximately $T = 2\pi/w = 2\pi A_1/v_1 = 2\pi * 100,000m/(0.3 * 300,000,000 m/s) = 0.007$ seconds.

¹⁰⁷ A good analogy can be found in sound waves, where the amplitude and frequency of the sound, rather than the exact phase at a given moment, determine our perception of its loudness and pitch.

¹⁰⁸ The two dimensional images do not contain the term $-\frac{GN_{M_1}m_pM_S}{2r_0}$ for the reasons discussed above.

¹⁰⁹ In order to demonstrate how the spirals are related to the potential energy waveforms, the three waveforms are overlaid with two dimensional calculated images of the potential energy of the given object. This requires displaying the waveforms and the images of the calculated potential energy using the same xy coordinates. Therefore, the equations of the waveforms were multiplied by respective factors of $5 * 10^{21} m/j$, $10^{22} m/j$ and $10^{20} m/j$, and shifted down by 0, 2.5 and -55 units (units of 1000 km) respectively. The method used to calculate the approximate number of SHPs in each group (N_{M_1} and N_{M_2}) will be described later in the chapter.

wavelength. This process further accounts for low particle density in the Cassini Division. The Cassini Division is located in the vicinity of a zonal maximum of the first SHP group with a velocity of $0.3c$ (see figures 5-8a and b), where the amplitude of the local oscillations nearly diminishes. In areas where the oscillation amplitude diminishes completely, the periodic driving force will reduce to zero, and the ring material will dissipate over time to produce a gap. In the remaining areas of the Cassini Division, where the oscillation amplitude is significantly reduced but not entirely eliminated, a very faint ring structure may be observed. Based on the above discussion, strong rings should be observed in regions where the amplitude of the outward moving oscillations is substantial. Looking at the same image, the relatively large amplitude of the oscillations produced by the upper waveform between $102,000 \text{ km}$ and the Cassini division (starting at about $117,000 \text{ km}$) explains the absence of gaps, as well as the relatively large optical depth of the B ring. An abundance of fine structure in the outer B ring can also be noted. As demonstrated in the figure, the oscillation amplitude of the contribution of the first SHP group in the middle B ring is significantly larger than the oscillation amplitude contributed by the second SHP group, however both contributions become comparable in size at the distance range of the upper B ring and the Cassini Division. Therefore, the fine structure oscillations contributed by the second group in the middle section of the B ring are insignificant (see Figure 5-8a), while in the general area of the Cassini Division the fine structure becomes relatively substantial. An enlarged view of the Cassini Division surrounded by the outer B ring and the inner A ring is provided in figure 5-8b. As expected, the ring structure in this area displays an abundance of fine structure.

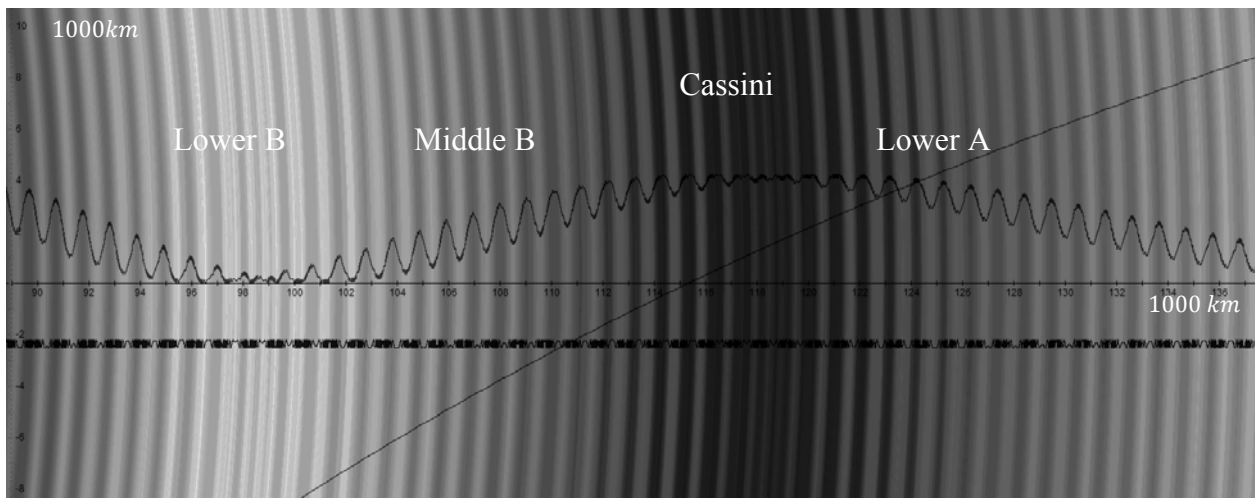


Figure 5-8a: UG calculated ring section.

Viewing the fine structure presented by the upper curve in figure 5-8b, the wavelengths of any two adjacent sections of rapidly oscillating waves are shown to increase in opposite directions. This may explain the observed occurrence of spiral density waves, where the wavelength decreases outward, as well as spiral bending waves, where the wavelength decreases inwards (See figure 5-7). Note that according to current theory, spiral density or bending waves are

thought to be created by gravitational interactions with Saturn's moons. However, in many instances, no sufficiently large moons were found in proper locations for creating them.

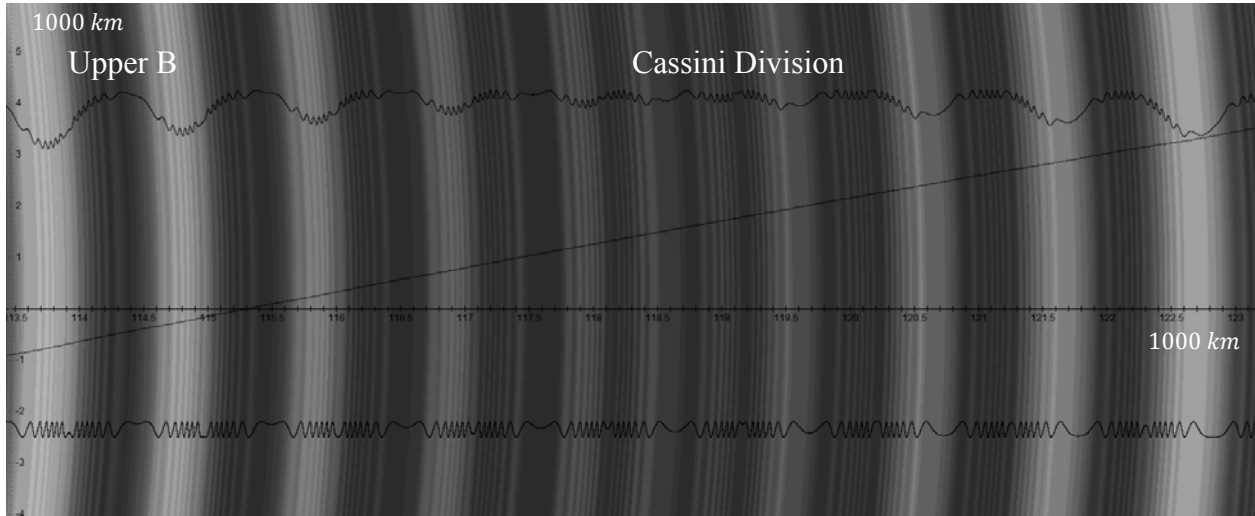


Figure 5-8b: UG calculated ring section.

Figure 5-8c displays an enlarged view of the middle B ring. The calculated waveforms overlaid on the two dimensional image demonstrate long stretches of over one hundred kilometers of little or no fine structure. In figure 5-8d, the calculated display is extended to cover Saturn's D, C, B and A rings and the Cassini division. Note the similarities between the oscillation patterns extending from about 83,000 km to 87,000 km, and between those extending from about 116,000 km to 122,000 km. This may account for the structural similarities observed between the C ring and the Cassini Division.

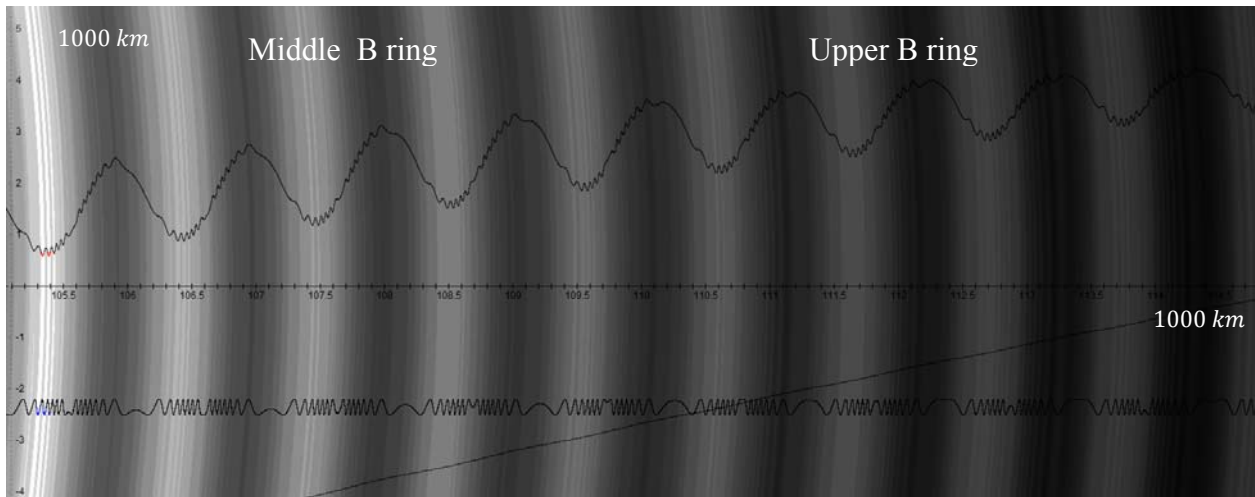


Figure 5-8c: UG calculated ring section.

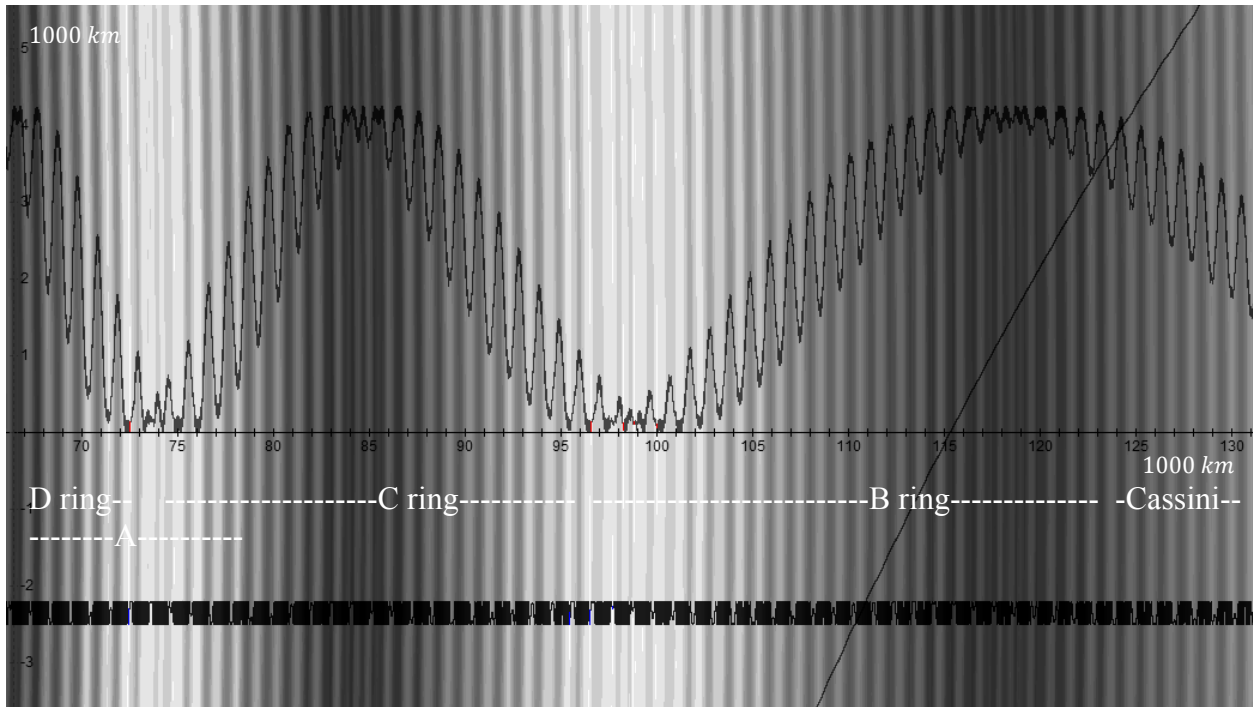


Figure 5-8d: UG calculated ring section.

Section V-3: The Phenomenon of Spokes

One of the more peculiar phenomena observed in Saturn's rings are the spokes, first observed by Voyager in 1980. Spokes are nearly radial structures, observed to appear intermittently in the B ring. Viewed from low phase angles (shown in figure 5-9c), they appear as dark markings along a bright underlying B ring. Conversely, spokes may appear brighter than the ring when viewed at high phase angles, or against the ring's unilluminated side (see figure 5-9d). A surprising property of the spokes is that they maintain their shape in spite of the differential rotation that occurs in the underlying B ring. This indifference to rotation is not consistent with orbital mechanics, and cannot be explained by Newtonian gravitational forces. As they are observed to rotate at approximately the same rate as the rotation of Saturn's magnetic field, spokes are commonly attributed to interactions of charged particles with Saturn's magnetic field, however the origin and exact nature of these features are not yet well understood.

According to the UG theory, the phenomenon of spokes can be explained as a by-product of a relativistic effect, where a pattern is generated as a consequence of the relativistic distortion of spacetime by the rotating SHP groups, and captured by the camera's matrix of sensors. This calculated phenomenon is demonstrated in figure 5-9a, where equation 5-3d was used in order to show that even a single SHP group is capable of creating spoke structures. The equation was applied using the parameters of the first SHP group ($M_1 = 1.15 * 10^{-8} \text{ kg}$, $v_1 = 0.3c$, $A_1 = 100 \text{ km}$, and for simplicity, $N_{M_1} = N_{m_p} = 1$). The resultant figure displays a two dimensional image of the rotation plane of Saturn's rings, drawn using a single threshold level $\epsilon_1 = 2.2 * 10^{-23} \text{ J}$ in order to maintain a high level of contrast. Consequently, any position on the ring

plane where $\xi_1(x, y, 0, t) = \frac{GN_{M_1}M_1N_{m_p}m_p\gamma^2(v_1)}{a} \left(e^{a/\dot{D}_{s_1}} \cos\left(\frac{bM_1m_p\gamma(v_1)}{\dot{D}_{s_1}}\right) - 1 \right) \geq 2.2 * 10^{-23} J$ was layered in gray, while any position where $\xi_1(x, y, 0, t) < 2.2 * 10^{-23} J$ was indicated in white. The resultant set of rings display features that fit the general description of spokes as observed in figures 5-9c and 5-9d.¹¹⁰ Moreover, the locations of the calculated spokes remain stationary over time relative to the frame of reference of the planetary center, which implies that they rotate with Saturn while maintaining their shape, as observed. It is further implied that these features are fixed within the coordinate axes. As the rotation rate of Saturn's magnetic field is very close to the overall rotation rate of the planet around its axis, the calculated spokes appear to rotate at approximately the same rate as Saturn's magnetic field.

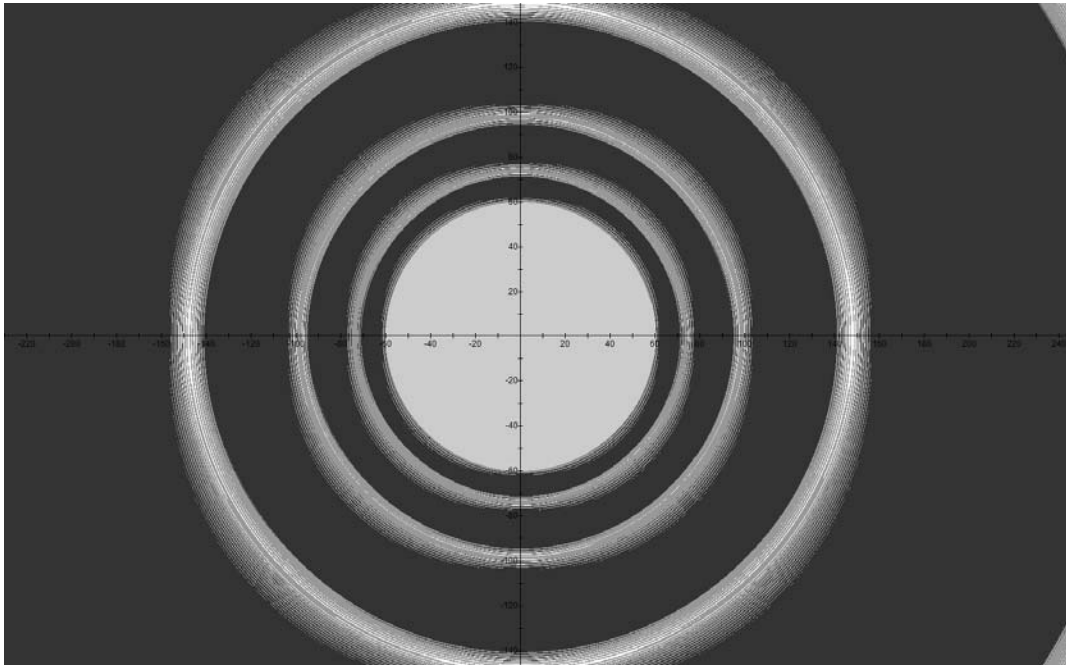


Figure 5-9a: Displays spoke features in the rings. The calculated figure was generated using parameters of $M_1 = 1.15 * 10^{-8} kg$, $v_1 = 0.3c$, $A_1 = 100 km$ and $N_{m_p} = 1$, where the point (x, y, t) is layered only if $\xi_1(x, y, t) > 2.2 * 10^{-23} J$ and $\dot{D}_{s_1} > 60,268 km$.

The visibility of spokes and the clarity of their patterns may depend on the angle between the Sun and the rotation plane of the rings, or on the angle between the camera and the rings' rotation plane.¹¹¹ This may account for the intermittent appearance of spokes in the B ring, which is currently attributed to their being a seasonal effect. In addition, although spokes are uniquely observed in the dense and massive B ring, the calculated figure shows that spoke

¹¹⁰ A clear demonstration, displayed in Figure 5-9b, was created using increased values of $M_1 = 1.385 * 10^{-8} kg$, $v_1 = 0.35c$ and a reduced radius of $A_1 = 55 km$, where the point $(x, y, 0, t)$ was layered only when $E_1(x, y, 0, t) > 4.56 * 10^{-22} J$. These values do not fit the Saturnian ring structure and are only intended to provide a more vivid display of spoke features.

¹¹¹ It is often the case with optical patterns that to be observed they must adhere to certain optimal geometrical conditions. For example, holograms may require a relatively narrow range of viewing and illumination angles, as well as a narrow range of wavelengths for the illuminating light. The quality of holograms also depends on the density as well as other properties of the film's emulsion. Slight variations in any of these parameters may make the difference between a sharp image and no image at all.

features can appear in other rings as well, suggesting that the visibility of the radial spokes may further depend on the density of ring matter or on the size of the ring particles.

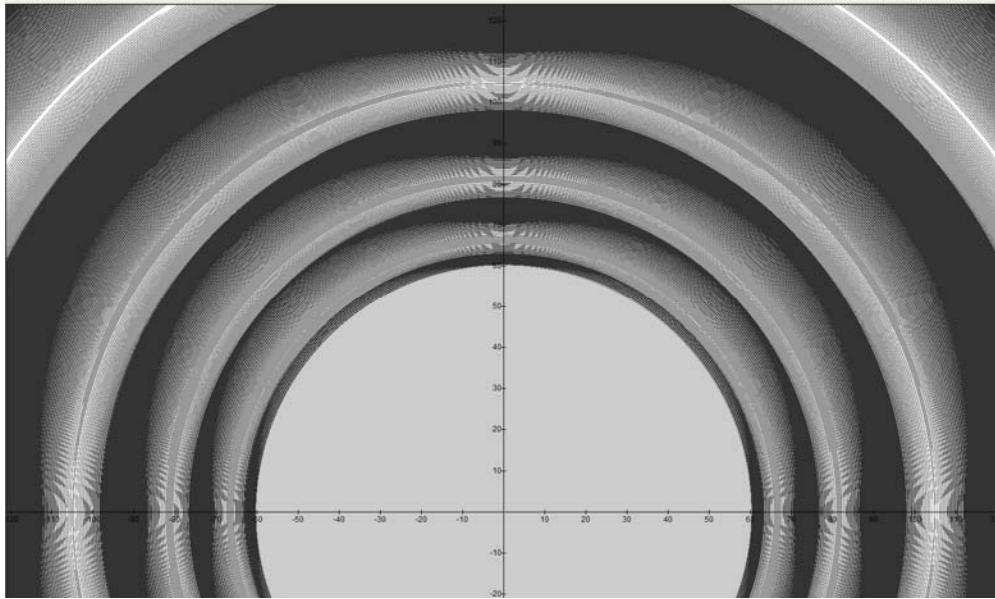


Figure 5-9b: In order to provide a vivid image of spoke features, the parameters were modified to $M_1 = 1.385 * 10^{-8} \text{ kg}$, $v_1 = 0.35c$ and $A_1 = 55 \text{ km}$, where the point (x, y, t) is layered only if $\xi_1(x, y, t) > 4.56 * 10^{-22} \text{ J}$ and $\dot{D}_{s_1} > 60,268 \text{ km}$.

Figure 5-9c

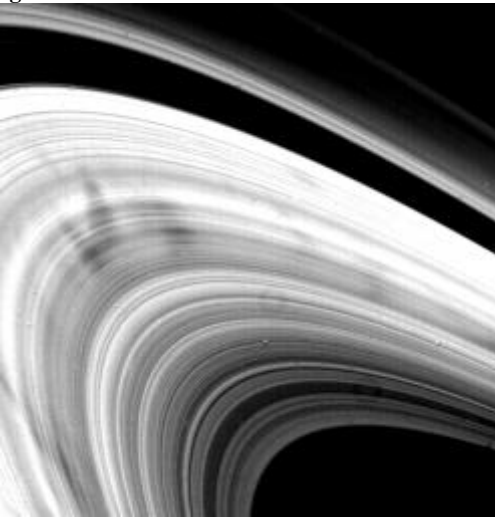
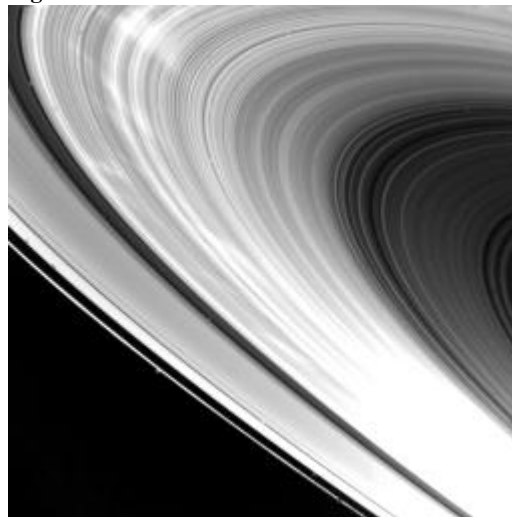


Figure 5-9d



Figures 5-9c and 5-9d: Voyager images of radial spokes in Saturn's B ring. Spokes appear dark against the B ring at low phase angles (5-9c) and bright against the B ring at high phase angles (5-9d).

Credit for figure 5-9c: image obtained by Voyager 2; NASA/JPL; <http://photojournal.jpl.nasa.gov/catalogue/PIA02275>.

Credit for image 5-9d: image obtained by Voyager 1; NASA/JPL; <http://photojournal.jpl.nasa.gov/catalogue/PIA02269>.

Section V-4: The Non-Circular Shape of the B Ring

Due to the effects of special relativity, superheavy particles rotating at relativistic velocities create a distortion of spacetime. As a result of this distortion, and of the finite speed of gravitation, the otherwise circular zonal minima are replaced by a distorted rotating spiral. Hence, the width of the ring will vary with azimuth, and its orbit will depart from a pure circular shape. This effect becomes stronger as the orbital speeds of the SHP groups increase and their radii of orbit are reduced. As demonstrated in figures 5-9a and 5-9b, the calculated zonal structure and its minima expand outwards, where the level of expansion varies with the azimuth of the ring section, resulting in a non-circular outer boundary of the rings, while the inner boundary retains a circular morphology. The non-circular structure of the outer edge of the rings resembles the boxiness observed in galaxies (see Chapter VII), as both phenomena are created by the same relativistic effect. Similar to the dynamics of the calculated radial spokes in Saturn's B ring, the calculated ring boundaries maintain their shape in spite of the differential rotation that occurs in the underlying B ring. In figures 5-9a and b, all of the calculated rings demonstrate some degree of boxiness.

Section V-5: The Dynamics of Ring Variability Over Time and Azimuth

Data obtained by Voyager and Cassini reveals that ring structure varies with time and azimuth. Figure 5-10a provides a composite image of four views of the outer edge of the B ring, assembled from images shuttered by Voyager 2 at two different times and at two different azimuths (Miner, Wessen & Cuzzi, 2007). An offset of about 50 km in the radius of the outer edge of the B ring as well as significant mismatch in its fine structure can be noted.¹¹² These findings can be explained by two different phenomena. Boxiness, explained above, may account for a large part of the 50 km offset of the outer edge of ring B between the two azimuths. In addition, as the zonal structure is driven by a rapidly rotating spiral that changes over time and azimuth, the ring pattern is also expected to shift over time and to change between different azimuths. Both SHP groups are calculated to complete a full rotation in about 0.00698 seconds, suggesting that some features of the fine structure of the rings must change at a rapid rate.

Figure 5-10b displays two calculated radial sections of the same region covering the outer edge of the B ring and the inner Cassini Division at two different times 0.0035 seconds apart. The images are positioned so that their large-scale pattern is aligned. Note that similar to observations, the fine structure in the outer B ring does not match between the calculated images. Mismatch is also observed, but to a lesser degree, in the Cassini Division.

¹¹² Similar dynamics have been observed in the D ring, where D72 was reported to have transformed from a bright, narrow ringlet of less than 40 km to a broad and diffuse structure which extends over 200 km during the 25 years that passed between NASA's Voyager and Cassini missions. In addition, the F ring is reported to be dynamic, and has changed significantly since the Voyager mission.

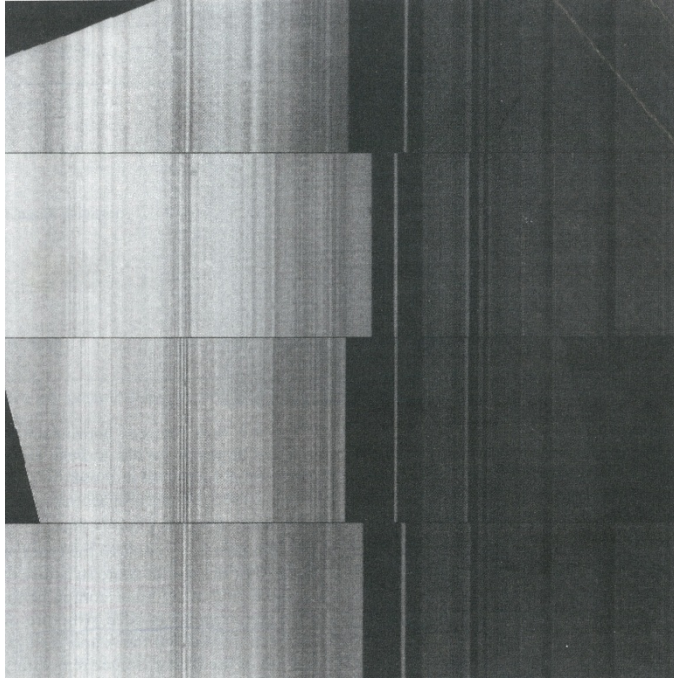


Figure 5-10a: The composite image of four views of the outer edge of the B ring assembled from images collected by the Voyager 2 Spacecraft. Displayed on the left is the bright B ring, at the center is the dark Huygens gap (of variable width) containing a narrow elliptical ringlet, and on the right is the Cassini Division (Voyager 2 image 260-1473, obtained from Miner, Wessen & Cuzzi, 2007).

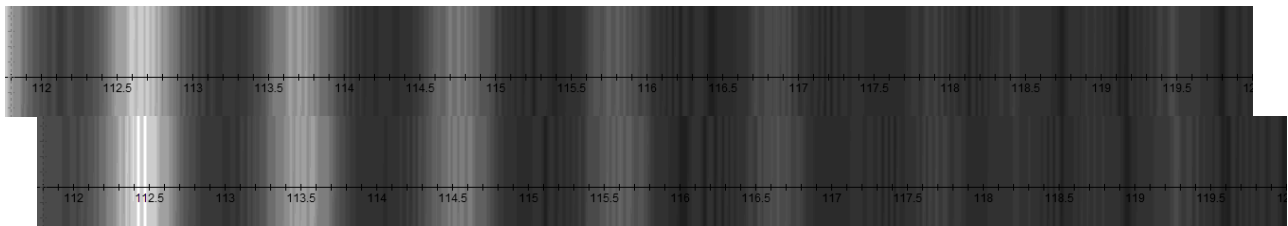


Figure 5-10b -----B ring----- --Cassini Division----

Section V-6: Estimating the Overall Mass and Abundance of Superheavy Particles of Mass M_1

Thus far, the following parameters of the two SHP groups were estimated: the SHP mass M_1 , the orbital radii A_1 and A_2 , the velocities v_1 and v_2 , and the approximate ratio of N_{M_2}/N_{M_1} , where N_{M_1} and N_{M_2} respectively denote the number of superheavy particles in the first and second SHP groups. In addition, the mass of the Saturn's ordinary matter M_s is already known. Still missing, however, is an assessment of the approximate values of N_{M_1} and N_{M_2} .¹¹³ Using Kepler's third law, the calculated orbital periods of each of the known satellites internal to the orbit of Lapetus (at about 3,561,300 km)¹¹⁴ were compared with their observed values. The calculated orbits were found to fall between -0.272% and 0.31% of the measured values (see

¹¹³ Note that if either one of N_{M_2} or N_{M_1} is known, the other can be easily derived via the known ratio of N_{M_2}/N_{M_1}

¹¹⁴ As the influence of superheavy particles reduces drastically above the SHP oscillation range ($r_1 \approx \frac{bM_1 m_p \gamma}{\pi} \lesssim 600,000 \text{ km}$), the SHP effect on satellites farther than Lapetus is not significant.

table 5-1). As the effect exerted by Saturn's superheavy particles is expected to cause the orbital periods of the satellites to deviate from their Keplerian predicted orbital periods, the measured deviations limit the possible number of SHPs of mass M_1 .

Assuming a circular orbit of radius r , the speed of a satellite u is related to its orbital period T via the equation $u = \frac{2\pi r}{T}$. Therefore, as the deviation of the satellite's orbital period from its predicted value, denoted ΔT , is small relative to T , the deviation of the square of the speed u^2 from the square of its Keplerian speed u_0^2 (where $\Delta(u^2) = u^2 - u_0^2$) can be expressed as

Equation 5-5

$$\frac{\Delta(u^2)}{u_0^2} = \frac{u^2 - u_0^2}{u_0^2} \approx \frac{\Delta\left(\frac{4\pi^2 r^2}{T^2}\right)}{\frac{4\pi^2 r^2}{T^2}} = -2 \frac{\Delta T}{T}$$

Kepler's law is fulfilled if and only if

Equation 5-6

$$\frac{1}{2} M_{sat} u_0^2 = \frac{GM_s M_{sat}}{2r}, \text{ or } u_0^2 = \frac{GM_s}{r}$$

where M_{sat} provides the mass of any one of the Saturnian satellites and M_s is the total mass of Saturn. Therefore, the deviation from Kepler's predicted orbital period is given by

Equation 5-7

$$\Delta(u^2) = -2u_0^2 \frac{\Delta T}{T} = -\frac{2GM_s \Delta T}{r T}$$

However, the centrifugal force applied to the satellite is given by

Equation 5-8

$$\frac{M_{sat} u^2}{r} = \frac{GM_s M_{sat}}{r^2} + \frac{GM_1 N_{M_1} (\gamma(v_1))^2 M_{sat}}{\dot{D}_{s_1}^2} \left(\cos\left(\frac{bM_1 \gamma(v_1) m_p}{\dot{D}_{s_1}}\right) - \frac{bM_1 \gamma(v_1) m_p}{a} \sin\left(\frac{bM_1 \gamma(v_1) m_p}{\dot{D}_{s_1}}\right) \right)$$

where the exponent term was replaced by 1, as $a \ll \dot{D}_{s_1}$. Also note that the contribution of the

second SHP group to the centrifugal force was dropped since $\frac{N_{M_2} (\gamma(v_2))^2}{N_{M_1} (\gamma(v_1))^2} \approx \frac{0.00665 * 5.026}{1.1} \approx$

0.03.^{115 116} Consequently, the overall influence of the second SHP group on the calculated velocity of the object is small relative to the influence of the first group, and can thereby be

¹¹⁵ Since the purpose of the present discussion is to estimate the number of superheavy particles, a quasi-relativistic, rather than a complete relativistic correction, was made by the inclusion of γ in the force equation.

¹¹⁶ The calculations in this section use the following values: $M_1 = 1.15 * 10^{-8} \text{ kg}$, $v_1 = 0.3c$, $v_2 = 0.895c$, $A_1 = 100 \text{ km}$, $N_{M_2}/N_{M_1} = 0.00665$.

neglected. Since $\frac{bM_1m_p\gamma(v_1)}{a}$ is of the order of 10^{22} , the cosine term is negligible and can be omitted. Thus,

Equation 5-9

$$u^2 = \frac{GM_s}{r} - \frac{GM_1^2 N_{M_1} (\gamma(v_1))^3}{r} \frac{bm_p}{a} \left(\frac{r}{\dot{D}_{s_1}}\right)^2 \sin\left(\frac{bM_1\gamma(v_1)m_p}{\dot{D}_{s_1}}\right)$$

Combining equations 5-6, 5-7 and 5-8, under the assumption that the entire deviation is due to the SHP effect, yields

$$\frac{GM_1^2 N_{M_1} (\gamma(v_1))^3}{r} \frac{bm_p}{a} \left(\frac{r}{\dot{D}_{s_1}}\right)^2 \sin\left(\frac{bM_1\gamma(v_1)m_p}{\dot{D}_{s_1}}\right) \approx \frac{2GM_s \Delta T}{r T}$$

or

Equation 5-10

$$N_{M_1} \approx \frac{2M_s}{M_1^2 (\gamma(v_1))^3} \frac{a}{bm_p} \frac{\Delta T}{T} \left(\frac{\dot{D}_{s_1}}{r}\right)^2 \frac{1}{\sin\left(\frac{bM_1\gamma(v_1)m_p}{\dot{D}_{s_1}}\right)}$$

According to table 5-1, the maximum deviation of an orbital period of a satellite is within $\pm\Delta T/T \approx 0.00312$ (see the satellite Anthe at $r \approx 197,700 \text{ km}$). Substituting $\frac{\Delta T}{T} < 0.0031$, $M_s = 5.6846 * 10^{26} \text{ kg}$, $v_1 = 0.3c$ (therefore, $\gamma(v_1) = 1.099$), and using the approximation of $\dot{D}_{s_1} \approx r$, equation 5-10 yields $N_{M_1} \approx 1.3 * 10^{10}$. The earlier estimate of $N_{M_2}/N_{M_1} = 0.00665$ thus provides $N_{M_2} = 8.4 * 10^7$, which translates to a total of $M_1(N_{M_1} + N_{M_2}) \approx 150.5 \text{ kg}$ of SHPs of mass $1.15 * 10^{-8} \text{ kg}$.

Hence, the overall SHP mass is negligible compared with the overall mass of Saturn's ordinary matter, and bears no influence on objects dominated by the ordinary matter external to the zonal oscillation range of the SHPs with ordinary matter.

Note, however, that the current published mass of Saturn was calculated from the orbital periods of its satellites, under the assumption that their motions are governed purely by Newtonian dynamics. If the SHP contribution is taken into account, the mass of Saturn may be altered by less than 0.3% (according to table 5-1), or by an amount of the order of $5 * 10^{23} \text{ kg}$.

Table 5-1: A comparison between the Keplerian calculated and the measured orbital periods of Saturn's Satellites (the calculation uses Kepler's third law, while arbitrarily assuming a perfect match for Mimas).

Satellite	semimajor axis (*1000 km)	calculated orbital period (Days)	measured orbital period (Days)	% change
Mimas	185.52	0.9424218	0.9424218	0
Enceladus	238.02	1.369554744	1.370218	0.048405179
Tethys	294.66	1.886431314	1.887802	0.072607505
Dione	377.4	2.734400117	2.736915	0.091887519
Rhea	527.04	4.512576593	4.5175	0.108985203
Titan	1221.83	15.92851895	15.945421	0.105999375
Hyperion	1481.1	21.25865545	21.276609	0.08438165
Iapetus	3561.3	79.26328361	79.330183	0.08433031
Pan	133.583	0.575819024	0.575	-0.142438957
Daphnis	136.50	0.594782521	0.594	-0.131737519
Atlas	137.67	0.602446088	0.6019	-0.090727402
Prometheus	139.353	0.613527034	0.613	-0.085976242
Pandora	141.70	0.629091758	0.6285	-0.094154062
Epimetheus	151.422	0.694932603	0.6942	-0.105531999
Janus	151.472	0.695276835	0.6945	-0.111855264
Methone	194	1.007770903	1.01	0.220702653
Anthe	197.70	1.036738494	1.04	0.313606348
Pallene	211	1.143096521	1.14	-0.271624679
Calypso	294.66	1.886431314	1.8878	0.072501638
Telesto	294.66	1.886431314	1.8878	0.072501638
Helene	377.40	2.734400117	2.7369	0.091339958
Polydeuces	377.40	2.734400117	2.74	0.204375303

Section V-7: Summary

A very simple model providing the interaction between two orbiting SHP groups composed of a single superheavy particle type and a spherically symmetric distribution of ordinary matter around the center of Saturn produces a zonal pattern that bears a close resemblance to the observed structure of Saturn's main body of rings, and can further account for a number of ring characteristics, including the appearance of spokes, gaps, ringlets, the appearance of spiral density and bending waves, and the general fine structure distribution. Note that the goal at this stage is limited to demonstrating the power of the UG theory and its ability to provide the general morphology and characteristics of complex systems on all distance scales via the use of the simplest model possible. No effort was made here to explain the remaining outer rings, such as the G and E rings, or to extend the discussion to model the formation and orbital locations of the Saturnian satellites. Saturn's main rings were selected for a UG analysis as they are the most complicated and the least understood rings observed to date. The same tools used for the analysis of the Saturnian system can be used for modeling the simpler rings and satellite systems of Jupiter, Uranus and Neptune.

The success achieved by this simple model in explaining the complex structure of Saturn's D, C, B, and A rings and the Cassini Division, coupled with the success of an even simpler model (using a single or binary SHP groups with as little as four parameters) in explaining various morphologies observed in galaxies and nebulae (in Chapter IV) provides a strong testament to the power of the UG theory, and further suggests that the addition of few more SHP groups, and additional fine-tuning of their parameters, may explain these complex systems down to very fine details. The UG approach suggests that the rings are generated by orbiting SHP groups, and provides a mechanism to keep them stable over a long period of time. As superheavy particles are most likely to be created by the collapse of the cloud of gas that formed the planet (see Chapter VII), planetary rings may be as old as their parent planets, and almost as old as the Solar System itself. This resolves the current contradiction, where according to the Newtonian scenario, the observed planetary rings could not have existed for more than a few tens of millions of years, while the Saturnian rings require a significantly longer period of time for developing their complex fine structure.

Chapter VI: The Potential Energy Spiral and the Constant Velocity Curve

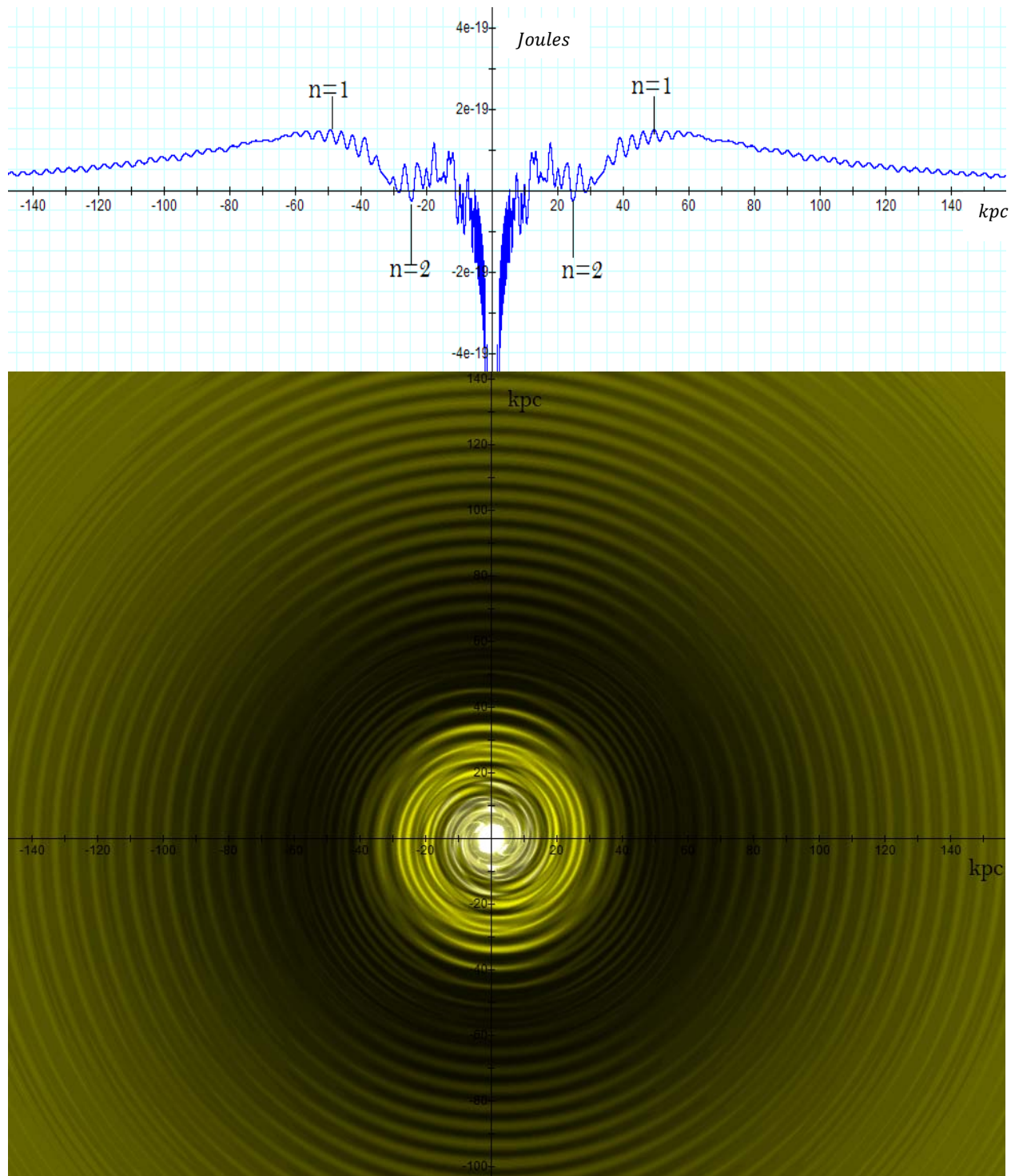


Figure 6-1: A galactic spiral calculated via equation 4-1-1a using the parameters $\Gamma = 1$, $M = 0.125 * 10^5 \text{ kg}$, $N_M = 1$, $A = 1.8 \text{ kpc}$, $M_G = 2.5 * 10^{38} \text{ kg}$, $N_{m_p} = 1$ and $v = 0.8c$. The lower image provides a two dimensional map of the potential energy contours of an ordinary particle of mass m_p , while the upper image of the figure displays its potential energy curve along the x axis. As shown, the spiral structure does not end at the last significant minimum contour $n = 2$ located at a radius of approximately 25 kpc , nor at the external zonal maximum $n = 1$ located at a radius of approximately 45 kpc to 50 kpc , and is demonstrated to extend well beyond these major zones. Note that as the distance between the ordinary test particle and the center

of the galaxy increases beyond the $n = 1$ maximum, the particle's potential energy declines gradually and eventually converges toward the Newtonian potential energy. When the rotation of the spiral is viewed over time, the oscillations displayed in the upper graph migrate outward, suggesting that the orbiting ordinary particles may be led outward by the rotating spiral, and eventually ejected out of the galaxy in the form of galactic wind.

The purpose of this chapter is to further explore the interaction between ordinary matter orbiting around the center of a spiral galaxy and the rotating spiral structure. In the following section, the large-scale potential energy spiral will be demonstrated to pump out ordinary matter such as interstellar gas and dust to beyond the $n = 1$ zonal maximum, creating the observed galactic outflow of gas. It will further be shown that the rotating potential energy spiral bears the effect of "equalizing" the velocity of orbiting matter, resulting in the relatively constant rotation curve observed in spiral galaxies. The critical influence of the rotating spiral on star formation will be examined in the final section of this chapter.

Section VI-1: The Formation of Galactic Density Waves

The theory of unified gravitation proposes that density waves occur due to the difference between the angular velocity of a rotating zonal pattern and the angular velocity of an orbiting object. In Chapter IV, the large-scale spiral structure was demonstrated to rotate at the same angular velocity as the galactic core and its superheavy particles. Following equation 4-1-1a, the potential energy of the object in a galaxy generated by a single SHP or binary SHP groups is given by

Equation 4-1-1a

$$V = -\frac{GN_M MN_{m_p} m_p \gamma^2(v)}{a} \left(e^{a/\dot{D}_{s_1}} \cos\left(\frac{bMm_p\gamma(v)}{\dot{D}_{s_1}}\right) - 1 \right) - \frac{GN_M MN_{m_p} m_p \gamma^2(v)\Gamma}{a} \left(e^{a/\dot{D}_{s_2}} \cos\left(\frac{bMm_p\gamma(v)}{\dot{D}_{s_2}}\right) - 1 \right) - \frac{Gm_p N_{m_p} M_G(r_0)}{r_0}$$

The variables used in the above equation are defined in Chapters III and IV, and $M_G(r_0)$ is equal to the mass of the ordinary matter enclosed in a sphere of radius r_0 around the galaxy center. Therefore, $\lim_{r_0 \rightarrow \infty} M_G(r_0) = M_G$, where M_G denotes the total mass of ordinary matter in the galaxy. As \dot{D}_{s_1} and \dot{D}_{s_2} are significantly larger than one parsec and a is of the order of $10^{-14} m$, the terms $e^{a/\dot{D}_{s_1}}$ and $e^{a/\dot{D}_{s_2}}$ are indistinguishable from 1. Therefore, the maximum potential energy of the object is given by $V_{max} \leq \frac{2GN_S MN_{m_p} m_p \gamma^2(v)}{a}$, where $N_S = (1 + \Gamma)N_M$ and the minimum potential energy is given by $V_{min} \geq -\frac{Gm_p N_{m_p} M_G(r_0)}{r_0}$. In order to remain trapped within the galactic disk at $a \ll r_0 < \frac{bm_p M \gamma(v)}{\pi}$, the total potential plus kinetic energy of the orbiting object must fall somewhere between V_{min} and V_{max} , leading to $\frac{1}{2}N_{m_p} m_p u^2(r_0) \leq V_{max} - V_{min} < \frac{2GN_S MN_{m_p} m_p \gamma^2(v)}{a} + \frac{GN_{m_p} m_p M_G(r_0)}{r_0}$, where $u(r_0)$ is the velocity of the orbiting object. Therefore,

Equation 6-1a

$$u(r_0) \lesssim \left(\frac{4GN_s M \gamma^2(v)}{a} + \frac{2GM_G(r_0)}{r_0} \right)^{1/2}$$

and the maximum possible velocity for a trapped object is in the vicinity of

Equation 6-1b

$$u_{max}(r_0) = \left(\frac{4GN_s M \gamma^2(v)}{a} + \frac{2GM_G(r_0)}{r_0} \right)^{1/2}$$

Thus, the upper bound of the velocity possible for an orbiting object is $w_{obj,max} = u_{max}(r_0)/r_0$.

Since $\lim_{r_0 \rightarrow \infty} M_G(r_0) = M_G$, the ratio between the angular velocity of the spiral pattern w and the maximum angular velocity $w_{obj,max}$ is given by

Equation 6-2a

$$\frac{w}{w_{obj,max}} = \frac{w}{(u_{max}(r_0)/r_0)} = \frac{wr_0}{\left(\frac{4GN_s M \gamma^2(v)}{a} + \frac{2GM_G(r_0)}{r_0} \right)^{1/2}} \rightarrow \frac{wr_0}{2} \left(\frac{a}{GN_s M \gamma^2(v)} \right)^{1/2}$$

as long as $\frac{aM_G}{2N_s M \gamma^2(v)} \ll r_0 < \frac{bm_p M \gamma(v)}{\pi}$. Therefore, $\frac{w}{w_{obj,max}}$ increases linearly with r_0 for any

value $\frac{aM_G}{2N_s M \gamma^2(v)} \ll r_0 < \frac{bm_p M \gamma(v)}{\pi}$ and $r_0 \gg a$. The corotation radius R_c , defined as the radial distance at which the velocity of the orbiting objects is equal to the angular velocity of the central core and the SHP groups, occurs when $w_{obj,max}(R_c) = w$, and is therefore given by

Equation 6-2b

$$R_c \approx \frac{1}{w} \left(\frac{4GN_s M \gamma^2(v)}{a} + \frac{2GM_G(R_c)}{R_c} \right)^{1/2}$$

Consequently, particles or objects with orbital radii larger than R_c can no longer keep up with w and begin to lag behind the rotation rate of the zonal pattern.

Figure 6-2 provides the graphic solution of the equation for R_c for the case of a galaxy with a spherically symmetric distribution of ordinary matter of mass $M_G = 10^{40} kg$ contained within a radius $R < 10 pc$ from the center of the galaxy (therefore, $M_G(r_0)$ is assumed to be virtually equal to the total mass of the galaxy for all distances $r > R$). The given galaxy is assumed to contain a single SHP group of $N_s = 50$ superheavy particles of particle mass $M = 0.125 * 10^5 kg$ rotating at a speed of $v = 0.8c$ in a circular orbit of radius of $A = 1.8 kpc$ around the center of the galaxy. In this figure, the functions $y = r_0$ (in violet) and $y =$

$\frac{1}{w} \left(\frac{4GN_s M \gamma^2(v)}{a} + \frac{2GM_G}{r_0} \right)^{1/2}$ (in red, using $w = v/A$) were drawn to provide $w/w_{obj,max} > 1$ when $r_0 > R_c \approx 13.5 pc$.

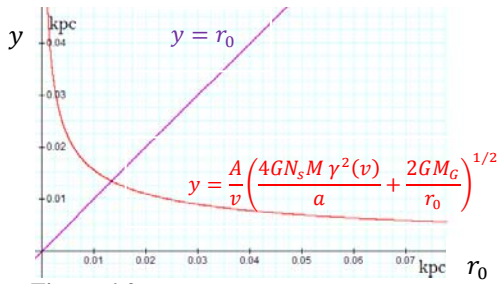


Figure 6-2

The pattern speed in this example is given by $w = v/A = 4.32 * 10^{-12} \text{ rd/sec}$. It would take the pattern $\frac{2\pi A}{v} = 46,083$ years to complete one full rotation, while a star moving at a speed of 250 km/s relative to the galaxy center in a circular orbit of radius of 10 kpc requires as many as 245.78 million years to complete a full rotation.

Section VI-2: The Outflow of Gas and Matter From Galaxies

As shown above, at distances of $r_0 > R_c$ the spiral maxima and minima rotate faster than the given ordinary object, and therefore overtake its orbit on a periodic basis. When the object's initial potential plus kinetic energy just prior to an encounter with a rotating maximum contour is lower than its potential energy at that maximum, the potential plus the kinetic energy of the object must be elevated to match or exceed its potential energy at the maximum. In addition, the rotating spiral applies a greater than zero net tangential force on the rotating object along its direction of movement, thereby resulting in a non-zero net work and in increasing the object's energy with every full spiral rotation.¹¹⁷ Unless the object loses this added energy via other interactions in between successive encounters, its energy level will steadily increase. The object's potential plus kinetic energy is thus expected to eventually exceed its potential energy at the highest maximum $n = 1$, and consequently the object will exit the galaxy.

In figure 6-3, the maxima of the relativistic oscillations beyond $n = 1$ decline with increasing distance and cannot confine the object, which breaks free and flies out in the tangential direction away from the galaxy. A collective outward flow of galactic matter may explain the observed large-scale outflow of gas from galaxies.

¹¹⁷ This results from the assumption that the object does not rotate in the opposite direction of the spiral. In the case where the object and the spiral rotate in opposing directions, the spiral will initially slow down and halt the object's rotation, before accelerating it in the opposite direction. From that point on, the energy of the object will begin to increase.

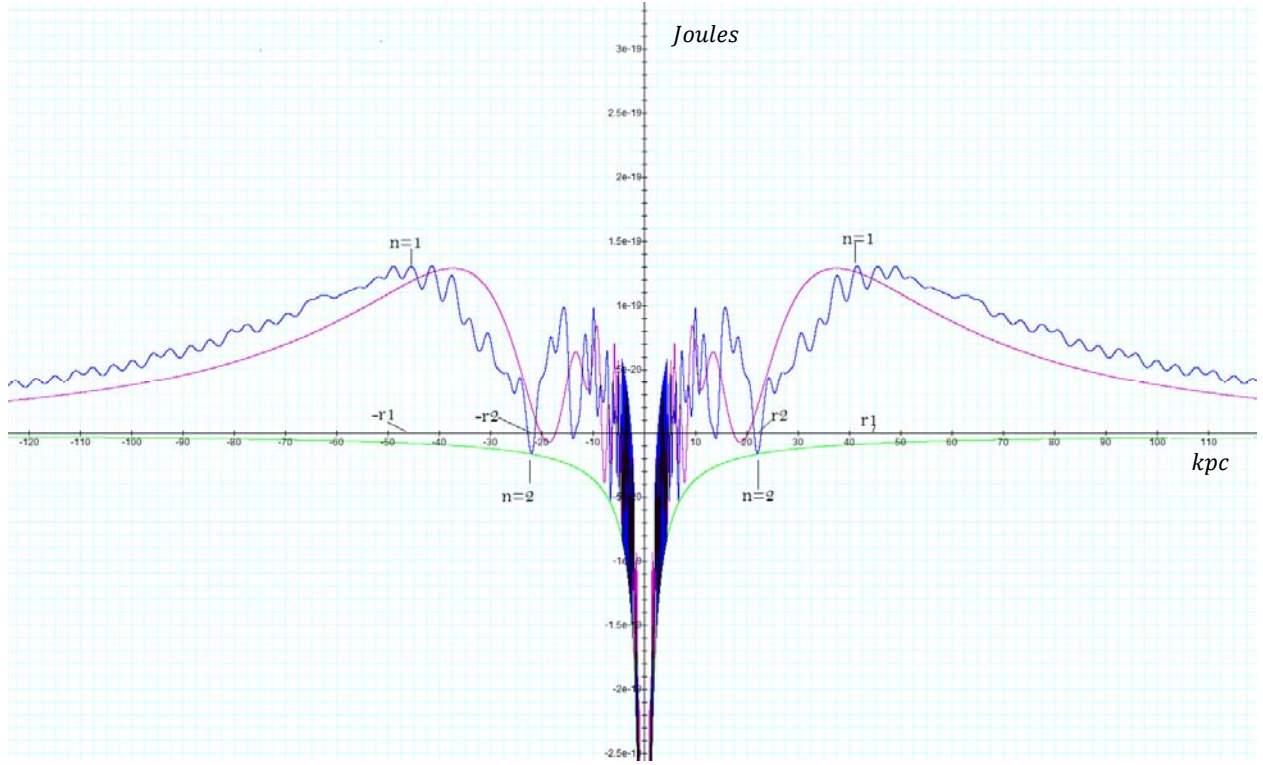


Figure 6-3: Provides the gravitational potential energy along the x axis between an ordinary particle of mass m_p and the binary SHP groups of a galaxy, described by the parameters $\Gamma = 1$, $A = 1.8 \text{ kpc}$, $N_M = 1$, $N_{m_p} = 1$ and $M_G = 10^{38} \text{ kg}$. Given non-relativistic SHP velocities of $v \ll c$, the potential energy derived via equation 4-1-1a demonstrates a long and steady decline beyond the $n = 1$ maximum (in violet) toward the $n = 0$ potential energy minimum. However, at a relativistic SHP velocity of $v = 0.75c$, the potential energy (in blue) provides outward propagating oscillations well beyond the external zonal maximum $n = 1$, while the $n = 1$ maximum contour shifts outward.

As the object's energy increases gradually over time, the object's potential plus kinetic energy at the time it crosses the $n = 1$ maximum and escapes the galaxy is approximately equal to the object's potential energy at this maximum (thus the kinetic energy of the object at this point is close to zero). Therefore, at $r_1 \gg a$ and $MN_S \ll M_G(r_1)$, the average overall potential plus kinetic energy of the object at the exact time of intersection with the zonal maximum $n = 1$ is given by $E = \frac{2GN_S MN_{m_p} m_p \gamma^2(v)}{a} - \frac{GN_{m_p} m_p M_G(r_1)}{r_1}$. After breaking away, the overall energy level of the test object remains approximately unchanged (assuming only a small contribution from other galaxies and minor SHP groups). At distances $r \gg r_1$, where the SHP contribution becomes negligible, the object's kinetic energy is equal to

$$E = \frac{1}{2} N_{m_p} m_p u(r)^2 - \frac{GN_{m_p} m_p M_G(r)}{r} \xrightarrow{r \rightarrow \infty} \frac{1}{2} N_{m_p} m_p u_\infty^2 \approx \frac{2GN_S MN_{m_p} m_p \gamma^2(v)}{a} - \frac{GN_{m_p} m_p M_G(r_1)}{r_1}$$

Consequently, the velocity of the galactic gas outflow u_∞ can be expected to approach

Equation 6-3a

$$u_\infty \approx \left(\frac{4GN_S M \gamma^2(v)}{a} - \frac{2GM_G(r_1)}{r_1} \right)^{1/2}$$

The approximate radius of the first maximum contour is given by $r_1 \approx \frac{bMm_p\gamma(v)}{\pi} \approx 2r_2$, where r_2 is equal to the approximate radius of the outermost substantial minimum contour, or roughly the radius of the galactic disk. Substituting $\frac{bMm_p\gamma(v)}{\pi}$ for r_1 and M_G for $M_G(r_1)$ in equation 6-3a,¹¹⁸

the speed of the ejected test object at far greater distances from the galaxy can also be written as **Equation 6-3b**

$$u_\infty \approx \left(\frac{4GN_sM\gamma^2(v)}{a} - \frac{2G\pi M_G}{bMm_p\gamma(v)} \right)^{1/2}$$

This process provides a possible explanation for the mechanism that drives the galactic outflow of gas and determines its velocity. Note that if the galaxy center contains a substantial amount of additional smaller SHPs (at sufficient quantity that their overall mass is larger than or comparable to N_sM), other outflow velocities may be detected. Such a phenomenon is observed in the Solar System, where solar wind is observed to have two different speeds at about 400 km/s and 750 km/s, suggesting significant contribution from at least two different SHP types.

Section VI-3: The Constant Galaxy Rotation Curve

According to Newton's theory of gravitation, one might expect that the speed of a star rotating beyond the main body of a galaxy mass should decrease inversely to the square root of the star's orbital radius. Mathematically stated,

Equation 6-4

$$u_{Newton} = \left(\frac{GM_G(r)}{r} \right)^{1/2}$$

Accordingly, at distances where $M_G(r) = M_G$, stars at the outer edge of a galactic disk would be expected to travel at much lower velocities than those near the middle. However, measurements of the rotation curves of a number of known spiral galaxies have demonstrated significant departure from the velocities predicted by Newtonian gravitation. Rather, stellar velocity was observed to remain roughly constant, or in some cases to increase slightly with distance from the center. To date, the theory of dark matter is the leading explanation for the galaxy rotation problem. Current theories predict that dark matter should account for about 22% of the mass of the observable universe, compared with only about 4% estimated for baryonic matter.¹¹⁹ As of yet, however, there is no direct evidence for the existence of dark matter, nor any clear and accepted theory that explains what exactly this matter is, what determines its distribution in galaxies and in the universe, why it has so little presence, if at all, within our Solar System, or how it influences galactic morphology. The hypothesis that the constant rotation curve observed

¹¹⁸ $M_G = M_G(r_1)$ indicates that the vast majority of the galaxy's ordinary matter is contained within its core and within the galactic disk.

¹¹⁹ The remaining 74% of the missing mass is believed, according to the current leading paradigm, to consist of dark energy.

in spiral galaxies is due to a massive dark halo surrounding a spiral disk allows Newton's gravitational theory to hold over cosmological scale distances. Consequently, most astronomers and physicists prefer this explanation to the alternative, that Newtonian dynamics require modification for application over cosmological distances.¹²⁰

Whereas the Newtonian rotation curve of equation 6-4 drops proportionally to $r^{-1/2}$, the UG rotation curve of equation 6-1a limits the speed of a rotating object to the range of $0 \leq u(r) < \left(\frac{4GN_s M \gamma^2(v)}{a} + \frac{2GM_G(r)}{r} \right)^{1/2}$ within the oscillation range of M and m_p at distances $r < \frac{bMm_p \gamma(v)}{\pi}$. Therefore, at relatively short distances¹²¹ $r < R$, $M_G(r) \propto r^3$ and $r \ll \frac{aM_G(r)}{2MN_s \gamma^2(v)}$, the rotation curve increases proportionally to r , in agreement with observations (see figure 6-5c at distances $r < 4 \text{ kpc}$). At distances $M_G(r) \approx M_G \propto R^3$, where $r \geq R$ and $r \ll \frac{aM_G(r)}{2MN_s \gamma^2(v)}$, the velocity of the orbiting object becomes $u(r) < \left(\frac{2GM_G}{r} \right)^{1/2}$.

At distances $r \gg \frac{aM_G(r)}{2MN_s \gamma^2(v)}$ and $A \ll r < \frac{bMm_p \gamma(v)}{\pi}$, the maxima and minima contours of both SHP groups (in the case of binary groups) almost coincide, and the contribution of ordinary matter is relatively small. Therefore, all the potential energy maxima within this range of distances demonstrate approximately the same potential energy of $\frac{2GN_s MN m_p m_p}{a}$, and all of the minima within this range have a potential energy of virtually zero joules or electron-volts (note that the external maximum $n = 1$ is slightly higher than the rest of the maxima within this range of distances and can thus contain the object within the galaxy).

When $r > R_c \approx \frac{1}{w} \left(\frac{4GN_s M \gamma^2(v)}{a} + \frac{2GM_G(R_c)}{R_c} \right)^{1/2}$, the spiral rotates faster than the ordinary object around the center of the galaxy, and therefore the overall potential plus kinetic energy of the object must be elevated during its periodic encounters with the spiral's local maxima to match or slightly exceed the highest potential energy encountered by the object. As the potential energy maxima are virtually equal, and the object remains trapped within the galaxy, its energy must be close to $\frac{2GN_s MN m_p m_p}{a}$. Therefore, the kinetic energy of the orbiting object will periodically approach zero upon encounter with a maximum contour in this range of distances, while upon encountering a minimum, the object's velocity becomes

$$u(r_{min}) \approx \left(\frac{2}{N_{m_p} m_p} \left(\frac{2GN_s MN m_p m_p}{a} - 0 \right) \right)^{1/2} = \left(\frac{4GN_s M \gamma^2(v)}{a} \right)^{1/2}$$

¹²⁰ The leading alternative theory of Modified Newtonian Dynamics, or MOND, is provided by Milgrom, M. 1983. ApJ., **270**, 371; Milgrom, M, Braun, E. 1988. ApJ., **334**, 130; McGaugh, S.S. and Blok, W.J.G. de. 1998. ApJ., **499**, 66; Blok W.J.G de, McGaugh, S.S. 1998. ApJ. **508**, 132; Begeman, K.G, Broeils, A.H., and Sanders, R.H. 1991. MNRAS, **249**, 523; Sanders, R.H. 1996. ApJ., **473**, 117; and Sanders, R.H., Verheijen M.A.W. 1998. ApJ., **503**, 97. Non-gravitational acceleration of halo gas rotation (due to magneto-hydrodynamical force) was also suggested as an alternative by Nelson, A.H. 1988. MNRAS. **233**, 115.

¹²¹ The dependency of $M_G(r)$ on r^3 can be derived by assuming a homogenous spherical distribution of $M_G(r) = \frac{4\pi}{3} \rho r^3$ for $r < R$, and $M_G(r) = M_G = \frac{4\pi}{3} \rho R^3$ for $r \geq R$, where the density of the ordinary matter ρ is assumed to be constant.

where $r \gg \frac{aM_G(r)}{2MN_s\gamma^2(v)}$ and $A \ll r < \frac{bMm_p\gamma(v)}{\pi}$. As the zonal spiral rotates, the object encounters an equal number of potential energy maxima and minima. Since matter tends to gravitate toward the minima potential energy, the object spends longer periods of time near the minima than near the maxima or near any other potential energy level in between. For this reason, the density of matter near the minima is far greater than the density of matter near the maxima. Most of the observed radiation generated by the galactic gas is therefore likely to have originated at or near the potential minima locations, where the velocity of the object is given approximately by $u(r_{min}) = \left(\frac{4GN_sM\gamma^2(v)}{a}\right)^{1/2}$. Consequently, the spectrum of the radiation emitted by the object's atoms appears redshifted when the matter moves away from the observer, or blue-shifted when the matter moves toward the observer, and is strongly skewed toward the shift associated with the velocity of the object at the minima $u(r_{min}) = \left(\frac{4GN_sM\gamma^2(v)}{a}\right)^{1/2}$. Note that $u(r_{min})$ is constant and independent of both the mass of the object as well as its distance from the center of the galaxy. As the minima are generally circular, the velocity of the object is almost tangential. Therefore, the spectral redshift or blueshift at the large distance range observed is of a relatively flat velocity curve.

Between the small and large-scale distances, there is a mid-range of distances at which $r < \frac{bMm_p\gamma(v)}{\pi}$, r is of the order of $\frac{aM_G(r)}{2MN_s\gamma^2(v)}$, and $M_G(r) \approx M_G$ is almost independent of r . At these distance ranges, the potential energy maxima and minima of the mid-range distances vary, and generally increase with distance. To analyze the velocity curve within this range in detail, the process described above can be repeated. Over time, the orbiting object drifts outward as its energy level increases due to the energy transferred to the object by the rotating spiral. Therefore, the overall potential plus kinetic energy of the object must be equal to or slightly higher than the highest energy maximum encountered by the object up to that point in time on its journey outward.¹²²

¹²² Note that this discussion assumes that the effect exerted on the given object by other orbiting objects is relatively small. As will be shown in Chapter VII, this assumption does not necessarily hold true for the case of elliptical galaxies.

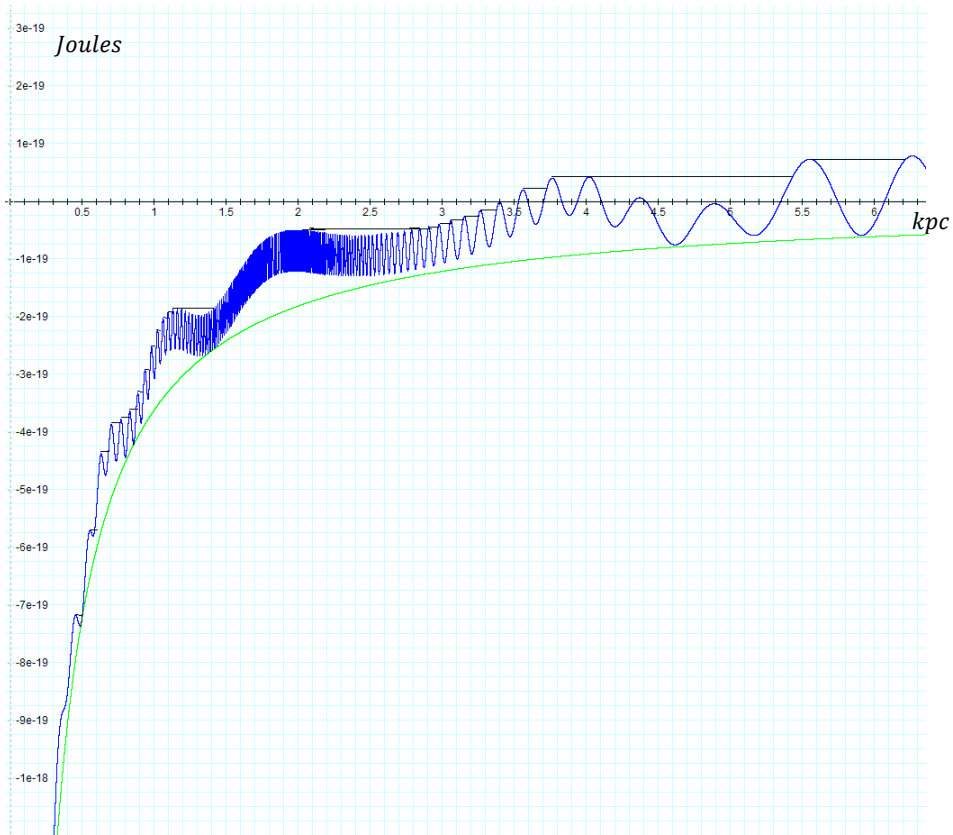


Figure 6-4a

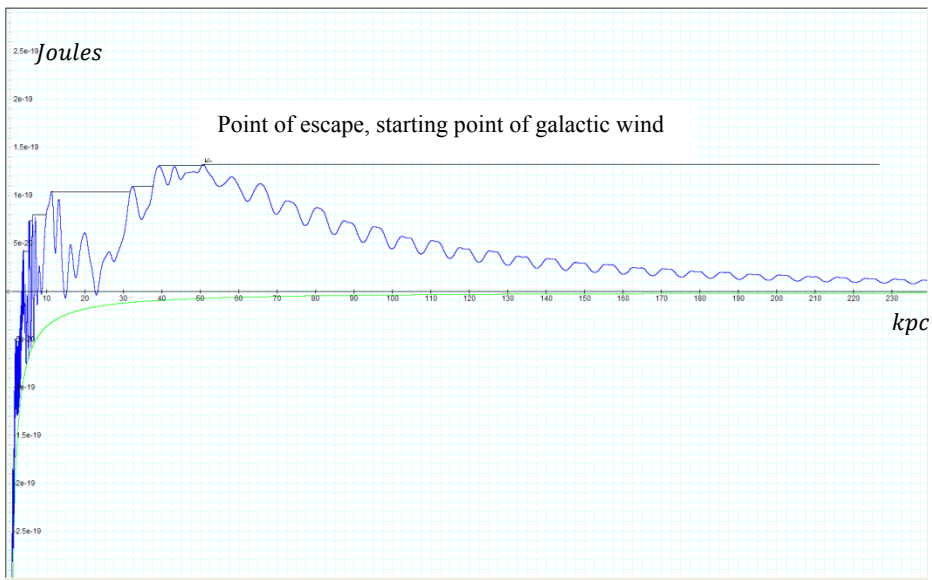


Figure 6-4b

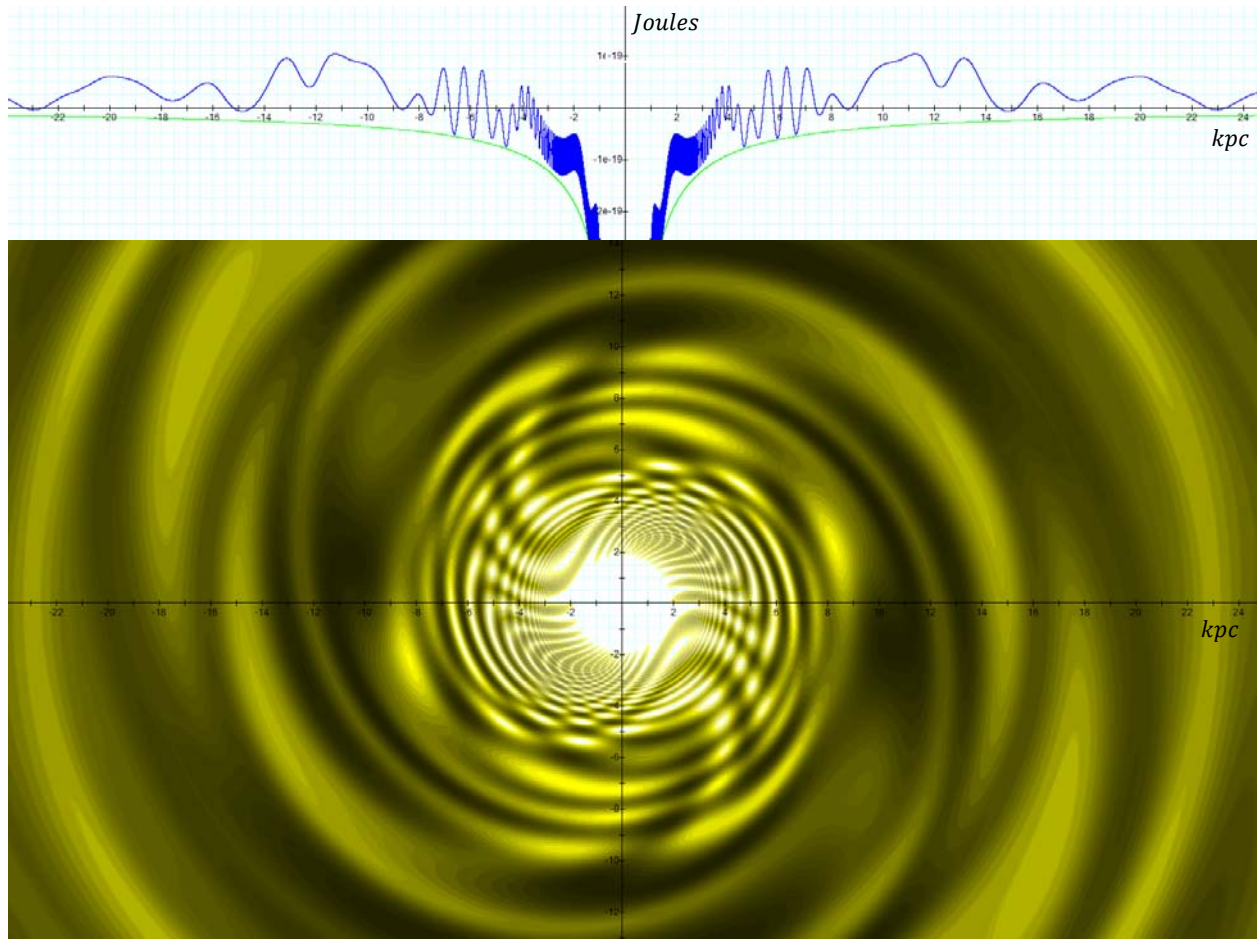


Figure 6-4c: Depicts a two dimensional contour map of the same galaxy provided in figures 6-4a and b, where the brighter colors denote lower potential energy of the test object.

Based on the above discussion, the potential plus the kinetic energy of the object as a function of the distance from the galaxy center is presented in figures 6-4a, 6-4b and 6-4c for the case of a single ordinary particle of mass m_p within a galaxy containing identical binary SHP groups ($\Gamma = 1$), each composed of a single SHP of mass $M = 0.156 * 10^5 \text{ kg}$, rotating at constant speed $v = 0.75c$ in a circular orbit of radius $A = 1.8 \text{ kpc}$ around the galaxy center. The mass of the ordinary matter at the center of the galaxy (within few parsecs) was selected to equal $M_G/N_s = 10^{38} \text{ kg}$. Figure 6-4c provides a two dimensional contour map of the potential energy of the test particle, as well as an additional perspective of the same galaxy displayed in a one dimensional graph of the particle's potential energy along the x axis.¹²³ Detailed waveforms of the one dimensional graph are provided in figures 6-4a (for $x = 0$ to 6 kpc) and 6-4b (for $x = 0$ to 230 kpc). The green curves in these figures provide the contribution of the galaxy's ordinary matter to the overall potential energy. The blue curve provides the overall potential energy contributed by the relativistic SHP groups and by the galaxy's ordinary matter. The black lines

¹²³ Note that when a series of graphs separated by a short time interval were calculated and displayed in rapid succession as a movie, the waves of figures 6-4a and 6-4b traveled outward, while the two dimensional map rotated counterclockwise, displaying spirals that converge outward.

provide the approximate overall potential plus kinetic energy of the object. Note that the overall potential plus kinetic energy of the object remains almost constant at the level of the highest maximum peak previously encountered by the object, with a slight positive slope.¹²⁴ Upon a successive encounter with a higher energy maximum, the object's energy level will abruptly increase to match the potential energy of the new maximum peak. This is reflected by a step increase between successive black lines, which are connected via a short segment of the blue potential energy curve. Consequently, the local velocity of the object at the time of the emittance

of a photon varies between $u = u_{min} \approx \left(2 \frac{V_{max} - V_{i,max}}{N_{m_p} m_p}\right)^{1/2}$ and $u = u_{max} \approx \left(2 \frac{V_{max} - V_{i,min}}{N_{m_p} m_p}\right)^{1/2}$,

where V_{max} denotes the highest potential energy encountered thus far by the object. $V_{i,max}$ and $V_{i,min}$ respectively provide the local maximum and minimum potential energy encountered at the given time. The value and the direction of \vec{u} determine the amount of redshift or blueshift of the photon when intercepted by the observer. As discussed above, the density of matter tends to be significantly higher at the potential energy minima, thus the distribution of the velocity u is

skewed strongly toward $u = u_{max} \approx \left(2 \frac{V_{max} - V_{i,min}}{N_{m_p} m_p}\right)^{1/2}$. Hence, the spectrum of the radiation

emitted by the object's atoms appears redshifted when matter is moving away from the observer or blueshifted when matter is moving toward the observer, and strongly skewed toward a wavelength shift associated with the velocity of

Equation 6-5

$$u \approx \left(2 \frac{V_{max} - V_{i,min}}{N_{m_p} m_p}\right)^{1/2} \approx \left(\frac{4GN_s M \gamma^2(v)}{a} + \Delta\left(\frac{GM_G}{r}\right)\right)^{1/2}$$

where $\Delta\left(\frac{GM_G}{r}\right) = -\frac{GM_G}{r_{max}} + \frac{GM_G}{r_{i,min}}$. As aforementioned, for distances $r \gg \frac{aM_G}{2N_s M \gamma^2(v)}$ or

$\left(\frac{r_{max} r_{i,min}}{r_{i,min} - r_{max}}\right) \gg \frac{aM_G}{2N_s M \gamma^2(v)}$, the velocity of the object is given by $u \approx \left(\frac{4GN_s M \gamma^2(v)}{a}\right)^{1/2}$. Due to this

concept, the rotation curve of the modeled galaxy was calculated by subtracting the potential energy waveform (the blue curve) from the potential plus kinetic energy waveform (indicated in black) displayed in figures 6-4a and 6-4b. Based on the above discussion, the overall potential plus kinetic energy is determined mainly by the highest maxima encountered prior to the given point in time V_{max} . As long as no higher maximum is encountered, the energy of the particle will increase only slightly with each rotation of the spiral, thus remaining nearly constant.

However, upon encountering a higher maximum $V_{i,max}$, the potential plus kinetic energy of the object will increase to the level of $V_{i,max}$, as demonstrated by the series of black lines in the figures. The calculated radius and potential energy of the maxima and minima shown in figures 6-4a and 6-4b are respectively provided in the columns x , V_{max} and $V_{i,min}$ of table 6-1. The Delta column of the table provides the approximately calculated kinetic energy of the object

¹²⁴ The slight positive slope is a consequence of the small increase in the object energy due to the work done by the spiral rotation.

upon encountering the minima of the spiral, given by $V_{max} - V_{i,min}$, and the column V_{Newton} provides the Newtonian potential energy of the galaxy's ordinary matter (indicated in green in figures 6-4a and 6-4b). Bear in mind that the waveforms and the two dimensional map of figures 6-4a to 6-4c (and therefore the set of values V_{max} and $V_{i,min}$ in table 6-1) were calculated under the assumption that each group contains a single SHP, and that the total mass of ordinary matter in the galaxy $M_G = 10^{38} kg$ is concentrated mainly in a sphere of radius $r < 0.375 kpc$. According to equation 4-1-1a (as well as to the second scaling theorem of the UG theory provided in appendix A), galactic morphology will remain unchanged as the number of superheavy particles in each SHP group and the mass of the ordinary matter M_G are multiplied by the same value N_s , while the potential energy and velocity of the object increase by a factor of N_s and $\sqrt{N_s}$ respectively. For example, selecting $N_s = 158$ will result in a total of 158 superheavy particles, and an overall ordinary matter mass of $N_s M_G = 1.58 * 10^{40} kg$. With this choice of N_s , the galaxy rotation curve expected according to Newtonian dynamics via equations 6-4 (multiplied by $N_s = 158$) and the overall UG rotation curve (which includes both the contribution of the galactic SHP groups and the contribution of ordinary matter calculated via $u \approx 0.001 \left(2 \frac{V_{max} - V_{i,min}}{N_{m_p} m_p} \right)^{1/2} \sqrt{N_s}$) are provided in the last two columns of the table. Note that the calculated velocities include a radial component as well. However, the assumption that the object's orbit is nearly circular implies that its rotational velocity is nearly equal to its overall velocity.

Figure 6-5a provides the graphs of the Newtonian (in blue) and the UG (in red) galactic velocities, as derived from the last two columns of table 1 and drawn as functions of the object's orbital radius.¹²⁵

¹²⁵ Note that as demonstrated by figure 6-4c, the potential energy is not rotationally symmetric, and may vary with the azimuth. Therefore, the velocity curve may also vary with the azimuth, in agreement with observations.

TABLE 6-1

x (kpc)	V_{max} (joules)	$V_{i,min}$ (joules)	Delta (joules)		V_{Newton} (joules)	x (kpc)	u ordinary matter (km/sec)	u overall (km/sec)
0.375			0	no minima	-9.64E-19	0.375	301.7	0.0
0.4875	-7.16E-19	-7.42E-19	2.54E-20		-7.42E-19	0.4875	264.6	69.3
0.5768	-5.69E-19	-5.79E-19	9.99E-21		-6.27E-19	0.5768	243.2	43.4
0.6639	-4.37E-19	-4.74E-19	3.70E-20		-5.45E-19	0.6639	226.8	83.6
0.858	-3.64E-19	-4.21E-19	5.67E-20		-4.21E-19	0.858	199.3	103.5
1.003	-2.52E-19	-3.06E-19	5.41E-20		-3.60E-19	1.003	184.3	101.1
1.147	-1.85E-19	-2.55E-19	6.93E-20		-3.15E-19	1.147	172.5	114.4
1.2548	-1.85E-19	-2.64E-19	7.86E-20		-2.64E-19	1.2548	157.8	121.8
1.339	-1.85E-19	-2.67E-19	8.14E-20		-2.67E-19	1.339	158.6	123.9
1.407	-1.85E-19	-2.57E-19	7.14E-20		-2.57E-19	1.407	155.7	116.1
1.544	-1.42E-19	-2.10E-19	6.78E-20		-2.34E-19	1.544	148.6	113.2
1.668	-9.55E-20	-1.64E-19	6.86E-20		-2.17E-19	1.668	143.0	113.8
1.7411	-7.47E-20	-1.44E-19	6.89E-20		-2.08E-19	1.7411	140.1	114.0
1.8093	-6.21E-20	-1.31E-19	6.86E-20		-2.00E-19	1.8093	137.4	113.8
1.917	-5.13E-20	-1.21E-19	6.96E-20		-1.89E-19	1.917	133.6	114.7
2	-4.99E-20	-1.20E-19	6.99E-20		-1.81E-19	2	130.5	114.9
2.1064	-4.99E-20	-1.22E-19	7.23E-20		-1.72E-19	2.1064	127.3	116.8
2.205	-4.99E-20	-1.25E-19	7.56E-20		-1.64E-19	2.205	124.4	119.4
2.298	-4.99E-20	-1.28E-19	7.79E-20		-1.57E-19	2.298	121.9	121.2
2.5	-4.99E-20	-1.28E-19	7.80E-20		-1.44E-19	2.5	116.7	121.4
2.71	-4.99E-20	-1.22E-19	7.20E-20		-1.33E-19	2.71	112.1	116.6
2.875	-4.62E-20	-1.15E-19	6.83E-20		-1.26E-19	2.875	109.0	113.5
3.1	-3.30E-20	-9.95E-20	6.65E-20		-1.17E-19	3.1	104.9	112.0
3.472	-1.42E-22	-6.08E-20	6.07E-20		-1.04E-19	3.472	99.2	107.0
3.886	4.13E-20	-2.33E-20	6.46E-20		-9.31E-20	3.886	93.7	110.4
4.2	4.29E-20	-4.32E-20	8.60E-20		-8.61E-20	4.2	90.1	127.4
4.619	4.29E-20	-7.83E-20	1.21E-19		-7.83E-20	4.619	86.0	151.2
5.165	4.29E-20	-5.85E-20	1.01E-19		-7.00E-20	5.165	81.3	138.3
5.911	7.36E-20	-5.82E-20	1.32E-19		-6.13E-20	5.911	76.1	157.7
6.632	7.93E-20	-5.04E-20	1.30E-19		-5.45E-20	6.632	71.7	156.5
7.515	7.93E-20	-1.34E-20	9.28E-20		-4.81E-20	7.515	67.4	132.3
8.634	7.93E-20	-2.73E-21	8.21E-20		-4.19E-20	8.634	62.9	124.5
12.25	1.05E-19	4.02E-20	6.44E-20		-2.95E-20	12.25	52.8	110.2
14.87	1.05E-19	-6.60E-21	1.11E-19		-2.43E-20	14.87	47.9	144.9
17.57	1.05E-19	1.45E-20	9.01E-20		-2.06E-20	17.57	44.1	130.4
22.94	1.05E-19	-3.66E-21	1.08E-19		-1.58E-20	22.94	38.6	143.0
27.49	1.05E-19	3.11E-20	7.35E-20		-1.32E-20	27.49	35.2	117.8
34.68	1.09E-19	7.51E-20	3.39E-20		-1.04E-20	34.68	31.4	79.9
41.66	1.30E-19	1.11E-19	1.92E-20		-8.71E-21	41.66	28.7	60.2
44.866	1.30E-19	1.17E-19	1.36E-20		-8.06E-21	44.866	27.6	50.7
49.12	1.30E-19	1.24E-19	6.40E-21		-7.36E-21	49.12	26.4	34.8
50.75	1.32E-19	escape point				50.75		

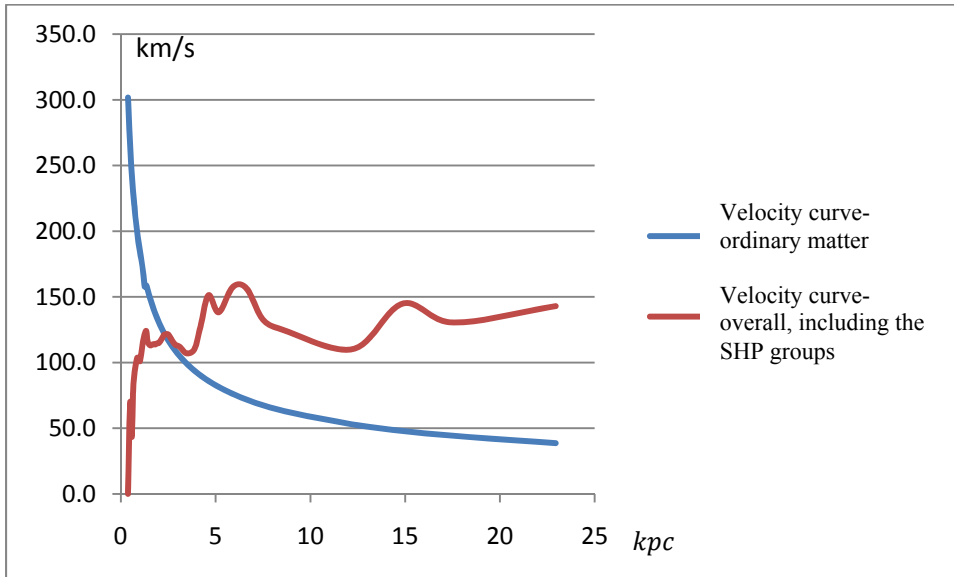


Figure 6-5a: The galaxy rotation curve within the disk range of distances between 0 *kpc* to 24 *kpc* (*x* axis) and velocity between 0 and 350 *km/s* (on the *y* axis).

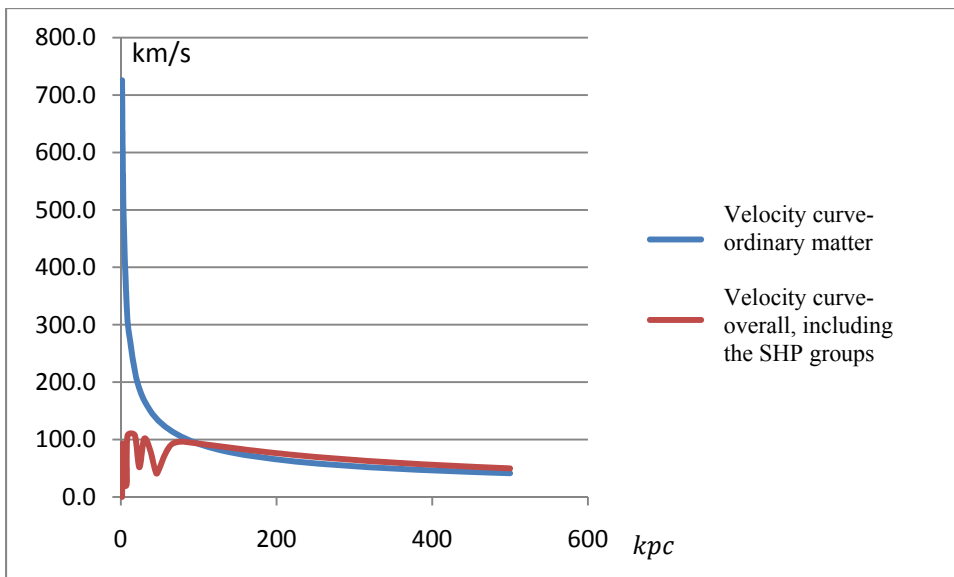


Figure 6-5b: The velocity curve of a galaxy similar to the one provided by figure 6-5a, where M_G/N_s increases from 10^{38} kg to $2.5 \times 10^{39} \text{ kg}$. The *x* axis provides the distance from the galactic center between 0 *kpc* and 500 *kpc*, and the *y* axis provides the object velocity between 0 and 800 *km/s*.

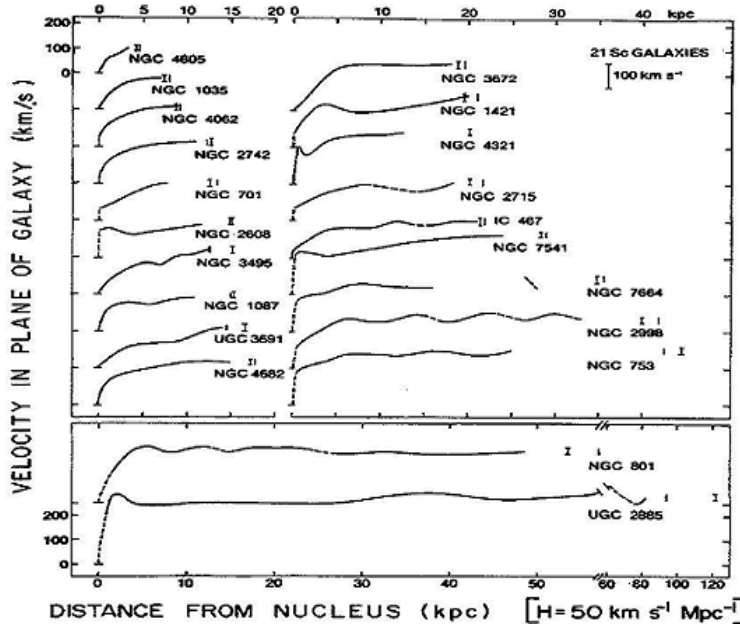


Figure 6-5c: Measured mean velocities in the plane of the galaxy, as a function of linear distance from the nucleus for 21 Sc galaxies, arranged according to increasing linear radius. The curve drawn is a rotation curve formed from the mean of velocities on both sides of major axis (Rubin, Ford & Thonard, 1980). The general trend is of rapid velocity rise to $v \approx 125 \text{ km/s}$ at about $r = 5 \text{ kpc}$, and slower rise or close to constant velocity thereafter.

Figure 6-5a provides the distance range between 0.375 kpc and 24 kpc . Within the range of $0.375 < r < 6.6 \text{ kpc}$, the UG rotation curve demonstrates an initial sharp increase in the velocity of the test object from $u = 0 \text{ km/s}$ to about $u = 158 \text{ km/s}$. At roughly 3 kpc to 5 kpc , the rotation curve levels and displays few oscillations within $\pm 25 \text{ km/s}$ around an average velocity curve of about 135 km/s , yet overall remains level relative to the sharp decrease demonstrated by the Newtonian rotation curve, which reduces proportionally to $(1/r)^{1/2}$. In addition, the approximately constant rotation curve increases slightly with distance, in good agreement with observation, as shown in figure 6-5c.¹²⁶ As demonstrated by figure 6-4b, the rotational velocity is not isotropic within the galaxy, and is dependent on the object's azimuth.

¹²⁶ Note that a choice of $N_s \approx 350$, rather than $N_s = 158$, would have resulted in the maximum velocity of about 235 km/s , which is closer to the range of velocities demonstrated by Andromeda. Also note that according to table 6-1, the velocity curve between 24 kpc and about 50 kpc is reduced significantly. However, while the theoretical velocity curve demonstrates a rapid decline at $r > 24 \text{ kpc}$ (for this example), the density of matter within this range of distances reduces significantly beyond the $n = 2$ minimum at about 24 kpc . Therefore, beyond the distance of 24 kpc , the velocity curve begins to decline towards the outermost $n = 1$ maximum, where its velocity nearly reduces to the Newtonian velocity. At this point, the object escapes the galactic disk. As the minima within the range of distances between $n = 1$ and $n = 2$ are shallow and relatively far from each other, the velocity curve in this distance range is less detectable. However, the constant rotation curves of some spiral galaxies were observed to end with a detectable sharp reduction in velocity, as demonstrated in the case of the velocity curves of NGC 2885 and NGC 7664 displayed in figure 6-5c.

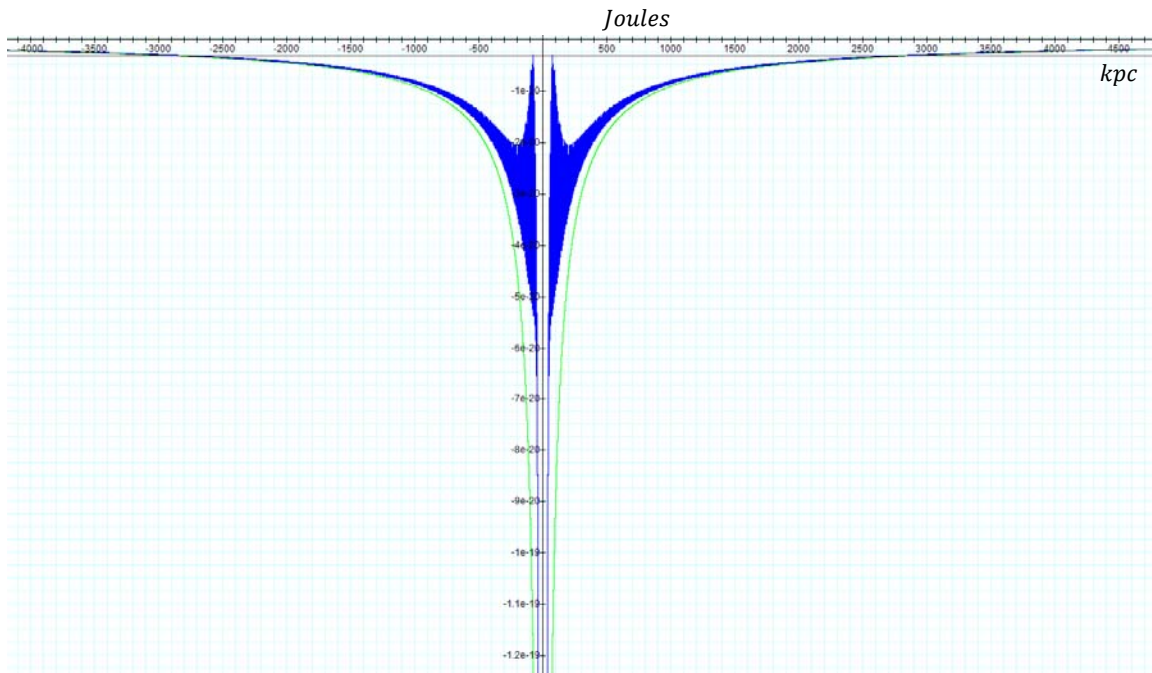


Figure 6-5d

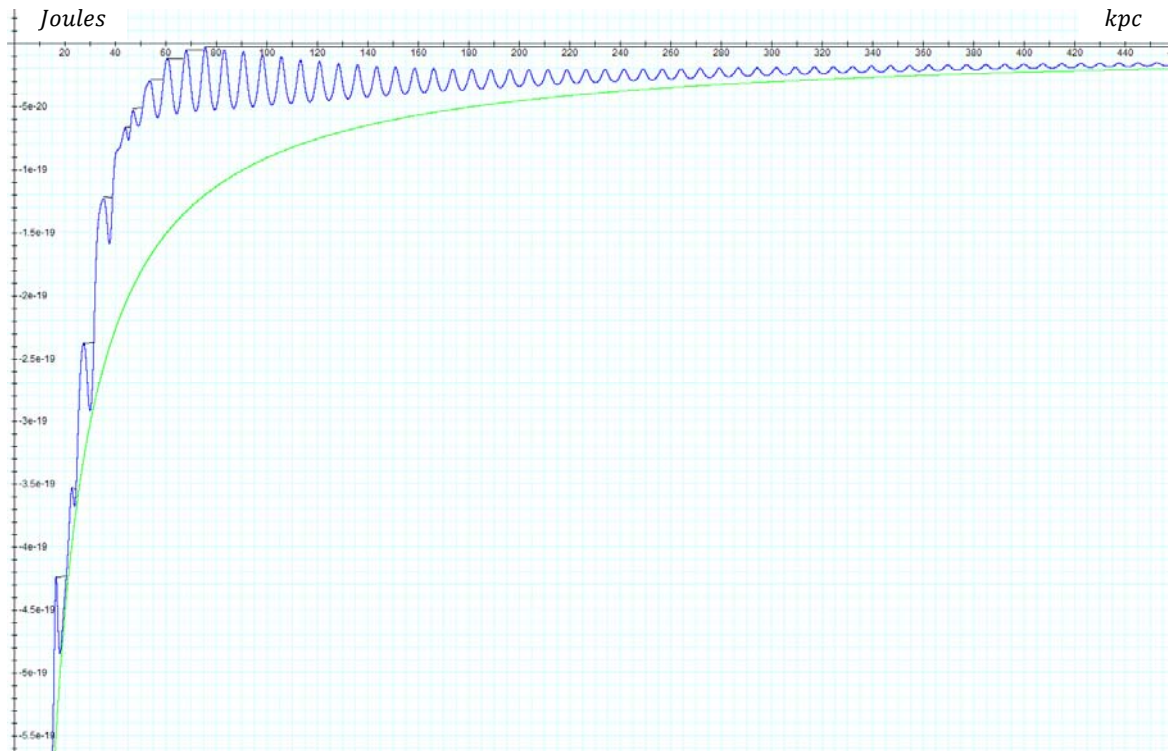


Figure 6-5e

A second example is provided in figures 6-5d and 6-5e for a galaxy with similar parameters, containing $M_G/N_s = 2.5 * 10^{39} \text{ kg}$ of ordinary matter (rather than 10^{38} kg).¹²⁷ Due

¹²⁷ As this example uses $N_s = 158$, the overall mass of the galaxy's ordinary matter is $3.95 * 10^{41} \text{ kg}$.

to the increased mass of the ordinary matter, the test particle remains trapped within the galaxy even when its potential plus kinetic energy is equal to its potential energy at the $n = 1$ maximum. As demonstrated, the encounter with a higher potential energy maximum abruptly elevates the potential plus kinetic energy level of the test particle. The particle's potential plus kinetic energy (indicated in black) remains almost constant at this level, demonstrating only a slight increase due to the rotation of the spiral, until the next encounter with a substantially higher potential energy maximum. Similar calculations lead to the rotation curve of the second galaxy displayed (for a given azimuth) in figures 6-5b.

There are a large number of possible combinations of SHP and ordinary matter parameters. The rotation curves of spiral galaxies therefore do not conform to a universal form, and different combinations may result in a different rotational curve. However, at distances $r > R_c$, where the central rotating spiral is sufficiently strong relative to the influence of the gravitational field of the galactic ordinary matter, the velocity curve of the galaxy will remain flat relative to the Newtonian velocity curve.

In summary, the UG theory is demonstrated to provide a constant velocity curve in spiral galaxies that is consistent with observations, without the need to assume the presence of yet undetected dark matter.

Section VI-4: The Influence of SHP Group Rotation on Star Formation in Galaxies

Observations demonstrate that new star formation is relatively low in elliptical galaxies, where the amount of interstellar gas is scarce, while a substantial amount of star formation takes place within gas-rich spiral galaxies. According to current theory, star formation occurs when a large cloud of gas exceeds a critical limit, such as the Jeans limit for an isolated cloud or the Bonnor-Ebert mass when the cloud is subjected to external pressure. It is well-understood that when the Brownian pressure created by the gas particles can no longer balance the gravitational force, the cloud will subsequently collapse toward its center to create a star. However, it is not yet well-understood what causes the observed fragmentation that enables stars to form in groups ranging from binary systems to stellar clusters containing hundreds of thousands of members, or what stops this fragmentation. In addition, the mechanisms that determine the mass and quantity of newly formed star systems are currently unknown. In section IV-1-2 of Chapter IV, galactic star formation via the interaction of binary SHP groups was discussed for the case of static or nearly static SHP groups, where as shown in figures 4-2a to 4-2e, the intersections of the minimum contours of two SHP groups create a local web of potential energy minima at which clouds of gas are formed. The collapses of these clouds become sites of star formation. It was further demonstrated that the number of intersections per volume of space increases as their distance from the nearest SHP group is reduced. In addition, the amount of matter at each intersection was shown to decrease at close proximity to a superheavy particle group, suggesting that the number of stars produced is inversely related to their size and mass. Finally, it was concluded that as the galaxy center is relatively far from both SHP groups (by as much as

1.8 *kpc* in the given examples), the stars produced at the intersection points within a given volume of space located near the galactic center are expected to be fewer in number and larger in size and mass than those produced in an equal volume of space located closer to either one of the SHP groups near the tips of the galactic bar.¹²⁸

Rapid SHP rotation may have the effect of converting star formation from a one-time event, by which thousands to hundreds of thousands of stars are formed at static minimum points, into a production line which over time creates more than $10^9 - 10^{12}$ stars. In the case of SHP rotation, at distances of $r < R_c$, orbiting matter can rotate at the same angular velocity as the rotating central core and its SHP groups, and can therefore keep pace with the rotating pattern. Hence, as in the static SHP scenario, at these short distances the stars remain confined to their place of birth within the galaxy. Consequently, the number of stars is limited by the number of minima intersections. However, as the SHP groups rotate around the galaxy center, at distances $r > R_c$ their zonal pattern rotates too fast for the newly generated stars to keep up, and the new stars begin to lag behind. As the zonal pattern continues to rotate, leaving behind the newly formed stars, its minima are shifted to nearby locations containing fresh interstellar gas. The accretion of matter at the new minima locations initiates a series of additional collapses, and a new set of stars is generated. This process is repeated with rotation, and by the time that the SHP groups have completed a full orbit around the galactic center, returning to their original positions, the stars created previously at these minima locations are expected to have relocated and to have been replaced with fresh interstellar gas, allowing the process to repeat all over again. The mechanism underlying the migration of stars away from their place of birth is as follows: As the minima of the pattern rotate away from the stars formed within them, the minima are replaced by their adjacent maxima contours. As these maxima cross paths with the slower moving stars, they elevate the overall potential plus kinetic energy of the stellar systems to match or slightly exceed their potential energy at the maxima. As the pattern continues to rotate faster than the orbiting new stars, the maxima contours move away from the stars' initial areas of formation, thus converting their elevated potential energy into kinetic energy, thereby accelerating them away from their original positions.

Consequently, by the time the following minimum arrives at a given location of star formation, the stars produced in the previous cycles have moved away from their original coordinates, vacating the area for an inflow of fresh interstellar gas, ready to collapse into new stars. This process may continue for as long as a new supply of interstellar gas and dust is available. As will be shown in Chapter VII, a constant supply of interstellar matter is expected

¹²⁸ In accordance with the UG stellar model, in 2008 Yusef-Zadeh and colleagues announced evidence of very young stars in a ring of gas near the heart of the Milky Way Galaxy. The researchers observed strong radio emissions from natural molecular masers, which form within dense collapsing clouds. The presence of these masers suggests that gas is collapsing to form protostars, which will eventually form into stars that are tens of times heavier than the Sun. In addition, these protostars share the same space with older stars (see Courtland, Rachel (July 23, 2008). "Stellar Nursery Found Near Milky Way's Violent Heart." *New Scientist*, <http://www.newscientist.com/article/dn14390>). Some stars were observed further in toward the galaxy center, only two light years away from Sagittarius A, currently believed to be a massive black hole. Sagittarius A is thus a likely candidate to be the rotating central core of the galaxy.

to be available until the superheavy particles generated at the galactic core become sufficiently massive to “lock” the galaxy, or to severely restrict any further inflow of ordinary matter.

Figures 6-6, 6-7 and 6-8 provide the potential energy of a test object in a galaxy using equation 4-1-1a with the set of parameters $\Gamma = 1$, $A = 1.8 \text{ kpc}$, $N_M = 1$, $N_{m_p} = 1$, $v = 0.75c$, and $M_G = 10^{38} \text{ kg}$.

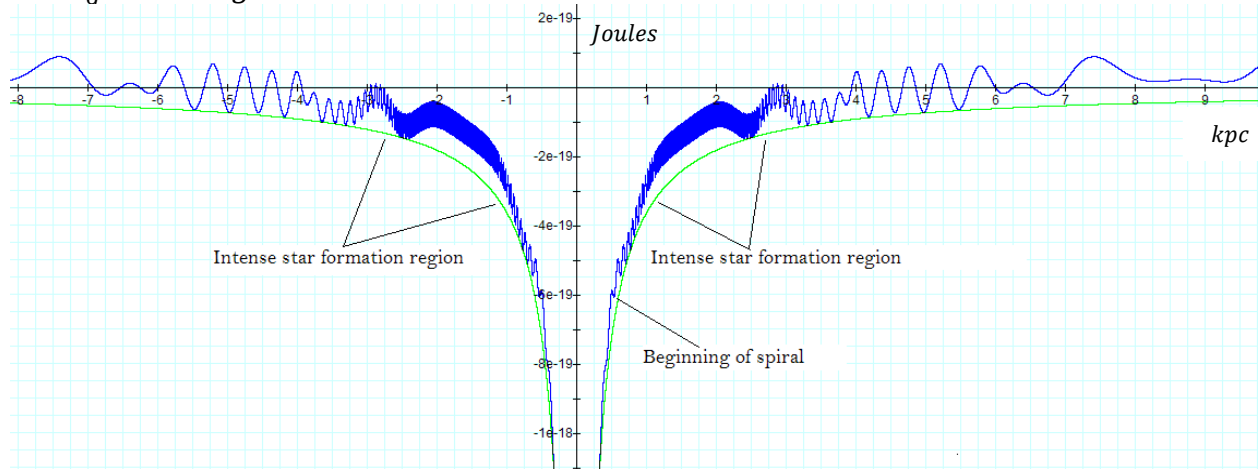


Figure 6-6a: Provides the potential energy of an ordinary particle of mass m_p along the x axis (which passes through the binary SHP groups of a galaxy) is described by the parameters $\Gamma = 1$, $A = 1.8 \text{ kpc}$, $N_M = 1$, $N_{m_p} = 1$, $v = 0.75c$, and $M_G = 10^{38} \text{ kg}$ of equation 4-1-1a. A high density of minima is demonstrated to occur between approximately $1 \text{ kpc} < |x| < 2.6 \text{ kpc}$, at which a large number of small stars are expected to be produced. In areas with a low density of minima, as observed deep in the galaxy center at $0.4 \text{ kpc} < |x| < 1 \text{ kpc}$, or at $|x| > 2.6 \text{ kpc}$, the amount of matter collapsing toward the minima is greater, resulting in the creation of larger, but fewer stars per volume of space. At distances $r < 0.3 \text{ kpc}$, minima and maxima cease to exist, allowing matter to collapse into a possible black hole.

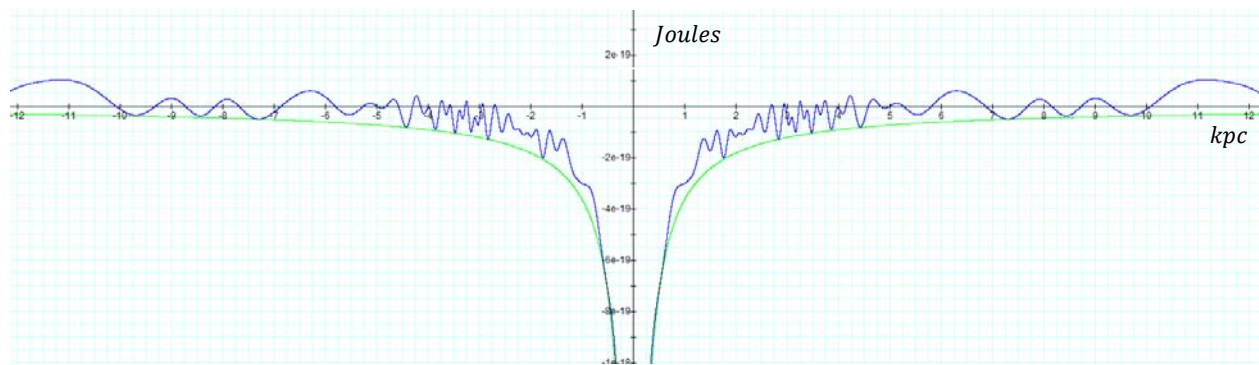


Figure 6-6b: Displays the same galaxy at a later time, where the rotated x axis becomes aligned perpendicular to the line connecting the two SHP groups. As the x axis is located relatively far from the two SHP groups (the closest points are 1.8 kpc away from either SHP group), the number of minima per volume of space along the x axis decreases, resulting in the production of fewer, yet more massive stars within the range of $1 \text{ kpc} < |x| < 2.6 \text{ kpc}$. At this orientation, when confined to the x axis, maxima and minima cease to exist below about $r \approx 0.8 \text{ kpc}$.

Figure 6-6a provides the potential energy of the object when the x axis is aligned with the two SHP groups positioned at $x = \pm 1.8 \text{ kpc}$ (or at about 30° to 40° from the plotted horizontal axis of figure 6-7). As the displayed x axis passes through the two SHP groups, the figure displays a high density of minima between approximately $1 \text{ kpc} < |x| < 2.6 \text{ kpc}$, where a large number of relatively small stars are expected to be produced. In areas with a low density of minima, as observed deep in the galaxy center at $0.4 \text{ kpc} < |x| < 1 \text{ kpc}$, or at $|x| > 2.6 \text{ kpc}$, the amount of

matter collapsing toward each minimum is relatively greater, resulting in the creation of larger, yet fewer stars per volume of space. Figure 6-6b displays the same hypothetical galaxy at a later time, where the rotated x axis becomes aligned perpendicular to the line connecting the two SHP groups. As the distance between the x axis and the two SHP groups increases (the closest points are 1.8 kpc away from either SHP group), the number of minima per volume of space along the x axis is reduced. Closer to the center of the galaxy, at $R < r < 0.3 \text{ kpc}$,¹²⁹ the slope of the potential energy due to the contribution of ordinary matter in the galactic core becomes greater than the contribution of the SHP group, and the oscillation maxima and minima appear washed out.¹³⁰ Consequently, the matter below roughly 0.3 kpc can collapse toward the center of the galaxy, where no fragmentation can occur, and the spiral cannot reach this area. In this model the spiral begins at approximately 0.5 kpc , thus matter below this distance cannot be carried outwards by the spiral. The same observations become clear in the two dimensional maps of the same galaxy provided in figures 6-7, 6-8 and 6-9, where the brighter colors denote lower potential energy of the test object. The SHP groups located within the area indicated by the white arcs¹³¹ are located near the tips of the bar and create an “interference” pattern of bright (minima) and dark (maxima) regions. As the SHP groups and their resultant zonal patterns rotate, matter in the vicinity of the maxima gravitate toward their nearest minimum, creating sufficiently high concentrations of matter to trigger a collapse in each of the minima. The size of a minimum, and to some extent its location, determine the amount of matter that may be enclosed in its vicinity, and therefore the size and the mass of the resultant star.

In order to obtain a more detailed analysis of the distribution of stars deep inside the galactic bulge, the mass of the ordinary matter was reduced to $M_G = 6 * 10^{36} \text{ kg}$ (approximately 3,000,000 times the mass of the Sun). The resultant figures 6-9a to 6-9c provide two dimensional maps of the galaxy center with the following parameters $\Gamma = 1$, $A = 1.8 \text{ kpc}$, $N_M = 1$, $N_{m_p} = 1$, $v = 0.75c$, and $M_g = 6 * 10^{36} \text{ kg}$, viewed in different resolutions at various locations within the center of the galactic disk.

¹²⁹ The parameter R denotes the radius of the central core, where the vast majority of the collapsed ordinary matter resides.

¹³⁰ Note that if one of the SHP groups was located at the center of the galaxy, $x = y = z = 0$, its maxima and minima would either disappear everywhere, or would exist anywhere, as long as $r < \frac{bMm_p}{\pi}$. However, since both of the SHP groups are located at a distance A from the center, their maxima and minima may be diminished close to the galactic center relative to the influence of the ordinary matter.

¹³¹ These areas appear white since the spatial oscillations became extremely dense to the point of overwhelming the display resolution, and were simply averaged out by the graphical program used.

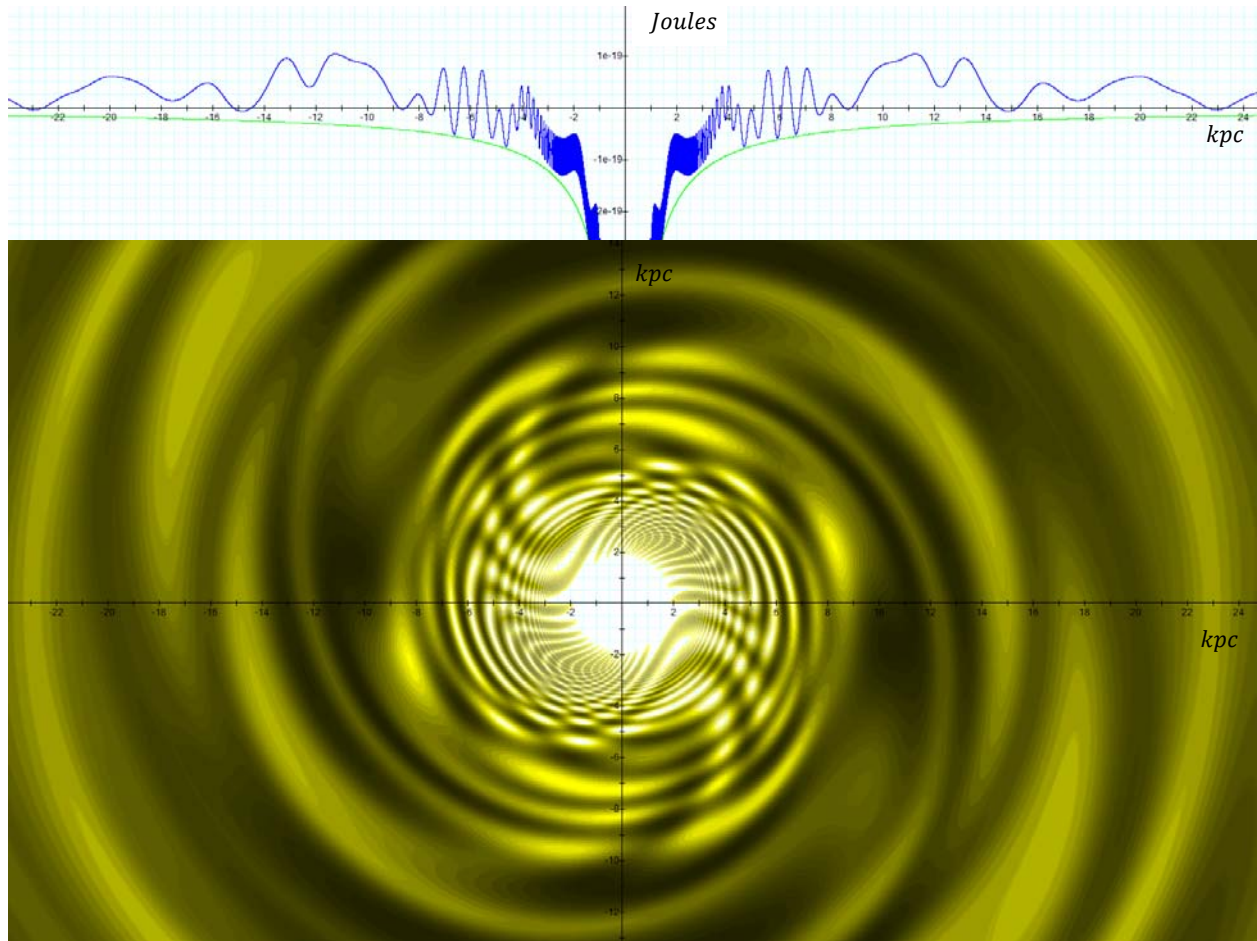


Figure 6-7: Depicts a two dimensional contour map of the same galaxy provided in figures 6-6a and 6-6b, where the brighter colors denote lower potential energy of the test object.

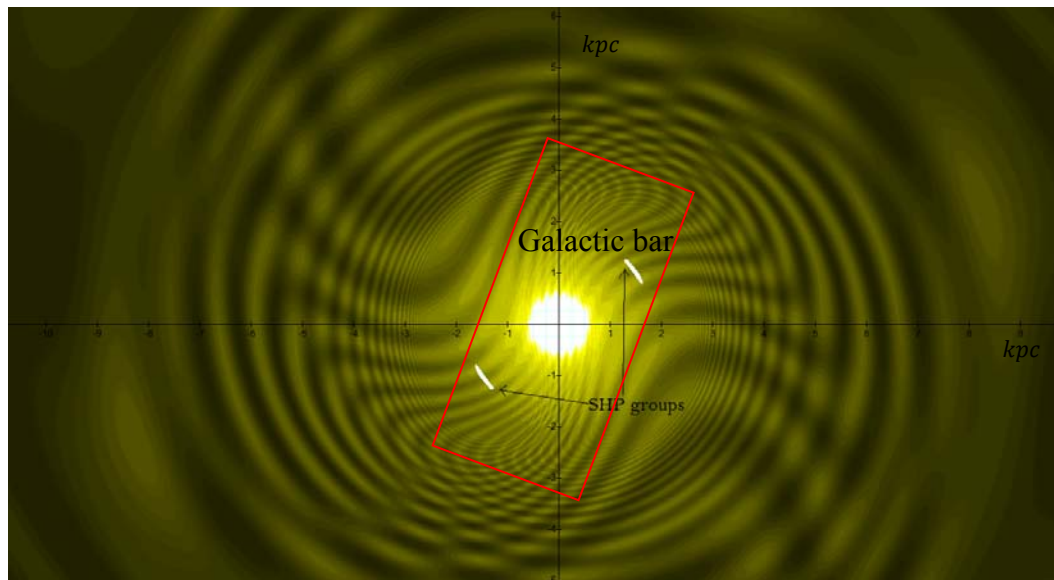


Figure 6-8: The same galaxy displayed in figure 6-7 is shown in higher resolution, where the locations of the SHP groups are indicated in white and the approximate area of the galactic bar is indicated in red. Note that a majority of the stars are produced in the general area of the tips of the bar, as the immediate areas surrounding the SHP groups are fragmented into many isolated clouds that may be too small to collapse.

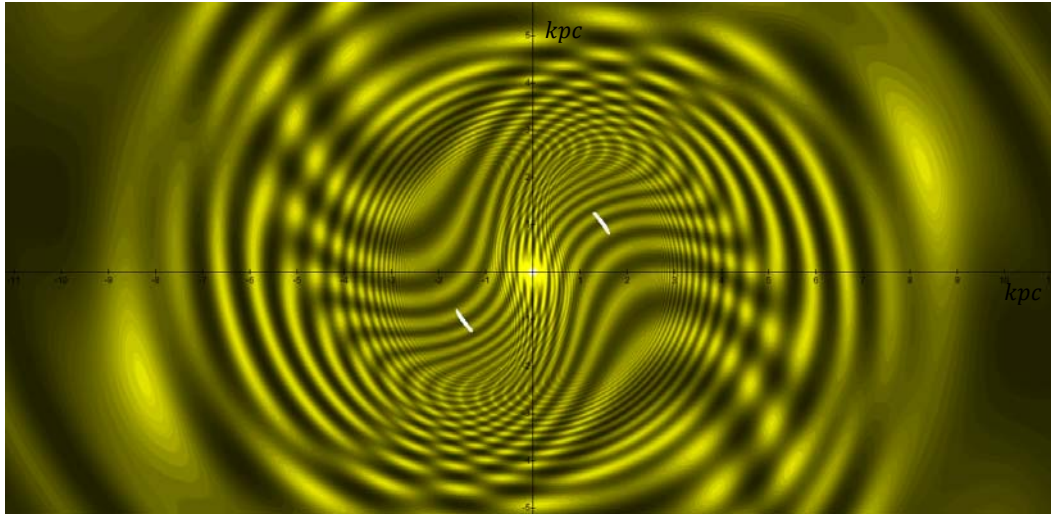


Figure 6-9a: Displays a two dimensional contour map of a similar galaxy with a reduced mass of ordinary matter, using the parameters $\Gamma = 1$, $A = 1.8 \text{ kpc}$, $N_M = 1$, $N_{m_p} = 1$, $v = 0.75c$ and $M_G = 6 * 10^{36} \text{ kg}$. Brighter colors denote lower potential energy of the test object. As can be seen, the SHP groups located within the area indicated by the bright arcs and are located near the tips of the bar and create an “interference” pattern of bright (minima) and dark (maxima) elliptical or arc regions. As the SHP groups and their resultant zonal patterns rotate, matter accumulates in the vicinity of the minima, thereby creating dense molecular clouds that collapse and create stars. Filaments occur in the long bright arcs near the central bulge. Note the pattern of a bar within a wider set of rings at the center of the figure.

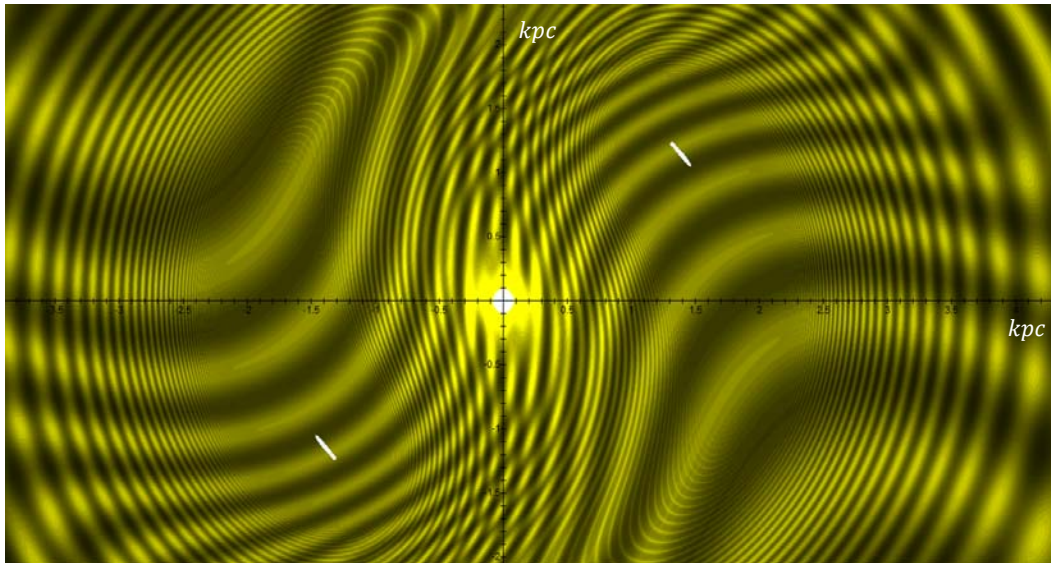


Figure 6-9b: Provides the same galaxy as figure 6-9a displayed in a higher spatial resolution.

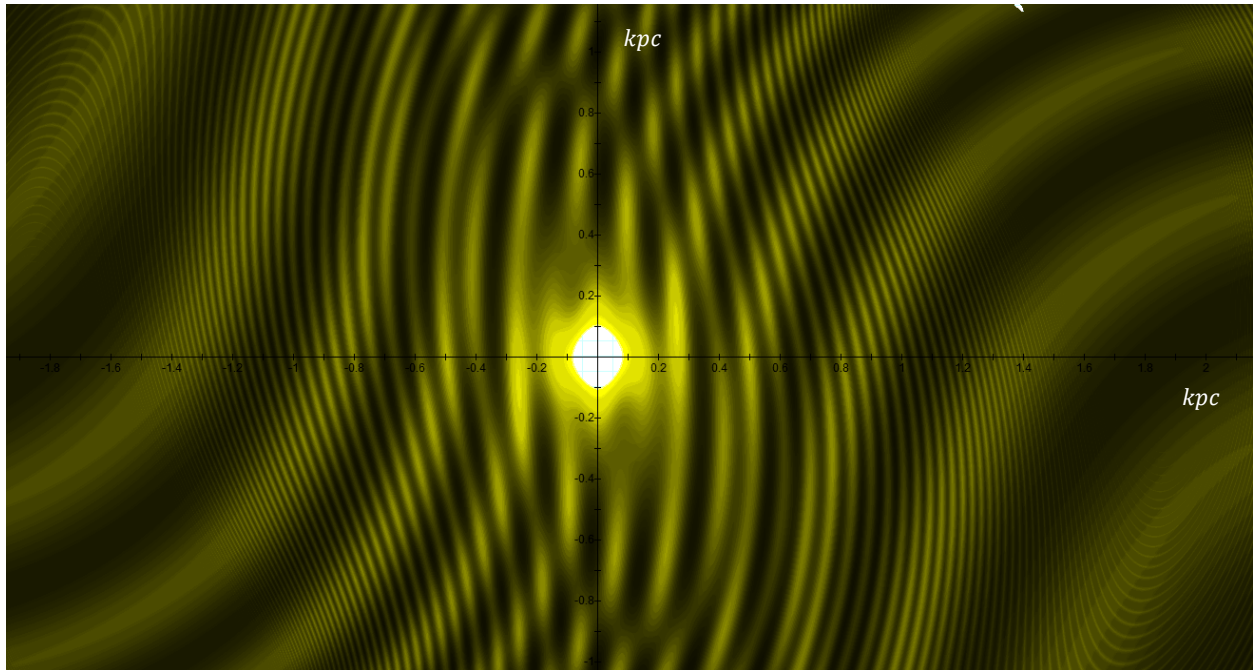


Figure 6-9c: Further increasing the resolution to concentrate on the central bulge displays a central bright area containing the rotating core of the galaxy (which may possibly be a black hole). The increase in the size of the stars as they approach the central core is apparent.

As aforementioned, with the exception of the region surrounding the central core at $r \ll 0.1 \text{ kpc}$, the minima are contained within the brightest areas of the figure. The geometry of the bright areas can be divided into elliptical regions, circular regions and arcs. The arc formations bear a strong resemblance to the patterns of observed filaments. All three geometrical patterns indicate regions that may either collapse into a star or produce dense molecular clouds or nebulae. The mass of a star can be expected to grow with the size of the area enclosed within the vicinity of its potential energy minimum. A filament is likely to be created in areas containing long continuous bright arcs.¹³² As previously discussed, the bright segments, or arcs, reduce in size and increase in number with increasing proximity to either one of the SHP groups. The existence of long arc regions may explain phenomena such as the filaments observed within galaxies and nebulae, as well as molecular clouds. Note that certain parallel sets of (bright) filaments resemble the structure of the Pillars of Creation of the Orion Nebula shown in figure 6-10. Also worth mentioning is the approximately circular string of about 6 to 8 large stars produced at distances of about 0.2 kpc to 0.8 kpc from the center of the galaxy.

In general, three types of rings are often observed in barred galaxies: nuclear rings, with radii of about 100 pc , elliptical inner rings of few kiloparsecs in diameter, which align and connect with the central bar, and outer rings, with radii of approximately 1.7 to 2.2 times the radius of the inner ring. It has been suggested to identify the nuclear rings with the inner

¹³² Note that while some of the segments displayed in the figures form genuine arcs, some of the longer, apparently continuous bright areas in the vicinity of the SHP groups are not actually continuous, but instead contain large numbers of distinct circular regions and arcs that are too small to appear separated. Zooming the display can help distinguish between the two possibilities (for example, compare figures 6-7, 6-8, 6-9a, 6-9b and 6-9c).

Lindblad resonance, the outer rings with the outer Lindblad resonance, and the inner rings with either the corotation resonance or with higher orders of the inner Lindblad resonances. However, observational data has not yet confirmed these claims. Note that figures 6-7, 6-8, and 6-9a to 6-9c provide rings that fit beautifully with these observations. However, in the calculated images, each of the three classes of rings includes several nearly concentric rings at very close proximity to each other.

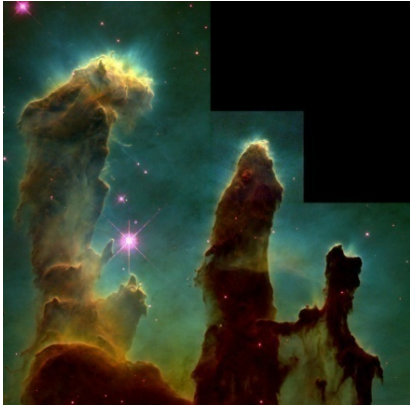


Figure 6-10: Pillars of Creation in the Eagle Nebula. Image credit: ESA/NASA; <http://hubblesite.org/gallery/album/pr1995044a>.

Interestingly, looking further into the center of the modeled galaxy, figure 6-11a provides a calculated image that resembles characteristics demonstrated by the central region of the Milky Way, provided in figure 6-11b, where Sagittarius A is likely to be the central rotating core.

Figure 6-11a: Calculated

Figure 6-11b

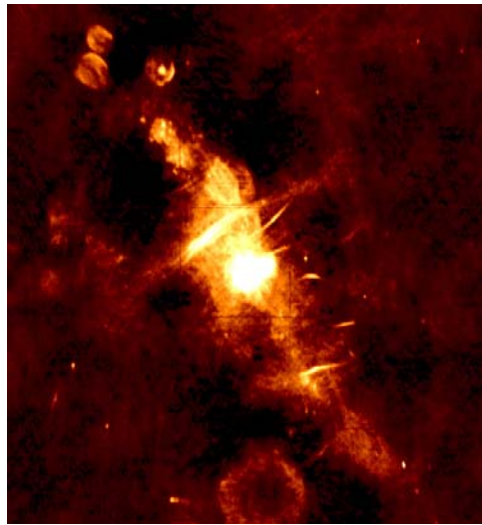
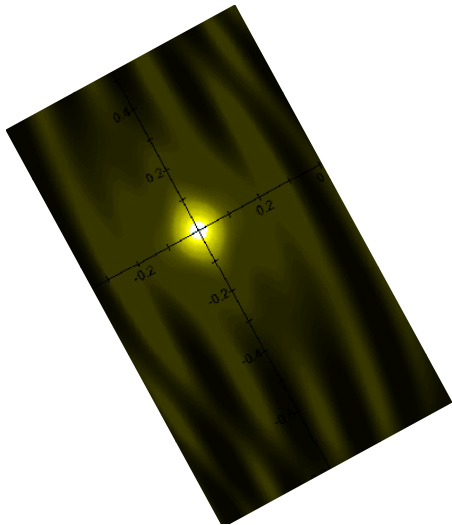


Figure 6-11: Zooming further into the center of the model galaxy (calculated in figure 6-11a) provides an image that resembles the characteristic demonstrated by the radio image of the central region of the Milky Way Galaxy depicted in figure 6-11b. The circular structure on the bottom of the right image may possibly indicate either a supernova remnant, or a ring around a superheavy particle group in orbit around Sagittarius A.

Image credit for figure 6-11b: N.E. Kassim et al., Naval Research Laboratory, NRAO/AUI/NSF; <http://www.nrao.edu/pr/2005/newsourc/>.

Chapter VII: The Effect of UG Theory on Cosmology

Modern cosmology relies on the Freidman-Lemaitre-Robertson-Walker (FLRW) metric. The FLRW metric is an exact solution of Einstein's field equations of general relativity under the assumption of a simply connected, homogeneous, isotropic expanding or contracting universe. The Freidman-Lemaitre-Robertson-Walker model serves as a first approximation for the evolution of the universe, however additional models have been added to provide for the deviation of the observed universe from homogeneity and isotropy. In order to understand the impact that the UG theory may have on cosmology, it is essential to first understand to what extent the UG theory is compatible with the general theory of relativity.

Section VII-1: The General Theory of Relativity and Unified Gravitation

For most engineering and scientific applications, the quantitative differences between Newton's theory of gravitation and Einstein's relativistic theories are insignificant. Special relativity and general relativity become important when velocities within the system of interest approach the speed of light, or in environments of high matter densities such as collapsed stars, neutron stars or black holes, or for analyzing systems of cosmological proportions.

Whereas Newton's potential energy equation is given by $V_N = -\frac{GmM}{r}$, the UG potential energy is described by

$$V_G = -\frac{GmM}{a} \left(e^{a/r} \cos\left(\frac{bmM}{r}\right) - 1 \right)$$

In contrast to Newtonian gravitation, the UG potential energy is a non-linear function of the mass of the fundamental test particle. Following equation 2-1-5, the acceleration of a non-relativistic test particle of mass m interacting with a particle of mass M at rest at the origin of the frame of reference is given by $\vec{a} = \frac{GM e^{a/r}}{r^2} \left(\cos\left(\frac{bmM}{r}\right) - \frac{bmM}{a} \sin\left(\frac{bmM}{r}\right) \right) \hat{r}$, instead of the Newtonian $\vec{a} = \frac{GM}{r^2} \hat{r}$. Therefore, within the potential energy oscillation zone at distances of the order of $r \leq bmM/\pi$ or $r \leq (bmM)^2/a$, the trajectory and acceleration of a free falling test particle becomes dependent on its mass.¹³³ However, at distances $r \gg a$, $r \gg bmM/\pi$ and $r \gg (bmM)^2/a$, the acceleration of the test particle approaches the Newtonian acceleration of $\frac{GM}{r^2}$, and becomes virtually independent of its mass m .

As the special theory of relativity is restricted to systems with relatively negligible gravitation, the deviation of the UG theory from Newton's theory of gravitation does not pose any additional conflict that has not already been expressed by the Newtonian theory. However, the general theory of relativity is based on Einstein's equivalence principle, stating that the trajectory of a free falling test particle depends only on its initial position and velocity, and is independent of its composition (and therefore independent of its mass). Consequently, at short

¹³³ A free falling object is an object that is influenced exclusively by the gravitational force.

distances such as $r \leq bmM/\pi$ and $r \leq (bmM)^2/a$, the UG theory is possibly at odds with general relativity.

Regardless of whether or not the UG theory is correct, the viability of the principle of equivalence and general relativity at short distances (under $10^{-6} m$) is arguable. In general relativity the applicability of the equivalence principle is restricted to distance scales where the gravitational field is uniform (with negligible tidal forces). Therefore, the equivalence principle cannot be applied at short distances, where the Newtonian forces may change drastically with any small deviation in the distance r . In addition, quantum effects become substantial at distances $r < 10^{-10} m$. Despite decades of enormous effort, the consolidation of general relativity with quantum mechanics has yet to succeed, raising further doubt about the viability of the equivalence principle at extremely short distances. Furthermore, according to the standard model, the strong interaction and the weak interaction are highly dependent on particle masses, and become dominant at distances of approximately $r < 10^{-15} m$. The exact equations of the strong and the weak forces within the standard model are unknown, however they are not likely to be linear with the mass of the test particle. Therefore, the equivalence principle may not be applied on such small scales, regardless of the validity of the UG theory.

It is important to determine when and where the UG equations substantially deviate from general relativity. According to equation 2-1-5 of the UG theory, the acceleration rates of free falling protons, neutrons and electrons are not identical when they gravitationally interact with ordinary matter at distances less than or of the order of $\frac{(bm_n)^2}{a}$. Therefore, in theory, within this range of distances, a free falling frame is not necessarily an inertial frame, as different free falling particles or objects within the same frame may demonstrate different rates of acceleration.

However, at interaction distances of $r \gg \frac{(bm_n)^2}{a} \approx 1.1 * 10^{-6} m$ (where $r \gg bm_n^2 \approx 2.5 * 10^{-10} m$ and $r \gg a$, thus $e^{a/r} = 1$), the gravitational force applied on a free falling ordinary particle is virtually Newtonian, and its acceleration is therefore independent of its mass. Consequently, in a UG world composed entirely of protons electrons and neutrons (as well as their anti-particles) the general theory of relativity provides a good approximation at distances of $r \gg \frac{(bm_n^2)^2}{a} \approx 1.1 * 10^{-6} m$. Consequently, in environments where ordinary matter interactions are dominant and the influence of superheavy particles can be regarded as negligible, the predictions made by general relativity, such as gravitational redshift (or blueshift), gravitational time dilation, the deflection of light by gravity (as in gravitational lensing) and the relativistic precession of apsides, hold true and are compatible with the UG theory.

According to the fourth UG postulate, however, massive superheavy particles are produced in environments of extremely high matter density, such as in the vicinity of collapsed stars, neutron stars or non-singular black holes.¹³⁴ When a test particle of mass m (or an object composed of particles of mass m) interacts with a massive SHP of mass M , the non-linear distance range of the UG force, where the cosine and the sine terms of equation 2-1-5

¹³⁴ The UG theory prevents the possibility of singularity (see section VII-2).

demonstrate oscillations, increases with the product of the two particles' masses mM . Therefore, if extremely large superheavy particles exist at the core of a planet (where the term $\frac{bm_p M}{\pi}$ is of the order of tens or hundreds of thousands of kilometers) or at the core of a galaxy (where $\frac{bm_p M}{\pi}$ is of the order of tens of kiloparsecs),¹³⁵ the gravitational oscillations create minimum points, arcs or contours. For the case of $m = m_p$, ordinary matter (such as the molecules or atoms of an object orbiting a planet, or of galactic interstellar gas) accumulates at the minima, and may create rings or spirals. As the UG oscillations are non-linear functions of the mass of the fundamental test particles, the isolated electrons, protons or superheavy particles may demonstrate substantially different rates of gravitational acceleration on large distance scales. Consequently, a free falling frame, and the free falling objects or particles within the frame, may not accelerate at the same rate, and cannot be assumed to follow the geodesics of curved spacetime geometry. Therefore, in regions of spacetime where rings and spirals are formed, the UG theory demonstrates greater deviation from the predictions of the general theory of relativity. Discrepancies between the results of the UG theory and general relativity, however, are relatively small in subsystems influenced by external SHPs when the subsystems are too mild to generate or sustain SHPs of their own, and their ordinary matter is almost exclusively arranged in the form of neutral atoms, molecules or more complex objects. In such a case, where all of the matter within a local free falling frame is composed exclusively of atoms and molecules of ordinary matter that interact with a strong external SHP, each atom or molecule accelerates as a rigid object. Therefore, all of the free falling objects within the local frame accelerate at the same rate as the frame itself (note that the mass of a neutron is almost equal to the mass of a proton, and the mass of the electrons bonded to the nucleus of the atom is almost negligible relative to the masses of the nucleons. The effect of the bonded electrons on the object's acceleration can therefore be neglected, and the effect of a neutron on the overall acceleration of the object is nearly identical to that of a proton.¹³⁶ Consequently, the acceleration of the free falling objects is very close to the acceleration rate of a free proton). Therefore, the equivalence principle is valid as long as the frame is sufficiently small to ensure that no significant tidal forces exist within its limits, and as long as the number of free electrons or positrons within the frame is negligible. When a significant number of free electrons or positrons exist within the local frame, their rate of acceleration according to the UG theory may vary from the acceleration of the protons, atoms and molecules within the frame,¹³⁷ as well as from the acceleration of the free falling frame.¹³⁸ Consequently, the equivalence principle is violated, and the frame does not constitute an inertial frame. The same is true for cases where a significant portion of the free falling objects within the given local frame are composed of massive SHP types as well.

¹³⁵ One parsec (pc) is equal to about $3.086 * 10^{16} m$, and $1 kpc = 3.086 * 10^{19} m$

¹³⁶ For further information, see Chapter VIII.

¹³⁷ In general relativity the term 'local frame' refers to a conceptual set of standardized clocks and measuring rods, which are also subjected to acceleration by the local gravitational field.

¹³⁸ This may be the case for galactic jets, pulsars or any plasma.

Section VII-2: Unified Gravitation and Black Holes

In the previous section it was demonstrated that in a world composed exclusively of ordinary matter, the UG theory would not demonstrate significant deviation from general relativity at distances greater than $10^{-5} m$. In such a scenario, the concept of a black hole event horizon, where neither a particle nor light can escape once trapped below the horizon, is supported by the UG theory.¹³⁹ It is important to note, however, that the UG theory rules out the concept of a black hole as a singularity. The fact that the UG potential energy equation oscillates between sets of maxima and minima, with a potential energy that approaches positive and negative infinities as $r \rightarrow 0$, requires an infinite amount of energy to physically combine two massive particles. Therefore, matter cannot collapse into singularity. Furthermore, in a universe containing a significant amount of superheavy particles, the UG theory provides a mechanism by which matter trapped within the event horizon of a black hole can eventually escape. As the matter within a black hole collapses toward its center, the pressure and temperature at the core become extremely high, to the point where sufficiently large superheavy particles may be created, generating their own repulsive zones. In cases where the SHP mass becomes sufficiently large, the oscillation range between the newly generated superheavy particles and ordinary matter matches or exceeds the radius of the black hole event horizon prior to the SHP creation. With a sufficiently high quantity of superheavy particles, the repulsive force between SHPs and ordinary matter may overcome the strong attractive forces exerted by the black hole's ordinary matter on matter located close to the former event horizon, making it possible for matter to escape.

Section VII-3: The Effect of Unified Gravitation on Cosmology - The Big Bang and the Expansion of the Universe

Hubble's discovery that the universe is not static, but expanding, led to the development of the Big Bang cosmological model, which attributes the beginning of our universe to an explosion from a very dense point singularity at about 14.5 billion years ago. The recent discovery that the universe is expanding at an accelerated rate forced the reintroduction of the cosmological constant, which was initially introduced into general relativity by Einstein in order to maintain a static universe, and later retracted in response to Hubble's discovery of the expansion of the universe. Throughout its development, the Big Bang model encountered significant problems, a few of which were addressed in the introductory chapter of this book.

An entirely different approach may be taken via the UG theory. The UG interaction between two particles has been demonstrated to produce zones of attraction and zones of repulsion. The UG repulsive force will be shown to account for the creation of large voids and

¹³⁹ This is true for any massive object composed exclusively of ordinary matter.

to explain the strong rejection between galactic entities,¹⁴⁰ which drives galaxies to recede away from each other on large distance scales and leads to the observed continuous, even accelerated expansion of the universe. The interplay between repulsive and attractive zones will be shown to account for the creation of galaxies, as well as for the creation of galactic groups, clusters and superclusters. Expansion due to repulsive forces, rather than due to an expansion of spacetime and subsequent inflation, may provide for a substantially simpler cosmological model, which avoids the paradoxes and inconsistencies inherent in the current Big Bang theory.

Section VII-4: Galactic Lock Out

As a first step, the UG theory will be shown to predict that sufficiently large and abundant superheavy particles within a galaxy may create a gravitational barrier that rejects, and therefore prevents most of the external ordinary matter from penetrating the galactic disk.¹⁴¹ In other words, the galaxy will become “locked,” and its growth halted. Consider, for example, an ordinary drifting object (or test particle) approaching a galaxy from infinity with a potential plus kinetic energy of close to zero.¹⁴² Initially, the object is located far beyond the maximal zonal range of the galactic SHPs and is thus gravitationally attracted by the galaxy’s ordinary matter.¹⁴³ As it accelerates towards the galaxy, however, the object may reach a distance where it is simultaneously attracted by the galaxy’s ordinary matter and conversely repelled by the galactic superheavy particles. Following equation 4-1-1, the object’s potential energy is given by

Equation 7-1

$$V = -\frac{GM_1 N_{M_1} m_p N_{m_p}}{a} \left(e^{a/r} \cos \left(\frac{bM_1 m_p}{r} \right) - 1 \right) - \frac{GM_G m_p N_{m_p}}{r}$$

and the force applied on the object is given by

Equation 7-2

$$F = \frac{GM_1 N_{M_1} m_p N_{m_p} e^{a/r}}{r^2} \left(\cos \left(\frac{bM_1 m_p}{r} \right) - \frac{bM_1 m_p}{a} \sin \left(\frac{bM_1 m_p}{r} \right) \right) + \frac{GM_G m_p N_{m_p}}{r^2}$$

Note that in order to concentrate on the essential factors, the above equations are based on a hypothetical scenario of a simple galaxy containing a single SHP group ($\Gamma = 0$) orbiting the center of the galaxy in a circular orbit of radius $A_1 \ll r$ at a non-relativistic and constant velocity (therefore, \dot{D}_{s_1} of equation 4-1-1 is equal to r , $\gamma = 1$, and equation 4-1-1a converges toward equation 7-1). The vast portion of the galaxy’s ordinary matter is assumed to be distributed symmetrically around the center of the galaxy within a sphere of radius R , where $a \ll R \ll r$. To further simplify the current discussion, the influence of other external bodies is assumed to be

¹⁴⁰ The term “galactic entity” refers to either a single galaxy, or to a galactic group (containing 2 to 50 galaxies), galactic clusters (containing 50 to 1000 galaxies), or galactic superclusters (containing more than 1000 galaxies).

¹⁴¹ The same mechanism should exist in stellar systems, and may also exist in planets

¹⁴² A “drifting” particle describes a particle with a total potential plus kinetic energy of close to 0 that begins its approach toward the galaxy from a very large distance with a negligible amount of kinetic energy.

¹⁴³ At distances exceeding the zonal range of the superheavy particles with ordinary matter, the UG contribution of the SHPs is negligible compared with the contribution of the galaxy’s ordinary matter.

negligible, and the effect of the rotation of both the galaxy and its SHP groups on the overall energy of the orbiting object is assumed to be relatively small.

Figures 7-1a and 7-1b display the overall potential energy (via equation 7-1) of an approaching single-particle object of mass m_p , as a function of its distance from the center of a galaxy containing a single SHP of mass $M_1 = 3.2 * 10^4 \text{ kg}$, and ordinary matter of a total mass of $M_G = 2 * 10^{38} \text{ kg}$.¹⁴⁴ The overall gravitational potential energy of the approaching particle due to contributions of the SHP and ordinary matter is indicated in violet. For comparison, the exclusive contribution of the galaxy's ordinary matter is displayed in blue. Note that in this example, a drifting particle of zero energy cannot come closer than a distance of about 1.05 Mpc from the center of the galaxy (see figure 7-1b). Consequently, the galaxy essentially becomes locked to an inflow of ordinary matter, forbidding the entrance of any external ordinary particle of mass m_p approaching with a potential plus kinetic energy below the $n = 1$ maximum of $E_p + E_k \leq 1.18 * 10^{-18} \text{ J}$. In addition, no circular orbit can exist between $51 \text{ kpc} < r < 2.11 \text{ Mpc}$, as within this range of distance both the overall gravitational force and the centrifugal force acting on the particle point outward, and thus cannot cancel each other out.¹⁴⁵

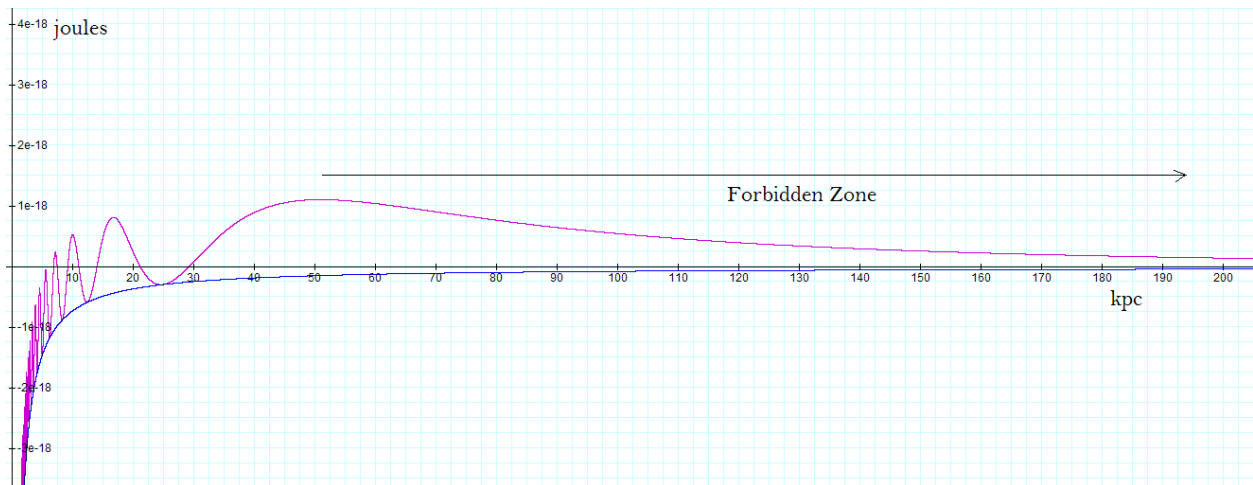


Figure 7-1a: The blue curve in this figure displays the overall potential energy (derived via equation 7-1) of an approaching single-particle object of mass m_p as a function of its distance from the center of a galaxy containing a spherically symmetric distribution of ordinary matter of a total mass of $M_G = 2 * 10^{38} \text{ kg}$. The addition of a single non-relativistic SHP of mass $M_1 = 3.2 * 10^4 \text{ kg}$ near the center of the galaxy is shown to elevate the potential energy of the approaching particle (indicated in violet) and creates a barrier at $r_1 \approx 51 \text{ kpc}$ of $V = 1.11 * 10^{-18} \text{ J}$ that keeps out all approaching particles of mass m_p with an overall potential plus kinetic energy of less than V . Within the resultant forbidden zone starting at r_1 , a particle of mass m_p cannot be confined in orbit. The minima below 30 kpc provide the locations of galactic rings, where the collapse of these rings results in the production of stars.

¹⁴⁴ In terms of the more general equation 4-1-1a, the parameters used are $\Gamma = 0$, $M_1 = 3.2 * 10^4 \text{ kg}$, $A_1 \approx 0$, $v_1 \approx 0$, $N_M = 1$, $N_{m_p} = 1$ and $M_G = 2 * 10^{38} \text{ kg}$.

¹⁴⁵ A forbidden zone is defined as a spherically symmetric volume of space around the center of a galaxy in which the orbit of an object composed exclusively of ordinary matter cannot be completely confined.

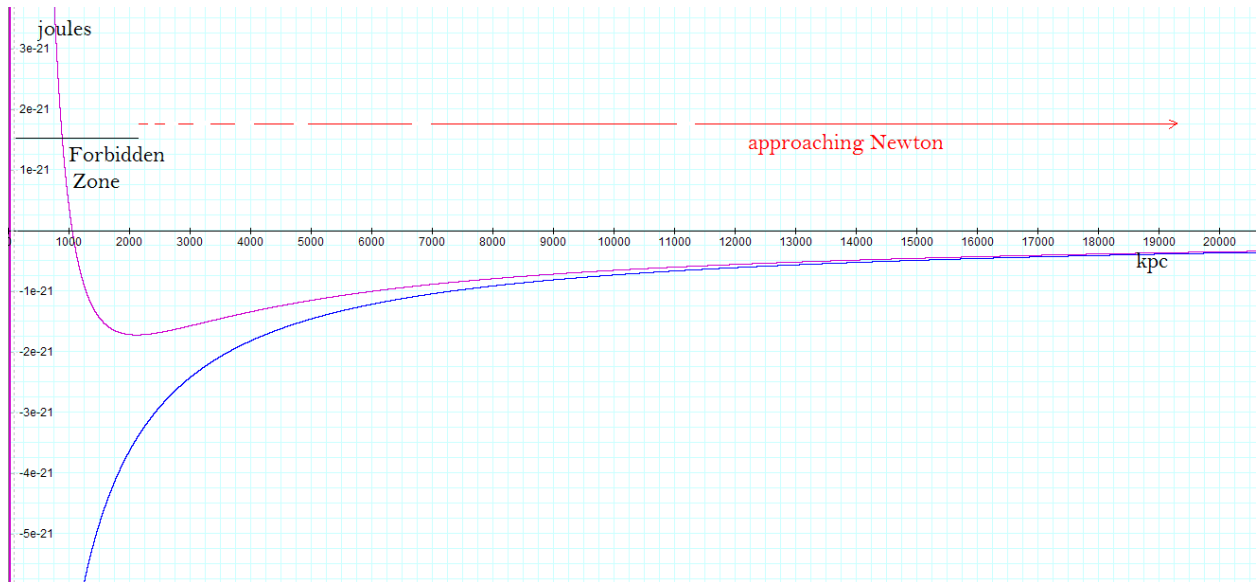


Figure 7-1b: The potential energy is displayed over a distance range 100 times greater. An external particle of mass m_p with an overall energy of $E \approx 0 \text{ eV}$ would be stopped by the SHP-generated barrier at about $1,050 \text{ kpc}$ (or 1.05 Mpc). The forbidden zone is demonstrated to extend all the way out to 2.11 Mpc . As the distance between the approaching particle and the center of the galaxy increases beyond $r = 2.11 \text{ Mpc}$, the relative contribution of the SHP to the potential energy of the test object declines, and the particle's potential energy converges toward the Newtonian curve (in blue).

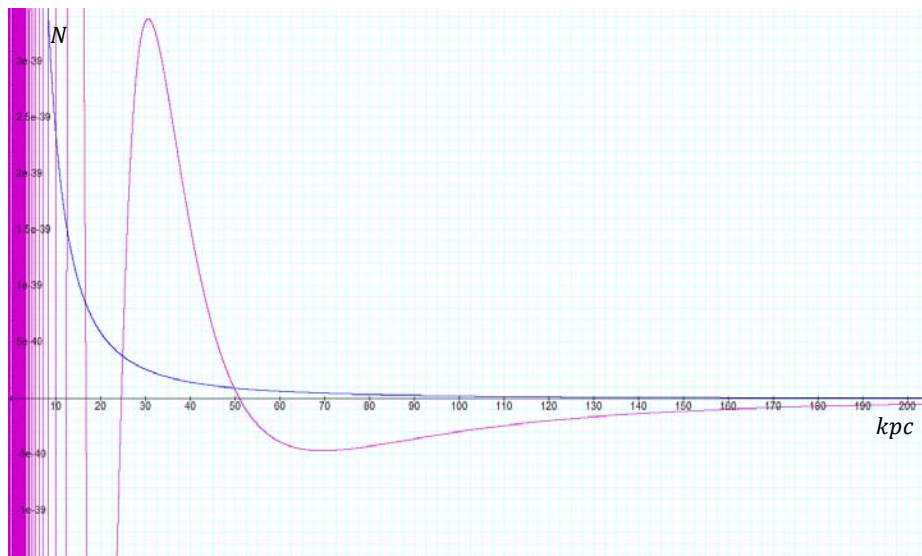


Figure 7-1c: Provides the force associated with the potential energy of the approaching particle using the same parameters as figures 7-1a, 7-1b and equation 7-2. Note the repulsive force above 51 kpc .

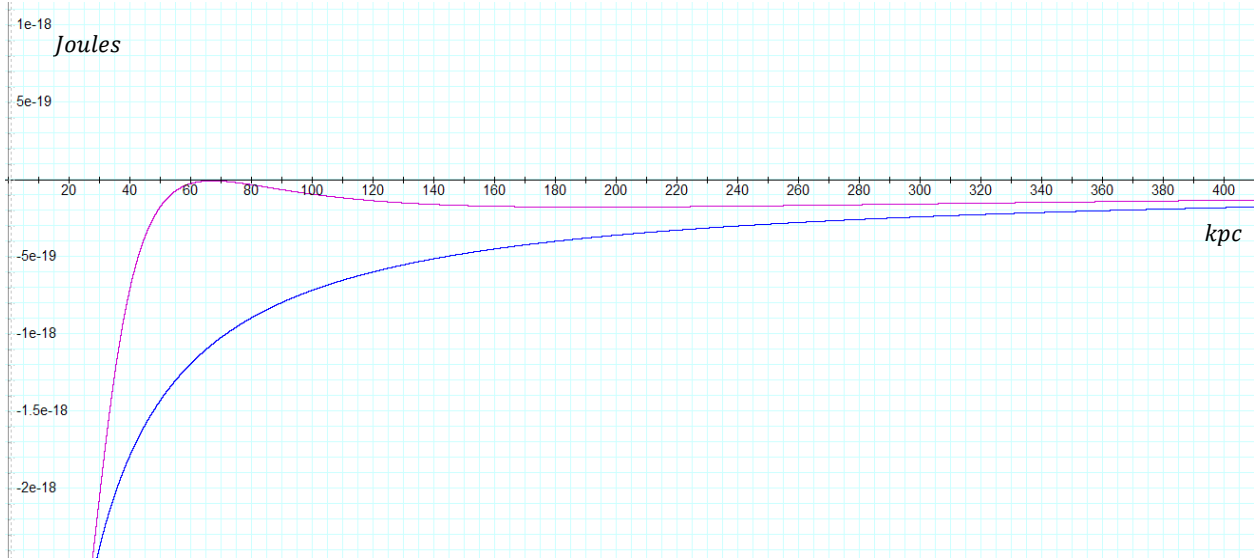


Figure 7-1d: The height of the barrier reduces as the total mass of the galaxy's ordinary matter (within the barrier boundaries) increases and/or as the number and mass of the dominant superheavy particles are reduced. A drifting particle of mass m_p with a potential plus kinetic energy of about zero electron volts is nearly prevented from entering the galaxy disk when the maximum potential energy is at $V = 0$. Such a case is demonstrated in this figure for a galaxy of overall ordinary mass (within the barrier boundaries) of $1.97 * 10^{39} \text{ kg}$ and when a single SHP of mass $M_1 = 3.2 * 10^4 \text{ kg}$ is located in the vicinity of the galactic center.

In general, the galaxy will begin to lock out ordinary matter when

$$V = -\frac{GM_1 N_{M_1} m_p N_{m_p}}{a} \left(e^{a/r} \cos\left(\frac{bM_1 m_p}{r}\right) - 1 \right) - \frac{GM_G m_p N_{m_p}}{r} > 0, \text{ or, as } e^{a/r} = 1, \text{ when}$$

$$M_G < \frac{M_1 N_{M_1} r}{a} \left(1 - \cos\left(\frac{bM_1 m_p}{r}\right) \right).$$

Substituting the approximate location of the maximum contour of the barrier at $r \approx bM_1 m_p / \pi$ will provide

$$M_G < \frac{2bM_1^2 N_{M_1} m_p}{\pi a} \approx 1.72 * 10^{39} \text{ kg}$$

where the parameter values used were $M_1 = 3.2 * 10^4 \text{ kg}$ and $N_{M_1} = 1$. A detailed graphical analysis is displayed in figure 7-1d, providing the mass $M_G \approx 1.97 * 10^{39} \text{ kg}$ as the galaxy's maximum amount of ordinary mass with which the galaxy is still locked to drifting objects composed of ordinary matter.

Section VII-5: The Construction of a Barrier, the Effect of a Barrier on the Fragmentation of a Collapsing Cloud and the Creation of a Series of Distinct Galactic Entities

According to current theory, the stages of star formation and the final state of a star are thought to depend on its overall mass. A star of a mass greater than eight solar masses must pass through successive stages of hydrogen, helium, carbon, neon, oxygen, and silicon fusion at its center. With the passing of each stage, the stellar core becomes increasingly hot and dense. The

evolution of stars is regarded as a long sequence of contractions, starting with the initial collapse of a molecular cloud, which is then halted by hydrogen burning, and ending with the formation of a neutron star or black hole. The contraction process pauses several times, as nuclear fusion provides the energy required to replenish the energy lost to radiation and neutrinos, as well as the outward pressure needed to balance the inward pull of the gravitational force. Upon the exhaustion of one type of fuel, the star contracts, heats up and burns the next higher element, usually created at a previous stage. Eventually, a core of iron-group elements is produced. Since no further energy-per-nucleon generating process is available, nuclear fusion is halted and the star is held by the pressure created by electron degeneration. As the amount of energy loss increases, the electrons combine into the iron-group nuclei, raising their neutron number. The energy of the stellar core again reduces to a level where it can no longer balance the inward gravitational forces, and the iron core collapses (at a rate of about a quarter of the speed of light) from approximately the size of the Earth to about 30 *km* in radius, creating a proto-neutron star. The collapse is halted by the short-range repulsive nuclear interactions. Note that according to the UG theory, short-range nuclear interactions are driven by repulsive zones of the UG gravitational equation 2-1-1 at distances of $r \lesssim a$.

Just before the initial stage of stellar or galactic formation, when the Brownian pressure created by the gas particles can no longer balance the gravitational force and the collapse of a gas cloud is set in motion, there are no central superheavy particles of substantial mass, and the potential energy curve of a test particle of mass m_p resembles the Newtonian potential energy (displayed by the blue curve in figures 7-1a and 7-1b). As the density of matter, the temperature and the pressure within the core of the collapsed star or galaxy increase substantially following each stage of collapse, the prevalence and the mass of the largest SHPs increase substantially, in accordance with postulate IV. With the production of more massive SHPs, the resultant potential energy of the object (presented by the violet curve) begins to increase and to depart from the Newtonian curve. Eventually, as long as the initial cloud is sufficiently massive, the pressure and temperature at its core will build up to high levels, where the production of superheavy particles yields an adequate number N_{M_1} and mass M_1 of a dominant SHP type to form a barrier that is capable of deflecting inward-drifting matter, thereby preventing the matter from penetrating the galactic disk. This will occur when $\frac{2bM_1^2N_{M_1}m_p}{\pi aM_G} > 1$ (see figures 7-1a and 7-1b). Since the transition to substantially larger SHPs takes place during a sudden and relatively short period of collapse, the rise of the barrier is almost instantaneous. As the barrier emerges, the slope of the potential energy, located between the newly formed $n = 1$ outer maximum contour and the adjacent external minimum (at approximately 51 *kpc* and 2.11 *Mpc* respectively in figures 7-1a to 7-1c) becomes negative. Consequently, gas and other ordinary matter objects orbiting within this distance range are suddenly subjected to a strong repulsive force and ejected outward in the direction of the external minimum.¹⁴⁶ As the volume of matter within the given

¹⁴⁶ For simplicity, it is assumed that the galaxy's potential energy is dominated by a single group of SHPs and by its ordinary matter. Therefore the maximum associated with $n = 1$ is well-defined.

distance range is emptied out, a large void is formed. At distances exceeding the outer minimum, the object's potential energy curve converges toward its Newtonian curve, thereby attracting ordinary matter and allowing for a continuous inward flow of matter. However, the vast majority of the inward flowing matter cannot penetrate the barrier and is instead deflected toward the outer minimum contour, where new centers of collapse may form, resulting in the fragmentation of the galactic entity into a series of sister galaxies. The same process is repeated again and again as the number of sister galaxies increases and the area covered by them expands outwards.

Section VII-6: UG Repulsion and the Generation of Stellar Novae and Supernovae

A similar process may explain what initiates the sudden massive expanding shell of gas and the high levels of radiation generated by stellar novae and supernovae. A sudden and drastic increase in the brilliance of a star is characteristic of a nova, where stellar explosion causes the star to become 10,000 to 100,000 times brighter than the Sun, and the cataclysmic supernova, where the exploding star can become billions of times as bright as the Sun before fading out of view. At its maximum brightness, the exploded star of the supernova may outshine the entire galaxy. Both novae and supernovae are characterized by a tremendous rapid brightening lasting few weeks, followed by slow dimming, and both show spectroscopically blueshifted emission lines, which imply that hot gases are blown outward. It is yet unknown how the collapse of a dying star creates an explosion that generates a massive outflow of gas and matter.

According to the fourth UG postulate, a significant increase in the temperature and pressure of a stellar core leads to the sudden creation of SHPs of significantly larger mass. A large and abrupt increase in temperature and pressure occurs during the initial collapse of the molecular cloud when the star is born, or at various stages of the stellar life cycle described in section VII-5. The initial collapse of a star results in a significant increase in temperature and pressure within the central core, which may produce pairs of substantially massive superheavy particles and anti-particles.¹⁴⁷

The birth of larger SHPs almost instantaneously elevates the potential energy curve, creating a barrier (for example, see the transition from the blue curve to the violet curve of figures 7-1a and b). Following the discussion of the previous section, the newly formed barrier produces a sudden massive expanding shell of gas, which drives out the vast amount of ordinary matter previously located between the newly formed $n = 1$ maximum and the newly formed external minimum. As the temperature in the collapsing core becomes sufficiently elevated, the collapse of the star is halted by the hydrogen burning process, producing higher temperatures and

¹⁴⁷ The newly generated superheavy particles are ejected from the central core and accelerated to relatively high (relativistic) velocities according to the process described in Chapter III-3 (note that a similar mechanism may solve the long-standing puzzle of why the compact object remaining after a supernova explosion is given a velocity kick away from the core. Observations over the last decade have shown that at birth neutron stars receive a large velocity kick of the order of a hundred to a thousand km/s (Hofflich, Kumar & Wheeler, 2004). Within the UG theory, the compact object may be a superheavy particle generated in or near the galactic central core, with sufficient kinetic energy to be ejected out of the central core together with ordinary matter trapped by the SHP zones.

increasing the outward pressure, thus balancing the inward gravitational force within the star. When its supply of hydrogen is nearly depleted, the collapse of the star is resumed. Energy released during this second collapse allows for the production of even larger SHPs, as the temperature and pressure within the stellar core are increased. Hence, the radius of the $n = 1$ maximum contour, which is proportional to the dominant SHP of mass M_1 , and the radius of the adjacent external minimum, which is dependent on $M_1 N_{M_1}$, are shifted outward, resulting in a significantly expanded barrier. The new, extended barrier once again triggers a sudden massive expanding shell of gas. This process is repeated through the series of collapses.

The creation of superheavy particles of greater mass produces a larger number of narrow minima within a shell contained between any two successive minima of the former dominant SHP type, resulting in an enormous number of local collapses toward the new set of minima. This process releases a vast amount of energy in the form of radiation, which together with the massive expanding shell of gas produced by the outer barrier, may explain the phenomenon of a nova or supernova.

A star that has experienced several stages of novae or supernovae is likely to have exhausted a majority of its core hydrogen (and possibly other light elements) and to produce heavier elements. Such a star is also likely to have already shed most of its outer layers via prior novae or supernovae or by its stellar wind (see section VI-2). Therefore, in the later stages of a supernova, a star is likely to lack the spectral lines of the lightest elements, while demonstrating a higher abundance of heavier elements in its spectrum, which may explain the various classifications of supernovae.

Section VII-7: The Fragmentation of a Galactic Entity and the Creation of Galactic Substructures

The creation of a series of distinct galactic entities by the collapse of a gas cloud was discussed in section VII-5. In this section, the interplay between attractive and repulsive zones within any galactic entity of a size larger than a typical galaxy (typically of larger than 1 Mpc) will be shown to provide a possible explanation for the fragmentation of a galactic entity into a group or a cluster of galaxies.

Assume, for example, that a specific galactic entity (the “parent entity”) produced by the collapse of a gas cloud is described by the same parameters used in figures 7-1a to 7-1c, with the exception of $M_1 = 10^6 kg$ and $M_G = 5 * 10^{40} kg$, and adheres to the same set of assumptions. The series of maxima and minima of the potential energy curve of the parent entity is demonstrated in figures 7-2a and 7-2b. As the density of matter in the vicinity of the minima becomes elevated, some of the minima develop into secondary centers of collapse, creating stars or smaller “offspring” galaxies, which generate sufficiently large SHPs of their own to produce a barrier. The secondary stars or galaxies consequently become locked to external drifting matter, diverting nearby matter to collapse at neighboring local minima.¹⁴⁸ As a result, a series of

¹⁴⁸ Note that the locations of the minima are determined by both the parent entity and its offspring substructures.

interconnected stars, galaxies or even galactic groups, clusters or superclusters are created at the minima, thereby fragmenting the matter within the galactic entity into a series of substructures. Note that the offspring substructures are separated into groups, where each group occupies a different minimum contour produced by the superheavy particles of the parent entity, and their disk planes should subsequently be oriented tangentially to the respective minima of the galactic parent.

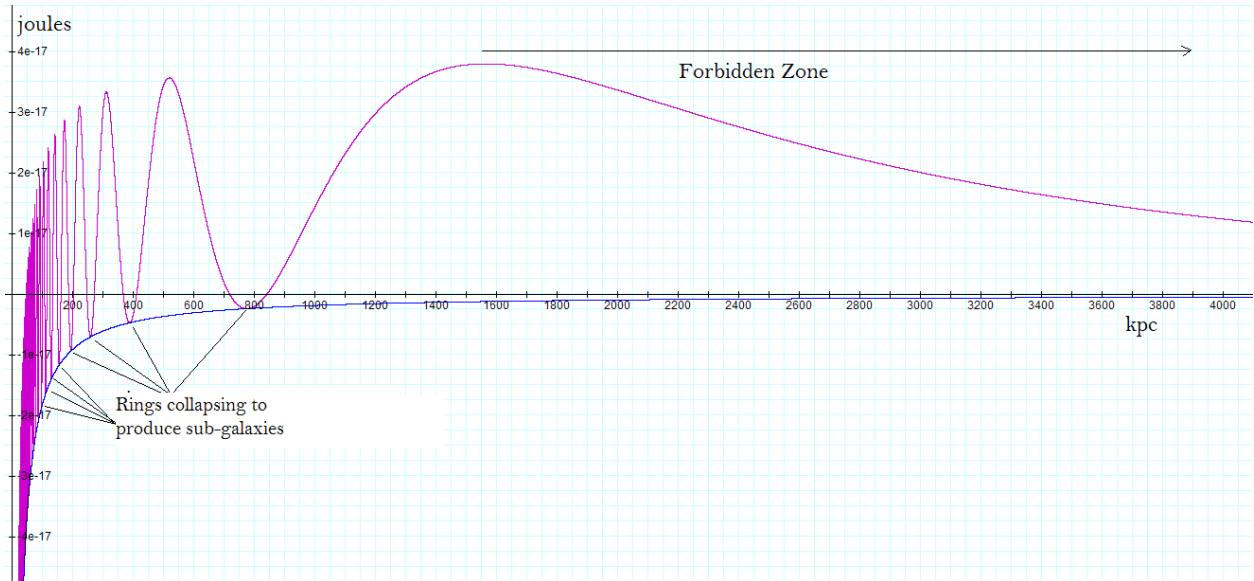
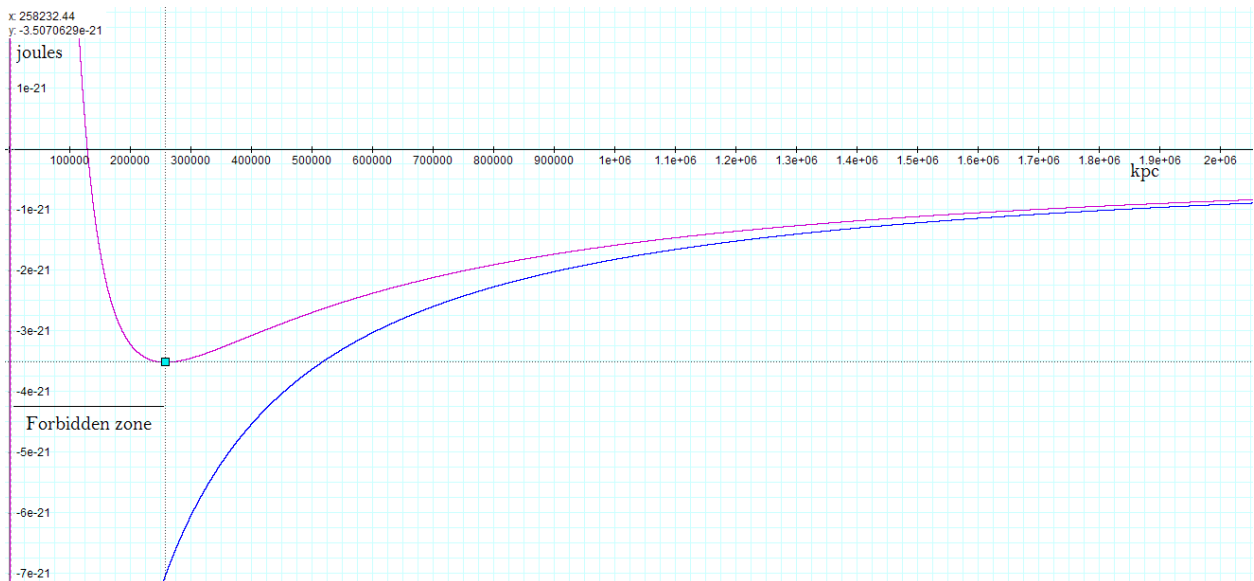


Figure 7-2a: Same as figure 7-1a, using higher values of $M_G = 5 * 10^{40} \text{ kg}$ and $M_1 = 10^6 \text{ kg}$. Rings collapse at the minima to produce galactic substructures.



Figures 7-2b: Same as Figure 7-2a displayed on a larger distance scale. The wide void (forbidden zone) which is shown to start at about 1.55 Mpc in Figure 7-2a is shown to extend all the way to 258 Mpc , where it starts to converge toward the ordinary matter Newtonian curve (in blue).

Further note that in figure 7-2b the void around the center of the parent galaxy is nearly a perfect sphere with a radius of 258 Mpc . However, in a more realistic scenario, where the space within

the void is additionally influenced by other galactic entities and the SHP groups move at relativistic speeds, the size and shape of the void become distorted. Consequently, the void may contain few local minima at which some galactic entities may form, and its geometry does not demonstrate perfect spherical symmetry. However, the average density of matter in the void is significantly reduced.

Finally, it is important to note that the process described above, by which a large galactic entity, or “parent” is broken into smaller “offspring” substructures, does not take into account the effect that the rotation of the large SHP groups may exert on the fragmentation of the parent structure. The process of star formation described in Chapters IV-1-2 and VI-4 may be extended to galactic groups, clusters and superclusters, to explain the fragmentation and distribution of galaxies within clusters.

Section VII-8: Gravitational Repulsion Between Galaxies

The rejection of ordinary matter by galaxies provides a mechanism by which galactic entities may repel each other at distances larger than the diameter of a supercluster. Repulsion between two galaxies will be shown to persist over a large range of distances, starting at a slightly larger distance than the oscillation range of ordinary matter of mass m_p with the dominant superheavy particles. The equation that describes the interaction between the two galaxies is given by

Equation 7-3

$$V = -\frac{GM_1N_{M_1}M_2N_{M_2}}{a} \left(e^{a/r} \cos \left(\frac{bM_1M_2}{r} \right) - 1 \right) - \frac{GM_1N_{M_1}M_{G_2}}{a} \left(e^{a/r} \cos \left(\frac{bM_1m_p}{r} \right) - 1 \right) \\ - \frac{GM_2N_{M_2}M_{G_1}}{a} \left(e^{a/r} \cos \left(\frac{bM_2m_p}{r} \right) - 1 \right) - \frac{GM_{G_1}M_{G_2}}{r}$$

where M_1 and M_2 denote the respective masses of the dominant SHP types of the two galaxies, N_{M_1} and N_{M_2} provide the total number of these SHPs in the respective galaxies, and M_{G_1} and M_{G_2} are the total mass of the ordinary matter within each of the galaxies. Note that the radii of the two galactic disks (which are close to $\frac{bM_1m_p}{2\pi}$ and $\frac{bM_2m_p}{2\pi}$ respectively) are assumed to be small relative to the distance r between their centers. The contributions of additional SHP groups and of other heavenly objects are assumed to be negligible.

The potential energy of the gravitational interaction between two identical galactic entities using the same structure and parameters as the latest example ($M_1 = M_2 = 10^6 \text{ kg}$, $N_{M_1} = N_{M_2} = 1$ and $M_{G_1} = M_{G_2} = 5 * 10^{40} \text{ kg}$) is depicted in figures 7-3a and 7-3b. The galaxies are shown to repel each other at distances stretching between $r \geq 1.56 \text{ Mpc}$ (which is the zonal oscillation range between the dominant SHPs and ordinary matter of mass m_p , denoted as r_{mor}) and $r \leq 2.87 \text{ Gpc}$ (which is the distance between the center of the galaxies and their outermost potential energy minimum, denoted as r_{omin}). In this example, the distance range of the repulsion between the galaxies is of the order of about one third of the estimated size of the

observable universe. Note that the existence of roughly spherical voids around each galactic entity must create a network of non-randomly distributed galaxies that are positioned along two dimensional sheets that form the walls of bubble-shaped regions of space, in agreement with observations.

As demonstrated in figure 7-3a, two isolated galaxies tend to cluster together when the distance separating them is less than the zonal oscillation range between their dominant superheavy particles and ordinary matter of mass m_p , denoted by r_{mor} , causing them to gravitate toward a local minimum. When the distance separating the two galaxies lies between r_{mor} and r_{omin} , the galaxies repel and accelerate away from each other.

The different terms of the force equation can be derived by computing the gradient of equation 7-3, which can be shown to reduce proportionally to either r^{-2} or to r^{-3} within the range $r_{mor} \ll r < r_{omin}$, and proportionally to r^{-2} at distances $r > r_{omin}$, where the effect of the SHP reduces significantly. At distances greater than r_{omin} , the galaxies begin to attract each other and the UG equations converge toward the Newtonian interactions between the ordinary matter of the given galaxies.

Figure 7-3a

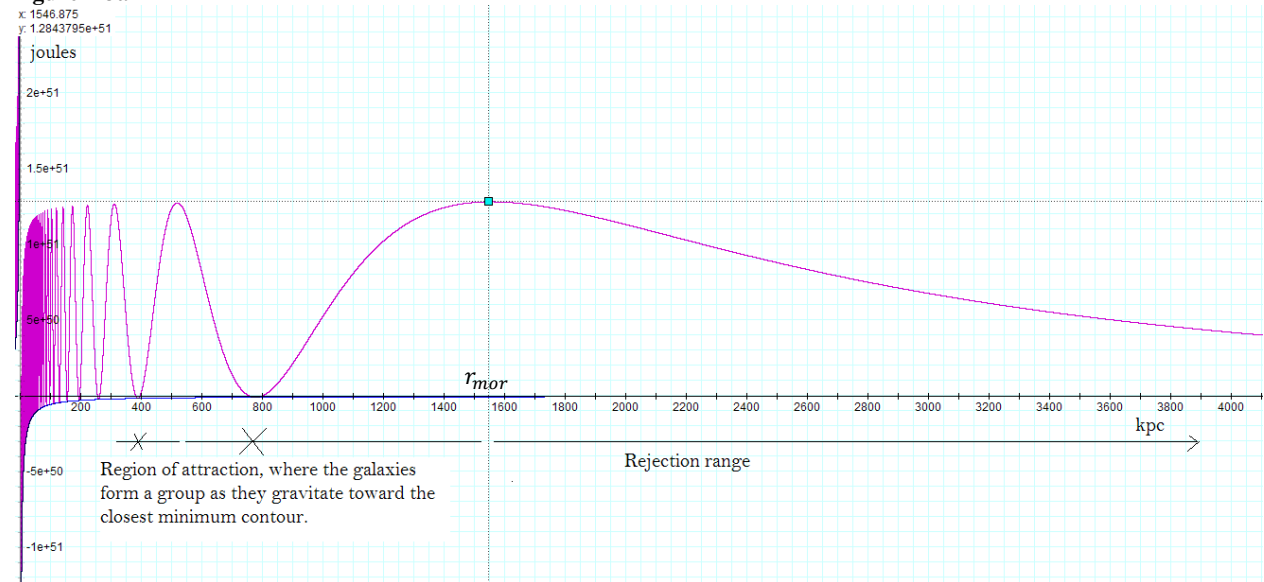


Figure 7-3b

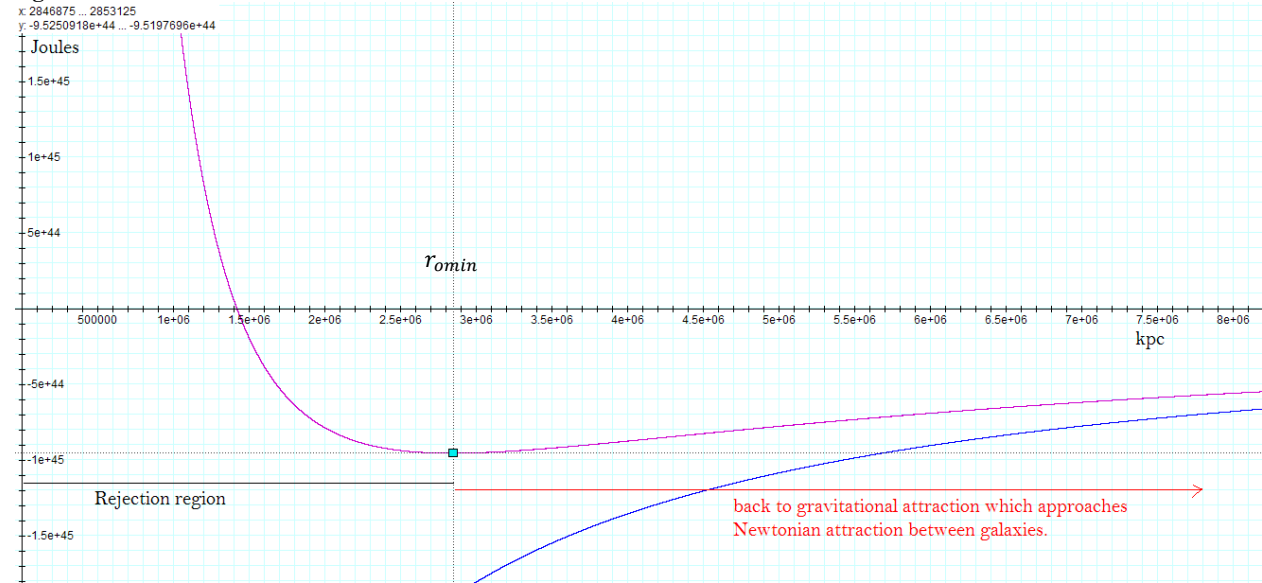


Figure 7-3: The potential energy is displayed as a function of the intergalactic distance due to the exclusive interaction of ordinary matter (blue curve), or due to the interaction between ordinary matter and superheavy particles of two identical galaxies using the parameters $M_1 = M_2 = 10^6 \text{ kg}$, $N_{M_1} = N_{M_2} = 1$ and $M_{G_1} = M_{G_2} = 5 * 10^{40} \text{ kg}$ via equation 7-3. At distances of $r < 800 \text{ kpc}$ the galaxies are bonded, creating a group (a). Between $1.56 \text{ mpc} < r < 2.847 \text{ Gpc}$ the galaxies reject each other (b).

Consequently, the velocity with which the two galaxies recede from each other between $r_{mor} \ll r < r_{omin}$ increases by an amount that is proportional to r^{-2} , and the velocity of two galaxies relative to each other converges quite rapidly to their maximum receding velocity at $r = r_{omin}$. As the galaxies drift apart beyond the relative distance $r = r_{omin}$, the velocity at which they recede from each other is gradually reduced by the attractive force between them. Whether the attractive force at $r > r_{omin}$ is sufficiently strong to eventually stop their motion away from each other depends on the value of their potential plus kinetic energy at $r = r_{mor}$. A positive initial energy indicates that the galaxies will continue to recede to infinity, whereas a negative initial energy implies that their motion away from each other will eventually come to a halt and begin to accelerate in the reverse direction, back toward one another. In the case of exactly zero energy, their receding will continue forever as the relative distance between the galaxies asymptotically approaches a maximum distance.

Section VII-9: The Expansion of the Universe

According to observation, the universe is expanding at an accelerated rate. Invoking the Copernican principle leads to the conclusion that the same isotropic expansion detected from Earth can be observed at the present time anywhere else in the universe. In the following discussion, the average size of a galactic cluster is denoted as \bar{C} , the average distance between adjacent galactic clusters is denoted as \bar{d}_G , and the average relative velocity of adjacent superclusters as they recede from each other is given by \bar{v}_G , where due to the Copernican principle, \bar{C} , \bar{d}_G and \bar{v}_G can be shown to be the same everywhere in the universe. Therefore, an

observer located in single galactic supercluster views adjacent superclusters located at a distance of \bar{d}_G as receding at an average velocity of \bar{v}_G , superclusters located at a distance of $2\bar{d}_G$ as receding at an average velocity of $2\bar{v}_G$, and so on. This leads to the conclusion that two distant galaxies should recede from each other at a speed proportional to the distance between them.¹⁴⁹
 150 151

As shown in the previous section, two isolated galaxies tend to cluster together when the distance separating them is shorter than r_{mor} , to repel each other at distances between r_{mor} and r_{omin} , or to attract each other at distances which exceed r_{omin} . The velocity of a pair of galactic clusters as they recede from each other was shown to increase, and to asymptotically approach the value of their velocity at r_{omin} . This may explain what causes the expansion of the universe. If the matter of the universe is contained within a sphere of radius R_{univ} , where R_{univ} is of an order of less than or equal to the average r_{omin} , the universe must expand in a uniform manner at an accelerating speed that asymptotically approaches a constant expansion velocity.¹⁵²

The UG theory further provides a mechanism to explain the observed acceleration of the expansion of the universe. As a substantial number of galactic cores enter into the next stage of collapse, significantly more massive SHPs are produced, thereby increasing the force with which the galactic entities repel each other. Invoking the cosmological principle, this process must occur everywhere in the universe at approximately the same time. Consequently, galaxies and galactic clusters are expected to repel each other with increasing force, escalating the expansion velocity of the universe.

Section VII-10: Additional Comments about Unified Gravitation and the Big Bang Model

The UG theory does not contradict, but can actually support the model of a relatively small and dense universe that at some point in time began to expand. However, there are two fundamental differences between the UG and the Big Bang expansions.

1. While the expansion of the universe according to the Big Bang is assumed to have started in a state of singularity, the $e^{a/r}$ term of the maxima of the UG equation 2-1-1 prevents the pre-expansion UG universe from becoming a point singularity.¹⁵³ Consequently, the initial pre-expansion UG Universe is expected to have been relatively small, yet infinitely larger than a singularity, eliminating the problems that arise from the Big Bang assumption that just prior to the beginning of the expansion, the universe was in a state of infinite temperature and infinite density, in which all known theories of physics would break down.

¹⁴⁹ Note that according to this statement, distant galaxies are expected to recede from each other at superluminal velocity. Superluminal velocities do not contradict the special theory of relativity in this case, as there is no global inertial system at which the velocity between the two galaxies can be measured.

¹⁵⁰ Note that the expansion of the universe, according to the current standard model of cosmology, is viewed as the expansion of the intervening space between galaxies, rather than as the expansion of galaxies into an empty space.

¹⁵¹ In accordance with general relativity and the cosmological principle, there is nothing external to the whole system of matter in the universe.

¹⁵² However, the speed of two given galactic clusters is likely to vary from the speed expected for the same clusters in isolation, as each one of them is affected by the entire mass of the universe, and not only by the other cluster.

¹⁵³ See the discussion of singularity in Chapter II and in section VII-2 of this chapter.

2. The expansion of the universe, according to the UG theory, is driven by the repulsive force between galactic entities, which results in an accelerated expansion as long as the universe did not grow sufficiently large for the distance between a majority of the entities to become larger than r_{omin} of the dominant SHPs in the universe.

These fundamental differences allow a UG-based cosmological model to avoid a number of problems presented by the Big Bang model. In particular, the fact that unified gravitation provides for the possibility of an accelerated expansion of the universe allows for the amount of time elapsed since the start of the expansion to be significantly larger than 14.5 billion years, resolving a potential recurrence of the age dilemma. As aforementioned, the initial size of the UG universe may have been extremely small, yet infinitely larger than a point singularity, and the universe may be substantially older than predicted by the Big Bang model. Consequently, the different regions of the universe had significantly more time to interact than previously estimated, thus avoiding the horizon problem. In addition, the UG model accounts for the observed tendency of matter within the universe to expand uniformly when viewed on large spatial scale, and to cluster when viewed on small spatial scale, therefore avoiding the problem of structure posed by the Big Bang theory. Note that since the UG scenario provides for a massive expansion of an extremely small initial universe, the theory is also consistent with the discovery of an almost uniform cosmic microwave background and with the theory of Big Bang nucleosynthesis. Finally, the expansion of the universe according to the UG theory is driven by the repulsive forces between massive SHPs and ordinary matter, rather than relying on the Friedmann-Lemaître-Robertson-Walker metric. Thus, the requirement that the density of matter and energy in the universe be equal to a critical density (within one part in 10^{60} according to the current Big Bang Theory) is eliminated, thereby avoiding the flatness problem. Consequently, the UG model does not need to rely on the assumption that an inflation process occurred in the early stages of the universe expansion, nor does it require the presence of dark matter and dark energy, and may thus provide a significantly simpler and potentially more stable theory than the current cosmological model.

It is further important to address what could have initiated the dramatic expansion of the universe. The UG explanation may involve a process similar to the processes described earlier in this chapter for the formation and dynamics of galactic entities. Consider, for example, a universe initially composed of a uniform cloud of gas as it begins to collapse toward its center, toward creating a single high-density core. As the production of sufficiently massive superheavy particles locks the galaxy disk to ordinary matter, excess matter is diverted to nearby secondary centers of collapse, generating a subset of galaxies. As the process is repeated, the collapsing universe becomes filled with galactic clusters and superclusters. Over time, the burning of hydrogen¹⁵⁴ is depleted and a second collapse of the galactic core ensues, resulting in the generation of heavier SHP types. At later stages of collapse, the production of sufficiently massive superheavy particles may create repulsion between clusters of galaxies, thus halting the

¹⁵⁴ Recall that the hydrogen burning process is responsible for stopping the initial collapse and thereby prevents the galactic core from collapsing further.

collapse of the universe and initiating an expansion via the mechanisms described in sections VII-8 and VII-9. Eventually, the distance between neighboring clusters will approach the average r_{omin} , and the effect of superheavy particles on the interaction between galactic clusters will become negligible. Consequently, at this point, the universe is expected to once again become compatible with the general theory of relativity. In cases where the amount of energy in the universe is insufficient to allow for continuous expansion, the universe may begin to contract. However, the existence of massive SHPs near the cores of galactic entities will prevent a full collapse, and the density of the universe may begin to oscillate around its average. This may occur as long as the population of massive superheavy particles remains stable over time. In case of significant decline in the SHP population, the universe will begin to collapse and the process described above will begin a new cycle.

Section VII-11: The Galactic Halo and the Transition From a Spiral to an Elliptical Galaxy

The rotation of a galaxy (as well as the rotation of its SHP groups) tends to confine stars and matter within its galactic disk. As discussed, the size of the galactic disk is determined by the radius of the second minima r_2 and is given approximately by

Equation 7-11-1

$$r_2 \approx \frac{bM_1m_p\gamma(v)}{2\pi}$$

This equation can also be used to estimate the mass of the dominant SHP type. Assuming that the average radius of a galactic disk of a spiral galaxy extends approximately to $r_2 = 30 \text{ kpc}$ and that $\gamma(v) = 1$ provides that $M_1 \approx \frac{2\pi r_2}{b m_p} = 3.86 * 10^4 \text{ kg}$. The same logic used in sections VII-4, 5, and 8 for determining the repulsion between galaxies can be applied to stellar systems, leading to the conclusion that stars may repel each other at certain distances. Hence, the number of stars that can be compressed into the galactic disk is limited. Consequently, in a galaxy containing an excess number of stellar systems that cannot be compressed into the disk must assume orbits within the halo. To quantify this statement, the maximum number of stars that may be contained within the galactic disk is of the order of $\frac{\pi r_2^2}{\pi R_a^2}$ and the maximum quantity of stars contained in the halo is of the order of $\frac{\frac{4}{3}\pi r_2^3}{\frac{4}{3}\pi R_a^3}$ respectively, where R_a is the average shortest distance between neighboring stars (therefore, the average stellar repulsion distance). In the case of a galaxy with $r_2 = 30 \text{ kpc}$ and $R_a = 1 \text{ pc}$, the approximate maximum number of stars within the galactic disk and halo are $9 * 10^8$ and $2.7 * 10^{13}$ stars respectively.¹⁵⁵

¹⁵⁵ Note that an increase in r_2 , according to the UG theory, would provide more space for stars to form within the galactic disk. However, the value of $r_2 \approx \frac{b m_p M_1}{2\pi}$ is determined by the mass of the dominant superheavy particles in the galactic center. Therefore, as the initial stellar quantity was substantially lower than $\frac{\pi r_2^2}{\pi R_a^2}$ (or $9 * 10^8$ in the current example), the rotation of the

The size and mass of a galaxy is determined by the mass of its dominant superheavy particles. Following the discussion of sections VII-4 and 5, the galaxy will eventually become locked to ordinary matter by the production of large SHPs, and the inflow of the gas which fuels the production of new stars will practically cease. Over time, the supply of interstellar gas within the galaxy will become depleted, as interstellar gas is used for the production of new stars, or is ejected from the galaxy in the form of galactic wind (see section VI-2). The resultant galaxy is expected to contain little or no cool interstellar gas or dust, and the majority of its stars are expected to reside within its halo. Furthermore, the galaxy is expected to appear to have no stellar disk, and as little or no new stars are produced, its stellar population is expected to consist of older stars. These characteristics are widely observed in the elliptical classification of galaxies.

Between the time that the galaxy becomes locked to ordinary matter and the depletion of its interstellar gas, a significant amount of matter, energy and angular momentum is lost in the form of galactic wind. Consequently, the rotating core of the galaxy (which is the engine of the galaxy) and its source of energy also lose energy and momentum, as well as matter that is pumped out by the rotating spiral. As a very limited amount of new gas enters the galaxy, the central core is deprived of additional fuel, and since its energy and momentum is reduced, the rate of rotation of the galactic core must slow down.¹⁵⁶ As the central core loses some of its mass $M_{central}$, and its rotation velocity reduces substantially ($\gamma^2(v)$ becomes closer to 1), the effect exerted on the velocity of the object by the SHP and the central core, which is proportional to $\left(\frac{4GN_s M \gamma^2(v)}{a} + GM_{central} \Delta \left(\frac{1}{r}\right)\right)^{1/2}$, decreases.¹⁵⁷ On the other hand, as the number of stars in the halo increases, and the mass and rotational velocity of the central core and the rotational velocity of the SHPs are reduced, the relative influence of nearby matter on the object increases. Consequently, the galaxy rotation curve may deviate substantially from constant velocity.

Section VII-12: Elliptical Morphology and Properties of Elliptical Galaxies

The elliptical shape of a galaxy is known not to correlate well with the rotation of the galaxy as a whole ^(Caroll & Ostlie, 2007, p. 988). A possible reason for the elliptical shape of the galaxy is that relativistic SHP groups distort the otherwise circular equi-potential contours into elliptical ones, in which case the level of ellipticity depends mainly on the velocity of the SHP groups. For the simple case of a galaxy containing a single SHP type of mass M_1 , the axes of the n^{th} minima are given by $\cos\left(\frac{bM_1 m_p \gamma(v_1)}{D_{1,n}}\right) \approx 1$, or for the outermost substantial minimum, by

$$D_{1,2} \approx \frac{bM_1 m_p \gamma(v_1)}{2\pi}.$$

galaxy confined all stars located within the r_1 maximum contour to the galactic disk, while stars located beyond this maximum were ejected from the galaxy in the form of galactic wind (see section VI-2).

¹⁵⁶ Note that upon the occurrence of another stage of collapse, the rotation rate of the galactic core will increase substantially.

¹⁵⁷ According to equation 6-5.

The apparent major axis α is given by $\alpha = D_{1,2} \approx \frac{bM_1 m_p \gamma(v_1)}{2\pi}$ (where the velocity of the SHP group at the time of emission is perpendicular to the distance between the location of the emission and the location of interception of the gravitational signal by the orbiting matter) and the apparent minor axis β is given by $\beta = D_{1,2} \gamma(v_1)^{-1} \approx \frac{bM_1 m_p \gamma(v_1)}{2\pi}$ (where the given velocity and the distance are parallel). Therefore, the observed ellipticity can be defined as $\epsilon = 1 - \beta/\alpha \approx 1 - \frac{D_{1,2}(\gamma(v_1))^{-1}}{D_{1,2}} = 1 - (\gamma(v_1))^{-1}$. The largest ellipticity observed is approximately $\epsilon = 0.7$, suggesting that $(\gamma(v_1))^{-1} = (1 - (v_1/c)^2)^{1/2} \geq 0.3$, or $v_1 \leq 0.954c$. Note that in the more realistic case of multiple SHP groups rotating on different rotational planes, the elliptical galaxy may be triaxial without a single preferred axis of rotation.

Section VII-13: The Boxiness vs. Diskiness of Elliptical Galaxies

Figure 7-4a: A calculated disk galaxy

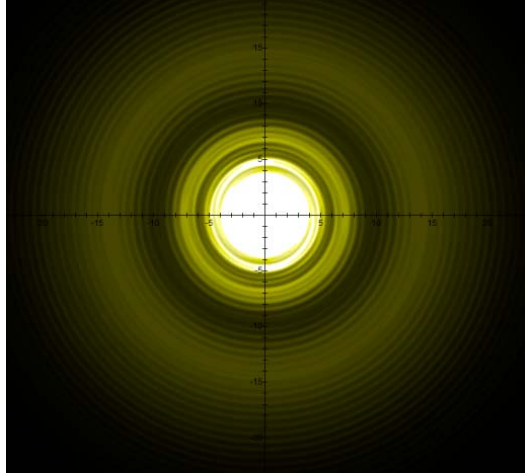
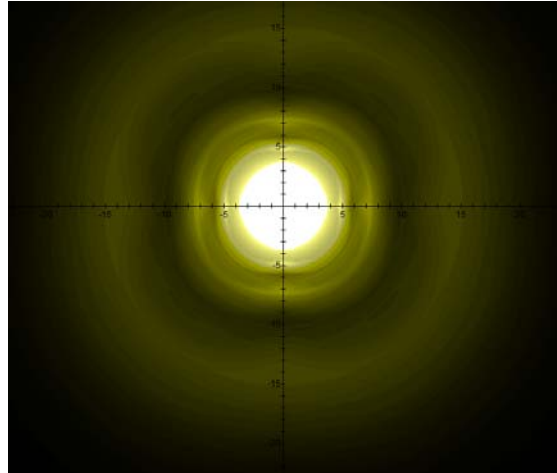


Figure 7-4b: A calculated boxy galaxy



Figures 7-4a and 7-4b: A calculated disk galaxy (7-4a) drawn using $A = 0.1 \text{ kpc}$ and a calculated boxy galaxy (7-4b) drawn using $A = 0.001 \text{ kpc}$. Both galaxies share the parameters $\Gamma = 1$, $M = 0.125 * 10^5$, $N_M = 1$, $M_G = 2.5 * 10^{38} \text{ kg}$ and $v = 0.45c$.

Ralf Bender, Jean-Luc Nieto and their collaborators proposed that many of the characteristics of elliptical galaxies are related to the degree of boxiness or diskiness that their isophotal surfaces demonstrate ^(Bender, 1992). It remained unclear, however, why a small portion of elliptical galaxies present a boxy appearance, while a majority of elliptical galaxies are disk. Figure 7-4b (calculated via equation 4-1-1a) demonstrates that a galaxy may take on a boxier appearance when the distance A is selected to be sufficiently small for a superheavy particle group moving at a relativistic velocity relative to the center of the galaxy. With $v = 0.45c$ and $A = 0.001 \text{ kpc}$, the isophotal surfaces in figure 7-4b demonstrate clear departure from elliptical morphology, particularly with increasing proximity to the galaxy center. Increasing A to 0.1 kpc in figure 7-4a modifies the morphology of the galaxy into a more spherical, or disk morphology.

Chapter VIII: Gravitational Ionization

Most of the observable universe consists of plasma, or partially ionized gas. The processes of ionization and their sources of energy are regarded as one of the important open questions in astrophysics. According to Newton's theory, the gravitational force between a proton and an electron is weaker than the electromagnetic force between them by a factor of about $2 * 10^{39}$. For this reason, the influence of gravitation on the atomic scale, specifically its ability to ionize an atom, is assumed to be non-existent. Furthermore, according to Newtonian dynamics, the gravitational acceleration of a particle is independent of its mass, a belief that led to Einstein's principle of equivalence. Consequently, under Newton's theory of gravitation and general relativity, free falling protons, electrons and neutrons are expected to accelerate at the exact same rate. Therefore, the ionization of atoms is extremely unlikely to be caused by the gravitational force.¹⁵⁸ Rather, current theories attribute ionization to either a thermal process or to strong electromagnetic fields.

However, massive ionization by the gravitational force alone is predicted and explained by the UG theory, even at distances of $r \gg a$, where the exponent $e^{a/r} = 1$. According to equation 2-1-2, at distances of $a \ll r < bMm_p/\pi$, the UG gravitational force between a superheavy particle of mass M and a nucleon of mass m_p is greater than the equivalent Newtonian force by an order of $\frac{bMm_p}{a} \approx 2.64 * 10^{30} * M$, and is thus capable of exceeding the electromagnetic force between an electron and a proton, given a sufficiently large SHP mass.¹⁵⁹
¹⁶⁰ In addition, the acceleration of a proton by a superheavy particle of mass M from a distance $r < \frac{bMm_p}{\pi}$ is expected to vary from the acceleration of an electron from the same distance.

Consider the simpler case of a hydrogen atom ^1_1H encircling the center of a star or galaxy dominated by a single SHP type of mass M surrounded by ordinary matter. To simplify the analysis, the velocity \vec{u} of the atom relative to the superheavy particle is assumed to be non-relativistic. The energy of the atom is thus given by

¹⁵⁸ An exception to this statement is when extremely strong tidal forces exist. For sufficiently strong tidal forces to occur over distances of the order of the diameter of an atom, the gradients of Newton's gravitational force must be enormous. Such gradients are theoretically possible within black holes. However, in order to experience such enormous gravitational tidal forces in the general relativity scenario, the atom must cross the black hole event horizon. In such a case, the ejected electrons must remain trapped within the black hole and cannot be detected by an outside observer, as even light cannot escape. Therefore, this process cannot produce any observable ionization.

¹⁵⁹ This value was calculated using $b = 0.9 * 10^{44}$, $a = 5.7 * 10^{-14}$ and $m_p = 1.674 * 10^{-27}$.

¹⁶⁰ Following the non-relativistic force equation 2-1-2, $\vec{F} = \frac{GMN_M m_p N_{m_p}}{r^2} \left(\cos\left(\frac{bMm_p}{r}\right) - \frac{bMm_p}{a} \sin\left(\frac{bMm_p}{r}\right) \right) \hat{r}$, the oscillation amplitude of the cosine term is negligible relative to the amplitude of the term $\frac{bMm_p}{a} \sin\left(\frac{bMm_p}{r}\right)$. Therefore, at the maxima the UG force becomes larger than the Newtonian force by a factor of $\frac{bMm_p}{a}$.

Equation 8-1

$$E_{Atom} = (m_e + m_p)c^2 - \frac{GMN_M m_p}{a} \left(e^{a/r} \cos\left(\frac{b m_p M}{r}\right) - 1 \right) - \frac{GMN_M m_e}{a} \left(e^{a/r} \cos\left(\frac{b m_e M}{r}\right) - 1 \right) + \frac{1}{2}(m_p + m_e)u^2 + E_{bond} - \frac{GM_G(r)(m_p + m_e)}{r}$$

where the atom is assumed to rotate in a circular orbit of radius r around a group of N_M SHPs of particle mass M concentrated in a small sphere of a radius that is negligible relative to r . The sphere of superheavy particles is assumed to be surrounded by a spherically symmetric distribution of ordinary matter of mass $M_G(r)$. The electron-proton bonding energy of a free atom E_{bond} must be negative, where at the ground state of the hydrogen atom, $E_{bond} = -13.6 \text{ eV}$.¹⁶¹ Note that only the terms $-\frac{GMN_M m_p}{a} \left(e^{a/r} \cos\left(\frac{b m_p M}{r}\right) - 1 \right)$ and $-\frac{GMN_M m_e}{a} \left(e^{a/r} \cos\left(\frac{b m_e M}{r}\right) - 1 \right)$ in equation 8-1 are non-linear functions of the proton and electron masses, and are therefore the only terms capable of generating a differential force that can separate the electron from the proton to ionize the atom.

The orbiting atom gravitates toward the potential energy minima generated by its interaction with the galactic superheavy particles and ordinary matter. The magnitudes and locations of the zonal oscillation maxima and minima of both the proton and the electron due to the dominant N_M SHPs of mass M can be derived via equations 2-1-1 and 2-1-42 respectively. Since the proton and the electron are independent particles of vastly different masses, their interactions with the superheavy particles generate distinct sets of potential energy minima. As the zonal oscillation range of the SHP-proton pair is proportional to bMm_p , and the zonal oscillation range of the SHP-electron pair is proportional to bMm_e , the radius of the proton's zonal oscillation range is about 1,836 times greater than that of the electron.

The characteristics of the interaction between the atom and the central superheavy particles can be viewed at three different distance ranges. At distances $r > bMm_p$, the UG potential energy of the proton and the electron approach their Newtonian form, and the differential gravitational force (as well as the total gravitational force) applied on the proton and the electron is negligible relative to the electromagnetic force between them. Therefore, the hydrogen atom remains intact.

At distances $\frac{bMm_e}{\pi} \ll r < \frac{bMm_p}{\pi}$, the UG force applied on the electron is still Newtonian, and therefore negligible. However, the protons (as well as neutrons) are within their zonal oscillation range with the SHPs and are attracted toward their nearest minimum r_{np} .¹⁶² Consequently, free protons, atoms, molecules and ions are drawn toward the nearest r_{np} minimum. As the UG force applied on the electron at this range of distances is negligible, the electron will remain bonded to the proton by the electromagnetic force.

¹⁶¹ The ionization energies of the other energy states of the hydrogen atom, are roughly equal to $13.6/k^2 \text{ eV}$, where k is an integer greater than zero.

¹⁶² For simplicity, the small difference between the mass of the proton and the neutron can be neglected.

Note that since $r \gg a$, the potential energy of the proton is given by $-\frac{GMN_M m_p}{a} \left(e^{a/r} \cos\left(\frac{bm_p M}{r}\right) - 1 \right) \rightarrow -\frac{GMN_M m_p}{a} \left(\left(1 + \frac{a}{r}\right) \cos\left(\frac{bm_p M}{r}\right) - 1 \right)$, and the minima occur where $\cos\left(\frac{bm_p M}{r_{n_p}}\right) \approx 1$. At these minima the potential energy is approximately $-\frac{GMN_M m_p}{r_{n_p}}$, which is equal to Newton's gravitational potential energy. Consequently, the atoms will assume circular Newtonian orbits. However, in contrast to Newton's theory, only a discrete (or quantized) set of orbits at close proximity to the minima are allowed.

At distances $a \ll r < \frac{bMm_e}{\pi}$, the electrons, as well as the protons and neutrons, are situated within their SHP zonal oscillation range. As the electron mass is about 1,836 times lighter than the mass of the protons (or neutrons), all protons, atoms, ions and molecules are attracted toward the nearest minimum of the proton's set of minima r_{n_p} . As long as the differential UG force between the hydrogen's proton and electron is smaller than the electromagnetic force which bonds them, the atom is likely to remain intact, and the electron is forced to follow the heavier proton and to gravitate toward the potential energy minima of the proton. The locations of these minima can be derived using equation 2-1-42. For the case where $MN_M \ll M_G(r)$ and $r < \frac{(bm_p)^2 M^3 N_M}{aM_G(r)}$, the energy minima of the proton and the electron occur at

Equation 8-2a

$$r_{n_p} = \frac{bm_p M}{(2n_p + 1)\pi - \arccos(\psi_p)}$$

where $\psi_p = \frac{aM_G(r_{n_p})}{(bm_p)^2 M^3 N_M} r_{n_p}$ and $r_{n_p} \ll bm_p M$, or $n_p \gg 1$. Thus,

Equation 8-2b

$$r_{n_p} \rightarrow \frac{bm_p M}{(2n_p + 1/2)\pi} \text{ as } n_p \rightarrow \infty$$

where minima occur at any integer $n_p \gg 1$, and where r_{n_p} of equation 8-2b fulfills $r_{n_p} < \frac{(bm_p)^2 M^3 N_M}{aM_G(r_{n_p})}$ and $r_{n_p} < \frac{bMm_p}{\pi}$. Similarly, the electrons are drawn by the UG force toward their own minima at approximately

Equation 8-2c

$$r_{n_e} = \frac{bm_e M}{(2n_e + 1)\pi - \arccos(\psi_e)}$$

where $\psi_e = \frac{aM_G(r_{n_e})}{(bm_e)^2 M^3 N_M} r_{n_e}$ and $r_{n_e} \ll bm_e M$, or $n_e \gg 1$, or

Equation 8-2d

$$r_{n_e} \rightarrow \frac{bm_e M}{(2n_e + 1/2)\pi} \text{ as } n_e \rightarrow \infty$$

where minima occur at any integer $n_e \gg 1$.

Since $m_p \approx 1,836 m_e$, there are 1,836 proton potential energy minima at distances greater than the first minimum of the SHP-electron UG interaction, and there are 1,836 proton potential energy minima between any two successive minimum contours of the electron.

According to equation 2-1-2, the UG force steering the electron toward its closest potential energy minimum is approximately $1,836^2$ times smaller than the force acting on the proton. Therefore, the atom settles in the immediate vicinity of the proton's potential energy minimum, and in the case of a weak local UG gravitational influence, the electron is prevented from approaching its own potential energy minimum by the electromagnetic force that bonds it to the proton. Since there are approximately 1,836 proton potential energy minima between any two successive electron potential energy minima, most of the electrons that are bonded to orbiting hydrogen atoms demonstrate orbital radii that deviate significantly from the radii of their UG minima. It will be shown that at some of these minima, the overall stability of the proton-electron system may increase due to the ionization of the hydrogen atom, while the barrier threshold of the ionization is either too small or non-existent, and therefore cannot prevent massive ionization. An atom is likely to be ionized at a given location if its overall energy is higher than the total sum of the energies of the ion and its displaced electron, where the electron's amount of displacement Δ is larger than, but of the same order of magnitude as the Bohr radius. For massive ionization to occur, the following equation must hold true at the radius where ionization takes place:¹⁶³

Equation 8-3

$$\begin{aligned} (m_e + m_p)c^2 - \frac{GM_N M m_p}{a} \left(e^{a/r} \cos\left(\frac{bm_p M}{r}\right) - 1 \right) - \frac{GM_N M m_e}{a} \left(e^{a/r} \cos\left(\frac{bm_e M}{r}\right) - 1 \right) + E_{bond} - \frac{GM_G(r)m_p}{r} - \frac{GM_G(r)m_e}{r} > \\ > (m_e + m_p)c^2 - \frac{GM_N M m_p}{a} \left(e^{a/r} \cos\left(\frac{bm_p M}{r}\right) - 1 \right) - \frac{GM_N M m_e}{a} \left(e^{a/|\vec{r} + \vec{\Delta}|} \cos\left(\frac{bm_e M}{|\vec{r} + \vec{\Delta}|}\right) - 1 \right) - \frac{GM_G(r)m_p}{r} \\ - \frac{GM_G(|\vec{r} + \vec{\Delta}|)m_e}{|\vec{r} + \vec{\Delta}|} \end{aligned}$$

where Δ is of the order of the radius of the hydrogen atom. Note that the loss of the electron has virtually no significant effect on the location of the ion (in this case, a proton), as $m_p \gg m_e$.

Also note that since $a \ll r$, $e^{a/|\vec{r} + \vec{\Delta}|} = e^{a/r} = 1$. Therefore, massive ionization will take place when

¹⁶³ Note that due to a quantum tunneling effect, ionization may also occur when the overall energy is increased due to ionization. However, in such a case the ionization rate would be low, and massive ionization would not occur.

Equation 8-4

$$-\frac{GMN_M m_e}{a} \left(\cos\left(\frac{bm_e M}{r}\right) - \cos\left(\frac{bm_e M}{|\vec{r} + \vec{\Delta}|}\right) \right) + E_{bond} - \frac{GM_G(r)m_e}{r} + \frac{GM_G(|\vec{r} + \vec{\Delta}|)m_e}{|\vec{r} + \vec{\Delta}|} > 0$$

With $|\vec{\Delta}|$ of the order of the Bohr radius, the term $-\frac{GM_G(r)m_e}{r} + \frac{GM_G(|\vec{r} + \vec{\Delta}|)m_e}{|\vec{r} + \vec{\Delta}|}$ is negligible relative to E_{bond} . Using the trigonometric equation

$\cos(x) - \cos(y) = -2\sin\frac{1}{2}(x + y)\sin\frac{1}{2}(x - y)$, $|\Delta| \ll r$, and $|E_{bond}| = -E_{bond}$ results in massive ionization occurring when

Equation 8-5

$$\sin\left(\frac{bm_e M}{r}\right) \sin\left(\frac{1}{2} \frac{bm_e M}{r^2} \Delta\right) > \frac{a|E_{bond}|}{2GMN_M m_e} > 0$$

As $\left| \sin\left(\frac{bm_e M}{r}\right) \sin\left(\frac{1}{2} \frac{bm_e M}{r^2} \Delta\right) \right| \leq 1$, massive ionization can happen only if $MN_M > \frac{a|E_{bond}|}{2Gm_e}$.

Therefore, massive ionization of hydrogen atoms at their ground state, where $E_{bond} = -13.6 \text{ eV}$, can occur only when $MN_M > 1.022 * 10^9 \text{ kg}$.

The gravitational ionization of other atoms or molecules can be treated similarly. Atomic ionization energy ranges between 3.8939 eV (for cesium) and 24.587 eV (for helium).

Therefore, massive atomic ionization at $a \ll r \ll bMm_e/\pi$ requires the total mass of the dominant SHP in the present scenario to be at least $MN_M > 2.926 * 10^8 \text{ kg}$.¹⁶⁴ Note that via equation 8-5, the removal of the last electron from the ground state of an atom with z protons will require approximately $\sin\left(\frac{bm_e M}{r}\right) \sin\left(\frac{1}{2} \frac{bm_e M}{r^2} \Delta\right) > \frac{13.6\text{eV} * za}{2GMN_M m_e}$.

The above discussion reveals two key concepts. First, a substantial portion of the massive amount of plasma detected in the universe may be produced via gravitational ionization. Second, the electrons freed by ionization settle into entirely different orbits than the orbits of ions or atoms.¹⁶⁵ In the following chapter, this phenomenon will be shown to explain the generation of the magnetic fields created by planets, stars and galaxies, and may be instrumental in understanding the observed phenomena of jets and pulsars.

¹⁶⁴ Lower MN_M values may be sufficient to ionize some large molecules, which may lower ionization energy.

¹⁶⁵ Note that in the first order of approximation, where the masses of the protons and neutrons are assumed to be equal and the mass of the bonded electrons is assumed to be negligible relative to the mass of protons, all ions, atoms and molecules share the same orbits. For a sufficiently large MN_M , these orbits may split into a series of nearby sub-orbits. For example, different isotopes of the same atom may demonstrate slightly different radii of orbit, or the orbital radius of an ion of a given element may differ slightly from the orbital radius of an atom of the same element.

Chapter IX: The General Structure and Composition of Planets and the Creation of their Magnetic Fields

Within our Solar System, the four inner planets have a solid surface, and are referred to as terrestrial planets. These planets display no planetary rings and few satellites. In contrast, the surfaces of the four outer planets are non-solid and composed of gases.¹⁶⁶ Gas planets are substantially more massive than terrestrial planets, and display broad rings and extensive satellite systems. The distinct differences in mass and radii between the terrestrial and gas planets raise questions as to whether their composition and structure are related to their size. A UG-based analysis will be applied to examine the relationship between the mass of planets and their resultant properties. It will be shown that under unified gravitation, the formation of a substantial ring and satellite system requires a planet of sufficient mass, and is mutually exclusive to having a solid surface.

Section IX-1: Planetary Ring and Satellite Systems of Terrestrial and Gas Planets

The temperature and pressure within the cores of less massive planets are less extreme, and are consequently expected to produce less massive superheavy particles. The maximal zonal oscillation ranges of the four terrestrial planets in the Solar System are thus expected to extend to shorter distances than the maximal zonal oscillation ranges of the four massive gas planets.

A mathematical formula relating the mass M_{SL} of the dominant SHP of a planet to the total planetary mass M_p is unknown. In the present case, it is assumed that the mass of the dominant SHP increases faster than the rate of growth of the radius of the planet R_p , which is roughly proportional to $M_p^{1/3}$.

A common spherical macroscopic object with a radius of the order of a few centimeters is too small to produce superheavy particles of a mass substantially larger than m_p . As the zonal oscillation range of two ordinary particles of mass m_p is of the order of $10^{-10} m$, the maximal zonal range of the object is negligible relative to its radius. The mass of a homogeneous object is proportional to the cube of its radius. The assumption made here, that on average the mass of the dominant SHP type of an object increases faster than the cube root of its mass, implies that the mass of the dominant SHP type increases faster than the radius of the object. Therefore, beyond a certain radial value, the object's maximal zonal oscillation range, which is proportional to M_{SL} , is expected to exceed its radius. In such a case, some of the potential energy minima of ordinary matter of mass m_p may occur above the surface of the object, creating areas of higher matter density, or rings. In order for the length of the zonal oscillation range of the dominant superheavy particles with ordinary matter to equal the radius of the object, the object's mass is expected to fall within the range between the mass of the largest known object without a ring system and the smallest object known to display a ring system. Hence, in our Solar System this

¹⁶⁶ Note that planetary gases may become compressed into liquids or solids further in toward their interiors.

mass value is expected to fall somewhere between the mass of the planet Earth and the mass of planet Uranus.

As an example, assume that within the range of masses covered by the eight Solar planets between $3 * 10^{23} kg < M_p < 2 * 10^{27} kg$ (see table 9.1), M_{SL} has an approximately linear dependency on the planet's overall mass (or $M_{SL} \approx \eta M_p$). For simplicity, the SHP velocities are assumed to be non-relativistic and the influence of less dominant SHP groups will not be taken into account. Applying the above simplifications, the radius of the planet R_p can be expressed by $R_p \approx \left(\frac{3}{4\pi\bar{\rho}_p}\right)^{1/3} M_p^{1/3}$, where $\bar{\rho}_p$ is defined as the average density of the planet.

The external ring, indexed $n = 2$,¹⁶⁷ is given by $R_z \approx \frac{bM_{SL}m_p}{2\pi}$. Therefore, rings may form when $R_z > R_p$, or

Equation 9-1-1

$$\frac{bM_{SL} m_p}{2\pi} \approx \frac{b\eta M_p m_p}{2\pi} > \left(\frac{3}{4\pi\bar{\rho}_p}\right)^{1/3} M_p^{1/3}$$

or

Equation 9-1-2

$$\eta > \eta_1 = \frac{2\pi}{bm_p M_p^{2/3}} \left(\frac{3}{4\pi\bar{\rho}_p}\right)^{1/3} = \frac{2.587 * 10^{-17}}{(M_p^2 \bar{\rho}_p)^{1/3}}$$

Table 9-1 provides the calculated values of η_1 for all of the planets in the Solar System. Given that the four terrestrial planets do not display planetary rings, while the four gas giants maintain rings, the value of η lies somewhere within the range

Equation 9-1-3

$$4.45 * 10^{-35} > \eta > 1.219 * 10^{-35}$$

Note, however, that the assumption of linearity ($M_{SL} \approx \eta M_p$) was used only as an example. In the case where the relation between M_{SL} and M_p is non-linear, as long as M_{SL} increases consistently at a higher rate than $M_p^{1/3}$, ring systems will occur exclusively in objects of a mass greater than some threshold mass value. Taking the above discussion one step further, when the zonal oscillations of the planetary superheavy particles with ordinary matter extend beyond the Roche limit of a planet, the rings located external to this limit are likely to coalesce to produce satellites. As discussed, this process can occur in planets of substantial mass, where the oscillation range of the SHP- m_p interaction exceeds the radii of the planets. This process may consequently account for the large number of satellites observed to encircle the four gas giants, and may further explain why terrestrial planets, which do not generate ring systems at which

¹⁶⁷ As previously discussed, the external ring between the $n = 0$ minimum and the $n = 1$ maximum demonstrates negligible amplitude and thus can be discounted. Note that this external ring may be observed as an extremely faint and diffused ring.

matter can accumulate and coalesce, have few satellites. According to unified gravitation, the moons of terrestrial planets are theorized to have been captured into orbit by the gravitational pull of their parent planet. These captured satellites may have originated external to the planetary system, or may have formed in tandem with their parent planet, in an adjacent orbit. In keeping with this scenario, Earth and its moon may have formed within virtually the same ring of the Sun, at two local minima generated by the “interference pattern” of various solar SHP groups.¹⁶⁸ As their masses increased, the gravitational interaction between the Earth and the moon became sufficiently strong and they began to orbit around each other, as well as around the Sun. Such a scenario may provide one or two satellites, however not the large quantity of satellites observed to orbit the giant gas planets.

Table 9-1

Planet	Density (kg/m^3) $\bar{\rho}_p$	Mass (kg) M_p	η_1
Jupiter	1,326	$1.8986 * 10^{27}$	$1.536 * 10^{-36}$
Saturn	687.3	$5.6846 * 10^{26}$	$4.274 * 10^{-36}$
Uranus	1,270	$8.681 * 10^{25}$	$12.19 * 10^{-36}$
Neptune	1,638	$1.0243 * 10^{26}$	$10.03 * 10^{-36}$
Earth	5,515	$5.9736 * 10^{24}$	$44.5 * 10^{-36}$
Mars	3,934	$6.4185 * 10^{23}$	$220.4 * 10^{-36}$
Venus	5,204	$4.868 * 10^{24}$	$52 * 10^{-36}$
Mercury	5,427	$3.3022 * 10^{23}$	$308.2 * 10^{-36}$

Section IX-2: Unified Gravitation and the Surface Structure of Gas and Terrestrial Planets

The UG explanation for the composition of planets, specifically the observation that the larger solar planets consist of non-solid surfaces, can be examined in the context of the discussion of the previous section. The existence of a ring system indicates that the zonal oscillation range generated by the planetary superheavy particles exceeds the radius of the planet. Therefore, the rapid oscillations of the potential energy create strong tidal forces that extend beyond the planetary surface and prevent surface layers of gases from transitioning to solid form. In smaller planets, the zonal oscillation range of the dominant superheavy particles is expected to terminate well below the planetary surface. Hence, the tidal forces applied on a planet’s surface by its superheavy particles are small, allowing ordinary matter on the planetary surface to solidify.

¹⁶⁸ For additional information, see figure 4-2 and footnote 63 in Chapter IV. Current theory holds that the Moon was created by a collision between Earth and an external body.

Section IX-3: The Composition of Earth's Core

As suggested in the third chapter, superheavy particles are generated deep within the cores of astronomical objects (probably as pairs of superheavy particles and anti-particles) with sufficient initial kinetic energy and momentum to allow for their ejection from the central core, yet not adequately large to set them free. Consequently, SHPs enter into approximately circular orbits of radii R_{orbit} around the central core, where the zonal oscillation range of the superheavy particles is given by $R_{zr} \approx \frac{bMm_p}{\pi}$. Ordinary matter is likely to coalesce in regions external to the zonal oscillation range of massive superheavy particles. Consequently, as long as $R_{zr} < R_{orbit}$ and $R_{zr} + R_{orbit} < R_p$, the inner core and the outer layers of the planet do not fall within the zonal oscillation range of large SHPs and are thus expected to solidify.¹⁶⁹ The middle section of the planet, between $R_{orbit} - R_{zr} < r < R_{orbit} + R_{zr}$, is located within the zonal oscillation range of large SHPs, and is thus expected to remain non-solid or viscous. Looking into the composition of our planet, the radius of Earth's solid inner core is 1,210 km and the radius of its outer liquid core lies between 1,210 km and 3,470 km from the planetary center. Above the liquid layers of the core lies the highly viscous mantle between 3,470 km and 6,370 km from the center of Earth,¹⁷⁰ and an additional 35 km of a solid outer crust. Using these values, the mass and orbital radii of the Earth's dominant superheavy particles can be estimated, where $R_{orbit} - R_{zr} \approx 1,210$ km and $R_{orbit} + R_{zr} \approx 3,470$ km provide $R_{orbit} \approx 2,340$ km and $R_{zr} \approx 1,130$ km, leading to $M \approx \frac{\pi R_{zr}}{b m_p} \approx 2.4 * 10^{-11}$ kg. Therefore, the mass of the dominant SHP within the Earth is expected to equal approximately $2.4 * 10^{-11}$ kg. Note that Earth may contain larger superheavy particles as well, but in quantities that are too minor to be noticed. Further note that based on unified gravitation, the outer core is not necessarily in a liquid or gas form. Rather, the outer core is more likely to be composed of layers of high matter density separated by layers of significantly lower density, where the layered structures rotate at lower angular velocities than the SHP groups, and are thus subjected to rotating density waves generated by the SHPs.

Section IX-4: The Creation of Planetary, Stellar and Galactic Magnetic Fields via Unified Gravitation

The Sun, the Earth and the other solar planets are known to have magnetic fields, a phenomenon described by Einstein as being one of the great unsolved problems facing modern physics. The exact cause for the observed magnetic fields remains unknown. Earth's magnetic

¹⁶⁹ Note that the center of the planet may be sufficiently massive to eliminate zonal oscillations, even in cases where the center is located within the oscillation range of the orbiting superheavy particles. In such a case, we can only rely on $R_{zr} + R_{orbit} < R_p$. Therefore, the mass of the dominant SHP may be larger than the mass calculated in this section.

¹⁷⁰ According to this model, the mantle lies on a downward slope of the potential beyond $n = 1$ at $r > r_1$. Therefore, the inner part of the mantle is almost liquid, whereas the outer mantle becomes increasingly solid.

field is presently believed to result from electric currents in its liquid outer core, however the origin of these currents is not well-understood.

As discussed in Chapter VIII, at distances below $r \approx \frac{bMm_e}{\pi}$, free electrons tend to gravitate toward their minima contours at about $r_{n_e} \approx \frac{bMm_e}{(2n_e-1/2)\pi}$, while below $r \approx \frac{bMm_p}{\pi}$, protons and ions (as well as neutral atoms, neutrons and molecules) tend to gravitate toward the minima of the ordinary matter m_p , at about $r_{n_p} \approx \frac{bMm_p}{(2n_p-1/2)\pi}$. Since $m_p \approx 1,836m_e$, there are 1,836 proton-SHP minima between any two successive electron-SHP minima.

Ionization may be caused by the UG gravitational force (as explained in Chapter VIII), by radiation (electromagnetic fields), or thermally (through collisions or radiation). In any case, if a free electron and an ion are within the electron-SHP zonal oscillation range, each will gravitate toward its nearest respective minimum and enter into an orbit. Each rotating charge is expected to generate a magnetic field of

Equation 9-4-1

$$B = \frac{\mu_0 q}{4\pi r^2} (\vec{u} \times \hat{r})$$

The total amount of negative and positive charges must be equal in order to maintain overall neutrality. According to the current paradigm (based on the electromagnetic/Newtonian scenario), the lighter electrons are expected to reach substantially higher velocities than the heavier ions, and the magnetic field generated by the ions is thus negligible. However, both thermal and radiation-driven ionization are random by nature. Substantially high temperatures are required for the generation of the massive ionization needed for the creation of the measured magnetic fields. At such high temperatures, the spatial and velocity distributions of the free electrons are expected to be entirely random. Therefore, the magnetic fields produced by the various electrons should cancel out, and no substantial global magnetic field should be observed.

According to the UG scenario, ions and protons are organized in a distinct set of orbits within the SHP-proton zonal oscillation range, dictated by an orderly set of minima. The same is true for the electrons within the SHP-electron oscillation range.¹⁷¹ The velocities of the nearby electrons and protons (or ions) are determined by the rotational velocity of the central core at

very short distances, or may be given by equation 6-5, $u \approx \left(\frac{4GN_s M \gamma^2(v)}{a} + \Delta \left(\frac{GM_G(r)}{r} \right) \right)^{1/2}$, at

larger distances. In either case, the velocity of the charged particles is independent of their masses. Consequently, in close proximity to the SHP groups, ions and protons travel at velocities that are comparable to the velocities of the electrons and rotate in the same direction within the same orbital plane, as dictated by the rotation of the SHP groups. Since all charges rotate in the same direction, the magnetic fields generated by the rotating positive charges point

¹⁷¹ Note that the ionization can be initiated not only by external radiation and a thermal process, but also by gravitational (UG) ionization. In either case, the ions and the electrons which are within their oscillation range with the SHPs, gravitated toward a potential energy minimum.

in a single direction, opposite to the direction of the contribution of the rotating negative charges.¹⁷² However, since the positive and negative charges are distributed in different sets of orbits, they are not likely to recombine, and their magnetic fields cannot entirely cancel each other out. As a result, a global planetary, stellar or galactic magnetic field may be generated.

In the specific case of Earth's magnetic field, the orbits of the dominant SHP groups were estimated in the previous section to reside within Earth's outer core. As the SHPs rotate around the center of Earth, they ionize nearby atoms and organize the free ions and electrons into separate orbits, therefore creating separate currents of ions and electrons within the outer core. These currents generate Earth's magnetic field via a dynamo effect, in accordance with current theory.

Section IX-5: The Solar Corona

Located above the Sun's transition region, the solar corona starts at about 1700 *km* above the photosphere and extends out into space without a well-defined outer boundary. The corona's energy output is nearly 10^{-6} of that of the photosphere. However, whereas the average temperature of the Sun's photosphere is 5800 kelvin, the corona's temperature is between one and three million Kelvin. The higher temperature of the corona rules out simple conduction of heat as its heating mechanism, and the exact process by which the corona is heated is still subject to debate.

A possible UG-driven theory proposes that the solar corona is located at the external minimum layer of a dominant SHP at $n = 2$, while the higher minima of $n \geq 4$ are positioned deep under the surface of the Sun, and are thus undetectable. As a result, a significantly higher density of matter is expected at the vicinity of the dominant SHP- m_p minimum $n = 2$, causing a dramatic elevation in temperature. Consequently, superheavy particles may be generated, and subsequently decay, at this minimum. Prior to their decay, these SHPs create a series of minima at which ordinary matter may concentrate to form the observed c (see figure 9.1).¹⁷³ The coronal loops may be generated by one or more superheavy particles of the same or of different masses located at varying distances from each other, thereby different loops may demonstrate entirely different structures. As new SHPs are created and then decay, coronal loops are expected to be transient. Figure 9-1 displays an observed coronal loop that appears almost identical in structure to a single lobe of the hourglass nebula MyCn18 discussed in chapter IV (a single lobe, since only the part of the overall structure that is located above the surface of the Sun is visible), suggesting that this particular coronal loop may also be generated by binary superheavy particles located at the $n = 2$ minimum.

¹⁷² In the present case, positive charges refer to ions and protons, and negative charges refer to electrons.

¹⁷³ The ionization and the strong magnetic fields created by the coronal SHPs may also play some role in determining the morphology of the coronal loops.

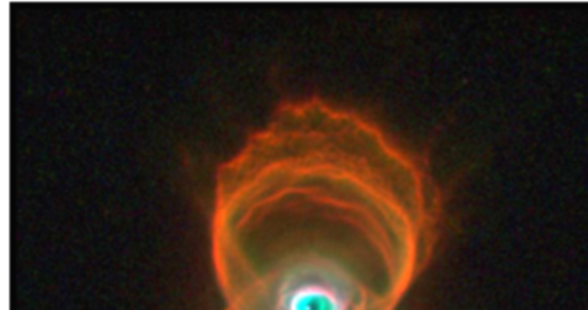
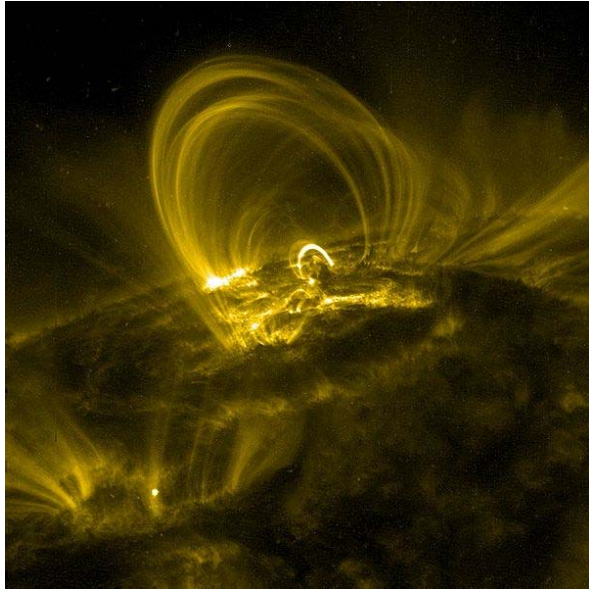


Figure 9-1: Coronal loops, image credit: TRACE NASA; <http://trace.lmsal.com/POD/TRACEpodarchive24.html>. In the fourth chapter, the hourglass structure of MyCn 18 was produced using a simple UG model of binary of stationary SHP groups. The resemblance between the structure of the coronal loop in figure 9-1 and a single lobe of MyCn 18 suggest that both structures may be governed by similar interactions.

Chapter X: The Question of Galactic Redshift Periodicity

Section X-1: Galactic Redshift Periodicity

Gravitational redshift is a well known phenomenon, first predicted by Einstein's relativity theories and then verified experimentally. According to general relativity, the redshift of a photon within the gravitational field of a non-rotating uncharged spherically symmetric mass $M_G(r)$ is viewed by a distant observer as

Equation 10-1-1

$$1 + \mathcal{L}(r) = 1 + \frac{\Delta\lambda}{\lambda} = \left(1 - \frac{2GM_G(r)}{rc^2}\right)^{-1/2}$$

where the redshift \mathcal{L} , and its equivalent velocity $v_{\mathcal{L}}$ are defined as

Equation 10-1-2

$$\mathcal{L} = \frac{\Delta\lambda}{\lambda} \text{ and } v_{\mathcal{L}} = c\mathcal{L}$$

where $\Delta\lambda$ provides the difference between the radiation wavelength measured at the inertial rest frame of the observer, denoted $\bar{\lambda}$, and the wavelength of the same radiation line emitted by a "free" atom measured at the inertial rest frame of the emitting atom, denoted λ .

Therefore, it is not surprising that the gravitational field of a galaxy may influence the amount of redshift of its radiation. However, it was not expected that the amount of redshift may show periodicity. The first researcher to observe such periodicity was William G. Tiftt in the 1970s (Tiftt, 1973). Tiftt reported that galaxies in the Coma Cluster show periodic redshift, with periodicity of about 72 km/s, followed by the later discovery of periodicity of about 36 km/s. A similar phenomenon was observed to occur in the redshift of quasars as well (Burbidge, 1968). Additional studies by Arp (Arp 1987), Tiftt (Tiftt 1980,1995, 2003), Napier (Napier, 1997) and their collaborators, conducted on larger sets of galaxies more widely distributed, seem to validate these findings. Specifically, in a limited trial on galaxies in the Virgo cluster, Bruce Guthrie and William Napier reported that away from the dense central core of the galaxy the redshifts were offset from each other in multiples of about 71 km/s, and further reported a periodicity of about 37.5 km/s in the Coma Cluster (Guthrie & Napier, 1990). While spiral galaxies were observed to display strong redshift periodicity, no significant periodicity was found for two separate groups of irregular galaxies. The increased accuracy achieved with the introduction of the 21 cm redshift measurements, and by correcting for the distortion effect caused by the velocity of the Solar System relative to the cosmic microwave background, led to the finding of additional redshift velocities.

General relativity can provide redshift periodicity to the extent reported only via a very particular distribution of matter. Such a distribution is very unlikely to form spontaneously or to persist for a long period of time. Consequently, it is quite difficult to explain the observations of

periodic redshift reported in a considerable number of galaxies. Therefore, the existence of redshift periodicity may require a paradigm shift, which can explain the great deal of skepticism among the astronomical community as to the merit of these findings. It has been suggested that the observed periodicity, or “quantization,” of galactic redshift may be due to measurement or analysis error, due to coincidence, or due to geometrical effects resulting from the correlated positions of galaxies ^(Sepulveda, 1987).

The UG theory suggests the occurrence of redshift periodicity, or quantization, resulting as a consequence of the tendency of ordinary matter to accumulate within a distinct set of potential energy minima created by the interaction between the galactic superheavy particles and the ordinary matter of the orbiting gas or objects. Substituting the distinct set of minima provided by equation 2-1-42, $r_n = \frac{bm_p M}{(2n+1)\pi - \arccos(\psi)} \rightarrow \frac{bm_p M}{(2n+1/2)\pi}$ (for $n \gg 1$), in equation 10-1-1 yields

$$1 + \mathcal{L}(r_n) = \left(1 - \frac{2GM_G(r_n)}{r_n c^2}\right)^{-1/2} \approx \left(1 - \frac{2GM_G(r_n)(2n + 1/2)\pi}{bm_p M c^2}\right)^{-1/2} \approx 1 + \frac{GM_G(r_n)(2n + 1/2)\pi}{bm_p M c^2}$$

As long as the vast majority of the mass of the galactic ordinary matter is within the distance $r < r_n$, $M_G(r_n) \approx M_G$ and $\mathcal{L}(r_n) \approx \frac{G(2n+1/2)\pi}{bm_p c^2} \left(\frac{M_G}{M}\right)$, thereby demonstrating a periodic redshift with a periodicity of $\Delta\mathcal{L} = \frac{2G\pi}{bm_p c^2} \left(\frac{M_G}{M}\right)$.¹⁷⁴ However, as the UG theory violates the equivalence principle at distances where rings or spiral arms occur, a UG analysis of redshift periodicity should not rely on an equation of general relativity. Therefore, an alternative approach is used, where the gravitational redshift is derived from the equivalence of mass and energy under special relativity.

In accordance with special relativity, the mass of the emitting electron and the masses of protons in the nucleus of the same atom deviate from their rest masses, due to their interactions with the galactic superheavy particles and ordinary matter. The rest masses of the electron and proton are denoted as m_e and m_p , and the masses of the interacting electron and proton are given by \bar{m}_e and \bar{m}_p respectively. Radiation occurs when an electron transitions from a higher energy quantum state to a lower energy quantum state, while the energy of the emitted radiation is equal to the energy difference between the two states. As the energy level of either atomic state depends on the mass of the electron as well as on the masses of protons, the emitted radiation energy measured by the distant observer will deviate from the energy measured in the inertial rest frame of an identical free atom.¹⁷⁵ Therefore, the effective masses of the electron and the protons deviate from their rest masses by a distinct set of values, resulting in a clear periodic set of wavelengths, rather than continuous radiation energies or wavelengths.

¹⁷⁴ Note that the much smaller UG contribution of the electrons was neglected.

¹⁷⁵ The effect of the galactic gravitational field on the mass of nucleons and electrons is also true for Newtonian gravitation within special relativity, with the exception that according to the UG theory, the atoms or molecules of a galaxy are likely to be arranged in the vicinity of distinct potential energy minima of the SHP-proton pairs, rather than in the continuous distribution predicted by the Newtonian theory.

The following discussion will provide a more rigorous analytical treatment of this phenomenon, specifically for the case of the hydrogen ${}^1_1\text{H}$ radiation lines. The hydrogen atom will be assumed to remain isolated and unaffected by nearby objects, and to travel in a circular orbit of radius r around a non-rotating galaxy center. The atom's orbital radius r is assumed to lie beyond the zonal oscillation range of ordinary matter of mass m_p and all but the dominant SHP type. The dominant superheavy particles of mass M are assumed to be located and at rest at the center of the galaxy. Note that the above assumptions are made for simplification, and do not significantly restrict the generality of the discussion.

Whereas the radiation energy is given by $\Delta E = h\nu = \frac{hc}{\lambda}$, where according to the law of conservation of energy, ΔE is the energy between the initial and final energy states of the emitting electron, where ν denotes the frequency of the radiation, and h is Planck's constant.

The following analysis is applied for the case of non-relativistic atom velocity, where the energy of a free particle (an electron or proton) of rest mass m and velocity u can be described accurately by the equation $E = mc^2 + \frac{1}{2}mu^2$. Initial studies of galactic redshift measured the redshift spectra of the transitions between the various hydrogen ($z = 1$) orbital levels. The electron orbital energy levels are given by¹⁷⁶

Equation 10-1-3a

$$E_{nj} = m_e c^2 - \frac{\mu Z^2 \alpha^2}{2n^2} - \frac{\mu Z^4 \alpha^4}{n^3(2j+1)} + \frac{3}{8} \frac{\mu Z^4 \alpha^4}{n^4} + \mu O(\alpha^6) = m_e c^2 + \mu \chi(n, j, z)$$

where m_e provides the rest mass of the electron, μ is the reduced mass of the electron-nucleus system in the inertial rest frame of the emitting atom, and z denotes the number of protons in the atom. The fine-structure constant α is defined as $\alpha = q_e^2 / 2hc\epsilon_0$, where q_e is the elementary charge, h is Planck's constant, c is the speed of light and ϵ_0 provides the vacuum permittivity. The quantum numbers of the hydrogen quantum states are denoted as n and j , where $n > 0$ is a positive integer, $j = \frac{1}{2}, \frac{3}{2}, \dots, n - \frac{1}{2}$, and where $\chi(n, j, z)$ is defined as

Equation 10-1-3b

$$\chi(n, j, z) = \frac{Z^2 \alpha^2}{2n^2} - \frac{Z^4 \alpha^4}{n^3(2j+1)} + \frac{3}{8} \frac{Z^4 \alpha^4}{n^4} + O(\alpha^6)$$

Note that $\chi(n, j, z)$ is independent of the masses of the protons and the electron. In the case of the hydrogen atom ${}^1_1\text{H}$, $z = 1$ and $\mu = \frac{m_e m_p}{m_e + m_p}$.

The wavelength of the radiation due to the electron's transition from level $E_{n_1 j_1}$ to level $E_{n_2 j_2}$ is subsequently given by

¹⁷⁶ For further reading, see *Quantum Field Theory* by Claude Itzykson and Jean-Bernard Zuber, Dover Publication, Inc., Mineola, New York, 2005.

Equation 10-1-4

$$\lambda = \frac{hc}{E_{n_2 j_2} - E_{n_1 j_1}} = \frac{hc}{\mu(\chi(n_2, j_2, z) - \chi(n_1, j_1, z))}$$

The observer is assumed to be positioned at sufficient distance from the galaxy to remain unaffected by its gravitational field. However, as the galactic superheavy particles and ordinary matter are expected to influence the masses of the electron and proton of the emitting hydrogen atom, and therefore its reduced mass $\bar{\mu}$, the actual observed radiation is equal to

Equation 10-1-5

$$\bar{\lambda} = \frac{hc}{\bar{\mu}(\chi(n_2, j_2, z) - \chi(n_1, j_1, z))}$$

where the redshift \mathcal{L} of the electron's orbital energy level is given by

Equation 10-1-6

$$\mathcal{L} = \frac{\bar{\lambda} - \lambda}{\lambda} = \left(\frac{1}{\bar{\mu}} - \frac{1}{\mu} \right) \mu = \frac{\mu}{\bar{\mu}} - 1$$

Defining $K_p = \frac{\bar{m}_p}{m_p}$ and $k_e = \frac{\bar{m}_e}{m_e}$ as the respective mass ratios of the proton and the electron, and substituting μ , $\bar{\mu}$, K_p and k_e for the case of hydrogen 1_1H ($z = 1$) in equation 10-1-6 yields

Equation 10-1-7

$$\mathcal{L} = \frac{\frac{m_e m_p}{m_e + m_p}}{\frac{k_e m_e K_p m_p}{k_e m_e + K_p m_p}} - 1 = \frac{1}{k_e} \frac{(k_e/K_p)m_e + m_p}{m_e + m_p} - 1$$

where $m_e \ll m_p$, and with the exception of extreme gravitational fields,

$(k_e/K_p)m_e \ll 1836m_e = m_p$. Therefore, $\mathcal{L} = \frac{1}{k_e} - 1$.

Later studies of redshift periodicity started using the more sensitive 21 *cm* line for quantifying redshift. The 21 *cm* line is assumed to be created by the magnetic field induced by the nucleus magnetic moment, resulting in the splitting of the triplet and the singlet spin state energy levels (this energy split is also called the hyperfine structure). The energy difference between the triplet and the singlet spin states at the ground level of the electron is given by

Equation 10-1-8

$$\Delta E_{hf_{n=1, j=1/2}} = \frac{4}{3} \mu \frac{m_e}{m_p} \alpha^4 g_p$$

where g_p provides the reduced gyromagnetic ratio of the proton. Following the same process, the \mathcal{L} redshift of the 21 *cm* line is given by

Equation 10-1-9

$$\mathcal{L} = \left(\frac{\frac{m_e m_p}{m_e + m_p}}{\frac{k_e m_e K_p m_p}{k_e m_e + K_p m_p}} \right) \left(\frac{\frac{m_e}{m_p}}{\frac{k_e m_e}{K_p m_p}} \right) - 1 = \frac{1}{k_e} \frac{m_e + (K_p / k_e) m_p}{m_e + m_p} - 1$$

Assuming that $(K_p / k_e) m_p \gg m_e$ provides

Equation 10-1-10a

$$\mathcal{L} = \frac{K_p}{k_e} - 1$$

If, in addition, $K_p \approx k_e$,

Equation 10-1-10b

$$\mathcal{L} = \frac{1}{k_e} - 1$$

yielding the same results as obtained for the case of the regular spectra of the hydrogen atom.

As observed, and demonstrated by the theory developed in Chapter III, the rotational velocities within and external to the galactic disk relative to the galaxy center are of the order of hundreds of km/s , too slow to cause any appreciable relativistic effects. This is also true in the case of an observer located outside of the given galaxy moving at a non-relativistic velocity relative to the galactic center. Therefore, no velocity-related relativistic corrections are required. However, according to Einstein's mass equation for a bonded electron-proton pair within a hydrogen atom $\frac{1}{2}H$, viewed by a distant observer, the energy of the proton is given by

Equation 10-1-11

$$\bar{m}_p c^2 = K_p m_p c^2 = m_p c^2 - \frac{G m_p M N_M}{a} \left(e^{a/r} \cos \left(\frac{b m_p M}{r} \right) - 1 \right) + \frac{1}{2} m_p u^2 - \frac{G m_p M_g(r)}{r} + E_{bond}$$

where E_{bond} provides the overall bonding energy of the proton to the electron, which must be negative,¹⁷⁷ \vec{u} is the rotational velocity of the atom around the galaxy center, and $M_g(r)$ is the mass of the ordinary matter within a sphere of radius r from the galaxy center. Additionally, the distribution of the galactic ordinary matter around the center of the galaxy is assumed to be spherically symmetric. Therefore,

Equation 10-1-12

$$(K_p - 1) m_p c^2 = - \frac{G m_p M N_M}{a} \left(e^{a/r} \cos \left(\frac{b m_p M}{r} \right) - 1 \right) + \frac{1}{2} m_p u^2 - \frac{G m_p M_g(r)}{r} + E_{bond}$$

Over time, the rotating atom is likely to gravitate toward an orbital radius near a potential energy minimum. Since the force applied on the proton at any of the minima is zero, the orbit

¹⁷⁷The value of E_{bond} must be negative in order for the electron to bond with the proton. In the general case, where the atom is part of a molecule or a larger object, E_{bond} may denote the overall bonding energy of the proton to the object as a whole. However, for simplicity, the current scenario deals with an isolated hydrogen atom.

must shift slightly from the minimum to allow the resultant gravitational force to balance the centrifugal force. However, due to the steep slopes of the potential energy at zonal indices $k \gg 0$, the orbital radii at which the overall energy minima occur must be very close to the radii where the overall potential energy of the atom has a local minimum. Using equation 2-1-42 and restricting the discussion to distances of $a \ll r \ll bm_p M$, where $MN_M \ll M_G(r)$ and $r <$

$\frac{(bm_p)^2 M^3 N_M}{aM_G(r)}$ confines the potential energy minima of the proton or the atom to

Equation 10-1-13a

$$r_{n_p} = \frac{bm_p M}{(2n_p + 1)\pi - \arccos(\psi_p)}$$

where $\psi_p = \frac{aM_G(r_{n_p})}{(bm_p)^2 M^3 N_M} r_{n_p}$ for $r_{n_p} \ll bm_p M$ or $n_p \gg 1$. For sufficiently large n_p (and therefore, sufficiently small r_{n_p}), $\psi_p \approx 0$, and

Equation 10-1-13b

$$r_{n_p} \approx \frac{bm_p M}{(2n_p + 1/2)\pi}$$

As $r_{n_p} \gg a$, equation 10-1-12 can be rearranged as follows:

Equation 10-1-14

$$K_p \approx 1 + \frac{GMN_M}{ac^2} \left[1 - \left(1 + \frac{a}{r} \right) \cos \left(\frac{bm_p M}{r} \right) \right] + \frac{1}{2} \left(\frac{u}{c} \right)^2 - \frac{GM_g(r)}{rc^2} + \frac{E_{bond}}{m_p c^2}$$

or

$$K_p \approx 1 + \frac{GMN_M}{ac^2} \left[1 - \cos \left(\frac{bm_p M}{r} \right) \right] + \frac{1}{2} \left(\frac{u}{c} \right)^2 - \frac{GM_g(r)}{rc^2} + \frac{E_{bond}}{m_p c^2}$$

At the range of interest $M_g(r) \gg MN_M$, substituting equation 10-1-13b in equation 10-1-14 provides a minimum contour at

Equation 10-1-15

$$K_p = 1 + \frac{GMN_M}{ac^2} - \frac{GM_g(r_{n_p})(2n_p + 1/2)\pi}{bMm_p c^2} + \frac{1}{2} \left(\frac{u}{c} \right)^2 + \frac{E_{bond}}{m_p c^2}$$

Similarly, for the electron,

Equation 10-1-16

$$\bar{m}_e c^2 = k_e m_e c^2 = m_e c^2 - \frac{Gm_e MN_M}{a} \left(e^{a/r} \cos \left(\frac{bm_e M}{r} \right) - 1 \right) + \frac{1}{2} m_e u^2 - \frac{Gm_e M_g(r)}{r} + E_{bond}$$

or

Equation 10-1-17

$$k_e = 1 + \frac{GMN_M}{ac^2} \left[1 - \cos \left(\frac{bm_e M}{r} \right) \right] + \frac{1}{2} \left(\frac{u}{c} \right)^2 - \frac{GM_g(r)}{rc^2} + \frac{E_{bond}}{m_e c^2}$$

The electron and the proton are bonded together, and thus travel at the same velocity around the galaxy center. However, as the masses of the electron and the proton differ substantially, the locations of the potential energy minima of their interaction with a superheavy particle of mass M vary accordingly. Since the proton mass is over 1,836 times larger than the mass of the electron, the atom is expected to reside near a minimum of the proton-SHP interaction, which may be at substantial distance from any minimum of the SHP-electron interaction. The electron is therefore subject to the UG gravitational force, which aims to draw the electron toward a UG potential energy minimum. However, the electron is usually prevented from migrating toward this minimum by its electromagnetic interaction with the proton. Hence, for the case of a non-ionized hydrogen atom, the location of the electron is given by

$r_{n_p} \approx \frac{bm_p M}{(2n_p+1/2)\pi}$, rather than by $r_{n_e} \approx \frac{bm_e M}{(2n_e+1/2)\pi}$. Substituting r_{n_p} for r in equation 10-1-17 provides

Equation 10-1-18

$$k_e = 1 + \frac{GMN_M}{ac^2} \left(1 - \cos \left(\frac{m_e}{m_p} (2n_p + 1/2)\pi \right) \right) + \frac{1}{2} \left(\frac{u}{c} \right)^2 - \frac{GM_G(2n_p + 1/2)\pi}{bMm_p c^2} + \frac{E_{bond}}{m_e c^2}$$

Using equations 10-1-15 and 10-1-18 yields

Equation 10-1-19

$$\begin{aligned} k_e &\approx K_p - \frac{GMN_M}{ac^2} \cos \left(\frac{m_e}{m_p} (2n_p + 1/2)\pi \right) + E_{bond} \left(\frac{1}{m_e c^2} - \frac{1}{m_p c^2} \right) \\ &= K_p - 1.3 * 10^{-14} MN_M \cos \left(0.00171(2n_p + 1/2) \right) + E_{bond} \left(\frac{1}{m_e c^2} - \frac{1}{m_p c^2} \right) \end{aligned}$$

The value of MN_M can be estimated from the rotational velocity of a typical spiral galaxy, shown in section VI-3 of chapter VI to be equal to $u \approx \left(\frac{4GMN_M}{a} \right)^{1/2}$. Thus, for a rotational velocity of $u = 300 \text{ km/sec}$, $MN_M \approx \frac{au^2}{4G} = 1.92 * 10^7 \text{ kg}$, which is far smaller than the overall galactic mass by a factor of the order of at least 10^{33} . Therefore,

$$0 \text{ J} < \left| 1.3 * 10^{-14} MN_M \cos \left(0.00171(2n_p + 1/2) \right) \right| < 2.5 * 10^{-7} \text{ J} \text{ and } \frac{1}{2} \left(\frac{u}{c} \right)^2 \approx 5 * 10^{-7} \text{ J}.$$

The magnitude of the term $E_{bond} \left(\frac{1}{m_e c^2} - \frac{1}{m_p c^2} \right)$ depends on the quantum state of the hydrogen atom. At the lowest ground state, $E_{bond} = -13.6 \text{ eV}$, and therefore $-13.6 \text{ eV} \leq E_{bond} < 0 \text{ eV}$.

Consequently, $0 \text{ J} \leq E_{bond} \left(\frac{1}{m_e c^2} - \frac{1}{m_p c^2} \right) < 2.656 * 10^{-5} \text{ J}$. As long as the value of

$$\frac{G(2n_p+1/2)\pi}{bm_p c^2} \left(\frac{M_G}{M} \right) \gg 2.7 * 10^{-5} \text{ J},$$

Equation 10-1-20

$$K_p \approx k_e \approx 1 - \frac{G(2n_p+1/2)\pi}{bm_p c^2} \left(\frac{M_G}{M} \right)$$

Substituting equation 10-1-20 in equation 10-1-7 (or equation 10-1-10b) yields the \mathcal{L} shift for the hydrogen orbital lines (as well as for the 21 cm line), given by

Equation 10-1-21

$$\mathcal{L} = \frac{1}{k_e} - 1 = \frac{1 - k_e}{k_e} \approx \frac{\frac{G(2n_p + 1/2)\pi}{bm_p c^2} \left(\frac{M_G}{M}\right)}{1 - \frac{G(2n_p + 1/2)\pi}{bm_p c^2} \left(\frac{M_G}{M}\right)}$$

Therefore, as long as $2.7 * 10^{-5} \ll \frac{G(2n_p + 1/2)\pi}{bm_p c^2} \left(\frac{M_G}{M}\right) \ll 1$,

Equation 10-1-22

$$\mathcal{L} \approx \frac{G(2n_p + 1/2)\pi}{bm_p c^2} \left(\frac{M_G}{M}\right)$$

where n_p is an integer. Note that \mathcal{L} demonstrates periodic behavior with a periodicity of

Equation 10-1-23

$$\mathcal{L}_{periodicity} = \frac{2G\pi}{bm_p c^2} \left(\frac{M_G}{M}\right)$$

Note that this intrinsic redshift is in addition to the expected redshift contributed by the velocity of the galaxy relative to the observer.

Using equation 10-1-23, a redshift periodicity of $\mathcal{L}_{periodicity} = \frac{72}{300000} = 2.42 * 10^{-4}$, which is equivalent to the reported redshift velocity of 72 km/sec, leads to¹⁷⁸

$\mathcal{L}_{periodicity} \approx \left(\frac{2G\pi}{bm_p c^2}\right) \frac{M_G}{M} \approx 3.093 * 10^{-44} \frac{M_G}{M} = 2.42 * 10^{-4}$. To achieve a periodicity of $\mathcal{L}_{periodicity} = 2.42 * 10^{-4}$, the ratio of the overall galaxy mass and the dominating SHP mass M is given by $\frac{M_G}{M} = 7.825 * 10^{39}$.

Similar calculations provide a value of $\frac{M_G}{M} = 3.9125 * 10^{39}$ for the case of $v_z = 36$ km/sec.

The above analysis, in addition to the fact that galaxies and galactic clusters are observed to produce a distinct set of redshifts with the same periodicity values shared by a significant number of unrelated galaxies, suggests that the ratios $\frac{M_G}{M}$ between the mass of the galactic center and the mass of the SHP tend to assume specific values.

¹⁷⁸ Note that the resultant periodicity of the redshift $\mathcal{L}_{periodicity} \approx 2.42 * 10^{-4}$ is indeed larger than the value $2.7 * 10^{-5}$ by a factor of 10 (even at the lowest $n_p = 1$ value) and less than 1 for all $0 < n_p < 4132$, fulfilling, within this range, the conditions required for the assumption that $K_p \approx k_e \approx 1 - \frac{GN_M k \pi}{bm_p c^2} \left(\frac{M_G}{M_N M}\right)$.

Section X-2: Unified Gravitation and the Redshifts of Quasars

Quasars, or quasi-stellar objects, are astronomical objects that are observed to emit highly redshifted radiation. According to the standard model of cosmology, large redshifts are interpreted as Doppler shifts, which lead to the following conclusions:

1. The large radiation redshifts observed in quasars indicates that they must recede from us at very high speeds.
2. More than 200,000 quasars are known with redshifts ranging between 0.06 and 6.5. Applying Hubble's law, which indicates that the velocity at which various galaxies are receding from Earth is proportional to their distance from us, leads to the conclusion that the known quasars are located between 790 million and 28 billion light years away from us, with most calculated to be over three billion light years away.
3. As the brightness of an object reduces proportionally to the square of its distance from the observer, quasars are presumed to be extremely luminous objects, radiating at rates that can exceed the output of average galaxies.
4. The great distances calculated between Earth and the known quasars lead to the conclusion that quasars were much more common in the early universe.

The assumption that substantial redshifts are due exclusively to Doppler effects has led to far-reaching conclusions. This assumption was challenged by Halton Arp's claim that the redshifts of quasars are not always an indication of their distances or their ages, as currently believed (Arp, 1988). Arp contested that many quasars with otherwise high redshifts can be linked to nearby objects of significantly lower redshifts, and are therefore nearby.

According to special relativity, the masses of the electron \bar{m}_e and the proton \bar{m}_p , as viewed by an external observer, cannot be negative, and therefore k_e and K_p cannot be negative. In the case of sufficiently small values of $\frac{M_G}{M}$ and n_p , the term $\frac{GM_G(2n_p+1/2)\pi}{bMm_p c^2}$ in equation 10-1-18 is negligible, and k_e may assume values greater or less than 1. Thus, the object's radiation frequency may either be blueshifted or redshifted due to gravitation. On the other extreme, in the case of $\frac{GM_G(2n_p+1/2)\pi}{bMm_p c^2} > \left| 1 + \frac{GMNM}{ac^2} \left(1 - \cos \left(\frac{m_e}{m_p} (2n_p + 1/2)\pi \right) \right) + \frac{1}{2} \left(\frac{u}{c} \right)^2 + \frac{E_{bond}}{m_e c^2} \right|$, k_e of equation 10-1-18 assumes a negative value, which is forbidden by special relativity. The physical meaning of this discrepancy is that the given emitting atom lies within the horizon of the object, thus its radiation is trapped in a black hole and cannot reach the external observer.

According to equation 10-1-18, at distance ranges where $1 > \frac{GM_G(2n_p+1/2)\pi}{bMm_p c^2} \gg \left| \frac{GMNM}{ac^2} \left(1 - \cos \left(\frac{m_e}{m_p} (2n_p + 1/2)\pi \right) \right) + \frac{1}{2} \left(\frac{u}{c} \right)^2 + \frac{E_{bond}}{m_e c^2} \right|$, $0 < k_e < 1$, and according to equation 10-1-7 (or 10-1-10b), the radiation redshift due to the gravitational interaction is given by $\mathcal{L} = \frac{1}{k_e} - 1 > 0$.

The matter trapped by the object is expected to accumulate mainly in vicinity of the potential energy minima. As noted above, at sufficiently high n_p indices, the radiation is trapped within a black hole, and cannot escape or be detected by the distant observer. Denote $n_{p,max}$ as the largest even integer index at which $k_e \approx 1 - \frac{G(2n_{p,max}+1/2)\pi}{bm_p c^2} \left(\frac{M_G}{M}\right) > 0$, where a minimum occurs.¹⁷⁹ As the potential energy slope is especially steep near a black hole horizon, and as the minimum $n_{p,max}$ is the closest minimum to the horizon, the density of ordinary matter in the vicinity of $n_{p,max}$ is likely to be significantly greater than the density anywhere external to the horizon. Hence, the redshift associated with the $n_{p,max}$ minimum may dominate the observed spectrum.¹⁸⁰

Following equation 10-1-21, in the case where $1 > \frac{G(2n_{p,max}+1/2)\pi}{bm_p c^2} \left(\frac{M_G}{M}\right) \rightarrow 1$, the redshift of the observed radiation will approach infinity. In cases where, in addition, $2 < n_{p,max} < 4$, most of the radiation emitted by the star is extremely redshifted, as observed in quasars. Thus, the astronomical object is expected to provide an intrinsic redshift that is significantly larger than the Doppler redshift created by the object's velocity relative to the observer. Therefore, according to the theory of unified gravitation, it is very possible that Arp's claim is in fact true, and that at least some of the observed quasars may be substantially closer, younger, smaller and less luminous than currently believed.

¹⁷⁹ Therefore, $n_{p,max}$ is the largest even integer where $k_e \approx 1 - \frac{G(2n_{p,max}+1/2)\pi}{bm_p c^2} \left(\frac{M_G}{M}\right) > 0$ and where the minimum is not washed out by the contribution of the object's ordinary matter.

¹⁸⁰ Note that the effect of the SHP rotation as well as the Doppler effect due to the relative speed between the distant galaxy and the observer, or due to the velocity of the emitting atom relative to the center of galaxy, are assumed in the present case to be relatively small.

Chapter XI: The UG Theory and Deep Inelastic Scattering (DIS)

Deep inelastic scattering experiments (DIS) provided the initial motivation for the development of a hadron constituent model. Deep inelastic electron-proton scattering experiments of the 1960s¹⁸¹ revealed a surprising weak fall-off of the deep inelastic cross sections with increasing q^2 and exhibited a scaling behavior previously predicted by Bjorken (Bjorken, 1969). Both observations strongly suggested the existence of a substructure in protons and neutrons. A preceding constituent model proposed by Richard Feynman offered a simple dynamical interpretation of the DIS results. Feynman postulated partons as the elementary constituents of hadrons, yet specified their identity only as far as basic particles relating under the strong interaction. Further development linked the parton model with the concept of quarks. Quarks, which were proposed independently by Gell-Mann (Gell-Mann, 1964) and Zweig as mathematically convenient building blocks of unitary symmetry, were the natural candidates for these elementary constituents. The early constituent quark model faced significant obstacles. To begin with, quarks had never been observed directly. The fact that quarks were never observed should have been explained by very strong interactions in their final state. The theory, however, required that the constituents of hadrons behave as free particles during virtual photon absorption. In addition, experimental results demanded significantly more than three constituents within the nucleon substructure. Resolving these, as well as additional inconsistencies, led to enhancements in the quark model and to the development of quantum chromodynamics (QCD). This resulted in a powerful, yet significantly more complex theory, postulating the additional concepts of gluons, colors, sea of quarks, quark confinement and the property of asymptotic freedom, with heavy reliance on renormalization techniques.

The quark and QCD models seem to provide adequate explanations for all available experimental data. Therefore, a choice has been made to first establish the credibility of the UG theory in the cosmic realm, where inconsistencies within the current theory are well documented. In this chapter, the UG theory will be employed on nuclear scale. It will be shown that the UG zonal structure generated by the interaction between two massive particles creates a dynamic substructure that naturally leads to the observed large-angle scattering, as well as to the weak fall-off of the DIS cross section, and provides a scaling phenomenon that resembles Bjorken scaling. Since the substructure is due to the interaction between a pair of particles, rather than due to constituent sub-particles, the UG theory does not require the assumption of quarks as real elementary particles.¹⁸²

Since the acceptance of quantum chromodynamics in the early 1970s, the quark structure of hadrons has become the dominant framework for theory development and experimental design. As a result, a significant portion of data collected from deep inelastic scattering has

¹⁸¹ at the Stanford Linear Accelerator Center (SLAC)

¹⁸² Note, however, that the UG theory does not necessarily contradict the existence of quarks as elementary constituents of hadrons.

generally been analyzed within this framework, and reflects its embedded assumptions. Some parameters commonly used in data presentation are

Equation 11-1

$$Q^2 = 4E_0E_f \sin^2\left(\frac{\theta}{2}\right) = -q^2$$

and

Equation 11-2

$$\chi = \frac{Q^2}{2Mc^2\nu}, \quad y = \frac{\nu}{E_0} = \frac{(1 - \cos(\theta))}{2}$$

where q denotes the four-momentum transfer function, E_0 represents the energy of the incident lepton, E_f represents the energy of the scattered lepton, ν provides the energy loss of the scattered lepton, or $\nu = E_0 - E_f$, θ indicates the scattering angle, M is the mass of the nucleon, χ is the Bjorken scale variable, y provides the fraction of the lepton's energy loss in the rest frame of the nucleon, and c is the speed of light. Reported experimental data commonly provides the values of the nucleon structure functions F_i as functions of some of the above parameters, as demonstrated in figure 11-7. According to the quark-QCD model, in the case of a high-energy DIS mediated by virtual photon exchange, the structure functions relate to the double differential cross section via the equation (see Devenish & Cooper-Sarkar, 2004)

Equation 11-3

$$\frac{d^2\sigma}{dq^2 dx} = \frac{4\pi\alpha^2}{Q^4\chi} [(1 - y)F_2(\chi, Q^2) + xy^2F_1(\chi, Q^2)]$$

where α is the fine structure constant. The experimental data is often presented in the form of the nucleon structure functions F_1 and F_2 after being subjected to a series of data processing routines, such as radiative corrections and Monte Carlo simulations, which are heavily dependent on the assumptions of the QCD model. The incorporation of these underlying assumptions within the data complicates the ability to apply the data to a new theory with an entirely different set of assumptions. Therefore, the following discussion will present evidence that the UG theory predicts DIS behavior using a related, yet not identical set of parameters.

According to the QCD model, the strong force acts between quarks and is mediated by gluons, while lepton-nucleon interactions are viewed as an electromagnetic interaction between charged leptons and charged quarks within the nucleons. Therefore, according to quantum chromodynamics, the fundamental process in DIS experiments is the electromagnetic scattering of two spin-1/2 point-like particles. In contrast, the UG model holds that there is no fundamental difference in the interactions between two nucleons, two leptons, or interactions involving a lepton and a nucleon. All of the above particles have a charge,¹⁸³ a mass and a spin,

¹⁸³ The electrical charge is equal to $\pm q_e$ or 0, where q_e denotes the charge of a proton.

and are assumed to interact with each other in accordance with the theory of unified gravitation and the electromagnetic theory.¹⁸⁴ According to the proposed UG model, the large scattering angles observed in high-energy collisions between a nucleon and a lepton are mainly attributed to the UG zone structure between the two colliding particles, rather than to electromagnetic interactions between the lepton and a hadron with a substructure composed of several elementary constituents. Historically, the quark-parton model (QPM) grew out of an attempt to provide a simple model to explain the results of the early deep inelastic scattering experiments, where the function F_2 was discovered to be independent of Q^2 at $\chi \approx 0.25$. QPM assumes that the nucleon consists of non-interacting point-like particles which serve as scattering centers. In contrast, according to the UG model, the UG gravitational field produced by the interaction between a rapidly approaching particle and a nucleon is viewed by the particle as an ‘onion’ with an infinite number of repulsive layers separated by attractive layers, where the layers consist of the potential energy maxima or minima respectively. It will further be demonstrated that due to relativistic spacetime distortion, the shape and size of the ‘onion’ and its layers are strongly affected by the momentary speed of the approaching particle, and may change drastically as the speed of the particle is reduced near the point of closest approach during a DIS event. The number of layers penetrated by the electron will be shown to depend mainly on the initial energy of the probing particle and on its impact parameter. Therefore, the idea of scattering by a sea of quarks is replaced by the concept of scattering via some of an infinite number of UG zones, where the zonal indices that contribute to the scattering are mainly determined by the impact parameter and by the overall energy of the probing particle.

The following analysis deals with a DIS collision between a nucleon and an electron. Note that the discussion is not limited to a collision between an electron and a nucleon, and may be extended to cover collisions between any two leptons, two nucleons, a lepton and a nucleon, or between any two massive particles. However, the discussion is limited to cases where the probing particle survives the collision.

Section XI-1-1: The Effect of the Velocity of Colliding Particles on Their UG Interaction

Based on the second UG postulate, equation 2-1-1 is valid when the interaction between a nucleon and an electron is viewed in the rest frame of the nucleon. For simplicity, the origin of the frame is set to coincide with the location of the nucleon. According to special relativity, the rest mass of the electron m_e and the distance r should be replaced by $m_e\gamma(v)$ and $r_d =$

$\sqrt{r^2 - \frac{v^2}{c^2} r_{\parallel}^2}$ respectively,¹⁸⁵ where \vec{v} is the velocity of the electron relative to the nucleon and r_{\parallel} is the distance component that is parallel to \vec{v} . Figure 11-1 provides the initial geometry of an electron-nucleon scattering, where a highly relativistic electron with the initial velocity of

¹⁸⁴ Note that this book does not deal with the weak force, which is viewed by the standard model as a separate force.

¹⁸⁵ To calculate r_d , $r^2 = r_{\parallel}^2 + r_{\perp}^2 + r_x^2$, where r_{\parallel} contracts to $r_{\parallel}/\gamma(v)$, $r_d^2 = r_{\parallel}^2/\gamma^2(v) + r_{\perp}^2 + r_x^2$. Thus, $r_d^2 = r^2 - r_{\parallel}^2 + r_{\parallel}^2/\gamma^2(v) = r^2 - r_{\parallel}^2(1 - \gamma^{-2}(v))$, or $r_d = \sqrt{r^2 - \frac{v^2}{c^2} r_{\parallel}^2}$.

$v = v_z = v_0$ and an impact parameter of B approaches the nucleon. The contribution of the nucleon to the UG potential energy of the electron is given by¹⁸⁶

Equation 11-4

$$V_G(\vec{r}, \vec{v}) = -\frac{Gm_em_p\gamma(v)}{a} \left(e^{a/\sqrt{r^2 - \frac{v^2}{c^2}r_{\parallel}^2}} \cos\left(\frac{bm_em_p\gamma(v)}{\sqrt{r^2 - \frac{v^2}{c^2}r_{\parallel}^2}}\right) - 1 \right)$$

where m_p is the rest mass of the nucleon and $r = \sqrt{x^2 + y^2 + z^2} = \sqrt{y^2 + z^2}$ when the x axis is selected to be perpendicular to the plane containing the vectors \vec{r} and \vec{v} . Note that at non-relativistic velocities, or when the vectors \vec{r} and \vec{v} are perpendicular, r coincides with the distance between the electron and the nucleon. At relativistic velocities, the true distance between these two particles is less than r , and is further dependent on the magnitude and the direction of the relative velocity \vec{v} . According to special relativity, only the distance component that is parallel to the relative velocity is contracted. This parallel component is given by

Equation 11-5

$$r_{\parallel} = r\cos(\theta) = \sqrt{r^2 - B^2} = r(1 - (B/r)^2)^{1/2}$$

Therefore, the variable \vec{r} (or r) should be considered as a parameter of the electron's trajectory, rather than the distance between the electron and the nucleon. In cases where the velocities are relativistic (and therefore, r may not be equal to the actual distance as viewed in the inertial frame of the nucleon) r will be referred to as the parametric distance, while the actual distance viewed in the nucleon's inertial frame of reference will be referred to as the apparent distance. At distances where $r \gg B$, $r_{\parallel} \approx r$, and equation 11-4 reduces to

Equation 11-6

$$V_G(\vec{r}, \vec{v}) = -\frac{Gm_em_p\gamma(v)}{a} \left(e^{a\gamma(v)/r} \cos\left(\frac{bm_em_p\gamma^2(v)}{r}\right) - 1 \right)$$

¹⁸⁶ Note that in the general case, the electron's potential energy V_G depends on the vectors \vec{r} and \vec{v} . However, in cases where it is clear that either v_{\parallel} or v_{\perp} are relatively insignificant, the notation $V_G(r, v)$ or $V_G(r, \gamma(v))$ may be used. For example, see equations 11-6 for the case of $v_{\perp} = 0$, or equation 11-7 for the case of $v_{\parallel} = 0$. In cases of non-relativistic velocity, where V_G becomes independent of v , the notations $V_G(r, \gamma(v) = 1)$ or $V_G(r)$ may be used.

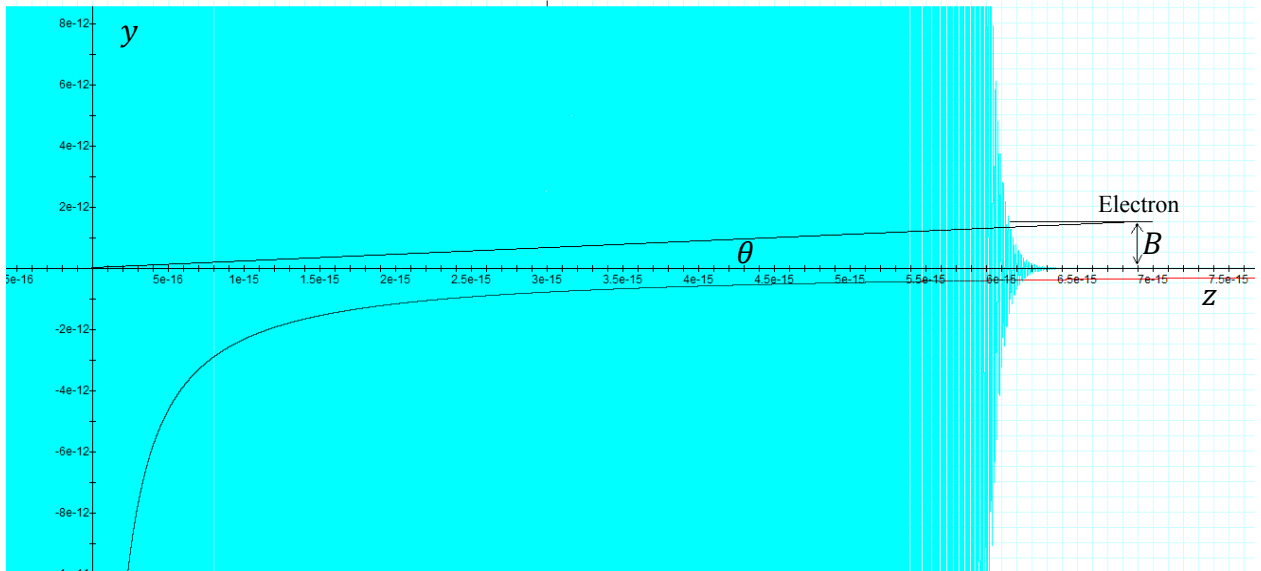


Figure 11-1a: An electron with an impact parameter of B approaches the nucleon at a velocity that corresponds with $\gamma(v) = 10$ in the direction parallel to the z axis. At this speed, the potential energy due to the UG force is provided in cyan and the electromagnetic force is provided in red for the case where the nucleon is a proton. The UG pattern (cyan) remains stable as long as the electron is located at sufficient distance from the nucleon and its velocity is about constant. As the electron approaches the nucleon, its UG potential energy increases abruptly to equal the overall energy of the electron (at about 6.3 fm), causing the electron to decelerate. As the electron's velocity is reduced, the UG pattern and the Coulomb potential energy collapse toward the proton, demonstrating the folding of the zonal structure described in section XI-2-2.

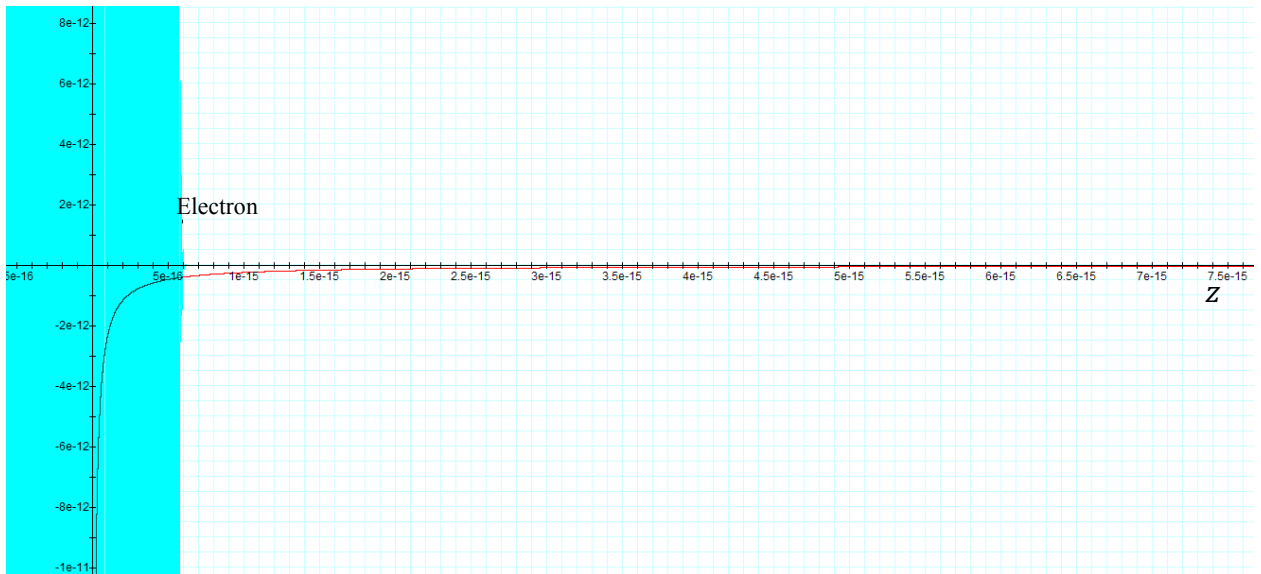


Figure 11-1b: Provides the contributions of the UG and the electromagnetic potential energy patterns as perceived by the electron after its speed is reduced to non-relativistic velocity, where $\gamma(v) = 1$.

Of special interest is the point of closest approach \vec{r}_{pca} of the electron to the nucleon, measured in the particle accelerator's frame of reference. As \vec{r}_{pca} is the closest point on the electron's trajectory toward the nucleon, its parallel component $r_{pca\parallel}$ must be equal to zero, and

the perpendicular component $r_{pca\perp}$ must be equal to r_{pca} ($r_{pca} = |\vec{r}_{pca}|$). Therefore, in the vicinity of the point of closest approach, equation 11-4 reduces to

Equation 11-7

$$V_G(\vec{r}, \vec{v}) = -\frac{Gm_em_p\gamma(v)}{a} \left(e^{a/r} \cos\left(\frac{bm_em_p\gamma(v)}{r}\right) - 1 \right)$$

At non-relativistic electron velocities, equation 11-4 becomes independent of v and reduces to¹⁸⁷

Equation 11-8

$$V_G(r) = V_G(\vec{r}, \vec{v}) = -\frac{Gm_em_p}{a} \left(e^{a/r} \cos\left(\frac{bm_em_p}{r}\right) - 1 \right)$$

It is important to realize that if the velocity of the electron remains relativistic throughout its entire journey, the scattering angle would be relatively small, and the scattering of the electron by the nucleon would not be highly inelastic (for example, see the trajectory of the electron in figure 11-3b, indicated in black). On the other extreme, in cases of deep inelastic scattering at the limit where the energy lost by the electron $\nu = (E_0 - E_f) \rightarrow \infty$ and $Q^2 = 4E_0E_f \sin^2\left(\frac{\theta}{2}\right) \rightarrow \infty$, the velocity of the electron in the vicinity of the point of impact (or the point of closest approach), denoted $\nu(\vec{r}_{pca})$, must become negligible, thus $\gamma(\nu(\vec{r}_{pca})) \rightarrow 1$ (see the electron trajectories in figure 11-3b, indicated in blue and green).¹⁸⁸ Due to their importance, events that provide extremely high values of ν and Q^2 will be classified as ‘high-loss deep inelastic events.’

The maxima and minima of the electron’s potential energy can be derived via $\vec{\nabla}V_G(\vec{r}, \vec{v}) = 0$. At non-relativistic velocities (which is the case in the immediate vicinity of the electron’s point of closest approach \vec{r}_{pca} during a high-loss DIS event), $\gamma(\nu(\vec{r}_{pca})) = 1$ and the potential energy minima and maxima occur only when

Equation 11-9a

¹⁸⁷ Note that at $\mathbf{z} \gg \mathbf{B}$, or when \vec{v} is perpendicular to \vec{r} , the potential energy $V_G(\vec{r}, \vec{v})$ is reduced to depend on r and ν (or $\gamma(\nu)$). At shorter distances, where \mathbf{z} approaches the impact parameter \mathbf{B} , V_G becomes dependent on ν , r_{\parallel} and r_{\perp} . In the non-relativistic case, V_G depends exclusively on r . Therefore, the notations $V_G(r, \gamma(\nu) = 1)$ and $V_G(r)$ will be used interchangeably throughout this chapter.

¹⁸⁸ The logic behind this statement is as follows: The initial energy E_0 of the electrons is fixed by the experimental setup. $Q^2 = 4E_0E_f \sin^2\left(\frac{\theta}{2}\right)$ increases as E_f increases and as $\theta \rightarrow \pi$. The energy loss of the scattered electron $\nu = (E_0 - E_f)$ is not directly dependent on the scattering angle θ , but increases with decreasing E_f . Thus, increasing E_f will increase Q^2 and decrease ν , and vice versa. Therefore, other than setting the highest possible value of the electrons’ initial energy E_0 , high values of both $\nu = (E_0 - E_f)$ and $Q^2 = 4E_0E_f \sin^2\left(\frac{\theta}{2}\right)$ can be achieved when E_f is within a specific range of energy values, and when the scattering angle θ is as close as possible to π . With this scattering geometry, the electron and the nucleon nearly undergo a head on collision, where the relative velocity of the electron nearly reduces to zero at the point of closest approach \vec{r}_{pca} . Hence, $\gamma(\nu(\vec{r}_{pca})) = 1$. As will be discussed later on in the chapter, the electron in such a case is effectively scattered by a hard sphere.

$$\vec{\nabla}V_G(\vec{r}, \vec{v}) = \frac{\partial V_G}{\partial r} \hat{r} = \frac{Gm_e m_p e^{a/r}}{r^2} \left(\cos\left(\frac{bm_e m_p}{r}\right) - \frac{bm_e m_p}{a} \sin\left(\frac{bm_e m_p}{r}\right) \right) \hat{r} \approx 0$$

Therefore, at the maxima or minima, $\tan\left(\frac{bm_e m_p}{r}\right) \approx \frac{a}{bm_e m_p}$, or

Equation 11-9b

$$r_n \approx \frac{bm_e m_p}{n\pi + \arctan(\Omega)} \text{ where } \Omega = \frac{a}{bm_e m_p}$$

At distances where the velocity of the electron is relativistic, the distortion of spacetime may introduce V_G dependency on θ through the velocity terms, and may modify the dependency of the potential energy V_G on the parametric distance r as well. As the velocity has no component along the inclination angle, V_G does not depend on φ , and therefore $\frac{\partial V_G}{\partial \varphi} = 0$. At distances $r \gg B$, the dependency of V_G on the azimuth angle θ becomes insignificant, leading to approximately $\frac{\partial v}{\partial \theta} = 0$ and $\frac{\partial V_G}{\partial \theta} = 0$. Therefore, at $r \gg B$, $\vec{\nabla}V_G \approx \frac{dV_G}{dr} = \frac{\partial V_G}{\partial r} + \frac{\partial V_G}{\partial v} \frac{\partial v}{\partial r}$. However, at the maxima or minima of the potential energy, $\vec{\nabla}V_G = 0$, and the force and acceleration must be equal to zero. Zero acceleration leads to $\frac{\partial v}{\partial r} = 0$, resulting in $\vec{\nabla}V_G \approx \frac{dV_G}{dr} = \frac{\partial V_G}{\partial r} = 0$. Consequently, the maxima or minima of V_G at parametric distances of $r \gg B$, where the velocity of the electron is relativistic, comply approximately with

Equation 11-10a

$$\vec{\nabla}V_G(\vec{r}, \vec{v}) = \frac{\partial V_G}{\partial r} \hat{r} = \frac{Gm_e m_p \gamma^2(v) e^{a\gamma(v)/r}}{r^2} \left(\cos\left(\frac{bm_e m_p \gamma^2(v)}{r}\right) - \frac{bm_e m_p \gamma(v)}{a} \sin\left(\frac{bm_e m_p \gamma^2(v)}{r}\right) \right) \hat{r} = 0$$

Therefore, at the maxima or minima, $\tan\left(\frac{bm_e m_p \gamma^2(v)}{r}\right) \approx \frac{a}{bm_e m_p \gamma(v)}$, or

Equation 11-10b

$$r_n \approx \frac{bm_e m_p \gamma^2(v_n)}{n\pi + \arctan(\Omega_n)}$$

where $\Omega_n = \frac{a}{bm_e m_p \gamma(v_n)}$ for the case of $r_n \gg B$. Note that at non-relativistic velocities, equations 11-10a and b reduce to equations 10-9a and 10-9b respectively. Similarly, in the case where \vec{r} is perpendicular to the relativistic velocity of the electron,

Equation 11-11

$$\vec{\nabla}V_G(\vec{r}, \vec{v}) = \frac{\partial V_G}{\partial r} \hat{r} = \frac{Gm_e m_p \gamma(v) e^{a/r}}{r^2} \left(\cos\left(\frac{bm_e m_p \gamma(v)}{r}\right) - \frac{bm_e m_p \gamma(v)}{a} \sin\left(\frac{bm_e m_p \gamma(v)}{r}\right) \right) \hat{r} \approx 0$$

Therefore, in the case where \vec{r} is perpendicular to the relativistic velocity of the electron, maxima or minima occur when

$$\tan\left(\frac{bm_em_p\gamma(v)}{r}\right) \approx \frac{a}{bm_em_p\gamma(v)}$$

where $r_n \gg B$ and $\vec{v}(r_n) \perp \vec{r}_n$, or

Equation 11-12

$$r_n \approx \frac{bm_em_p\gamma(v_n)}{n\pi + \arctan(\Omega_n)}$$

where $\Omega_n = \frac{a}{bm_em_p\gamma(v_n)}$. Note, however, that at distances less than or of the order of the electron's impact parameter B , the azimuth angle θ starts to vary substantially along the trajectory of the electron. Consequently, at these small distances, equations 11-10 to 11-12 are not entirely accurate for relativistic electron velocities, while 11-9a and 11-9b remain accurate at non-relativistic velocities.

Section XI-1-2: The Effect of Quantum Mechanics on DIS

Before diving deeper into a UG analysis of deep inelastic scattering, it is important to determine the highest level of precision that can be achieved in calculating how close the electron came to the nucleon. The natural tendency is to assume that the quantum uncertainty principle restricts the level of precision of this distance. This is the case, according to quantum mechanics, when the forces acting between the particles are Newton's gravitational force and/or the electromagnetic force. However, this is not the case for the exponential UG force.

As discussed above, the velocity of the probing electron of a high-loss deep inelastic event (an event where $Q^2 = 4E_0E_f \sin^2\left(\frac{\theta}{2}\right) \rightarrow \infty$ and $v = (E_0 - E_f) \rightarrow \infty$) should become non-relativistic ($\gamma(v(\vec{r}_{pca})) = 1$) at the point of closest approach \vec{r}_{pca} . Given a high-loss DIS event, \vec{r}_{pca} is located between the $n - 1$ minimum and the n^{th} maximum of the most external zone indexed n with potential energy maximum higher than the local overall energy of the electron. The UG potential energy of the electron at the n^{th} maximum can therefore be calculated by substituting equation 11-9b in equation 11-8, providing

Equation 11-1-1

$$V_{G,n} = -\frac{Gm_em_p}{a} \left(e^{a(n\pi + \arctan(\Omega))/(bm_em_p)} \cos(n\pi + \arctan(\Omega)) - 1 \right)$$

Given the high level of energy required for deep inelastic scattering, the term -1 is negligible relative to the exponent, thus

Equation 11-1-2

$$V_{G,n} = \frac{Gm_em_p}{a} e^{a(\arctan(\Omega))/(bm_em_p)} \cos(\arctan(\Omega)) (-1)^{n+1} e^{an\pi/(bm_em_p)}$$

or

Equation 11-1-3a

$$V_{G,n} = A(m_e, m_p)(-1)^{n+1}e^{an\pi/(bm_em_p)}$$

where $A(m_e, m_p) = \frac{Gm_em_p}{a} e^{a(\arctan(\Omega))/(bm_em_p)} \cos(\arctan(\Omega))$. Maxima occur when the integer n is odd, thus $(-1)^{n+1} = 1$. Therefore, the potential energy at the nearest maximum is approximately given by

Equation 11-1-3b

$$V_{G,n} = A(m_e, m_p)e^{an\pi/(bm_em_p)}$$

In the case of a neutron, the electromagnetic interaction between the probing electron and the neutron is zero. In the case of a proton, the electromagnetic potential energy at the point of closest approach is given approximately by the Coulomb equation at the nearest maximum indexed n ,

Equation 11-4

$$V_E = \frac{Kqe^2}{\sqrt{r^2 - \frac{v^2}{c^2}r_{\parallel}^2}}$$

which can be reduced to $\frac{Kqe^2}{r}$ at non-relativistic electron velocities.

V_E is a monotonic function of the parametric distance r and does not have any maxima or minima. Consequently, the value of V_E at the n^{th} maximum or minimum of the UG potential energy V_G in the case of a non-relativistic electron velocity is given by

Equation 11-1-5

$$V_{E,n} = \frac{Kq^2(n\pi + \arctan(\Omega))}{bm_em_p}$$

The uncertainty principle restricts the certainty of simultaneously measuring the electron's momentum and position via the inequality $\Delta p_i \Delta x_i \geq \frac{\hbar}{2}$, where i denotes the coordinates of x , y or z . The uncertainty of the location of the electron Δ can be approximated by $\Delta \approx 2r =$

$$\sqrt{\sum_{i=1}^3 \Delta x_i^2} \approx \sqrt{3}\Delta x_i, \text{ or } \Delta x_i \approx \frac{2r}{\sqrt{3}}. \text{ A similar calculation will yield } \Delta E \approx c\Delta P \approx c\sqrt{3}\Delta p_i.$$

Therefore, the amount of kinetic energy required by the uncertainty principle is given by

$$\Delta E \approx c\sqrt{3}\Delta p_i \approx \frac{\sqrt{3}\hbar c}{2\Delta x_i} \approx \frac{3\hbar c}{4r}$$

At the maxima and minima of V_E ,
Equation 11-1-6

$$\Delta E \approx \frac{3\hbar c(n\pi + \arctan(\Omega))}{4bm_e m_p}$$

In figure 11-2 the absolute value of the UG gravitational potential energy of the electron $|V_{G,n}|$ of equation 11-1-2 is displayed in blue, the absolute value of the electromagnetic potential of the electron $|V_E|$ of equation 11-1-5 is displayed in red, and the absolute value of the uncertainty of the amount of energy due to the uncertainty principle $|\Delta E|$ of equation 11-1-6 is provided in violet, as functions of the zonal index n .¹⁸⁹

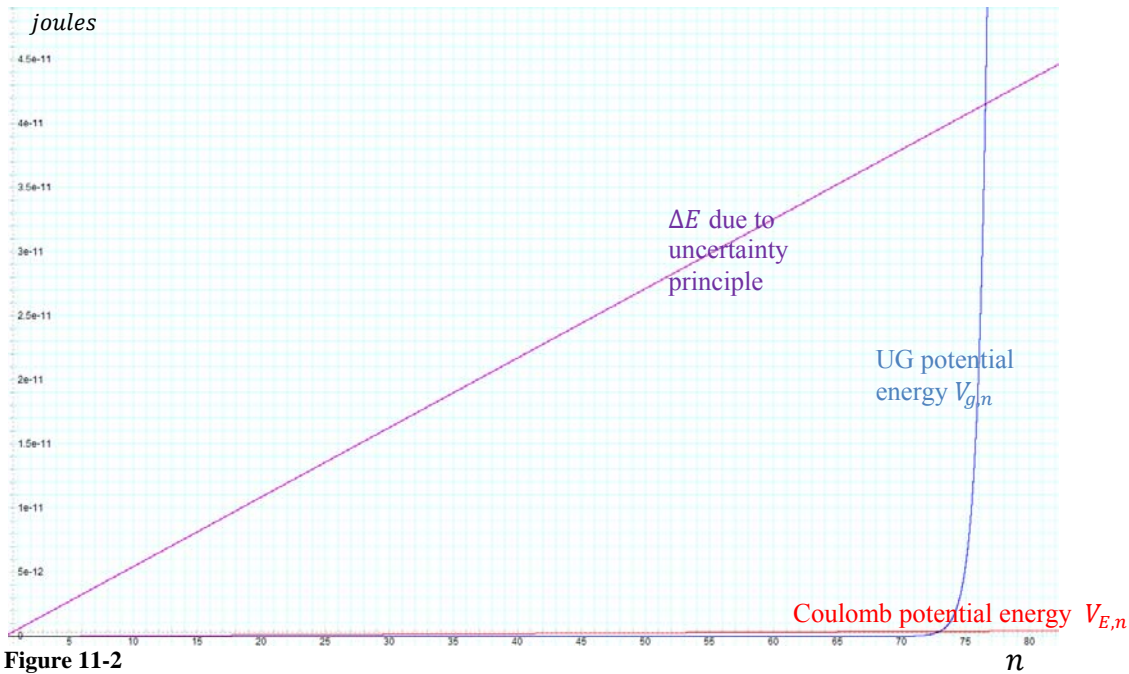


Figure 11-2

As demonstrated in the figure, below $n = 73$ the UG force is virtually zero, and is thus negligible relative to the Coulomb force in the case where the interacting nucleon is a proton.¹⁹⁰ Moreover, throughout the range of distances associated with the maxima and minima $n = 0$ to $n = 76$, the uncertainty principle forces the energies to become so high that any effort to accurately localize the electron in relation to the nucleon is doomed to fail. However, due to the rapid exponential growth of the UG interaction, the UG potential energy dominates over the Coulomb interaction at $n > 73$, and over the kinetic energy associated with the uncertainty principle at $n > 76$, which is roughly associated with energy levels above 0.4 Gev . At energies higher than or of the order of 1 Gev (for $n > 76$), quantum effects become negligible and the

¹⁸⁹ Using equation 11-9b (or equation 11-12, where $\gamma(v) = 1$) leads to $\arctan(\Omega) \approx 0.394 \text{ rd}$.

¹⁹⁰ Note that the distance between the electron and the nucleon increases with decreasing n .

scattering can be localized and viewed using classical physics methodology, thus making it possible to locate the zone of closest approach in spite of the uncertainty principle.¹⁹¹ Consequently, classical (non-quantum) methodology should provide a reasonable approximation and will be used here for the analysis of high-energy DIS events.

Section XI-2-1: The Effect of Special Relativity on the Range of the UG Interaction

According to equation 11-8 for the non-relativistic case ($v \ll c$), the strength of the UG interaction between two nucleons, or between a nucleon and an electron at a distance of $r > 1.5 * 10^{-15} m$ is negligible. Therefore, the effective range of the UG force on the nuclear scale, for the case of non-relativistic electrons, is less than $1.5 * 10^{-15} m$. Consequently, a non-relativistic electron of an impact parameter of $B \gtrsim 1.5 * 10^{-15} m$ would demonstrate exclusively an electromagnetic interaction with a proton, and virtually no interaction with a neutron. Under these conditions, the interaction is too weak to create substantial inelastic scattering. According to equation 2-1-1 and 2-1-2, at non-relativistic velocities the UG interaction is comprised of a central force that is independent of the speed of the electron relative to the nucleon. However, as shown in equations 11-4, 11-6 and 11-7, at relativistic velocities the UG potential energy is indirectly dependent on the electron's velocity due to relativistic spacetime distortions and due to relativistic mass–energy equivalence. Therefore, at parametric distances where a low-velocity electron is anticipated to remain unaffected by its UG interaction with the nucleon, a relativistic electron may be significantly influenced. Hence, the effective range of the UG interaction may depend heavily on the relative velocity of the electron.

Consider an electron moving toward a nucleon with a kinetic energy of $1 Gev = 1.602 * 10^{-10} J$ at a sufficiently large distance that the overall potential energy of the electron is negligible.¹⁹² The Lorentz factor $\gamma(v_0)$ of the electron before the impact with the nucleon is therefore given by

Equation 11-2-1

$$\gamma(v_0)m_e c^2 \approx 1.602 * 10^{-10} J, \text{ or } \gamma(v_0) = 1953.9 \text{ (or approximately } \gamma(v_0) = 2000)$$

In the case of highly relativistic electrons, the effect of the electromagnetic interaction on the value of the Lorentz factor γ is relatively small, even for the case of interaction with a proton. According to equation 11-5, at distances of $r \gg B$ the velocity of the electron is virtually parallel to the \vec{r} vector. Therefore, the distance between the electron and the proton measured in the rest

¹⁹¹ Note that this analysis does not imply that the electromagnetic interaction and the uncertainty principle are completely negligible at $n > 76$, as they may still bear some influence on the zero intersections of the gravitational potential energy V_G . In addition, the electromagnetic force may pull the electron closer to the nucleon, thereby reducing its impact parameter. As previously noted, the impact parameter plays a crucial role in determining the outcome of the DIS event.

¹⁹² Note that the rest mass energy of the electron (of about $0.511 Mev$) is relatively negligible.

frame of the proton is given by $r/\gamma(v(r))$.¹⁹³ According to equation 11-6, the distance r_c at which the UG interaction is about equal to the electromagnetic interaction is given by

Equation 11-2-2a

$$\frac{Gm_p m_e \gamma(v(r_c))}{a} e^{a\gamma(v(r_c))/r_c} \approx \frac{kq_e^2 \gamma(v(r_c))}{r_c}$$

or

Equation 11-2-2b

$$\frac{a}{r_c} \approx \gamma^{-1}(v(r_c)) \left[\ln \left(\frac{kq_e^2}{Gm_p m_e} \right) + \ln \left(\frac{a}{r_c} \right) \right]$$

The equation may be solved for a/r_c by either a titration technique, or via graphical calculator. For the case of a non-relativistic electron ($\gamma(v(r_c)) = 1$), the solution of equation 11-2-2b provides

Equation 11-2-2c

$$\frac{a}{r_c} \approx 95.1757 \text{ or } r_c \approx \frac{a}{95.1757} \approx 0.6 * 10^{-15} m$$

Therefore, at distances of less than $0.6 * 10^{-15} m$, the UG interaction between a proton and a non-relativistic electron (relative to the proton) becomes stronger than the electromagnetic interaction between them, yet becomes weaker than their electromagnetic interaction at distances greater than $0.6 * 10^{-15} m$. The same calculation shows that the range of the UG dominance is extended by a factor of about 2,172 to $1.3 * 10^{-12} m$ in the case of a relativistic electron, where $\gamma(v(r_c)) = 2,000$.

Section XI-2-2: DIS and the Relativistic Effect of the Folding and Unfolding of the Particles' Zonal Structure

In high-energy head on collisions, a large amount of energy is converted to potential energy by the electron as it encounters the point of closest approach with the nucleon. During this process, the momentum and the velocity of the electron relative to the particle accelerator's frame of reference are drastically reduced. To preserve the overall momentum, the nucleon's momentum, and therefore velocity, must increase significantly. However, since the nucleon is strongly bonded to other nucleons within the atomic nucleus, and the atom itself is bonded to other atoms or molecules, a substantial portion of the transferred energy and momentum are dispersed to the surrounding nucleons and molecules. These losses of energy and momentum, as well as additional loss of energy and momentum in the form of radiation, result in an inelastic

¹⁹³ Note that at DIS events the nucleon demonstrates substantial acceleration. Consequently, its rest frame can be inertial for only a brief period of time.

scattering, where the final energy of the electron (as viewed in either the reference frame of the particle accelerator or of the nucleon) reduces significantly. The amount of change in the energy and momentum of the electron depends strongly on its initial energy and momentum, and on its impact parameter. The explosive growth of the exponential term of equation 11-4 as a function

of $\frac{a}{\sqrt{r^2 - \frac{v^2}{c^2} r_{\parallel}^2}}$ at distances of $\sqrt{r^2 - \frac{v^2}{c^2} r_{\parallel}^2} \ll a$, as well as the sharp increase in the frequency of

the oscillations of the cosine term as $r \rightarrow 0$, cause the trajectories of the probing electrons to behave in a chaotic manner. This behavior appears to be random, as a minute difference in an electron's initial impact parameter or velocity may result in drastically different scattering angles, as well as in a different final momentum and energy. Therefore, although the overall magnitude of the electromagnetic interaction in high-energy deep inelastic scattering is very small compared with the UG interaction, the electromagnetic effect may be significant in such a chaotic system, where a tiny perturbation may result in an entirely different trajectory.

Consequently, regardless of the fact that the initial energy and momentum of all of the electrons in the beam are virtually identical, the trajectories of different electrons may vary considerably. Thus, the point of closest approach between different electrons, and their amount of energy and momentum at these points, may vary substantially. In experiments using particle accelerators the velocities of the probing electrons within a beam are all virtually equal. Therefore, the most influential factor in determining the characteristics of the scattering event is the impact parameter B of the electron, and to a lesser degree, whether the nucleon is a proton or a neutron.

In cases where the impact parameter of the electron is sufficiently small, the electron will approach the first impenetrable maximum barrier, where the electron's potential energy at its peak exceeds the overall energy of the electron. This outer maximum is expected to have an odd integer index, denoted as the k_B maximum. As the overall energy of the electron is insufficient to penetrate the k_B barrier, the electron will either be deflected to the side or scattered backward by the barrier, in either case demonstrating a large scattering angle and a substantial loss of energy. In high-energy DIS collisions, the rate of reduction of the UG amplitude as a function of an increasing parametric distance r is high, and the slopes of the barrier at high zonal indices are extremely steep. Consequently, the electron's energy must have been greater than the maxima of most of the preceding zonal maxima encountered prior to the point of closest approach, and the electron's trajectory should have been minimally affected by the majority of these preceding zones. Therefore, the electron will be scattered by the k_B maximum zone in the same manner as it would be scattered by a hard object of the same approximate shape as the contour of the k_B zone barrier, where the electron's kinetic energy is equal to zero.

The UG zonal structure generated by the interaction between the nucleon and the electron consists of an infinite series of concentric barriers around the nucleon, where the height and density of the barriers approach infinity as $r \rightarrow 0$. At non-relativistic velocities, these concentric barriers are spherical and their distance from the nucleon is independent of the electron's velocity. However, in the case of relativistic electron velocities (relative to the nucleon), the shape of the barriers begins to resemble a series of elongated ellipses, where their major axes are

aligned perpendicular to the velocity of the electron. The heights and locations of these barriers, which are fixed in the case of non-relativistic electron velocities, become highly dependent on the speed of the electron at relativistic electron velocities.

According to equation 11-5, at parametric distances $r \gg B$, $r_{\parallel} = r$ and $r_{\perp} \approx B \ll r$. Therefore, the potential energy of the electron is given by equation 11-6, and the coordinates of the potential energy maxima (at odd k) and minima (at even k) are given by 11-10b, or $r_k \approx \frac{bm_em_p\gamma^2(v_k)}{k\pi + \arctan(\Omega_k)}$, where $\Omega_k = \frac{a}{bm_em_p\gamma(v_k)}$. For a high-loss deep inelastic scattering event with a large deflection angle to occur, the electron's potential energy at the barrier maximum must match or exceed its overall energy at the point of impact.¹⁹⁴ The equations may be simplified by defining the function $h(r) = \frac{\gamma(v(r))}{\gamma(v_0)}$. Since the lowest possible value for the Lorentz factor is $\gamma(v) = 1$, $h(r) \geq 1/\gamma(v_0)$, and as the electron is expected to lose energy in a DIS event, $h(r)$ is typically less than 1. Denote q_n as the electric charge of the nucleon and define $E_L(r)$ as the amount of energy lost by the electron by the time it arrived at the parametric distance r (when viewed in the rest frame of the nucleon).¹⁹⁵ Using equation 11-6 for the UG potential energy, the overall energy of the electron at any given parametric distance $r \gg B$ along its trajectory is given by **Equation 11-2-4**

$$E(r, \gamma(v)) = -\frac{Gm_em_ph(r)\gamma(v_0)}{a} \left(e^{ah(r)\gamma(v_0)/r} \cos\left(\frac{bm_em_ph^2(r)\gamma^2(v_0)}{r}\right) - 1 \right) - \frac{kq_eq_nh(r)\gamma(v_0)}{r} + h(r)\gamma(v_0)m_e c^2 + E_L(r) = \gamma(v_0)m_e c^2$$

Where, the small contribution of the particles' spin is neglected.

At DIS events, the UG maxima must be located at sufficiently short distances, where the Coulomb term $\frac{kq_eq_nh(r)\gamma(v_0)}{r}$ is negligible relative to the UG potential energy. Furthermore, at such high energies the -1 term within the parentheses is insignificant compared with the large exponent term required for DIS and can be dropped.

In cases where the energy of the electron on impact is just short of being equal to its potential energy at the k^{th} zonal maximum, as viewed in the rest frame of the nucleon, we can substitute $r = r_k \approx \frac{bm_em_p\gamma^2(v_k)}{k\pi + \arctan(\Omega_k)} = \frac{bm_em_ph^2(r_k)\gamma^2(v_0)}{k\pi + \arctan\left(\frac{a}{bm_em_ph(r_k)\gamma(v_0)}\right)}$ (where k is an odd positive integer) in equation 11-2-4 to provide

¹⁹⁴ Note that in deep inelastic scattering, the energy associated with the electron's rest mass is negligible relative to its overall energy and therefore can be neglected.

¹⁹⁵ As the nucleon is accelerated significantly during the DIS event, its rest frame is not inertial, and consequently, the overall energy and momentum of the system is not preserved. Therefore, $E_L(r) \neq 0$ is possible. While this frame of reference is not inertial over the entire period of the DIS event, it can be viewed as an inertial frame at any parametric distance r for a brief period of time. Therefore, equation 11-2-4 is valid.

Equation 11-2-5

$$\frac{Gm_e m_p h(r_k) \gamma(v_0)}{a} e^{\frac{a \left(k\pi + \arctan\left(\frac{a}{bm_e m_p h(r_k) \gamma(v_0)}\right) \right)}{bm_e m_p h(r_k) \gamma(v_0)}} \cos\left(\arctan\left(\frac{a}{bm_e m_p h(r_k) \gamma(v_0)}\right)\right) = (1 - h(r_k)) \gamma(v_0) m_e c^2 - E_L(r_k)$$

Multiplying both sides by $\left(\frac{Gm_e m_p h(r_k) \gamma(v_0) c^2}{a}\right)^{-1}$ and then taking the log of both sides of the equation yields

Equation 11-2-6

$$\frac{a \left(k\pi + \arctan\left(\frac{a}{bm_e m_p h(r_k) \gamma(v_0)}\right) \right)}{bm_e m_p h(r_k) \gamma(v_0)} = \ln\left(\frac{ac^2}{Gm_p}\right) - \ln\left(\cos\left(\arctan\left(\frac{a}{bm_e m_p h(r_k) \gamma(v_0)}\right)\right)\right) - \ln(h(r_k)) + \ln(1 - h(r_k)) + \ln\left(1 - \frac{E_L(r_k)}{(1 - h(r_k)) \gamma(v_0) m_e c^2}\right)$$

The point of closest approach, denoted as \vec{r}_{pca} , generally occurs in the case of DIS somewhere within the k_B zone, but is assumed for the moment to occur very close to the k_B^{th} zonal maximum. Therefore, at this point in space and time, $r_{\parallel} = 0$ and $r_{\perp} = r_{pca}$. Consequently, r_{pca} provides the actual distance between the electron and the nucleon, as viewed in the rest frame of the nucleon. In the general case, the electron's velocity $v(\vec{r}_{pca})$ may be substantial, or even relativistic, and the resultant electron scattering would not be highly inelastic. However, as discussed, for a DIS event to occur where $Q^2 = 4E_0 E_f \sin^2\left(\frac{\theta}{2}\right) \rightarrow \infty$ and $v = (E_0 - E_f) \rightarrow \infty$, the electron should become non-relativistic at the point of closest approach r_{pca} , with $\gamma(v(r_{pca})) = 1$ and $h(r_{pca}) = 1/\gamma(v_0)$. Therefore, $\left|\arctan\left(\frac{a}{bm_e m_p h(r_{pca}) \gamma(v_0)}\right)\right| = \arctan\left(\frac{a}{bm_e m_p}\right) = 0.3936$, $\ln\left(\cos\left(\arctan\left(\frac{a}{bm_e m_p h(r_{pca}) \gamma(v_0)}\right)\right)\right) = \ln\left(\cos\left(\arctan\left(\frac{a}{bm_e m_p}\right)\right)\right) = -0.0796$, and $\ln\left(\frac{ac^2}{Gm_p}\right) = 93.628$.

As almost all of the energy of the electron is delivered to the nucleon, while a significant portion of the nucleon's energy dissipates into the network of surrounding nucleons, atoms and molecules, the electron's loss of energy $E_L(\vec{r}_{pca})$ must be substantial. The energy loss $E_L(\vec{r}_{pca})$ may cause the electron to stop its forward motion toward the nuclei earlier, at a more external repulsive zone, and may consequently lower the value of k_B . Substituting the above equalities in equation 11-2-6 yields

Equation 11-2-7

$$k_b \leq \frac{bm_em_p}{a\pi} \left[\ln\left(\frac{ac^2}{Gm_p}\right) + 0.0796 - \ln(1/\gamma(v_0)) + \ln(1 - 1/\gamma(v_0)) \right] - \frac{\arctan\left(\frac{a}{bm_em_p}\right)}{\pi}$$

$$= 0.766[93.71 - \ln(1/\gamma(v_0)) + \ln(1 - 1/\gamma(v_0))] - 0.1253$$

For example, provided that $\gamma(v_0) \approx 2000$, the first maximum contour at which the potential energy of the electron exceeds its initial overall energy is indexed $k_b \approx 77$. Note that energy losses may reduce k_b to an odd $k_b \leq 75$. Intuition would suggest that as the electron was stopped by the k_b maximum, it should have passed through all minima and maxima of $n < k_b$, and could not have reached any of the minima and maxima of index $n > k_b$. This will not be shown to be the case, however. While the electron indeed had to pass all minima and maxima of $n < k_b$, it will be shown that the electron also had to pass maxima and minima between k_b and $k \gg k_b$.

At parametric distances r , where the potential energy of the electron is still small relative to its overall energy, $v(r) \approx v_0$; hence $h(v(r))$ is still approximately 1. Therefore, no substantial energy loss has yet occurred, and E_L is negligible, leading to $\frac{E_L}{(1-h(r_k))\gamma(v_0)m_e c^2} \ll 1$.

As $\gamma(v_0) \gg 1$, $\frac{a}{bm_em_ph(r_k)\gamma(v_0)} \ll 1$, and consequently, $0 < \arctan\left(\frac{a}{bm_em_ph(r_k)\gamma(v_0)}\right) \ll 1$. Following equation 11-2-6,

Equation 11-2-8

$$k \approx \frac{bm_em_ph(r_k)\gamma(v_0)}{a\pi} \left[\ln\left(\frac{ac^2}{Gm_p}\right) - \ln(h(r_k)) + \ln(1 - h(r_k)) \right]$$

For the example of $\gamma(v_0) = 2000$, at the point where $h = 0.9999$ or $h = 0.99$, the calculated index k of the last encountered maximum is given by $k = 129,393$ and $k = 135,115$ respectively, which are obviously much larger than the index of $k_b (\approx 77)$.

Therefore, before being stopped by the nucleon at the $k_b \leq 77$ maximum, the electron managed to pass substantially more than 135,115 zones. The question arises as to how it is possible that an electron in motion towards a nucleon, after successfully passing through 135,115 zones, ended up being stopped by a maximum barrier of an index as low as $k_b \leq 77$. After all, the electron could not have reached the 135,115th zone without first passing through all of the $k_b \leq 77$ maxima. Additionally, the electron's potential energy at the 135,115th maximum should be substantially higher than its potential energy at the 77th maximum. Therefore, it seems odd that the electron could be stopped by a low energy maximum barrier after having passed a substantially higher energy barrier earlier.

The amplitude ratio between any two successive maxima (or minima) of indices k and $k - 2$ can be calculated by substituting r_k and r_{k-2} of equation 11-10b in equation 11-6. As long

as the overall energy of the electron is substantially greater than the local potential energy maxima $E(r) \gg V_G(r, \gamma(v))$, or as long as the electron's velocity is non-relativistic (therefore, $\gamma(v) = 1$), $\gamma(v)$ changes only slightly between two successive maxima, and $\gamma(v_k) \approx \gamma(v_{k-2})$. Therefore, provided that at high-energy collisions $e^{a\gamma(v_k)/r_k} \gg 1$, the ratio of two successive maxima or minima peaks is given by

Equation 11-2-9

$$\frac{V_G(r_k, \gamma(v_k))}{V_G(r_{k-2}, \gamma(v_{k-2}))} = \frac{-\frac{Gm_e m_p \gamma(v_k)}{a} \left(e^{a\gamma(v_k)/r_k} \cos\left(\frac{bm_e m_p \gamma^2(v_k)}{r_k}\right) \right)}{-\frac{Gm_e m_p \gamma(v_k)}{a} \left(e^{a\gamma(v_k)/r_{k-2}} \cos\left(\frac{bm_e m_p \gamma^2(v_k)}{r_{k-2}}\right) \right)}$$

or

Equation 11-2-10

$$\frac{V_G(r_k, \gamma(v_k))}{V_G(r_{k-2}, \gamma(v_{k-2}))} = \frac{\left(e^{a \left(k\pi + \arctan\left(\frac{a}{bm_e m_p \gamma(v_k)}\right) \right) / bm_e m_p \gamma(v_k)} \cos\left(k\pi + \arctan\left(\frac{a}{bm_e m_p \gamma(v_k)}\right) \right) \right)}{\left(e^{a \left((k-2)\pi + \arctan\left(\frac{a}{bm_e m_p \gamma(v_k)}\right) \right) / bm_e m_p \gamma(v_k)} \cos\left((k-2)\pi + \arctan\left(\frac{a}{bm_e m_p \gamma(v_k)}\right) \right) \right)}$$

or

Equation 11-2-11

$$\frac{V_G(r_k, \gamma(v_k))}{V_G(r_{k-2}, \gamma(v_{k-2}))} = e^{2a\pi/bm_e m_p \gamma(v_k)} = e^{2.609/\gamma(v_k)} = 13.59^{1/\gamma(v_k)}$$

With the example used above, where $\gamma(v_0) = 2000$, the ratio in regions where $v_k = v_0$ is given

by $\frac{V_G(r_k, \gamma(v_0))}{V_G(r_{k-2}, \gamma(v_0))} = 1.0013$, compared with $\frac{V_G(r_k, \gamma(v_0))}{V_G(r_{k-2}, \gamma(v_0))} = 13.59$ in regions where the electron

moves at non-relativistic velocities. The ratio of the electron's potential energy between the 77th maximum viewed by the electron at close to zero velocity (where $\gamma(v_{77}) = 1$) and the

135,115th maximum viewed at $\gamma = 0.99 * 2000 = 1980$ is given by $\frac{V_G(r_{77}, \gamma(v_{77})=1)}{V_G(r_{135,115}, \gamma(v_{135,115})=1980)} \approx$

$$\frac{-\frac{Gm_e m_p}{a} (e^{a/r_{77}})}{-\frac{Gm_e m_p * 1980}{a} (e^{1980a/r_{135,115}})} \approx 5.05 * 10^{-4} e^{(a\pi/bm_e m_p)(77-135,115/1980)} = 46.45. \text{ Therefore, the potential}$$

energy of the non-relativistic electron at the time it was stopped by the 77th maximum substantially exceeds the potential energy of the relativistic electron of $\gamma \geq 1980$ at the 135,115th maximum. This explains how an electron can have a sufficient amount of energy to pass the 135,115th maximum barrier, yet not enough energy to pass the earlier 77th maximum barrier.

However, the above explanation does not account for how an electron that just passed the zonal maximum indexed 135,115 can encounter the same 77th maximum for a second time while still moving toward the nucleon. The explanation is as follows: While the parametric distance r is reduced monotonically as the electron approaches the nucleon, the apparent distance of the electron from the nucleon fluctuates wildly, at times increasing and at times decreasing with the reduction of r . As it moves through the zones toward the nucleon, the electron accelerates when approaching a potential energy minimum and decelerates as it approaches a maximum. When approaching a potential energy maximum, v and $\gamma(v)$ decrease. Consequently, the apparent distance between the electron and the nucleon (as viewed by the nucleon), as well as the potential energy ratio between two successive maxima (or minima), increases. The opposite occurs when the electron approaches a minimum, in which case v and $\gamma(v)$ increase, and the apparent distance between the electron and the nucleon (as viewed by the nucleon), as well as the potential energy ratio between two successive maxima or minima, decreases. In effect, as demonstrated by figures 11-1a and 11-1b, the entire zonal pattern folds in when the velocity of the electron is decreased, causing the pattern's maxima and minima to move inward toward the nucleon. Conversely, the pattern unfolds when the velocity of the electron is increased, as the maxima and the minima move outward, away from the nucleon. The speed of folding or unfolding depends on the rate of change of the electron's Lorentz factor γ . Early on, when the distance between the electron and the nucleon is relatively large and the UG interaction is quite weak, the relative velocity of the electron is about constant, and the rate of folding and unfolding of the UG pattern is negligible. In a DIS event, as the electron approaches the point of closest approach \vec{r}_{pca} the maxima and the minima fluctuations become enormous, causing related fluctuations in the value of $\gamma(v)$. The size and rate of these fluctuations determine the speed and the extent of the folding and unfolding of the pattern. The speeds of the few folds preceding r_{pca} become large and may exceed the velocity of the electron. Hence, some of the maxima already passed by the electron may fold or unfold at a significantly faster rate than the speed of the electron, thus overtaking the electron. It is therefore feasible, and even expected, that in a DIS event the electron will encounter the same maximum or minimum multiple times as it moves toward the nucleon.

Section XI-3: The Weak Fall-off of the DIS Cross Section

Prior to calculating the approximate UG equation that describes the weak fall-off of the DIS cross section, the underlying principle responsible for this phenomenon can be demonstrated by the set of figures 11-3a to 11-3d. Again, consider a high-loss DIS event at the limit $Q^2 = 4E_0E_f \sin^2\left(\frac{\theta}{2}\right) \rightarrow \infty$ and $v = (E_0 - E_f) \rightarrow \infty$. As discussed, in such an event the electron is scattered by the outermost impenetrable zone indexed k_b in the same manner as it would have been scattered by hard object. However, the velocity of the electron becomes non-relativistic at the point of impact. At non-relativistic velocities the zone structure is spherically symmetric

around the nucleon, and therefore depends on the absolute value of the distance between the electron and the nucleon, $(\Delta x^2 + \Delta y^2 + \Delta z^2)^{1/2}$. In addition, at non-relativistic speeds, when $n > 75$, the ratio between two successive potential energy maxima $V_G(r_{n+2})/V_G(r_n)$ was shown by equation 11-2-11 to be approximately 13.59. The UG potential energy waveform, indicated in violet in figure 11-3a, is displayed as a function of the distance between the electron and the nucleon along an arbitrary axis within the plane defined by the electron's velocity vector and the distance vector between the electron and the nucleon. The green concentric circles provide the UG potential energy maxima contours within this plane. Note that while the potential energy of successive maxima increases by a factor of 13.59, the distance between them decreases proportionally to n^2 (see equation 2-1-16), where n denotes the zonal index. Therefore, the UG slopes rapidly become extremely steep.¹⁹⁶

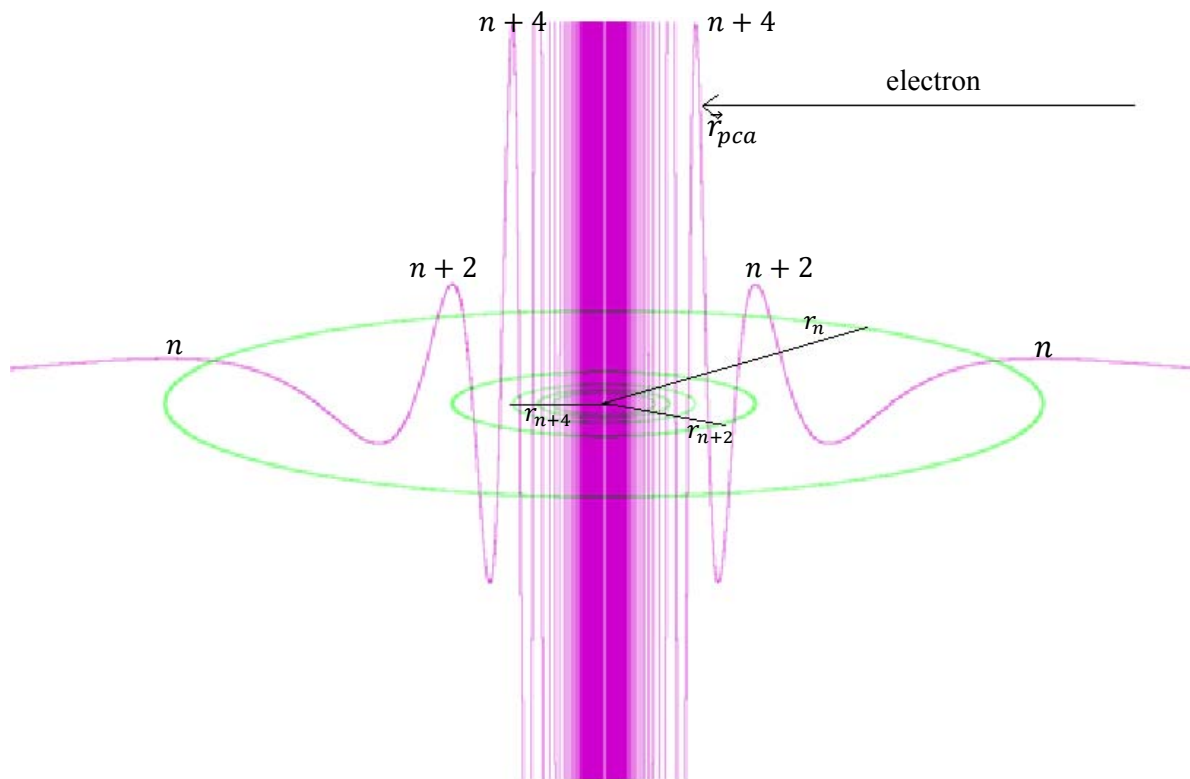


Figure 11-3a

The overall energy of the electron illustrated in figure 11-3a is lower than its potential energy at the $n + 4$ maximum. As the electron passes the n^{th} maximum, its overall energy is significantly larger than its potential energy. Note that the electron retains most of its kinetic energy; therefore only a small portion of its energy can be transferred to the nucleon, and subsequently dispersed to nearby nucleons, atoms and molecules. When the impact parameter of the electron is larger than r_{n+1} , the electron will not reach the maximum $n + 2$, and the amount of energy lost is relatively small. As a result, the scattering event is only slightly inelastic. At an

¹⁹⁶ Note that lower mass values were used for the figures in this chapter in order to view more maximum and minimum peaks.

impact parameter of $r_{n+3} < B < r_{n+2}$, the electron passes the higher potential energy maximum $n + 2$, and a greater portion of its kinetic energy is transferred directly to the nucleon and indirectly to nearby nucleons, atoms and molecules. Consequently, the scattering becomes increasingly inelastic. At an impact parameter of $B < r_{n+4}$, the electron proceeds toward the $n + 4$ maximum. Since the electron's potential energy at this maximum exceeds its overall energy, the electron's motion toward the nucleon is halted as it reaches the point at which its potential energy is equal its overall energy, at \vec{r}_{pca} .¹⁹⁷ As the electron does not have sufficient energy to continue to move toward the nucleon, it is scattered in the same manner as it would have been scattered by a hard object. Note that as the overall energy of the electron at the impact point \vec{r}_{pca} is equal to its potential energy, the velocity of the electron relative to the nucleon is reduced to $v(\vec{r}_{pca}) = 0$ and its Lorentz factor is reduced to $\gamma(v(\vec{r}_{pca})) = 1$. Since the electron becomes non-relativistic on impact, the UG zones viewed in the particle accelerator's frame of reference appear spherically symmetric around the nucleon, and the hard scattering object becomes a hard scattering sphere of radius r_{pca} . Hence, the high-loss DIS cross section becomes approximately equal to $\pi(r_{n+4})^2$. Note that the higher the energy of the probing electron, the smaller the radius of the hard sphere becomes.

Adhering to equation 11-2-11, in a DIS event, in regions where the electron moves at non-relativistic velocities, the ratio between the potential energy of an electron at two successive maxima $V_G(r_{n+2})/V_G(r_n)$ is equal to 13.59. Increasing the energy by a factor of 13.59 will therefore reduce the DIS cross section by a factor of

$$\frac{\sigma_{n+2}}{\sigma_n} \approx \frac{\pi(r_{n+2})^2}{\pi(r_n)^2} \approx \frac{\left(\frac{bm_e m_p}{(n+2)\pi}\right)^2}{\left(\frac{bm_e m_p}{n\pi}\right)^2} \approx \frac{n^2}{(n+2)^2} \rightarrow 1 \text{ when } n \rightarrow \infty. \text{ Therefore, as } n \text{ increases, the DIS cross}$$

section is reduced. However, as n increases, the DIS cross section fall-off becomes exceedingly weak. This phenomenon is demonstrated in figures 11-3b to 11-3d.

Figure 3-11b depicts three electrons with the same energy and different impact parameters. The solid sphere indicates the impenetrable hard sphere at the given level of energy, while the concentric circles indicate the radii of the lower external maxima, which can be penetrated as the potential energy of the electron at the maxima is lower than the overall energy of the probing electrons. In particular, the electron's potential energy at the surface of the hard sphere is roughly given by $V_G(r_{n+6}) = 13.59V_G(r_{n+4}) = 13.59^2V_G(r_{n+2}) = 13.59^3V_G(r_n)$. As displayed, the two electrons with the smaller impact parameters (indicated by blue and green trajectories) hit the hard sphere and are deflected by it. The electron with the largest impact parameter (indicated by a black trajectory) passes near the nucleon without colliding with the hard sphere, with only slight elastic deflection by the lower indexed maxima and minima. Increasing the energy of the electrons at the impact point (r_{pca}) by a factor of 13.59⁵

¹⁹⁷ Note that the energy at the impact point \vec{r}_{pca} within the nucleon's frame of reference is not equal to the initial energy of the electron. This is due to energy losses endured, as well as to the fact that the nucleon's frame of reference cannot remain inertial for a sufficient amount of time, due to the acceleration of the nucleon.

(to $13.59^8 V_G(r_n)$) results in the reduction of the radius of the hard sphere to r_{n+16} , where neither of the outer two electrons (black and green) collide with the hard sphere.¹⁹⁸

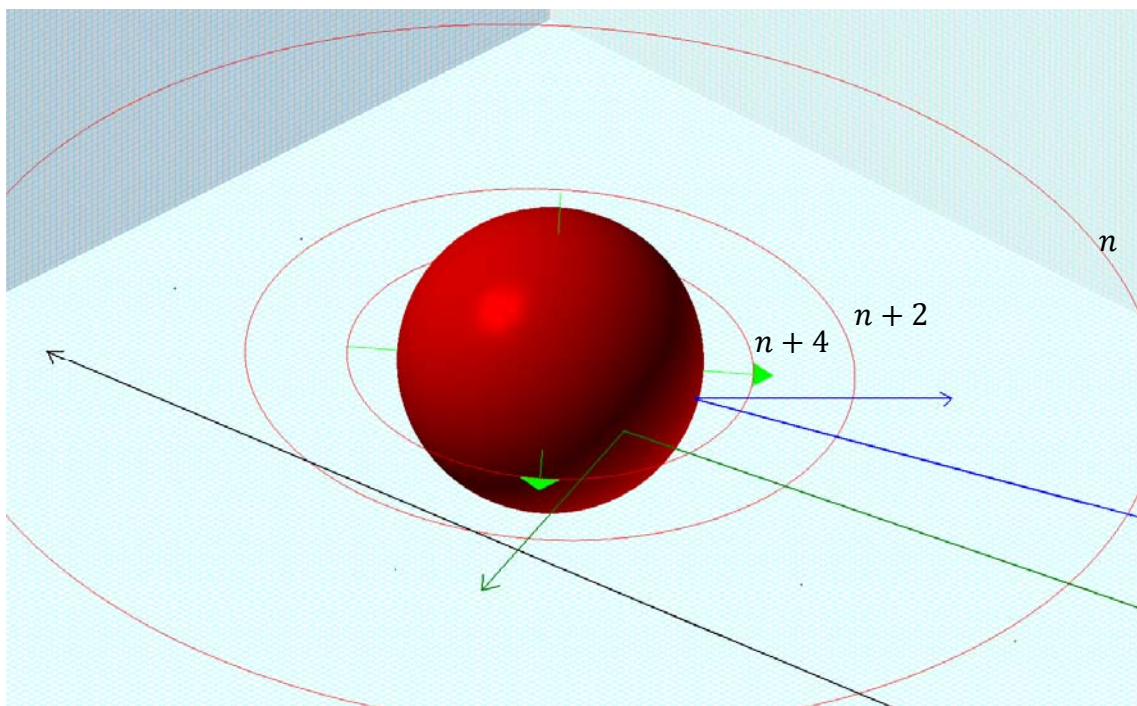


Figure 11-3b

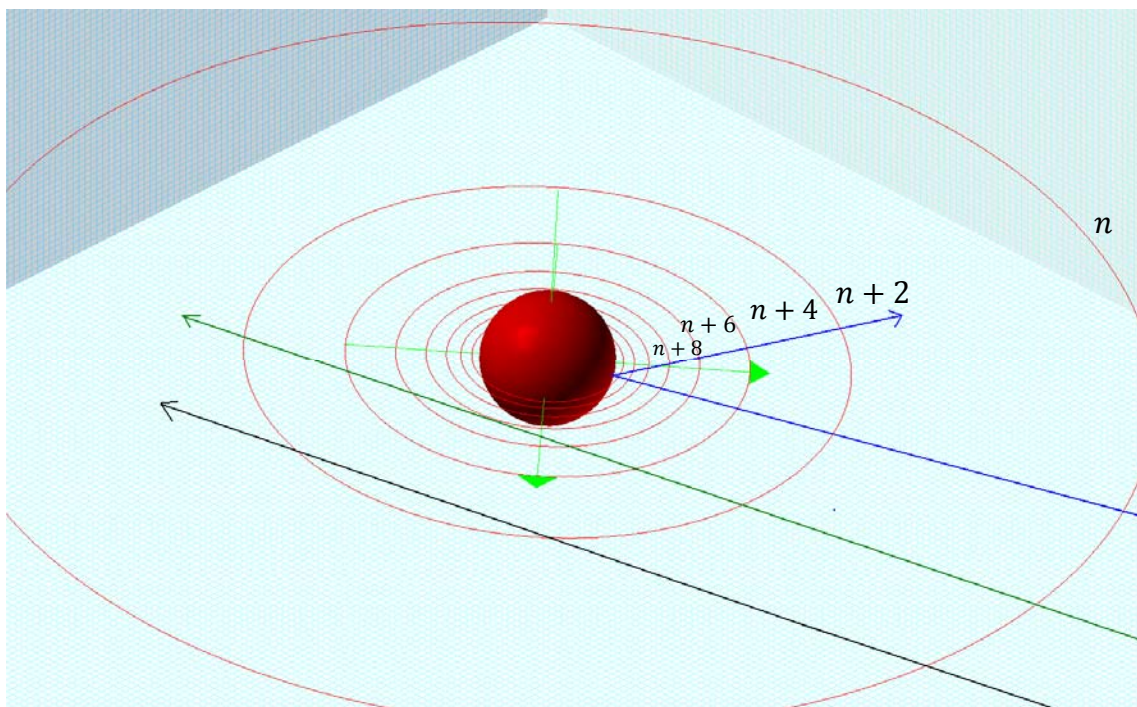


Figure 11-3c

¹⁹⁸ The index increase from $n + 6$ to $n + 16$ (by 10), rather than to $n + 11$ (by 5) reflects that there are five minima in addition to the five maxima separating the radii of the two hard spheres.

In figure 11-3d the impact energy of the electrons is further increased to about $13.59^{12}V_G(r_n)$, resulting in the reduction of the radius of the hard sphere to r_{n+24} . As shown in the figure, at high zonal indices the spherical maxima become compacted together to the extent that increasing the electrons' energy by a large factor results in little reduction in the radii of the hard sphere, thus diminishing the rate of reduction of the DIS cross section.

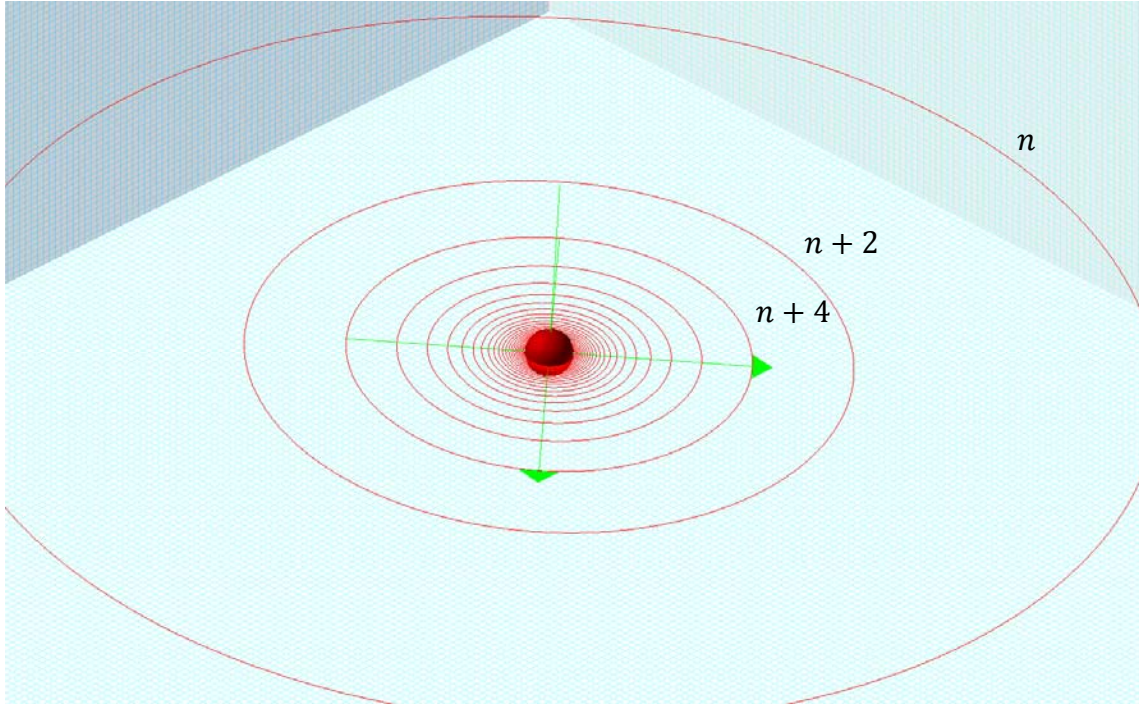


Figure 11-3d

Recall that close to the impact point where the electron's velocity is no longer relativistic, the effect of any zone $n = k_b - 2l$ is smaller than the 'hard sphere' effect of the k_b zone by a factor of at least $13.59^{2(l-1)}$. Thus, the effect of any zone $n < k_b - 4$ can be regarded as negligible.¹⁹⁹ The trajectory of the electron can consequently be expected to be deflected slightly by the maxima $k_b - 4$ and $k_b - 2$, and by the minima $k_b - 3$ and $k_b - 1$, before colliding with the hard sphere of a radius greater than $R \approx r_{k_b}$, where r_{k_b} is the radius of the k_b maximum contour. In summary, the highest DIS losses occur when the electron's impact parameter is sufficiently small. As a result, the electron is scattered as it would have been scattered by a hard sphere, where the radius of the sphere is equal to the distance of the point of closest approach $r_{pca} = |\vec{r}_{pca}|$. On the other hand, in cases where the impact parameter of the electron is sufficiently large, the energy of the electron at the point of closest approach (located at zone k) is higher than the maximum potential energy of zone k , thus $E_{pca} > V(r_k, \gamma(v_{pca}) = 1)$. In this scenario, the

¹⁹⁹ Note however, that as the velocity of the electron was higher and may have been relativistic when passing through the previous maximum, the ratio between two successive maxima may reduce to below 13.59.

electron will not collide with the hard sphere and its velocity at the point of closest approach \vec{r}_{pca} may still be relativistic. As the potential energy of the electron reduces drastically with its distance from the nucleon, the scattering becomes more elastic with an increased impact parameter.

Armed with the above insights, the task at hand is to apply the same principles and approximations for the development of a more precise mathematical description of the weak fall-off of the DIS cross section. At the point of closest approach \vec{r}_{pca} (viewed in the frame of reference of the particle accelerator), the electron's velocity is either zero or perpendicular to \vec{r} ($r_{\parallel} = 0$ and $r_{\perp} = r_{pca}$). Therefore, the dynamics of the interaction at that point are determined by equations 11-7 and 11-12. However, the electron's energy at the point of closest approach $E_{pca} = E(r_{pca})$ is not observable. To simplify the analysis, it is assumed that $E_{pca}(E_0, E_f)$ (or alternatively, $E_{pca}(E_0, v)$) is a monotonic function of the electron's initial energy E_0 and its final energy E_f (or v), and that its behavior is consistent with²⁰⁰ $\lim_{E_f \rightarrow E_0} E_{pca} = \lim_{v \rightarrow 0} E_{pca} = E_0$ and, on average, $\frac{dE_{pca}}{dE_0} > 0$, $\frac{dE_{pca}}{dE_f} > 0$, $\frac{dE_{pca}}{dv} = H < 0$ and $\lim_{v \rightarrow \infty, E_f \rightarrow \infty} E_{pca} = \infty$.

Expanding to the first Taylor term,

Equation 11-3-1

$$E_{pca} \approx E_0 - Hv = (1 - H)E_0 + HE_f$$

where H is a constant.

The index of the maximum of the zone containing \vec{r}_{pca} will be denoted as k . Consider the specific case where the parametric distance between the nucleon and the point of closest approach is infinitesimally larger than the radius of the k^{th} maximum contour, $r_k < r_{pca} \rightarrow r_k$. In this case, the potential energy of the electron in the nucleon's frame of reference is given by **Equation 11-3-2**

$$V_G(r_{pca}, \gamma(v(r_{pca}))) \rightarrow V_G(r_k, v(r_k)), \text{ where } v \perp r_k = -\frac{Gm_e m_p \gamma(v(r_k))}{a} \left(e^{a/r_k \cos\left(\frac{bm_e m_p \gamma(v(r_k))}{r_k}\right)} - 1 \right)$$

and the maxima occur when

Equation 11-3-3

$$r_{pca} \rightarrow r_k = \frac{bm_e m_p \gamma(v(r_k))}{k\pi + \arctan(\Omega_k)}$$

where $\Omega_k = \frac{a}{bm_e m_p \gamma(v(r_k))}$. Substituting r_k of equation 11-3-3 in equation 11-3-2 yields

²⁰⁰ Note that the nucleon is accelerated by the electron. Therefore, its frame of reference can be regarded as an inertial frame for only a brief period of time. Consequently, the law of conservation of energy does not apply.

Equation 11-3-4

$$V_G(r_{pca}, \gamma(v(r_{pca}))) \rightarrow V_G(r_k, v(r_k) = v_{\perp}(r_k)) \\ = -\frac{Gm_e m_p \gamma(v(r_k))}{a} \left(e^{a((k\pi + \arctan(\Omega_k)))/bm_e m_p \gamma(v(r_k))} \cos(k\pi + \arctan(\Omega_k)) - 1 \right)$$

In cases of deep inelastic scattering, $e^{a((k\pi + \arctan(\Omega_k)))/bm_e m_p \gamma(v(r_k))} \gg 1$, and at a UG maximum, k is an odd integer. Therefore,

Equation 11-3-5

$$V_G(r_{pca}, \gamma(v(r_{pca}))) \rightarrow V_G(r_k, v(r_k), v(r_k) = v_{\perp}(r_k)) = \\ \frac{Gm_e m_p \gamma(v(r_k))}{a} \left(e^{a(k\pi + \arctan(\Omega_k))/bm_e m_p \gamma(v(r_k))} \cos(\arctan(\Omega_k)) \right)$$

To simplify the equation, define

Equation 11-3-6

$$D(m_e, m_p, \gamma(v(r_k))) = \frac{Gm_e m_p \gamma(v(r_k))}{a} \left(\cos(\arctan(\Omega_k)) \right)$$

Therefore, equation 11-3-5 can be stated as

Equation 11-3-7

$$V_G(r_{pca}, \gamma(v(r_{pca}))) \rightarrow V_G(r_k, v(r_k)) = D(m_e, m_p, \gamma(v(r_k))) e^{a(k\pi + \arctan(\Omega_k))/bm_e m_p \gamma(v(r_k))}$$

or, as of equations 11-3-3 and 11-3-7,

Equation 11-3-8

$$r_{pca} \rightarrow r_k = \frac{bm_e m_p \gamma(v(r_k))}{k\pi + \arctan(\Omega_k)} = \frac{a}{\left[\ln(V_G(r_k, \gamma(v(r_k)))) - \ln(D(m_e, m_p, \gamma(v(r_k)))) \right]}$$

As discussed above, when the kinetic energy of an electron is substantial at r_{pca} , the influence of the nucleon on the electron's trajectory will be relatively small, resulting in either an elastic scattering, or in a weak inelastic scattering. For a substantial DIS event to take place at the limits of $Q^2 = 4E_0 E_f \sin^2\left(\frac{\theta}{2}\right) \rightarrow \infty$ and $v = (E_0 - E_f) \rightarrow \infty$, the kinetic energy of the electron at r_{pca} should be minimal, leading to $v(r_{pca}) \approx 0$ and $\gamma(v(r_{pca})) = 1$. Therefore, in the case of a substantial DIS event, the parametric (and apparent) distance of $r_k < r_{pca} \rightarrow r_k$ is given by

Equation 11-3-9

$$r_k < r_{pca} \rightarrow r_k = \frac{bm_e m_p}{k\pi + \arctan\left(\frac{a}{bm_e m_p}\right)} = \frac{a}{\left[\ln(V_G(r_k, \gamma = 1)) - \ln(D(m_e, m_p, \gamma = 1)) \right]}$$

However, in the usual case of a high-loss deep inelastic scattering event, the electron will not collide directly with the peak of the k^{th} maximum, and will instead reach somewhere between $r_{k-2} > r > r_k$, where $V_G(r_{k-2}, \gamma(v(r_{k-2})) = 1) < V_G(r, \gamma(v(r)) = 1) \approx E_{pca} < V_G(r_k, \gamma(v(r_k)) = 1)$.²⁰¹ As discussed above, for a substantial inelastic event to occur, the electron must become non-relativistic on impact with $\gamma(v) = 1$, somewhere within the k^{th} zone or at the tip of the $k - 2$ maximum. As E_{pca} may be anywhere within the range of $V_G(r_{k-2}, \gamma(v(r_{k-2})) = 1) < E_{pca} < V_G(r_k, \gamma(v(r_k)) = 1)$, the maximum potential energy at the $k - 2$ maximum is of the order of $\frac{E_{pca}}{13.59} \lesssim V_G(r_{k-2}, \gamma(v(r_{k-2})) = 1) \lesssim E_{pca}$. For the general maxima, the maximum potential energy at $k - 2n$ (at non-relativistic velocities) for an integer $n \geq 1$ is given by $\frac{E_{pca}}{13.59^n} \lesssim V_G(r_{k-2n}, \gamma(v(r_{k-2n})) = 1) \lesssim \frac{E_{pca}}{13.59^{n-1}}$. Therefore, in the case of deep inelastic scattering, only the contributions of the preceding two or three maxima have a significant effect. This is in agreement with experimental results, where 1 to 3 resonances are generally found in graphs of the double differential cross section as function of energy (or vs. energy lost, $\nu = E_0 - E_f$).²⁰²

To calculate the approximate scattering cross section, we begin once again with a high-loss DIS event where the impact energy of the electron E_{pca} is slightly lower than $V_G(r_k, \gamma(v(r_k)) = 1)$ and its impact parameter B is sufficiently small to produce hard sphere scattering. Therefore, r_{pca} is slightly larger than r_k . In this case, the k^{th} maximum contour cannot be penetrated by the probing electron, which can only reach as deep as $r_{pca} \approx r_k$. As the electron's velocity is already reduced to a non-relativistic speed near the point of closest approach, the shape of the k^{th} maximum is perceived by the electron to be spherically symmetric.

As discussed, in the case of a DIS event, the sharp steepness of the UG exponent as a function of distance is so explosive near the point of closest approach that the electron's course and direction of motion remain largely unaffected by most of the UG maxima and minima encountered, with the exception of the last few extremely narrow zones between $k - 6$ and k . Therefore, the interaction distance and the interaction time associated with DIS events, during which the electron's overall energy and direction of motion have been significantly altered, are extremely short. For this reason, although the electron's direction of motion may have changed substantially, the effect of this change on its impact parameter is minimal. Consequently, all electrons with an impact parameter of $B \leq r_k$ and an impact energy of $V_G(r_{k-2}, \gamma(v(r_{k-2})) = 1) < E_{pca} < V_G(r_k, \gamma(v(r_k)) = 1)$ will scatter in the same manner as they would have been scattered by a hard sphere of radius r_k . Electrons of the same range of energy, with impact parameters within the range $r_k < B < r_{k-2}$ (as calculated for non-relativistic electrons) may undergo a weak

²⁰¹The reason for the assumption that $E_{pca} > V_G(r_{k-2}, \gamma(v(r_{k-2})) = 1)$ is that the electron had to pass the $k - 2$ maximum just before impact with the k^{th} zone, and then had to pass the maximum again immediately after the impact, on its way toward the detector.

²⁰²Note that there is also a split of the potential energy maxima due to the slight difference in mass between the proton and the neutron, which may impact the number of resonances.

inelastic scattering, while electrons with impact parameters of $B \gg r_{k-2}$ will undergo an elastic scattering, or will remain unaffected.

As the cross section of a hard sphere of radius r is given by $\sigma = \pi r^2$, the deep inelastic scattering event for the case of an impact energy E_{pca} of just under $V_G(r_k, \gamma = 1)$ is given by

Equation 11-3-10

$$d\sigma(E_{pca} \rightarrow V_G(r_k, \gamma = 1)) = d\sigma(V_G(r_k, \gamma = 1)) = d\sigma_k \approx \pi r_k^2 dE_{pca} = \pi \left[\frac{bm_e m_p}{k\pi + \arctan\left(\frac{a}{bm_e m_p}\right)} \right]^2 dE_{pca} = \frac{\pi a^2}{[\ln(V_G(r_k)) - \ln(D(m_e, m_p))]^2} dE_{pca}$$

where E_{pca} is less than yet almost equal to $V_G(r_k)$.^{203 204} Similarly, if the energy is just under $V_G(r_{k-2})$, where $v(r_{k-2}) \approx 0$ and $\gamma(v(r_{k-2})) = 1$,

Equation 11-3-11

$$d\sigma(E_{pca} \rightarrow V_G(r_{k-2}, \gamma = 1)) = d\sigma(V_G(r_{k-2}, \gamma = 1)) = d\sigma_{k-2} \approx \pi r_{k-2}^2 dE = \pi \left[\frac{bm_e m_p}{(k-2)\pi + \arctan\left(\frac{a}{bm_e m_p}\right)} \right]^2 dE_{pca} = \frac{\pi a^2}{[\ln(V_G(r_{k-2})) - \ln(D(m_e, m_p))]^2} dE_{pca}$$

In a DIS event, where $k \gg 1$, $\left| \arctan\left(\frac{a}{bm_e m_p}\right) \right| < \pi/2 \ll (k-2)\pi < k\pi$. Therefore,

Equation 11-3-12

$$\frac{d\sigma_k}{d\sigma_{k-2}} \approx \frac{\pi \left[\frac{bm_e m_p}{k\pi + \arctan\left(\frac{a}{bm_e m_p}\right)} \right]^2}{\pi \left[\frac{bm_e m_p}{(k-2)\pi + \arctan\left(\frac{a}{bm_e m_p}\right)} \right]^2} \approx \left(\frac{k-2}{k} \right)^2 = 1 - 4/k + 4/k^2$$

and consequently, $d\sigma_{k-2} > d\sigma_k$. Based on the above assumptions, the case of $E_f \rightarrow \infty$ leads to $E_{pca} \rightarrow \infty$, and therefore to $k \rightarrow \infty$, and subsequently to $d\sigma_k \rightarrow d\sigma_{k-2}$ while $d\sigma_k < d\sigma_{k-2}$. For the general case of an electron with an impact energy of

Equation 11-3-13

$$V_G(r_{k-2}, \gamma(v(r_k)) = 1) < E_{pca} < V_G(r_k, \gamma(v(r_k)) = 1) \ll E_0$$

²⁰³ In cases where $\gamma(v(r_k)) = 1$, the notations $V_G(r_k) = V_G(\vec{r}_k, v(r_k))$ and $D(m_e, m_p) = D(m_e, m_p, \gamma(v(r_k)))$ may be used.

²⁰⁴ The DIS cross section can be written as $\sigma = \int_{E_{pca}=-\infty}^{\infty} d\sigma(E_{pca})$. However, in the case of a negative E_{pca} value, the electron would remain trapped, and would never reach the detector. Therefore, E_{pca} cannot be negative. In addition, as the electron is extremely unlikely to gain energy during the scattering event, $\int_{E_{pca}=E_0}^{\infty} d\sigma(E_{pca})$ should be negligible. Therefore, the overall UG cross section can be expressed as $\sigma = \int_{E_{pca}=-\infty}^{\infty} d\sigma(E_{pca}) = \int_{E_{pca}=0}^{E_0} d\sigma(E_{pca}) = \int_{E_{pca}=0}^{E_0} \frac{d\sigma(E_{pca})}{dE_{pca}} dE_{pca}$.

As V_G is a continuous function of r , there is always a radius B_c where $r_k < B_c < r_{k-2}$ and $E_{pca} = V_G(r_{B_c}, \gamma(v(r_{B_c})) = 1)$. At an impact parameter B of less than B_c , an electron with an impact energy of E_{pca} will be scattered by the zone containing the k^{th} maximum in the same manner as it would have been scattered by a hard sphere of radius B_c . Therefore, at the limits of $v = (E_0 - E_f) \rightarrow \infty$ and $Q^2 = 4E_0E_f \sin^2\left(\frac{\theta}{2}\right) \rightarrow \infty$, the cross section of the DIS event must comply with

Equation 11-3-14

$$d\sigma_k \approx \pi r_k^2 dE_{pca} \leq \pi B_c^2 dE_{pca} \approx d\sigma(E_{pca}) \leq \pi r_{k-2}^2 dE_{pca} \approx d\sigma_{k-2}$$

Therefore, according to equations 11-3-11 and 11-3-12, for $k \rightarrow \infty$ (or $E_{pca} \rightarrow \infty$),

Equation 11-3-15

$$\frac{\pi a^2}{[\ln(V_G(r_{k-2})) - \ln(D(m_e, m_p))]^2} dE_{pca} \approx d\sigma_{k-2} \rightarrow d\sigma_k \approx \frac{\pi a^2}{[\ln(V_G(r_k)) - \ln(D(m_e, m_p))]^2} dE_{pca}$$

In order to comply with equations 11-3-13, 11-3-14 and 11-3-15, $d\sigma(E_{pca})$ must comply with

Equation 11-3-16

$$d\sigma(E_{pca}) = \frac{\pi a^2}{[\ln(E_{pca}) - \ln(D(m_e, m_p))]^2} dE_{pca}$$

Consequently, equation 11-3-16 provides a weak fall-off of $\frac{d\sigma(E_{pca})}{dE_{pca}}$ relative to the fall-off demonstrated by their elastic scattering, which is proportional to E_0^{-2} . Note that this general behavior is consistent with experimental observations. However, $E_{pca}(E_0, \nu)$ is not observable. Using the approximation given in equation 11-3-1 of $E_{pca} \approx E_0 - H\nu$, where both E_0 and ν are observables, provides

$$d\sigma(\nu) \approx \frac{d\sigma(E_{pca})}{dE_{pca}} \frac{dE_{pca}}{d\nu} d\nu = \frac{-H\pi a^2}{[\ln(E_0 - H\nu) - \ln(D(m_e, m_p))]^2} d\nu$$

which also provides a similar weak fall-off of $\frac{d\sigma(\nu)}{d\nu}$.

Section XI-4: Unified Gravitation and the Phenomenon of Bjorken Scaling

Bjorken scaling, demonstrated in figure 11-7, is the observed high-loss DIS behavior where $F_1(x, Q^2) \rightarrow \tilde{F}_1(x)$ and $F_2(x, Q^2) \rightarrow \tilde{F}_2(x)$ when $Q^2 = 4E_0E_f \sin^2\left(\frac{\theta}{2}\right) \rightarrow \infty$ and $\nu = (E_0 - E_f) \rightarrow \infty$. As discussed, high-loss DIS events adhering to $\nu \rightarrow \infty$ and $Q^2 \rightarrow \infty$ occur when the electron is scattered by a hard sphere of radius r_{pca} , where the velocity of the electron at the impact point of \vec{r}_{pca} yields $\gamma(v(\vec{r}_{pca})) = 1$.

From the UG perspective, scaling becomes apparent when the UG force dominates over the electromagnetic interaction and over the range of energy affected by the uncertainty principle. Therefore, according to section XI-1-2, $E_0 \gg E_f \gg V_G(r_{75}, v(r_{75}))$.

The physical underlying principle that leads to the observed Bjorken scaling is demonstrated in figures 11-4a to 11-4e. The illustration in figure 11-4a provides a tilted three dimensional image of the UG potential energy. The illustration displays only three consecutive maxima and one visible minimum out of an infinite set of maxima and minima in the vicinity of the $n = k_b$ maximum.

Figure 11-4b provides an illustration of the three dimensional geometry of the deep inelastic scattering of the electron by the zone $n = k_b$ at $r_n < r_{pca} < r_{n-1}$, where the blue area resides on the $V = E_{pca}$ plane and $E_{pca} = E(r_{pca})$ is the energy of the electron on impact (at r_{pca}). The electron's energy is thus given by $E_{pca} = V_G(r_{n-2}) + \Delta < V_G(r_n)$, where Δ is small relative to $V_G(r_n) - V_G(r_{n-2})$. Consequently, the electron contains sufficient energy to pass the $n - 2$ maximum, but not enough energy to penetrate the n^{th} zone. The DIS cross section is equal to the circular area contained within the outer circumference defined by the intersection of the three dimensional UG surface with the blue $V = E_{pca}$ plane. At a higher electron energy, where E_{pca} is just below the maximum $V_G(r_n)$, as shown in figure 11-4c, the electron collides with the n^{th} zone at a point slightly external to r_n and the DIS cross section is slightly reduced. Note that as the energy of the probing electrons changes continuously between $V_G(r_{n-2}) < E_{pca} < V_G(r_n)$ (approximately between the energy levels shown in figure 11-4b and 11-4c), the DIS cross section reduces continuously, and becomes almost a linear function of the electron's energy level. However, as the energy E_{pca} becomes infinitesimally larger than $V_G(r_n)$, the electron has sufficient energy to pass the $V_G(r_n)$ maximum. As the electron passes through r_n , its potential energy begins to fall drastically, and its velocity increases as its potential energy is converted to kinetic energy. After crossing the $n + 1$ minimum, the electron's potential once again increases until colliding with the zone containing the higher $V_G(r_{n+2})$ maximum at the point \vec{r}_{pca} located between $r_{n+2} < r_{pca} < r_{n+1}$. Consequently, the DIS cross section is reduced by more than $\pi(r_n^2 - (r_{n+1})^2)$. Therefore, as the energy of the electron in the vicinity of r_n changes from being infinitesimally lower than the maximum $V_G(r_n)$ to infinitesimally higher than $V_G(r_n)$, the DIS cross section reduces abruptly, resulting in a discontinuity. Such a transition is demonstrated in figure 11-4d. As the electron's impact energy E_{pca} increases continuously

between $V_G(r_n) < E_{pca} < V_G(r_{n+2})$, the cross section will reduce continuously until the energy of the electron becomes equal to $V_G(r_{n+2})$, where another discontinuity occurs. Hence, a discontinuity is expected to occur when the energy of the electron at the point of impact is equal to its potential energy at any given non-relativistic UG maximum.

It will be shown that the reduction of the DIS cross section can be described to depend on two independent parameters. The first parameter is the zone index that determines the electron's impact energy levels E_{pca} at which discontinuities in the DIS cross section occur, as well as the DIS cross section values on either side of each discontinuity. The second parameter controls the approximately linear relationship between the DIS cross section and the electron's energy at the point of closest approach, within the range of energies lying between two successive maxima. Note that at high zonal indices the slopes of the UG potential energy become extremely steep (as demonstrated by figure 11-3a), and the difference between the radii of two successive maxima becomes negligible.

At the energy range between the two maxima there is no notable change in the cross section or in the radius of the hard sphere, consequently creating an effect similar to Bjorken scaling, where the cross section depends on a single parameter (in this case, the potential energy maximum index). However, at low zonal indices the slopes are less steep, and the difference between the radii of two successive maxima is significant. Therefore, in the energy range between the two maxima, the radius and cross section of the hard sphere change notably as functions of the electron's impact energy E_{pca} , thereby creating a visible break in scaling at low DIS energies.

The above principles can be applied for the development of a more detailed mathematical description of these scaling behaviors. As stated, Bjorken scaling is the observed high-loss DIS behavior where $F_1(x, Q^2) \rightarrow \tilde{F}_1(x)$ and $F_2(x, Q^2) \rightarrow \tilde{F}_2(x)$ when $Q^2 = 4E_0E_f \sin^2\left(\frac{\theta}{2}\right) \rightarrow \infty$ and $\nu = (E_0 - E_f) \rightarrow \infty$. Bear in mind that these high-loss DIS events occur when the electron is scattered by a hard sphere of radius r_{pca} , where the velocity of the electron at the impact point of \vec{r}_{pca} yields $\gamma(v(\vec{r}_{pca})) = 1$. As \vec{r}_{pca} is located within the k^{th} zone, the electron's velocity either reduces to a non-relativistic velocity of $\gamma(v(r_{pca})) = 1$, or alternatively, the overall energy of the electron as it passes through the $k - 2$ maximum is slightly higher than its potential energy with $\gamma(v(r_{k-2})) = 1$.²⁰⁵

Consider the case where the electron's impact energy $E_{pca} \ll E_0$ is just under the potential energy of $V_G(r_k)$ at the k^{th} maximum. Therefore, an electron with a sufficiently large impact parameter of $B > r_k$ avoids collision with an impenetrable hard sphere, as demonstrated in black in figure 11-3b, or in black and green in figure 11-3c.

²⁰⁵ In the non-quantum approach, the overall energy of the electron must be somewhat above $V_G(r_{k-2}, v(r_{k-2}))$ as it passes through this maximum, otherwise the electron would not be able to enter and subsequently exit the k^{th} zone, which contains r_{pca} , on its way toward the detector.

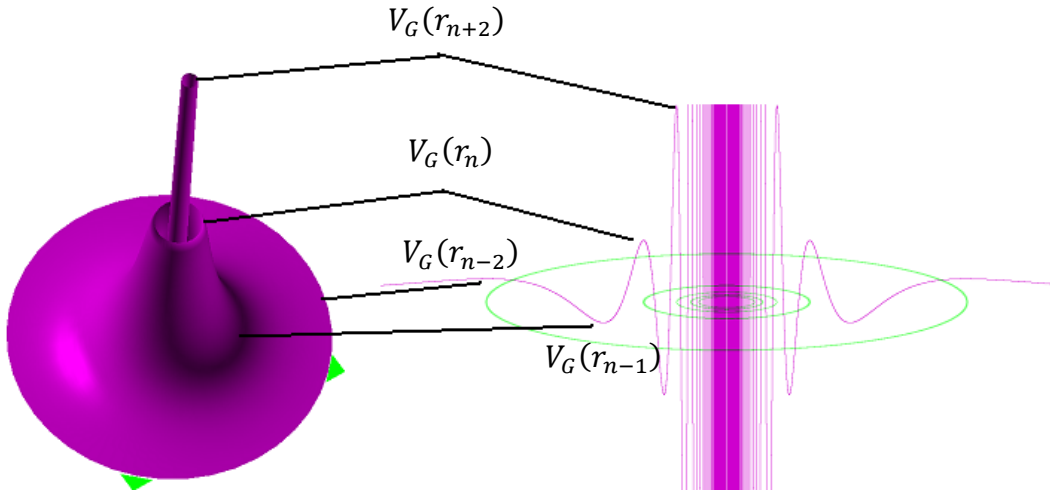


Figure 11-4a

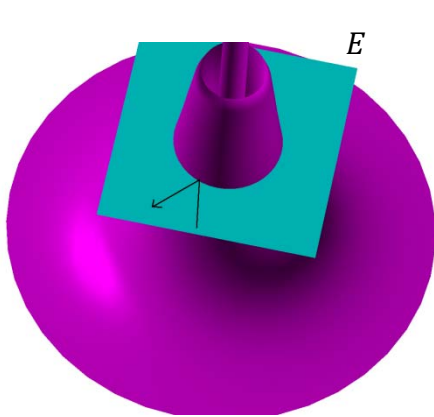


Figure 11-4b
 $V_G(r_{n-2}) + \Delta = E_{pca} < V_G(r_n)$

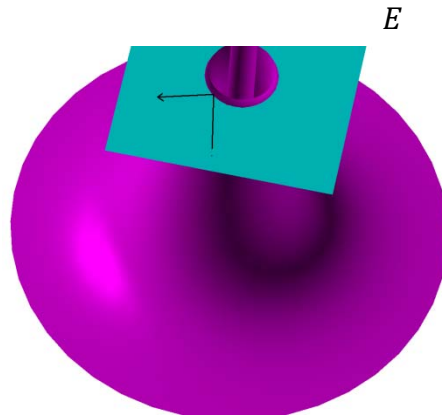


Figure 4-11c
 $V_G(r_{n-2}) < E_{pca} = V_G(r_n) - \Delta$

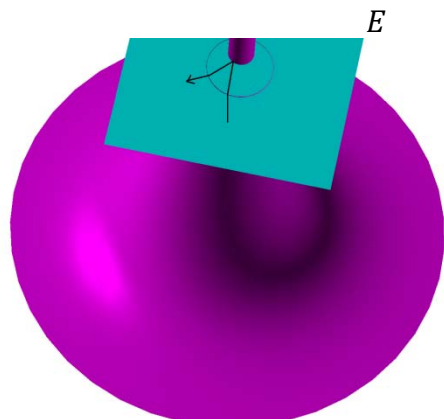


Figure 11-4d
 $E_{pca} = V_G(r_n) + \delta, \delta \rightarrow 0$

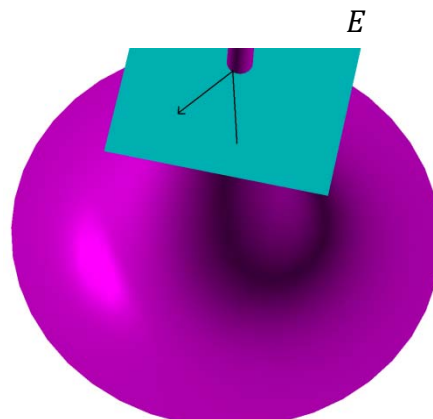


Figure 11-4e
 $E_{pca} = V_G(r_n) + \Delta < V_G(r_{n+2})$

The absolute value of the potential energy of the electron at any of the remaining maxima and minima of $n < k$ is significantly lower than E_{pca} . Therefore, throughout its trajectory the

electron retains a substantial portion of its kinetic energy with γ significantly larger than 1, and undergoes an elastic scattering with a relatively small scattering angle. However, electrons with an impact parameter of $B \lesssim r_k$ collide with an impenetrable hard sphere with a radius of r_k , as indicated in blue and green in figure 11-3b, or in blue in figure 11-3c. The potential energy of a non-relativistic electron at the maximum indexed $k - 2n$ is equal to $V_G(r_k)/13.59^n \approx E_{pca}/13.59^n \ll E_{pca}$, where n is an integer greater than zero. Hence, at least 92.6% of the electron's energy at the $k - 2$ maximum, and over 99% of the electron's energy at indices of $k - 4$ or lower must have been in the form of kinetic energy when encountered by the electron. Consequently, the effect of the maxima and minima of $n \leq k - 2$ on the electron's path is relatively small. In addition, the electron retains the majority of its velocity and kinetic energy when it encounters any maximum of $n \leq k - 2$, while the velocity and kinetic energy of the electron may increase as it encounters a minimum of $n \leq k - 1$.²⁰⁶ Therefore, the electron is abruptly halted within the k^{th} zone at about $r = r_k$, leading to $\gamma(v(r_k)) = 1$. Consequently, the cross section $d\sigma(E_{pca})$ of electrons with an impact energy of $V_G(r_k) - dE_{pca} < E_{pca} < V_G(r_k) - \delta$, where $0 < \delta \rightarrow 0$ is equal to

Equation 11-4-1

$$d\sigma(E_{pca} \rightarrow V_G(r_{k+})) \rightarrow d\sigma(V_G(r_k)) = d\sigma_k = \pi r_k^2 dE_{pca} \approx \pi \left[\frac{bm_e m_p}{k\pi + \arctan\left(\frac{a}{bm_e m_p}\right)} \right]^2 dE_{pca}$$

Bjorken scaling should take place at distances where the effects of the electromagnetic force and the uncertainty principle are negligible. Note that the effects of the electromagnetic force and the uncertainty principle were shown to become insignificant relative to the UG force at $k \geq 77$.

Since $\arctan\left(\frac{a}{bm_e m_p}\right) = 0.3936 \ll 77\pi \ll k\pi$ the following holds true:

Equation 11-4-2

$$d\sigma(E_{pca} \rightarrow V_G(r_{k+})) \approx d\sigma_k = d\sigma(V_G(r_k)) \approx \pi r_k^2 dE_{pca} \approx \pi \left[\frac{bm_e m_p}{k\pi} \right]^2 dE_{pca}$$

Similarly, for the case where E_{pca} is just under the potential energy $V_G(r_{k-2})$ of the $k - 2$ maximum,

Equation 11-4-3

$$\begin{aligned} d\sigma(E_{pca} \rightarrow V_G(r_{k-2})) &\approx d\sigma_{k-2} = d\sigma(V_G(r_{k-2})) \approx \pi r_{k-2}^2 dE_{pca} \approx \pi \left[\frac{bm_e m_p}{(k-2)\pi + \arctan\left(\frac{a}{bm_e m_p}\right)} \right]^2 dE_{pca} \\ &\approx \pi \left[\frac{bm_e m_p}{(k-2)\pi} \right]^2 dE_{pca} \approx \frac{d\sigma_k k^2}{(k-2)^2} dE > d\sigma_k \end{aligned}$$

Defining $Q_d = \frac{V_G(r_k) - E_{pca}}{V_G(r_{k-2})} = \frac{V_G(r_{k-2}) e^{\left(\frac{2a\pi}{bm_e m_p}\right)} - E_{pca}}{V_G(r_{k-2})} = 13.59 - \frac{E_{pca}}{V_G(r_{k-2})}$ provides

²⁰⁶ At even n indices, r_n is a minimum and its potential energy is negative. Therefore, it is possible that the velocity and the kinetic energy of the electron as it encounters these minima may be larger than their initial values.

Equation 11-4-4a

$$E_{pca} = (13.59 - Q_d)V_G(r_{k-2})$$

The impact energy E_{pca} of the electron can therefore be fully defined by the variables Q_d and k .

Hence, $d\sigma(E_{pca})$ can be expressed as $\left(\frac{d^2\sigma(E_{pca})}{dQ_d dk}\right) dQ_d dk$.²⁰⁷

In the case of an electron with an impact energy level falling anywhere between its potential energy at the k^{th} maximum and the $k - 2$ maximum, E_{pca} is given by

Equation 11-4-4b

$$V_G(r_{k-2}) < E_{pca} = (13.59 - Q_d)V_G(r_{k-2}) < V_G(r_k)$$

where

Equation 11-4-4c

$$0 < Q_d < e^{\left(\frac{2a\pi}{bm_e m_p}\right)} - 1 = 12.59$$

In such cases, an electron with an initial impact parameter of $B < r_k$ will have sufficient energy to penetrate the $k - 2$ zone and to reach the k^{th} zone. As the $k - 2$ maximum and the $k - 1$ minimum are not negligible relative to E_{pca} , the electron will be deflected as it passes the $k - 2$ maximum, and again as it passes the $k - 1$ minimum. These deflections influence the energy and momentum of the electron, and therefore its direction of propagation. However, as the combined width of these zones is extremely narrow, the deflections exert little effect on the actual location where the electron encounters the k^{th} zone. Therefore, whether or not the given electron collides with a hard sphere depends mainly on the electron's initial impact parameter B .²⁰⁸ With $E_{pca} \approx V_G(\vec{r}_{pca}) < V_G(r_k, \gamma = 1)$, the electron does not have sufficient energy to penetrate the k^{th} zone, and consequently, in the case of $B < r_k$, the electron is deflected by a hard sphere and its forward motion toward the nucleon is halted at the impact point. In the specific case of a high-loss DIS event, where the energy lost by the electron $\nu = E_0 - E_f \rightarrow \infty$ and $Q^2 = 4E_0 E_f \sin^2\left(\frac{\theta}{2}\right) \rightarrow \infty$, the scattering angle approaches π and the electron's relative velocity at the point of closest approach (or impact point) becomes about zero, leading to $V_G(r_k + \varepsilon_{E_{pca}}, \gamma = 1) = E_{pca}$. Note that it was taken into consideration that the rest mass of the electron as well as its nearly diminished kinetic energy at the impact point $r_k + \varepsilon_{E_{pca}}$ are negligible relative to the impact energy E_{pca} . Since the electron is scattered by a nearly hard

²⁰⁷ Note that the potential energy maxima are odd integers, therefore dk is not continuous, and instead changes in steps of two.

²⁰⁸ Note that the UG and the electromagnetic interactions are both long-range forces. In proton-electron scattering, at all distances greater than nuclear scale, the UG contribution is negligible compared with the electromagnetic contribution (by a factor of approximately 10^{39}) and can be neglected. However, at such distances the electromagnetic force reduces the impact parameter B by pulling the electron toward the proton. This may explain why the cross section of a proton-electron DIS is observed to be larger than the cross section of a neutron-electron DIS as the Bjorken scale variable $\chi \rightarrow 1$.

sphere of radius $r_k + \varepsilon_{E_{pca}}$, its cross section is given by $d\sigma(E_{pca}) = \pi (r_k + \varepsilon_{E_{pca}})^2 dE_{pca}$.

Consequently, the minimum value of $\varepsilon_{E_{pca}}$ is at the limit $E_{pca} = \lim_{\delta \rightarrow 0} V_G(r_k + \delta, \gamma = 1)$, and $\varepsilon_{E_{pca}} \rightarrow 0$ as the distance between the point of closest approach and the nucleon converges toward r_k . On the other hand, the maximal value of $\varepsilon_{E_{pca}}$, denoted $\varepsilon_{k,max}$, is associated with the minimum energy E_{pca} with which the electron can penetrate the $k - 2$ zone as it approaches and recedes from the impact point on its way to the detector. This energy value is significantly more difficult to calculate for several reasons. First, the velocity of the electron as it encounters the $k - 2$ maximum is unknown, and may be relativistic, and consequently may affect the height and the perceived location of the $k - 2$ maximum. In addition, the amount of energy lost by the electron during the time it spent between the distances of the $k - 2$ maximum and $r_k + \varepsilon_{E_{pca}}$ is substantial, thus the energy of the electron as it passes through the $k - 2$ maximum is uncertain. However, it is clear that $r_k + \varepsilon_{k,max} < r_{k-2}$, where r_{k-2} is the radius of the $k - 2$ maximum, as perceived by a non-relativistic electron.

In the case of an electron with an impact energy of E_{pca} , where $V_G(r_{k-2}, \gamma = 1) < E_{pca} \approx V_G(r_{pca}) < V_G(r_k, \gamma = 1)$, and an impact parameter of $r_k + \varepsilon_{E_{pca}} < B < r_{k-2}$, the electron will escape the k^{th} zone without colliding with its impenetrable hard sphere. The electron will then re-enter zone $k - 1$ on its way toward the detector, while retaining a non-zero and possibly relativistic velocity at the point of closest approach r_{pca} within the k^{th} zone. At an impact parameter B just above $r_k + \varepsilon_{E_{pca}}$, the scattering may still be significantly inelastic, however, as the value of B approaches r_{k-1} , the scattering becomes less inelastic.

Consequently, DIS cross sections demonstrate discontinuity at energy levels that match the potential energy of the zonal maxima. In the case of a close encounter between the electron and the $k - 2$ maximum, the cross section reduces abruptly from $\pi r_{k-2}^2 dE_{pca}$ to $\pi (r_k + \varepsilon_{k,max})^2 dE_{pca}$. As the electron's impact energy E_{pca} continues to increase between $V_G(r_{k+\varepsilon_{k,max}}, \gamma = 1)$ and $V_G(r_k, \gamma = 1)$, the cross section decreases gradually toward $d\sigma_k = \pi r_k^2 dE_{pca}$. The next discontinuity occurs at the energy $E_{pca} = V_G(r_{k+2+\varepsilon_{k+2,max}}, \gamma = 1)$, where the cross section reduces abruptly from $\pi r_k^2 dE_{pca}$ to $\pi (r_{k+2} + \varepsilon_{k+2,max})^2 dE_{pca}$. This pattern of discontinuities, or scaling gaps, depicted in Figure 11-5 will be shown to occur, and to provide a scaling phenomenon that is similar to Bjorken scaling.

As discussed, since V_G is a continuous function of the parametric distance r , for any E_{pca} compliant with $V_G(r_{k-2}, \gamma = 1) < E_{pca} < V_G(r_k, \gamma = 1)$, there is a distance ε_k at which $E_{pca} = V_G(r_k + \varepsilon_k, \gamma = 1)$, where $r_k < r_k + \varepsilon_k < r_{k-2}$. Therefore,

Equation 11-4-5

$$d\sigma(E_{pca}) = d\sigma\left((13.59 - Q_d)V_G(r_{k-2})\right) \approx \pi(r_k + \varepsilon_k)^2 dE_{pca}$$

where the value of ε_k depends on the values of k and Q_d . For a high-loss deep inelastic scattering to take place, the potential energy at the point of closest approach must comply with $V_G(\vec{r}_{pca}, \gamma = 1) \approx E_{pca} > 0$ and $\gamma(v(\vec{r}_{pca})) = 1$. The zero crossing of the potential energy of a non-relativistic electron preceding r_k can be denoted as $r_{k-1/2}$. Thus, $V_G(r_{k-1/2}, \gamma = 1) = 0$, where $r_k < r_{k-1/2} < r_{k-1}$. At the impact point \vec{r}_{pca} , where $V_G(r_{pca}, \gamma = 1) \approx E_{pca}$, the slope of the potential energy V_G must be negative. Further note that E_{pca} must be positive for the electron to escape the nucleon and reach the detector. Therefore, the range of distances between $r_{k-1/2} < r_{pca} < r_{k-2}$ can be ruled out as possible distances for scattering by a hard sphere. Consequently, the value of ε_k is restricted to the range of $0 < \varepsilon_k < r_{k-1/2} - r_k$. This creates a discontinuity in the cross section function, as the cross section of $E_{pca} = V_G(r_{k-2})$ is given by

$\lim_{\delta \rightarrow +0} (d\sigma(V_G(r_{k-2}) - \delta)) = \pi(r_{k-2})^2 dE_{pca}$, while the DIS cross section of an infinitesimally higher impact energy $E_{pca} = V_G(r_{k-2}) + \delta$ results in $\lim_{\delta \rightarrow +0} (d\sigma(V_G(r_{k-2}) + \delta)) \approx \pi(r_k + \varepsilon_k)^2 dE_{pca}$, where $r_k < r_k + \varepsilon_k < r_{k-1/2} < r_{k-1} < r_{k-2}$. These discontinuities (or gaps), denoted as Δ_k , are given by

Equation 11-4-6

$$\Delta_k = \lim_{\delta \rightarrow +0} (d\sigma(V_G(r_{k-2}) - \delta) - d\sigma(V_G(r_{k-2}) + \delta)) \approx \pi(r_{k-2})^2 dE_{pca} - \pi(r_k + \varepsilon_k)^2 dE_{pca}$$

or

Equation 11-4-7

$$(\pi(r_{k-2})^2 - \pi(r_k + \varepsilon_k)^2) dE_{pca} > \Delta_k > (\pi(r_{k-2})^2 - \pi(r_{k-1})^2) dE_{pca}$$

Recall that the velocity of the electron upon being scattered by the higher potential energy barrier is non-relativistic. Hence, the above inequalities can also be estimated for the non-relativistic electron,

Equation 11-4-8

$$\Delta_k > (\pi r_{k-2}^2 - \pi r_{k-1}^2) dE_{pca} > \left\{ \pi \left[\frac{bm_e m_p}{(k-2)\pi + \arctan\left(\frac{a}{bm_e m_p}\right)} \right]^2 - \pi \left[\frac{bm_e m_p}{(k-1)\pi + \arctan\left(\frac{a}{bm_e m_p}\right)} \right]^2 \right\} dE_{pca}$$

As $\arctan\left(\frac{a}{bm_e m_p}\right) = 0.3936 \ll (k-2)\pi$,

Equation 11-4-9

$$\Delta_k > \frac{(bm_e m_p)^2}{\pi} \left[\left(\frac{1}{k-2} \right)^2 - \left(\frac{1}{k-1} \right)^2 \right] dE_{pca} = \frac{(bm_e m_p)^2}{\pi} \left(\frac{2k-3}{(k-2)^2(k-1)^2} \right) dE_{pca} \rightarrow \frac{2(bm_e m_p)^2}{k^3 \pi} dE_{pca}$$

as $k \rightarrow \infty$

and

Equation 11-4-10

$$\Delta_k < (\pi r_{k-2}^2 - \pi r_k^2) dE_{pca} < \left\{ \pi \left[\frac{bm_e m_p}{(k-2)\pi + \arctan\left(\frac{a}{bm_e m_p}\right)} \right]^2 - \pi \left[\frac{bm_e m_p}{k\pi + \arctan\left(\frac{a}{bm_e m_p}\right)} \right]^2 \right\} dE_{pca}$$

J and $1.28 * 10^{-23} \sigma$

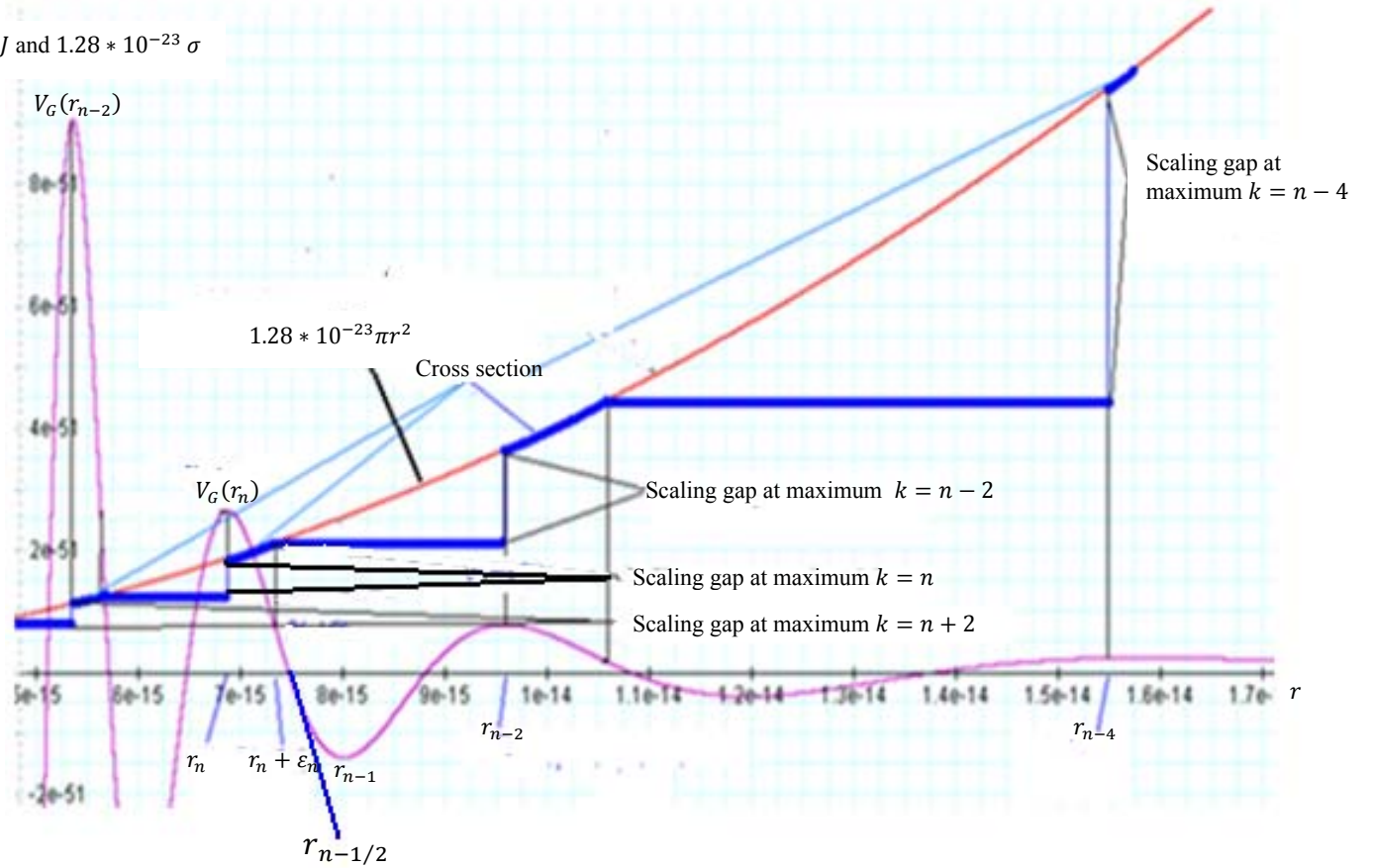


Figure 11-5: Provides an illustration of the DIS cross section of particles such as electrons by a nucleon (note that for the purpose of clarity, the mass of the scattered particle used in this example is slightly larger than mass of an electron, allowing for the clear identification of more than three maxima in the graph). The figure further includes the curve of $1.28 * 10^{-23} J/m^2 * \pi r^2$, which is proportional to the hard sphere cross section of a zone. The multiplication factor is included in order to allow the hard sphere cross section to be displayed in the same figure, along the zone energies. Discontinuity in the cross section can be noted at every maximum, creating cross section ‘scaling gaps’ between the zones and generating a phenomenon similar to the observed Bjorken scaling. The degree of curvature of the cross section between any two successive discontinuities becomes increasingly insignificant as $d\sigma$ and r reduce, and as k increases (where the zone maximum index, given by an odd integer k , is analogous to χ , where χ is the Bjorken scale variable). This increase in the cross section curvature at low k indices (low χ values) explains the break in scaling at low values of χ .

As $\arctan\left(\frac{a}{bm_e m_p}\right) < \pi/2 \ll (k-2)\pi < k\pi$,

Equation 11-4-11

$$\Delta_k < \left(\pi \left[\frac{bm_e m_p}{(k-2)\pi} \right]^2 - \pi \left[\frac{bm_e m_p}{k\pi} \right]^2 \right) dE_{pca} = \frac{(bm_e m_p)^2}{\pi} \left(\frac{4k-4}{k^2(k-2)^2} \right) dE_{pca} \rightarrow \frac{4(bm_e m_p)^2}{k^3 \pi} dE_{pca} \text{ as } k \rightarrow \infty$$

Therefore, the width of the k^{th} discontinuity in the cross section is consistent with

$$\frac{(bm_em_p)^2}{\pi} \left(\frac{2k-3}{(k-2)^2(k-1)^2} \right) dE_{pca} < \Delta_k < \frac{(bm_em_p)^2}{\pi} \left(\frac{4k-4}{k^2(k-2)^2} \right) dE_{pca}, \text{ which converges to}$$

$$\frac{2(bm_em_p)^2}{k^3\pi} dE_{pca} < \lim_{k \rightarrow \infty} \Delta_k < \frac{4(bm_em_p)^2}{k^3\pi} dE_{pca} \text{ as } k \rightarrow \infty.$$

Consequently, deep inelastic scattering results in a series of discontinuities that resemble the behavior of Bjorken scaling. The next step is to determine the behavior of the double differential cross section as a function of Q_d and the zonal index k .

Knowledge of the value of ε_k is required for the calculation of the cross section scaling pattern. The approach taken here is to approximate $V_G(r)$ by a linear function lying between the potential energy of a non-relativistic electron at the maximum $V_G(r_k)$, located at r_k , and the preceding zero crossing $V_G(r_{k-1/2}) = 0$, located at $r_{k-1/2}$. Note that the selection of the non-relativistic values of $V_G(r_k)$ and $V_G(r_{k-1/2})$ is driven by the realization that for a DIS event to occur, the velocity of the electron at the impact location of $r_k + \varepsilon_k$ should be close to zero. The slope S_V of this function is given by

Equation 11-4-12

$$S_V = \frac{V_G(r_k) - V_G(r_{k-1/2})}{(r_k - r_{k-1/2})} = \frac{V_G(r_k)}{(r_k - r_{k-1/2})}$$

Therefore, the distance r at which a particle with an impact energy of $V_G(r_{k-2}) < E_{pca} < V_G(r_k)$ will encounter a potential energy equal to E_{pca} is given approximately by

Equation 11-4-13

$$\frac{E_{pca}}{(r - r_{k-1/2})} = S_V = \frac{V_G(r_k)}{(r_k - r_{k-1/2})}$$

or

Equation 11-4-14

$$r = \frac{E_{pca}(r_k - r_{k-1/2})}{V_G(r_k)} + r_{k-1/2}$$

At a minimum, $E_{pca} = V_G(r_\varepsilon)$ cannot be lower than $V_G(r_{k-2})$. Otherwise, the electron would remain trapped between the k^{th} maximum and the $k - 2$ maximum, and would not reach the detector. Solving specifically for the minimum at $r_\varepsilon = r_k + \varepsilon_k$, where $E_{pca} = V_G(r_\varepsilon) = V_G(r_{k-2})$, provides

Equation 11-4-15

$$r_\varepsilon = \frac{V_G(r_{k-2})}{V_G(r_k)} (r_k - r_{k-1/2}) + r_{k-1/2}$$

According to equation 11-8, non-relativistic V_G zero crossings occur where $\cos\left(\frac{bm_em_p}{r_{k-1/2}}\right) = e^{-a/r_{k-1/2}}$. In a high-energy DIS experiment the UG exponent $e^{a/r_{k-1/2}}$ must be very large. Subsequently, $e^{-a/r_{k-1/2}} \approx 0$. Thus, $r_{k-1/2} \approx \frac{bm_em_p}{(k-1/2)\pi}$. Defining $\Omega = \arctan\left(\frac{a}{bm_em_p}\right)$ and using equations 11-4-15, 11-2-11 and 11-9b (with $\gamma = 1$ at both r_k and r_{k-2}), as well as the above expression for $r_{k-1/2}$, yields

Equation 11-4-16

$$r_\varepsilon \approx e^{-2a\pi/(bm_em_p)} \left[\frac{bm_em_p}{k\pi + \Omega} - \frac{bm_em_p}{(k-1/2)\pi} \right] + \frac{bm_em_p}{(k-1/2)\pi}$$

or

Equation 11-4-17

$$r_\varepsilon \approx \frac{bm_em_p}{(k-1/2)\pi} \left\{ e^{(-2a\pi/(bm_em_p))} \left[\frac{-1-2\Omega/\pi}{2(k+\Omega/\pi)} \right] + 1 \right\}$$

and

Equation 11-4-18

$$d\sigma(E_{pca}) \cong \pi r_\varepsilon^2 dE_{pca} = \frac{1}{\pi} \left\{ \frac{bm_em_p}{(k-1/2)} \left\{ e^{(-2a\pi/(bm_em_p))} \left[\frac{-1-2\Omega/\pi}{2(k+\Omega/\pi)} \right] + 1 \right\} \right\}^2 dE_{pca} \text{ when } E_{pca} \text{ is just above } V_{k-2}$$

In the general case, in which the electron's impact energy E_{pca} in the rest frame of the nucleon is within the range $V_G(r_{k-2}) < E_{pca} \leq V_G(r_k)$, the cross section $d\sigma(E_{pca})$ (using equation 11-4-14) is given approximately by

Equation 11-4-19

$$d\sigma(E_{pca}) \approx \pi r_E^2 dE_{pca} \approx \pi \left(\frac{E_{pca}}{V_G(r_k)} (r_k - r_{k-1/2}) + r_{k-1/2} \right)^2 dE_{pca}$$

or

Equation 11-4-20

$$d\sigma(E_{pca}) \approx \pi r_E^2 dE_{pca} \approx \pi \left(\left(\frac{E_{pca}}{V_G(r_k)} \right) \left[\frac{bm_em_p}{k\pi + \Omega} - \frac{bm_em_p}{(k-1/2)\pi} \right] + \frac{bm_em_p}{(k-1/2)\pi} \right)^2 dE_{pca}$$

or

Equation 11-4-21

$$d\sigma(E_{pca}) \approx \frac{1}{\pi} \left(\frac{bm_em_p}{(k-1/2)} \right)^2 \left[\frac{-E_{pca}(1+2\Omega/\pi)}{2(k+\Omega/\pi)V_G(r_k)} + 1 \right]^2 dE_{pca}$$

Substituting equation 11-1-2, where k is an odd integer, into equation 11-4-21 yields

Equation 11-4-22

$$d\sigma(E_{pca}) \approx \frac{1}{\pi} \left(\frac{bm_e}{2(k+\Omega/\pi)(k-1/2)} \right)^2 \left[\frac{-E_{pca}(1+2\Omega/\pi)}{A(m_p, m_e)e^{(ka\pi/bm_em_p)} + 2(k+\Omega/\pi)} \right]^2 dE_{pca}$$

Under the condition where $V_G(r_{k-2}) < E_{pca} < V_G(r_k)$, equation 11-1-3b at the maxima $V_G(r_{k-2})$ and $V_G(r_k)$ provides

Equation 11-4-23

$$A(m_p, m_e)e^{(k-2)(a\pi/bm_em_p)} < E_{pca} < A(m_p, m_e)e^{k(a\pi/bm_em_p)}$$

Substituting equations 11-4-23 and 11-4-4a in equation 11-4-22 yields

Equation 11-4-24

$$d\sigma(E_{pca}) \approx \frac{1}{\pi} \left(\frac{bm_em_p}{(k + \Omega/\pi)(2k - 1)} \right)^2 \left[-(13.59 - Q_d)(1 + 2\Omega/\pi)e^{(-2a\pi/bm_em_p)} + 2(k + \Omega/\pi) \right]^2 dE_{pca}$$

Substituting the estimated values $a = 5.7 * 10^{-14} m$, $b \approx 0.9 * 10^{44} m/kg^2$ and the given masses of the electron and proton into equation 11-4-24, with the realization that at close to a 180° scattering angle the velocity at the point of closest approach is non-relativistic, results in

Equation 11-4-25

$$d\sigma(E_f) = \frac{d^2\sigma(E_f)}{dQ_d dk} dQ_d dk = 6 * 10^{-27} \left(\frac{1}{(k + 0.125)(2k - 1)} \right)^2 [-0.092(13.59 - Q_d) + 2(k + 0.125)]^2 dQ_d dk$$

where according to equation 11-4-4c, $0 < Q_d < 12.59$. Figures 11-6a and 11-6b illustrate the resulting scaling behavior by displaying the ‘hard sphere’ cross section $\frac{d^2\sigma}{dQ_d dk}$ as a function of Q_d . Each waveform is associated with the inelastic scattering produced by electron collisions with a given k^{th} zone, where k is an odd integer.

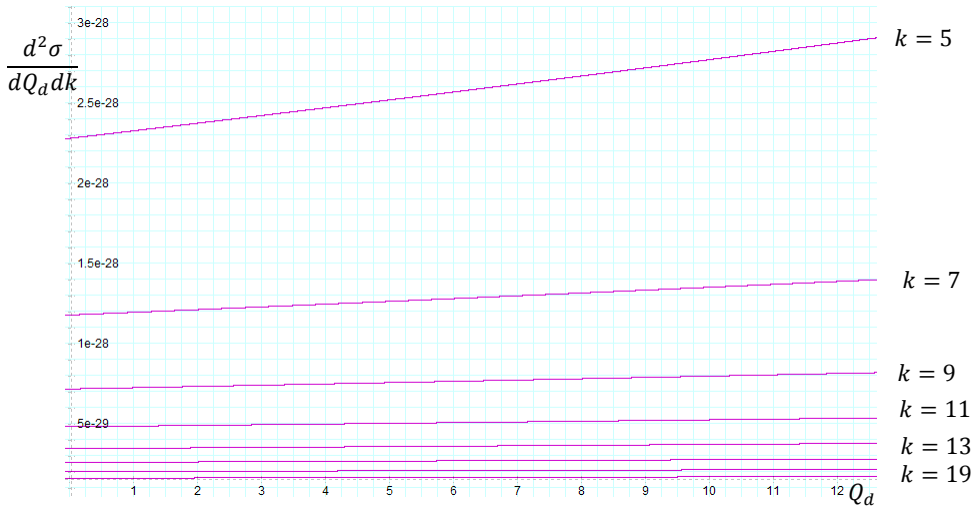


Figure 11-6a: Display of the UG DIS double differential cross section scaling, calculated via equation 11-4-25, due to repulsive zones above $k = 5$. Note that within the provided range of energies, where $k < 73$, the effect of the UG scaling may be masked by the much larger electromagnetic interaction, as well as by the effect of the uncertainty principle. Nevertheless, the figure is displayed in order to effectively demonstrate the scaling break that occurs at relatively low k values.

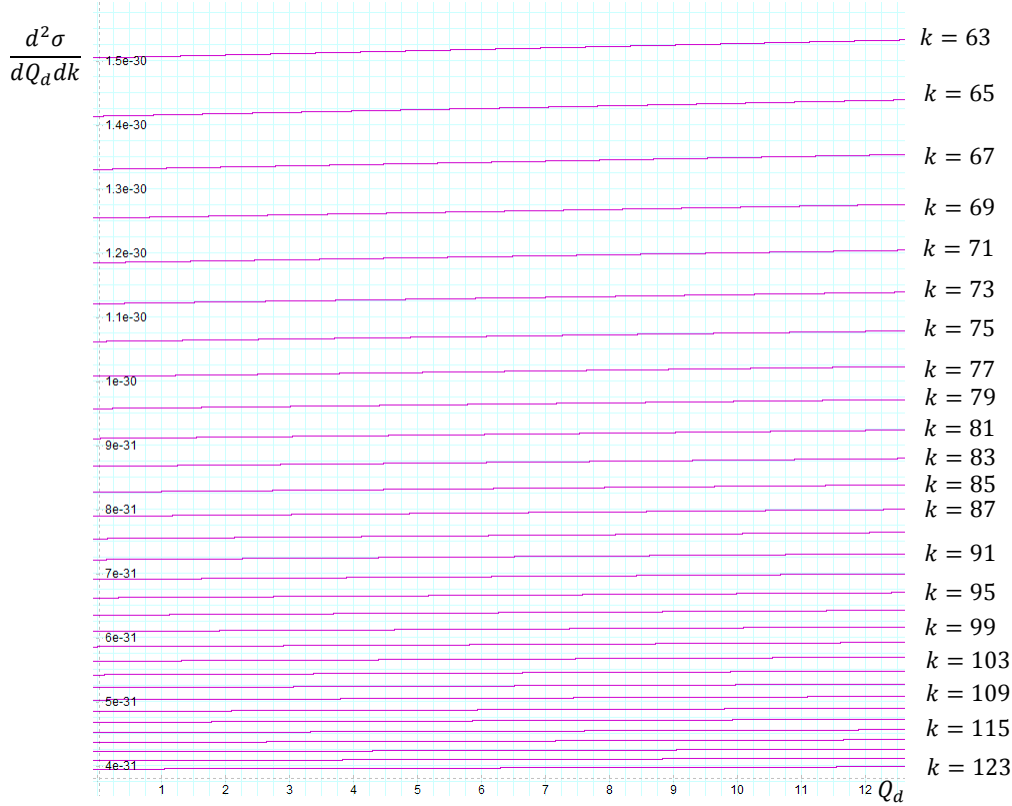


Figure 11-6b: Display of the calculated double differential cross section of a UG deep inelastic scattering in the range between $k = 63$ and $k = 123$. Across most of this range of energy, the UG interaction dominates over the effects of the electromagnetic interaction, and the uncertainty principle. The displayed cross section provides clear scaling properties, as well as a break in the scaling at low k values. The scaling pattern in figures 11-6a and b bears a resemblance to the observed Bjorken scaling pattern of the form factor $F_2(x, Q^2)$ provided in Figure 11-7 within the range of $0.0009 < \chi < 0.275$, where an odd k is analogous to the Bjorken variable χ and the factor Q_d is analogous to Q^2 .

As demonstrated in equation 11-4-25, and in figures 11-6a and 11-6b, the dependency of the DIS double differential cross section on Q_d is relatively weak, and therefore provides a scaling pattern similar to the observed Bjorken scaling. Similar to Bjorken scaling, the calculated scaling of equation 11-4-25 displays a break in the scaling at low values of k , in which the cross section $\frac{d^2\sigma}{dQ_d dk}$ is increased with increasing Q_d . As anticipated, an increase in χ (signifying that the scattering becomes more inelastic) corresponds with an increase in k , while an increase in Q^2 corresponds with an increase in Q_d .²⁰⁹

Using equations 11-3-16 and 11-4-4a, the scaling and the break in the scaling at low k values are given by

²⁰⁹ Providing that experimental data becomes available in this form (where the overall DIS cross section is dependent on Q_d and on odd k , rather than on χ and Q^2), the values of the UG constants a and b could be calculated with greater accuracy.

Equation 11-4-26

$$d\sigma(E_f) = \frac{d^2\sigma}{dQ_d dk} dQ_d dk = \frac{\pi a^2}{\left[\ln(E_{pca}) - \ln(D(m_e, m_p)) \right]^2} dQ_d dk$$

$$= \frac{\pi a^2}{\left[\ln(V_G(r_{k-2})) + \ln(13.59 - Q_d) - \ln(D(m_e, m_p)) \right]^2} dQ_d dk$$

where $0 = \ln(1) \leq \ln(13.59 - Q_d) \leq \ln(13.59) = 2.609$.

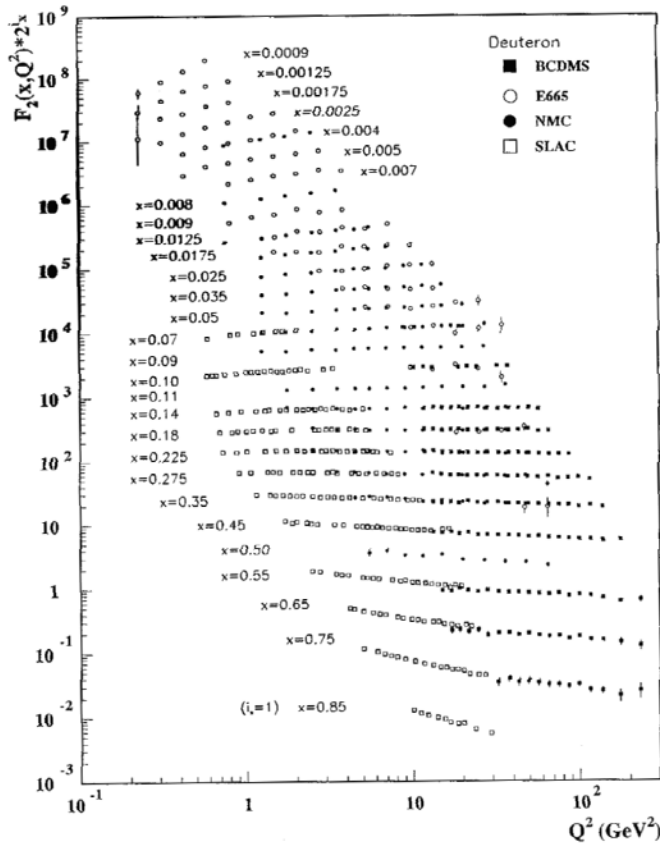


Figure 11-7: The deuteron structure function F_2^d measured in electromagnetic scattering of electrons (SLAC) and muons (BCDMS, E665, NMC) on a fixed target, shown as a function of Q^2 for bins of fixed x . Statistical and systematic errors added in quadrature are shown. For the purpose of plotting, F_2^d has been multiplied by 2^{i_x} , where i_x is the number of the x bin, ranging from 1 ($x = 0.85$) to 29 ($x = 0.0009$). References: H1-C. Adloff et al., Eur. Phys. J. C21, 33 (2001); C. Adloff et al., Eur. Phys. J. hep-ex/0304003; ZEUS-S. Chekanov et al., Eur. Phys. J. C21,443 (2001); BCDMS-A.C. Benvenuti et al., Phys. Lett. B223, 485 (1989); E665-M.R. Adams et al., Phys Rev. D54, 3006 (1996); NMC-M. Arneodo et al., Nucl. Phys. B483, 3 (97); SLAC-L.W. Whitlow et. Al., Phys. Lett. B282, 475 (1992). (Source: "16. Structure Functions" by B. Foster, A.D. Martin and M.G. Vinceter, citation: W. M. Yao et al., Journal of Physics G 33, 1 (2006) available on the PDG WWW pages (URL: <http://pdg.lbl.gov/>) July 2006.)

Equation 11-4-26 demonstrates that when $\ln(13.59 - Q_d) \ll \ln(V_G(r_{k-2}))$ for odd k , $\frac{d^2\sigma}{dQ_d dk}$ is almost independent of Q_d (thus resulting in the scaling phenomenon). At lower odd k indices, where $\ln(13.59 - Q_d)$ is not negligible compared with $\ln(V_G(r_{k-2}))$, $\frac{d^2\sigma}{dQ_d dk}$ declines with decreasing Q_d , generating the break in scaling observed for low k (or low χ) values. In either case, the DIS cross section fall-off with decreasing Q_d (or increasing E_{pca} and decreasing Q^2) is significantly weaker than the elastic scattering (which falls off proportionally to $1/E_0^2$). As stated above, this weaker fall-off provided by the UG theory is consistent with reported experimental data in the range of $0 < \chi < 0.275$.

Appendix A: The UG Scaling Theorems

Nebulae and galaxies are observed to come in many shapes and sizes. This raises the question of whether the morphology observed for an astronomical object of a given size can recur in astronomical objects on an entirely different distance scale. As satellites, planets, stars, nebulae, galaxies and clusters of galaxies are assumed to be governed by the same gravitational law, it is logical to suppose that the same morphology can be observed across distance scales. According to the UG theory, for any given system consisting of a test object that rotates around a source object with an orbital radius significantly larger than the constant a (approximately larger than the size of an atom), the following UG scaling theorem can be applied:

A-1: The First UG Scaling Theorem

Consider a system containing a test object with $j = 1$ to J groups of N_{m_j} particles of mass m_j located at \vec{r}_j moving at velocities \vec{u}_j relative to the center of the source object. The source object contains $k = 1$ to K groups of N_{M_k} particles of mass M_k located at \vec{s}_k moving at velocities of \vec{v}_k relative to its center.²¹⁰ The UG potential energy of the test object is therefore given by

$$V_G \left(\left\{ \vec{r}_j, m_j, N_{m_j}, \vec{u}_j \right\}_{j=1 \text{ to } J}, \left\{ \vec{s}_k, M_k, N_{M_k}, \vec{v}_k \right\}_{k=1 \text{ to } K} \right) \\ = -\frac{G}{a} \left(\sum_{j=1}^J \sum_{k=1}^K N_{m_j} m_j N_{M_k} M_k \gamma^2 (|\vec{v}_k - \vec{u}_j|) \left[e^{a/\dot{D}_{jk} \cos \left(\frac{b M_k m_j \gamma (|\vec{v}_k - \vec{u}_j|)}{\dot{D}_{jk}} \right)} - 1 \right] \right)$$

The UG potential energy between the two objects of the system scaled via $m_j \rightarrow P m_j$, $M_k \rightarrow Q M_k$, $\vec{r}_j \rightarrow P Q \vec{r}_j$ and $\vec{s}_k \rightarrow P Q \vec{s}_k$, where P and Q are rational numbers²¹¹ and all velocities $\{\vec{u}_j\}$ and $\{\vec{v}_k\}$ remain unaltered, yields

$$V_G \left(\left\{ P Q \vec{r}_j, P m_j, N_{m_j}, \vec{u}_j \right\}_{j=1 \text{ to } J}, \left\{ P Q \vec{s}_k, Q M_k, N_{M_k}, \vec{v}_k \right\}_{k=1 \text{ to } K} \right) = \\ P Q V_G \left(\left\{ \vec{r}_j, m_j, N_{m_j}, \vec{u}_j \right\}_{j=1 \text{ to } J}, \left\{ \vec{s}_k, M_k, N_{M_k}, \vec{v}_k \right\}_{k=1 \text{ to } K} \right)$$

where the angular velocity of any particle in the scaled system is reduced by a factor of PQ ($w_j \rightarrow w_j/PQ$ and $w_k \rightarrow w_k/PQ$).

²¹⁰ Note that this description is sufficiently general to describe any real astronomical system, as it is always possible to select the SHP groups in such a way that each one includes only a single particle. Thus, $N_{m_j} = 1$ and $N_{M_k} = 1$ for all j and k , and the number of particles in the system is equal to $J + K$.

²¹¹ Although the values of P and Q can mathematically be any real number, P and Q only have a physical meaning as integers or rational numbers, since the number of particles must be given by an integer.

Proof:

Denote $\vec{r}_{jk} = \vec{r}_j - \vec{s}_k = (r_{jk_{\perp}}^2 + r_{jk_{\parallel}}^2 + r_{jk_{\perp}}^2)^{1/2}$ and $r_{jk} = |\vec{r}_{jk}|$, where within the plane defined by the vectors \vec{v}_k and \vec{u}_j , $r_{jk_{\perp}}$ is the \vec{r}_{jk} component that is perpendicular to the vector $\vec{v}_k - \vec{u}_j$, $r_{jk_{\parallel}}$ is the \vec{r}_{jk} component that is parallel to the vector $\vec{v}_k - \vec{u}_j$ within the plane, and $r_{jk_{\perp}}$ is the \vec{r}_{jk} component that is perpendicular to the plane. Since only the parallel component of \vec{r}_{jk} is contracted by the relativistic effect, the distance between the two particles, as viewed in the inertial frame of either particle, is given by

$$\dot{D}_{jk} = \left(r_{jk_{\perp}}^2 + \frac{r_{jk_{\parallel}}^2}{\gamma^2(|\vec{v}_k - \vec{u}_j|)} + r_{jk_{\perp}}^2 \right)^{1/2} = \left(r_{jk}^2 - r_{jk_{\parallel}}^2 + \frac{r_{jk_{\parallel}}^2}{\gamma^2(|\vec{v}_k - \vec{u}_j|)} \right)^{1/2} = \left(r_{jk}^2 - r_{jk_{\parallel}}^2 \left(1 - \frac{1}{\gamma^2(|\vec{v}_k - \vec{u}_j|)} \right) \right)^{1/2}$$

with $\gamma(|\vec{v}_k - \vec{u}_j|) = \left(1 - \frac{|\vec{v}_k - \vec{u}_j|^2}{c^2} \right)^{-1/2}$. Thus,

$$\dot{D}_{jk} = \left(r_{jk}^2 - \frac{|\vec{v}_k - \vec{u}_j|^2}{c^2} r_{jk_{\parallel}}^2 \right)^{1/2} = \left(r_{jk}^2 - \frac{|\vec{v}_k - \vec{u}_j|^2}{c^2} r_{jk}^2 \left(\frac{\hat{r}_{jk} \cdot (\vec{v}_k - \vec{u}_j)}{|\vec{v}_k - \vec{u}_j|} \right)^2 \right)^{1/2}$$

or

$$\dot{D}_{jk} = r_{jk} \left(1 - \left(\frac{\hat{r}_{jk} \cdot (\vec{v}_k - \vec{u}_j)}{c} \right)^2 \right)^{1/2}$$

On scales significantly larger than nuclear scale, the distance between the two objects is substantially greater than a ; hence, $e^{a/\dot{D}_{jk}}$ becomes indistinguishable from 1. Therefore, **Equation A-1-1**

$$V_G \left(\left\{ \vec{r}_j, m_j, N_{m_j}, \vec{u}_j \right\}_{j=1 \text{ to } J}, \left\{ \vec{s}_k, M_k, N_{M_k}, \vec{v}_k \right\}_{k=1 \text{ to } K} \right) = -\frac{G}{a} \left(\sum_{j=1}^J \sum_{k=1}^K N_{m_j} m_j N_{M_k} M_k \gamma^2 (|\vec{v}_k - \vec{u}_j|) \left[\cos \left(\frac{b M_k m_j \gamma (|\vec{v}_k - \vec{u}_j|)}{r_{jk} \left(1 - \left(\frac{\hat{r}_{jk} \cdot (\vec{v}_k - \vec{u}_j)}{c} \right)^2 \right)^{0.5}} \right) - 1 \right] \right)$$

Scaling $m_j \rightarrow P m_j$, $M_k \rightarrow Q M_k$, $\vec{r}_j \rightarrow PQ \vec{r}_j$ and $\vec{s}_k \rightarrow PQ \vec{s}_k$ and using the identity $PQ \vec{r}_j - PQ \vec{s}_k = PQ(\vec{r}_j - \vec{s}_k) = PQ \vec{r}_{jk}$, while retaining the same sets of velocities \vec{u}_j and \vec{v}_k , provides

Equation A-1-3

$$\begin{aligned}
 & V_G \left(\left\{ PQ\vec{r}_j, Pm_j, N_{m_j}, \vec{u}_j \right\}_{j=1 \text{ to } J}, \left\{ PQ\vec{s}_k, QM_k, N_{M_k}, \vec{v}_k \right\}_{k=1 \text{ to } K} \right) \\
 &= -\frac{G}{a} \left(\sum_{j=1}^J \sum_{k=1}^K PN_{m_j} m_j N_{M_k} QM_k \gamma^2 (|\vec{v}_k - \vec{u}_j|) \left[\cos \left(\frac{bQM_k Pm_j \gamma (|\vec{v}_k - \vec{u}_j|)}{PQr_{jk} \left(1 - \left(\frac{\hat{r}_{jk} \cdot (\vec{v}_k - \vec{u}_j)}{c} \right)^2 \right)^{0.5}} \right) - 1 \right] \right) = \\
 &= -\frac{G(PQ)}{a} \left(\sum_{j=1}^J \sum_{k=1}^K N_{m_j} m_j N_{M_k} M_k \gamma^2 (|\vec{v}_k - \vec{u}_j|) \left[\cos \left(\frac{bM_k m_j \gamma (|\vec{v}_k - \vec{u}_j|)}{r_{jk} \left(1 - \left(\frac{\hat{r}_{jk} \cdot (\vec{v}_k - \vec{u}_j)}{c} \right)^2 \right)^{0.5}} \right) - 1 \right] \right)
 \end{aligned}$$

Thus,

$$\begin{aligned}
 & V_G \left(\left\{ PQ\vec{r}_j, Pm_j, N_{m_j}, \vec{u}_j \right\}_{j=1 \text{ to } J}, \left\{ PQ\vec{s}_k, QM_k, N_{M_k}, \vec{v}_k \right\}_{k=1 \text{ to } K} \right) = \\
 & (PQ) V_G \left(\left\{ \vec{r}_j, m_j, N_{m_j}, \vec{u}_j \right\}_{j=1 \text{ to } J}, \left\{ \vec{s}_k, M_k, N_{M_k}, \vec{v}_k \right\}_{k=1 \text{ to } K} \right)
 \end{aligned}$$

as claimed in the first part of the first theorem.

Note that for the first theorem to hold true, the set of velocities $\{\vec{u}_j\}$ and $\{\vec{v}_k\}$ must remain unchanged.²¹² In the contrary case, the terms $\gamma(|\vec{v}_k - \vec{u}_j|)$ and $\left(1 - \left(\frac{\hat{r}_{jk} \cdot (\vec{v}_k - \vec{u}_j)}{c} \right)^2 \right)^{0.5}$ would cause significant distortion in the scaled system. Therefore, to preserve the morphology, all the particles of the scaled system must travel at the same velocity as their counterparts in the original system. In the case of solid rotation, where a group of particles (within either object of the original system) rotate as a solid sub-object around the center of the source object with an angular momentum w , the group of particles travels at a velocity of wr_j (or ws_k). As $r_j \rightarrow PQr_j$ and $s_k \rightarrow PQs_k$ the angular velocity of the scaled sub-object must be scaled to $w \rightarrow w/PQ$ in order for the velocity of the particles of the scaled system to equal the velocity of the particles of the original system. While different sections of the original system may demonstrate different angular velocities, all the angular velocities of all of the particles in the scaled system must be reduced by the same factor of w/PQ , proving the second part of the first theorem.

A-2: The Second UG Scaling Theorem

The potential energy is linear with the number of particles of each type.

²¹² Note that in the case where all of the particles of the original system as well as the scaled system are non-relativistic, the theorem can be extended to allow for the scaling of all velocities by a fixed factor U , where $\{\vec{u}_j\} \ll c$, $\{\vec{v}_k\} \ll c$, $\{U\vec{u}_j\} \ll c$, and $\{U\vec{v}_k\} \ll c$. In such a case, the morphology of the system will remain unaltered, while all of its angular velocities will increase by a factor of U .

Therefore, scaling up the number of particles of all the groups within the test or the source objects by factors of N_α and N_β respectively yields

$$\begin{aligned} V_G \left(\left\{ \vec{r}_j, m_j, N_\alpha N_{m_j}, \vec{u}_j \right\}_{j=1 \text{ to } J}, \left\{ \vec{S}_k, M_k, N_\beta N_{M_k}, \vec{v}_k \right\}_{k=1 \text{ to } K} \right) \\ = N_\alpha N_\beta V_G \left(\left\{ \vec{r}_j, m_j, N_{m_j}, \vec{u}_j \right\}_{j=1 \text{ to } J}, \left\{ \vec{S}_k, M_k, N_{M_k}, \vec{v}_k \right\}_{k=1 \text{ to } K} \right) \end{aligned}$$

Proof:

Equation A-1-4

$$\begin{aligned} V_G \left(\left\{ \vec{r}_j, m_j, N_\alpha N_{m_j}, \vec{u}_j \right\}_{j=1 \text{ to } J}, \left\{ \vec{S}_k, M_k, N_\beta N_{M_k}, \vec{v}_k \right\}_{k=1 \text{ to } K} \right) \\ = -\frac{G}{a} \left(\sum_{j=1}^J \sum_{k=1}^K N_\alpha N_{m_j} m_j N_\beta N_{M_k} M_k \gamma^2 (|\vec{v}_k - \vec{u}_j|) \left[\cos \left(\frac{b M_k m_j \gamma (|\vec{v}_k - \vec{u}_j|)}{r_{jk} \left(1 - \left(\frac{\hat{r}_{jk} \cdot (\vec{v}_k - \vec{u}_j)}{c} \right)^2 \right)^{0.5}} \right) - 1 \right] \right) = \\ = -N_\alpha N_\beta \left\{ \frac{G}{a} \left(\sum_{j=1}^J \sum_{k=1}^K N_{m_j} m_j N_{M_k} M_k \gamma^2 (|\vec{v}_k - \vec{u}_j|) \left[\cos \left(\frac{b M_k m_j \gamma (|\vec{v}_k - \vec{u}_j|)}{r_{jk} \left(1 - \left(\frac{\hat{r}_{jk} \cdot (\vec{v}_k - \vec{u}_j)}{c} \right)^2 \right)^{0.5}} \right) - 1 \right] \right) \right\} \end{aligned}$$

Thus,

$$\begin{aligned} V_G \left(\left\{ \vec{r}_j, m_j, N_\alpha N_{m_j}, \vec{u}_j \right\}_{j=1 \text{ to } J}, \left\{ \vec{S}_k, M_k, N_\beta N_{M_k}, \vec{v}_k \right\}_{k=1 \text{ to } K} \right) \\ = N_\alpha N_\beta V_G \left(\left\{ \vec{r}_j, m_j, N_{m_j}, \vec{u}_j \right\}_{j=1 \text{ to } J}, \left\{ \vec{S}_k, M_k, N_{M_k}, \vec{v}_k \right\}_{k=1 \text{ to } K} \right) \end{aligned}$$

Note that in contrast to the first theorem, the second theorem is valid at all distances, including the nuclear range where $r \leq a$.

References

- Amram, P., Mendes de Oliveira, C., Boulesteik, J., and Balkowski, C. 1998. *A&A.*, **330**, 881-893.
- Anderson, J.D., Laing, P.A., Lau, E.L., Liu, A.S., Nieto, M.M., and Turyshev, S.G. 1998. *Phys. Rev. Lett.*, **81**, 2858.
- Arp, H. 1987. *JApA.*, **8**, 241-255.
- Arp, H. 1989. *Quasars* (Cambridge: Cambridge University Press).
- Arp, H. 1996. *A&A.*, **316**, 57.
- Arp, H. 1997. *A&A.*, **319**, 33.
- Arp, H. 1997. *JApA.*, **18**, 393-406.
- Arp, H. 1998. *Seeing Red* (Montreal: Apeiron).
- Arp, H. C., Bi, H.G., Chu, Y., and Zhu, X. 1990. *A&A.*, **239**, 33.
- Arp, H., Russell, D. 2001. *ApJ.*, **549** (2), 802-819.
- Arp, H., Roscoe, D., and Fulton, C. 2005. *ArXiv:astro-ph/0501090v1*.
- Arp, H., Burbidge, E. M., Carosati, D. 2008. *A&A.*, manuscript no. NGC4410aa.
- Bajan, K., Flin, P, Godlowski, W., and Pervushin, V.P., 2006, eprint *arXiv:astro-ph/0606294*, to be published in *Physics of Particles and Nuclei*.
- Beaton, R. L., Athanassoula, E., Majewski, S. R., Guhathakurta, P., Skrutskie, M.F., Patterson, R.J., and Bureau, M. 2005. *American Astronomical Society Meeting 207*, #135.03; *Bulletin of the American Astronomical Society*, **37**, 1387.
- Begeman, K.G., Broeils, A.H., and Sanders, R.H. 1991. *MNRAS*, **249**, 523.
- Bekenstein, J. 2004. *Phys. Rev. D* **70**, 083509.
- Bell, M.B. 2002. *ArXiv:astro-ph/0211091v1*.
- Bell, M.B., McDiarmid, D. 2006. *ApJ.*, **648** (1), 140-147.
- Bender, R., Burnstein, D, and Faber, S.M. 1992. *ApJ.*, **399**, 462.
- Bender et al. 2005. *ApJ.*, **631**, 280.
- Bhattacharjee, P. and Sigl, G. 2000. *Phys. Rept.* **327**, 109-247, *arXiv: astro-ph/9811011*.
- Binney, J. and Tremaine, S. 2008. *Galactic Dynamics*, 2nd ed. (Princeton/Oxford: Princeton University Press).
- Bjorken, J.D. 1969, *Phys. Rev.*, **179**, 154.
- Blok, W.J.G de and McGaugh, S.S. 1998. *ApJ.*, **508**, 132.

- Burbidge, E.M. 1995. *A&A.*, **298**, L1.
- Burbidge, E.M., Beaver, E.A., Cohen, R.D., Junkkarinen, V.T., and Lyons, R.W. 1996. *AJ.*, **112**, 2533.
- Burbidge, E.M., and Burbidge, G. R. 1967, *ApJ.*, **148**, L107.
- Burbidge, E.M., Burbidge, G.R., Solomon, P.M., and Strittmatter, P.A. 1971. *ApJ.*, **170**, 233.
- Burbidge, G. 1968, *ApJ.*, **154**, L41.
- Burbidge, G. 1996, *A&A.*, **309**, 9.
- Burbidge, G., Hewitt, A., Narlikar, J. V., and Das Gupta, P. 1990, *ApJS*, **74**, 675.
- Burbidge, G., Hoyle, F., and Schneider, P. 1997. *A&A.*, **320**, 8.
- Burbidge, G., and Napier, W.M. 2001. *AJ.*, **121**:21-30.
- Buta, R. J., Byrd, G.G., and Freeman, T. 2003. *AJ.*, **125**: 634–666.
- Byrd, G., Freeman, T., Howard, S., and Buta, R.J. 2008. *AJ.*, **135**: 408–413.
- Carroll, B.W, Ostlie, D.A. 2007. *An Introduction to Modern Astrophysics* (San Francisco, CA: Pearson Addison-Wesley).
- Courtland, Rachel (July 23, 2008). “Stellar Nursery Found Near Milky Way’s Violent Heart.” *New Scientist*, <http://www.newscientist.com/article/dn14390>.
- Croasdale, M.R. 1989. *ApJ.*, **345**, 72-83.
- Devenish, R., and Cooper-Sarkar, A. 2004. *Deep Inelastic Scattering*, New York: Oxford University Press.
- Eckhardt, D. H. 1993. *Phys. Rev. D*, **48** (8), 3762.
- French, A.P. 1968. *Special Relativity*, MIT Introductory Physics Series.
- Fridman, A. M. and Gorkavyi, N. N. 1994. *Physics of Planetary Rings* (Springer Netherlands).
- Friedman, J.I. 1991. Nobel Lecture, *Rev. Mod. Phys.* **63**, 615.
- Gell-Mann, M. 1964. *Phys. Lett.* **8**, 214.
- Gillies, G.T. 1997. *Rep. Prog. Phys.* **60**, 151.
- Godłowski, W., Bajan, K., and Flin, P. 2006. *Astronomische Nachrichten*, **327** (1), 103-113.
- Guth, A.H. 1981. *Phys. Rev., D* **23**, 347.
- Guthrie, B.N.G., and Napier, W.M. 1990. *MNRAS*, **243**, 431-442.
- Guthrie, B.N.G., and Napier, W.M. 1991. *MNRAS*, **253**, 533-544.

- Hawkins, E., Maddox, S.J., Merrifield M.R. 2002. MNRAS, **336**, L13.
- Hedman, M.M., Burns, J.A, and Showalter, M.R. 2007. Icarus **188**, 89–107.
- Hoag, A.A. 1950. AJ., **55**, 170.
- Hoflich, P., Kumar, P., and Wheeler, J. C. 2004. *Cosmic Explosions in Three Dimension-: Asymmetries in Supernovae and Gamma-ray Bursts* (Cambridge: Cambridge University Press).
- Holba, A., Horvath, I., Lukacs, B., and Paal, G., 1992. Ap&SS, **198** (1), 111-120.
- Holba, A., Horvath, I., Lukacs, B., and Paal, G., 1994. Ap&SS, **222** (1), 65-83.
- Itzykson, C. and Zuber, J.B. 2005. *Quantum Field Theory* (Mineola, NY: Dover Publications, Inc).
- Lin C. C. and Shu, F.H. 1964. ApJ., **140**, 646.
- Lin C. C., Yuan C., & Shu F. H. 1969. ApJ, **155**, 721.
- Mayya, Y.D., Bizyaev, D., Romano, R., Garcia-Barreto, J. A., and Vorobyov, E.I. 2005. ApJ., **620**, L35-L38.
- McGaugh, S.S., and Blok, W.J.G. de 1998. ApJ., **499**, 66.
- Men'shchikov, A.B., Schertl, D., Tuthill, P.G., Weigelt, G., and Yungelson, L.R. 2002. A&A, **393**, 867-885.
- Milgrom, M. 1983. ApJ, **270**, 365; 371.
- Milgrom, M and Braun, E. 1988. ApJ., **334**, 130.
- Miner, E.D., Wessen, R.R, Cuzzi, J. N. 2007. *Planetary Ring Systems* (Springer Praxis).
- Napier, W. M. and Guthrie, B.N.G. 1997. JApA., **18**, 455-463.
- NASA HQ (December 12, 2007). "Saturn's Rings May be Old Timers." Press release. Retrieved 2007-12-27. Archive copy at the Internet Archive http://www.nasa.gov/mission_pages/cassini/media/cassini20071212.html.
- Navabi, A. A. and Riazi, N. 2003. JApA., **24**, 3-10.
- Nelson, A.H. 1988. MNRAS. **233**, 115.
- O'Connor, J.A., Redman, M.P., Holloway, A.J., Bryce, M., Lopez, J.A. and Meaburn, J. 2000. ApJ., **531**, 336-344.
- Paal, G., Horvath, I., and Lukacs, B. 1992. Ap&SS., **191**, 1, 107-124.
- Rubin, V.C. and Ford Jr., W.K. 1970. AJ., **159**, 379.
- Rubin, V.C., Ford Jr., W.K., and Thonard, R. 1980. AJ., **238**, 471.
- Rudnick, L., Brown, S., and Williams, L.R. 2007. AarXiv:astro-ph/0704.0908.
- Sandage, A. 1961. *Hubble Atlas of Galaxies* (Washington D.C.: Carnegie Institution of Washington).
- Sanders, R.H. 1996. ApJ., **473**, 117.

- Sanders, R.H., Verheijen, M.A.W. 1998. *ApJ.*, **503**, 97.
- Sarkar S. 2002. arXiv:hep-ph/0202013v2.
- Sepulveda, E. 1987. *Bulletin of the American Astronomical Society*, **19**, 689.
- Smolin, L. 2006. *The Trouble with Physics*, (Boston/New York: Houghton Mifflin Company).
- Smullin, S.J., Geraci, A.A., Weld, D. M., Chiaverini, J., Holmes S., and Kapitulnik, A. 2006, arXiv: hep-ph/0508204 v2.
- Tang, S.M. and Zhang, S.N. 2005, *ApJ*, **633** (1), 41-51 .
- Tift, W. G. 1973. *ApJ.*, **179**, 29-44.
- Tift, W.G. 1980. *ApJ.*, **236**, 70-74.
- Tift, W.G. 1995. *Ap&SS.*, **227**, 25-39.
- Tift , W.G. 1997. *JApA.*, **18**, 415-433.
- Tift, W.G. 1997. *ApJ.*, **485**, 465.
- Tift, W.G. 2003. *Ap&SS.*, **285** (2), 429-449.
- Trimble, V. Aschwanden, M.J., and Hansen, C.J. 2006. [arXiv:0705.1730](https://arxiv.org/abs/0705.1730).
- Tuthill, P.G., and Lloyd, J.P. 2007. *Science* 13, vol. **316**, no. 5822, p. 247.
- Vorontsov-Velyaminov, B.A. 1959. *Atlas and Catalogue of Bright Galaxies*, (Austin, TX: The University of Texas Press).
- Zhang, C.Y., and Kwok, S. 1998. *ApJS*, **117**, 341-359.
- Zwicky, F. 1933. *Helvetica Physica Acta*, **6**, 110.
- Zwicky, F. 1937. *ApJ*, **86**, 217.

Index

A

A ring, 14, 108, 111, 112, 116, 117, 119, 121
Abell 39, 10, 83, 84
age problem, 16, 172
Andromeda galaxy, 12, 88, 89, 90, 91, 102, 146
ansae, 12, 78, 88, 91
Anthe, 129, 130
arc, 74, 153, 154
Aristotle, 2
Arp
 Arp, Halton, 84, 188, 196, 197, 243
Asteroid belt, 19
asymptotic freedom, 198
Atlas, 117, 130, 245, 246

B

B Ring, 3, 126
bar
 galactic bar, 19, 93, 94, 95, 97, 99, 149, 151,
 152, 153, 155
barred spirals, 19, 155
barrier, 120, 160-166, 179, 210, 211, 213, 214,
 231
Big Bang, 4, 5, 16, 17, 18, 159, 160, 171, 172
Bjorken Scaling, 4, 15, 198, 199, 225, 226, 228-
 230, 232, 233, 236, 243
black holes, 4, 159
blueshift, 139, 142, 157
Bohr radius, 6, 179, 180
boxiness, 126, 175
Brahe,
 Brahe, Tycho 1
Brownian pressure, 148, 164

C

C ring, 111, 112, 114, 122
Calypso, 130
Cassini, 3, 14, 106, 108, 111-114, 116, 117, 120,
 122, 126, 127, 131
Cassini Division, 3, 106, 108, 111, 113, 116, 120,
 122, 126, 127, 131
central bulge, 81, 82, 88, 91, 99, 100, 153, 154
classical mechanics, 1
color

(of quarks) 198

Coma Cluster, 15, 188
companion galaxies, 3, 102
Copernican principle, 17, 170
coronal loops, 186
cosmic microwave background, 172, 188
cosmological constant, 17, 18, 159
cosmological principle, 17, 171
Coulomb
 force, potential energy, 5, 7, 20, 21, 23, 24,
 34, 35, 58, 59, 202, 206, 207, 211
critical density, 16, 172
cross section, 15, 199, 215, 217, 219, 220, 222,
 224, 225, 230, 231, 233, 235, 236, 238

D

D ring, 14, 111, 112, 114, 115, 117, 118, 126,
 251
D73 ringlet, 111, 112
Daphnis, 105, 130
dark energy, 5, 15, 17, 18, 137, 172
dark matter, 5, 15, 16, 18, 24, 137, 148, 172
deep inelastic scattering
 DIS, 4, 5, 15, 198, 199, 200, 203, 205, 208,
 210, 211, 221-226, 229, 230-236, 238
density wave, 14, 19, 84, 85, 117-119, 121, 133
Dione, 130
Diskiness, 175
Doppler effect
 Doppler shift, 196, 197

E

E ring, 105, 109
Eagle Nebula, 155
Earth, 4, 2, 17, 19, 36, 51, 52, 74, 164, 170, 182-
 184, 186, 196
Einstein
 Einstein, Albert, 2, 3, 17, 19, 21, 30, 58, 156,
 159, 176, 184, 188, 192
electromagnetic force, 7, 21, 36, 58, 176-179,
 202, 205, 208, 228, 229
electromagnetic force, 20, 24
electron, 8, 9, 20, 23, 24, 27-29, 36-38, 66, 67,
 138, 157, 158, 163, 164, 176-180, 185, 186,
 189-194, 196, 198, 200-235, 237

elementary particles, 198
elliptical galaxy, 19, 84, 100, 139, 148, 173-175
Enceladus, 105, 130
Encke Gap, 14, 119
Epimetheus, 130
equivalence principle, 2, 4, 156-158, 189
ESO 350-40, 13, 102
ESO 510-G13, 103
event horizon, 159, 176
expansion of spacetime, 160
expansion of the universe, 4, 15, 16, 159, 160,
170-172

F

F ring, 105, 108, 117, 126
Feynman, 198
filaments, 75, 77, 154
fine structure constant, 199
flatness problem, 16, 172
flocculent spiral, 9, 11, 91, 99
flyby anomaly, 19
folding
 (relativistic effect), 202, 209, 215
fragmentation
 (of stars or galaxies), 4, 163, 166
Freidman-Lemaitre-Robertson-Walker metric,
16, 172

G

galactic bulge, 50, 99, 151
galactic core, 72, 81, 133, 150, 151, 172, 174
galactic disk,
 galaxy disk, 52, 53, 67, 72, 81, 83, 85, 86, 93,
 95, 96, 100, 133, 137, 146, 151, 160, 164,
 173, 174, 192
galactic group, 160, 166, 168
galactic halo, *see halo*
galactic lock out, 160, 163
galactic rings, 20, 24, 29, 161
galactic void
 cosmic void, 15, 17, 50, 91, 92, 159, 165
galactic wind, 15, 72, 119, 133, 174
galaxy, 5, 8, 9, 13-19, 24-26, 28, 29, 43, 50-53,
60, 64, 65, 69, 71, 72, 74, 78, 84, 85, 91, 99,
100, 102, 107, 119, 126, 131, 133, 135-139,
146, 148, 154, 155, 160, 165-175, 180, 188,
189, 195, 196, 239

galaxy rotation curve,
 velocity curve, 5, 14, 15, 132, 133, 137-139,
 142, 143, 145, 146, 148, 174
Galileo
 Galilei, Galileo, 1, 2, 5, 13, 104
gaps, 19, 24, 105, 111, 114, 115, 117, 120, 121,
230, 231, 232
gas planets, 19, 104, 106, 181, 183
general theory of relativity
 general relativity, 2, 4, 5, 15-19, 27, 30, 51,
 106, 156-159, 173, 176, 188, 189
geodesics, 158
globular clusters, 16
gluon, 198, 199
grand design spiral, 91
gravitation
 gravitational force, 1, 3-9, 13, 15-23, 26, 27,
 31, 34, 36, 37, 41, 44, 52, 53, 56, 59, 65,
 66, 70, 79, 86, 104, 106, 108, 118, 119,
 126, 133, 137, 148, 156, 157, 161, 164,
 166, 172, 176, 177, 181, 183, 184, 185,
 189, 193, 194, 196, 197, 200, 205
gravitational constant G , 3, 8, 18, 28, 36
gravitational ionization, *see ionization*
gravitational lensing, 52, 157
gravitational shepherding, 105
Guth's inflation theory, *see inflation*

H

hadron, 198, 200
halo
 galactic halo, 53, 54, 60, 138, 173, 174
Heisenberg's uncertainty principle, *see*
 uncertainty principle
Helene, 130
Hoag's Object, 10, 84
horizon problem, 16, 172
hourglass nebula, 9, 82, 83, 186
Hubble classification, 71, 84
Hubble sequence, 84
Hubble's law, 196
Hubble space telescope, 10, 96
hydrogen atom, 7, 28, 38, 176, 177, 179, 190-
192, 194
hyperfine structure, 191
Hyperion, 130

I
 Iapetus, 130
 impact parameter, 200-203, 205, 208, 210, 216, 217, 219, 222, 224, 226, 229, 230
 inertial frame, 3, 7, 51, 52, 56, 57-64, 157, 158, 200, 201, 211, 220, 240
 infinities, 17, 40, 159
 inflation, 5, 15-18, 160, 172
 inner core
 (Earth), 184
 ionization, 15, 176, 177, 179, 180, 185, 186
 irregular galaxies, 188

J
 Janus, 130
 Jupiter, 19, 104, 105, 131, 183

K
 Kepler
 Kepler, Johannes, 1
 Kepler's laws of planetary motion, 1, 2, 42, 110, 120, 127, 128, 130
 Keplerian dynamics, 2, 15, 108
 Keplerian orbit, 120
 Kuiper belt, 19
 Kuiper cliff, 19

L
 law of conservation of angular momentum, 86
 law of conservation of energy, 190
 leading spiral arms, 11
 lenticular galaxy, 3, 100
 lepton, 8, 199, 200
 Lin
 Lin, C. C., 84, 245
 Lindblad
 Lindblad, Bertil, 84, 155
 Lindblad resonance, 155
 Lloyd
 Lloyd, James, P., 100, 101, 246
 Lorentz resonances, 19, 104
 Lorentz transformations, 58, 59, 63

M
 M81, 10, 96

magnetic fields, 15, 19, 21, 78, 180, 184, 185, 186
 Mars, 183
 maximal zonal range, 40, 160
 Maxwell gap, 114
 Mercury, 19, 183
 meteoroid bombardment, 105
 Methone, 130
 Milky Way Galaxy, 78, 149, 155
 Mimas, 115, 117, 130
 missing mass problem, 15, 137
 molecular clouds, 153, 154
 MOND
 Modified Newtonian Dynamics, 138
 Moon, 2, 74, 182
 morphology, 3, 4, 10, 12, 19, 50-53, 58, 63, 67, 69-71, 78-86, 88, 90-93, 95-97, 100, 102, 106, 109, 110, 112, 126, 131, 137, 143, 175, 182, 186, 239, 241
 MWC 922, 101
 MyCn 18, 9, 80, 82, 83, 86, 187

N
 NASA, 9, 10, 11, 12, 13, 14, 80, 82, 83, 90, 96, 98, 100-103, 105, 106, 111, 113-117, 119, 125, 155, 187, 245
 nearly Newtonian environment, 42, 44
 nebula, 9, 19, 50, 69, 71, 78, 79, 81, 84, 91, 131, 154, 239
 Neptune, 19, 104, 105, 131, 183
 neutron star, 52, 164
 neutron, 8, 20, 23, 24, 27, 29, 36-38, 157, 176-178, 180, 185, 198
 Newton
 Newton, Isaac, 1-7, 11, 13, 15, 16, 18-25, 27, 30, 31, 36, 44, 99, 104, 106, 108, 119, 137, 138, 156, 176, 178, 205
 Newton's laws
 law of universal gravitation, 1, 3, 7, 19, 36
 laws of motion, 1, 3, 19
 NGC 2859, 84
 NGC 3081, 84
 NGC 4622, 10, 11, 97, 100
 NGC 488, 11, 99
 NGC 6028, 84
 NGC 6302, 79, 80
 NGC-2346, 79, 80

no-hair theorem, 30
nova, 4, 15, 19, 165, 166
nucleon, 4, 5, 20, 23, 24, 34, 35, 38, 158, 189,
199, 200, 208, 209, 212, 216
nucleosynthesis, 172
nucleus
Andromeda's nucleus, 12, 88
atom nucleus, 5, 8, 24, 29, 34, 35, 47, 96,
158, 189, 190, 191, 209
galaxy nucleus, 146

O

Occam's Razor, 1, 4, 6, 7, 27, 59
orbital resonances, 19, 24, 104, 105
Orion Nebula, 154
oscillation range, *see zonal range*
outer core
(Earth), 184, 185, 186

P

Pallene, 130
Pan, 105, 108, 117, 130
Pandora, 108, 117, 130
particle accelerator, 29, 202, 209, 210, 220
partons, 198
Philosophiae Naturalis Principia Mathematica, 2
photosphere, 186
Pillars of Creation, 154, 155
Pioneer 10, 19
Pioneer 11, 19
Pioneer anomaly, 19
Planck
Planck's constant, 18, 190
planetary magnetic fields, 19
planetary ring system
planetary rings, 4, 5, 13, 15, 19, 24, 26, 29,
40, 42, 50, 67, 103-106, 108-112, 118, 120,
131, 181-183, 245
planet
planetary system, 2, 4, 8, 9, 15, 19, 26, 28,
29, 42, 43, 64, 65, 131, 160, 180-184, 239
plasma, 158, 176, 180
plateau, 114
polar ring galaxy, 103
Polydeuces, 130
positron, 9, 29, 158
principle of Galilean relativity, 2, 3

Prometheus, 117, 130
proton, 5, 8, 20, 23, 24, 27, 34, 36-38, 67, 157,
158, 176-178, 180, 185, 186, 189, 190, 198
protostars, 149

Q

quantum chromodynamics
QCD, 198, 199
quantum mechanics, 17, 20, 157, 205
quark, 29, 198, 199
quark confinement, 29, 198
quark-parton model
QPM, 200
quasars, 196, 197, 243

R

Red Rectangle, 100, 101
Red Square, 100, 101
redshift periodicity
redshift quantization, 15, 188, 189, 191, 195
rejection zones, 50, 67, 78
relativistic precession of apsides, 157
renormalization, 17, 198
Rhea, 130
ring system, *see planetary ring system*
ringlets, 20, 24, 105, 111, 114, 115, 118, 131
Roche limit, 104, 108, 182

S

satellite, 9, 19, 24, 43, 67, 68, 80, 104-108, 110,
117, 127-129, 131, 181-183, 239
Saturn, 3, 5, 13, 14, 19, 24, 53, 67, 103-113,
117-120, 122, 123, 125-131, 183, 245
Saturn's ring system, 13, 111, 118
scaling theorem, *see UG scaling theorem*
sea of quarks, 198, 200
shell structure, 8, 24
shepherd satellite,
shepherd moon, 19, 105
Shu
Shu, Frank, 84, 245
singlet, 191
singularity, 16-18, 40, 157, 159, 171, 172
Smolin
Smolin, Lee, 18, 246
solar corona, 4, 186

Solar System, 2, 5, 19, 42, 74, 79, 105, 106, 131, 137, 181, 182, 188
 Southern Crab Nebula, 80, 81, 82
 special theory of relativity
 special relativity, 3, 4, 21, 52, 58, 59, 65, 126, 156, 188, 189, 196, 200, 201, 208, 244
 spin
 (particle spin), 20, 21, 30, 191, 199, 211
 spiral arms, 58, 81, 84, 86, 88, 91, 93, 96, 99, 189
 spiral bending waves, 14, 117, 121
 spiral density waves, 14, 117, 121
 spiral galaxy, 10, 11, 19, 97, 133, 173, 194
 spokes, 109, 123-126
 standard model, 4, 5, 7, 18, 29, 157, 171, 196, 200
 star formation, 13, 15, 19, 74, 75, 78, 84, 100, 133, 148, 149, 163, 168
 star
 stellar system, 5, 9, 15, 16, 19, 28, 29, 43, 54, 59, 64, 65, 74, 75, 77, 78, 91, 137, 148-154, 156, 157, 161, 164-167, 173, 174, 180, 239
 stellar core, 163, 165, 166
 stellar wind
 solar wind, 19, 166
 strong interaction
 strong force, 3, 4, 7, 8, 15, 20, 21, 34, 157, 198
 structure problem, 17
 superclusters, 160, 166, 168, 170, 172
 superheavy particles
 SHP, 3, 4, 9, 28-30, 36, 40-42, 44, 47, 50-55, 58-61, 64-91, 93-97, 99-101, 103, 106-113, 117-121, 123, 126-129, 131, 133, 134, 136-138, 141, 143, 148, 150-154, 157-170, 172, 173-191, 194, 195, 197, 239
 supernova, 15, 19, 165, 166
 supernova 1987A, 102

T

Teleso, 130
 terrestrial planet, 15, 19, 181, 182, 183
 Tethys, 130
 tidal forces, 52
 Tiff
 Tiff, William, G., 188, 246

time dilation, 21, 157
 Titan, 130
 trailing spiral arms, 88, 91, 97
 triplet, 191
 Tuthill, Peter, G., 100, 101, 246

U

UG postulates, 21, 22, 23, 24, 28, 29, 59, 157, 165, 200
 UG Postulate I, 21
 UG Postulate II, 22, 59
 UG Postulate III, 23
 UG Postulate IV, 28, 64
 UG scaling theorem, 199, 239, 241
 UGC 9562, 84
 uncertainty principle
 Heisenberg's uncertainty principle, 7, 205, 206, 207, 208, 225, 228, 235, 236
 unfolding
 (relativistic effect), 4, 209
 Unified Gravitation
 UG, 3, 4, 8, 9, 20, 21, 104, 156, 159, 171, 183, 184, 196, 225
 Uranus, 19, 104-107, 118, 131, 182, 183
 Uranian ring system, 105

V

Venus, 183
 Virgo cluster, 188
 void, *see galactic void*
 Voyager, 105, 111, 123, 125, 126, 127

W

weak fall-off
 of a DIS cross section 15, 198, 215, 220, 224

Z

zonal range,
 zonal oscillation range, 26, 35, 40, 41, 43, 44, 45, 48, 65, 67, 103, 107, 127, 129, 138, 159, 160, 168, 169, 177, 178, 181-185, 190
 zones of attraction, 31, 159
 zones of repulsion, 31, 159
 Zwicky,
 Zwicky, Fritz, 15, 246